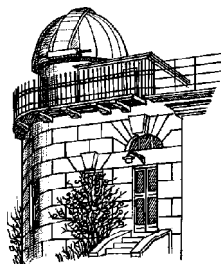


ISSN 1810-4215

ODESSA ASTRONOMICAL PUBLICATIONS

Volume 28 Issue 2
(2015)



Odessa
«AstroPrint»

FOREWORD

This issue of the “Odessa Astronomical Publications” (vol. 28, issue 2) includes articles that were presented at the 5-th Gamow Memorial International Conference dedicated to the 111-th birth anniversary of George Gamow “Astrophysics and Cosmology after Gamow: progress and perspectives” and the 15-th Odessa International Astronomical Gamow Conference-School “Astronomy and beyond: Astrophysics, Cosmology, Cosmophysics, Astroparticle Physics, Radioastronomy and Astrobiology”. The Conference and the Gamow’s School were also devoted to the 150th anniversary of Odessa National University, 50 years of discovery of CMB radiation, 110 years of special relativity and light quanta and 100 years of general relativity.

The Conference was organized by Odessa I.I.Mechnikov National University (Astronomical Observatory and Astronomy and Theoretical Physics Departments), Radio-Astronomical Institute of NASU of Ukraine, Ukrainian Astronomical Association, Euro-Asian Astronomical Society, Odessa Astronomical Society, South Scientific Centre of NAS of Ukraine.

Co-chairs of SOC: G.S.Bisnovaty-Kogan (SRI RAS, Moscow, Russia) and V.M.Shulga (IRA NASU, Kharkov, Ukraine). Vice-chairs: A.I.Zhuk (AO ONU, Odessa, Ukraine) and M.I.Ryabov (IRA NASU, Odessa, Ukraine).

The scientific program included the following section: “Cosmology, gravitation, astroparticle physics and high energy physics” (33 reports), “Astrophysics” (27 reports) (subsection “Virtual Observatory and Intensive data” – 11 reports), “Radioastronomy” (13 reports), “Sun, Solar activity and Astrobiology” (14 reports) and “Solar system” (15 reports).

About 120 scientists from Ukraine, Russia, Belarus, Italy, Poland, France, Switzerland, Egypt, Kazakhstan, Azerbaijan, Czech Republic, Georgia and USA took part in the Gamow conference. During the conference it was presented 20 plenary and 113 section reports!

Vice-chairs of SOC A.I.Zhuk and M.I.Ryabov



CONTENTS

Foreword	100
Contents	101
COSMOLOGY, GRAVITATION, ASTROPARTICLE PHYSICS, HIGH ENERGY PHYSICS	
ASPECTS OF STRING PHENOMENOLOGY IN PARTICLE PHYSICS AND COSMOLOGY	
Antoniadis I.	105
DISCRETE COSMOLOGY APPLICATION CONCERNING DARK MATTER HALOS	
Brilenkov R.D.	113
THE DOMINANCE OF DARK ENERGY LEADS TO REDUCTION OF THE ENTROPY OF GALAXIES FLOW AND ENTROPY OF THE UNIVERSE	
Bukalov A.V.	114
THE MODEL FOR FINAL STAGE OF GRAVITATIONAL COLLAPSE MASSLESS SCALAR FIELD	
Gladush V.D., Mironin D.V.	116
FIVE DIMENSIONAL BOOSTS AND ELECTROMAGNETIC FIELD IN KALUZA-KLEIN THEORY	
Gladush V.D., Al-Shawaf Nadim	121
STABILITY OF STELLAR SYSTEMS ORBITING SGR A*	
Kahil Magd E.	126
PERTURBATIONS OF FRIEDMAN-LEMAITRE-ROBERTSON-WALKER SPACETIMES IN GEROCH-HELD-PENROSE FORMALISM	
Novák J.	132
THE DETERMINATION OF THE MORPHOLOGICAL TYPES OF GALAXY CLUSTERS USING CLUSTER CARTOGRAPHY	
Panko E.A., Emelyanov S.I.	135
BIG RIP AND OTHER SINGULARITIES IN ISOTROPIC HOMOGENEOUS COSMOLOGICAL MODELS WITH ARBITRARY EQUATION OF STATE	
Parnovsky S.L.	137
ON THE MECHANISM OF THE FORMATION OF MAGNETOHYDRODYNAMIC VORTICES IN THE SOLAR PLASMA	
Pashitskii E.A.	141
THE PROPERTIS OF TIDAL FORCES IN THE KERR METRIC	
Rasulova A.M.	147
X-RAY SPECTRAL PROPERTIES OF THE ISOLATED AGNs: NGC 1050, NGC 2989, ESO 317-038, ESO 438-009	
Vavilova I.B., Vasylenko A.A., Babyk Iu.V., Pulatova N.G.	150
ASTROPHYSICS	
THE KINEMATICS PARAMETERS OF THE GALAXY USING DATA OF MODERN ASTROMETRIC CATALOGUES	
Akhmetov V.S., Fedorov P.N., Velichko A.B., Shulga V.M.	154
"ASYMPTOTIC PARABOLA" FITS FOR SMOOTHING GENERALLY ASYMMETRIC LIGHT CURVES	
Andrych K.D., Andronov I.L., Chinarova L.L., Marsakova V.I.	158
A MODIFICATION OF GAUSS' METHOD FOR PRELIMINARY DETERMINATION OF A CELESTIAL BODY'S ORBIT	
Bazyey A.A.	161
RESULTS OF DOUBLE STARS OBSERVATIONS AT NIKOLAEV OBSERVATORY	
Bodryagin D.V., Maigurova N.V.	163

INVESTIGATION OF DIFFUSE INTERSTELLAR BANDS OF ORGANIC MOLECULES IN THE SPECTRA OF CEPHEID STARS Kashuba S.V., Andrievsky S.M., Chehonadskih F.A., Korotin S.A., Kovtyukh V.V., Luck R.E.....	166
NUCLEAR MAGICS AT MAGNETOROTATIONAL SUPERNOVA EXPLOSION Kondratyev V.N., Korovina Yu.V., Mishenina T.V.	168
THREE-DIMENSIONAL NUMERICAL HYDRODYNAMICAL SIMULATION OF LOW/HARD AND HIGH/SOFT STATES IN ACCRETION DISCS OF MICROQUASARS AND QUASARS ON BASE OF UNDEFINED PRECESSION Nazarenko V.V., Nazarenko S.V.	171
THE RELATIVE WAVELENGTH INDEPENDENCE OF IR LAGS IN ACTIVE GALACTIC NUCLEI: IMPLICATIONS FOR THE DISTRIBUTION OF THE HOT DUST Oknyansky V.L., Gaskell C.M., Shimanovskaya E.V.	175
REVISION OF THE PHENOMENOLOGICAL CHARACTERISTICS OF THE ALGOL-TYPE STARS USING THE NAV ALGORITHM Tkachenko M.G., Andronov I.L., Chinarova L.L.	181
PHOTOMETRY AND MODULATION OF LIGHT CURVES IN THE BLAZHKO STAR V365 HER Udovichenko S.N.	186
Subsection “VIRTUAL OBSERVATORIES AND INTENSIVE DATA”	
COMPARISON OF ZERO ZONE CATALOGUES OF THE FON PROGRAM BASED ON THE KYIV AND KITAB OBSERVATIONS Andruk V.M., Relke H., Protsyuk Yu.I., Muminov M.M., Ehgamberdiev Sh.A., Yuldoshev Q.X., Golovnia V.V.	188
CATALOG OF POSITIONS AND B MAGNITUDES OF STARS IN THE CIRCUMPOLAR REGION OF NORTHEN SKY SURVEY (FON) PROJECT Andruk V.M., Pakuliak L.K., Golovnia V.V., Ivanov G.A., Yizhakevych O.M., Protsyuk Yu.I., Shatokhina S.V.	192
CATALOGUES OF THE FAINT OBJECTS IN THE AREAS WITH GAMMA-RAY BURSTS Golovnia V.V., Protsyuk Yu.I., Andruk V.M., Vavilova I.B., Pakuliak L.K., Kulyk I.V., Romanyuk Ya.O., Baransky O.R.	196
RESEARCH OF THE LONG-TERM BEHAVIOUR OF THE PLEIADES BY USING OF PHOTOGRAPHIC PLATES FROM UKRVO DIGITAL ARCHIVE AND BALDONE OBSERVATORY Kazantseva L.V., Andruk V.M., Shatokhina S.V., Protsyuk Yu.I., Eglitis I., Eglite M.	198
CROSS-MATCHING OF VERY LARGE CATALOGS Martynov M.V., Bodryagin D.V.	200
DETERMINATION OF PROPER MOTIONS OF CIRCUMPOLAR STARS BY USING IMAGES FROM UKRVO PLATE ARCHIVES Protsyuk Yu., Andruk V., Mazhaev A., Kovylianska O., Protsyuk S., Golovnya V.	202
DATA PROCESSING OF PLATES CONTAINING IMAGES OF URANUS AND NEPTUNE FROM UKRVO DIGITAL ARCHIVE: STRUCTURE, QUALITY ANALYSIS Protsyuk Yu., Yizhakevych O., Kovylianska O., Protsyuk S., Andruk V., Kashuba S., Kazantseva L.	204
CREATION OF LARGE CATALOGUES BY USING OF VIRTUAL OBSERVATORIES Protsyuk Yu.I., Kovalchuk O.M.	207
THE COMPILED CATALOGUE OF PHOTOELECTRIC UBVR STELLAR MAGNITUDES IN THE TYCHO2 SYSTEM Relke E., Protsyuk Yu.I., Andruk V.M.	211
CATALOG OF ASTRONOMICAL POSITIONS OF SATURN’S MOONS OBTAINED BY PHOTOGRAPHIC OBSERVATIONS AT THE MAO NASU IN 1961-1991 Yizhakevych O.M., Andruk V.M., Pakuliak L.K.	213

RADIOASTRONOMY

THE STUDY OF EXTRAGALACTIC SOURCES 3C 446 AND 3C 345 WITH USING THE SINGULAR SPECTRUM AND WAVELET ANALYSIS Donskykh G.I., Ryabov M.I., Sukharev A.L., Aller M.F.	217
MONITORING THE COMMUNICATION CHANNEL FROM PUSCHSHINO TO MOSCOW IN THE PROJECT OF SPACE RADIO TELESCOPE "RADIOASTRON" Dumsky D.V., Isaev E.A., Samodurov V.A., Isaev K.A.	222
SECULAR DECREASE THE FLUX OF SUPERNOVA REMNANT CAS A ON MONITORING RESULTS TO RADIOTELESCOPE "URAN-4" IRA NASU Gorbynov A.A., Ryabov M.I., Panishko S.K.	224
LIGHT CURVE TYPES OF CLASSIC T TAURI STARS Ismailov N.Z., Adygezalzaade H.N.	227
HE I 5876 LINE STRUCTURE IN THE SPECTRA OF IL CEP A Ismailov N.Z., Khalilov O.V., Bahaddinova G.R.	231
SEASONAL VARIATIONS OF THE IONOSPHERE SCINTILLATIONS PARAMETERS OBTAINED FROM THE LONG OBSERVATIONS OF THE POWER COSMIC RADIO SOURCES AT THE DECAMETER WAVE RANGE Lytvynenko O.A., Panishko S.K.	235
LUMINOSITY-LINEAR SIZE RELATION FOR GALAXIES AND QUASARS WITH STEEP RADIO SPECTRUM Miroshnichenko A.P.	238
THE DAILY 110 MHZ SKY SURVEY (BSA FIAN): ON-LINE DATABASE, SCIENCE AIMS AND FIRST RESULTS OF DATA PROCESSING Samodurov V.A., Rodin A.E., Kitaeva M.A., Isaev E.A., Dumsky D.V., Churakov D.D., Manzyuk M.O.	242
HIGH-FREQUENCY CUTOFF IN TYPE III BURSTS Stanislavsky A.A., Konovalenko A.A., Volvach Ya.S., Koval A.A.	246
ON THE E/P-COSMIC RAYS AS MEDIATORS OF VISCOUS FORCES THAT CREATE SHOCK AND VORTEX STRUCTURES IN THE RADIO GALAXIES Tsvyk N.O.	248
DECAMETER PULSARS AND TRANSIENTS SURVEY OF THE NORTHERN SKY. STATUS, FIRST RESULTS, MULTIPARAMETRIC PIPELINE FOR CANDIDATE SELECTION Zakharenko V.V., Kravtsov I.P., Vasylieva I.Y., Mykhailova S.S., Ulyanov O.M., Shevtsova A.I., Skoryk A.O., Zarka P., Konovalenko O.O.	252
SUN, SOLAR ACTIVITY AND ASTROBIOLOGY	
EVALUATION OF CORONAL SHOCK WAVE VELOCITIES FROM THE II TYPE RADIO BURSTS PARAMETERS Galanin V.V., Isaeva E.A., Kravetz R.O.	256
CONNECTION BETWEEN THE CME VELOCITIES AND DECAMETER RADIO BURSTS PARAMETERS FROM URAN-4 OBSERVATIONS Galanin V.V., Isaeva E.A., Kravetz R.O.	259
THE REACTION OF PHOSPHORUS-CONTAINING INTRACELLULAR INCLUSIONS TO SPACE WEATHER CHANGES Gromozova E.N., Kachur T.L., Voychuk S.I., Kharchuk M.S.	261
LONGTERM CHANGES OF SOLAR ACTIVITY ASYMMETRY Leiko U.M.	264
PROBLEM OF MISTAKES IN DATABASES, PROCESSING AND INTERPRETATION OF OBSERVATIONS OF THE SUN. I. Lozitska N. I.	266

SIMULTANEOUS MAGNETIC FIELD MEASUREMENTS IN SUNSPOTS USING SPECTRAL LINES WITH DIFFERENT LANDE FACTORS Osipov S.N., Lozitsky V.G.....	268
PECULIARITIES OF A GROUP RESPONSE OF CARDIOVASCULAR SYSTEM OF VOLUNTEERS AT DIFFERENT LATITUDES TO CHANGES OF SPACE WEATHER PARAMETERS Parshina S.S., Samsonov S.N., Manykina V.I., Afanasyeva T.N., Vishnevsky V.V., Petrova P.G., Petrova V.D., Strekalovskaya A.A., Tokayeva L.K., Kaplanova T.I., Potapova M.V.	270
SUN'S POLAR MAGNETIC FIELD REVERSALS IN SOLAR CYCLE 24 Pishkalo M.I., Leiko U.M.....	272
SOLAR SYSTEM	
THE PHYSICAL PARAMETERS OF THE GAS AND DUST IN COMETARY ATMOSPHERES Churyumov K.I., Ponomarenko V.O., Kleschonok V.V.	274
STUDY OF QUASI-PERIODIC VARIATIONS IN DRAG OF ARTIFICIAL SATELLITE DURING 23–24 SOLAR CYCLES Komendant V.H., Ryabov M.I., Sukharev A.L.	277
THE STUDY OF INDICATRICES OF SPACE OBJECT COATINGS IN A CONTROLLED LABORATORY ENVIRONMENT Koshkin N., Burlak N., <u>Petrov M.</u> , Strakhova S.	281
RESEARCHES OF LONG-TERM VARIATIONS IN URANUS AND NEPTUNE SPECTRA Kuznyetsova Yu., Vidmachenko A., Matsiaka O., Shliakhetskaya Y., Yushkin M., Krushevskaya V.	285
IDENTIFICATION OF EMISSION LINES IN A METEOR SPECTRUM OBTAINED ON AUGUST 2, 2011 Mozgova A.M., Borovicka J., Spurny P., Churyumov K.I.	289
THE RESULTS OF OBSERVATIONS OF MUTUAL PHENOMENA OF THE GALILEAN SATELLITES OF JUPITER IN 2009 AND 2015 IN NIKOLAEV ASTRONOMICAL OBSERVATORY Pomazan A., Maigurova N., Kryuchkovskiy V.....	292
SYNCHRONIZATION OF TERRESTRIAL PROCESSES WITH FREQUENCIES OF THE EARTH-MOON-SUN SYSTEM Sidorenkov N.S.....	295
EFFECT OF NON-SPHERICITY OF GRAVITATIONAL FIELD OF THE ASTEROID ON THE ITS SATELLITES ORBITS EVOLUTION Troianskyi V.V.	299

COSMOLOGY, COSMOMICROPHYSICS AND GRAVITATION

ASPECTS OF STRING PHENOMENOLOGY IN PARTICLE PHYSICS AND COSMOLOGY

I. Antoniadis^{1,2}

¹ LPTHE, UMR CNRS 7589 Sorbonne Universités, UPMC Paris 6, F-75005 Paris

² A.Einstein Center, Institute for Theoretical Physics, Bern U, Sidlerstrasse 5, CH-3012 Bern

ABSTRACT. We discuss possible connections between several scales in particle physics and cosmology, such as the electroweak, inflation, dark energy and Planck scales. We then describe the phenomenology of a model of supersymmetry breaking in the presence of a tiny (tunable) positive cosmological constant. The model is coupled to the MSSM, leading to calculable soft supersymmetry breaking masses and a distinct low energy phenomenology that allows to differentiate it from other models of supersymmetry breaking and mediation mechanisms.

Keywords: String theory, extra dimensions, supersymmetry, scale hierarchies, inflation, de Sitter space

1. Introduction

If String Theory is a fundamental theory of Nature and not just a tool for studying systems with strongly coupled dynamics, it should be able to describe at the same time particle physics and cosmology, which are phenomena that involve very different scales from the microscopic four-dimensional (4d) quantum gravity length of 10^{-33} cm to large macroscopic distances of the size of the observable Universe $\sim 10^{28}$ cm spanned a region of about 60 orders of magnitude. In particular, besides the 4d Planck mass, there are three very different scales with very different physics corresponding to the electroweak, dark energy and inflation. These scales might be related via the scale of the underlying fundamental theory, such as string theory, or they might be independent in the sense that their origin could be based on different and independent dynamics. An example of the former constrained and more predictive possibility is provided by TeV strings with a fundamental scale at low energies due for instance to large extra dimensions transverse to a four-dimensional braneworld forming our Universe [1]. In this case, the 4d Planck mass is emergent from the fundamental string scale and inflation should also happen around the same scale [2]. We will first review this possibility, focussing on its compatibility with cosmological observations.

We will then adopt a second more conservative approach, assuming that all three scales have an independent dynamical origin. Moreover, we will assume the presence of low energy supersymmetry that allows for an elegant solution of the mass hierarchy problem, a unification of fundamental forces as indicated by low energy data and a natural dark matter candidate due to an unbroken R-parity. The assumption of independent scales implies that supersymmetry breaking should be realized in a metastable de Sitter vacuum with an infinitesimally small (tunable) cosmological constant independent of the supersymmetry breaking scale that should be in the TeV region. In a recent work [3], we studied a simple $N = 1$ supergravity model having this property and motivated by string theory. Besides the gravity multiplet, the minimal field content consists of a chiral multiplet with a shift symmetry promoted to a gauged R-symmetry using a vector multiplet. In the string theory context, the chiral multiplet can be identified with the string dilaton (or an appropriate compactification modulus) and the shift symmetry associated to the gauge invariance of a two-index antisymmetric tensor that can be dualized to a (pseudo)scalar. The shift symmetry fixes the form of the superpotential and the gauging allows for the presence of a Fayet-Iliopoulos (FI) term, leading to a supergravity action with two independent parameters that can be tuned so that the scalar potential possesses a metastable de Sitter minimum with a tiny vacuum energy (essentially the relative strength between the F- and D-term contributions). A third parameter fixes the Vacuum Expectation Value (VEV) of the string dilaton at the desired (phenomenologically) weak coupling regime. An important consistency constraint of our model is anomaly cancellation which has been studied in [5] and implies the existence of additional charged fields under the gauged R-symmetry.

In a more recent work [6], we analyzed a small variation of this model which is manifestly anomaly free without additional charged fields and allows to couple in a straight forward way a visible sector containing the minimal supersymmetric extension of the Standard Model (MSSM) and studied the mediation of super-

symmetry breaking and its phenomenological consequences. It turns out that an additional ‘hidden sector’ field z is needed to be added for the matter soft scalar masses to be non-tachyonic; although this field participates in the supersymmetry breaking and is similar to the so-called Polonyi field, it does not modify the main properties of the metastable de Sitter (dS) vacuum. All soft scalar masses, as well as trilinear A-terms, are generated at the tree level and are universal under the assumption that matter kinetic terms are independent of the ‘Polonyi’ field, since matter fields are neutral under the shift symmetry and supersymmetry breaking is driven by a combination of the $U(1)$ D-term and the dilaton and z -field F-term. Alternatively, a way to avoid the tachyonic scalar masses without adding the extra field z is to modify the matter kinetic terms by a dilaton dependent factor.

A main difference of the second analysis from the first work is that we use a field representation in which the gauged shift symmetry corresponds to an ordinary $U(1)$ and not an R-symmetry. The two representations differ by a Kähler transformation that leaves the classical supergravity action invariant. However, at the quantum level, there is a Green-Schwarz term generated that amounts an extra dilaton dependent contribution to the gauge kinetic terms needed to cancel the anomalies of the R-symmetry. This creates an apparent puzzle with the gaugino masses that vanish in the first representation but not in the latter. The resolution to the puzzle is based to the so called anomaly mediation contributions [7, 8] that explain precisely the above apparent discrepancy. It turns out that gaugino masses are generated at the quantum level and are thus suppressed compared to the scalar masses (and A-terms).

2. Effective Planck mass and the inflation scale

Low scale gravity with large extra dimensions is actually a particular case of a more general framework, where the UV cutoff is lower than the Planck scale due to the existence of a large number of particle species coupled to gravity [9]. Indeed, it was shown that the effective UV cutoff M_{UV} is given by

$$M_{UV}^2 = M_P^2/N, \quad (1)$$

where the counting of independent species N takes into account all particles which are not broad resonances, having a width less than their mass. For instance, in braneworld gravity with n large extra dimensions of average size R , the particle species are the Kaluza-Klein (KK) excitations of the graviton (and other possible bulk modes), whose number at a given energy scale E_* is given by

$$N \simeq R^n E_*^n. \quad (2)$$

Here, we work out the consequences of this scale dependence of the strength of gravity for inferring various quantities during inflation [2], which we take to be driven by a single field for economy of discussion and because the data doesn’t compel us to consider otherwise [10]. As is to be expected, all dimensionless observables such as the amplitude and spectral properties of the perturbations are unaffected by the changing strength of gravity at inflationary energies. However, when one tries to *infer* an absolute energy scale for inflation, one finds that it is undetermined commensurate with (1) up to the unknown spectrum of universally coupled species between laboratory scales and the inflationary scale, the details of which we elaborate upon in the following.

According to the inflationary paradigm, the primordial perturbations observed in the CMB were created at horizon crossing during the quasi de Sitter (dS) phase of early accelerated expansion sourced by the inflaton field. Therefore all quantities that enter calculations of primordial correlation functions (which we subsequently relate to observables in the CMB) refer to quantities at the scale at which inflation occurred. We denote all quantities measured at the scale of inflation with a starred subscript. The dominant contribution to the temperature anisotropies comes from adiabatic perturbations¹ sourced by the comoving curvature perturbation \mathcal{R} , defined as the conformal factor of the 3-metric h_{ij} in comoving gauge:

$$h_{ij}(t, x) = a^2(t) e^{2\mathcal{R}(t, x)} \hat{h}_{ij}; \quad \hat{h}_{ij} := \exp[\gamma_{ij}] \quad (3)$$

with $\partial_i \gamma_{ij} = \gamma_{ii} = 0$ defining transverse traceless graviton perturbations. The temperature anisotropies are characterized by the dimensionless power spectrum for \mathcal{R} , whose amplitude is given by

$$\mathcal{P}_{\mathcal{R}} := \frac{H_*^2}{8\pi^2 M_*^2 \epsilon_*} = \mathcal{A} \times 10^{-10}, \quad (4)$$

where $\epsilon_* := -\dot{H}_*/H_*^2$, H_* being the Hubble factor during inflation. Given that \mathcal{R} is conserved on super-horizon scales (in the absence of entropy perturbations), this immediately relates to the amplitude of the late time CMB anisotropies, which fixes $\mathcal{A} \sim 22.15$ [10]. The tensor anisotropies are characterized by the tensor power spectrum

$$\mathcal{P}_{\gamma} := 2 \frac{H_*^2}{\pi^2 M_*^2}, \quad (5)$$

Taking the ratio of the above with (4), we find the tensor to scalar ratio

$$r_* := \frac{\mathcal{P}_{\gamma}}{\mathcal{P}_{\mathcal{R}}} = 16\epsilon_*. \quad (6)$$

¹In what follows, we assume that all of the extra species have sufficiently suppressed couplings to the inflaton during inflation (e.g. either through derivative couplings or as Planck suppressed interactions) so that isocurvature perturbations are not significantly generated. This is trivially true for hidden sector fields.

Therefore any determination of r_* , either through direct measurements of the stochastic background of primordial gravitational waves or through their secondary effects on the polarization of the CMB [11, 12, 13] allows us in principle to fix the scale of inflation:

$$H_* = M_* \left(\frac{\pi^2 \mathcal{A} r_*}{2 \cdot 10^{10}} \right)^{1/2} := \Upsilon = 1.05 \sqrt{r_*} \times 10^{-4}. \quad (7)$$

We see that any measurements of r_* determines the scale of inflation *up to our ignorance of the effective strength of gravity at the scale H_** , given by $M_* \sim \frac{M_P}{\sqrt{N}}$, where N is the effective number of all universally coupled species up to the scale H_* — whether they exist in the visible sector or in any hidden sector. Note that as one lowers the scale of strong gravity, the maximum reheating temperature T_i is necessarily lowered as well, since it cannot be higher than the inflation scale. Conservatively, T_i cannot be too far below the TeV scale without spoiling the standard scenarios of big bang cosmology— in particular, mechanisms for Leptogenesis and Baryogenesis which can occur no lower than the electroweak scale [14]. We note as a consistency check on the above considerations, that although additional species increase the strength of gravity, the ratio H_*^2/M_*^2 is independent of N and is fixed by observable quantities. Therefore the effects of strong gravity are evidently negligible during inflation even if M_* is much smaller than the macroscopic strength of gravity M_{pl} . Hence inflationary dynamics, in particular the dynamics of adiabatic fluctuations remain weakly coupled independent of N and the usual computation of adiabatic correlators can be implemented [15].

In the case of extra species as KK graviton modes, the fundamental higher-dimensional gravity scale (1) with N given in (2) for $E_* = M_{UV}$ leads to the usual relation between the 4d and $(4+n)$ d Planck scales

$$M_P^2 = M_{UV}^{2+n} R^n. \quad (8)$$

On the other hand, during inflation N counts all KK states with mass less than the Hubble scale H_* :

$$N = (H_* R)^n, \quad (9)$$

and the effective gravity scale becomes

$$M_* = M_P / \sqrt{N} = M_{UV} (M_{UV}/H)^{n/2}, \quad (10)$$

where we used the relations (8) and (10). Equation (7) then yields:

$$H_* = M_* \Upsilon = M_{UV} (M_{UV}/H)^{n/2} \Upsilon \Rightarrow M_{UV} \Upsilon^{2/(n+2)}, \quad (11)$$

where we used eq. (10). It follows that H_* is one to three orders of magnitude below the fundamental gravity scale M_{UV} for the range $0.001 \lesssim r_* \lesssim 0.1$. The ratio H_*/M_* is of course fixed by (7). The inflation scale H_*

can then be as low as the weak scale in low scale gravity models with large extra dimensions, consistently with observations.

In the following, we assume that the electroweak, inflation, gravity and dark energy scales have an independent dynamical origin and examine the corresponding conditions to the microscopic theories. More precisely, we address the question of supersymmetry breaking in dS space with an infinitesimal (tunable) cosmological constant.

3. Conventions

Throughout this paper we use the conventions of [16]. A supergravity theory is specified (up to Chern-Simons terms) by a Kähler potential \mathcal{K} , a superpotential W , and the gauge kinetic functions $f_{AB}(z)$. The chiral multiplets z^α, χ^α are enumerated by the index α and the indices A, B indicate the different gauge groups. Classically, a supergravity theory is invariant under Kähler transformations, viz.

$$\begin{aligned} \mathcal{K}(z, \bar{z}) &\longrightarrow \mathcal{K}(z, \bar{z}) + J(z) + \bar{J}(\bar{z}), \\ W(z) &\longrightarrow e^{-\kappa^2 J(z)} W(z), \end{aligned} \quad (12)$$

where κ is the inverse of the reduced Planck mass, $m_p = \kappa^{-1} = 2.4 \times 10^{15}$ TeV. The gauge transformations of chiral multiplet scalars are given by holomorphic Killing vectors, i.e. $\delta z^\alpha = \theta^A k_A^\alpha(z)$, where θ^A is the gauge parameter of the gauge group A . The Kähler potential and superpotential need not be invariant under this gauge transformation, but can change by a Kähler transformation

$$\delta \mathcal{K} = \theta^A [r_A(z) + \bar{r}_A(\bar{z})], \quad (13)$$

provided that the gauge transformation of the superpotential satisfies $\delta W = -\theta^A \kappa^2 r_A(z) W$. One then has from $\delta W = W_\alpha \delta z^\alpha$

$$W_\alpha k_A^\alpha = -\kappa^2 r_A W, \quad (14)$$

where $W_\alpha = \partial_\alpha W$ and α labels the chiral multiplets. The supergravity theory can then be described by a gauge invariant function

$$\mathcal{G} = \kappa^2 \mathcal{K} + \log(\kappa^6 W \bar{W}). \quad (15)$$

The scalar potential is given by

$$\begin{aligned} V &= V_F + V_D \\ V_F &= e^{\kappa^2 \mathcal{K}} \left(-3\kappa^2 W \bar{W} + \nabla_\alpha W g^{\alpha\bar{\beta}} \bar{\nabla}_{\bar{\beta}} \bar{W} \right) \\ V_D &= \frac{1}{2} (\text{Re} f)^{-1 AB} \mathcal{P}_A \mathcal{P}_B, \end{aligned} \quad (16)$$

where W appears with its Kähler covariant derivative

$$\nabla_\alpha W = \partial_\alpha W(z) + \kappa^2 (\partial_\alpha \mathcal{K}) W(z). \quad (17)$$

The moment maps \mathcal{P}_A are given by

$$\mathcal{P}_A = i(k_A^\alpha \partial_\alpha \mathcal{K} - r_A). \quad (18)$$

In this paper we will be concerned with theories having a gauged R-symmetry, for which $r_A(z)$ is given by an imaginary constant $r_A(z) = i\kappa^{-2}\xi$. In this case, $\kappa^{-2}\xi$ is a Fayet-Iliopoulos [17] constant parameter.

4. The model

The starting point is a chiral multiplet S and a vector multiplet associated with a shift symmetry of the scalar component s of the chiral multiplet S

$$\delta s = -ic\theta, \quad (19)$$

and a string-inspired Kähler potential of the form $-p \log(s + \bar{s})$. The most general superpotential is either a constant $W = \kappa^{-3}a$ or an exponential superpotential $W = \kappa^{-3}ae^{bs}$ (where a and b are constants). A constant superpotential is (obviously) invariant under the shift symmetry, while an exponential superpotential transforms as $W \rightarrow We^{-ibc\theta}$, as in eq. (14). In this case the shift symmetry becomes a gauged R-symmetry and the scalar potential contains a Fayet-Iliopoulos term. Note however that by performing a Kähler transformation (12) with $J = \kappa^{-2}bs$, the model can be recast into a constant superpotential at the cost of introducing a linear term in the Kähler potential $\delta K = b(s + \bar{s})$. Even though in this representation, the shift symmetry is not an R-symmetry, we will still refer to it as $U(1)_R$. The most general gauge kinetic function has a constant term and a term linear in s , $f(s) = \delta + \beta s$.

To summarise,²

$$\begin{aligned} \mathcal{K}(s, \bar{s}) &= -p \log(s + \bar{s}) + b(s + \bar{s}), \\ W(s) &= a, \\ f(s) &= \delta + \beta s, \end{aligned} \quad (20)$$

where we have set the mass units $\kappa = 1$. The constants a and b together with the constant c in eq. (19) can be tuned to allow for an infinitesimally small cosmological constant and a TeV gravitino mass. For $b > 0$, there always exists a supersymmetric AdS (anti-de Sitter) vacuum at $\langle s + \bar{s} \rangle = b/p$, while for $b = 0$ (and $p < 3$) there is an AdS vacuum with broken supersymmetry. We therefore focus on $b < 0$. In the context of string theory, S can be identified with a compactification modulus or the universal dilaton and (for negative b) the exponential superpotential may be generated by non-perturbative effects.

²In superfields the shift symmetry (19) is given by $\delta S = -ic\Lambda$, where Λ is the superfield generalization of the gauge parameter. The gauge invariant Kähler potential is then given by $\mathcal{K}(S, \bar{S}) = -p\kappa^{-2} \log(S + \bar{S} + cV_R) + \kappa^{-2}b(S + \bar{S} + cV_R)$, where V_R is the gauge superfield of the shift symmetry.

The scalar potential is given by:

$$\begin{aligned} V &= V_F + V_D \\ V_F &= a^2 e^{\frac{2}{3}l^{p-2}} \left\{ \frac{1}{p}(pl - b)^2 - 3l^2 \right\} \quad l = 1/(s + \bar{s}) \\ V_D &= c^2 \frac{l}{\beta + 2\delta l} (pl - b)^2 \end{aligned} \quad (21)$$

In the case where S is the string dilaton, V_D can be identified as the contribution of a magnetized D-brane, while V_F for $b = 0$ and $p = 2$ coincides with the tree-level dilaton potential obtained by considering string theory away its critical dimension [18]. For $p \geq 3$ the scalar potential V is positive and monotonically decreasing, while for $p < 3$, its F-term part V_F is unbounded from below when $s + \bar{s} \rightarrow 0$. On the other hand, the D-term part of the scalar potential V_D is positive and diverges when $s + \bar{s} \rightarrow 0$ and for various values for the parameters an (infinitesimally small) positive (local) minimum of the potential can be found.

If we restrict ourselves to integer p , tunability of the vacuum energy restricts $p = 2$ or $p = 1$ when $f(s) = s$, or $p = 1$ when the gauge kinetic function is constant. For $p = 2$ and $f(s) = s$, the minimization of V yields:

$$b/l = \alpha \approx -0.183268 \quad , \quad p = 2 \quad (22)$$

$$\frac{a^2}{bc^2} = A_2(\alpha) + B_2(\alpha) \frac{\Lambda}{b^3 c^2} \approx -50.6602 + \mathcal{O}(\Lambda) \quad (23)$$

where Λ is the value of V at the minimum (i.e. the cosmological constant), α is the negative root of the polynomial $-x^5 + 7x^4 - 10x^3 - 22x^2 + 40x + 8$ compatible with (23) for $\Lambda = 0$ and $A_2(\alpha)$, $B_2(\alpha)$ are given by

$$A_2(\alpha) = 2e^{-\alpha} \frac{-4 + 4\alpha - \alpha^2}{\alpha^3 - 4\alpha^2 - 2\alpha} \quad ; \quad B_2(\alpha) = 2 \frac{\alpha^2 e^{-\alpha}}{\alpha^2 - 4\alpha - 2} \quad (24)$$

It follows that by carefully tuning a and c , Λ can be made positive and arbitrarily small independently of the supersymmetry breaking scale. A plot of the scalar potential for certain values of the parameters is shown in figure 1.

At the minimum of the scalar potential, for nonzero a and $b < 0$, supersymmetry is broken by expectation values of both an F and D-term. Indeed the F-term and D-term contributions to the scalar potential are

$$\begin{aligned} V_F|_{s+\bar{s}=\frac{\alpha}{b}} &= \frac{1}{2} a^2 b^2 e^\alpha \left(1 - \frac{2}{\alpha} \right)^2 > 0, \\ V_D|_{s+\bar{s}=\frac{\alpha}{b}} &= \frac{b^3 c^2}{\alpha} \left(1 - \frac{2}{\alpha} \right)^2 > 0. \end{aligned} \quad (25)$$

The gravitino mass term is given by

$$(m_{3/2})^2 = e^{\mathcal{G}} = \frac{a^2 b^2}{\alpha^2} e^\alpha. \quad (26)$$

Due to the Stueckelberg coupling, the imaginary part of s (the axion) gets eaten by the gauge field, which acquires a mass. On the other hand, the Goldstino, which

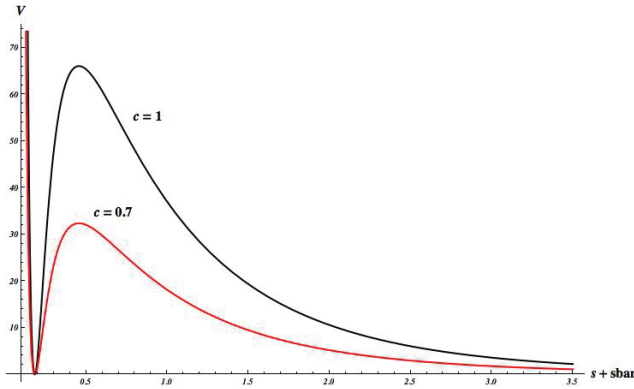


Figure 1: A plot of the scalar potential for $p = 2$, $b = -1$, $\delta = 0$, $\beta = 1$ and a given by equation (23) for $c = 1$ (black curve) and $c = 0.7$ (red curve).

is a linear combination of the fermion of the chiral multiplet χ and the gaugino λ gets eaten by the gravitino. As a result, the physical spectrum of the theory consists (besides the graviton) of a massive scalar, namely the dilaton, a Majorana fermion, a massive gauge field and a massive gravitino. All the masses are of the same order of magnitude as the gravitino mass, proportional to the same constant a (or c related by eq. (23) where b is fixed by eq. (22)), which is a free parameter of the model. Thus, they vanish in the same way in the supersymmetric limit $a \rightarrow 0$.

The local dS minimum is metastable since it can tunnel to the supersymmetric ground state at infinity in the s -field space (zero coupling). It turns out however that it is extremely long lived for realistic perturbative values of the gauge coupling $l \simeq 0.02$ and TeV gravitino mass and, thus, practically stable; its decay rate is [5]:

$$\Gamma \sim e^{-B} \quad \text{with} \quad B \approx 10^{300}. \quad (27)$$

5. Coupling a visible sector

The guideline to construct a realistic model keeping the properties of the toy model described above is to assume that matter fields are invariant under the shift symmetry (19) and do not participate in the supersymmetry breaking. In the simplest case of a canonical Kähler potential, MSSM-like fields ϕ can then be added as:

$$\begin{aligned} \mathcal{K} &= -\kappa^{-2} \log(s + \bar{s}) + \kappa^{-2} b(s + \bar{s}) + \sum \varphi \bar{\varphi}, \\ W &= \kappa^{-3} a + W_{MSSM}, \end{aligned} \quad (28)$$

where $W_{MSSM}(\phi)$ is the usual MSSM superpotential. The squared soft scalar masses of such a model can be shown to be positive and close to the square of the gravitino mass (TeV^2). On the other hand, for a gauge kinetic function with a linear term in s , $\beta \neq 0$ in eq. (20), the Lagrangian is not invariant under the

shift symmetry

$$\delta \mathcal{L} = -\theta \frac{\beta c}{8} \epsilon^{\mu\nu\rho\sigma} F_{\mu\nu} F_{\rho\sigma}. \quad (29)$$

and its variation should be canceled. As explained in Ref. [5], in the 'frame' with an exponential superpotential the R-charges of the fermions in the model can give an anomalous contribution to the Lagrangian. In this case the 'Green-Schwarz' term $\text{Im}s F \bar{F}$ can cancel quantum anomalies. However as shown in [5], with the minimal MSSM spectrum, the presence of this term requires the existence of additional fields in the theory charged under the shift symmetry.

Instead, to avoid the discussion of anomalies, we focus on models with a constant gauge kinetic function. In this case the only (integer) possibility³ is $p = 1$. The scalar potential is given by (21) with $\beta = 0$, $\delta = p = 1$. The minimization yields to equations similar to (22), (23) and (24) with a different value of α and functions A_1 and B_1 given by:

$$\begin{aligned} b(s + \bar{s}) &= \alpha \approx -0.233153 \\ \frac{bc^2}{a^2} &= A_1(\alpha) + B_1(\alpha) \frac{\Lambda}{a^2 b} \approx -0.359291 + \mathcal{O}(\Lambda) \quad (30) \\ A_1(\alpha) &= 2e^\alpha \alpha \frac{3 - (\alpha - 1)^2}{(\alpha - 1)^2}, \quad B_1(\alpha) = \frac{2\alpha^2}{(\alpha - 1)^2}, \end{aligned}$$

where α is the negative root of $-3 + (\alpha - 1)^2(2 - \alpha^2/2) = 0$ close to -0.23 , compatible with the second constraint for $\Lambda = 0$. However, this model suffers from tachyonic soft masses when it is coupled to the MSSM, as in (28). To circumvent this problem, one can add an extra hidden sector field which contributes to (F-term) supersymmetry breaking. Alternatively, the problem of tachyonic soft masses can also be solved if one allows for a non-canonical Kähler potential in the visible sector, which gives an additional contribution to the masses through the D-term.

Let us discuss first the addition of an extra hidden sector field z (similar to the so-called Polonyi field [19]). The Kähler potential, superpotential and gauge kinetic function are given by

$$\begin{aligned} \mathcal{K} &= -\kappa^{-2} \log(s + \bar{s}) + \kappa^{-2} b(s + \bar{s}) + z \bar{z} + \sum \varphi \bar{\varphi}, \\ W &= \kappa^{-3} a(1 + \gamma \kappa z) + W_{MSSM}(\varphi), \\ f(s) &= 1 \quad , \quad f_A = 1/g_A^2, \end{aligned} \quad (31)$$

where A labels the Standard Model gauge group factors and γ is an additional constant parameter. The existence of a tunable dS vacuum with supersymmetry

³If $f(s)$ is constant, the leading contribution to V_D when $s + \bar{s} \rightarrow 0$ is proportional to $1/(s + \bar{s})^2$, while the leading contribution to V_F is proportional to $1/(s + \bar{s})^p$. It follows that $p < 2$; if $p > 2$, the potential is unbounded from below, while if $p = 2$, the potential is either positive and monotonically decreasing or unbounded from below when $s + \bar{s} \rightarrow 0$ depending on the values of the parameters.

breaking and non-tachyonic scalar masses implies that γ must be in a narrow region:

$$0.5 \lesssim \gamma \lesssim 1.7. \quad (32)$$

In the above range of γ the main properties of the toy model described in the previous section remain, while $\text{Re} z$ and its F-auxiliary component acquire non vanishing VEVs. All MSSM soft scalar masses are then equal to a universal value m_0 of the order of the gravitino mass, while the B_0 Higgs mixing parameter is also of the same order:

$$\begin{aligned} m_0^2 &= m_{3/2}^2 \left[(\sigma_s + 1) + \frac{(\gamma + t + \gamma t)^2}{(1 + \gamma t)^2} \right], \\ A_0 &= m_{3/2} \left[(\sigma_s + 3) + t \frac{(\gamma + t + \gamma t^2)}{1 + \gamma t} \right], \\ B_0 &= m_{3/2} \left[(\sigma_s + 2) + t \frac{(\gamma + t + \gamma t^2)}{(1 + \gamma t)} \right], \end{aligned} \quad (33)$$

where $\sigma_s = -3 + (\alpha - 1)^2$ with α and $t \equiv \langle \text{Re} z \rangle$ determined by the minimization conditions as functions of γ . Also, A_0 is the soft trilinear scalar coupling in the standard notation, satisfying the relation [20]

$$A_0 = B_0 + m_{3/2}. \quad (34)$$

On the other hand, the gaugino masses appear to vanish at tree-level since the gauge kinetic functions are constants (see (31)). However, as mentioned in Section , this model is classically equivalent to the theory⁴

$$\begin{aligned} \mathcal{K} &= -\kappa^{-2} \log(s + \bar{s}) + z\bar{z} + \sum_{\alpha} \varphi \bar{\varphi}, \\ W &= (\kappa^{-3} a(1 + z) + W_{\text{MSSM}}(\varphi)) e^{bs}, \end{aligned} \quad (35)$$

obtained by applying a Kähler transformation (12) with $J = -\kappa^{-2} bs$. All classical results remain the same, such as the expressions for the scalar potential and the soft scalar masses (33), but now the shift symmetry (19) of s became a gauged R-symmetry since the superpotential transforms as $W \rightarrow W e^{-ibc\theta}$. Therefore, all fermions (including the gauginos and the gravitino) transform⁵ as well under this $U(1)_R$, leading to cubic $U(1)_R^3$ and mixed $U(1) \times G_{\text{MSSM}}$ anomalies. These anomalies are cancelled by a Green-Schwarz (GS) counter term that arises from a quantum correction to the gauge kinetic functions:

$$f_A(s) = 1/g_A^2 + \beta_A s \quad \text{with} \quad \beta_A = \frac{b}{8\pi^2} (T_{R_A} - T_{G_A}), \quad (36)$$

⁴This statement is only true for supergravity theories with a non-vanishing superpotential where everything can be defined in terms of a gauge invariant function $G = \kappa^2 \mathcal{K} + \log(\kappa^6 W \bar{W})$ [21].

⁵The chiral fermions, the gauginos and the gravitino carry a charge $bc/2$, $-bc/2$ and $-bc/2$ respectively.

where T_G is the Dynkin index of the adjoint representation, normalized to N for $SU(N)$, and T_R is the Dynkin index associated with the representation R of dimension d_R , equal to $1/2$ for the $SU(N)$ fundamental. An implicit sum over all matter representations is understood. It follows that gaugino masses are non-vanishing in this representation, creating a puzzle on the quantum equivalence of the two classically equivalent representations. The answer to this puzzle is based on the fact that gaugino masses are present in both representations and are generated at one-loop level by an effect called Anomaly Mediation [7, 8]. Indeed, it has been argued that gaugino masses receive a one-loop contribution due to the super-Weyl-Kähler and sigma-model anomalies, given by [8]:

$$\begin{aligned} M_{1/2} &= -\frac{g^2}{16\pi^2} \times [(3T_G - T_R)m_{3/2} + (T_G - T_R)\mathcal{K}_{\alpha} F^{\alpha} \\ &\quad + 2\frac{T_R}{d_R} (\log \det \mathcal{K}|_R)_{,\alpha} F^{\alpha}]. \end{aligned} \quad (37)$$

The expectation value of the auxiliary field F^{α} , evaluated in the Einstein frame is given by

$$F^{\alpha} = -e^{\kappa^2 \mathcal{K}/2} g^{\alpha\bar{\beta}} \bar{\nabla}_{\bar{\beta}} \bar{W}. \quad (38)$$

Clearly, for the Kähler potential (31) or (35) the last term in eq. (37) vanishes. However, the second term survives due to the presence of Planck scale VEVs for the hidden sector fields s and z . Since the Kähler potential between the two representations differs by a linear term $b(s + \bar{s})$, the contribution of the second term in eq. (37) differs by a factor

$$\delta m_A = \frac{g_A^2}{16\pi^2} (T_G - T_R) b e^{\kappa^2 \mathcal{K}/2} g^{\alpha\bar{\beta}} \bar{\nabla}_{\bar{\beta}} \bar{W}, \quad (39)$$

which exactly coincides with the ‘direct’ contribution to the gaugino masses due to the field dependent gauge kinetic function (36) (taking into account a rescaling proportional to g_A^2 due to the non-canonical kinetic terms).

We conclude that even though the models (31) and (35) differ by a (classical) Kähler transformation, they generate the same gaugino masses at one-loop. While the one-loop gaugino masses for the model (31) are generated entirely by eq. (37), the gaugino masses for the model (35) after a Kähler transformation have a contribution from eq. (37) as well as from a field dependent gauge kinetic term whose presence is necessary to cancel the mixed $U(1)_R \times G$ anomalies due to the fact that the extra $U(1)$ has become an R-symmetry giving an R-charge to all fermions in the theory. Using (37), one finds:

$$\begin{aligned} M_{1/2} &= -\frac{g^2}{16\pi^2} m_{3/2} [(3T_G - T_R) - \\ &\quad (T_G - T_R) \left((\alpha - 1)^2 + t \frac{\gamma + t + \gamma t^2}{1 + \gamma t} \right)] \end{aligned} \quad (40)$$

For $U(1)_Y$ we have $T_G = 0$ and $T_R = 11$, for $SU(2)$ we have $T_G = 2$ and $T_R = 7$, and for $SU(3)$ we have $T_G = 3$ and $T_R = 6$, such that for the different gaugino masses this gives (in a self-explanatory notation):

$$\begin{aligned} M_1 &= 11 \frac{g_Y^2}{16\pi^2} m_{3/2} \left[1 - (\alpha - 1)^2 - \frac{t(\gamma + t + \gamma t)}{1 + \gamma t} \right], \\ M_2 &= \frac{g_2^2}{16\pi^2} m_{3/2} \left[1 - 5(\alpha - 1)^2 - 5 \frac{t(\gamma + t + \gamma t^2)}{1 + \gamma t} \right], \\ M_3 &= -3 \frac{g_3^2}{16\pi^2} m_{3/2} \left[1 + (\alpha - 1)^2 + \frac{t(\gamma + t + \gamma t^2)}{1 + \gamma t} \right] \end{aligned} \quad (41)$$

6. Phenomenology

The results for the soft terms calculated in the previous section, evaluated for different values of the parameter γ are summarised in Table 1. For every γ , the corresponding t and α are calculated by imposing a vanishing cosmological constant at the minimum of the potential. The scalar soft masses and trilinear terms are then evaluated by eqs. (33) and the gaugino masses by eqs. (41). Note that the relation (34) is valid for all γ . We therefore do not list the parameter B_0 .

In most phenomenological studies, B_0 is substituted for $\tan\beta$, the ratio between the two Higgs VEVs, as an input parameter for the renormalization group equations (RGE) that determine the low energy spectrum of the theory. Since B_0 is not a free parameter in our theory, but is fixed by eq. (34), this corresponds to a definite value of $\tan\beta$. For more details see [22] (and references therein). The corresponding $\tan\beta$ for a few particular choices for γ are listed in the last two columns of table 1 for $\mu > 0$ and $\mu < 0$ respectively. No solutions were found for $\gamma \lesssim 1.1$, for both signs of μ . The lightest supersymmetric particle (LSP) is given by the lightest neutralino and since $M_1 < M_2$ (see table 1) the lightest neutralino is mostly Bino-like, in contrast with a typical mAMSB (minimal anomaly mediation supersymmetry breaking) scenario, where the lightest neutralino is mostly Wino-like [23].

To get a lower bound on the stop mass, the sparticle spectrum is plotted in Figure 2 as a function of the gravitino mass for $\gamma = 1.1$ and $\mu > 0$ (for $\mu < 0$ the bound is higher). The experimental limit on the gluino mass forces $m_{3/2} \gtrsim 15$ TeV. In this limit the stop mass can be as low as 2 TeV. To conclude, the lower end mass spectrum consists of (very) light charginos (with a lightest chargino between 250 and 800 GeV) and neutralinos, with a mostly Bino-like neutralino as LSP (80 – 230 GeV), which would distinguish this model from the mAMSB where the LSP is mostly Wino-like. These upper limits on the LSP and the lightest chargino imply that this model could in principle be excluded in the next LHC run.

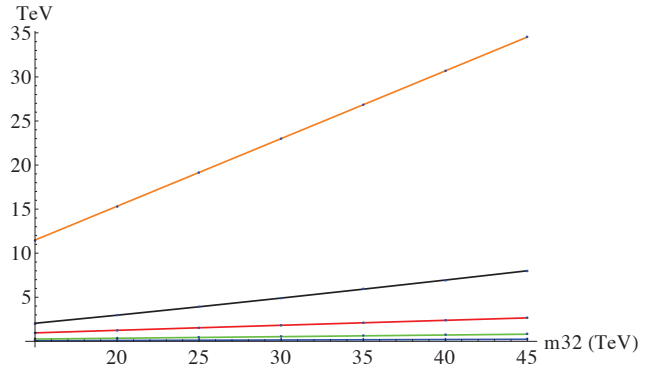


Figure 2: The masses (in TeV) of the sbottom (yellow), stop (black), gluino (red), lightest chargino (green) and lightest neutralino (blue) as a function of $m_{3/2}$ for $\gamma = 1.1$ and for $\mu > 0$. No solutions to the RGE were found when $m_{3/2} \gtrsim 45$ TeV. The lower bound corresponds to a gluino mass of 1 TeV.

In order for the gluino to escape experimental bounds, the lower limit on the gravitino mass is about 15 TeV. The gluino mass is then between 1-3 TeV. This however forces the squark masses to be very high (10 – 35 TeV), with the exception of the stop mass which can be relatively light (2 – 15 TeV).

7. Non-canonical Kähler potential for the visible sector

As mentioned already in Section 4, an alternative way to avoid tachyonic soft scalar masses for the MSSM fields in the model (28), instead of adding the extra Palonyi-type field z in the hidden sector, is by introducing non-canonical kinetic terms for the MSSM fields, such as:

$$\begin{aligned} \mathcal{K} &= -\kappa^{-2} \log(s + \bar{s}) + \kappa^{-2} b(s + \bar{s}) + (s + \bar{s})^{-\nu} \sum \varphi \bar{\varphi} \\ W &= \kappa^{-3} a + W_{MSSM}, \\ f(s) &= 1, \quad f_A(s) = 1/g_A^2, \end{aligned} \quad (42)$$

where ν is an additional parameter of the theory, with $\nu = 1$ corresponding to the leading term in the Taylor expansion of $-\log(s + \bar{s} - \varphi \bar{\varphi})$. Since the visible sector fields appear only in the combination $\varphi \bar{\varphi}$, their VEVs vanish provided that the scalar soft masses squared are positive. Moreover, for vanishing visible sector VEVs, the scalar potential and its minimization remains the same as in eqs. (refbsalpha). Therefore, the non-canonical Kähler potential does not change the fact that the F-term contribution to the soft scalar masses squared is negative. On the other hand, the visible fields enter in the D-term scalar potential through the derivative of the Kähler potential with respect to s . Even though this has no effect on the ground state of the potential, the φ -dependence of the D-term scalar potential does result in an extra contribution to the

γ	t	α	m_0	A_0	M_1	M_2	M_3	$\tan \beta(\mu > 0)$	$\tan \beta(\mu < 0)$
0.6	0.446	-0.175	0.475	1.791	0.017	0.026	0.027		
1	0.409	-0.134	0.719	1.719	0.015	0.025	0.026		
1.1	0.386	-0.120	0.772	1.701	0.015	0.024	0.026	46	29
1.4	0.390	-0.068	0.905	1.646	0.014	0.023	0.026	40	23
1.7	0.414	-0.002	0.998	1.588	0.013	0.022	0.025	36	19

Table 1: The soft terms (in terms of $m_{3/2}$) for various values of γ . If a solution to the RGE exists, the value of $\tan \beta$ is shown in the last columns for $\mu > 0$ and $\mu < 0$ respectively.

scalar masses squared which become positive

$$\nu > -\frac{e^\alpha(\sigma_s + 1)\alpha}{A(\alpha)(1 - \alpha)} \approx 2.6. \quad (43)$$

The soft MSSM scalar masses and trilinear couplings in this model are:

$$\begin{aligned} m_0^2 &= \kappa^2 a^2 \left(\frac{b}{\alpha}\right) \left(e^\alpha(\sigma_s + 1) + \nu \frac{A(\alpha)}{\alpha}(1 - \alpha)\right) \\ A_0 &= m_{3/2}(s + \bar{s})^{\nu/2}(\sigma_s + 3) \\ B_0 &= m_{3/2}(s + \bar{s})^{\nu/2}(\sigma_s + 2) \end{aligned} \quad (44)$$

where σ_s is defined as in (33), eq. (31) has been used to relate the constants a and c , and corrections due to a small cosmological constant have been neglected. A field redefinition due to a non-canonical kinetic term $g_{\varphi\bar{\varphi}} = (s + \bar{s})^{-\nu}$ is also taken into account. The main phenomenological properties of this model are not expected to be different from the one we analyzed in section with the parameter ν replacing γ . Gaugino masses are still generated at one-loop level while mSUGRA applies to the soft scalar sector. We therefore do not repeat the phenomenological analysis for this model.

References

- [1] I. Antoniadis, N. Arkani-Hamed, S. Dimopoulos and G. R. Dvali, Phys. Lett. B **436** (1998) 257 [arXiv:hep-ph/9804398]
- [2] I. Antoniadis and S. P. Patil, Eur. Phys. J. **C75** (2015) 182 [arXiv:1410.8845 [hep-th]].
- [3] I. Antoniadis and R. Knoops, Nucl. Phys. B **886** (2014) 43 [arXiv:1403.1534 [hep-th]].
- [4] F. Catino, G. Villadoro and F. Zwirner, JHEP **1201** (2012) 002 [arXiv:1110.2174 [hep-th]]; G. Villadoro and F. Zwirner, Phys. Rev. Lett. **95** (2005) 231602 [hep-th/0508167].
- [5] I. Antoniadis, D. M. Ghilencea and R. Knoops, JHEP **1502** (2015) 166 [arXiv:1412.4807 [hep-th]].
- [6] I. Antoniadis and R. Knoops, [arXiv:1507.06924 [hep-ph]].
- [7] L. Randall and R. Sundrum, Nucl. Phys. B **557** (1999) 79 [hep-th/9810155]; G. F. Giudice, M. A. Luty, H. Murayama and R. Rattazzi, JHEP **9812** (1998) 027 [hep-ph/9810442].
- [8] J. A. Bagger, T. Moroi and E. Poppitz, JHEP **0004** (2000) 009 [hep-th/9911029].
- [9] G. Dvali, arXiv:0706.2050 [hep-th]; Int. J. Mod. Phys. A **25** (2010) 602 [arXiv:0806.3801 [hep-th]]; G. Dvali and M. Redi, Phys. Rev. D **77** (2008) 045027 [arXiv:0710.4344 [hep-th]]; R. Brustein, G. Dvali and G. Veneziano, JHEP **0910** (2009) 085 [arXiv:0907.5516 [hep-th]]; G. Dvali and C. Gomez, Phys. Lett. B **674** (2009) 303.
- [10] P. A. R. Ade *et al.* [Planck Collaboration], Astron. Astrophys. (2014) [arXiv:1303.5076 [astro-ph.CO]]; arXiv:1303.5082 [astro-ph.CO].
- [11] A. G. Polnarev, Sov. Astron. **29**, 607 (1985).
- [12] M. Kamionkowski, A. Kosowsky and A. Stebbins, Phys. Rev. Lett. **78**, 2058 (1997) [astro-ph/9609132].
- [13] U. Seljak and M. Zaldarriaga, Phys. Rev. Lett. **78**, 2054 (1997) [astro-ph/9609169].
- [14] M. Trodden, Rev. Mod. Phys. **71**, 1463 (1999) [hep-ph/9803479]; S. Davidson, E. Nardi and Y. Nir, Phys. Rept. **466**, 105 (2008) [arXiv:0802.2962 [hep-ph]].
- [15] C. Cheung, P. Creminelli, A. L. Fitzpatrick, J. Kaplan and L. Senatore, JHEP **0803**, 014 (2008) [arXiv:0709.0293 [hep-th]].
- [16] D. Z. Freedman and A. Van Proeyen, Cambridge, UK: Cambridge Univ. Pr. (2012) 607 p.
- [17] P. Fayet and J. Iliopoulos, Phys. Lett. B **51** (1974) 461; Phys. Lett. B **69** (1977) 489.
- [18] I. Antoniadis, J. -P. Derendinger and T. Maillard, Nucl. Phys. B **808** (2009) 53 [arXiv:0804.1738 [hep-th]].
- [19] J. Polonyi, Hungary Central Inst Res - KFKI-77-93 (77,REC.JUL 78) 5p.
- [20] H. P. Nilles, Phys. Rept. **110** (1984) 1
- [21] S. Ferrara, L. Girardello, T. Kugo and A. Van Proeyen, Nucl. Phys. B **223** (1983) 191
- [22] J. R. Ellis, K. A. Olive, Y. Santoso and V. C. Spanos, Phys. Lett. B **573** (2003) 162 [hep-ph/0305212]
- [23] T. Gherghetta, G. F. Giudice and J. D. Wells, Nucl. Phys. B **559** (1999) 27 [hep-ph/9904378].

DISCRETE COSMOLOGY APPLICATION CONCERNING DARK MATTER HALOS

R.D. Brilenkov

Odessa I.I.Mechnikov National University,
Dvoryanskaya st. 2, Odessa 65082, Ukraine,
ruslan.brilenkov@gmail.com

ABSTRACT. We applied discrete cosmology for investigation of the density profiles of dark matter (DM) halos of clusters of galaxies. Comparing the derived velocity dispersion with the experimental data for the Coma cluster, we found the effective radius for the mass distribution inside this galaxy cluster. Our estimates give an opportunity to restrict the parameters of the Navarro-Frenk-White profile for considered cluster.

Keywords: dark matter, clusters of galaxies.

It is generally known, our Universe is dark: dark energy and dark matter contribute approximately 69% and 26% into total mass-energy balance in the Universe, respectively.

We found potentials, which satisfy the Poisson equation and give us an opportunity to consider motion of test massive bodies and light taking into account gravitational attraction to inhomogeneities inside the galaxies, groups and clusters of galaxies and cosmological expansion of the Universe:

$$\Delta\Phi = \frac{1}{R} \frac{d^2}{dR^2}(R\Phi) = 4\pi G_N \rho_{\text{ph}},$$

where G_N is the Newtonian gravitational constant and ρ_{ph} is the physical rest mass density of the bound system.

After that we introduce the distance radius of zero acceleration surface (at which the gravitational attraction and cosmological expansion compensate each other):

$$R_H = \left[\frac{G_N M}{\ddot{a}/a} \right]^{1/3}$$

Using the NFW density profile of DM halo of clusters of galaxies as the most commonly used profile:

$$\rho_{\text{ph}}(R) = \frac{4\rho_s}{\frac{R}{R_s} \left(1 + \frac{R}{R_s}\right)^2}, \quad R_s = \text{const}, \quad \rho_s = \rho(R_s)$$

we obtain, with the help of the observable data, the preferable profile parameters for the Coma cluster: $R_{200} \approx 1.77 h^{-1} \text{ Mpc} = 2.61 \text{ Mpc}$ and the concentration parameter $c = 3 \div 4$

The most galaxies are concentrated inside a sphere of effective radius $R_{\text{eff}} \sim 3.7 \text{ Mpc}$ for the Coma cluster (Abell 1656).

We also found line-of-sight velocity dispersion 1004 km s^{-1} . The observations give very close value 1008 km s^{-1} for this cluster.

Acknowledgements. I would like to thank my supervisors Alexander Zhuk and Maxim Eingorn who helped me to get these results.

References

- Eingorn M., Zhuk A.: 2012, Hubble flows and gravitational potentials in observable Universe, *JCAP*, **09**, 026; arXiv:1205.2384.
Eingorn M., Kudinova A., Zhuk A.: 2013, Dynamics of astrophysical objects against the cosmological background, *JCAP*, **04**, 010; arXiv:astro-ph/1211.4045.
Eingorn M., Zhuk A.: 2014, Remarks on mechanical approach to observable Universe, *JCAP*, **05**, 024; arXiv:astro-ph/1309.4924.

THE DOMINANCE OF DARK ENERGY LEADS TO REDUCTION OF THE ENTROPY OF GALAXIES FLOW AND ENTROPY OF THE UNIVERSE

Aleksandr V. Bukalov

The Centre for Physical and Space Research, International Institute of Socionics,
Melnikova str., 12, Kyiv-050, 04050, Ukraine, *bukalov.physics@socionic.info*

ABSTRACT. The existence of the Hubble flow recession of galaxies in terms of dominance of dark energy density, vacuum energy, reduces the gravitational entropy of clusters of galaxies, reducing the gravitational entropy of the Universe as a whole. Global dominance of dark energy leads to a decrease in entropy of the Universe within the cosmic event horizon.

Keywords: Hubble flow, movement of galaxies, clusters of galaxies, dark energy, entropy of the Universe

The dominance of dark energy in the modern era leads to the dominance of anti-gravitation of gravity on cosmological scales. I.D.Karachentsev (Karachentsev & Kashlbadze, 2006; Karachentsev, 2005; Karachentsev et al., 2009; Karachentsev, Karachentseva & Huchtmeier, 2007) and A.D.Chernin (Chernin, Teerikorpi, Baryshev, 2003; Chernin et al., 2007; Chernin et al., 2009; Chernin et al., 2012; Chernin et al., 2013; Chernin et al., 2007; Chernin et al., 2012; Chernin, 2013; Teerikorpi & Chernin, 2010), studying the motions of galaxies in clusters, have shown that anti-gravity effects manifest themselves not only on a cosmic scale, but the scale of clusters of galaxies, for example – the Local Group, including our galaxy (the Milky Way) galaxy Andromeda and dozens of other smaller galaxies. M. Eingorn and A. Zhuk also studied in detail these issues (Brilenkov, Eingorn & Zhuk, 2015; Eingorn & Zhuk, 2012). Observations and modeling have shown that at distances of 1–3 Mpc from the center of the gravity bounded Local Group of galaxies it is observed the local flow of divergent dwarf galaxies. The velocities of these galaxies are proportional to the distance from the center. A.D.Chernin et al. (2012) have shown that such flows, which are observed in other clusters at different scales, form under the influence of dark energy. So, for Local Groups zone of zero gravity in which the gravitational force is balanced by the force of attraction and anti-gravitation is the $R_{ZG} \approx 1.3 \div 1.4$ Mpc. Therefore, when $R > R_{ZG}$ the flow of recession of galaxies starts. A.D.Chernin and colleagues studied the behavior of galaxies streams, build charts based on experimental data and numerical simulation and showed that the phase trajectories of the local stream tend to phase attractor $V = H_x R$, that corresponds to the Hubble law. In this case $H_x = (8\pi G\rho_x/3)^{1/2}$ is determined by the local density of dark energy (Chernin, 2013). Therefore, when $R > R_{ZG}$ flow of

receding galaxies starts. In this case the phase trajectories of the local flow tend to phase attractor $V = H_x R$, that is, obey the Hubble law. From experimental diagram of velocities of galaxies we can estimate that the spread of own velocities of galaxies with $R < R_{ZG}$ reaches $\Delta V_{\max} = \pm 150$ km/s, the average is $\Delta V = \pm 70$ km/s, while when $R > R_{ZG}$ velocity spread to the theoretical velocity of Hubble divergence flow averages about $\Delta V = 12$ km/s (Bukalov, 2014). Antigravity of dark energy, or the energy of the vacuum, reduces the dispersion of velocity galaxies. The difference in entropy in areas with $R < R_{ZG}$ and $R > R_{ZG}$ is negative, so “evaporation” of the galaxies from gravitationally bound clusters reduces its gravitational entropy. Thus the anti-gravitation area causes a decrease in entropy of “gas of galaxies” at different levels of the hierarchy, in clusters and superclusters. In fact, gravitationally bound system, such as a group or cluster of galaxies, has gravitational entropy more than a galaxy outside the gravitational cluster and moving in an anti-gravitational environment. The “evaporation” of the galaxies gravitationally bound cluster reduces its gravitational entropy. Thus, the area of anti-gravitation causes a decrease in the entropy “gas galaxies” at different levels of the hierarchy – in clusters and superclusters.

Based on the results of numerical modeling of flow of galaxies recession, in which were obtained the minimum and maximum velocity of flow $V_{\min} = H_x R(1+2x^{-3}-3x^{-2})^{1/2}$ and $V_{\max} = H_x R(1+3x^{1/2})$, where $x = R/R_{ZG}$ (Chernin, 2013), we can write in general form the expression for the entropies difference:

$$\Delta S = \ln \frac{(V_{2_{\max}} - V_{2_{\min}})^2}{(V_{1_{\max}} - V_{1_{\min}})^2}. \quad (1)$$

We have obtained the entropy flow of galaxies similar to the gas. But if we use obtained by Chernin A.D. (2013) vacuum cooling factor as ratio of velocities, the logarithm of the square of this factor also provides an estimate of entropy changes. However, we can consider the more general expression for the evaluation of gravitational entropy of the system. We express the acceleration as equivalent to the Unruh vacuum temperature of accelerated moving body, for example a galaxy:

$$\frac{\hbar \ddot{a}}{2\pi c k_B} = \frac{\hbar g}{2\pi c k_B} + \frac{\hbar a}{2\pi c k_B} = -\frac{\hbar G M}{2\pi c k_B R^2} + \frac{\hbar c^2}{2\pi c k_B \cdot 3} \Lambda R, \quad (2)$$

or taking a positive temperature T_G , corresponding to the gravitational acceleration g , by analogy with the temperature of the black holes, we obtain a negative temperature value of the vacuum T_v , which corresponds to the anti-gravity acceleration: $\Delta k_B T = k_B T_G - k_B T_v$.

Thus, the entropy S_v is negative, which means that the effects of the vacuum can be attributed to the negative entropy, or information, that is the ability to the information arranging ordering. This explains the shift to the orderly movement of galaxies at $R > R_{ZG}$.

However, on the scale of the Universe there is a similar law accelerating recession superclusters of galaxies under the influence of dark energy (Chernin, 2013). This means that in a similar manner gravitational entropy decreases at the level of interaction of superclusters of galaxies also. Hence, the dominance of dark energy, or vacuum energy, on cosmological scales leads to the orderly movement of galaxies at the level of clusters and superclusters, reducing gravitational entropy of the Universe as a whole, as was shown earlier by the author (Bukalov, 2014). Therefore, in the Universe, which is expanding with acceleration under the influence of anti-gravity vacuum, gravitational entropy due to the contribution of gravitating matter should decrease with time. Thus, in the present Universe inside the Hubble radius are about 10^9 clusters of galaxies, like the Local Group. With continued accelerated expansion of the Universe it will be only a local group. All the other galaxies will be an observer outside the event horizon, which tends to $H^{-1} = r_\Lambda$, the radius of de Sitter space. Thus gravitational entropy associated with the supercluster of galaxies decrease in 10^9 times.

Turning to the cosmological scale and the Friedmann equation:

$$\ddot{a}_U = -\frac{4\pi}{3}G(\rho_M + 3p_M)a + (\rho_V + 3p_V)a, \quad (3)$$

where a is the scale factor, from $p_M=0$, $\rho_V = -p_V$ we get (Bukalov, 2014).

$$\ddot{a}_U = -\frac{4\pi G}{3}(\rho_M - 2p_V)a. \quad (4)$$

When $a \approx R_H \approx 1.36 \cdot 10^{26} \text{m}$, $\Omega_M \approx 0.318$, $\Omega_V = 0.682$, $\Omega_r \approx 5 \cdot 10^{-4}$, $z=0$

$$\begin{aligned} \ddot{a}_U &= -\frac{4\pi}{3}G_N \rho_c (0.318(1+z)^3 + \Omega_r(1+z)^4 - \\ &- 2 \cdot 0.682) \cdot R_H = \frac{4\pi}{3}G_N \rho_c \cdot 1.046a = \\ &= 3.46 \cdot 10^{-10} \text{m s}^{-2}. \end{aligned} \quad (5)$$

$$\Delta \ddot{a}_V = g - 2\ddot{a}_U \quad (6)$$

$$k_B \Delta T = k_B T_g - 2k_B T_V = -1.046k_B T_H = -k_B T_U \quad (7)$$

$$T_U = \frac{\hbar \ddot{a}_U}{2\pi c k_B} = 1.4 \cdot 10^{-30} \text{K}. \quad (8)$$

This is the temperature of the quantum radiation of accelerated body to the outside distant observer. According to M.B. Mensky (1978) such temperature is negative. Therefore for the Universe the entropy change will be:

$$\frac{\partial S_U}{\partial t} \approx \frac{S_U}{t_U} \approx -2.4 \cdot 10^{52} \text{J/s}. \quad (9)$$

Thus, when $z < 0.745$, $\partial S_U / \partial t < 0$.

From our results it follows that the vacuum is a reservoir of negative entropy, or ordering, which manifests itself in the period of its domination. Therefore, the vacuum can induce an increase in ordering of the movement patterns the universe. This impact is **the macroscopic quantum cosmological effect**.

The existence of the Hubble flow of receding galaxies under the domination of dark energy density, vacuum energy, leads to a decrease of gravitational entropy of galaxy clusters, reducing gravitational entropy of the universe as a whole.

With the gradual disappearance of black holes with their entropy and radiation, as well as the galaxies themselves over the cosmic event horizon, the entropy of the observable universe will only decrease, and negative entropy, or the degree of ordering of information, will increase asymptotically approaching a constant value.

References

- Birrell N.D., Davies P.C.W. Quantum fields in curved space. Cambridge University Press, 1982.
- Bisnovatyi-Kogan G.S., Chernin A.D.: 2012, *Astrophys. Space Sci.*, **338**, 337.
- Bukalov A.V.: 2014, in Proc. of 14th International Gamow Summer School.
- Chernin A., Teerikorpi P., Baryshev Yu.: 2003, *Adv. Space Res.*, **31**, 459; astro-ph/0012021.
- Chernin A.D. et al.: 2007, *Astron. Astrophys.*, **467**, 933.
- Chernin A.D. et al.: 2007, *Astron. Astrophys. Trans.*, **26**, 275.
- Chernin A.D. et al.: 2009, *Astron. Astrophys.*, **507**, 1271.
- Chernin A.D. et al.: 2012, *Astron. Astrophys.*, **539**, 4.
- Chernin A.D. et al.: 2012, *Astron. Rep.*, **56**, 653.
- Chernin A.D. et al.: 2013, *Astron. Astrophys.*, **553**, 101.
- Chernin A.D.: 2013, *UFN (Uspehi fiz. nauk)*, **183**, 741.
- Egan C.A., Lineweaver C.H.: 2010, *Astrophys. J.*, **710**, 1825; arXiv:0909.3983 [astro-ph.CO].
- Brilenkov R., Eingorn M., Zhuk A.: 2015, arXiv: 1507.07234.
- Eingorn M., Zhuk A.: 2012, arXiv:1205.2384.
- Gibbons G.W., Hawking S.W.: 1977, *Phys. Rev. D*, **15**, 2738.
- Karachentsev I.D., Kashlbadze O.G.: 2006, *Astrophys.*, **49**, 3.
- Karachentsev I.D.: 2005, *Astron. J.*, **129**, 178.
- Karachentsev I.D. et al.: 2009, *Mon. Not. R. Astron. Soc.*, **393**, 1265.
- Karachentsev I.D., Karachentseva V.E., Huchtmeier W.K.: 2007, *Astron. Lett.*, **33**, 512.
- Mensky M.B.: 1978, *TMF*, **115** (2), 215.
- Perlmutter S. et al.: 1999, *Astrophys. J.*, **517**, 565.
- Riess A.G. et al.: 1998, *Astron. J.*, **116**, 1009.
- Teerikorpi P., Chernin A.D.: 2010, *Astron. Astrophys.*, **516**, A93.

THE MODEL FOR FINAL STAGE OF GRAVITATIONAL COLLAPSE MASSLESS SCALAR FIELD

V.D. Gladush¹, D.V. Mironin²

Dnipropetrovsk National University, Gagarin Ave, 725014, Ukraine,
¹vgladush@gmail.com, ²dmyronin1993@mail.ru

ABSTRACT. It is known that in General relativity, for some spherically symmetric initial conditions, the massless scalar field (SF) experience the gravitational collapse (Choptuik, 1989), and arise a black hole (BH). According Bekenstein, a BH has no "hair scalar", so the SF is completely under the horizon. Thus, the study of the final stage for the gravitational collapse of a SF is reduced to the construction of a solution of Einstein's equations describing the evolution of a SF inside the BH. In this work, we build the Lagrangian for scalar and gravitational fields in the spherically symmetric case, when the metric coefficients and SF depends only on the time. In this case, it is convenient to use the methods of classical mechanics. Since the metric allows an arbitrary transformation of time, then the corresponding field variable (g_{00}) is included in the Lagrangian without time derivative. It is a non-dynamic variable, and is included in the Lagrangian as a Lagrange multiplier. A variation of the action on this variable gives the constraint. It turns out that Hamiltonian is proportional to the constraint, and so it is zero. The corresponding Hamilton-Jacobi equation easily integrated. Hence, we find the relation between the SF and the metric. To restore of time dependence we using an equation $\partial L / \partial \dot{q} = \partial S / \partial q$. After using a gauge condition, it allows us to find solution. Thus, we find the evolution of the SF inside the BH, which describes the final stage of the gravitational collapse of a SF. It turns out that the mass BH associated with a scalar charge G of the corresponding SF inside the BH ratio $M = G/(2\sqrt{\kappa})$.

Keywords: scalar field, black hole, Einstein equations.

1. Introduction

One of the most interesting objects in astrophysical and cosmological applications of General relativity (GR) is a scalar field. However, the models with scalar field known only for the simplest configurations, due to the difficulties of obtaining analytical solutions. So for a massless scalar field in General relativity is widely known spherically symmetric static solution of Fisher (1948) and its various later modifications (Janis, Newman, Winicour (1968); Wyman (1981); Agnese and La Camera. (1985)). Analytical solutions for the system of static scalar and electromagnetic fields in General relativity for spherical symmetry built Bronnikov (1972), Zaitsev, Kolesnikov and Radynov (1972), and then Korkina (1976) in different coordinate systems. All these solutions are unstable and

have naked singularity. It turns out that for systems with a scalar field analogue of Birkhoff theorem on the uniqueness of the solution fails, and in addition, there is no conserved scalar charge. Therefore, a static configuration with a scalar field which satisfies the Einstein equations, due to negligible fluctuations, coming out of this mode and begins to evolve.

For dynamic spherically symmetric problems, due to the obvious difficulties in obtaining solutions of Einstein's equations in closed form, most of the work performed numerically. Roberts (1989) has built one of the few analytical solutions in closed form. Initially, he scheduled to use it as a counter-example to the hypothesis of cosmic censorship. However, later Brady (1994); Oshiro, Nakamura and Tomimatsu (1994) rediscovered this solution in the context of critical gravitational collapse

Spherically symmetric collapse of a scalar field is the perfect model for studying the dynamics of strong field in general relativity. Therefore, in this model used analytical and numerical methods. In particular, Christodoulou (1987) rigorously established global existence and uniqueness of solutions of the Einstein equations for a scalar field. He proved that the space of General relativity together with spherically symmetric scalar field with a sufficiently weak (in some sense) initial data evolves in Minkowski space-time, while the class sufficiently strong data forms a BH.

The behavior of the scalar field near the threshold of BH formation was first investigated Choptuik (1993). He numerically solved the Einstein equations for spherically symmetric systems of the gravitational and massless scalar fields with minimal coupling. He studied the gravitational collapse for different sets of one-parameter families of the initial data. For example, they can be taken as a family of Gaussian pulses

$$\varphi(0, v) = p v^2 \exp(-(v - v_0)^2 / \sigma^2).$$

Suppose that for a given family the parameter p is chosen in such a way that for small values of p the gravitational field in during the evolution of is too weak to form a BH (the field is scattered), while for large values of parameter p is formed BH. Then between these two limits, there is a critical value of this parameter p^* in which first formed the BH. Solutions for which $p < p^*$ are called subcritical and solving for $p > p^*$ – supercritical, respectively. Choptuik proved that in the collapse may occur arbitrarily small BH. Moreover, when $p > p^*$ the mass of the BH is given by

$$M_{BH}(p) \propto \left| p - p^* \right|^\beta,$$

where the exponent β has a universal value $\gamma = 0.374$ for all 1-parameter families of scalar field data. There are still a number of other features critical gravitational collapse of a scalar field, for example, discrete and continuous self-similarity, and others. Work Choptuik is an example of when the discovery of a new phenomenon in General relativity was done numerically. The discovery of universal properties of critical collapse is one of significant achievements the numerical relativity (Novikov & Frolov, 2001).

2. The action and its reduction

Consider the evolution of spherically symmetric massless scalar field in the supercritical case, when $p > p^*$. In this case, at the final stage of the gravitational collapse is formed the black hole with a mass $M_{BH}(p)$. The residual relaxation phenomena associated with scattering of the remnants of the scalar field at infinity, do not affect the black hole and can be ignored.

According to the no-hair theorem Chase (1970) and Bekenstein (1972), the BH has no of neutral "scalar hairs" (as, indeed, and charged), therefore on the final stage of the gravitational collapse a scalar field is completely under the horizon, inside a black hole. Beyond the BH, we have the free vacuum gravitational field described by the Schwarzschild solution. Thus, the study of the final stage the gravitational collapse a scalar field, by definition, is to construction of the solution of Einstein equations describing the evolution of scalar field inside the BH and satisfying appropriate boundary conditions.

In view with the above, we assume that the space-time inside a BH is described by the spherically symmetric metric, depending on time

$$ds^2 = e^{v(t)} c^2 dt^2 - e^{\lambda(t)} dr^2 - e^{\mu(t)} d\sigma^2, \\ d\sigma^2 = d\theta^2 + \sin^2 \theta d\alpha^2.$$

For simplicity, consider the evolution of the homogeneous scalar field $\psi = \psi(t)$. Note that the metric admits an arbitrary gauge transformation time $t = t(\tilde{t})$, which induces the transformation of the metric coefficient $e^{\tilde{v}} = e^v (dt / d\tilde{t})^2$. Thus, there is a gauge arbitrariness in the definition of the metric function $e^v = N^2$.

$$S = \int \Lambda \sqrt{-g} d^4 x. \\ \Lambda = -\frac{1}{4\pi} \left[\frac{c^4}{4k} R - \frac{1}{2} g^{\mu\nu} \varphi_{,\mu} \varphi_{,\nu} \right].$$

Here scalar curvature R in this case is equal to

$$R = -2e^{-\mu} - \frac{e^{-v}}{c^2} (2\ddot{\mu} + \ddot{\lambda} + \frac{3}{2} \dot{\mu}^2 + \dot{\mu}\dot{\lambda} - \\ - \dot{\mu}\dot{v} + \frac{1}{2} \dot{\lambda}^2 - \frac{1}{2} \dot{v}\dot{\lambda}), \\ \sqrt{-g} = e^{\mu+(v+\lambda)/2} \sin \theta,$$

where the point denotes d/dx^0 . After the integration over the angles, the action takes the form

$$S = \int L dx^0 dr, \\ L = \frac{1}{2c^2} \left[\frac{c^4}{2k} (2\ddot{\mu} + \ddot{\lambda} + \frac{3}{2} \dot{\mu}^2 + \dot{\mu}\dot{\lambda} - \dot{\mu}\dot{v} + \frac{1}{2} \dot{\lambda}^2 - \frac{1}{2} \dot{v}\dot{\lambda}) + \dot{\varphi}^2 \right] e^{\frac{\lambda-v}{2} + \mu} + \frac{c^4}{2k} e^{\frac{v+\lambda}{2}}.$$

Since the Lagrangian and the field variables is independent from the coordinate r , it possible to be limited to the one-dimensional system with the action

$$\tilde{S} = \int L dx^0.$$

Extracting total time derivative, we obtain an effective Lagrangian

$$\tilde{L} = -\frac{1}{2c^2} \left[\frac{c^4}{2k} \left(\frac{1}{2} \dot{\mu}^2 + \dot{\mu}\dot{\lambda} \right) - \dot{\varphi}^2 \right] e^{\frac{\lambda-v}{2} + \mu} + \frac{c^4}{2k} e^{\frac{v+\lambda}{2}}.$$

For diagonalization of the Lagrangian, we make a change of field variables

$$\mu = \omega - \lambda, \quad v = \rho - \lambda.$$

Then

$$\tilde{L} = \frac{1}{2} \left[\frac{\dot{\varphi}^2}{c^2} - \frac{c^3}{4k} (\dot{\omega}^2 - \dot{\lambda}^2) \right] e^{\omega - \rho/2} + \frac{c^4}{2k} e^{\rho/2}.$$

In the new variables, the metric takes the form

$$ds^2 = e^{-\lambda} (e^\rho c^2 dt^2 - e^\omega d\sigma^2) - e^\lambda dr^2.$$

3. The equation of Hamilton-Jacobi in the minisuperspace

To solve the problem under consideration is convenient to use the methods of classical mechanics. From the point of view of the classical mechanics, the metric coefficients and a scalar field in the resulting Lagrangian are the generalized coordinates (coordinates of a minisuperspace Wheeler-DeWitt).

Note that the metric allows arbitrary gauge transformation of time, and the corresponding metric variable e^ρ enters the Lagrangian without time derivative. Therefore, it is a non-dynamic variable and is included in the Lagrangian as the Lagrange multiplier. Variation of the Lagrangian on this variable gives us the constraint:

$$\frac{\partial \tilde{L}}{\partial \rho} = -\frac{1}{4} \left[\frac{\dot{\varphi}^2}{c^2} - \frac{c^2}{4k} (\dot{\omega}^2 - \dot{\lambda}^2) \right] e^{\omega - \rho/2} + \frac{c^4}{4k} e^{\rho/2} = 0.$$

Next, we find momenta, conjugate of the dynamic variables $\{\varphi, \omega, \lambda\}$:

$$p_\varphi = \frac{\partial \tilde{L}}{\partial \dot{\varphi}} = \frac{\dot{\varphi}}{c^2} e^{\omega - \rho/2}, \quad p_\omega = \frac{\partial \tilde{L}}{\partial \dot{\omega}} = -\frac{c^2}{4k} \dot{\omega} e^{\omega - \rho/2}, \\ p_\lambda = \frac{\partial \tilde{L}}{\partial \dot{\lambda}} = \frac{c^2}{4k} \dot{\lambda} e^{\omega - \rho/2},$$

and Hamiltonian

$$H = \frac{1}{2} \left[\left(c^2 p_\varphi^2 - \frac{4k}{c^2} (p_\omega^2 - p_\lambda^2) \right) e^{\frac{\rho}{2} - \omega} \right] - \frac{c^4}{2k} e^{\frac{\rho}{2}}.$$

Comparing the Hamiltonian with the constraint, it is easy to see that they are proportional

$$H = -2 \frac{\partial \tilde{L}}{\partial \rho}.$$

Hence, by virtue of Lagrangian constraint $\partial L / \partial \rho = 0$ it follows the Hamiltonian constraint

$$\frac{1}{2} c^2 p_\varphi^2 - \frac{2k}{c^2} (p_\omega^2 - p_\lambda^2) e^{\frac{\rho}{2} - \omega} - \frac{c^4}{2k} e^{\frac{\rho}{2}} = 0.$$

The latter is a consequence of the invariance of the theory with respect to gauge transformations $t = t(\tilde{t})$. Next, substituting momenta

$$p_\varphi = \frac{\partial S}{\partial \varphi}, \quad p_\lambda = \frac{\partial S}{\partial \lambda}, \quad p_\omega = \frac{\partial S}{\partial \omega}$$

in the Hamiltonian constraint, we come to the Hamilton-Jacobi equation (HJE)

$$c^2 \left(\frac{\partial S}{\partial \varphi} \right)^2 - \frac{4k}{c^2} \left(\frac{\partial S}{\partial \omega} \right)^2 + \frac{4k}{c^2} \left(\frac{\partial S}{\partial \lambda} \right)^2 = \frac{c^4}{k} e^{\omega}.$$

This equation is one-dimensional minisuperspace analogue of the Peres equation in the functional derivatives in a superspace. The variable $e^{\rho/2}$ is not included in the GJE and is not related with the minisuperspace dynamics. Thus, the 3-geometry minisuperspace with coordinates φ , e^λ , e^ω is defined by diffeomorphic invariant way. It is easy to see that this equation is the GJE for the geodesic in minisuperspace in terms minisupermetric (in a potential space). Indeed, let us rewrite the action for the diagonalized Lagrangian

$$\tilde{S} = \iint \left[\left(\frac{\dot{\varphi}^2}{2c^2} - \frac{c^3}{8k} (\dot{\omega}^2 - \dot{\lambda}^2) \right) e^{\omega - \rho/2} + \frac{c^4}{2k} e^{\rho/2} \right] dx^0.$$

Nondynamical variable can be eliminated. In order to do this we find the variable $e^{\rho/2}$ from the constraint equation

$$e^{\rho/2} = \frac{\sqrt{k}}{c^2} \sqrt{\frac{\dot{\varphi}^2}{c^2} - \frac{c^2}{4k} (\dot{\omega}^2 - \dot{\lambda}^2)} e^{\omega/2},$$

and substitute into the action. The result is

$$\tilde{S} = \int \tilde{L} dx^0 = \frac{c^2}{\sqrt{k}} \int e^{\omega/2} \sqrt{\frac{\dot{\varphi}^2}{c^2} - \frac{c^2}{4k} (\dot{\omega}^2 - \dot{\lambda}^2)} dx^0.$$

From here we have

$$\tilde{S} = \frac{c^2}{\sqrt{k}} \int e^{\omega/2} \sqrt{\frac{d\varphi^2}{c^2} - \frac{c^2}{4k} (d\omega^2 - d\lambda^2)}.$$

It is easy to show that the equations resulting from the variational principle $\delta S = 0$ together with the constraint are equivalent to the Einstein equations for the original

metric. Taking the differential from the action and placed in the square, we obtain the interval in a minisuperspace

$$d\tilde{S} = \frac{c^2}{\sqrt{k}} e^{\omega/2} \sqrt{\frac{d\varphi^2}{c^2} - \frac{c^2}{4k} (d\omega^2 - d\lambda^2)},$$

$$d\tilde{S}^2 = G_{ab} dq^a dq^b = \frac{c^4}{k} e^{\omega} \left[\frac{d\varphi^2}{c^2} - \frac{c^2}{4k} (d\omega^2 - d\lambda^2) \right].$$

4. Solutions of the Hamilton-Jacobi equation

We are searching the solution GJE in the form

$$S = a\lambda + b\varphi + V(\omega).$$

Then the function $V(\omega)$ is determined by the integral

$$V(\omega) = \int \sqrt{A^2 - e^{\omega} \varepsilon^2} d\omega,$$

where

$$A^2 = a^2 + \frac{c^4}{4k} b^2, \quad \varepsilon^2 = \frac{c^6}{4k^2}.$$

Thus, we find for the action

$$S = a\lambda + b\varphi + \int \sqrt{A^2 - e^{\omega} \varepsilon^2} d\omega.$$

From the relations

$$\frac{\partial S}{\partial a} = \ln N, \quad \frac{\partial S}{\partial b} = \varphi_0,$$

we find the connection between the scalar field φ and metric functions λ , e^ω . In order to restore the time dependence, we use the equation

$$p_\omega = \frac{\partial L}{\partial \dot{\omega}} = \frac{\partial S}{\partial \omega}.$$

As a result, we obtain

$$-\frac{c^2}{4k} e^{\omega - \rho/2} \dot{\omega} = \sqrt{A^2 - e^{\omega} \varepsilon^2}.$$

Choosing the gauge condition

$$e^{\rho/2} = 1,$$

we find

$$\int \frac{e^{\omega} d\omega}{\sqrt{A^2 - e^{\omega} \varepsilon^2}} = -\frac{4k}{c^2} t.$$

Hence we obtain the equation

$$e^{\omega} = B^2 - c^2 t^2.$$

Where

$$B^2 = \frac{k}{c^2} \left(\frac{4k}{c^4} a^2 + b^2 \right).$$

Thus the metric takes the form

$$ds^2 = e^{-\lambda} \left(e^{\rho} c^2 dt^2 - (B^2 - c^2 t^2) d\sigma^2 \right) - e^{\lambda} dr^2.$$

Furthermore, we find the remaining variables φ and λ , as function of time t . From the relations

$$\frac{\partial S}{\partial a} = \ln N, \quad \frac{\partial S}{\partial b} = \varphi_0,$$

it follows that

$$\lambda + a \int \frac{d\omega}{\sqrt{A^2 - e^{\frac{\omega}{\varepsilon}}}} = \ln N,$$

$$\varphi + \frac{c^4 b}{4k} \int \frac{d\omega}{\sqrt{A^2 - e^{\frac{\omega}{\varepsilon}}}} = \varphi_0.$$

Taking into account

$$e^{\omega} = B^2 - c^2 t^2, \quad B^2 = \frac{k}{c^2} \left(\frac{4k}{c^4} a^2 + b^2 \right),$$

$$A^2 = a^2 + \frac{c^4}{4k} b^2, \quad \varepsilon^2 = \frac{c^6}{4k^2},$$

from here we find

$$e^{\lambda} = N \left| \frac{B+ct}{B-ct} \right|^p, \quad p = \frac{2ak}{Bc^3},$$

$$\varphi = \varphi_0 + \frac{cb}{2B} \ln \left| \frac{B+ct}{B-ct} \right|,$$

where

$$B^2 = \frac{1}{c^6} (4k^2 a^2 + kb^2 c^4), \quad N = \text{const.}$$

Thus, the metric and the scalar field inside the BH take the form

$$ds^2 = N^{-1} \left(\frac{B+ct}{B-ct} \right)^{-p} \left[c^2 dt^2 - (B^2 - c^2 t^2) d\sigma^2 \right] -$$

$$- N \left(\frac{B+ct}{B-ct} \right)^p dr^2.$$

$$\varphi = \varphi_0 + \frac{cb}{2B} \ln \left| \frac{B+ct}{B-ct} \right|, \quad -B < ct < B.$$

5. Determination constants

To find the constant, we can use the correspondence principle. When the scalar field vanishes, the resulting solution should be the same with the Schwarzschild solution in the T-region. Therefore, we put $b=0$, $\varphi_0=0$. Then

$$B = \frac{2ka}{c^3}, \quad p=1.$$

$$ds^2 = N^{-1} \left[\frac{2ka/c^3 + ct}{2ka/c^3 - ct} c^2 dt^2 - \left(\frac{2ka}{c^3} - ct \right)^2 d\sigma^2 \right] -$$

$$- N \frac{2ka/c^3 + ct}{2ka/c^3 - ct} dr^2.$$

After replacing

$$T = \frac{2ka}{c^4} - t,$$

we have

$$ds^2 = N^{-1} \left[\left(\frac{4ka}{c^4 T} - 1 \right)^{-1} c^2 dT^2 - c^2 T^2 d\sigma^2 \right] -$$

$$- N \left(\frac{4ka}{c^4 T} - 1 \right) dr^2.$$

This metric coincides with the Schwarzschild solution

$$ds^2 = \left(1 - \frac{2km}{c^2 R} \right) c^2 dt^2 - \left(1 - \frac{2km}{c^2 R} \right)^{-1} dR^2 - R^2 d\sigma^2$$

in the T-region, when we replace $cT \rightarrow R$, $r \rightarrow ct$ and choice the constants $N=1$, $a=mc/2$. Thus, the solution can be written in the form

$$ds^2 = \left(\frac{B+ct}{B-ct} \right)^{-p} \left[c^2 dt^2 - (B^2 - c^2 t^2) d\sigma^2 \right] -$$

$$- \left(\frac{B+ct}{B-ct} \right)^p dr^2,$$

$$\varphi = \varphi_0 + \frac{G}{2B} \ln \left| \frac{B+ct}{B-ct} \right|,$$

$$-B < ct < B, \quad B = \frac{1}{c^2} \sqrt{k^2 m^2 + kG^2},$$

$$p = \frac{km}{\sqrt{k^2 m^2 + kG^2}},$$

where we introduced the scalar charge $G=cb$.

6. Conclusion

In the obtained solution about free scalar field, except the scalar charge, any other constants should not be. Therefore, we should put $m=0$ and $p=0$. Then we have

$$B = \frac{\sqrt{kG}}{c^2}.$$

In this case, the metric and scalar field take the form

$$ds^2 = c^2 dt^2 - dr^2 - c^2 (t_G^2 - t^2) d\sigma^2,$$

$$\varphi = \frac{c}{2\sqrt{k}} \ln \left| \frac{t_G + t}{t_G - t} \right|, \quad -t_G < t < t_G.$$

where we have introduced the constant

$$t_G = \frac{B}{c} = \frac{\sqrt{kG}}{c^3}.$$

We take into account that at a maximum expansion (at the boundary of BH), when $t=t_G$, the scalar field vanishes, $\varphi_0=0$. This metric correspond the scalar field confinement under the horizon BH by the gravitational interaction.

Note that the spatial part of the metric describes a

metric of hypercylinder $R^1 \otimes S^2$.

$$dl^2 = dr^2 + c^2(t_G^2 - t^2)d\sigma^2.$$

Here $R = c\sqrt{t_G^2 - t^2}$ is the radius of hypercylinder, which when time changing within $-t_G < t < t_G$ first increases $0 < R < ct_G$, and then decreases $ct_G > R > 0$. At $t = t_G$ we have a singularity. The radius $R = t_G$ corresponds to the horizon in the Schwarzschild metric.

Note that this solution has an analogue in the R-region, which are considered by Denisova et al (1999). Their metrics can be rewritten as

$$ds^2 = c^2 dt^2 - dR^2 - (R^2 - R_0^2) d\sigma^2.$$

Where $R_0^2 < R^2 < \infty$. When $R^2 = R_0^2$ this metric has a naked singularity. This metric corresponds to a scalar field coupled gravitational interaction

$$\psi = \frac{c^2}{2\sqrt{k}} \ln \frac{R - R_0}{R + R_0},$$

and physically is not connected with the interior of a black hole with collapsing scalar field, because it is another solution.

Note that after replacing the time coordinate

$$T = \sqrt{t_G^2 - t^2}, \quad 0 < T < t_G,$$

the obtained metric inside a BH with a scalar field takes the form

$$ds^2 = \frac{c^2 dT^2}{t_G^2 / T - 1} - dr^2 - c^2 T^2 d\sigma^2.$$

It turns out that scalar curvature $R_{\beta\alpha\gamma}^{\alpha} g^{\beta\gamma}$ and Kretschman invariant $K = R_{\alpha\beta\alpha\gamma} R^{\alpha\beta\alpha\gamma}$ on the boundary $t = 0$ ($T = t_G$) are the finite quantities, while in the center, when $t = t_G$ ($T = 0$) they go to infinity. Since the boundary $t = 0$ ($T = t_G$) is regular, therefore it can be matched with the external vacuum solution for the BH, i.e. with the Schwarzschild metric. From the matched condition of the angular parts of the metrics, we obtain the relation between the scalar charge G , collapsed scalar field, and the BH mass M :

$$G = 2M\sqrt{k}.$$

Note that the mass function

$$M = \frac{c^2}{2k} R \left(1 + (\nabla R)^2 \right),$$

for the given solution takes the form

$$M = \frac{c^2}{2k} \frac{c^2 t_G^2}{c\sqrt{t_G^2 - t^2}}.$$

Hence, at the boundary value of time $t = 0$, we have

$$M(0) = \frac{c^2}{2k} ct_G = \frac{G}{2\sqrt{k}}.$$

This again confirms the connection the BH mass with the scalar charge into the BH. In the center of $t = t_G$ and mass function diverge.

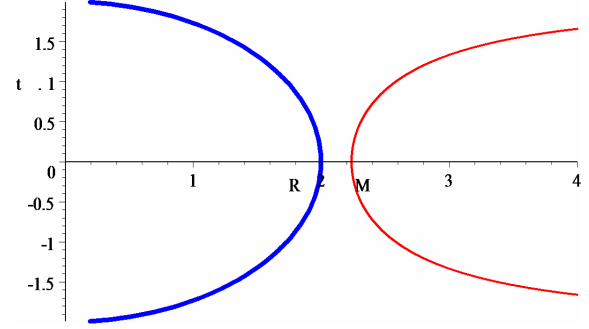


Figure 1: The behavior of the mass function and the hypercylinder radius in universe with homogeneous scalar field.

The behavior of the mass function and the hypercylinder radius represented on the figure 1.

Here, the ordinate represents time t , and abscissa is the radius of hypercylinder R and the mass function M . We see that when the time changes from $-t_G$ to $t_G = \sqrt{k}G/c^3 = 2kM/c^3$ the hypercylinder radius grows from zero, reaches the maximum is equal to $ct_G = \sqrt{k}G/c^2 = 2kM/c^2$ at $t = 0$ and then decreases again to zero. At the same time the mass function simultaneously decreases and reaches a minimum is equal of the mass $M(0) = c^3/2kt_G = G/2\sqrt{k} = M_{BH}$ external BH at $t=0$ is and rises again to infinity.

Therefore, we obtained formulas describing the evolution of the homogeneous scalar field inside the BH. It corresponds to the final stage of the gravitational collapse some scalar field with such initial conditions that lead to the homogeneous distribution of the scalar field inside the BH.

References

- Fisher I.Z.: 1948, *JETF*, **18**, 636.
 Janis A.I., Newman E.T., Winicour J.: 1968, *Phys. Rev. Lett.* **20**, 878.
 Wyman M.: 1981, *Phys. Rev. D*, **24**, 839.
 Agnese A.G., La Camera M.: 1985, *Phys. Rev. D*, **31**, 1280.
 Bronnikov K.A.: 1972, *Preprint ITF-72-20P*.
 Zaitsev N.A., Kolesnikov S.M., Radynov A.G.: 1972, *Preprint ITF-72-21P*.
 Korkina M.P.: 1976, *Preprint ITF-76-93P*.
 Roberts M.D.: 1989, *GRG*, **21**, 907.
 Brady P.R.: 1994, *Class. Quant. Grav.*, **11**, 1255.
 Oshiro Y., Nakamura K., Tomimatsu A.: 1994, *Prog. Theor. Phys.* (arXiv: gr-qc/9402017).
 Christodoulou D.: 1987, *Commun. Math. Phys.* **109**, 613.
 Choptuik M.W.: 1993, *Phys. Rev. Letters* **70**, 9.
 Novikov I.D., Frolov V.P.: 2001, *UFN*, **171**, 307.
 Chase J.E.: 1970, *Commun. Math. Phys.*, **19**, 276.
 Bekenstein J.D.: 1972, *Phys. Rev. Letters*, **28**, 452; 1972, *Phys. Rev. D*, **5**, 1239 and 2403.
 Denisova I.P., Mehta B.V., Zubrilov A.A.: 1999, *GRG*, **31**, 821.

FIVE DIMENSIONAL BOOSTS AND ELECTROMAGNETIC FIELD IN KALUZA-KLEIN THEORY

V.D. Gladush¹, Nadim Al-Shawaf²

¹ Dnipropetrovsk National University, Gagarin Ave,
725014, Ukraine, *vgladush@gmail.com*

² Uppsala University, Sweden, *tms2006@gmail.com*

ABSTRACT. A stationary, spherically symmetric, 5D Kaluza-Klein theory exhibits 5D boosts. After reduction of 5D vacuum Einstein action of a diagonal 5D metric, we obtained Einstein equations with energy-momentum tensor of a massless scalar field. Applying a 5D boost generates a non-diagonal metric with an electric field. This electric field is trivial, since it can be removed by a reverse 5D boost. Existence of such kind of trivial fields is analyzed on the example previously known solutions. Transformation properties of physical fields relative to 5D boosts examined. This symmetry is a subgroup of $SL(3, R)$ symmetries of 5D equations, rewritten in 3 + 2-decomposition in stationary, spherically symmetric case. This symmetry also can be used to generate new solutions. The solution with trivial electric field is obtained from diagonal 5D metric by a simple symmetry transformation, which reduces to the coordinate 5D boosts.

Keywords: Kaluza-Klein theory, decomposition, electric field, symmetry.

1. Introduction

In a framework of the usual 5D Kaluza-Klein theory (KK), we consider M^5 space with the following 5D metric:

$${}^{(5)}ds^2 = {}^{(5)}g_{AB}dx^A dx^B, \quad (1)$$

where $\{A, B = 0, 1, 2, 3, 4\} = \{\mu, \nu = 0, 1, 2, 3\} \cup \{4\}$, x^μ – are space-time coordinates, $x^4 = z$ – fifth coordinate.

As it is known, KK theory is based on two postulates:

1. Cylindrical condition, according to which, the space M^5 admits a space-like Killing vector $\vec{\xi}$. In the corresponding coordinate system it has the form $\vec{\xi} = \partial/\partial z$, that leads to metric's independence of the fifth coordinate z , that is ${}^{(5)}g_{AB} = {}^{(5)}g_{AB}(x^\mu)$.
2. Closure condition, which states that the space M^5 is closed relative to coordinate z .

Four dimensional physical space can be derived by dimensional reduction of M^5 space, and it's corresponding action. This can be accomplished by orthogonal 4 + 1 splitting of M^5 space, and then projecting all quantities on the physical space-time M^4 . In result we get the following form of the 5D metric:

$$\begin{aligned} {}^{(5)}ds^2 &= {}^{(5)}g_{\mu\nu}dx^\mu dx^\nu + 2{}^{(5)}g_{\mu 4}dx^\mu dx^4 + {}^{(5)}g_{44}dz^2 \\ &= V^{-1}h_{\mu\nu}dx^\mu dx^\nu - V^2(dz + A_\mu dx^\mu)^2, \end{aligned} \quad (2)$$

where:

$${}^{(5)}g_{\mu\nu} = V^{-1}h_{\mu\nu} - V^2 A_\mu A_\nu, \quad (3)$$

$${}^{(5)}g_{4\nu} = -V^2 A_\nu, \quad {}^{(5)}g_{44} = -V^2. \quad (4)$$

This splitting leads to the following physical space-time metric:

$$h_{\mu\nu} = {}^{(5)}g_{\mu\nu} - \frac{{}^{(5)}g_{4\nu} {}^{(5)}g_{4\mu}}{{}^{(5)}g_{44}}, \quad (5)$$

and the following electromagnetic field:

$$A_\nu = \frac{{}^{(5)}g_{4\nu}}{{}^{(5)}g_{44}}, \quad (6)$$

while the scalar field is:

$$V^2 = -(\vec{\xi}, \vec{\xi}) = -{}^{(5)}g_{44}. \quad (7)$$

After orthogonalization of the 5D action

$$S = -\frac{1}{4\pi L} \int d^5x \sqrt{{}^{(5)}g} \quad {}^{(5)}R \quad (8)$$

we extract a full derivative, and then integrating by the periodic coordinate z we get:

$$\begin{aligned} S &= -\frac{1}{4\pi L} \int d^4x \sqrt{h} \left\{ {}^{(4)}R - \frac{1}{2} \frac{(\nabla V)^2}{V^2} + \right. \\ &\quad \left. + \frac{V^3}{4} F_{\mu\nu} F^{\mu\nu} \right\}. \end{aligned} \quad (9)$$

Using the following natural variable substitution:

$$V = e^{\varphi/\sqrt{3}} \quad (10)$$

we get the following 5D metric:

$$\begin{aligned} {}^{(5)}ds^2 &= e^{-\varphi/\sqrt{3}} h_{\mu\nu} dx^\mu dx^\nu - \\ &- e^{2\varphi/\sqrt{3}} (dz + A_\mu dx^\mu)^2 \end{aligned} \quad (11)$$

and following 4D action of Einstein's form:

$$\begin{aligned} S &= -\frac{1}{4\pi L} \int d^4x \sqrt{h} \left\{ {}^{(4)}R - \frac{1}{2} (\nabla\varphi)^2 + \right. \\ &\left. + \frac{1}{4} e^{\sqrt{3}\varphi} F_{\mu\nu} F^{\mu\nu} \right\}. \end{aligned} \quad (12)$$

where $F_{\mu\nu} = A_{\nu,\mu} - A_{\mu,\nu}$ is an electromagnetic tensor, φ is a massless scalar field.

In summary, 5D variational principle for 5D manifold with a metric that subject to cylindrical and closure conditions, is equivalent to a 4D variation principle of a system with an interacting scalar, electromagnetic and gravitational fields, and above mentioned action.

2. Stationary space of 5D theory and boosts

Suppose that on M^5 space, in addition to the space-like Killing vector $\vec{\xi}_4$, there is also a time-like Killing vector $\vec{\xi}_0 = \partial/\partial x^0$ orthogonal to space directions. Thus we have

$$\text{ortgonal} \vec{\xi}_a = \frac{\partial}{\partial x^a} \quad (a = 0, 4). \quad (13)$$

Those two vectors induce a "2+3 splitting" of M^5 space, and the metric becomes:

$$\begin{aligned} {}^{(5)}ds^2 &= {}^{(2)}ds^2 + {}^{(3)}ds^2 \\ &= \gamma_{ab}(x^k) dx^a dx^b - h_{ij}(x^k) dx^i dx^j, \end{aligned} \quad (14)$$

where $\{a, b = 0, 4\}$ and $\{i, j, k = 1, 2, 3\}$. The Killing vector $\vec{\xi}_a$ is subject to the transformations:

$$\vec{\eta}_{\tilde{a}} = L_{\tilde{a}}^b \vec{\xi}_b = L_{\tilde{a}}^b \frac{\partial}{\partial x^b} = \frac{\partial}{\partial x^{\tilde{a}}}, \quad (15)$$

where $\vec{\eta}_{\tilde{a}}$ – new Killing vectors, $L_{\tilde{a}}^b$ – a constant invertible matrix. Herewith, this "2+3 splitting" of the metric (14) is form invariant. This transformation, can be also induced by the following linear coordinate transformation $\{x^0, x^4\} = \{\tilde{x}^a\}$:

$$\begin{aligned} \tilde{x}^{\tilde{a}} &= L_{\tilde{a}}^b x^b, \quad L_{\tilde{a}}^b L_c^{\tilde{a}} = \delta_c^b, \\ \det \|L_{\tilde{a}}^b\| &= L_0^0 L_4^4 - L_4^0 L_0^4 = \pm 1. \end{aligned}$$

In this text we will use only the positive sign. This transformations keeps the interval ${}^{(2)}ds^3$ structure unchanged. While the 2D metric $\gamma_{ab}(x^k)$ transforms according to:

$$\tilde{\gamma}_{\tilde{a}\tilde{b}}(\tilde{x}^k) = L_{\tilde{a}}^b L_{\tilde{b}}^c \gamma_{bc}(x^k).$$

Let the metrics $\tilde{\gamma}_{\tilde{a}\tilde{b}}(\tilde{x}^k)$ and $\gamma_{ab}(x^k)$ are asymptotically flat, i.e. in spatial infinity our metric is pseudo-euclidean:

$$\lim_{r \rightarrow \infty} \gamma_{ab}(x^k) = \eta_{ab}, \quad \lim_{r \rightarrow \infty} \tilde{\gamma}_{\tilde{a}\tilde{b}}(\tilde{x}^k) = \eta_{\tilde{a}\tilde{b}},$$

where η_{ab} – is 2D Minkowski tensor. Then:

$$\begin{aligned} \eta_{\tilde{a}\tilde{b}} &= \lim_{r \rightarrow \infty} \tilde{\gamma}_{\tilde{a}\tilde{b}}(\tilde{x}^k) = \lim_{r \rightarrow \infty} L_{\tilde{a}}^a L_{\tilde{b}}^b \gamma_{ab}(x^k) \\ &= L_{\tilde{a}}^a L_{\tilde{b}}^b \lim_{r \rightarrow \infty} \gamma_{ab}(x^k) = L_{\tilde{a}}^a L_{\tilde{b}}^b \eta_{ab}. \end{aligned}$$

Thus, those transformations, at infinity approaches 2D Lorentz transformations, or 5D boosts in $\{x^a\} = \{x^0 = t, x^4 = z\}$ coordinates, with a property:

$$L_{\tilde{a}}^a L_{\tilde{b}}^b \eta_{ab} = \eta_{\tilde{a}\tilde{b}}. \quad (16)$$

In consequence, we have 2D Lorentz transformations:

$$\begin{aligned} x^0 &= \frac{\tilde{x}^0 + v\tilde{x}^4/c}{\sqrt{1 - V^2/c^2}} = \tilde{x}^0 \cosh \alpha + \tilde{x}^4 \sinh \alpha, \\ x^4 &= \frac{\tilde{x}^4 + v\tilde{x}^0/c}{\sqrt{1 - V^2/c^2}} = \tilde{x}^0 \sinh \alpha + \tilde{x}^4 \cosh \alpha, \end{aligned}$$

where:

$$\tanh \alpha = \frac{v}{c},$$

Herewith, the physical quantities transforms as:

$$\tilde{h}_{\tilde{0}\tilde{0}} = -\frac{\det \gamma_{ab}}{\sqrt{-V^{-1}h_{00} \sinh^2 \alpha + V^2 (A_0 \sinh \alpha + \cosh \alpha)^2}};$$

$$\tilde{A}_{\tilde{0}} = \frac{(V^{-3}h_{00} - A_0^2 - 1) \tanh \alpha - A_0 (1 + \tanh^2 \alpha)}{V^{-3}h_{00} \tanh^2 \alpha - (A_0 \tanh \alpha + 1)^2};$$

$$\tilde{V}^2 = -V^{-1}h_{00} \sinh^2 \alpha + V^2 (A_0 \sinh \alpha + \cosh \alpha)^2.$$

Note that the metric' determinant

$$\det \gamma_{ab} = \gamma_{00}\gamma_{44} - (\gamma_{04})^2 = -\frac{h_{00}}{V} = \text{inv} \quad (17)$$

actually an invariant.

Those transformations, physically corresponds to using a moving frame of reference of the fifth coordinate \tilde{x}^4 , which according to the Kaluza-Klein postulates, is closed.

Let our initial metric be diagonal, this will correspond to that there is no electromagnetic field. Owing to 5D boosts, and bearing in mind that $\gamma_{04} = 0$, and $A_0 = \gamma_{04}/\gamma_{44} = 0$ we get:

$$\tilde{h}_{\tilde{0}\tilde{0}} = \frac{-Vh_{00}}{\sqrt{V^2 \cosh^2 \alpha - V^{-1}h_{00} \sinh^2 \alpha}}, \quad (18)$$

$$\tilde{A}_{\tilde{0}} = \frac{(V^{-1}h_{00} - V^2) \tanh \alpha}{V^{-1}h_{00} \tanh^2 \alpha - V^2}, \quad (19)$$

$$\tilde{V}^2 = V^2 \cosh^2 \alpha - V^{-1}h_{00} \sinh^2 \alpha. \quad (20)$$

So we see that after 5D Lorentz transformations, the metric becomes non-diagonal. In 4D physical space-time it will correspond the appearance of the electromagnetic field. This means that we actually generating electromagnetic field with its correspondent effective electric charge. This electric field corresponds to a global 5D boost, so we call it trivial field, due to the fact that applying backward 5D boost (by coordinate transformation $\tilde{x}^{\tilde{a}} = L_{\tilde{b}}^{\tilde{a}} x^b$) this field can be removed (a removable electric charge).

To find the condition under which this electromagnetic field can be removed, we consider the transformation of the metric $^{(2)}ds^2$ by the 2D boost $x^b = L_{\tilde{a}}^b \tilde{x}^{\tilde{a}}$:

$$\tilde{\gamma}_{\tilde{a}\tilde{b}}(\tilde{x}^k) = L_{\tilde{a}}^a L_{\tilde{b}}^b \gamma_{ab}(x^k), \quad (21)$$

$$\det(\tilde{\gamma}_{\tilde{a}\tilde{b}}) = \det \gamma_{ab} = inv. \quad (22)$$

From this we have:

$$\tilde{\gamma}_{\tilde{0}\tilde{0}} = \gamma_{00} \cosh^2 \alpha + \gamma_{04} \sinh 2\alpha + \gamma_{44} \sinh^2 \alpha \quad (23)$$

$$\tilde{\gamma}_{\tilde{0}\tilde{4}} = \frac{1}{2}(\gamma_{00} + \gamma_{44}) \sinh 2\alpha + \gamma_{04} \cosh 2\alpha, \quad (24)$$

$$\tilde{\gamma}_{\tilde{4}\tilde{4}} = \gamma_{00} \sinh^2 \alpha + \gamma_{04} \sinh 2\alpha + \gamma_{44} \cosh^2 \alpha \quad (25)$$

The requirement $\tilde{\gamma}_{\tilde{0}\tilde{4}} = 0$ leads us to the needed condition for 5D metric to be diagonalizable:

$$\frac{\gamma_{04}(x^k)}{\gamma_{00}(x^k) + \gamma_{44}(x^k)} = -\frac{1}{2} \tanh 2\alpha = const. \quad (26)$$

In terms of physical quantities, this conditions takes the form:

$$\frac{V^{-3}h_{00} - A_0^2 - 1}{A_0} = \coth \alpha + \tanh \alpha = const. \quad (27)$$

While the rest of the metric components will transform as:

$$\tilde{\gamma}_{\tilde{0}\tilde{0}} = \frac{\gamma_{00} \cosh^2 \alpha - \gamma_{44} \sinh^2 \alpha}{\cosh 2\alpha}, \quad (28)$$

$$\tilde{\gamma}_{\tilde{4}\tilde{4}} = \frac{\gamma_{44} \cosh^2 \alpha - \gamma_{00} \sinh^2 \alpha}{\cosh 2\alpha}. \quad (29)$$

Analyzing the conditions that will keep fifth coordinate space-like (i.e. conserve metric signature) when electric field is generated, with a consideration of the initial values $\gamma_{04} = 0$, and $A_0 = \gamma_{04}/\gamma_{44} = 0$, we have:

$$\tilde{V}^2 = V^2 \cosh^2 \alpha - V^{-1}h_{00} \sinh^2 \alpha \geq 0$$

$$\frac{v^2}{c^2} = \tanh^2 \alpha \leq \frac{V^3}{h_{00}} = \frac{(\gamma_{44})^2}{-\det \gamma_{ab}} = \frac{-\gamma_{44}}{\gamma_{00}}.$$

Thus, the allowed global boosts is when the coordinate velocity not larger than:

$$v \leq c \sqrt{-\frac{\gamma_{44}}{\gamma_{00}}}. \quad (30)$$

For asymptotically flat space, we conclude the expected result of $v \leq c$. With higher speeds, horizons are formed, and the meaning of fifth coordinate does change.

3. Examples of a removable and unremovable electric charge

3.1. A removable electric charge

In Chodos and Detweiler (1982) work, they obtained the following solution:

$$^{(5)}ds^2 = -e^\mu dt^2 + 2\tilde{A} dt dx + \varphi^2 dx^2 + e^\beta [dr^2 + r^2 d\sigma^2] \quad (31)$$

$$= ^{(4)}ds^2 + \varphi^2 (dx + A dt)^2, \quad (32)$$

$$^{(4)}ds^2 = -e^\nu dt^2 + e^\beta [dr^2 + r^2 d\sigma^2] \quad (32)$$

$$A = \frac{\tilde{A}}{\varphi^2}, \quad e^\nu = e^\mu + \frac{\tilde{A}^2}{\varphi^2} \quad (33)$$

where

$$\varphi^2 = a_1 \psi^{p_1} + a_2 \psi^{p_2}, \quad \psi = \left(\frac{r-B}{r+B} \right)^{\lambda/2B}, \quad (34)$$

$$e^\nu = e^\beta e^\mu + \frac{\tilde{A}}{\varphi^2} = \frac{\psi^2}{\varphi^2}, \quad (35)$$

$$e^\beta = \left(1 - \frac{B^2}{r^2} \right)^2 \frac{1}{\psi^2}, \quad (36)$$

$$\tilde{A} = \sqrt{-a_1 a_2} (\psi^{p_1} - \psi^{p_2}), \quad (37)$$

$$e^\mu = a_2 \psi^{p_1} + a_1 \psi^{p_2}, \quad (38)$$

$$A = \frac{\tilde{A}}{\varphi^2} = \frac{\sqrt{-a_1 a_2} (\psi^{p_1} - \psi^{p_2})}{a_1 \psi^{p_1} + a_2 \psi^{p_2}}, \quad (39)$$

$$E \equiv F_{rt} e^{-\nu/2} = \frac{Q}{r^2 \varphi^3} e^{-\beta/2}, \quad (40)$$

$$p_{1,2} = 1 \pm \sqrt{1 + \kappa}, \quad \kappa = 4 \left(\frac{4B^2}{\lambda^2} - 1 \right), \quad (41)$$

$$Q^2 = -a_1 a_2 (1 + \kappa) \frac{\lambda^2}{G}, \quad a_1 + a_2 = 1, \quad (42)$$

where $a_1, a_2, p_1, p_2, \lambda$, and B — constants.

We rewrite this metric in the form:

$$^{(5)}ds^2 = -(a_2 \psi^{p_1} + a_1 \psi^{p_2}) dt^2 + 2(\sqrt{-a_1 a_2} (\psi^{p_1} - \psi^{p_2})) dt dx + (a_1 \psi^{p_1} + a_2 \psi^{p_2}) dx^2 + e^\beta [dr^2 + r^2 d\sigma^2]$$

or:

$$^{(5)}ds^2 = -\psi^{p_2} (\sqrt{a_1} dt + \sqrt{-a_2} dx)^2 + \psi^{p_1} (\sqrt{-a_2} dt + \sqrt{a_1} dx)^2 + e^\beta [dr^2 + r^2 d\sigma^2]. \quad (43)$$

Now we see that the transformation:

$$T = \sqrt{a_1}t + \sqrt{-a_2}x, \quad (44)$$

$$X = \sqrt{-a_2}t + \sqrt{a_1}x \quad (45)$$

will give us the diagonal form of the metric:

$$-^{(5)}ds^2 = \psi^{p_2} dT^2 - \psi^{p_1} dX^2 - e^\beta [dr^2 + r^2 d\sigma^2], \quad (46)$$

So we have here an example of the removable electric field (charge).

In their work, authors claims that this is a general spherically symmetric solution of KK theory. However, in a general solution, there should be 4 independent parameters, more precisely: m - mass, q - electromagnetic charge, g - scalar charge, v - boost parameter. But here we have actually only three parameter: m , g , v , moreover, electromagnetic charge is actually some function of the rest of parameters, $q = q(v, m, g)$. So for the obtained electric field is an open question about the sense of the thus obtained electric field and charge

Frolov et al. (1987) carried out a formal embedding of the Kerr metric in the flat space M^5 , and then applied a boost. By this procedure they obtaining electromagnetic field, and even the scalar field. Of course, those are trivial fields, that can be removed by another global boost. Note that those authors reference to works of Gibbons (1982), Gibbons and Wiltshire (1985), where this method been developed.

We note also the work Vladimirov and Popov (1982), which uses a similar method of generating an electric field.

Apart from the question of the interpretation of this removable electric field, there are still problems related to the relationship between the the closure condition space 5D and 5D boost. In addition to that, it is appropriate to ask if there are solutions where electromagnetic field A_0 is unremovable by this procedure, and with an independent charge parameter q .

3.2. Unremovable Electric Charge

In work Gladush (1980), there is a solution of spherically-symmetric configuration of interacting scalar, electromagnetic and gravitational fields of 5D KK theory, with the following reduced metric and Lagrangian:

$$\Lambda = -\frac{1}{4\pi} \left[\frac{c^4}{4\kappa} R - \frac{1}{2} (\nabla\psi)^2 + \frac{1}{4} F_{\mu\nu} F^{\mu\nu} e^{\psi\sqrt{6}} \right], \quad (47)$$

$$^{(5)}ds^2 = \frac{1}{2} e^{-\psi\sqrt{2/3}} d\tau^2 - e^{2\psi\sqrt{2/3}} (dz + f dt)^2, \quad (48)$$

where 4D metric is:

$$^{(4)}ds^2 = e^\nu dt^2 - e^{-\nu} [dr^2 + (r^2 - a^2) d\sigma^2] \quad (49)$$

while the gravitational potential, scalar field, and electric field are:

$$e^\nu = u^{G\sqrt{3\kappa}/2a} \left[\frac{A+1}{2} u^{-p} - \frac{A-1}{2} u^p \right]^{-1/2} \quad (50)$$

$$\psi = -\frac{1}{4} \ln \left[u^{\frac{G}{a}} \left(\frac{A+1}{2u^p} - \frac{A-1}{2u^{-p}} \right) \sqrt{\frac{3}{\kappa}} \right] \quad (51)$$

$$f = \frac{q}{2p} \frac{1 - u^{2p}}{A + 1 - (A - 1) u^{2p}}, \quad (52)$$

$$u = \frac{r - a}{r + a}, \quad p = \frac{\sqrt{\kappa^2 m^2 - \kappa q^2}}{a}, \quad (53)$$

$$A = \frac{\pm \kappa m}{\sqrt{\kappa^2 m^2 - \kappa q^2}}, \quad (54)$$

$$a^2 = \kappa^2 m^2 - \kappa q^2 + \kappa G^2, \quad \kappa^2 m^2 - \kappa q^2 > 0 \quad (55)$$

Here, we have three independent parameters $\{m, q, G\}$, and the fourth parameter v can be included by applying some boost. There is no global transformation with constant coefficients, that can be used to remove the electromagnetic field, thus this field is unremovable.

In the work of Bronikov and Shikin (1977) a similar problem is solved for a system of interacting scalar, electromagnetic and gravitational fields, and with an action similar to above mentioned. But the field was interpreted not in the context of 5D theory. Also they used harmonic time gauge for the metric. However if we analyze it in the context of 5D theory, one finds that the electric field here as well is unremovable.

4. A symmetrical approach for constructing new solutions of 5D KK theory

For stationary spaces, in KK theory there is a method of constructing solutions by using internal symmetries of KK equations. This method has been developed in the papers of Maison Kramer and Neugebauer (1969), Maison (1979), Dobiash and Maison (1982), Clement (1986), Cvetic and Youm (1995) and others.

The stationary metric(14) 5D KK theory in 2+3 splitting: be rewritten as:

$$ds^2 = \gamma_{ab}(x^k) dx^a dx^b - \frac{\tilde{h}_{ij}(x^k)}{\tau} dx^i dx^j, \quad (56)$$

$$\tau = |\det \|\gamma_{ab}\||. \quad (57)$$

Then the 5D lagrangian for vacuum 5D space of KK theory is:

$$L = \sqrt{^{(5)}g} R,$$

by omitting the divergence, it can be rewritten as Lagrangian for the 4D space

$$L = \sqrt{\tilde{h}} \left\{ {}^{(3)}R - \frac{1}{4} \left[\gamma^{ab} \gamma^{cd} \gamma_{ac,k} \gamma_{bd,l}^{,k} + \gamma^2 (\tau^{-1})_{,k} (\tau^{-1})_{,l} \tilde{h}^{kl} \right] \right\}. \quad (58)$$

Furthermore, we introduce a symmetrical unimodular matrix 3×3 :

$$\chi = \begin{pmatrix} \gamma_{ab} & 0 \\ 0 & \tau^{-1} \end{pmatrix}, \quad (59)$$

such that $\det \chi = 1$. Then the Lagrangian can be rewritten as (σ -model):

$$L = \sqrt{\tilde{h}} \left\{ {}^{(3)}R - \frac{1}{4} Sp(\gamma^{-1} \gamma_{,k} \gamma^{-1} \gamma^{,k}) \right\}. \quad (60)$$

From this we get the following equations:

$$(\chi^{-1} \chi^{,k})_{;k} = 0, \quad (61)$$

$${}^{(3)}R_{ij} = \frac{1}{4} Sp(\chi^{-1} \chi_{,i} \chi^{-1} \chi_{,j}). \quad (62)$$

This system is invariant under group $SL(3, R)$ transformations of 3D matrices:

$$\chi \longrightarrow N \chi N^T, \quad N \in SL(3, R). \quad (63)$$

To force this metric γ_{ab} be asymptotically flat space, we should have at infinity:

$$\chi = \begin{pmatrix} 1 & & \\ & -1 & \\ & & -1 \end{pmatrix}. \quad (64)$$

Only the subgroup $SO(1, 2)$ of the group $SL(3, R)$ can satisfy this property. Now we can generate new solutions by applying some transformation of the group $SO(1,2)$ to a known solution. For the class of metrics under our consideration, we only need the transformations $\widetilde{SO}(1, 2) \subset SO(1, 2)$, which can conserve the block structure of the matrix χ .

We see that the analyzed Lorentz transformation $L(2) = O(1, 1)$ is actually a subgroup of $\widetilde{SO}(1, 2)$ $\tilde{x}^{\tilde{a}} = L_{\tilde{b}}^{\tilde{a}} x^{\tilde{b}}$. So we have:

$$O(1, 1) \subset \widetilde{SO}(1, 2) \subset SO(1, 2) \subset SL(3, R).$$

While the transformed matrix χ has the structure:

$$N = \begin{pmatrix} L_{\tilde{b}}^{\tilde{a}} & 0 \\ 0 & 1 \end{pmatrix}, \quad (65)$$

where $L_{\tilde{b}}^{\tilde{a}}$ are the 2D boosts matrix, that reduces to the Lorentz coordinate transformations. The set of solutions that can be obtained by this method is not very big. The group $O(1, 1)$ that induced by coordinate transformation can give us solutions only with trivial electric field. Hence we see the place of coordinate transformations that generate the trivial electric fields, among the entire set of transformations $SO(1,2)$, which in the general case generate a nontrivial field.

We also see that the physically significant transformations $\widetilde{SO}(1, 2)$ – are a map of one KK space (solution) to another one, that can not be reduced to simple coordinate transformations.

5. Conclusion

We observed that a phenomenon of generating an electric field can be interpreted as 5D rotation. In general, electric field is a result of local 5D rotations of 5D manifold (i.e. existence of local inertial 5D reference frames), that defined by additional local dynamical degrees of freedom. The corresponding integral of motion gives the conserved charge, as an independent parameter, This is the case of non trivial unremovable electrical field (charge).

References

- Chodos A., Detweiler S.: 1982, *GRG*, **14**, 879.
- Frolov V., Zelnikov I, Bleyer U.: 1987, *Annalen der Physik*, **7**, 371.
- Gibbons G.: 1982, *Nucl. Phys.*, **B207**, 337.
- Gibbons G., Wiltshire D.: 1985, *University of Cambridge preprint*.
- Vladimirov Yu. S., Popov A.D.: 1982, *Problems in Gravitation Theory and Particle Theory*. Atomizdat, Moscow, **13**, 66.
- Gladush V.D.: 1980, *Izv. Vuzov, Fiz.*, **3**, 74.
- Bronikov K., Shikin G.: 1977, *Izv. Vuzov, Fiz.*, **9**, 25.
- Kramer Von D., Neugebauer G.: 1969, *Annalen der Physik*, **1-2**, 479.
- Maison D.: 1979, *GRG*, **10**, 717.
- Dobiasch P., Maison D.: 1982, *GRG*, **14**, 231.
- Clement G.: 1986, *GRG*, **18**, 861.
- Cvetic M., Youm D.: 1995, arXiv:hep-th/9503082.

STABILITY OF STELLAR SYSTEMS ORBITING SGR A*

Magd E. Kahil

October University for Modern Sciences and Arts (MSA),
October City, Giza, Egypt,
Egyptian Relativity Group (ERG)
mkahil@msa.eun.eg

ABSTRACT. Path equations of different orbiting objects in the presence of very strong gravitational fields are essential to examine the impact of its gravitational effect on the stability of each system. Implementing an analogous method, used to examine the stability of planetary systems by solving the geodesic deviation equations to obtain a finite value of the magnitude of its corresponding deviation vectors. Thus, in order to know whether a system is stable or not, the solution of corresponding deviation equations may give an indication about the status of the stability for orbiting systems. Accordingly, two questions must be addressed based on the status of stability of stellar objects orbiting super-massive black holes in the galactic center.

1. Would the deviation equations play the same relevant role of orbiting planetary systems for massive spinning objects such as neutron stars or black holes?
2. What type of field theory which describes such a strong gravitational field?

Keywords: Stellar systems: Stability – Galaxy: SgrA* – Strong fields: bi-metric theory – Path and Path deviation equations: Orbiting particles.

1. Introduction

The problem of stability in our study is centered only on examining the stability of orbits in a very strong gravitational fields. In our Galaxy, S-stars are counted to be good candidates, to explain such a phenomenon. S-Stars are of spectral class B, that have been traced near infrared. The characteristic behavior of these stars as they are very fast orbital motions around the Galactic Center, with orbital periods more than 16 years, high eccentricities $e > 0.2$, and their distances from the Galactic Center is between $10^0 - 10^2 mpc$ (Han, 2014), which is greater than the center's radius $r \gg r_g$ where r_g its Schwarzschild radius. Also, a stringent condition is taken based on $\frac{m}{M} < 10^{-5}$, where m and M are masses of stellar object and center of SgrA* respectively (Iorio, 2011). One of most brightest member of this group is S2, which takes about 16 years to re-

volve about the center of Galaxy with a radial speed $10,000 km/sec$ and its mass is about $15m_{sun}$ (Meyer et al., 2012). Recently, another type of stars S0-102 with lesser brightness and shorter period about 11.5 years. Unlike, the orbits of satellites, planets or pulsars in the galactic center the orbital periods are much longer leading to the relativistic effects increase more steeply with small radius and very high velocities than classical effects leading to the involvement of relativity is strongly appear around the peri-center passage. Accordingly, S-stars can be counted as clocks in orbit around a black hole moving on geodesics (Angelil et al., 2014). Any slight effective perturbation on these trajectories can be obtained by obtaining its corresponding geodesic deviation equations.

In general the problem of stability is not only related to geodesic deviation equations, but to path deviation equations of spinning object for a point mass particle (Mohseni, 2010), which can also be extended to be charged and spinning charged objects. However, a slight problem can be emerged which is the solution of these deviation equations are completely affected by a coordinate system. Yet, Wanas and Bakry (2008) developed an approach based on determining a scalar value of the geodesic deviation capable for detecting the status of stability of any a certain planetary system in the presence of weak gravitational fields (Wanas & Bakry, 2008).

In the present work, we are going to examine stability conditions in the presence of a strong gravitational field, using Verozub's version of bi-metric theory of gravity, which is one of the most appealing theories (Verozub, 2015).

2. Equations of motion for orbiting objects

It is well known that from observational methods, to confirm that both planetary and stellar objects are exhibiting two types of motion revolving and spinning to become stable in their orbits. From this perspective, it is important to study stability of these systems by causing a slight perturbation that affects these com-

bined motion and checks whether the object remains in the orbit or lose it forever. Such a technique is required to solve the path deviation equations of these objects. Accordingly, it is vital to obtain these equations from perturbing the original path equation. In case of planets/stellar objects, several authors have recommended Mathisson-Papapetrou- Dixon equations (MPD) to be most reliable set of equation for describing such a situation (Dixon, 1970).

$$\frac{DP^\mu}{DS} = F^\mu, \quad (1)$$

$$\frac{DS^{\mu\nu}}{DS} = M^{\mu\nu}, \quad (2)$$

where P^μ is the momentum vector, $F^\mu = \frac{1}{2}R^\mu_{\nu\rho\delta}S^{\rho\delta}U^\nu$, $R^\alpha_{\beta\rho\sigma}$ is the Riemann curvature, $\frac{D}{Ds}$ is the covariant derivative with respect to a parameter S , $S^{\alpha\beta}$ is the spin tensor, and $M^{\mu\nu} = P^\mu U^\nu - P^\nu U^\mu$ such that $U^\alpha = \frac{dx^\alpha}{ds}$ is the unit tangent vector to the geodesic.

Using the following identity on both equations (1) and (2)

$$A^\mu_{;\nu\rho} - A^\mu_{;\rho\nu} = R^\mu_{\beta\nu\rho}A^\beta, \quad (3)$$

such that A^μ is an arbitrary vector. Multiplying both sides with vectors, U^ρ and Ψ^ν as well as using the following condition (Heydari-Fard et al., 2005)

$$U^\alpha_{;\rho}\Psi^\rho = \Psi^\alpha_{;\rho}U^\rho, \quad (4)$$

and Ψ^α is its deviation vector associated to the unit vector tangent U^α . Also in a similar way:

$$S^{\alpha\beta}_{;\rho}\Psi^\rho = \Phi^{\alpha\beta}_{;\rho}U^\rho,$$

one obtains the corresponding deviation equations (Mohseni, 2010)

$$\frac{D\Phi^\mu}{DS} = F^\mu_{;\rho}\Psi^\rho, \quad (5)$$

$$\frac{D\Phi^{\mu\nu}}{DS} = M^{\mu\nu}_{;\rho}\Phi^\rho \quad (6)$$

where Φ^α , $\Phi^{\alpha\beta}$ are the spin path deviation and the spin tensor deviation associated to a path characterized by a parameter S and $(;)$ is the covariant derivative in Riemannian spaces.

In our study, it is worth mentioning that in case of S-systems, the orbiting systems are becoming MPD with $S^{\mu\nu}$ is constant.

Thus,

$$\frac{DU^\mu}{DS} = \frac{1}{2m}F^\mu, \quad (7)$$

$$\frac{DS^{\mu\nu}}{DS} = 0, \quad (8)$$

with taking into consideration that

$$S^{\mu\nu}U_\mu = 0.$$

Accordingly, one transform V^α to U^α in the following way:

$$V^\alpha = U^\alpha + \sigma \frac{D\Psi^\alpha}{Ds}$$

where $V^\alpha = \frac{dx^\alpha}{dS}$ the tangent vector describing the spinning motion, S its associated geodesic parameter and σ is an arbitrary parameter acting as a spin angular momentum ratio (Bini & Gerlhalico, 2014).

Thus,

$$\frac{D}{DS}V^\alpha = \frac{D}{Ds}(U^\alpha + \sigma \frac{D\Psi^\alpha}{Ds}) \frac{ds}{dS}$$

as well as

$$S^{\mu\nu} = \hat{s}(\Psi^\mu U^\nu - \Psi^\nu U^\mu),$$

such that $\sigma = \frac{\hat{s}}{m}$. Thus,

$$\frac{D}{DS}V^\alpha = \frac{\hat{s}}{m}R^\mu_{\nu\rho\sigma}U^\rho\Psi^\sigma U^\beta \frac{ds}{dS},$$

Let $\frac{ds}{dS} = 1$, we obtain

$$\frac{D}{DS}V^\alpha = \frac{\hat{s}}{m}R^\mu_{\nu\rho\sigma}U^\rho\Psi^\sigma U^\beta, \quad (9)$$

the above equation gives an indication that the path equation of a spinning particle is expressed in terms of its corresponding geodesic deviation vector.

Such a result can be also extended to study the motion of binary pulsar, PSR-J0737-3039. It is composed of two neutrons stars, located at a distance $10^9 km$ from the Galactic Center, of negligible intrinsic rotations regarding to the orbital period of about 2.4 hours, and their total mass is about $0.7M_{sun}$. This can give that

$$\begin{aligned} \frac{D}{DS}V_1^\alpha - \frac{D}{DS}V_2^\alpha &= \frac{D}{Ds}(U^\alpha + \sigma_1 \frac{D\Psi^\alpha}{Ds}) \frac{ds}{dS} \\ &\quad - \frac{D}{Ds}(U^\alpha + \sigma_2 \frac{D\Psi^\alpha}{Ds}) \frac{ds}{dS}. \end{aligned}$$

where σ_1 and σ_2 the angular momentum ratio of each neutron star of this binary pulsar, to obtain the following equation

$$\frac{D}{DS_1}V_1^\alpha - \frac{D}{DS_2}V_2^\alpha = (\sigma_1 - \sigma_2)R^\alpha_{\rho\delta\beta}U^\delta U^\rho \Psi^\beta,$$

in which V_1^α and V_2^α are two tangent vector associated to each spinning object in the binary system.

Consequently, we find out that

$$\frac{D\bar{V}^\alpha}{DS} = (\sigma_1 - \sigma_2)R^\alpha_{\rho\delta\beta}U^\delta U^\rho \Psi^\beta \quad (10)$$

such that, $\bar{V}^\alpha = V_1^\alpha - V_2^\alpha$.

3. The relationship between stability and geodesic deviation

It is well known that stability of planetary / stellar systems can be represented by a path deviation equation for an orbiting object.

Consequently, the stability tensor can be defined as follows:

$$H_\gamma^\alpha \Psi^\gamma = R_{\beta\omega\gamma}^\alpha U^\beta U^\omega \quad (11)$$

where H_γ^α is the stability tensor defined as (Di Bari & Cipriani, 2000).

Thus geodesic deviation equation may be expressed in terms of stability tensor;

$$\frac{D^2 \Psi^\alpha}{DS^2} = H_\beta^\alpha \Psi^\beta \quad (12)$$

which is reduced to

$$\frac{d^2 \Psi^\mu}{dS^2} + 2\Gamma_{\nu\rho}^\mu \frac{d\Psi^\nu}{dS} U^\rho + \Gamma_{\nu\rho,\sigma}^\mu U^\nu U^\rho \Psi^\sigma = 0, \quad (13)$$

provided that (Di Bari & Cipriani, 2000)

$$g_{\mu\nu} \Psi^\mu \Psi^\nu = \text{constant}.$$

Also, equation (9) and (10) can be written in terms of stability tensor in following way

$$\frac{D}{DS} V^\alpha = \sigma R_{\sigma}^\alpha \Psi^\sigma, \quad (14)$$

and

$$\frac{D\bar{V}^\alpha}{DS} = (\sigma_1 - \sigma_2) H_\beta^\alpha \Psi^\beta. \quad (15)$$

Such a result for linearized systems gives rise to indicate that geodesic deviation vector can determine the spin path equation for S-stars and binary pulsar that are expressed by MPD equations. In order to obtain the solution, one must solve its corresponding field equation and define a certain coordinate system, to obtain the value of the deviation vector.

However, Wanas and Bakry (1995) introduced an approach, for examining the stability problem for any planetary system, being a covariant coordinate independent which can be explained in the following way (Wanas & Bakry, 1995).

Let $\Psi^\alpha(S)$ is obtained from the solutions of the deviation equation in a given interval [a,b] in which $\Psi^\alpha(S)$ behave monotonically. These quantities can become sensors for measuring the stability of the system are

$$q^\alpha \stackrel{\text{def.}}{=} \Psi^\alpha(S) = C^\alpha f(S), \quad (16)$$

where C^α are constants and $f(S)$ is a function known from the metric. If $f(S) \rightarrow \infty$, the system becomes unstable otherwise it is stable. This approach has been applied previously in examining the stability of some cosmological models (Wanas & Bakry, 1995)

using two geometric structures (Wanas, 1986). The above approach has been modified by obtaining the scalar value of the deviation vector which gives rise to become independent of any coordinate system (Wanas & Bakry, 2008)

$$q \stackrel{\text{def.}}{=} \lim_{s \rightarrow b} \sqrt{\Psi^\alpha \Psi_\alpha}. \quad (17)$$

If $q \rightarrow \infty$ then the system is unstable, otherwise it is always stable.

Now for spinning objects with precession, we suggest the above condition be extended to include the spin deviation tensor $\Phi^{\mu\nu}$ as

$$\bar{q} \stackrel{\text{def.}}{=} \lim_{s \rightarrow b} \sqrt{\Phi^{\alpha\beta} \Phi_{\alpha\beta}}. \quad (18)$$

Thus, for such a member in stellar/planetary system is stable, if and only if the magnitude of the scalar value of both spin deviation vectors Φ^α and spin deviation tensors $\Phi^{\alpha\beta}$ to be real numbers respectively. i.e. either $q \rightarrow \infty$ or $\bar{q} \rightarrow \infty$ the assigned member is unstable. Accordingly, a strong stability condition must be admitted if both q and \bar{q} are satisfying the following conditions:

$$\lim_{s \rightarrow \infty} (\Phi_\alpha \Phi^\alpha) = 0, \quad (19)$$

and

$$\lim_{s \rightarrow \infty} (\Phi_{\alpha\beta} \Phi^{\alpha\beta}) = 0. \quad (20)$$

4. Geodesic and geodesic deviation: The Bazanski approach

Geodesic and geodesic deviation equations can be obtained simultaneously by using the Bazanski Lagrangian (Bazanski, 1989):

$$L = g_{\alpha\beta} U^\alpha \frac{D\Psi^\beta}{DS}, \quad (21)$$

where L is the lagrangian function.

Thus, it can be found clearly, if one takes the variation with respect to the deviation vector Ψ^ρ to get geodesic equations:

$$\frac{dU^\alpha}{dS} + \Gamma_{\mu\nu}^\alpha U^\mu U^\nu = 0. \quad (22)$$

Also, the same technique can be applied to get the variation with respect to the tangent vector U^ρ to get the geodesic deviation equations:

$$\frac{D^2 \Psi^\alpha}{DS^2} = R_{\beta\gamma\delta}^\alpha \Psi^\gamma U^\beta U^\delta. \quad (23)$$

The above Lagrangian has been modified to describe the path equation of a charged object to take the following form (Kahil, 2006);

$$L = g_{\alpha\beta} U^\alpha \frac{D\Psi^\beta}{DS} + \frac{e}{m} F_{\alpha\beta} U^\alpha \Psi^\beta$$

where $\frac{e}{m}$ is the ratio of charge to mass of any charged object, $F_{\mu\nu}$ is an electromagnetic field tensor. Taking the variation with respect to $\Psi^{alpha\rho}$ one obtains

$$\frac{dU^\alpha}{dS} + \Gamma_{\mu\nu}^\alpha U^\mu U^\nu = \frac{e}{m} F_{\nu}^\mu U^\nu. \quad (24)$$

While taking the variation with respect to U^α one obtains its corresponding deviation equations:

$$\frac{D^2\Psi^\alpha}{DS^2} = R_{\mu\nu\rho}^\alpha U^\mu U^\nu \Psi^\rho + \frac{e}{m} (F_{\nu}^\alpha \frac{D\Psi^\nu}{DS} + F_{\nu;\rho}^\alpha U^\nu \Psi^\rho). \quad (25)$$

Also the corresponding Papapetrou Equation for rotating objects without precession can be obtained from the following Lagrangian:

$$L = g_{\alpha\beta} U^\alpha \frac{D\Psi^\beta}{DS} + \frac{1}{2m} F_\mu \Psi^\mu \quad (26)$$

Taking the variation with respect to Ψ^α , we obtain the spin path equation,

$$\frac{dU^\alpha}{dS} + \Gamma_{\mu\nu}^\alpha U^\mu U^\nu = \frac{1}{2} F^\alpha \quad (27)$$

and taking the variation with respect to U^α , we obtain the spin deviation equation

$$\frac{D^2\Psi^\alpha}{DS^2} = R_{\beta\gamma\delta}^\alpha U^\beta U^\gamma \Psi^\delta + \frac{1}{2} F_{;\rho}^\alpha \Psi^\rho. \quad (28)$$

In case of the Dixon equation for spinning charged objects can be obtained in a similar way from the following Lagrangian

$$L = g_{\alpha\beta} U^\alpha \frac{D\Psi^\beta}{DS} + \frac{1}{2m} (F_\mu + e F_{\mu\nu} U^\nu) \Psi^\mu. \quad (29)$$

Taking the variation with respect to Ψ^μ we obtain

$$\frac{dV^\alpha}{dS} + \Gamma_{\mu\nu}^\alpha U^\mu U^\nu = \frac{e}{m} F_{\nu}^\mu U^\nu + \frac{1}{2m} F^\mu. \quad (30)$$

While its corresponding deviation equation can be obtained by taking the variation with respect to U^α

$$\frac{D^2\Psi^\alpha}{DS^2} = R_{\mu\nu\rho}^\alpha U^\mu U^\nu \Psi^\rho + \frac{e}{m} (F_{\nu}^\alpha U^\nu)_{;\rho} \Psi^\rho + \frac{1}{2} F_{;\rho}^\alpha \Psi^\rho. \quad (31)$$

Similarly, we can modified the Lagrangian (21) to obtain spin equation and spin deviation equation for rotating objects with precession in the following way:

$$L = g_{\alpha\beta} P^\alpha \frac{D\Psi^\beta}{DS} + F_\alpha \Phi^\alpha \quad (32)$$

where

$$P^\alpha = mU^\alpha + U_\beta \frac{DS^{\alpha\beta}}{DS}.$$

In order to obtain an equation of spinning object with precession, we take the variation with respect to the deviation vector Φ^α

$$\frac{DP^\alpha}{DS} = F^\alpha. \quad (33)$$

And for its spin deviation equation, we take the variation with respect to U^α to become:

$$\frac{D^2\Phi^\alpha}{DS^2} = R_{\mu\nu\rho}^\alpha P^\mu U^\nu \Phi^\rho + F_{;\rho}^\alpha \Phi^\rho. \quad (34)$$

While for its precession part it can be obtained using the following condition:

$$P_\mu S^{\mu\nu} = 0,$$

to give

$$\frac{DS^{\alpha\beta}}{DS} = P^\mu U^\nu - P^\nu U^\mu.$$

5. Stability of motion in bimetric theory of gravity: the Verozub approach

In this section, we are showing that the treatment of the stability problem in strong fields may be explained in the presence of bimetric theory of gravity. This type of bimetric theories was proposed by Rosen in 1940, who regarded gravity can be expressed in flat space. Due to considering that, all objects of the Riemannian space are functions in Minkowski space (Rosen, 1973). But such a type of visualization gives no physical meaning, with inconsistency with observations as well as there is no relation between the two metrics (Verozub, 2015). Recently, Verozub has introduced a new version of bimetric theory of gravity, stemmed from a well known principle of Poincare that properties of space-time are relative to the properties of used measuring instruments, together with the Einstein idea of the relativity of properties of space-time with respect to the distribution of matter (Verozub, 2008).

It is well known that in general relativity that test particles in gravitational field move on geodesics in a Riemannian space. Accordingly, one may figure out that the differential equations for obtaining the metric tensor $g_{\mu\nu}(x)$ of any distribution of matter must keep the geodesic equations invariant under coordinate transformations. Surprisingly, it can be found that these equations are also invariant under geodesic mapping of space time V into \bar{V} upon replacing $\Gamma_{\alpha\beta}^\mu \rightarrow \bar{\Gamma}_{\alpha\beta}^\mu$ of the Christoffel symbols in any fixed coordinate system to become

$$\bar{\Gamma}_{\alpha\beta}^\mu = \Gamma_{\alpha\beta}^\mu + \delta_\alpha^\mu \phi_\beta + \delta_\beta^\mu \phi_\alpha \quad (35)$$

where $\phi_\mu(x)$ is a vector field. Moreover, transformations of the metric tensors are obtained by solving the

partial differential equation

$$\bar{g}_{\mu\nu;\alpha} = 2\phi_\alpha(x)\bar{g}_{\beta\gamma}(x) + \phi_\beta(x)\bar{g}_{\gamma\alpha}(x) + \phi_\gamma(x)\bar{g}_{\alpha\beta}(x), \quad (36)$$

in which the semi-colon is related here to the covariant derivative of V .

Thus, this field can be expressed in a Riemannian space in terms of two metrics before and after the geodesic mapping of from one space time into another in the following way:

$$\phi_\alpha = \frac{1}{n+1}(\bar{\Gamma}_{\alpha\mu}^\mu - \Gamma_{\alpha\mu}^\mu) = \frac{1}{2(n+1)}\frac{\partial}{\partial x^\alpha} \ln|\frac{\bar{g}}{g}|. \quad (37)$$

Thus, Verozub's version of bimetric theory of gravity has two important results, geodesic transformations are playing the role of gauge transformations while coordinates transformation are acting the same way as in electrodynamics. It also gives a full description of motion of small particles of a perfect isentropic fluid able to describe gravity in strong gradational fields of a super-massive black hole Sgr A* at the Galactic Center. Also, the theory has neither singularities nor event horizon.

From this perspective, we aim to study stability of orbiting objects like S2 and binary pulsar PSR-J0737-3039, by obtaining their geodesic and geodesic deviations vectors.

Implementing Verzob's version one can find that the trajectories of a test particles are geodesics are in the co-moving reference frame, (CRF), described by $g_{\mu\nu}(\psi)$, such that $\psi_{\mu\nu}$ is a tensor field of spin 2 gravity, as found in Riemannian space of non zero curvature. While, the same test particle is observed in an inertial reference frame (IRF) as a point mass moves under the influence of a force field $\psi_{\mu\nu}$, as existed in Minkowski space (Verozub 2008).

Accordingly, the line element of the IRF is defined as follows:

$$d\sigma^2 = \eta_{\mu\nu}(x)dx^\mu dx^\nu, \quad (38)$$

where $\eta_{\mu\nu}$ is the Minkowski metric and its corresponding CRF line element is defined as

$$dS^2 = g_{\mu\nu}(\psi)dx^\mu dx^\nu \quad (39)$$

leading to define its corresponding affine connection:

$$\bar{\Gamma}_{\beta\rho}^\alpha = \frac{1}{2}g^{\alpha\delta}(\psi)(g_{\beta\delta,\rho} + g_{\delta\rho,\beta} - g_{\beta\rho,\delta}).$$

Applying the Bazanski approach, we obtain geodesic and geodesic deviation equations of Verozub's version for bimetric theory of gravity:

$$L(\psi) = g_{\alpha\beta}(\psi)U^\alpha \frac{D\Psi^\beta}{DS} \quad (40)$$

This can be seen clearly if one takes the variation with respect to the deviation vector Ψ^ρ to get the geodesic equations:

$$\frac{dU^\alpha}{dS} + \bar{\Gamma}_{\mu\nu}^\alpha(\psi)U^\mu U^\nu = 0 \quad (41)$$

Also, the same technique can be applied to get the variation with respect to the tangent vector U^ρ to get the geodesic deviation equations:

$$\frac{D^2\Psi^\alpha}{DS^2} = \bar{R}_{\beta\gamma\delta}^\alpha(\Psi)\Psi^\gamma U^\beta U^\delta \quad (42)$$

where \bar{R} is the Riemann Curvature described by the affine connection $\bar{\Gamma}_{\beta,\rho\sigma}^\alpha$ for the (CRF). Thus the stability equation in this case becomes:

$$\frac{D^2\Psi^\alpha}{DS^2} = \hat{H}_{\cdot\gamma}^\alpha(\psi)\Psi^\gamma. \quad (43)$$

as $\hat{H}_{\cdot\beta}^\alpha$ is the stability tensor defined in CRF. Thus, the deviation vector in CRF in Riemannian space can be expressed as a separation vector of these particles under the action of a force field $\psi_{\mu\nu}$ in Minkowski space, which can be reduced to (Verozub, 2015):

$$\frac{\partial^2\eta^\alpha}{\partial^2\tau} + \frac{\partial^2 U}{\partial x^\alpha \partial x^\beta} \eta^\beta = 0, \quad (44)$$

where $\eta^\alpha = \frac{\partial x^\alpha}{\partial \xi}$, $x^\mu = x^\mu(\tau, \xi)$ such that η^α is the separation vector and U is the gravitational potential as measured in the flat space. If we apply the Wanas-Bakry condition on the scalar of the separation vector between two geodesics in a Minkowski space we can easily find

$$\tilde{q} = \lim_{\tau \rightarrow \bar{b}} \sqrt{\eta^\alpha \eta_\alpha}$$

, where the solutions of $\eta(\tau)$ in a given interval $[\bar{a}, \bar{b}]$ behave monotonically. If $\tilde{q} \rightarrow \infty$ then the system is unstable, otherwise it is always stable. Consequently, the strong stability condition becomes

$$\lim_{\tau \rightarrow \infty} (\eta_\alpha \eta^\alpha) = 0. \quad (45)$$

Accordingly, we can conclude that in a strong gravitational field, in covariant stability condition is examined by obtaining the scalar value of its associated separation vectors as defined in IRF rather than its equations. Such an approach gives the finiteness of the scalar value for the separation vector an indicator to decide whether the orbiting system is stable or not.

6. Discussion and concluding remarks

In this study, we have examined the stability of rotating objects in the presence of very strong gravitational field. One of most promising theories is the bimetric version of Verozub. The objects are considered as test particles due to the stringent condition $\frac{m}{M} < 10^{-5}$, e.g the S-stars are considered as test particles moving on geodesics and acting as clocks for the SgrA*. It has been assumed that the stability criterion may be estimated its status by extending the covariant stability condition method of Wanas-Bakry to examine S-stars

and PSR J0737-3039. The stability of these systems are mainly dependent on obtaining the corresponding deviation vectors and then finding their scalar value in each case. Yet, an additive step may be obtained due to Verozub's bimetric theory, is the scalar part of the separation vectors obtained in IRF as defined in flat space is becoming a good candidate to examine the stability condition.

Moreover, we have obtained a relationship between the spin tensor of a rotating object with its corresponding deviation vector. This result leads to identify the stability condition without finding out the spin deviation vector as an indicator of stability conditions, and examining only the stability condition on their corresponding deviation vector. Accordingly, we have obtained a quick method to estimate whether the system is stable or not without going to lengthy calculation to determine the scalar value for the spin deviation vector, such an advantage works in favor of testing stability conditions for S-stars or binary pulsars orbiting SgrA*.

Acknowledgments. The author would like to thank Professor A.Zhuk and the organizing committee of the Conference of Fifth Gammov for their hospitality and good atmosphere of discussions during the conference period.

References

- Angelil R., Saha P.: 2014, *MNRS*, **444**(2), 3780.
Bazanski S.L.: 1989, *J. Math. Phys.*, **30**, 1018.
Bini D., Geralico A.: 2014, *Phys Rev.*, **D84**,104012.
Di Bari M., Cipriani P.: 2000, *Chaotic Universe*, 444.
Dixon W.G.: 1970, *Proc. R. Soc. London, Ser. A*, **314**, 499.
Han Wen-Biao: 2014, *A&A*, **14**, 1415.
Heydrai-Fard, Mohseni, M., Sepanigi, H.R.: 2005, *Phys. Lett. B*, **626**, 230.
Iorio L.: 2011, *Phys. Rev.*, **D84**, 124001.
Kahil M.E.: 2006, *J. Math. Physics*, **47**, 052501.
Meyer et al.: 2012, *Science*, **125506**.
Mohseni M.: 2010, *Gen. Rel. Grav.*, **42**, 2477.
Papapetrou A.: 1951, *Proc. R. Soc. London, Ser. A*, **209**, 248.
Rosen N.: 1973, *Gen. Relativ. and Gravit.*, **4**, 435.
Verozub L.: 2008, *Annalen der Physik*, **27**, 28.
Verozub L.: 2015, *Space-time Relativity and Gravitation*, Lamberg Academic Publishing.
Wanas M.I.: 1986, *Astrophys. Space Sci.*, **127**, 21.
Wanas M.I., Bakry M.A.: 1995, *Astrophys. Space Sci.*, **228**, 239.
Wanas M.I., Bakry M.A.: 2008, *Proc. MGXI, part C*, 2131.

PERTURBATIONS OF FRIEDMAN-LEMAITRE-ROBERTSON-WALKER SPACETIMES IN GEROCH-HELD-PENROSE FORMALISM

J. Novák

Department of theoretical physics, Charles University,
V Holešovičkách 2, Prague-Libeň, 180 00, Czech republic, jan.janno.novak@gmail.com

ABSTRACT. We will use Geroch-Held-Penrose formalism for decoupling of quantity $d\Psi_4$, which is responsible for tensorial perturbations, in Bianchi equations. We will concentrate on the case, where we eliminate the source terms.

Keywords: Friedman-Lemaitre-Robertson-Walker spacetime, Geroch-Held-Penrose formalism, Newman-Penrose formalism, Weyl scalars

1. Introduction

Our goal is to use the Geroch-Held-Penrose formalism (GHP - formalism) in reformulation of perturbations of Friedman-Lemaitre-Robertson-Walker spacetime (FLRW ST). GHP - formalism (a more compact version of NP - formalism) is a convenient formalism, because it allows us to work with partial differential equations of the first order. The scalar and tensor perturbations are for us the most interesting because of the origin of structure. I will show, how to apply the GHP-formalism for decoupling of the quantity $d\psi_4$ in Bianchi equation. These calculations are done for the case of the simplified right-hand side (RHS without sources).

2. NP-formalism

NP- and GHP-formalisms are mathematical approaches which help us, for example, in perturbation theory to simplify calculations in standard General Relativity. We decompose the metric with respect to the null tetrad and then we project all quantities on this tetrad (in the NP-formalism). The basic quantities are spin-coefficients - projections of the derivatives of the null tetrad, then projections of the Ricci tensor and already mentioned Weyl scalars. We could then rewrite the Einstein's equations by the 18 Ricci, 8+3 Bianchi and 4 commutation equations, which are only first order PDE's, when we define new derivatives in the direction of the tetrad $(D, \Delta, \delta, \bar{\delta})$. Let us to introduce,

Table 1: Spin coefficients

$$\begin{aligned} \alpha &= \frac{1}{2}(S_{214} + S_{344}) & \nu &= S_{242} & \tau &= S_{312} \\ \beta &= \frac{1}{2}(S_{213} + S_{343}) & \kappa &= S_{311} & \sigma &= S_{313} \\ \gamma &= \frac{1}{2}(S_{212} + S_{342}) & \pi &= S_{241} & \mu &= S_{243} \\ \epsilon &= \frac{1}{2}(S_{211} + S_{341}) & \rho &= S_{314} & \lambda &= S_{244} \end{aligned}$$

for illustration, the basic quantities and equations now:

we will denote the 12 spin coefficients by S_{ijk} (standard notation is with γ), where the three indices mean, which element of the tetrad we are using (where the null tetrad is defined in standard way), Table 1.

For example:

$$\rho = m^\mu l_{\mu;\nu} \bar{m}^\nu$$

Projections of the Ricci tensor (we will omit the brackets by tetrad indices in this part of thesis):

$$\Phi_{(i)(j)}, \quad i, j = 0, 1, 2, 3,$$

$$\Phi_{(0)(0)} = -\frac{1}{2} R_{\mu\nu} l^\mu l^\nu$$

So, let's define the projections of the Ricci tensor by the following notation, [1]:

$$\begin{aligned} \Phi_{00} &= -\frac{1}{2} R_{11}, \quad \Phi_{01} = -\frac{1}{2} R_{13}, \quad \Phi_{10} = -\frac{1}{2} R_{14}, \\ \Phi_{12} &= -\frac{1}{2} R_{23}, \quad \Phi_{21} = -\frac{1}{2} R_{24}, \quad \Phi_{22} = -\frac{1}{2} R_{22}, \\ \Phi_{11} &= -\frac{1}{4}(R_{12} + R_{34}), \quad \Lambda = \frac{1}{12}(R_{12} - R_{34}), \\ \Phi_{02} &= -\frac{1}{2} R_{33}, \quad \Phi_{20} = -\frac{1}{2} R_{44}. \end{aligned} \quad (1)$$

Weyl scalars (5 in dimension 4):

$$\Psi_i, \quad i = 0, 1, 2, 3, 4 \quad (2)$$

$$\begin{aligned}
 \Psi_0 &= l^\mu m^\nu l^\rho m^\sigma C_{\mu\nu\rho\sigma}, \\
 \Psi_1 &= l^\mu n^\nu l^\rho m^\sigma C_{\mu\nu\rho\sigma}, \\
 \Psi_2 &= l^\mu m^\nu \bar{m}^\rho n^\sigma C_{\mu\nu\rho\sigma}, \\
 \Psi_3 &= n^\mu l^\nu n^\rho \bar{m}^\sigma C_{\mu\nu\rho\sigma}, \\
 \Psi_4 &= n^\mu \bar{m}^\nu n^\rho \bar{m}^\sigma C_{\mu\nu\rho\sigma}.
 \end{aligned} \tag{3}$$

Now we present one Ricci, one Bianchi and one commutation relation:

Ricci identities (18 equations)

$$D\rho - \delta^* \kappa - \rho^2 - \sigma\bar{\sigma} - \rho\epsilon - \rho\bar{\epsilon} + \bar{\kappa}\tau + (3\alpha + \bar{\beta} - \pi)\kappa = \Phi_{00}, \tag{4}$$

Bianchi identities (11 equations)

$$\begin{aligned}
 -\delta^* \Psi_0 + D\Psi_1 + (4\alpha - \pi)\Psi_0 - 2(2\rho + \epsilon)\Psi_1 = \\
 \delta\Phi_{00} - 3\kappa\Psi_2 - D\Phi_{01} + 2(\epsilon + \bar{\rho})\Phi_{01} - \bar{\kappa}\Phi_{02} + \\
 + (\bar{\pi} - 2\bar{\alpha} - 2\beta)\Phi_{00} + 2\sigma\Phi_{10} - 2\kappa\Phi_{11},
 \end{aligned} \tag{5}$$

Commutation relations (4 equations):

$$\Delta D - D\Delta = (\gamma + \bar{\gamma})D + (\epsilon + \bar{\epsilon})\Delta - (\bar{\tau} + \pi)\delta - (\tau + \bar{\pi})\bar{\delta}. \tag{6}$$

We can rotate the tetrad and we can get a transformation property of these quantities. However, there exists also a more compact version of the NP-formalism, so called GHP-formalism. One makes the following re-definitions of the derivative operators:

$$\mathfrak{p} = D - p\epsilon - q\bar{\epsilon}, \tag{7}$$

$$\mathfrak{p}' = \Delta - p\gamma - q\bar{\gamma}, \tag{8}$$

$$\mathfrak{d} = \delta - p\beta - q\bar{\alpha}, \tag{9}$$

$$\mathfrak{d}' = \bar{\delta} - p\bar{\beta} - q\alpha. \tag{10}$$

We have 4 different operators and two, so called, dualities in dimension 4 (star - duality, $(p, q) \rightarrow (p, -q)$), is for exchange of the vector l and m , the prime duality,

Table 2: Relations among projections of Ricci tensor

$$\begin{array}{cccc}
 \Phi'_{00} = \Phi_{22} & \Phi'_{11} = \Phi_{11} & \Phi'_{10} = \Phi_{12} & \Phi'_{02} = \Phi_{20} \\
 \Phi'_{00} = \Phi_{02} & \Phi'_{01} = -\Phi_{01} & \Phi^*_{10} = \Phi_{12} & \Phi^*_{11} = -\Phi_{11} \\
 \Phi^*_{22} = \Phi_{20} & \Phi^*_{12} = \Phi_{10} & \Phi^*_{02} = \Phi_{00} & \Phi^*_{20} = -\Phi_{22} \\
 \Lambda' = \Lambda & \Phi^*_{21} = -\Phi_{21} & \Lambda^* = -\Lambda &
 \end{array}$$

Table 3: GHP-type

$$\begin{array}{ccc}
 \Phi_{00} : (2, 2) & \Phi_{01} : (2, 0) & \Phi_{10} : (0, 2) \\
 \Phi_{11} : (0, 0) & \Phi_{22} : (-2, -2) & \Phi_{12} : (0, -2) \\
 \Phi_{21} : (-2, 0) & \Phi_{20} : (-2, 2) & \Phi_{02} : (2, -2) \\
 \Lambda : (0, 0) & &
 \end{array}$$

$(p, q) \rightarrow (-p, -q)$, for the exchange of the l and n ; we could not use both dualities in HD, because we have odd dimensions)

$$\Sigma\eta, \Sigma = \left\{ \mathfrak{p}, \mathfrak{p}', \mathfrak{d}, \mathfrak{d}' \right\}, \tag{11}$$

where Σ is an operator acting on a quantity η .

But we need the notion of the GHP scalars when we make the following transformations:

$$l^\nu \rightarrow \lambda^{-1} l^\nu, \tag{12}$$

$$n^\mu \rightarrow \lambda n^\mu, \tag{13}$$

$$m^\rho \mapsto e^{i\theta} m^\rho. \tag{14}$$

We say that a quantity η is a GHP-scalar of type (p, q) , if it transforms like (analogical definition for the case of higher dimensions is in [2]):

$$\eta \rightarrow \lambda^{(p+q)/2} e^{i(p-q)\theta/2} \eta. \tag{15}$$

We will use the star and prime duality in a standard way, [1]. We see the relations among perturbations of Ricci tensor in Table 2.

And the types for these quantities are in Table 3.

3. Computations

Now we will apply the GHP-formalism in perturbation theory of FLRW ST. It will be done, of course, in classical manner. However, we obtain a new result with this formalism.

Reference [3] will be of great importance for us, where the following fact can be found: the only non-vanishing spin coefficients for the case of FLRW are α , β , γ , μ and ρ . These are the same non-zero spin coefficients as for the case of the Schwarzschild solution. This fact can be employed in the analysis of unperturbed equations. This means that we can get rid of

many terms in the resulting equations. We get rid of α , β , γ and ϵ because they are absorbed into \flat and $\bar{\delta}$ (\flat' and $\bar{\delta}'$). Together there are 12 spin coefficients, thus there remain yet 8 more: τ , σ , κ , μ , ρ , λ , π and ν ;

The course of action will be now the following. We will write the general Bianchi equations for the case of FLRW ST with sources. We will show our result for the special case of simplified right-hand side.

We have the following 2 equations in GHP formalism for the case of FLRW ST. We have 8 equations in standard NP-formalism, but this formalism is even more efficient. (We stress once again that we have sources on the right hand side of the equations contrary to the Schwarzschild ST.) The equations read

$$\flat\Psi_1 - \bar{\delta}'\Psi_0 + \tau'\Psi_0 - 4\rho\Psi_1 + 3\kappa\Psi_2 = \flat\Phi_{01} - \bar{\delta}\Phi_{00} - \bar{\pi}\Phi_{00} - 2\bar{\rho}\Phi_{01} + \bar{\kappa}\Phi_{02} + 2\kappa\Phi_{11} - 2\sigma\Phi_{10}, \quad (16)$$

$$\flat\Psi_2 - \bar{\delta}'\Psi_1 - \sigma'\Psi_0 + 2\tau'\Psi_1 - 3\rho\Psi_2 + 2\kappa\Psi_3 = \flat'\Phi_{00} - \bar{\delta}'\Phi_{01} - \bar{\rho}'\Phi_{00} + 2\bar{\tau}\Phi_{01} - 2\rho\Phi_{11} - \bar{\sigma}\Phi_{00}^* + 2\tau\Phi_{10} + 2\flat\Lambda, \quad (17)$$

where we defined the NP components of the Weyl tensor in the standard way.

The Ψ_0 and Ψ_4 are connected with the tensor perturbations, Ψ_1 and Ψ_3 are connected with the vector perturbations and Ψ_2 is connected with the scalar perturbations according to the [3]^{1, 2}

Now we will follow the approach presented in [4]. The difference, as we already mentioned, is that we have sources on the RHS. However, we can make the same steps: we will take the first equation and we will apply operator $\bar{\delta}$, we make the star duality and we add the first and this modified equation. Then we plug from the Ricci identities, we eliminate some of these combinations of spin coefficients (we make also prime and star dualities of these Ricci identities) and we arrive at the following result (the second equation could be obtained in a similar way).

¹ We can use their boost weights like an argument.

² In the case of non-zero sources we have also other two equations:

$$-\flat' - 2\tau^* + \pi^*\Phi_{01} + [-\flat - 2\tau^* + \bar{\pi}^*]\Phi_{12} + [\bar{\delta} - 2(\rho^* + \bar{\rho}^*)]\Phi_{11} - [-\bar{\delta}' + \mu^* + \bar{\mu}^*]\Phi_{02} + \bar{\sigma}^*\Phi_{02}^* + \sigma^*\Phi_{20}^* - \bar{\kappa}^*\Phi_{12}^* - \kappa^*\Phi_{21}^* + 3\bar{\delta}\Lambda = 0, \quad (18)$$

$$[\bar{\delta} - 2\tau + 2\pi^*]\Phi_{11} - 3\bar{\delta}\Lambda + [-\flat + 2\rho + \bar{\rho}]\Phi_{12} + [-\flat' - 2\bar{\mu} - \mu]\Phi_{01} + [\bar{\delta}' - \tau^* + \pi]\Phi_{02} - \kappa\Phi_{22} + \bar{\nu}\Phi_{00} + \sigma\Phi_{21} - \bar{\lambda}\Phi_{10} = 0. \quad (19)$$

$$\begin{aligned} & [\flat'\flat - \bar{\delta}'\bar{\delta} - (4\rho' + \bar{\rho}')\flat - \rho\flat' + (4\tau' + \bar{\tau})\bar{\delta} + \\ & \tau\bar{\delta}' + 4\rho\rho' - 4\tau\tau' - 2\Psi_2 + 2\Lambda]\Psi_4 + \\ & [4\flat\kappa' - 4\bar{\delta}\sigma' - 4(\bar{\rho} - 2\rho)\kappa' + \\ & 4(\bar{\tau} - 2\tau)\sigma' + 10\Psi_3]\Psi_3 + \\ & [-4\sigma'\flat' + 4\kappa'\bar{\delta}' - 12\kappa'\tau' + 12\rho'\sigma' - 3\Psi_0]\Psi_2 = 0. \end{aligned} \quad (20)$$

This equation contains information from both (16) and (17). It is interesting that for this case of FLRW spacetimes, we have cancellations of all extra terms in front of Ψ_2 and Ψ_3 . The terms in the brackets in front of Ψ_2 and Ψ_3 are exactly the same (except of one term $3\Psi_0\Psi_2$) as for the case of the Schwarzschild spacetime. This means that when we will make perturbations of these equations, the second and third term disappear. So, we obtain a decoupling of the quantity $d\Psi_4$.

This is other new information, when we compare it with [3]. Here we were interested in equations without sources, i.e. when we put just delta-function on the RHS. But in later work we could be interested in the same problem but with sources, as was already suggested in this article. It is an advantage to write all sources in one compact form.

4. Conclusion

I have been studying perturbation theory of FLRW ST in GHP formalism. We obtained a new interesting observation, which could be used for other research in the realm of Cosmological Perturbation Theory.

References

- Chandrasekhar S.: 1983, Mathematical theory of black holes, *Oxford University Press*, 668.
- Durkee M., Pravda V., Pravdová A., Reall H.S.: 2010, Generalization of the Geroch-Held-Penrose formalism to higher dimensions, *Class.Quantum Grav.*, **27**.
- Sharma S., Khanal U.: 2014, Perturbations of FRW ST's in NP formalism, *International Journal of Modern Physics D*.
- Stewart J.M., Walker M.: 2014, *Proc. R.Soc. Lond. A*, 49-74.

THE DETERMINATION OF THE MORPHOLOGICAL TYPES OF GALAXY CLUSTERS USING CLUSTER CARTOGRAPHY

E.A. Panko, S.I. Emelyanov

V.O. Suckomlinsky Nikolaev National University, Kalinenkov Astronomical Observatory
Nikolskaya, 24, Nikolaev, 54030, Ukraine
panko.elena@gmail.com

ABSTRACT. We discuss the possibility of using the Cluster Cartography set for the determined morphological types of galaxy clusters. The applied morphological scheme was proposed by Panko (2013). The morphological types are determined using numerical criteria based on three parameters: concentration to the cluster center, the signs of preferential direction or plane in the cluster (filamentary substructure), and the positions of the brightest galaxies. However, structures like galaxy clusters need visual preview for classification. The Cluster Cartography set constructs the individual cluster map in different forms and allows to estimate previously cluster type.

Keywords: Galaxies: clusters: morphological types.

1. Introduction

The morphology of galaxy clusters reflects the physical conditions in the cluster space. One can note the galaxy clusters have a special place in hierarchy of large-scale structures. They are the part of a continuous range of large-scale construction of Universe: galaxies \Rightarrow groups \Rightarrow clusters \Rightarrow superclusters \Rightarrow cosmological large scale structure. Galaxy cluster virialization time is about 10^9 yr, and it is less than Hubble time. In contrary, galaxy superclusters virialization time – about $10^{10.5}$ – is bigger than Hubble time. As a result the galaxy clusters are not biggest bound structures in the Universe, they are only biggest virialized ones. The galaxy clusters are small in comparison to Universe. At the same time, on the galaxy clusters scale, their components have not had a chance to separate during collapse and a cluster is probably a representative sample of the Universe. In particular, the part of dark matter (DM) in galaxy clusters must be the same, as in whole Universe. The determination of morphological types of galaxy clusters will be useful for detailed study of the large scale structures.

Panko (2013) summarized the classical schemes, including both famous Bautz – Morgan (1970), Rood – Sastry (1971) systems and less popular López-Cruz

at al. (1997) and López-Cruz & Gaztanaga (2001) ones. Improved and integrated scheme (Panko 2013) allows to assign the morphological types corresponding to cluster “concentration” (from *C* – compact, to *I* – intermediate, and *O* – open), “flatness signs” (*L* – line or *F* – flat, and no symbol if no indication of flatness is present) and the role of bright galaxies (*cD* or *BG*, if the bright cluster members role is significant). Other peculiarities are noted as *P*. “Flatness signs” can correspond to filamentary substructure or preferential plane in cluster. The designations can be combined, for example *CFcD* or *ILP*. Unfortunately, like to morphology of galaxies case, programmatic way does not allow to distinguish morphology without visual preview and control.

We create the Cluster Cartography set (hereafter CC) for simplification of the galaxy clusters classification.

2. Observational Data

The CC set was create for morphology classification of galaxy clusters of the “A Catalogue of Galaxy Clusters and Groups” (Panko & Flin, 2006, hereafter PF). The PF Catalogue was constructed on Münster Red Sky Survey Galaxy Catalogue (Ungrue et al., 2003, hereafter MRSS) as the observational basis. Each PF galaxy cluster has the list of galaxies in the cluster field inclusive for each galaxy information accordingly to MRSS, specifically RA_{2000} and Dec_{2000} , r_F magnitude, major and minor axes and positional angle of major axis of galaxy best-fitted ellipse (Ungrue et al., 2003).

2. The Cluster Cartography set

The cluster map is constructed in rectangular coordinates recalculated into arcseconds. The equatorial coordinates were recalculated to rectangular ones centered in the cluster center by usual way. The CC set allows to construct the cluster map in four modes:

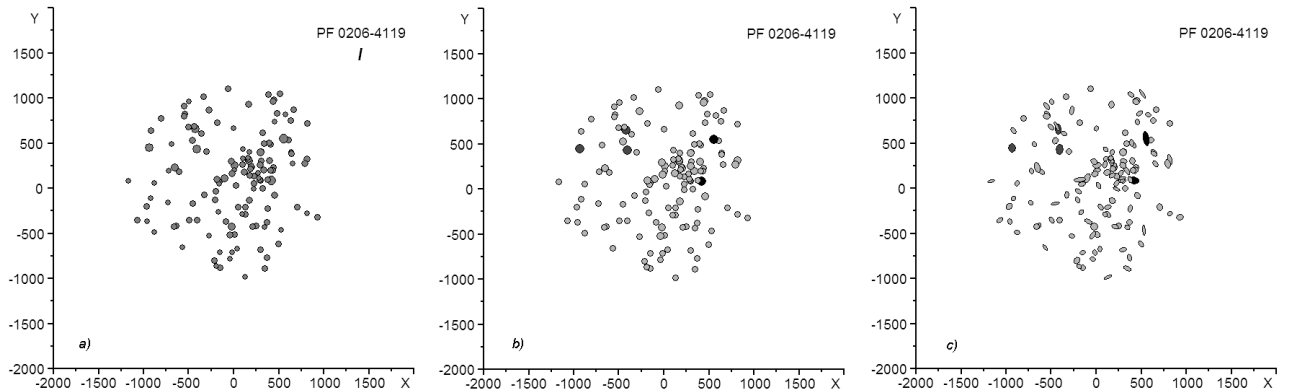


Figure 1: The modes of cluster mapping. All maps constructed for the same I -type cluster PF 0206-4119.

- all symbols are circles and have the same size;
- all symbols are circles and the symbol size corresponds to magnitude of galaxy (Fig. 1a and b);
- the symbol size corresponds to magnitude of galaxy and each symbol illustrates the galaxy shape and orientation in the projection on the celestial sphere (Fig. 1c);
- the symbols illustrates the galaxy shape and orientation in the projection on the celestial sphere, but size of symbol corresponds to galaxy size in arcseconds.

Additionally brightest galaxies can be marked by darker gray shades (Fig. 1b and c).

The shown in Fig.1b CC mode allows to estimate the morphological type according to Panko (2013) and the select the clusters for numerical definition. The analyze of distribution of ellipticities of galaxies in the cluster notes to one more parameter in classification – the part of E-type galaxies (Panko & Flin, 2014). E-rich and S-rich galaxy clusters were recognized by Oemler in 1974. The galaxy shape and orientation mode was added for previous estimation of positions of E-type galaxies in the cluster field. In our data set (accordingly to MRSS) we can divide galaxies only to elliptical and non-elliptical. Galaxies with ellipticity $E > 0.5$ can be lenticular or spiral (near edge-on view) or interactive ones. Positions of these galaxies in E-poor clusters is important in connection with Morphology – Density relation (Dressler, 1980).

The diameter of circle symbol m' was calculated using galaxy magnitude m as:

$$m' = 3 \cdot 2^{0.6(18.5-m)} + 6 \quad (1)$$

The coefficients can be changed in case of need, but for typical map size – 4000×4000 arcsec – the symbol sizes calculated according to (1) are optimal.

The sizes of major and minor axes ($2a$ and $2b$) for shown in Fig. 1c CC mode are calculated from m' and

ellipticity E as:

$$2a = \frac{m'}{\sqrt[4]{1 - 2E + E^2}}; \quad 2b = \frac{(m')^2}{2a} \quad (2)$$

Note, the ellipticity $E = 1 - \frac{b}{a}$. The equations (2) transform the circle to ellipse with the same area and connect symbol axes with galaxy magnitude. We use MRSS data for maps shown real galaxy size with magnitudes noted as shades of gray in CC mode 4.

2. Conclusion

We tested the CC set in different modes on 247 rich PF galaxy clusters. It allows to estimate galaxy cluster morphological type quickly. We will use the CC set in future work for study of 1746 PF galaxy clusters with richness 50 and more. About of 1200 galaxy clusters in this list have no morphological types and using the CC set allows to improve our data set.

Acknowledgements. This research has made use of NASA's Astrophysics Data System.

References

- Bautz P. & Morgan W.W.: 1970, *ApJ*, **162**, L149.
 Dressler A.: 1980 *ApJ*, **236**, 351.
 López-Cruz O., Yee H.K.C., Brown J.P., et al.: 1997, *ApJ*, **475**, L97.
 López-Cruz O. & Gaztanaga E.: 2001, *arXiv:astroph/0009028*.
 Oemler A.Jr.: 1974, *ApJ*, **194**, 1.
 Panko E. & Flin P.: 2006, *J. Astr. Data*, **12**, 1.
 Panko E.: 2013, *Odessa Astr. Publ.*, **26**, 90.
 Panko E. & Flin P.: 2014, *Odessa Astr. Publ.*, **27**, 32.
 Rood H.J. & Sastry G.N.: 1971, *PASP*, **83**, 313.
 Ungruue R., Seitter W.C. & Duerbeck, H.W.: 2003, *J. Astr. Data*, **9**,1.

BIG RIP AND OTHER SINGULARITIES IN ISOTROPIC HOMOGENEOUS COSMOLOGICAL MODELS WITH ARBITRARY EQUATION OF STATE

S.L. Parnovsky

Astronomical Observatory, Taras Shevchenko National University of Kyiv,
3 Observatorna Str., 04053, Kyiv, Ukraine, *par@observ.univ.kiev.ua*

ABSTRACT. We study the possible types of future singularities in the isotropic homogeneous cosmological models for the arbitrary equation of state of the contents of the Universe. We obtain all known types of these singularities as well as two new types using a simple approach. No additional singularity types are possible. We name the new singularities type “Big Squeeze” and “Little Freeze”. The “Big Squeeze” is possible only in the flat Universe after a finite time interval. The density of the matter and dark energy tends to zero and its pressure to minus infinity. This requires the dark energy with a specific equation of state that has the same asymptotical behaviour at low densities as the generalised Chaplygin gas. The “Little Freeze” involves an eternal expansion of the Universe. Some solutions can mimic the Λ CDM model.

Keywords: Relativistic cosmology

1. Introduction

During almost a century, cosmologists considered only two possible scenarios of the future of our Universe – an eternal expansion of open or flat Universe or future recollapse of the closed Universe with the “Big Crunch”. Nowadays we know that the Universe contains not only several types of matter, including the dark matter, baryonic matter and massless particles, but also the mysterious dark energy (DE). We know about its existence only for the last few decades. Honestly, we know very little about DE properties, in particular about the DE equation of state.

Even for the simplest type of the DE equation of state

$$p = w\rho \quad (1)$$

with $w = \text{const}$, where p is the pressure and ρ is the mass density, the Universe can meet its end in absolutely different way. If $w < -1$ we deal with so-called phantom energy. In this case during the finite time period the matter and energy density, the Hubble parameter H and the scale factor of the Universe a increase to infinity. Such type of possible future singularity was

discovered by Caldwell, Kamionkowski and Weinberg (2003) and called “Big Rip”.

Note that the latest estimations of the w value do not reject this possibility. The data on the cosmic microwave background spectra from the Planck and WMAP satellites together with ground measurements and data from baryonic acoustic oscillations (BAO) provide the estimation $w = -1.13_{-0.25}^{+0.23}$ at 95% confidence level (CL). The 9-year data from the WMAP satellite plus the determination of the Hubble constant and BAO data provide estimations $w = -1.073_{-0.089}^{+0.090}$ for the flat Universe and $w = -1.19 \pm 0.12$ for the non-flat Universe at 68% CL. Adding 472 type Ia supernovae data improves these estimations to $w = -1.084 \pm 0.063$ and $w = -1.122_{-0.067}^{+0.068}$, respectively.

Thus, the possibility of the “Big Rip” sealing the fate of the Universe is not to be taken lightly. This is not the only theoretically possible type of cosmological singularity except “Big Bang” and “Big Crunch”. Their first classification was carried out by Nojiri, Odintsov and Tsujikawa (2005). Four possible types were found for the singularities at $t = t_0$ with finite t_0 . They include:

- **Type I** $a, \rho, |p| \rightarrow \infty$ (“Big Rip”)
- **Type II** $a \rightarrow a_0; \rho \rightarrow \rho_0; |p| \rightarrow \infty$ (“sudden”)
- **Type III** $a \rightarrow a_0; \rho, |p| \rightarrow \infty$ (it was named “Big Freeze” lately)
- **Type IV** $a \rightarrow a_0; \rho, |p| \rightarrow 0$ and higher derivatives of the Hubble parameter H diverge.

There are some singularities with $t_0 = \infty$, too. The “Little Rip” singularity (Frampton, Ludwick and Scherrer, 2012) similar to the “Big Rip”, but with eternal expansion is among them.

Some types of singularities were found and demonstrated for some specific equations of state. Cosmologists considered the particular cases of the phantom generalised Chaplygin gas equation of state, tachyon field, scalar fields with specific potentials, etc. Naturally, a question arose, whether all the possible singularity types have been considered.

In this article we try to give an exhaustive answer to this question for the isotropic and homogeneous Universe. To make it worse, in addition to unknown DE equation of state we have three possible signs of space curvature. We are interesting in the complete list of the possible types of future singularities for an arbitrary equation of state for three signs of space curvature. We consider an arbitrary equation of state $p(\rho)$ without any constraints except $\rho \geq 0$. In particular we do not use the strong energy condition $\rho + 3p > 0$.

2. The search for future singularities in FLRW Universe

We consider the homogeneous isotropic Universe with the Friedmann-Lemaître-Robertson-Walker (FLRW) metric

$$ds^2 = dt^2 - a(t)^2 [d\chi^2 + F^2(\chi)dO^2], \quad (2)$$

where $a(t)$ is the scale factor, $dO^2 = d\Theta^2 + \cos^2(\Theta)d\varphi^2$ is the distance element on a unit sphere, $F(\chi) = \sin(\chi)$ and $k = 1$ for the closed Universe, $F(\chi) = \sinh(\chi)$ and $k = -1$ for the open one, and $F(\chi) = \chi$ and $k = 0$ for the spatially flat models. We use the system of units in which $G = 1$ and $c = 1$. This Universe is filled by all kinds of matter and dark energy with a mass density ρ and an effective pressure $p(\rho)$. In this system of units the energy density ε coincides with ρ . The Einstein equations for the metric (2) reduce to the well-known Friedmann equations. We need the expression for the Hubble parameter $H = a^{-1}da/dt$

$$H^2 = \frac{8\pi}{3}\rho - \frac{k}{a^2} \quad (3)$$

and the hydrodynamical equation or the energy conservation equation

$$\frac{d\rho}{dt} = -3(\rho + p)H. \quad (4)$$

The Friedmann equation for the scale factor

$$\frac{d^2a}{dt^2} = -\frac{4\pi}{3}a(\rho + 3p) \quad (5)$$

follows from the equations (3) and (4).

2.1. Flat model

We start from the flat model with $k = 0$. The equation (3) provides the expression $H = (8\pi\rho/3)^{1/2}$. After substituting it into (4) we obtain a simple equation with the solution

$$\Delta t = t_0 - t_1 = -\frac{1}{2(6\pi)^{1/2}} \int_{\rho_1}^{\rho_0} \frac{d\rho}{\rho^{1/2}(\rho + p(\rho))}. \quad (6)$$

Here the subscript 1 corresponds to the initial parameters (i.e. t_1 is “now”) and the subscript 0 corresponds to the parameters of the Universe in the future at time t_0 after a time interval Δt . We will denote the instant of time of any terminal cosmological singularity as t_0 , and use (6) to analyse their properties. After finding the dependence $\Delta t(\rho)$ we find the inverse function $\rho(\Delta t)$ and $H(\Delta t)$, the integration of the last one gives $\ln(a)$.

The first thing to check is the finiteness of Δt . If the integral in (6) diverges we obtain $t_0 = \infty$ and this case deals with the asymptotic evolution in the future. An example of such solution is the “Little Rip”.

We are going to go over all possible types of singularity. We consider three possible cases for ρ_0 . It can be infinite, finite and nonzero, or equal to zero. Let us consider it one by one.

2.1.1 Infinite terminal density

Let us start with a well-known “Big Rip” singularity to illustrate our approach. We consider the equation of state (1). If $w = -1$ we deal with the effective cosmological constant. According to (4) in this case the density and the pressure are constant. If $w > -1$ the values of ρ and H decrease in time because of (4). If $w < -1$ the values of ρ and H increase due to (4) and become infinite at time t_0 . Equation (6) gives us in this case the relations

$$\rho_1 = \frac{1}{6\pi(1+w)^2\Delta t^2}, \quad H = \frac{2}{3|1+w|\Delta t}. \quad (7)$$

This is the so-called “Big Rip” case. The scale factor of the Universe diverges $a \propto \Delta t^{-\frac{2}{3|1+w|}}$.

A somewhat similar case is when w is not constant, but asymptotically tends to -1 : $\rho/p \xrightarrow{\rho \rightarrow \infty} -1$. Let us assume that it follows the power law

$$\rho + p \xrightarrow{\rho \rightarrow \infty} -A\rho^\alpha \quad (8)$$

with $\alpha < 1$, $A = \text{const}$. The integral in (6) is finite at $1/2 < \alpha < 1$. In this case we have the “Big Rip” with $H \propto \Delta t^{1/(1-2\alpha)}$, $\ln a \propto \Delta t^{2(1-\alpha)/(1-2\alpha)}$. It occurs later and has a sharper shape for the same initial value ρ_1 in comparison with the equation of state (1).

If $\alpha < 1/2$ the integral in (6) becomes divergent and we have to put $t_0 = \infty$. This is the so-called “Little Rip” introduced in (Frampton, Ludwick and Scherrer, 2012). In this case we rewrite (6) in the form

$$\Delta t = t - t_1 = -\frac{1}{2(6\pi)^{1/2}} \int_{\rho_1}^{\rho(t)} \frac{d\rho}{\rho^{1/2}(\rho + p(\rho))}. \quad (9)$$

This case corresponds to an eternally accelerating expansion of the Universe: $H \propto t^{1/(1-2\alpha)}$, $\ln a \propto t^{2(1-\alpha)/(1-2\alpha)}$.

In the intermediate case $\alpha = 1/2$ we must take into account a possible logarithmic divergence and consider

the equation of state with the asymptote $\rho + p \xrightarrow{\rho \rightarrow \infty} -A\rho^{1/2}(\ln \rho)^\beta$. At $\beta > 1$ we deal with the unconventional ‘‘Big Rip’’ with $\ln \rho \propto \Delta t^{1/(1-\beta)}$, at $\beta < 1$ we deal with the ‘‘Little Rip’’ with $\ln \rho \propto t^{1/(1-\beta)}$. At $\beta = 1$ we consider the equation of state with the asymptotic $\rho + p \xrightarrow{\rho \rightarrow \infty} -A\rho^{1/2}(\ln \rho)(\ln \ln \rho)^\gamma$. There is the ‘‘Big Rip’’ with $\ln \ln \rho \propto \Delta t^{1/(1-\gamma)}$ at $\gamma < 1$ and the ‘‘Little Rip’’ with $\ln \ln \rho \propto t^{1/(1-\gamma)}$ at $\gamma > 1$.

So far we considered cases with $a \xrightarrow{\rho \rightarrow \infty} \infty$, but this is not required. For example, a type III singularity has finite t_0 and a_0 values, but $\rho, H, |p| \xrightarrow{t \rightarrow t_0} \infty$.

Let us consider this type of singularity. From $H = a^{-1}da/dt \xrightarrow{t \rightarrow t_0} \infty$ and $a(t) \xrightarrow{t \rightarrow t_0} a_0$ we see that $a(t)$ is regular, but da/dt diverges at $t = t_0$. This is possible if the scale factor has a power-law asymptote

$$a(t) \xrightarrow{t \rightarrow t_0} a_0 - B(t_0 - t)^\lambda \quad (10)$$

with $0 < \lambda < 1$. This yields $H \xrightarrow{t \rightarrow t_0} \lambda B(t_0 - t)^{\lambda-1}/a_0$. From (3) we obtain for this case $\rho(t) \propto (t_0 - t)^{2(\lambda-1)}$. After substituting these expressions in (4) we get $\rho(t) + p(t) \propto (t_0 - t)^{\lambda-2}$. This corresponds to the equation of state (8) with $\alpha = \frac{2-\lambda}{2-2\lambda}$, $\lambda = \frac{2\alpha-2}{2\alpha-1}$. In this case $\alpha > 1$ and $|p| \propto \rho^\alpha \gg \rho$ in the vicinity of the singularity.

Let us consider this type of singularity directly from (6). If $\rho \xrightarrow{t \rightarrow t_0} \infty$ but $\rho/p \xrightarrow{\rho \rightarrow \infty} 0$, e.g. $p(\rho) \xrightarrow{\rho \rightarrow \infty} -A\rho^\alpha$ with $\alpha > 1$, $A = const$ we also have a singularity with $H \propto \Delta t^{1/(1-2\alpha)}$, $\ln a \propto \Delta t^{2(1-\alpha)/(1-2\alpha)} = \Delta t^\lambda$. Note that at $\alpha < 1$ we get the ‘‘Big Rip’’ case considered above. But in the case of the ‘‘Big Freeze’’ singularity the scale factor tends to some constant value.

If we deal with the power law (10) for the scale factor with some noninteger $\lambda > 1$ we have no ‘‘Big Freeze’’ singularity, but some higher derivatives of H diverge. If $1 < \lambda < 2$ both parts of the Friedmann equation (5) diverge, if $\lambda > 2$ both of them tend to zero. This case corresponds to $\rho \xrightarrow{t \rightarrow t_0} 0$, $|p| \xrightarrow{t \rightarrow t_0} \infty$ and we will consider it later.

Is a version of the ‘‘Big Freeze’’ with $t_0 = \infty$ possible? It could be named the ‘‘Little Freeze’’ similarly to the situation with the ‘‘Big Rip’’ and the ‘‘Little Rip’’. In this case instead of (10) we consider an asymptotic behaviour of the scale factor in the form $a(t) \xrightarrow{t \rightarrow \infty} a_0 - Bt^\lambda$ with $\lambda < 0$. According to (3) and (4) we have in this case $\rho(t) \propto t^{2\lambda-2} \xrightarrow{t \rightarrow \infty} 0$ and $p(t) \propto t^{\lambda-2} \xrightarrow{t \rightarrow \infty} 0$. This possibility will be considered later, too.

2.1.2 Finite terminal density

Let us consider singularities with a nonsingular $\rho \xrightarrow{t \rightarrow t_0} \rho_0 \neq 0$. In this case all nontrivial solutions require $p + \rho$ factor to diverge or vanish according to

(6). In the first case $|p| \rightarrow \infty$, the second one corresponds to the crossing the line $\rho + p = 0$. It corresponds to the equation of state of the cosmological constant, separating the phantom energy domain with an effective $w < -1$ from the domain of not so exotic matter $w > -1$. We will see that the possibility of such crossing depends on the parameters of the equation of state.

We start with considering solutions with finite t_0 . Both cases could be described by a single power-law asymptote of the equation of state

$$\rho + p(\rho) \xrightarrow{\rho \rightarrow \rho_0} C(\rho - \rho_0)^\mu \quad (11)$$

with $C = const$.

At $\mu < 0$ the modulus of the pressure tends to infinity, at $\mu > 0$ the $\rho + p$ reaches zero. The finiteness of t_0 is possible only at $\mu < 1$. In this case we have $\rho(t) - \rho_0 \propto \Delta t^{1/(1-\mu)}$, $\rho(t) + p(t) \propto \Delta t^{\mu/(1-\mu)}$. The singularity with $\mu < 0$ and $|p| \xrightarrow{\rho \rightarrow \rho_0} \infty$ is referred to as the type II or sudden singularity. The value of H tends to finite H_0 , so the scale factor linearly increases.

The achievement of $\rho + p = 0$ condition in finite time is possible if $0 < \mu < 1$. Thus, the Universe can change the type of its equation of state from phantom energy to a more ordinary one, but only for such kind of the asymptote of the equation of state.

At $\mu > 1$ we obtain $t_0 = \infty$, i.e. the asymptotic approximation of $\rho + p = 0$ condition. The evolution of such a Universe at the terminal stage practically coincides with the evolution of the flat Universe with a cosmological constant and without any other types of matter. There is no spacetime singularity in this case. Using the approximation (11) we obtain the asymptotes $\rho(t) - \rho_0 \propto t^{1/(1-\mu)}$, $\rho(t) + p(t) \propto t^{\mu/(1-\mu)} \rightarrow 0$ at $t \rightarrow \infty$. This solution can mimic the Λ CDM model.

2.1.3 Zero terminal density

This last possibility assumes $\rho_0 = H_0 = 0$, which means that a scale factor tends to some extremum. But this does not mean an asymptotic expansion or contraction of the Universe is impossible. One simple example is the case $a \propto t^\eta$, $0 < \eta < 1$ when the Universe keeps expanding, but H decreases and tends to zero.

Let us consider the power-law asymptote of the equation of state

$$\rho + p \xrightarrow{\rho \rightarrow 0} -D\rho^\nu \quad (12)$$

and substitute it into (6). The integral in (6) is finite at $\nu < 1/2$, which yields finite t_0 . In this case $\rho \propto \Delta t^{2/(1-2\nu)} \xrightarrow{t \rightarrow t_0} 0$, $H \propto \Delta t^{1/(1-2\nu)} \xrightarrow{t \rightarrow t_0} 0$, $\rho + p \propto \Delta t^{2\nu/(1-2\nu)}$. If $0 < \mu < 1/2$, pressure tends to zero. This is a type IV singularity. If $\lambda = 1 + 1/(1 - 2\nu)$ is a noninteger number, the higher derivatives of $H \propto \Delta t^{\lambda-1}$ diverge. The condition $0 < \mu < 1/2$ means $\lambda > 2$, so the first derivative of H is finite, as well as both sides of the Friedmann equation (5). The value of

Table 1: Possible cosmological singularities except “Big Bang” and “Big Crunch”

T	Nickname	EoS	ρ_0	$ p_0 $	$p_0 + \rho_0$	a_0	ρ	$p + \rho$	a
$t \rightarrow t_0, \Delta t = t_0 - t \rightarrow 0$									
I	“Big Rip”	(1), $w < -1$	∞	∞	$-\infty$	∞	$\propto \Delta t^{-2}$	$\propto \Delta t^{-2}$	$a \propto \Delta t^{-2/(3 1+w)}$
I	“Big Rip”	(8), $1/2 < \alpha < 1$	∞	∞	$-\infty$	∞	$\propto \Delta t^{2/(1-2\alpha)}$	$\propto \Delta t^{2\alpha/(1-2\alpha)}$	$\ln a \propto \Delta t^{2(1-\alpha)/(1-2\alpha)}$
III	“Big Freeze”	(8), $\alpha > 1$	∞	∞	$-\infty$	a_0	$\propto \Delta t^{2/(1-2\alpha)}$	$\propto \Delta t^{2\alpha/(1-2\alpha)}$	$\lambda = (2\alpha - 2)/(2\alpha - 1)$
II	“sudden”	(11), $\mu < 0$	ρ_0	∞	$-\infty$	a_0	$\rho - \rho_0 \propto \Delta t^A$	$\propto \Delta t^{\mu A}$	$a \rightarrow a_0 - H_0 \Delta t$
IV		(12), $0 < \nu < 1/2$	0	0	0	a_0	$\propto \Delta t^{2/(1-2\nu)}$	$\propto \Delta t^{2\nu/(1-2\nu)}$	$\lambda = (2 - 2\nu)/(1 - 2\nu)$
New	“Big Squeeze”	(12), $\nu < 0$	0	∞	$-\infty$	a_0	$\propto \Delta t^{2/(1-2\nu)}$	$\propto \Delta t^{2\nu/(1-2\nu)}$	$\lambda = (2 - 2\nu)/(1 - 2\nu)$
$t \rightarrow \infty$									
	“Little Rip”	(8), $0 < \alpha < 1/2$	∞	∞	$-\infty$	∞	$\propto t^{2/(1-2\alpha)}$	$\propto t^{2\alpha/(1-2\alpha)}$	$\ln a \propto t^{2(1-\alpha)/(1-2\alpha)}$
	“Little Rip”	(8), $\alpha < 0$	∞	∞	0	∞	$\propto t^{2/(1-2\alpha)}$	$\propto t^{2\alpha/(1-2\alpha)}$	$\ln a \propto t^{2(1-\alpha)/(1-2\alpha)}$
	“Little Freeze”	(12), $1/2 < \nu < 1$	0	0	0	a_0	$\propto t^{2/(1-2\nu)}$	$\propto t^{2\nu/(1-2\nu)}$	$a \rightarrow a_0 - Bt^B$
	“Little Freeze”	(12), $\nu > 1$	0	0	0	∞	$\propto t^{2/(1-2\nu)}$	$\propto t^{2\nu/(1-2\nu)}$	$\ln a \propto t^{2(\nu-1)/(2\nu-1)}$

λ is the same as in (10). We can introduce the effective barotropic index $w = p/\rho \propto \Delta t^{(2\nu-2)/(1-2\nu)} \rightarrow \infty$.

If $\mu < 0$ we have $|p| \xrightarrow[t \rightarrow t_0]{} \infty$. This is a new type of the future singularity, which we name “Big Squeeze”. It combines certain properties of the sudden singularity and the type IV singularity. It corresponds to $1 < \lambda < 2$ in (10). The first derivative of H and both sides of the Friedmann equation (5) diverge. The asymptotics near this singularity type are $\rho \propto \Delta t^{2/(1-2\nu)} \xrightarrow[t \rightarrow t_0]{} 0$, $H \propto \Delta t^{1/(1-2\nu)} \xrightarrow[t \rightarrow t_0]{} 0$, $|p| \propto \Delta t^{2\nu/(1-2\nu)} \xrightarrow[t \rightarrow t_0]{} \infty$, $a \xrightarrow[t \rightarrow t_0]{} a_0 + \text{const} \Delta t^{(2-2\nu)/(1-2\nu)} \rightarrow a_0$. It requires the equation of state (12) with negative ν . The example is the generalized Chaplygin gas which occurs in some cosmological theories.

At $1/2 < \nu < 1$ the integral in (6) diverges and $t_0 = \infty$. In this case $\rho \propto t^{2/(1-2\nu)} \xrightarrow[t \rightarrow \infty]{} 0$, $H \propto t^{1/(1-2\nu)} \xrightarrow[t \rightarrow \infty]{} 0$, $\rho + p \propto t^{2\nu/(1-2\nu)} \xrightarrow[t \rightarrow \infty]{} 0$, $a \xrightarrow[t \rightarrow \infty]{} a_0 - Bt^{(2\nu-2)/(2\nu-1)}$. This is the mentioned above solution which could be named the “Little Freeze”. In this case the effective barotropic index $w = p/\rho \propto t^{(2\nu-2)/(1-2\nu)} \rightarrow \infty$.

At $\nu = 1/2$ we can take into account the possible logarithmic factor and consider the asymptotic equation of state $\rho + p \xrightarrow[\rho \rightarrow 0]{} -D\rho^{1/2}(\ln \rho)^\beta$. At $\beta > 1$ we deal with the unconventional type IV singularity with $\ln \rho \propto \Delta t^{1/(1-\beta)}$, at $\beta < 1$ we deal with the “Little Freeze” with $\ln \rho \propto t^{1/(1-\beta)}$. At $\beta = 1$ we consider the equation of state with the asymptotic $\rho + p \xrightarrow[\rho \rightarrow 0]{} -A\rho^{1/2}(\ln \rho)(\ln \ln \rho)^\gamma$, etc.

At $\nu > 1$ we deal with the expanding Universe and $\ln a \propto t^{(2\nu-2)/(2\nu-1)} \xrightarrow[t \rightarrow \infty]{} \infty$ at $D > 0$ in spite of $H \propto t^{1/(1-2\nu)} \xrightarrow[t \rightarrow \infty]{} 0$. This is the new “Little Freeze” case. The higher derivatives of H diverge. At $\nu = 1$ the Universe expands according to power law $a \propto t^{2/3D}$. The effective barotropic index $w = p/\rho \rightarrow -1$.

2.2. Open and closed models

The second term in the right-hand side of (3) does not affect the properties of the singularities with $\rho, H \rightarrow \infty$ and $\rho \rightarrow \rho_0 \neq 0, H \rightarrow H_0 \neq 0$. The only exception is the “Big Crunch” singularity with $a \rightarrow 0$ which we do not study in this paper.

But we must revise a possibility of the existence and the properties of singularities with $H \rightarrow 0$ or $\rho \rightarrow 0$. A simple analysis shows that in all cases we have no new type of singularity. The equation of state (12) with $\nu < 1$ could provide the type IV or the “Big Squeeze” singularities only for the flat model.

3. Conclusion

We tabulate all main cases of the cosmological singularities in Table 1. T and EoS mean type and equation of state, λ corresponds to (10), $A = 1/(1-\mu)$, $B = 2(1-\nu)/(1-2\nu)$. The terminal values denoted ρ_0 and a_0 are finite and nonzero. Note that the “Big Squeeze” and the type IV cases are possible only for the flat Universe. The asymptote (11) of the equation of state at $0 < \mu < 1$ corresponds to changing the type of energy from phantom one to ordinary one or vice versa. At $\mu > 1$ it provides an eternal near- Λ CDM expansion of the Universe.

Acknowledgements. Publications are based on the research provided by the grant support of the State Fund For Fundamental Research (project F64/42-2015).

References

- Caldwell R.R., Kamionkowski M., Weinberg N.N.: 2003, *Phys. Rev. Lett.*, **91**, 071301.
 Nojiri S., Odintsov S.D., Tsujikawa S.: 2005, *Phys. Rev. D*, **71**, 063004.
 Frampton P.H., Ludwick K.J., Scherrer R.J.: 2011, *Phys. Rev. D*, **84**, 083001.

ON THE MECHANISM OF THE FORMATION OF MAGNETO-HYDRODYNAMIC VORTICES IN THE SOLAR PLASMA

E. A. Pashitskii

Institute of Physics, National Academy of Sciences of Ukraine,
pr. Nauki 46, Kyiv, 03680 Ukraine, *pashitsk@iop.kiev.ua*

ABSTRACT. Based on the magnetohydrodynamic (MHD) equations for an incompressible conductive viscous fluid, the possible mechanism of the formation of giant MHD vortices recently discovered in the solar atmosphere (chromosphere) is analyzed. It is assumed that these vortices arise in the regions of the solar surface (photosphere) with ascending flows of hot plasma that arrives from the inner regions of the Sun as a result of thermal convection and is accelerated upward under the action of the chromospheric plasma pressure gradient. It is shown that, under the assumption of plasma incompressibility and flow continuity, the ascending plasma flows induce converging radial plasma flows, which create the convective and Coriolis nonlinear hydrodynamic forces due to the nonzero initial vorticity of the chromospheric plasma caused by Sun's rotation. The combined action of these two forces leads to the exponential acceleration of the solid-body rotation of plasma inside the ascending flow, thereby creating a vortex that generates an axial magnetic field, in agreement with astrophysical observations.

Keywords: solar plasma, MHD vortex

1. Introduction

Recent publication [1] reported observation of cylindrically symmetric vortex structures with characteristic radii of $R \approx 500$ km in the solar atmosphere in the UV spectral region. There may be more than 10^4 such structures simultaneously on the Sun's surface. These vortices penetrate through the entire chromosphere reaching the lower layers of the solar corona at an altitude of 2500 km. The existence of such magnetohydrodynamic (MHD) vortices, which were earlier predicted in [2–4], is now confirmed by means of precision optical measurements of the Doppler shifts of the absorption lines of iron, calcium, and helium ions [5] corresponding to the vortex motion of the chromospheric plasma with velocities on the order of 4 km/s. It was suggested in [1] that such MHD vortices could be responsible for the heating of the corona plasma up to temperatures of several million degrees due to dissipation of the energy of Alfvén [6–10] and magnetosonic [11] waves excited by the vortex plasma motion. In [1], vortex structures were simulated numerically by using the MHD equations for a perfectly conducting ideal incompressible fluid with allowance for the processes of radiative energy transfer. It was assumed in [1] that an MHD vortex is accelerated due to its radial compression by con-

verging plasma flows, provided that the initial angular momentum of the vortex is conserved.

However, as will be shown below, an MHD vortex in plasma cannot be regarded as a conservative system in which the angular momentum is constant, because there is a permanent influx of matter with a nonzero vorticity into the vortex core from the surrounding chromospheric plasma, i.e., such a vortex is an open nonequilibrium system. As a result, the mechanism of the formation and evolution of an MHD vortex in the solar chromosphere cannot be considered completely established. In the present work, we analyze a possible mechanism of the formation of an MHD vortex in the solar chromosphere and the accompanying generation of magnetic fields and ohmic heating of the chromospheric plasma in the framework of an approximate description based on the MHD equations for an incompressible viscous fluid with a finite conductivity [12]. It is assumed that such vortices are initiated by the ascending flows of hot plasma that arise in some “hot spots” on the Sun's surface, i.e., in the regions of the photosphere where hot plasma rises from the inner regions of the Sun as a result of convection. This hot plasma expands and rapidly flows upwards in the gravitational field through the surrounding colder chromospheric plasma, whose pressure rapidly drops with altitude. Under the conditions of the flow continuity and plasma incompressibility, the ascending vertical flow creates converging radial flows. At a nonzero initial vorticity of the chromospheric plasma caused by the Sun's rotation, such converging flows give rise to convective and Coriolis nonlinear hydrodynamic forces. The combined action of these two forces leads to the acceleration of the solid-body rotation of plasma in the core of the MHD vortex, similar to the mechanism of the formation of air vortices in the Earth's atmosphere (such as whirlwinds, tornadoes, and typhoons) earlier analyzed in [13]. Here, we analyze axisymmetric vortex solutions to the nonlinear MHD equations with separable variables that satisfy the continuity equation and cause the kinematic and magnetic viscosities of an incompressible conductive fluid to vanish. Such solutions satisfy the principle of the minimum entropy generation in an open nonequilibrium system [13], i.e., correspond to the minimum dissipation rate of the kinetic and magnetic energies of the MHD vortex. It is shown that the vortex state is characterized by the exponential growth of both the azimuthal rotation velocity of the MHD vortex and the axial magnetic field, which qualitatively agrees with the observations [14,15] of the local concentration of the magnetic field under vortex motion of the solar plasma.

Such a growing magnetic field generates an azimuthal electric current in the external shell of the MHD vortex, which should lead to the ohmic heating of plasma in the chromosphere and lower layers of the solar corona. It is shown that, due to the instability of the growing tangential discontinuity of the azimuthal velocity at the boundary of the vortex core, strong local turbulence with an anomalously high viscosity develops in the surface layer, which leads to the dissipation of MHD vortices.

2. Basic equations for the description of MHD vortices in the solar chromosphere

To describe MHD vortices in the solar chromosphere, we will use the well-known set of MHD equations for an incompressible viscous conductive fluid [14].

We note that the MHD approximation can be used to describe electron-ion plasma only if the cyclotron radii of ions and electrons, as well as their Debye screening lengths and their free path lengths along the magnetic field, are smaller than the characteristic spatial scales of the problem (in particular, the MHD vortex dimensions). Such an approximation can also be used to describe a weakly ionized plasma with a high particle collision frequency and low electric conductivity. At the same time, plasma in a magnetic field can be assumed to be incompressible if the velocity of its macroscopic motion is lower than both the adiabatic sound speed $c_s = \sqrt{\Gamma P / \rho}$ (where Γ is the adiabatic index) and the Alfvén velocity $c_A = H / \sqrt{4\pi\rho}$.

Let us analyze cylindrical axisymmetric (i.e., independent of the azimuthal angle φ) vortex flows of a conductive fluid (plasma) in which the self-consistent magnetic field has only the azimuthal and axial components, $\mathbf{H}(0, H_\varphi, H_z)$. In this case, the set of MHD equations in cylindrical coordinates with allowance for the gravity acceleration g (which is directed vertically downward, i.e., in negative z direction) takes the form

$$\frac{\partial v_r}{\partial t} + v_r \frac{\partial v_r}{\partial r} + v_z \frac{\partial v_r}{\partial z} - \frac{v_\varphi^2}{r} \quad (1)$$

$$= -\frac{1}{\rho} \frac{\partial}{\partial r} \left(P + \frac{H_\varphi^2 + H_z^2}{8\pi} \right) + \frac{H_\varphi^2}{4\pi\rho r} + v \cdot \Delta v_r,$$

$$\frac{\partial v_\varphi}{\partial t} + v_r \frac{\partial v_\varphi}{\partial r} + v_z \frac{\partial v_\varphi}{\partial z} + \frac{v_r v_\varphi}{r} \quad (2)$$

$$= \frac{1}{4\pi\rho} H_z \frac{\partial H_\varphi}{\partial z} + v \cdot \Delta v_\varphi,$$

$$\frac{\partial v_z}{\partial t} + v_r \frac{\partial v_z}{\partial r} + v_z \frac{\partial v_z}{\partial z} = -\frac{1}{\rho} \frac{\partial}{\partial z} \left(P + \frac{H^2}{8\pi} \right) \quad (3)$$

$$-g + \frac{1}{4\pi\rho} H_z \frac{\partial H_z}{\partial z} + v \cdot \Delta v_z,$$

$$\frac{\partial H_\varphi}{\partial t} + v_r \frac{\partial H_\varphi}{\partial r} + v_z \frac{\partial H_\varphi}{\partial z} \quad (4)$$

$$= H_z \frac{\partial v_\varphi}{\partial z} + \frac{v_r H_\varphi}{r} + v_m \cdot \Delta H_\varphi,$$

$$\frac{\partial H_z}{\partial t} + v_r \frac{\partial H_z}{\partial r} + v_z \frac{\partial H_z}{\partial z} = H_z \frac{\partial v_z}{\partial z} + v_m \cdot \Delta H_z, \quad (5)$$

where v_r , v_φ , and v_z are the radial, azimuthal, and axial components of the hydrodynamic velocity of the fluid, respectively, v and v_m are the kinematic and magnetic viscosities, and the Laplace operator is

$$\Delta = \frac{\partial^2}{\partial r^2} + \frac{1}{r} \frac{\partial}{\partial r} + \frac{\partial^2}{\partial z^2}. \quad (6)$$

We note that terms v_φ^2 / r and $v_r v_\varphi / r$ on the left-hand side of equations (1) and (2) describe the centrifugal force and the local Coriolis nonlinear hydrodynamic force, respectively.

In this case, the continuity equation for an incompressible fluid, $\text{div } \mathbf{v} = 0$, and Maxwell's equation for the solenoidal magnetic field, $\text{div } \mathbf{H} = 0$, take the form

$$\frac{\partial v_r}{\partial r} + \frac{v_r}{r} + \frac{\partial v_z}{\partial z} = 0; \quad \frac{\partial H_z}{\partial z} = 0. \quad (7)$$

The simplest formal solutions to Eqs. (7) with the separable variables r and z in the region $r \leq R_0$ have the form

$$v_r(r) = -\beta \cdot r; \quad v_z(z) = v_{z_0} + \alpha \cdot z; \quad (8)$$

$$H_z = h = \text{const}.$$

where the parameters α and β are related by the formula

$$(\alpha - 2\beta) = 0. \quad (9)$$

3. Ascending flows of plasma in solar chromosphere

The expression for the radial velocity $v_r(r)$ in Eq. (8) describes an incompressible radial plasma flow converging toward the axis that is induced by the ascending plasma flow the axial velocity of which increases linearly along z axis, $v_z(z) = v_{z_0} + \alpha z$. According to time-independent equation (3),

$$v_z \frac{\partial v_z}{\partial z} = -\frac{1}{\rho} \frac{\partial P}{\partial z} - g + v \frac{\partial^2 v_z}{\partial z^2}, \quad (10)$$

such a velocity can appear under the action of the pressure P , which decreases with altitude according to the square law

$$P(z) = P_0 - \rho(az + bz^2), \quad (11)$$

where $a = (\alpha v_{z_0} + g)$ and $b = \alpha^2 / 2$. As will be shown below, such a dependence of the pressure on z can occur in the gravitational field at relatively low altitudes, provided that the plasma temperature sufficiently fast drops with altitude.

Let us suppose that hot plasma in a certain region of radius R_0 in the solar photosphere flows up due to thermal convection in the gravitational field. This plasma expands and flows upward under the action of the buoyancy force in the colder denser chromospheric plasma. As the plasma flows up and expands, it plasma cools down, so that its temperature in the initial stage decreases almost linearly with altitude,

$$T(z) \approx T_0 \cdot (1 - \chi z); \quad \chi = -\left(\frac{\partial \ln T}{\partial z} \right)_{z=0} > 0. \quad (12)$$

In this case, to within second-order terms in z , the barometric formula for the pressure of the chromospheric plasma in the Sun's gravitational field takes the form

$$P(z) = P_0 \cdot \exp\left\{-\frac{mgz}{k_B T(z)}\right\} \quad (13)$$

$$\approx P_0 \cdot \left[1 - \frac{mgz}{k_B T_0} - \frac{mg}{k_B T_0} \left(\chi - \frac{mg}{2k_B T_0}\right) z^2\right].$$

For $\chi > mg/2k_B T_0$, this formula coincides with the adopted dependence (11) of the pressure on the z coordinate if we set $a = P_0 \cdot mg/k_B T_0$ and $b = (\chi - mg/2k_B T_0) \cdot a$ (where m is the mass of a hydrogen atom). As a result, we obtain two equations for determining two parameters, v_{z0} and α , entering into the expression for the increasing velocity of the ascending flow,

$$\alpha v_{z0} = g \cdot \left(\frac{c_s^2}{\Gamma} \frac{m}{k_B T_0} - 1\right) > 0, \quad (14)$$

$$\alpha^2 = \frac{mg}{k_B T_0} \cdot \left(2\chi - \frac{mg}{k_B T_0}\right) > 0.$$

Taking into account the parameters of plasma in the lower layers of the solar chromosphere ($c_s \approx 10$ km/s and $T_0 \approx 6000$ K) and the value of the gravity acceleration on the Sun's surface ($g \approx 274$ m/s²), we obtain $\alpha v_{z0} \approx 57.5$ m/s² and $mg/k_B T_0 \approx 5.5 \cdot 10^{-6}$ m⁻¹. However, in this case, the parameter χ , which has the dimension of the reciprocal length and characterizes the cooling rate of hot plasma with altitude, remains undefined, due to which the values of α and v_{z0} cannot be estimated independently (see below).

Note that the radius R_0 of the ascending flow should increase with altitude, which prevents separation of the variables r and z in the MHD equations. However, if the longitudinal inhomogeneity scale L of the plasma flow radius is much larger than R_0 , then, with a high degree of precision, we can set $R_0 = const$, which substantially simplifies the problem and allows us to investigate the main physical processes affecting the dynamics and evolution of MHD vortices in the solar atmosphere by means of an approximate procedure of separation of variables without recourse to complicated computer simulations.

4. Solid-body vortex rotation of plasma

Let's assume that at $r \leq R_0$ the azimuthal components of the velocity and magnetic field are independent of z and have the form

$$v_\phi(r) = \omega \cdot r; \quad H_\phi(r) = \gamma \cdot r. \quad (15)$$

After the substitution of expressions (8) and (15) into Eqs. (1)–(5), a large number of terms on the right-hand sides (including those containing Laplace operator (6)) vanish. This corresponds to the zero kinematic and magnetic viscosities of the incompressible conductive fluid (plasma),

i.e., in fact to the nondissipative solid-body rotation of the MHD vortex core at $r < R_0$.

Substituting Eqs. (8) and (15) into Eqs. (1), (2), (4), and (5) and assuming that the parameters γ, ω and h are functions of t , we obtain the following set of first-order equations that describe the dynamics of the MHD vortex core:

$$\omega^2(t) - \beta^2 = \frac{1}{r\rho} \cdot \frac{\partial P}{\partial r} + \frac{\gamma^2(t)}{2\pi\rho}, \quad (16)$$

$$\frac{d\omega}{dt} - 2\beta \cdot \omega(t) = 0, \quad (17)$$

$$\frac{dh}{dt} - \alpha \cdot h(t) = 0. \quad (18)$$

In this case, Eq. (4) is reduced to the condition $d\gamma/dt = 0$, which is a consequence of the mutual compensation of the nonlinear terms $v_r \partial H_\phi / \partial r$ and $v_r H_\phi / r$ on the right- and left-hand sides of Eq. (4). This allows us to neglect the azimuthal component of the self-consistent magnetic field H_ϕ in the MHD vortex.

Since, according to Eq. (9), we have $\alpha = 2\beta$, solutions to Eqs. (17) and (18) have the form

$$\omega(t) = \omega(0) \cdot e^{\alpha t}, \quad h(t) = h(0) \cdot e^{\alpha t}, \quad (19)$$

where $\omega(0)$ and $h(0)$ are the initial values of the angular plasma rotation velocity and axial magnetic field, respectively.

Equation (16) governs spatial distribution and temporal behavior of plasma pressure in the core of the MHD vortex, which has the following form in the cyclostrophic regime of rotation of an incompressible fluid:

$$P(r, z, t) = \tilde{P}_0 + \frac{\rho r^2}{2} [\omega^2(t) + \omega^2(0) - \beta^2] - \frac{\rho z^2}{2} \alpha^2(t) - \rho z \tilde{g}, \quad (20)$$

where \tilde{P}_0 is the pressure at the vortex axis (see below), and $\tilde{g} = g + v_{z0} \alpha$.

5. Exponential regime of MHD vortex evolution

It follows from Eq. (19) that the angular velocity of the solid-body rotation of the MHD vortex core and the axial component of the self-consistent magnetic field increase exponentially with a characteristic time of $t_{exp} = 1/\alpha$.

We see that the source of the exponential acceleration of the vortex core rotation is the linear increase in the axial velocity of the ascending flow of incompressible plasma, $v_z(z) = (v_{z0} + \alpha z)$, as it propagates upward in the gravitational field of the Sun through the solar chromosphere, in which the temperature and pressure decrease with increasing altitude.

The value of α can be estimated by equating the velocity of the ascending flow $v_z(z) = v_{z0} + \alpha z$ to the speed of sound at the upper boundary of the solar chromosphere,

$L \approx 2500$ km. In the rarefied upper layers of the chromospheric plasma, the speed of sound is $\tilde{c}_s = \sqrt{2k_B \tilde{T} / m}$, where $\tilde{T} \approx 3 \cdot 10^4$ K, so that $\tilde{c}_s \approx 20$ km/s. Assuming that $v_{z0} \leq \tilde{c}_s$, we find that $\alpha \leq \tilde{c}_s / L \approx 8 \cdot 10^{-3} \text{ s}^{-1}$ and the characteristic time of the exponential evolution of the MHD vortex is $t_{\text{exp}} \geq L / \tilde{c}_s \approx 2$ min.

It should be noted that the exponential growth of the axial magnetic field $H_z(t) = h(t)$ qualitatively agrees with the local concentration of the magnetic field during the vortex motion of the chromospheric plasma observed in [14, 15]. In this case, the local Alfvén velocity $c_A(t) = H_z(t) / \sqrt{4\pi\rho}$ inside the vortex core grows exponentially in time (see (19)).

According to expression (20), the plasma pressure on the vortex axis at $z=0$ in the cyclostrophic regime of vortex rotation is

$$\tilde{P}_0(0,t) \approx P_0 - \frac{\rho R_0^2}{2} \cdot \omega^2(t). \quad (21)$$

According to Eqs. (19) and (21), this pressure decreases exponentially in time and vanishes at the time

$$t_0 = \frac{1}{2\alpha} \cdot \ln \left[\frac{2P_0}{\rho R_0^2 \cdot \omega^2(0)} \right] \approx \frac{1}{\alpha} \cdot \ln(c_s / V_0), \quad (22)$$

where $V_0 = R_0 \cdot \omega(0)$ is the initial azimuthal velocity of the vortex motion of plasma ($V_0 \ll c_s$). Since the negative pressure in the system leads to instability (collapse), an MHD vortex cannot exist at $t > t_0$. The time t_0 can be approximately estimated if we assume that, in the order of magnitude, the initial value of the angular velocity $\omega(0)$ coincides with the average solar atmosphere vorticity caused by the nonuniform (liquid-like) rotation of the Sun's surface with the angular velocity varying with latitude from $\Omega \approx 1/28$ day on the equator to $\Omega \approx 1/33$ day at a latitude of 75° . Estimates show that the initial vorticity is $\omega(0) \approx 2 \cdot 10^{-6} \text{ s}^{-1}$, which is one order of magnitude higher than the vorticity caused by the global Coriolis force on the solar surface.

As a result, the initial azimuthal velocity of plasma at the boundary of a vortex of radius $R_0 \approx 500$ km is $V_0 \approx 1$ m/s. Taking into account that the density of the chromospheric plasma on the Sun's surface is on the order of $\rho \approx 5 \cdot 10^{-9} \text{ g/cm}^3$ and the temperature is $T \approx 6000$ K and assuming that the density of hydrogen atoms is $n \approx 3 \cdot 10^{15} \text{ cm}^{-3}$, we find using the approximation of an ideal gas that the speed of sound is $c_s \approx 10$ km/s. Hence, with allowance for the above estimate of α and disregarding dissipation of the vortex kinetic energy (see below), we find that the maximum time of the exponential evolution of an MHD vortex is $t_0 \approx 15 / \alpha \approx 30$ min.

On the other hand, it should be taken into account that the solid-body rotation of the vortex core begins to decelerate when the azimuthal velocity at $r = R_0$ becomes compara-

ble with the speed of sound, because, at such velocities, the compressibility effects come into play and the fluid (plasma) acquires a nonzero bulk viscosity. Therefore, taking into account the exponential growth of the rotation velocity of the vortex core, the maximum azimuthal velocity $v_\phi^{\text{max}}(R_0, t_s) = V_0 \cdot \exp(\alpha \cdot t_s) \approx c_s$ is reached over a time $t_s = 1 / \alpha \cdot \ln(c_s / V_0)$, which coincides with t_0 . We note that the velocity of the vortex motion of the chromospheric plasma determined from the Doppler shift of the spectral lines is 4 km/s, which is half as large as the speed of sound, whereas according to computer simulations, the vortex velocity at altitudes of 2500 km, where the speed of sound is $c_s \approx 20$ km/s, can reach 15 km/s.

The time $t_0 \approx t_s$ also determines the maximum values of the axial component of the magnetic field inside the vortex core, $H_z = h(0) \cdot \exp(\alpha t_0)$, and the corresponding local Alfvén velocity $c_A^{\text{max}} = \sqrt{h^2(0) / 4\pi\rho} \cdot \exp(\alpha t_0)$. Assuming that the factor in front of the exponential in the last expression is on the order of the initial vortex velocity $V_0 \approx 1$ m/s, we find that $c_A^{\text{max}} \approx 10$ km/s. In this case, the magnetic field reaches its maximum value of $H_z^{\text{max}} \approx 250$ G, which agrees with observational data [14, 15].

Note that the excitation of Alfvén and magnetosonic waves in the MHD vortex core cannot lead to vortex deceleration and plasma heating, because the Alfvén velocity grows according to the same exponential law as the azimuthal velocity of plasma rotation, whereas the speed of sound decreases due to a decrease in the pressure in the vortex core.

6. Instability of the tangential discontinuity of the azimuthal velocity and local turbulence on the surface of the MHD vortex core

The exponential growth of the angular velocity of the solid-body plasma rotation in the MHD vortex core, where the radial and axial velocities are directly proportional to the radius r , is caused, as was mentioned above, by the combined action of the convective and Coriolis nonlinear hydrodynamic forces, which are equal in magnitude. However, in the external region $r \geq R_0$, where the radial and azimuthal velocities are proportional to r^{-1} , these forces, as can be easily verified, have opposite signs and exactly balance one other. As a result, there is no acceleration of the initial vorticity $\omega(0)$. Therefore, the azimuthal velocity experiences an exponentially growing jump (tangential discontinuity) at the vortex core boundary.

As was shown for the first time in [13], the exponential growth of the velocity jump leads to the absolute instability of surface perturbations accompanied by the growth of their amplitude according to the double exponential law of the form

$$|\xi_k(t)| = |\xi_k(0)| \cdot \exp \left\{ \frac{kV_0}{2\alpha} \cdot (e^{\alpha t} - \alpha t) \right\}, \quad (23)$$

where $\xi_k(0)$ is the initial perturbation with the wavenumber k at $t = 0$.

Such instability develops much faster than the exponential acceleration of the solid-body rotation of the MHD vortex core. As a result, a strongly turbulent state is rapidly established near the vortex surface. Turbulence is localized in a layer of thickness δ , which is comparable with the maximum amplitude of turbulent pulsations $l^* = |\xi_k|_{\max}$. The amplitude reaches its maximum value $|\xi_k|_{\max} \equiv |\xi_k(t_{\max})|$ at the time t_{\max} at which the velocity of turbulent pulsations

$$\tilde{v}_k(t) \equiv \frac{d\xi_k}{dt} = |\xi_k(t)| \cdot \frac{kV_0}{2} \cdot (\exp\{\alpha t\} - 1) \quad (24)$$

becomes equal to the speed of sound c_s and the effects of compressibility and finite viscosity come into play. It is well known that the wavenumber k of the most unstable surface perturbations has the same order of magnitude as the reciprocal thickness of the transition layer $1/\delta$. Hence, we have

$$l^* \approx \delta \approx |\xi_k|_{\max} \approx \pi / k_{\max}. \quad (25)$$

At $\alpha t_{\max} \gg 1$, expression (24) yields

$$t_{\max} \approx \frac{1}{\alpha} \cdot \ln \left(\frac{c_s}{\pi V_0} \right) \leq t_0. \quad (26)$$

Thus, the peak amplitude of turbulent pulsations cannot exceed

$$|\xi_k|_{\max} = \xi_0 \cdot \exp \left\{ \frac{kV_0}{2\alpha} \cdot \exp(\alpha t_0) \right\}. \quad (27)$$

Taking the logarithm of expression (27) with allowance for relationships (23) and (25), we obtain to within logarithmic accuracy the following transcendental equation for the characteristic scale length of turbulent pulsations l^* and, accordingly, the effective width δ of the turbulent transition layer on the vortex core boundary:

$$\delta \approx \frac{c_s}{2\alpha \cdot \ln(\delta / \xi_0)} \approx \frac{600}{\ln(\delta / \xi_0)} \text{ km}. \quad (28)$$

Assuming that the amplitude ξ_0 of the initial fluctuations of quasineutral plasma is on the order of the Debye screening length $D = \sqrt{k_B T / 8\pi e^2 n_e}$, which, at a chromospheric plasma temperature of $T \approx 6000$ K and an electron density of $n_e \approx 3 \cdot 10^{15} \text{ cm}^{-3}$, is $D \approx 10^{-5} \text{ cm}$, we find that the thickness of the turbulent region surrounding an MHD vortex is $\delta \approx 25 \text{ km}$, which corresponds to $\ln(\delta / D) \approx 25$. If the amplitude of turbulent pulsations is known, then, applying the dimensionality analysis, we find that the turbulent viscosity of plasma inside the turbulent layer is $\nu^* \approx c_s \cdot l^* / 3 \approx 8 \cdot 10^7 \text{ m}^2/\text{s}$.

The anomalously large effective viscosity of the turbulent layer improves the stability of the MHD vortex core during its evolution. In this regard, it may be supposed that the observed filamentary structure of strong solar flares is caused by the simultaneous formation of a large number of MHD vortices in the photospheric hot spots.

7. Deceleration of MHD vortices due to viscous energy dissipation and ohmic losses in the turbulent layer

As we mentioned above, solutions with separable variables correspond to zero kinematic and magnetic viscosities of the incompressible conductive fluid (plasma) both inside the MHD vortex core at $r \leq R_0$ and in the external region $r \geq (R_0 + \delta)$. However, the kinetic energy of the vortex should dissipate inside the turbulent surface layer of thickness $\delta \ll R_0$ with an anomalously large turbulent viscosity ν^* . The energy dissipation rate per unit vortex length is determined by the relationship

$$\frac{dE_{kin}^*}{dt} = -\frac{\rho\nu^*}{2} \int dV \left(\frac{\partial v_\phi}{\partial r} \right)^2 \approx -\pi R_0 \delta \rho \nu^* \frac{R_0^2 \omega^2(t)}{\delta^2}. \quad (29)$$

On the other hand, the kinetic energy (per unit length) of the accelerated solid-body rotation of the vortex core is determined by the expression

$$E_{kin}(t) = \pi \rho \int_0^{R_0} r dr \cdot v_\phi^2(r, t) = \frac{\pi}{4} \rho R_0^4 \cdot \omega^2(t). \quad (30)$$

In this case, the growth rate of the kinetic energy of vortex rotation accelerated under the action of the convective and Coriolis hydrodynamic forces is

$$\frac{dE_{kin}}{dt} = \frac{\pi}{2} \alpha \rho R_0^4 \cdot \omega(t) \frac{d\omega}{dt} \approx \frac{\pi}{2} \alpha \rho R_0^4 \cdot \omega^2(t). \quad (31)$$

Comparing expressions (29) and (31), we obtain the following condition for the weak dissipation of the vortex energy: $\nu^* < \alpha \cdot R_0 \cdot \delta / 2$. For the above parameter values, $\nu^* \approx 8 \cdot 10^7 \text{ m}^2/\text{s}$, $\alpha \approx 8 \cdot 10^{-3} \text{ s}^{-1}$, $R_0 \approx 500 \text{ km}$, and $\delta \approx 25 \text{ km}$, the left- and the right-hand sides of this inequality are nearly equal to one another, i.e., the rate of kinetic energy dissipation is nearly equal to the energy gain caused by the convective and Coriolis forces. As a result, in the final stage of evolution under the condition of strong turbulence in the surface layer, the MHD vortex reaches a regime of steady-state rotation and gradually dissipates.

There is another energy dissipation mechanism in an MHD vortex that is related to ohmic losses leading to Joule heating. The heat is generated by the electric currents induced by the growing magnetic fields that flow in plasma with a finite conductivity. According to Maxwell's equations

$$\text{rot } \mathbf{H} = \frac{4\pi}{c} \cdot \mathbf{j}, \quad \text{rot } \mathbf{E} = -\frac{1}{c} \frac{\partial \mathbf{H}}{\partial t} \quad (32)$$

the generation of magnetic fields during the exponential evolution of MHD vortices should be accompanied by the generation of electric currents \mathbf{j} and electric fields \mathbf{E} , which are related to one another via Ohm's law $\mathbf{j} = \sigma \mathbf{E}$. However, taking into account that the vortex evolution is a relatively slow process, we can consider only the first of Maxwell's equations. In particular, the axial magnetic field, which is uniform inside the vortex core and vanishes

in the transition layer of thickness δ , induces the azimuthal current

$$j_\varphi(t) = -\frac{c}{4\pi} \cdot \frac{\partial H_z(t)}{\partial r} \approx -\frac{c \cdot h(t)}{4\pi\delta}. \quad (33)$$

in this layer.

The azimuthal current of density (33) that flows inside the turbulent surface layer should lead to heat release in this layer, the power of which per unit vortex length is

$$Q \approx 2\pi R_0 \delta \cdot j_\varphi^2 / \sigma = c^2 R_0 \cdot h^2(t) / 8\pi\delta\sigma. \quad (34)$$

Here $\sigma = e^2 n_e \cdot \tau_e / m_e$ is the electron conductivity of the chromospheric plasma with the electron density $n_e \approx 3 \cdot 10^{15} \text{ cm}^{-3}$, m_e is the mass of an electron, and $\tau_e \approx 10^{-13} \text{ s}$ is the average time of electron–electron and electron–ion Coulomb collisions at an electron temperature of $T_e \approx 10^4 \text{ K}$. Hence, in the order of magnitude, we have $\sigma \approx 10^9 \text{ s}^{-1}$.

As a result, setting $h(t) \approx h(0) \cdot \exp(\alpha t_0)$, we find that the Joule heating power in the final stage of MHD vortex evolution is $Q \approx 1 \text{ MJ/km}$.

Joule losses must slow down the MHD vortex rotation, determined by relationships (38). The slowing down will be weak if

$$\frac{dE_{kin}(t)}{dt} = \frac{\pi}{2} \alpha \rho R_0^4 \cdot \omega^2(t) \gg Q(t). \quad (35)$$

Taking into account that the angular velocity $\omega(t)$ and the longitudinal magnetic field $h(t)$ grow according to the same exponential law, we can rewrite inequality (43) in the form

$$\frac{c^2 \cdot c_A^2(0)}{\pi \alpha \cdot \delta \cdot \sigma \cdot R_0 \cdot V_0^2} \ll 1, \quad (36)$$

which shows that, for the above parameter values, $\alpha \approx 8 \cdot 10^{-3} \text{ s}^{-1}$, $\sigma \approx 10^9 \text{ s}^{-1}$, $\delta \approx 25 \text{ km}$, and $R_0 \approx 500 \text{ km}$, the Joule losses weakly affect MHD vortex dynamics if $V_0 > c_{A0}$.

Due to ohmic heat release in the MHD vortex shell, additional heating and ionization of the chromospheric plasma, followed by its recombination upon cooling, take place. This should lead to the glow of MHD vortices in the visible and UV spectral regions. Since MHD vortices can reach the lower layers of the solar corona, heat released due to the ohmic heating of plasma, along with that released due to the dissipation of the magnetic and kinetic energies of vortices during their decay, can play a significant role in the heating of the solar corona to temperatures as high as 10^6 K . However, this issue requires additional study, which goes beyond the scope of the present work.

To conclude, it should be emphasized that the initial local vorticity of the solar plasma in the regions where MHD vortices begin to form can have opposite signs, so that the vortices in different solar hemispheres can rotate in different directions. Accordingly, the self-consistent axial magnetic fields generated by such vortices should have opposite directions. Thus it can be energetically advantageous for the magnetic field lines of the adjacent pairs of such vortices and anti-vortices to be closed into loops, which are indeed often observed in solar atmosphere.

Acknowledgements. The author is grateful to A.B. Mikhailovskij, N.S. Erokhin, D.D. Sokolov, and A.V. Stepanov for useful discussions of the problems touched upon in this work, as well as V.I. Pentegov for his help in preparing this manuscript for publication.

References

1. Wedermeyer-Böhm S., Scullion E., Steiner O. et al.: 2012, *Nature*, **486**, 505.
2. Wedermeyer-Böhm S., van der Voort L. R.: 2009, *Astron. Astrophys.*, **507**.
3. De Pontieu B., McIntosh S. W., Carlsson M., et al.: 2007, *Science*, **318**, 1574.
4. Cirtain J. W., Golub L., Lundquist L., et al.: 2007, *Science*, **318**, 1580.
5. Lemen J. R., Title A. M., Akin D. J., et al.: 2012, *Sol. Phys.*, **275**, 17.
6. McIntosh S. W., De Pontieu B., Carlsson M., et al.: 2011, *Nature*, **475**, 477.
7. Fedun V., Shelyag S., Verth G., et al.: 2011, *Ann. Geophys.*, **29**, 1029.
8. Van Ballegooijen A., Asgari-Targhi M., Cranmer S., DeLuca E.: 2011, *Astrophys. J.*, **736**, 3.
9. Kitiashvili I., Kosovichev A., Mansour N., Wray A.: 2011, *Astrophys. J.*, **727**, L50.
10. Attie R., Innes D., Potts H.: 2009, *Astron. Astrophys.*, **493**, L13.
11. Shelyag S., Keys P., Mathioudakis M., Keenan F. P.: 2011, *Astron. Astrophys.*, **526**, A5.
12. Landau L. D., Lifshitz E. M.: *Electrodynamics of Continuous Media* (Fizmatgiz, Moscow, 1959; Pergamon, Oxford, 1960).
13. Pashitskii E. A.: 2010, *JETP*, **110**, 1026.
14. Balmaceda L., Domingues S. V., Palacios J., et al.: 2010, *Astron. Astrophys.*, **513**.
15. Zhang J., Liu Y.: 2011, *Astrophys. J.*, **741**, L7.

THE PROPERTIS OF TIDAL FORCES IN THE KERR METRIC

A.M.Rasulova^{1,2}

¹Theoretical Physics and Astronomy Department, The Herzen University, Moika 48
St. Petersburg, 191186, Russia,

²Institute of Limnology, RAS, Sevastyanov st. 9.
St. Petersburg, 196105, Russia, *ARasulova@gmail.com*

ABSTRACT. The expression for the tidal forces of the two relativistic protons at a distance of the order of the Compton wavelength near a rotating black hole is found. The analysis shows that the tidal forces are dependent on the plane of incidence and sharply increase with increasing Lorentz factor.

Keywords: General relativity - geodesic deviation: Black hole - Kerr metric: Tidal forces.

1. Introduction

The problem of deviation of geodesic is important in the study of motion of n-interacting particles in strong gravitational fields and in particular, the study of the deformation of the gas and dust clouds in the vicinity of black holes.

When driving two or more closely spaced particles in curved space-time their is a deviation of geodesic lines. General view of the geodesic deviation equation of the n-dimensional Riemannian manifold was obtained by T. Levi-Civita in 1925 Ref. 1. For the 4-dimensional space deviation equation for structureless massless particles was investigated in Refs. 2–3 by J.L. Sing.

The system of units $G = c = 1$ is used in the paper.

2. The Kerr Metric

The Kerr's metric in Boyer-Lindquist coordinates has the form [4]:

$$ds^2 = \rho^2 \frac{\Delta}{\Sigma^2} dt^2 - \frac{\Sigma^2}{\rho^2} \left[d\varphi - \frac{2aMr}{\Sigma^2} dt \right]^2 \sin^2\theta - \frac{\rho^2}{\Delta} dr^2 - \rho^2 d\theta^2, \quad (1)$$

where

$$\Delta = r^2 - 2Mr + a^2, \quad (2)$$

$$\rho^2 = r^2 + a^2 \cos^2\theta, \quad (3)$$

$$\Sigma^2 = (r^2 + a^2)^2 - a^2 \Delta \sin^2\theta, \quad (4)$$

and M is the black hole mass, aM its angular momentum $0 \leq a \leq 1$. The event horizon of the Kerr's black hole corresponds to the coordinate:

$$r_h = M + \sqrt{M^2 - a^2}. \quad (5)$$

The static limit surface is defined by the value:

$$r_{st} = M + \sqrt{M^2 - a^2 \cos^2\theta}. \quad (6)$$

The region of space-time between the static limit and the event horizon is called ergosphere.

In view of the equation (1) metric tensors are Ref.5:

$$g^{ij} = \begin{pmatrix} \Sigma^2/\rho^2\Delta & 0 & 0 & 2aMr/\rho^2\Delta \\ 0 & -\Delta/\rho^2 & 0 & 0 \\ 0 & 0 & -\frac{1}{\rho^2} & 0 \\ 2aMr/\rho^2\Delta & 0 & 0 & -(\Delta - a^2\sin^2\theta)/\rho^2\Delta\sin^2\theta \end{pmatrix}. \quad (7)$$

The nonzero components of the curvature tensor in the Kerr metric have the form [5]:

$$R_{1023} = -aM \cos\theta (3r^2 - a^2 \cos^2\theta) \frac{1}{\rho^6}, \quad (8)$$

$$R_{1230} = -\frac{aM \cos\theta}{\rho^6} (3r^2 - a^2 \cos^2\theta) \Sigma^{-2} \times [(r^2 + a^2)^2 + 2a^2 \Delta \sin^2\theta], \quad (9)$$

$$R_{1302} = \frac{aM \cos\theta}{\rho^6} (3r^2 - a^2 \cos^2\theta) \Sigma^{-2} \times [2(r^2 + a^2)^2 + a^2 \Delta \sin^2\theta], \quad (10)$$

$$-R_{3002} = R_{1213} = -\frac{aM \cos\theta}{\rho^6} (3r^2 - a^2 \cos^2\theta) \times \frac{3a\Delta^{1/2}}{\Sigma^2} (r^2 + a^2) \sin\theta, \quad (11)$$

$$-R_{1220} = R_{1330} = -\frac{Mr}{\rho^6} (r^2 - 3a^2 \cos^2\theta) \times \frac{3a\Delta^{1/2}}{\Sigma^2} (r^2 + a^2) \sin\theta, \quad (12)$$

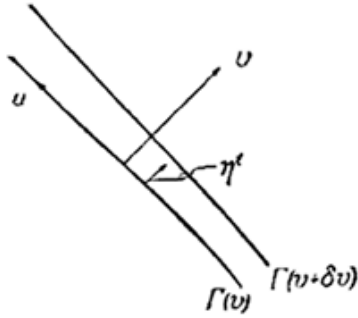


Figure 1: The deviation of curve $\Gamma(v)$ from curve $\Gamma(v + \delta v)$.

$$-R_{1010} = R_{2323} = \frac{Mr}{\rho^6}(r^2 - 3a^2 \cos^2 \theta) = R_{0202} + R_{0303}, \quad (13)$$

$$-R_{1313} = R_{0202} = \frac{Mr}{\rho^6}(r^2 - 3a^2 \cos^2 \theta) \Sigma^{-2} \times [2(r^2 + a^2)^2 + a^2 \Delta \sin^2 \theta], \quad (14)$$

$$-R_{1212} = R_{0303} = -\frac{Mr}{\rho^6}(r^2 - 3a^2 \cos^2 \theta) \Sigma^{-2} \times [(r^2 + a^2)^2 + 2a^2 \Delta \sin^2 \theta]. \quad (15)$$

3. The equations of geodesic deviation

If there is a pair of adjacent curves $\Gamma(v)$ and $\Gamma(v + \delta v)$ (Fig.1), then the equation of geodesic deviation for structureless infinitely close particles has the form:

$$\frac{d^2 \eta^i}{ds^2} + R_{jkm}^i U^j \eta^k U^m = 0, \quad (16)$$

where η^i — infinitesimal vector deviation, $R_{jkm}^i = g^{il} R_{l jkm}$ — Riemann tensor, U^m — 4-speed.

A solution of equation (16) is a vector of deviation of world lines that covariantly describes the relative acceleration between geodesic lines.

Let us consider the equations of geodesic deviation in the Kerr metric. We find the equation of geodesic deviation for relativistic structureless particles that have only radial velocity component, hence:

$$U^i = \Gamma(1, V, 0, 0) \quad (17)$$

where $\Gamma = \frac{1}{\sqrt{1-V^2}}$ is Lorentz factor.

From the equations (16) and curvature tensor in the Kerr metric (8)—(15) in this case, the equation of the deviation will have the form:

$$\frac{D^2 \eta^0}{ds^2} = \Gamma^2 [g^{03}(R_{3002} - R_{0303}) + g^{03}V(R_{1230} + R_{1330} - R_{1302}) + V^2(g^{00}R_{1010} - g^{03}R_{1313})], \quad (18)$$

$$\frac{D^2 \eta^1}{ds^2} = -g^{11} \Gamma^2 R_{1010} (1 + V), \quad (19)$$

$$\frac{D^2 \eta^2}{ds^2} = g^{22} \Gamma^2 [R_{0202} + V(R_{1220} + R_{1302}) - R_{1212} V^2], \quad (20)$$

$$\frac{D^2 \eta^3}{ds^2} = \Gamma^2 [-g^{33}R_{0303} + g^{33}V(R_{1230} + R_{1330} - R_{1302}) + V^2(g^{03}R_{1010} - g^{33}R_{1313})]. \quad (21)$$

From these equations it is seen that the relative acceleration between the infinitely close to the world lines will be directly proportional to the square of the Lorentz factor.

To evaluate the tidal forces of the proton in the Kerr metric we use the following restrictions:

- let proton with mass $m_p = 1.67 \cdot 10^{-27}$ kg is in motion along a geodesic so that the deviation is proportional to the Compton wavelength $\lambda_C^p = 1.32 \cdot 10^{-15}$ m,
- let movement only occurs in the equatorial plane $\theta = \frac{\pi}{2}$,
- the black hole has the following parameters: $M = 10^6$, $a = 0.98$,
- motion occurs at a coordinate of distance of r from horizon of black hole $r = 10^{-5} r_h$,
- the proton velocity is $V = (1 - 10^{-15})c$.

If we consider the assumptions given above, then calculations made by us lead to the work of the tidal forces $F = 4.156 \cdot 10^9$ Newton's. For example, the same force on the surface of the Sun is about $4.5 \cdot 10^{-26}$ Newtons.

For different values of velocities of particles obtain the tidal forces by numerical calculations for protons are given in the Fig. 2. The graph shows that the tidal forces increase with the speed of the proton in the center of mass of the order of 10^{-19} Newtons with $V = 0.9c$ up to 10^{19} Newtons with $V = (1 - 10^{-20})c$.

Dependence of tidal forces on the mass and the specific angular momentum of the black hole is shown in Fig. 3 and Fig. 4 respectively. It is important to note that tidal forces are maximal for black holes of stellar mass and are minimal for a supermassive black holes. For example, if the black hole mass is of about mass of Sun then it creates tidal forces near horizon order 10^{15} Newtons and supermassive black holes with mass $10^9 M_\odot$ creates tidal forces order 10^6 Newtons. A similar effect was observed in Ref. 6 for a Schwarzschild

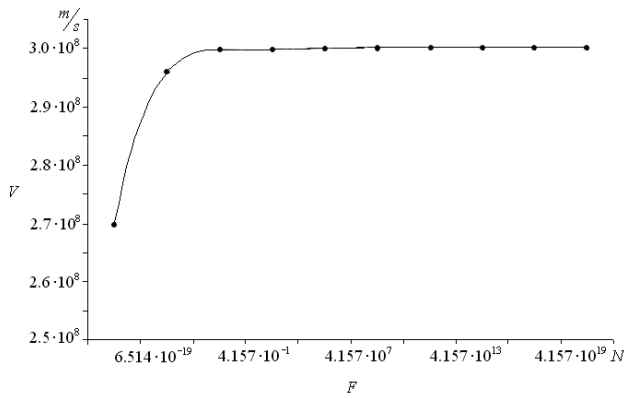


Figure 2: The dependence of the tidal force F on the speed of the proton V .

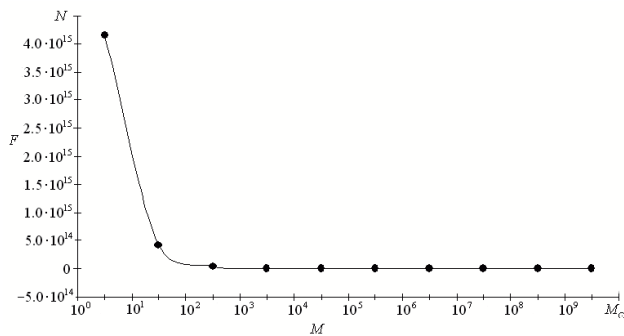


Figure 3: The dependence of the tidal force F on the black hole mass M .

black hole. Also if there is an increase of specific angular momentum of the black hole then there is an increase of the tidal forces near the horizon.

Acknowledgements. The author expresses her sincere gratitude to her research supervisor Professor Andrei Grib for the problem statement and numerous discussions. The work was supported by Russian Foundation for Basic Research, grant 15-02-06818-a.

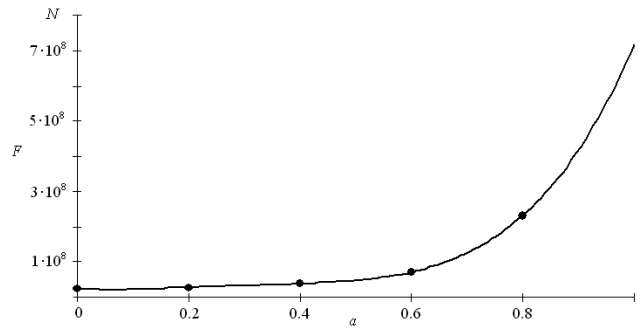


Figure 4: The dependence of the tidal force F on the specific angular momentum of the black hole a .

References

1. Levi-Civita T.: 1926, *The absolute differential calculus*, London: Blackie and Son.
2. Synge J.L.: 1934, *Element Ann. Math.*, **35**, 705.
3. Synge J.L.: 1960, *Relativity: The General Theory*, North-Holland, Amsterdam; Interscience, New-York.
4. Shapiro S.L., Teukolsky S.A.: 1983, *Black Holes, White Dwarfs and Neutron Stars*, Cornell Univ., Ithaca, New York.
5. Chandrasekhar S.: 1983, *The Mathematical Theory of Black Holes*, Oxford Univ. Press, Oxford.
6. Misner C.W., Thorne K.S., Wheeler J.A.: 1973, *Gravitation*, Freeman and Company Limited.

X-RAY SPECTRAL PROPERTIES OF THE ISOLATED AGNs: NGC 1050, NGC 2989, ESO 317-038, ESO 438-009

I.B. Vavilova, A.A. Vasylenko, Iu.V. Babyk, N.G. Pulatova

Main Astronomical Observatory of the NAS of Ukraine,
27 Akademika Zabolotnogo St., Kyiv, MSP 03680, Ukraine, irivav@mao.kiev.ua

ABSTRACT. We have analyzed the spectral data obtained by XMM-Newton, Swift, Chandra, and INTEGRAL space observatories for several isolated AGNs from 2MIG catalogue, for which the available X-ray data were accessed. Among these objects were CGCG 179-005, NGC 6300, NGC 1050, NGC 2989, WKK 3050, ESO 438-009, and ESO 317-038. We determined corresponding spectral models and values of their parameters (spectral index, intrinsic absorption etc.). X-ray spectra for bright galaxies, NGC 6300 and Circinus, were analyzed up to 250 keV and their characteristics of emission features were determined in 6-7 keV range.

We present the results for NGC 1050, NGC 2989, ESO 317-038, and ESO 438-009, for which their spectral parameters were obtained for the first time.

Keywords: Active galaxy nuclei – X-ray; Objects: NGC 1050, NGC 2989, ESO 317-038, ESO 438-009

1. Introduction

The most galaxies with active nuclei (AGNs) in the Local Universe are in a low-luminosity state (Ptak et al., 2000; Ho et al., 2009; Maia et al., 2003; Pulatova et al., 2015). In this sense, the principal question is why this state is related also to X-ray activity of the isolated galaxies with active nuclei (AGNs). The answer will be helpful to explain the AGN's paradigm in detail as well as to get a response to the internal evolution of galaxy activity as well as to investigate the influence of halo matter (baryonic/dark) on the formation and productivity of AGN's engine.

With this goal we have analyzed the data obtained by XMM-Newton, Swift, Chandra, and INTEGRAL X-ray observatories to find the X-ray spectra of a good quality for several isolated AGNs from 2MIG catalogue (Karachentseva et al., 2010). We have selected such objects as CGCG 179-005, NGC 6300, NGC 1050, NGC 2989, WKK 3050, ESO 438-009, and ESO 317-038 and determined their main spectral properties. In this paper we describe briefly our results for NGC 1050, NGC 2989, ESO 438-009, and ESO 317-038, for which their spectral parameters were not previously studied.

2. Data processing

The Swift/BAT spectra were derived from the 70-month hard X-ray Survey (Baumgartner et al. 2013). The reduced Swift /XRT products were taken by using the XRT products generator (http://www.swift.ac.uk/user_objects/) (Evans et al. 2007, 2009, 2010) with HEASOFT 6.15.1 software package in UKSSDC (UK Swift Science

Data Centre) archive. We only used the data taken in the photon counting (PC) mode in such a manner that we were able to identify the precise locations of our targets without any contamination. Only events with energy in the range of 0.3–10 keV with grades 0–12 were included.

The XMM-Newton MOS and PN data were processed using the standard software packages XMM SAS ver. 11.0 (Science Analysis Software) according to the guidelines of XMM-Newton User's Manual. Because of its higher sensitivity, we use the EPIC/PN spectrum for the analysis of NGC 1050, although duration of exposure for EPIC/MOS has been slightly longer (but it has less data as compared to PN). Only patterns corresponding to single and double events (pattern ≤ 4) were taken into account for the PN camera. Filter FLAG=0 was applied to exclude bad pixels and events that are at the edge of a CCD. The ARFGEN and RMFGEN tasks were used to create ancillary and response files. Spectra were binned according to the luminosity of each source.

The XMM-Newton/XRT and BAT spectra were treated together and analyzed using XSpec ver.12.6 software. Since observations for each instrument are not simultaneous, a cross-calibration constants C have been introduced in our models. In order to derive the luminosities we used the standard Λ CDM cosmological model with parameters $H_0 = 70$ (km/s)/Mpc, $\Lambda = 0.73$, $\Omega_m = 0.27$ (Bennett, 2003) as well as the Galactic absorption (see Table 1) has already been taken into account in the fitting.

The Chandra data was analyzed with CIAO software package (Chandra Interactive Analysis of Observations, version 4.7 (Fruscione et al. 2006) and the latest realize of calibration files. The standard reprocessing and screening routines to create new level=2 event files were made using *chandra repro* script. To extract the source and background spectra with ARF and RMF files we have used *specextract* script. The XSpec environment version 12.6.0 was used to model all spectra with absorbed power law model. The errors of best-fit parameters correspond of 1σ confidence level.

3. Results

The main spectral parameters of NGC 1050, NGC 2989, ESO 317-038 and ESO 438-009 are given in Table 1, namely, Column (1): Object name; Column (2): Right Ascension from NASA/IPAC Extragalactic Data base (NED); Column (3): Declination (NED); Column (4): Redshift (NED); Column (5): X-ray Observatory/ Instrument; Column (6): Observation exposures in ks; Column (7): Galactic absorption in units of 10^{20} cm⁻² (by Kalberla

Table 1. The main spectral parameters of NGC 1050, NGC 2989, ESO 317-038 and ESO 438-009 for the absorbed power law fits to the data

(1) Object (Type)	(2) RA (deg) (J2000)	(3) Dec. (deg) (J2000)	(4) z	(5) Instrument	(6) Exposure (ks)	(7) N_{H} 10^{20} cm^{-2}	(8) L, 10^{40} erg/s	(9) N_{H} 10^{22} cm^{-2}	(10) Phot. index
NGC 1050 (Sy2)	40.648	34.764	0.013	XMM- Newton/ EPIC PN	9.507*	5.67	2.15±0.23 (0,5-2 keV)	47.43±0.81 (10^{22} cm^{-2})	2.0 (fixed)
NGC 2989 (AGN)	146.355	-18.374	0.014	Swift/ XRT	27.8*	4.34	2.19 (0,5-2 keV)	5.07 ^{+0.10} _{-0.05} (10^{20} cm^{-2})	1.69±0.68
ESO 317-038 (AGN)	157.440	-38.349	0.015	Swift/ XRT+BAT	14.4*+8482	6.0	27.1	17.05 ^{+32.59} _{-14.12} (10^{22} cm^{-2})	1.7 (fixed)
ESO 438-009 (Sy1.5)	167.700	-28.501	0.024	Swift/ XRT+BAT	17.4*+7242	5.26	357	4.61 ^{+4.76} _{-3.40} (10^{21} cm^{-2})	1.89±0.08

* Exposure time in ks (EPIC PN/Swift XRT) after the data screening

et al. 2005 (LAB map)); Column (8): Luminosity, L, in units of 10^{40} erg/s in 2-10 keV range; Column (9): Intrinsic absorption in units of 10^{22} cm^{-2} ; Column (10): Photon Index.

NGC 1050 has been observed by XMM-Newton (2013-02-27, ID 0693540201). X-ray spectrum has a bad quality and the data beyond ~5 keV are absent. It was fitted by the model $phabs*(zbody+zpo)$, where $tbabs$ corresponds to the Galactic absorption. Because of a lack of data in the middle range, we have fixed a value of the photon index as $\Gamma = 2.0$. We determined the values of flux in 0.5-2.0 keV as $(5.64 \pm 0.59) \cdot 10^{14} \text{ ergs/cm}^2/\text{s}$ and black-

body model as $kT = 189 \pm 23 \text{ eV}$ ($\chi^2/\text{dof} = 15.41/11 = 1.4$). Other parameters are summarized in Table 1 and the best fitting spectrum is presented in Figure 1 (left panel).

X-ray observational data for NGC 1050 are presented for the first time.

NGC 2989 has been observed twice by Swift/ XRT (2008-10-06/08), duration of exposure in XRT/PC mode was 14125 s and 13672 s. A lower limit of spectrum was 2.5 keV. We fitted it by the model $phabs* zphbs*zpo$, where $phabs$ corresponds to the Galactic absorption. A value of the photon index was determined as $\Gamma = 1.69 \pm 0.68$, $\chi^2/\text{dof} = 9.06/9$. The main parameters are summarized in Table 1 and its spectrum is presented in Figure 1 (left panel). The errors are caused by the poor quality of the XRT data.

ESO 317-038 has been observed six times by Swift/XRT from 2011-02-24 to 2011-03-20, duration of exposure in XRT/PC mode was $623 \div 4909 \text{ s}$. A spectral analysis was conducted altogether with the Swift/BAT observational data and allowed us to enlarge a spectral range till 195 keV. A lower limit of spectrum was also 2.5 keV. We fitted its spectrum by the model $phabs*zphbs* cutoffpl$, where $phabs$ corresponds to the Galactic absorption. We fixed a value of the photon index as $\Gamma = 1.7$ and energy as $E_{\text{cut-off}} = 500 \text{ keV}$. Luminosity is $2.71 \cdot 10^{41} \text{ ergs/s}$ in 2.0-10 keV, $6.31 \cdot 10^{42} \text{ ergs/s}$ in 14-195 keV (Swift BAT 70-Month Hard X-ray Survey). The main parameters are

summarized in Table 1 and its spectrum is presented in Figure 1 (right panel). The errors are caused by the poor quality of the XRT data.

ESO 438-009 has been observed three times by Swift/XRT from 2010-11-02 to 2010-11-08, duration of exposure in the XRT/PC mode is $1172 \div 6429 \text{ s}$. A spectral analysis was conducted altogether with the Swift/BAT observational data and allowed us to enlarge a spectral range till 195 keV. A lower limit of spectrum is 0.5 keV. We fitted its spectrum by the model $phabs* zxicpf* cut offpl$, where $zxicpf$ corresponds to the absorption by the ionized matter with the overlap factor C (we fixed $C=1$). We determined the photon index as $\Gamma = 1.86 \pm 0.06$, cut-off energy was fixed as $E_{\text{cut-off}} = 500 \text{ keV}$. Intrinsic ionized absorption is $N_{\text{H}} = 4.61^{+4.76}_{-3.40} 10^{21} \text{ cm}^{-2}$ and ionization rate $\log \xi = 2.35^{+0.44}_{+0.68}$, $\chi^2/\text{dof} = 134.51/116$. Luminosity is $L_x = 2.73 \cdot 10^{42} \text{ ergs/s}$ in 0.5-2.0 keV, $4.94 \cdot 10^{41} \text{ ergs/s}$ in 2.0-10 keV, $1.24 \cdot 10^{43} \text{ ergs/s}$ in 14-195 keV (Swift BAT 70-Month Hard X-ray Survey). The main parameters are summarized in Table 1 and its spectrum is presented in Figure 1 (right panel).

4. Brief discussion

One can see, the studied galaxies are of low activity (X-ray luminosity is less than 10^{42} ergs/s) that is consistent with our previous research (Pulatova et al., 2015), where we found that isolated AGNs in the Local Universe are mostly faint in X-ray. Altogether with these new data, a mean luminosity for 17 the 2MIG isolated AGNs without companions is $L_x \sim 1.9 \cdot 10^{42} \text{ ergs/s}$ in the soft 2-10 keV range (see, for comparison, results by Halderson (2001). The same estimations were derived by Anderson et al. (2013) for subsets of 2MIG galaxies: the average luminosity L_x within 50 kpc is $1.0 \cdot 10^{40} \text{ ergs/s}$. They found also that that 1/2 of the total emission is extended and about 1/3 of the extended emission comes from hot gas.

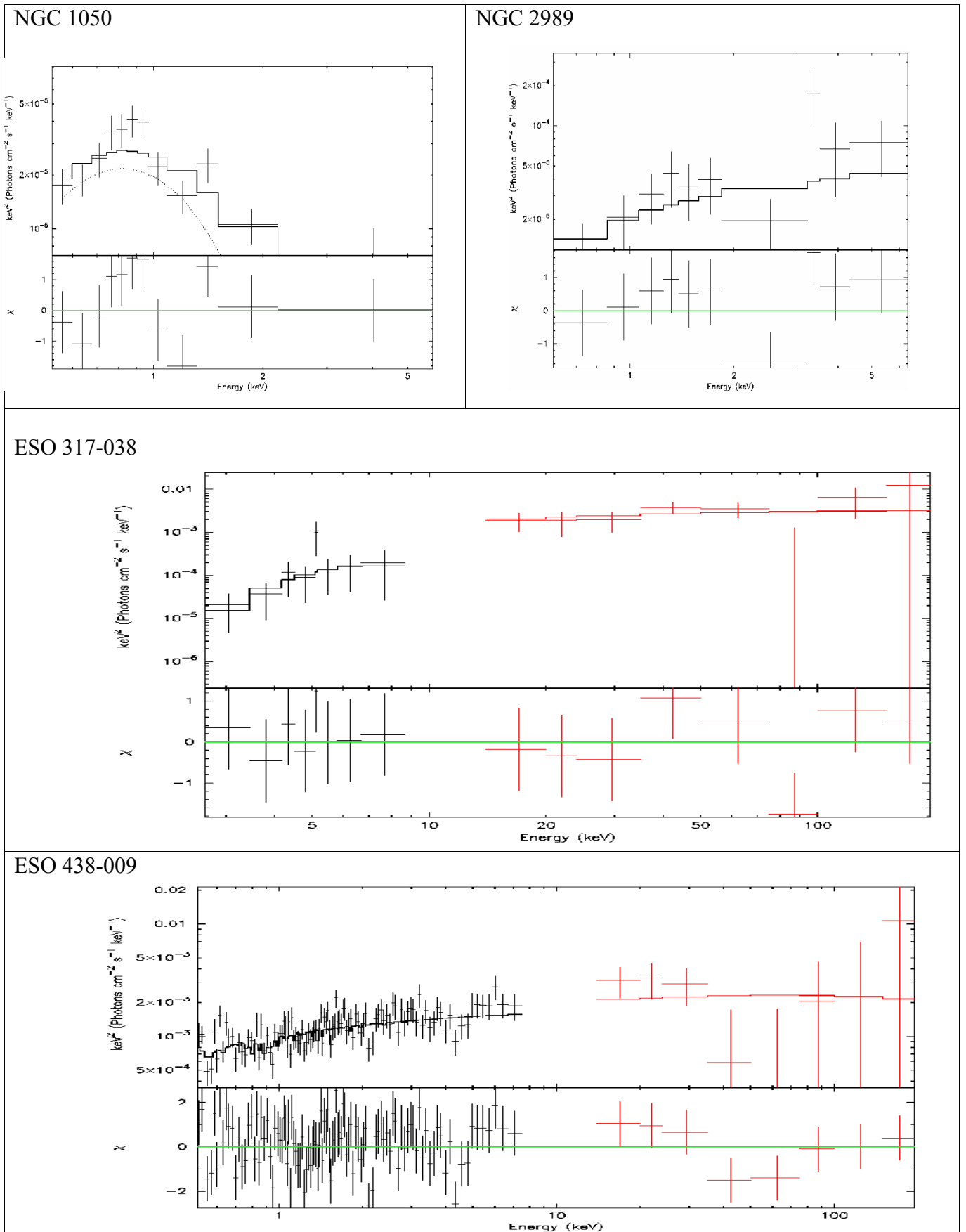


Figure 1: Unfolded spectrum of the isolated galaxies with active nuclei (their parameters are in Table 1). *Top:* NGC 1050 and NGC 2989; the spectra were obtained in 0,5-10 keV range with XMM-Newton/XRT/BAT (best fitting spectra) and Swift respectively. *Down:* ESO 317-038 and ESO 438-009; the broad-band spectra were obtained in 0,5-150 keV range with Swift and INTEGRAL (red)

The authors (Melnyk et al., 2013) in their research with two selected samples XMM-LSS field (X-ray galaxies and AGNs) have studied an environment effect and found that AGNs, including soft X-ray AGNs, when comparing to X-ray galaxies, prefer to be located in lower galaxy overdensities. It is in a good agreement with our estimations on the influence of choice of isolation criteria for spatial analysis and physical/morphological properties of host galaxies (Vavilova, 2009; Elyiv, 2009). At the same time, we do not confirm the conclusion that the softest AGNs are of Sy1 type.

We noted in our research (Pulatova et al., 2015) that Sy 1 type galaxies appear to be more luminous than of Sy 2 type. Some AGNs of our sample have the spectral energy distribution almost flat from the infrared to X-ray part of spectrum, as result the spectral index is ~ 1 , although it is usually steeper.

The stronger X-ray flux, than X-ray continuum is produced by lower energy photons. These photons are scattered to higher energies by relativistic electrons using Compton scattering. The fraction of the power emitted in the X-ray flux is almost four times bigger in AGNs than in normal galaxies. Using such property, we conclude that X-ray soft emission from the studied objects is in favor of the presence of AGN's engine. Additional evidences are the normalized excess variances (variability amplitudes) that anti-correlate with black hole masses. Our preliminary estimations point out (Chesnok et al., 2010) that the isolated AGNs in the Local Universe possess a low-mass black holes (intermediate values, 10^5 - $10^6 M_{\text{Sun}}$) being closer to their primordial mass (Ludlam et al., 2015).

To investigate the correlation between photon index of power law model and X-ray flux for each AGNs we have used additional data of XMM-Newton and Chandra observatories. Figure 2 shows the distribution of slopes of spectra of the isolated AGNs over X-ray flux. It was found a clear correlation between these values: the slope is 1.3. At the same time, we did not find correlation between the photon index and luminosity of the studied X-ray isolated AGNs.

Acknowledgements. This study is partially supported in frame of the Target Program of Scientific Space Research of the National Academy of Sciences of Ukraine (2012-2016).

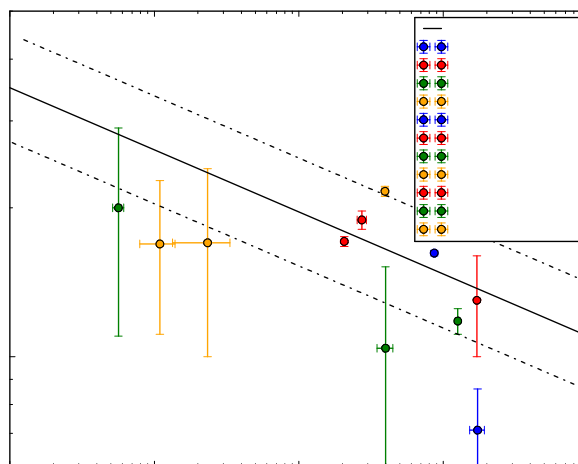


Figure 2: The Flux - Photon Index relation for X-ray sample of the isolated AGNs. The solid line corresponds to the simple power law model with slope 1.3, while two dotted lines correspond to the standard deviation.

References

- Anderson M.E. et al.: 2013, *ApJ*, **762**, Is. 2, article id. 106.
 Baumgartner W. H. et al.: 2013, *ApJSS*, **207**, 19.
 Bennett C.L. et al.: 2003, *ApJSS*, **148**, 1.
 Chesnok et al.: 2009, *Kinemat. Phys. Celest. Bodies*, **25**, issue 2, 107.
 Chesnok N. et al.: 2010, *AIP Conf. Series.*, **1206**, 328.
 Elyiv A.A. et al.: 2009, *MNRAS*, **394**, Is. 3, 1409.
 Evans P. A. et al.: 2007, *A&A*, **469**, 379.
 Evans P. A. et al.: 2009, *MNRAS*, **397**, 1177.
 Evans P. A. et al.: 2010, *A&A*, **519**, A102.
 Fruscione et al.: 2006, SPIE Proc. 6270, 62701V, D.R. Silvia & R.E. Doxsey, eds.
 Halderson E.L. et al.: 2001, *AJ*, **122**, 637.
 Ho L.C.: 2009, *ApJ*, **699**, 626.
 Hwang H.S. et al.: 2012, *A&A*, **538**, A15.
 Kalberla P. M. et al.: 2005, *A&A*, **440**, 775.
 Karachentseva V.E. et al.: 2010, *Astrophys. Bull.*, **65**, 1.
 Ludlam R.M. et al.: 2015, *MNRAS*, **447**, 2112.
 Maia M.A.G. et al.: 2003, *ApJ*, **126**, 1750.
 Melnyk O.V. et al.: 2013, *A&A*, **557**, id. A81.
 Ptak A. et al.: 1999, *ApJSS*, **120**, 179.
 Pulatova N.G. et al.: 2015, *MNRAS*, **447**, 2209.
 Vasylenko A.A. et al.: 2015, *Ap&SS*, DOI: 10.1007/s10509-015-2585-z
 Vavilova I. B. et al.: 2009, *Astron. Nachr.*, **330**, 1004.
 Vol'vach A.E. et al.: 2011, *Astron. Reports*, **55**, 608.

ASTROPHYSICS

THE KINEMATICS PARAMETERS OF THE GALAXY USING DATA OF MODERN ASTROMETRIC CATALOGUES

V.S. Akhmetov¹, P.N. Fedorov^{1,2}, A.B. Velichko¹, V.M. Shulga^{2,1}

¹ Institute of Astronomy of Kharkiv National University,

Sums'ka 35, 61022 Kharkiv, Ukraine, *akhmetov@astron.kharkov.ua*

² Institute of Radio Astronomy, National Academy of Sciences of Ukraine,

Chervonopraporna 4, 61002, Kharkiv, Ukraine, *shulga@rian.kharkov.ua*

ABSTRACT. Based on the Ogorodnikov-Milne model, we analyze the proper motions of XPM2, UCAC4 and PPMXL stars. To estimate distances to the stars we used the method of statistical parallaxes herewith the random errors of the distance estimations do not exceed 10%. The method of statistical parallaxes was used to estimate the distances to stars with random errors no larger than 14%. The linear solar velocity relative to the local standard of rest, which is well determined for the local centroid ($d \approx 150$ p), was used as a reference.

We have established that the model component that describes the rotation of all stars under consideration about the Galactic Y axis differs from zero. For the distant ($d < 1000$ pc) PPMXL and UCAC4 stars, the mean rotation about the Galactic Y axis has been found to be $M_{13}^- = -0.75 \pm 0.04$ mas yr⁻¹. As for distances greater than 1 kpc M_{13}^- derived from the data of only XPM2 catalogue becomes positive and exceeds 0.5 mas yr⁻¹. We interpret this rotation found using the distant stars as a residual rotation of the ICRS/Tycho-2 system relative to the inertial reference frame.

Keywords proper motions, reference systems, Galaxy: kinematics and dynamics: late-type.

1. Introduction

The method used in this work allows not only to determine kinematic parameters of the Galaxy but also to estimate the inertiality of the proper catalogues from the study of components of the solid-body rotation tensor, which describe the rotation about the X, Y axes in the galactic coordinate system.

Since the Sun is located inside the giant stellar-gaseous complex known as the Gould belt (≈ 500 pc in radius), the involvement of sufficiently distant stars, which would be free of the effects of both the near-solar flows and the local stellar system on the whole, is vital for the reliable application of the method.

The aim of this work is to study kinematic pa-

rameters of the large number of stars depending on their distances. To estimate the latter we applied the method of comparison of statistical parallaxes with the velocity of the Sun (Olling R. et al.: 2003), which is currently known quite reliably (Schönrich R. et al., 2010). $(U, V, W) = (11.1_{-0.75}^{+0.69}, 12.24_{-0.47}^{+0.47}, 7.25_{-0.36}^{+0.37})$ km s⁻¹

2. The model

In the present work, we use a rectangular galactic coordinate system with the axes directed in the following way: from the observer towards the galactic center ($l = 0^\circ, b = 0^\circ$, axis X or axis 1), along the galactic rotation ($l = 90^\circ, b = 0^\circ$, axis Y or axis 2), and towards the Northern pole of the Galaxy ($b = 90^\circ$, axis Z or axis 3). Within the Ogorodnikov-Milne model, we use the designations introduced by Clube S. (1972, 1973) and applied in the works by du Mont D. (1977, 1978). As is known, (Ogorodnikov, 1965), when using only the proper motions of stars, one of the diagonal elements of the local deformation tensor remains to be undefined. That is why we determine the differences of the form: $(M_{11}^+ - M_{22}^+)$ and $(M_{33}^+ - M_{22}^+)$.

The conditional equations are written in the following form:

$$\begin{aligned} \mu_l \cos b &= (1/r)(X_0 \sin l - Y_0 \cos l) \\ &- M_{32}^- \cos l \sin b - M_{13}^- \sin l \sin b \\ &+ M_{21}^- \cos b + M_{12}^+ \cos 2l \cos b \\ &- M_{13}^+ \sin l \sin b + M_{23}^+ \cos l \sin b \\ &- 0.5(M_{11}^+ - M_{22}^+) \sin 2l \cos b, \quad (1) \end{aligned}$$

$$\begin{aligned} \mu_b &= (1/r)(X_0 \cos l \sin b + Y_0 \sin l \sin b - Z_0 \cos b) \\ &+ M_{32}^- \sin l - M_{13}^- \cos l \\ &- 0.5 M_{12}^+ \sin 2l \sin 2b + M_{13}^+ \cos l \cos 2b \\ &+ M_{23}^+ \sin l \cos 2b \\ &- 0.5(M_{11}^+ - M_{22}^+) \cos^2 l \sin 2b \\ &+ 0.5(M_{33}^+ - M_{22}^+) \sin 2b, \quad (2) \end{aligned}$$

where X_0, Y_0, Z_0 are components of the peculiar velocity of the Sun, $M_{12}^-, M_{13}^-, M_{23}^-$ - components of the vector of the solid-body rotation of the small circum-solar vicinity about the corresponding axes. According to the rectangular coordinate system we selected, the following rotations are positive: from axis 1 to axis 2, from axis 2 to axis 3, and from axis 3 to axis 1.

M_{21}^+ and M_{12}^+ values (mas yr⁻¹) are connected with the Oort constants A and B (km s⁻¹ kpc⁻¹) respectively through the proportionality factor of 4.74. Each of the $M_{12}^+, M_{13}^+, M_{23}^+$ values describes deformation of the velocity field in the corresponding plane.

The diagonal terms of the local deformation tensor $M_{11}^+, M_{22}^+, M_{33}^+$ describe the general contraction or extension of the whole stellar system. The set of conditional equations (1), (2) involves eleven unknown variables which are found using the least squares method. As can be seen from the equation (1), two pairs of unknown variables M_{13}^- and M_{13}^+ as well as M_{32}^- and M_{23}^+ have the same coefficients $\sin l \sin b$ and $\cos l \sin b$, respectively. This has the result that the unknowns are resolved poorly. A quantity $1/r$ is a parallactic factor, which is put to equal unity in solving the system of equations (1), (2). In this case stars are projected to the unit sphere. With this approach all parameters under determination are proportional to the heliocentric distance of the considered centroid and expressed in the same units as components of proper motions of stars namely in mas yr⁻¹. Applying a such approach allow us to eliminate completely the effect of the distance errors in data analyzed. Indeed, when the method with known distances to the stars is applied left-hand side of (1) and (2) equations have to be multiplied by 4.74 r, while right-hand side - by r, and then the desired unknowns will be distorted by the errors in determining the stellar distances. At present, the reliable distances to individual stars (with errors of <10%) allow the circum-solar vicinity of 100 pc in radius to be analyzed, but this is insufficient for the purposes of the present work.

3. Used catalogues

XPM2. The XPM2 astrometric catalogue recently created in the Research Institute of Astronomy of the V. N. Karazin Kharkiv National University but until now unpublished is presently the only bulk one that contains highly accurate proper motions of about one billion stars. There is a full coverage of the sky in the declination range $90^\circ \leq \delta \leq 90^\circ$. The accuracy of proper motions of faint stars in the XPM2 catalogue is within 3 to 10 mas yr⁻¹. As concerns its own proper motions, the XPM2 catalogue is a realization of the optical reference system independent on HCRF.

UCAC4. The UCAC4 astrometric catalogue (Zacharias, 2013), at present, is a catalogue, which con-

tains highly accurate proper motions of stars up to 16 mag. The sky coverage is full in the declination interval $90^\circ \leq \delta \leq 90^\circ$. The accuracy of proper motions for faint stars ranges from 3 to 10 mas yr⁻¹. The catalogue expands the system of ICRS/Tycho-2 towards the faint stars.

PPMXL. The PPMXL catalogue contains 910,468,710 entries, including stars, galaxies, and bogus entries. Of these, 412,410,368 are in 2MASS, i.e., 2MASS is used to determine proper motions and the J,H,Ks magnitudes are given in the catalogue. The resulting typical individual mean errors of the proper motions range from 4 mas yr⁻¹ to more than 10 mas yr⁻¹ depending on observational history. We used only those stars from the catalogue, for which at least one of the stellar magnitudes $b1$ or $b2$ is given. If both of them are presented, the magnitude was accepted to equal $(b1 + b2)/2$. Ultimately, a number of stars we used from the PPMXL catalogue, made 750 millions.

4. Estimation of the group distances

To obtain the estimates of distances to the stars, we used a statistical method (Olling R. et al., 2003). For the value of the known velocity of the Sun's peculiar motion relative to the LSR values from the work (R. Schonrich R. et al., 2009) were adopted. $(U, V, W) = (11.1_{-0.75}^{+0.69}, 12.24_{-0.47}^{+0.47}, 7.25_{-0.36}^{+0.37})$ km s⁻¹. The parallax has been calculated from the formulas:

$$\pi U = 4.74 X/U; \quad \pi W = 4.74 Z/W, \quad (3)$$

where X and Y are the components of the group velocity of stars (in mas yr⁻¹) received from the solution of equations (1), (2). Since component Y can be distorted by the asymmetric drift velocity (Dennin et. al, 1998), it was not used to determine the group parallaxes. The distance d is found from the relationship: $d = 1/\pi$. In this case the error of distance can be estimated from the relationship

$$e_d = \left(\frac{e_\pi}{\pi}\right) d, \quad (4)$$

while the e_π value for the motion along Z coordinate was estimated in the following way:

$$e_\pi^2 = 4.74(e_W/W)^2 Z^2 + 4.74(e_Z/W)^2 \quad (5)$$

A similar relationship can be derived for the motion along the X coordinate.

At first we apply this method to the HIPPARCOS catalogue. Grouping was based on trigonometric parallaxes of the catalogue, herewith $e_\pi/\pi < 1$. Derived statistical distances to the stars depending on trigonometric ones are presented in Fig. 1. It is seen from the figure that no significant systematic distortions in statistical distances are observed, as well as the fact that

for the distances larger that 200 pc, the errors in determining statistical distances are less that the errors of trigonometric distances. Further, we apply the method to the analysis of stars from the UCAC4, XPM2 and PPMXL catalogues.

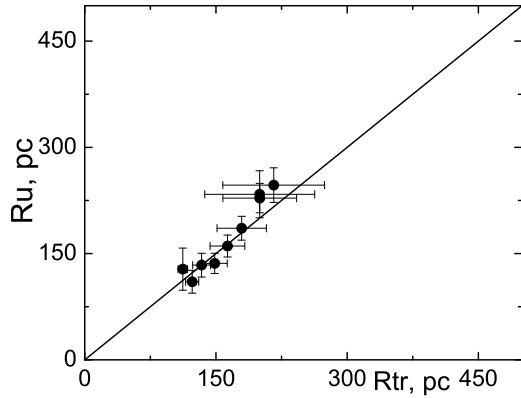


Figure 1: Statistical distances of stars depending on trigonometric ones calculated by data of the HIPPARCOS catalogue.

5. Results of calculations

The several results of solving (1), (2) equation system derived on the basis of stars of mixed spectral composition from XPM2, UCAC4 and PPMXL catalogues depending on the distance are presented in Fig. 2. We have used virtually all stars from the XPM2 catalogue (about 1 billion), with a constraint imposed on the modulus of a star tangential velocity $|\mu_t| = \sqrt{(\mu_\alpha \cos \delta)^2 + (\mu_\delta)^2} < 150 \text{ mas yr}^{-1}$. All the stars have been grouped according to their magnitudes, with the magnitude interval width of 1 mag in each group. Each of these intervals, in turn, was divided into 1633 Sharlie areas. The resulting data (the mean proper motions) were used to solve the system of equation (1), (2). Thus, the average distance derived using the procedure described above was assigned to the each interval of magnitudes. Random errors of all parameters under determination are $0.05 - 0.10 \text{ mas yr}^{-1}$, while those of $(M_{11}^+ - M_{22}^+)$ and $(M_{33}^+ - M_{22}^+)$ are twice as much in the each interval of magnitudes. The procedures for obtaining the data needed to solve the system of equations (1), (2) for XPM2, UCAC4 and PPMXL catalogues are the same.

The distances found and utilized in the work show that the considered stars are located on average outside the boundaries of the local spiral arm (Orion arm), or the Local stellar system. This serves as a reason to consider the rotation about the galactic axis Y found

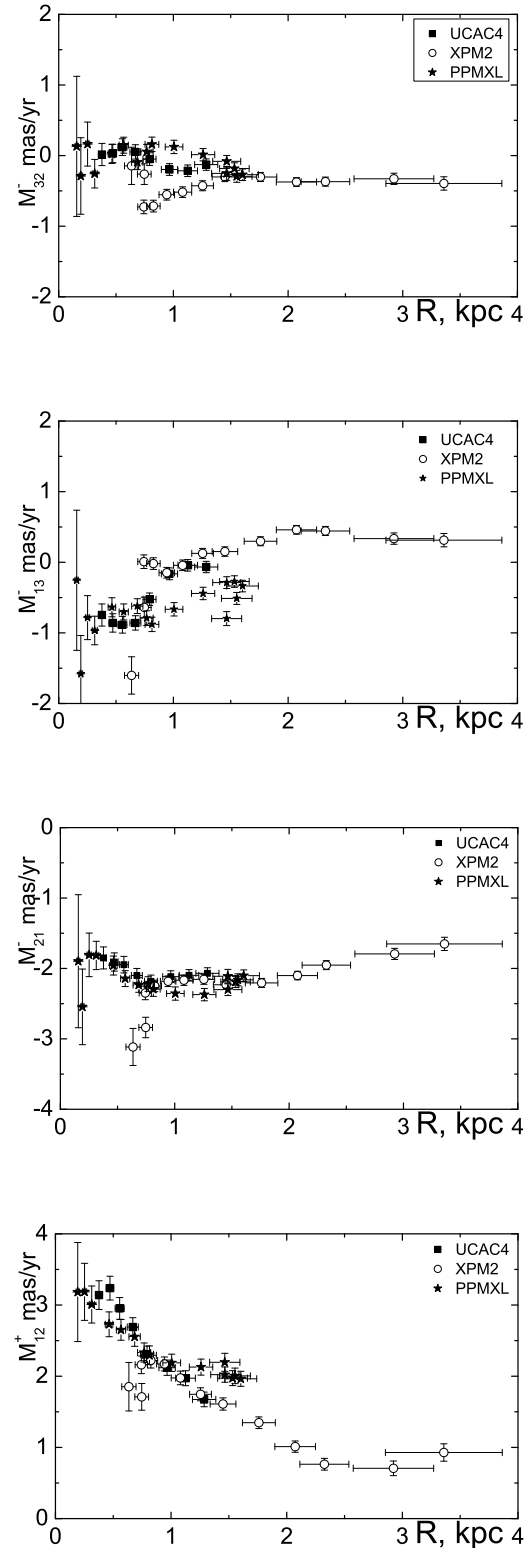


Figure 2: Kinematic parameters inferred from the proper motions of XPM2, UCAC4 and PPMXL stars vs. distances.

with the use of relatively faint stars, as a residual rotation of the ICRS/Tycho-2 (Hög, 2000) system relative to the extragalactic system of coordinates.

As can be seen from the figures, the dependences of kinematic parameters derived from the data of XPM2 catalogue are provided from the distance of about 600-700 pc. It is well seen that the components of rotation tensor for the stars of UCAC4 and PPMXL catalogues are almost coincided with each other within the interval of distances from 0 to 1 kpc and slightly different from those for XPM2 catalogue.

We also show a component of the deformation tensor in the XY plane for all the three catalogues. As can be seen from Fig. 2, the dependences of parameters M_{12}^+ are very similar in the range from 0 to 1.5 kpc. The dependence is extended by the data from only the XPM2 catalogue at distances greater than 1.5 kpc and these data do not contradict the previous ones. We present in the Fig. 3 the dependence of the angular velocity of the Galaxy rotation obtained from the formula $\omega = (M_{21}^- - M_{12}^+)$ on the heliocentric distance.

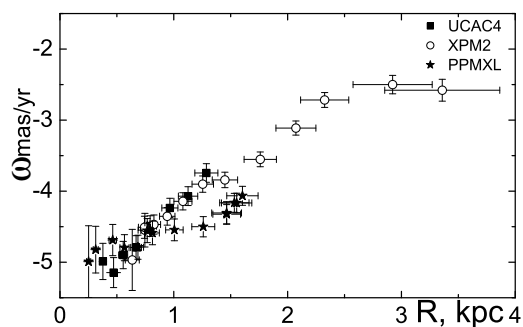


Figure 3: The dependence of the angular velocity of the Galaxy rotation on the heliocentric distance: $\omega = (M_{21}^- - M_{12}^+)$

As can be seen from this figure, there are no differences in the behavior of the dependence of ω on the heliocentric distance to the stars from XPM2 and UCAC4 catalogues up to 1.25 kpc. As for larger distances (only XPM2 catalogue) the behavior of this dependence does not change. The angular rotation velocity derived from the data of the PPMXL catalogue differs from values derived from the data of XPM2 and UCAC4 catalogues by more than 0.5 mas yr^{-1} at the distance interval from 1 to 1.6 kpc. It was surprising for us that although the PPMXL catalogue contains virtually the same amount of stars as the XPM2 one, the distances derived from statistical parallaxes of PPMXL stars do not exceed 1.6 kpc.

6. Conclusions

As a result of the work performed, it was established that for relatively close stars ($d < 1000$ pc) one component of the Ogorodnikov-Milne model which describes the rotation about the galactic axis Y and two components which describe deformations in the YZ and XY planes, depend on the heliocentric distance. We associate it with the kinematic specialities of the Local group of stars. As for farther stars, in average, the existence of the deformations in YZ and XY planes is seen.

Besides, for the distant stars of the Tycho2/UCAC4 and Tycho2/PPMXL catalogue systems, located in the distance > 1000 pc from the Sun, the mean value of the rotation about the galactic axes Y is about $+0.30 \text{ mas yr}^{-1}$ that we interpret as the residual rotation of the ICRS/Tycho-2 system relative to the inertial coordinate system.

The angular rotation velocity of the Galaxy can be represented by the linear dependence on the heliocentric distance and change from -5 mas yr^{-1} to -3 mas yr^{-1} in the distance range from 0.5 kpc to 2 kpc.

References

- Olling R. et al.: 2003, *ApJ*, **599**, 275.
- Schönrich R. et al.: 2010, *MNRAS*, **403**, 1829.
- Clube S.: 1972, *MNRAS*, **159**, 289.
- Clube S.: 1973, *MNRAS*, **161**, 445.
- du Mont D.: 1977, *A&A*, **61**, 127.
- du Mont D.: 1978, *A&A*, **66**, 441.
- Ogorodnikov K.F.: 1965, *Dynamics of stellar systems*. Fizmatgiz [in russian].
- Zacharias N. et al.: 2013, *ApJ*, **145**, 44.
- Dennen W. et al.: 1998, *MNRAS*, **298**, 387.
- Roeser S. et al.: 2010, *ApJ*, **139**, 2440.
- Hög E. et al.: 2000, *A&A*, **355**, L27.

"ASYMPTOTIC PARABOLA" FITS FOR SMOOTHING GENERALLY ASYMMETRIC LIGHT CURVES

K.D.Andrych¹, I.L.Andronov², L.L.Chinarova¹, V.I.Marsakova¹

¹ Department of Astronomy and Astronomical Observatory, Odessa National University, Marazlievskaya 1V, 65014, Odessa, Ukraine, katyaandrych@gmail.com, lidia_chinarova@mail.ru, v.marsakova@onu.edu.ua

² Department "High and Applied Mathematics, Odessa National Maritime University, Mechnikova Str., 34, 65029, Odessa, Ukraine, tt_ari@ukr.net

ABSTRACT. A computer program is introduced, which allows to determine statistically optimal approximation using the "Asymptotic Parabola" fit, or, in other words, the spline consisting of polynomials of order 1,2,1, or two lines ("asymptotes") connected with a parabola. The function itself and its derivative is continuous. There are 5 parameters: two points, where a line switches to a parabola and vice versa, the slopes of the line and the curvature of the parabola. Extreme cases are either the parabola without lines (i.e.the parabola of width of the whole interval), or lines without a parabola (zero width of the parabola), or "line+parabola" without a second line. Such an approximation is especially effective for pulsating variables, for which the slopes of the ascending and descending branches are generally different, so the maxima and minima have asymmetric shapes. The method was initially introduced by Marsakova and Andronov (1996OAP....9...127M) and realized as a computer program written in QBasic under DOS. It was used for dozens of variable stars, particularly, for the catalogs of the individual characteristics of pulsations of the Mira (1998OAP....11...79M) and semi-regular (2000AP....13..116C) pulsating variables. For the eclipsing variables with nearly symmetric shapes of the minima, we use a "symmetric" version of the "Asymptotic parabola". Here we introduce a Windows-based program, which does not have DOS limitation for the memory (number of observations) and screen resolution. The program has an user-friendly interface and is illustrated by an application to the test signal and to the pulsating variable AC Her.

Keywords: Stars: variable – stars: binary – stars: cataclysmic – stars: pulsating

1. Introduction

Variable stars are important sources of information on structure and evolution of stars, They are observed by many professional and amateur astronomers, which have generally different photometrical systems. In this case, it is not easy to reduce all the data to some effective system, thus such observations are used for high-amplitude variables, e.g. Mira – type stars, cataclysmic binaries or semi – regular variables. A huge part of observations of such objects was obtained by

amateurs and stored in national (but really international) databases like AAVSO (<http://aavso.org>), AFOEF (<http://cdsarc.u-strasbg.fr/afoev/>), VSOLJ (<http://vsolj.cetusnet.org/>). Photographical surveys ("Sky Patrol") produced "one or few per night" observations, which are not suitable for short – period (or aperiodic stars with a short time – scale of variability). The most abundant collections of photo negatives are stored in the AAVSO (Harvard Observatory), Sonneberg observatory, and Astronomical Observatory of the Odessa National University. Nowadays, there are numerous "photometric surveys" based on the CCD observations from ground-based and space telescopes. They are very important in studying variable stars (including the newly discovered ones) "in the past".

However, for eclipsing and pulsating variables, there is another very popular mode of observations: time series, which are obtained during a time interval, which is shorter than a photometric period – close to the minimum of eclipsing binaries, or to the maximum of pulsating variables. Then from the light curve is determined a single parameter – the moment of the extremum and its accuracy (needed, but often ignored). These individual extrema are published in the journals "Variable Stars. Supplement" ("Peremennyye Zvezdy. Prilozhenie"), "Information Bulletin on Variable Stars", "Open European Journal on Variable Stars" et al. and are used for studies of the period changes using the method of the "O-C" diagrams (see Tsessevich, 1971 for more details).

The methods for determination of the extrema were based on the Pogson's method of chords, Hertzsprung's method of fitting the data to some "standard curve", method of "tracing paper" (see e.g. Tsessevich (1971) for a review). Kwee and van der Woerden (1956) proposed a very popular method, which was implemented in some computer programs. However, it generally produces unreal small error estimates and thus is to be replaced by fitting the data with some approximating function (e.g. Andronov, 1994, 2005; Andronov & Marsakova, 2006; Mikulašek, 2007).

These methods are based on the assumptions of "symmetry" (suitable for eclipses of binary stars) and "asymmetry" (suitable for maxima of pulsating and cataclysmic variables). For latter, Marsakova and Andronov (1996) proposed the method of "asymptotic parabolae", which was successfully used for determination of characteristics of thousands of maxima and minima of individual cycles of variability of

single and binary stars of different types (Marsakova & Andronov, 1998).

As in the electronic tables (Microsoft Excel, Open/Libre Office, GNUmeric), the smoothing functions are algebraic polynomials. The polynomials were applied for the determination of more than 6500 extrema (and the error estimates) of semi-regular variables by Chinarova and Andronov (2000).

The method was also realized later in the programs VSCalc (Breus, 2007) and PERANSO (<http://peranso.com>).

2. Basic Equations

In this work, we present application of algebraic polynomials and asymptotic parabolae for determination of extrema. Following Andronov (1994, 2005), we make a mathematical model (smoothing function) for the signal:

$$x_C(t) = \sum_{\alpha=1}^m C_{\alpha} f_{\alpha}(t) \quad (1)$$

Here C_{α} are called “the coefficients” and $f_{\alpha}(t)$ – “the basic functions”. The coefficients C_{α} are usually determined by minimizing the test function

$$\Phi_m = \sum_{jk=1}^n h_{jk} (x_j - x_{Cj})(x_k - x_{Ck}), \quad (2)$$

which uses the observed x_j and computed $x_{Cj} = x_C(t_j)$ values. Obviously, results are dependent on the matrix h_{jk} , which is similar to the “metric tensor” in the differential geometry. In the electronic tables, the matrix h_{jk} is oversimplified to the unitary matrix (Kronecker symbol) δ_{jk} (equal to 1, if $j = k$, and else 0). More general case is $h_{jk} = w_k \delta_{jk}$, $w_k = \sigma_0^2 / \sigma_k^2$, σ_0 – the “unit weight error” and σ_k – the accuracy of the observation x_k .

For the derivative of degree s , the Eq. (1) may be extended to

$$x_C^{(s)}(t) = \sum_{\alpha=1}^m C_{\alpha} f_{\alpha}^{(s)}(t) \quad (3)$$

Obviously, the case $s = 0$ corresponds to the initial function, $s = -1$, to the integral etc. The error estimate of this value is

$$\sigma[x_C^{(s)}(t)] = \sum_{\alpha\beta=1}^m R_{\alpha\beta} f_{\alpha}^{(s)}(t) f_{\beta}^{(s)}(t), \quad (4)$$

Where $R_{\alpha\beta}$ is the covariation matrix of the statistical errors of the coefficients. Usually it is replaced by a simplified expression

$$R_{\alpha\beta} = \sigma_{0m}^2 A_{\alpha\beta}^{-1}, \quad (5)$$

$$A_{\alpha\beta} = \sum_{jk=1}^m h_{jk} f_{\alpha}(t_j) f_{\beta}(t_k) \quad (6)$$

This approximation (5) is valid, only if the matrix $h_{jk} = \sigma_0^2 \mu_{jk}^{-1}$, where μ_{jk} is the covariation matrix of errors of the observations and σ_0^2 is an arbitrary positive constant. Andronov (1997) studied even more complicated case, when h_{jk} are dependent on the time shift (like in the wavelet analysis). The classical case $w_k = \sigma_0^2 / \sigma_k^2$ was described e.g. by Anderson (??), Andronov (1994, 2003), Mikulášek (2007, 2015).

Marsakova and Andronov (1996) proposed a method of asymptotic parabola. The idea is that the part of the light curve near an extremum is approximated by two straight lines, which are connected by a piece of the parabola in a way that the function and its first derivative are continuous.

Free parameters for this approximation are the transition points between the parabola and straight lines corresponding to the ascending and descending branches. Extreme cases are the ordinary parabola and a broken line. The remaining three parameters – the slope of the lines and the vertical offset defined by the method of least squares.

The extremum of the smoothing function is determined in an usual way, by solving equation for the first derivative: $x'_C(t) = 0$ analytically or numerically by determining a maximum or minimum at a discrete grid of arguments, and then using iterations

$$t_e := t_e - \frac{x'_C(t)}{x''_C(t)} \quad (7)$$

with a corresponding statistical error estimate:

$$\sigma[t_e] = \frac{\sigma[x'_C(t_e)]}{|x''_C(t_e)|} \quad (8)$$

(cf. Andronov 1994, Mikulášek 2007). Obviously, this estimate is valid for a parabolic shape of the extremum and is not valid for flat extrema (e.g. total eclipses in binary stars). To determine of the statistically optimal number of parameters, we have computed approximations for few values of $m=2\dots m_{\max}$, where $m_{\max} = 10$ or smaller, and used m , which corresponds to the minimum of $\sigma[t_e]$.

The computations stopped, when the degree of degeneracy

$$\gamma = \det(\mathbf{A}) / \prod_{\alpha=1}^m A_{\alpha\alpha}$$

of the matrix of normal equation becomes smaller than the limiting value $\gamma_{\min} = 10^{-9}$.

3. Applications

For an illustration, we have used a part of the light curve of the RV – type pulsating star AC Her. We have used the international AAVSO database (<http://aavso.org>). After filtering of the photometrical data for outliers and other filters, the total number of the observations $N=23540$. The detailed analysis is in preparation. We have chosen a smaller part well covered by the observations.

In Fig. 1, the approximation using the “asymptotic parabola” is shown for few dozens cycles.

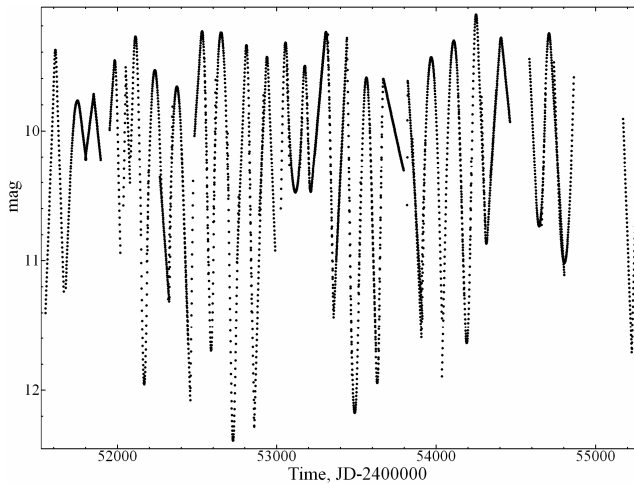


Figure 1: The “asymptotic parabola” approximation to the light curve of AC Her. The curve is compiled from the individual approximations of observations in the intervals surrounding maxima and minima.

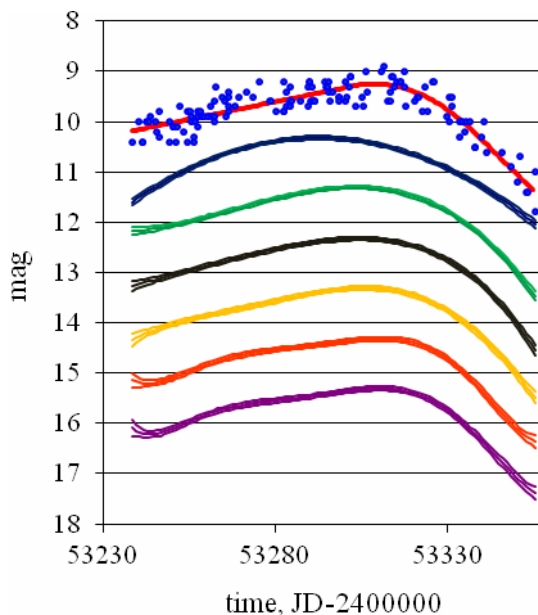


Figure 2: Original data (circles), approximations and “ $\pm 1\sigma$ error corridor” (lines) for the asymptotic parabola (upper curve) and algebraic polynomials with number of parameters $m=3..8$.

An excellent approximation is seen at those parts where approximations near minimum and maximum overlap. Totally we determined characteristics of 749 extrema.

Fig. 2 shows approximations using the “asymptotic parabola” and low-order algebraic polynomials of one of the extrema.

One may note that a maximum of the parabola is significantly shifted as compared to other approximations. However, the parabola corresponds to the best accuracy estimate of the time of extremum.

The dependences of the error estimates of the smoothing function are shown in Fig. 3. For this data set, the most accurate approximation corresponds to $m=3$ (parabola), the statistical errors increase with m .

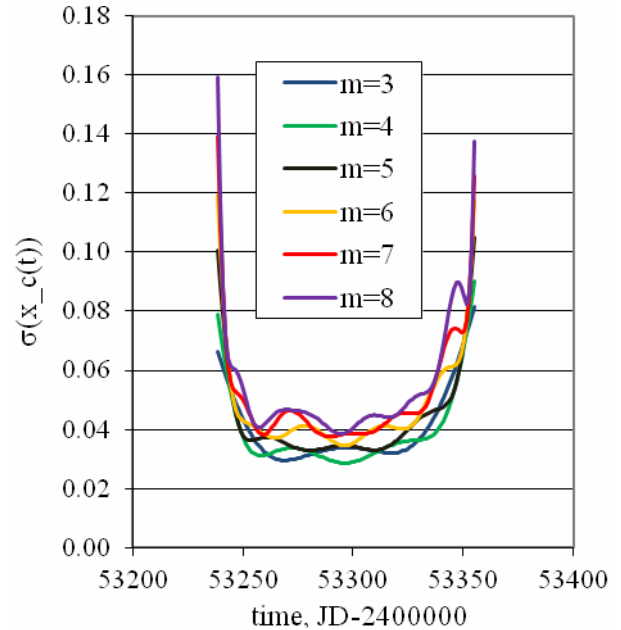


Figure 3: Scheme of internal and external contacts in eclipse.

4. Conclusions

The program was developed in the computer language VBA for Excel. It allows to determine the characteristics of extrema (maxima or minima) using the polynomial approximation with choosing a statistically optimal degree.

Results are applied to the pulsating variable S Aql.

The program will be used for further determination of extrema of variable stars of different types using our observations as well as observations from the virtual observatories and photometric databases like AAVSO, AFOEV, VSOLJ etc.

References

- Andronov I.L.: 1994, *Odessa Astron. Publ.*, **7**, 49 (1994OAP.....7...49A).
- Andronov I.L.: 2003, *ASPC*, **292**, 391 (2003ASPC..292..391A)
- Andronov I.L.: 2005, *ASPC*, **335**, 37 (2005ASPC..335...37A)
- Andronov I.L., Marsakova V.I.: 2006, *Ap*, **49**, 370 (2006Ap....49..370^a).
- Breus V.V. // *Odessa Astron. Publ.*, 2007, v.20. P. 32 (2007OAP....20...32B).
- Chinarova L.L., Andronov I.L.: 2000, *OAP.*, **13**, 116 (2000OAP....13..116C).
- Kwee K.K., van Woerden H.: 1956, *BAN*, 12, 327, (1956BAN....12..327K).
- Marsakova V.I., Andronov I.L.: 1996, *Odessa Astron. Publ.*, **9**, 127 (1996OAP.....9...127M).
- Marsakova V.I., Andronov I.L.: 1998, *Odessa Astron. Publ.*, **11**, 79 (1998OAP....11...79M).
- Mikulášek Z.: 2007, *OAP* **20**, 138, (2007OAP....20..138M)
- Mikulášek Z.: 2015, *A&A*, **584A**, 8, (2015A&A...584A...8M).
- Tsessevich V.P.: 1980, *Variable Stars and their Observations* (in Russ.), Moscow, Nauka, 176pp.

A MODIFICATION OF GAUSS' METHOD FOR PRELIMINARY DETERMINATION OF A CELESTIAL BODY'S ORBIT

A.A.Bazyey

Dpt of Astronomy, Odessa National University
Shevchenko Park, Odessa 65014, Ukraine

ABSTRACT. A modification of classical Gauss' method for determination of Keplerian elements from the observed positions is considered in this paper. The modification involves the exhaustive enumeration of all possible orbital plane positions in order to improve the method's reliability. It has been shown that such an approach requires a priori information on the pattern of the celestial body's motion, particularly, whether its motion is direct or retrograde.

Key words: orbit determination methods, celestial mechanics

Introduction

The method for determination of orbital elements of celestial bodies was developed by C.F.Gauss as early as at the beginning of the 19th century when the first asteroids were discovered. Up to the present time, this method has been successfully employed for preliminary orbit determination for both circumsolar and near-Earth orbital motion.

However, the method presents some limitations in its usage (Samotokhin et al., 2014). In particular, the orbital arc whose length is used for calculations should not be too long as in this case difficulties with solution of some equations may emerge. On the other hand, the orbital arc should not be too short as in this case uncertainties associated with observational errors may occur.

Numerical experiment

These and other limitations of Gauss' method can be overcome by exploiting capabilities of modern computers. Keplerian elements define the size and shape of the conic (the semi-major axis and eccentricity); a celestial body's position at a given instant of time (the time of perigee passage); the conic section orientation within the orbital plane (the argument of perigee); and, finally, the orbital plane position with regard to the reference coordinate system (the inclination and longitude of the ascending node).

At a two-body approximation the orbital plane always intersects the centre of gravity. With this fact the orbital plane position can be independently determined using the method of exhaustive enumeration of all possible values of inclination and longitude of the ascending node (Bondarenko et al., 2014a). All orbital elements can be derived for each pair of elements i and Ω using Gauss' method for determination of orbital elements from two position vectors and instants of time (Escobal, 1970). Based on these orbital elements, it is possible to define a celestial body's position for the current i and Ω . Using the differences between the observed and calculated in such a manner positions (O-C), it is possible to select the inclination and longitude of the ascending node which define the actual position of the orbital plane. It is evident that it is the minimum difference (O-C) that corresponds to the actual position of the orbital plane.

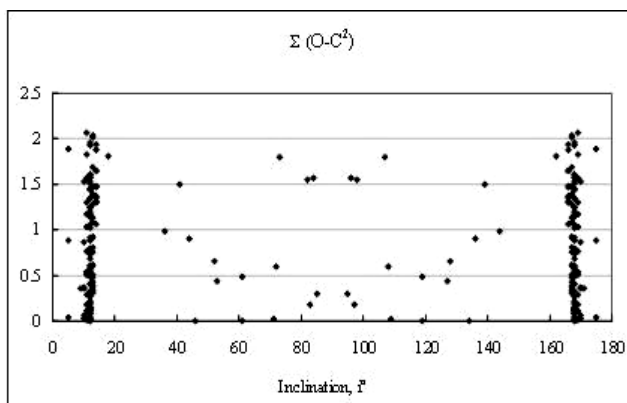


Figure 1. The distribution of the sum of squared differences between the observed and calculated positions of the test celestial body for different orbital inclinations.

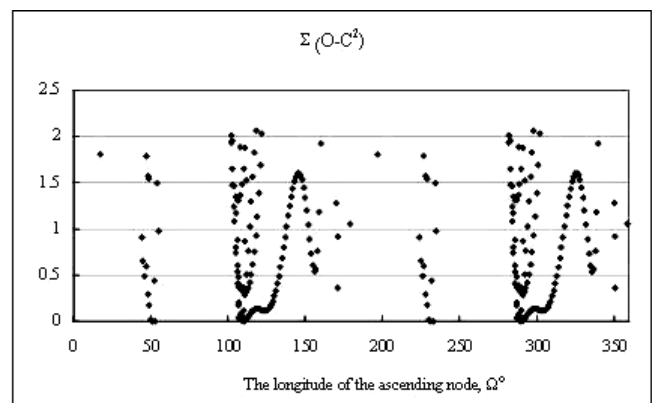


Figure 2. The distribution of the sum of squared differences between the observed and calculated positions of the test celestial body for different longitudes of the ascending node.

To study the behaviour of the dependence of the sum of squared differences ($O-C$) on the adopted values of inclination and longitude of the ascending node, we set up a numerical experiment. In this experiment we simulated the search of the position of a test celestial body's orbital plane. Keplerian elements for the heliocentric orbit were selected as follows:

the semi-major axis $a=2.48255$ AU;
 the eccentricity $e=0.15326$;
 the time of perigee passage 19.06.2011;
 the argument of perigee $\omega=79.325^\circ$;
 the longitude of the ascending node $\Omega=108.395^\circ$;
 the inclination $i=10.252^\circ$.

Using the methods described in (Bondarenko et al., 2014b), we determined the sums of squared differences ($O-C$) for all possible pairs of orbital elements, namely the inclination $0 \leq i \leq 180^\circ$ and longitude of the ascending node $0 \leq \Omega < 360^\circ$. From this data set we selected only those values which meet the following requirement:

$$\Sigma \sqrt{(O-C)^2} \leq 1.4'.$$

The obtained dependencies are shown in Figs. 1 and 2.

The dependence of $\Sigma(O-C)^2$ on the inclination is reflection symmetric with regard to the value $i=90^\circ$, and it exhibits the largest number of the selected values $\Sigma(O-C)^2$ near $i=10.5^\circ$ and $i=169.5^\circ$.

The dependence of $\Sigma(O-C)^2$ on the longitude of the ascending node is the same for the ranges $0 \leq \Omega < 180^\circ$ and $180^\circ \leq \Omega < 360^\circ$, and it exhibits the largest number of the selected values $\Sigma(O-C)^2$ near $\Omega=108.5^\circ$ and $\Omega=288.5^\circ$.

Conclusion

Thus, to ultimately determine the orbital plane using a modified Gauss' method suggested in (Bondarenko et al., 2014a), a priori information on the pattern of the celestial body's motion is required, particularly, whether its motion is direct or retrograde. This requirement is similar to that one for the application of Gauss' method for determination of orbital elements from two position vectors and instants of time (Escobal, 1970).

References

- Bondarenko Yu.S., Vavilov D.E., Medvedev Yu.D.: 2014, *Solar System Research*, **48**, No 3, 212-216.
 Bondarenko Yu.S., Vavilov D.E., Medvedev Yu.D.: 2014, *Astronomical News Letter*, **48**, No 3, 1-5.
 Escobal P. *Methods of Orbit Determination*. Moscow: Mir, 1970.
 Samotokhin A.S., Khutorovskiy Z.N.: 2014, *The Working Papers of M.V.Keldysh Institute of the Applied Mathematics*, No **44**, 31.

RESULTS OF DOUBLE STARS OBSERVATIONS AT NIKOLAIEV OBSERVATORY

D.V.Bodryagin, N.V.Maigurova

Research Institution “Mykolaiv Astronomical Observatory”,
Observatorna St.1, 54030, Mykolaiv, Ukraine

ABSTRACT. The results of double stars observations at Nikolayev Observatory during 2013-2014 are presented. The Washington Double Stars Catalogue (WDS) was used for observation program composing. The observation volume was obtained with usage two telescopes equipped CCD-cameras. Precise modern epoch CCD-observations allowed to make new proper motion values. The position angles and separations for 214 double stars were measured. Results are going to be submitted to WDS.

Keywords: Stars: double stars, binary stars, proper motions

1. Introduction

The main reason to be interested in double stars is a possibility to obtain total mass of a double-star system from studying their relative motions. Mass estimates are of huge importance to theorists on stellar evolution. According to modern double stars researches, the percentage of stars included into double or multiple systems is in range from 30 to 70%. The main source of information about these objects is the Washington Double Star Catalog (WDS) [1]. WDS contains more than 132,000 objects on July, 2015 each of which gives measures for the positional angle and separation of two components. Visual double stars are two that appear close together in the sky visually, but are not necessarily anywhere near one another in space. If visual doubles are gravitationally attached they are called visual binaries. Similar proper motions for both components is one of criteria for distinguish them. If the difference of their proper motions is small comparing to their common proper motion, the pair is probably physical. The proper motions for 1.5% of main component and for 20% second component are absent in WDS catalog. The most of the doubles are available for observations with small telescopes. That's why we have performed double stars observations in Nikolaev.

2. Observations: Instrumentation, Program

The observations were made at two telescopes which were created in the RI NAO: mobile multi-channel automatic telescope (Mobitel) with D=500 mm, F=3000 mm and Axial meridian circle (AMC) with D=180 mm, F=2500 mm.

Both telescopes are equipped with the CCD cameras and getting images in drift scan mode. We have obtained frames with scale 1.32" and 0.83" per pixel and field of view 24'×28' and 42.6'×42.6' for AMC and Mobitel, respectively. These parameters allow us to have enough

reference stars for astrometric reductions and obtaining positions of the stars with high accuracy.

For observational program we selected WDS objects which are most appropriate to be observed by our telescope and in the expected time frame (the full time of exposure is 102s and 85s at equator). For the main selection criteria we used a magnitude limit of 17^m and 14.5^m and a separation bigger than two FWHM.

The regular observations of double stars were carried out during 2013-2014. The statistical information about volume of observations is given in table 1. There are not only program objects in column 4; we also selected other WDS doubles from the other observations, which appeared in the imaged field.

Table 1. Statistics of observations

Period	Telescope	Σ stars	Mean N*
2013	AMC	2420	4
2014	AMC	1848	3.5
2013	Mobitel	124859	8
2014	Mobitel	87767	9

*The average number of star observations

3. Processing and Results

Processing of obtained observations included two steps: getting astrometrical parameters (coordinates, proper motions, magnitudes) and measures of double stars parameters (position angle and separation).

Astrometric reductions for equatorial coordinates of objects were performed with Astrometrica software [2]. Connection model between the tangential and the measured coordinates was polynomial 2nd order for AMC and polynomial 4th order for Mobitel. The catalogs UCAC2 [3] and UCAC4 [4] were used as reference catalogs. After processing whole volume of observations the coordinates in right ascension and declination at mean observational epoch were averaged. The mean standard errors of catalog position were about 30 mas in both coordinates and that allows us to obtain new proper motions with accuracy about 4-5 mas/year when the catalog USNO A2.0 was used as source of second epoch positions. Then we cross-matched our positional data with WDS catalog and other astronomical catalogs for calculations new proper motions of the primary and secondary double components and for selection all WDS doubles which were appeared in the imaged field. The results of search WDS double stars and following cross-matching are summarized in table 2. Cross-matching was made with usage

service CDS-Upload X-Match realized by TOPCAT software [5].

Table 2. Results of cross-matching

	WDS	USNO A2.0	PPMXL	2mass	UCAC4	TYCHO2
AMC	127	118	123	127	127	74
Mobitel	234	216	222	234	230	55

The comparison of obtained proper motions has shown a good agreement with other sources. The mean external accuracy of the obtained proper motions is about 8 mas/year in both coordinates based on the comparison with other catalogs (Tycho2, PPMXL, UCAC4, WDS).

The comparison results of obtained proper motions with WDS proper motions are shown in figure 1.

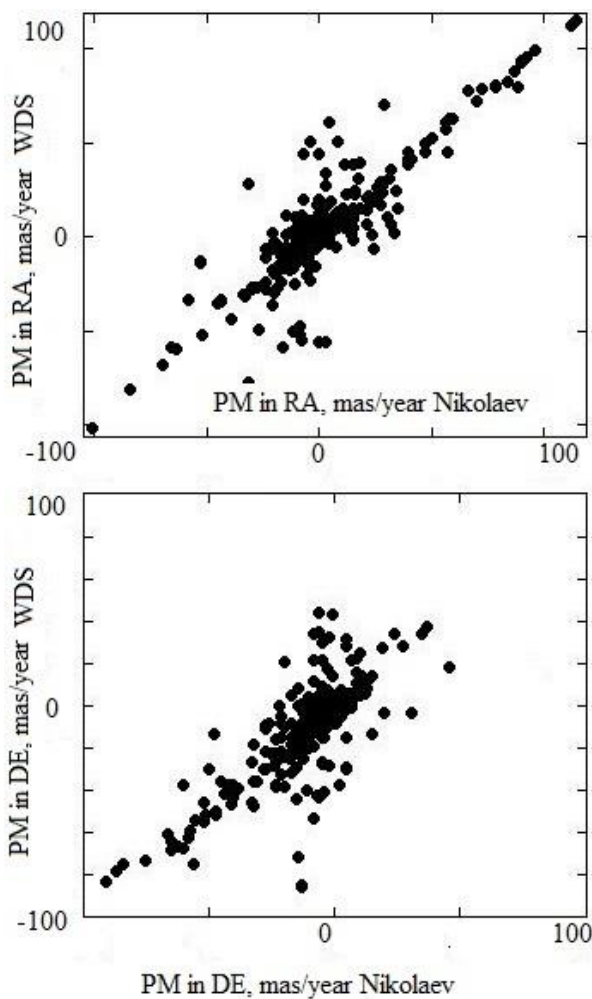


Figure 1: Obtained proper motion vs WDS proper motions (top – right ascension, bottom – declination).

The figure 1 have shown that criteria of common proper motions for distinguishing visual binary stars work better for stars with high proper motions, when values of their error much less than values of proper motions.

Measures of double stars were made with usage REDUC software [6]. We used previously determined exact values of orientation angle and image inclination regarding the celestial equator from astrometric reductions for

calibration. Unfortunately, the AMC limiting magnitude fallen down significantly by the technical reasons and we can't see the secondary component in most frame there. We have measured only observations obtained at Mobitel.

There were obtained 1802 positions for 199 WDS stars. The mean number of measurements of a star is about 8. The distributions of observations in stellar magnitudes and magnitude differences between main and secondary component measured by REDUC are given in figure 2.

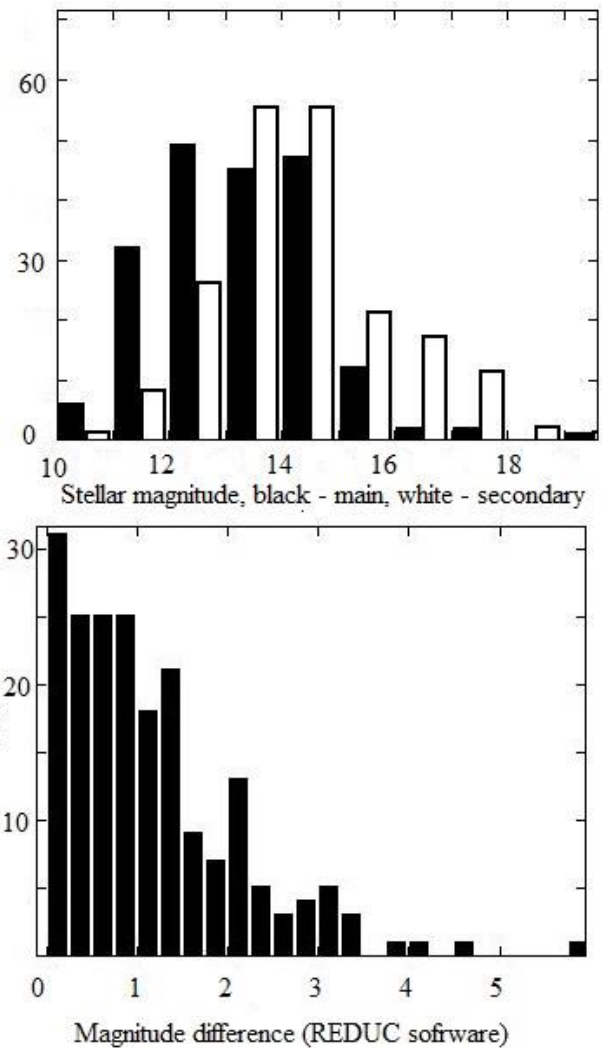


Figure 2: Distribution of double stars in stellar magnitude (top – stellar magnitude of main (black column) and secondary (white column), bottom – magnitude difference between the components, obtained REDUC software)

The position angle (PA) of the secondary with respect to the primary and angular distance between the two stars (separation) between components were measured. The mean standard error of PA is 0.5° , separation – $0.15''$. The distribution of standard errors in PA and separation are shown in figure 3.

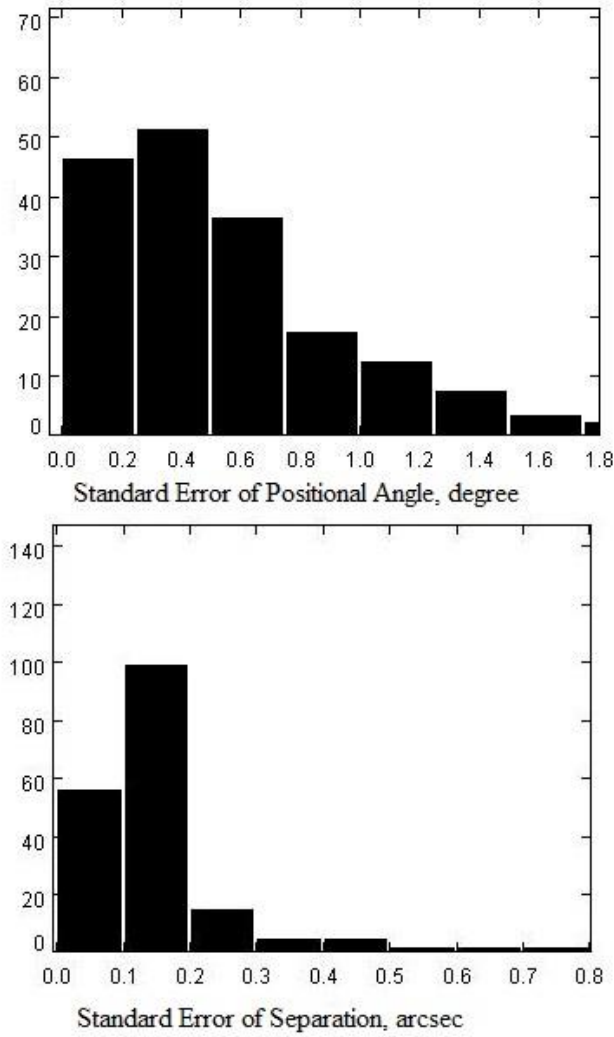


Figure 3: Distribution of standard errors of measurements

We have compared our results with WDS data. It can be seen from figure 4 that they are in good accordance with each other.

4. Conclusions

The equatorial coordinates and proper motions of 361 WDS stars were obtained basing on CCD observations during 2013-2014 yr. Average accuracy of the catalog star position is about 30 mas in both coordinates. The new proper motions for WDS star were calculated with usage USNO A2.0 as the first epoch. Parameters for 199 WDS doubles (PA and separations) were obtained. The standard deviation is 0.5° for PA and $0.15''$ for separation.

The results of measurements are going to be sent to WDS database.

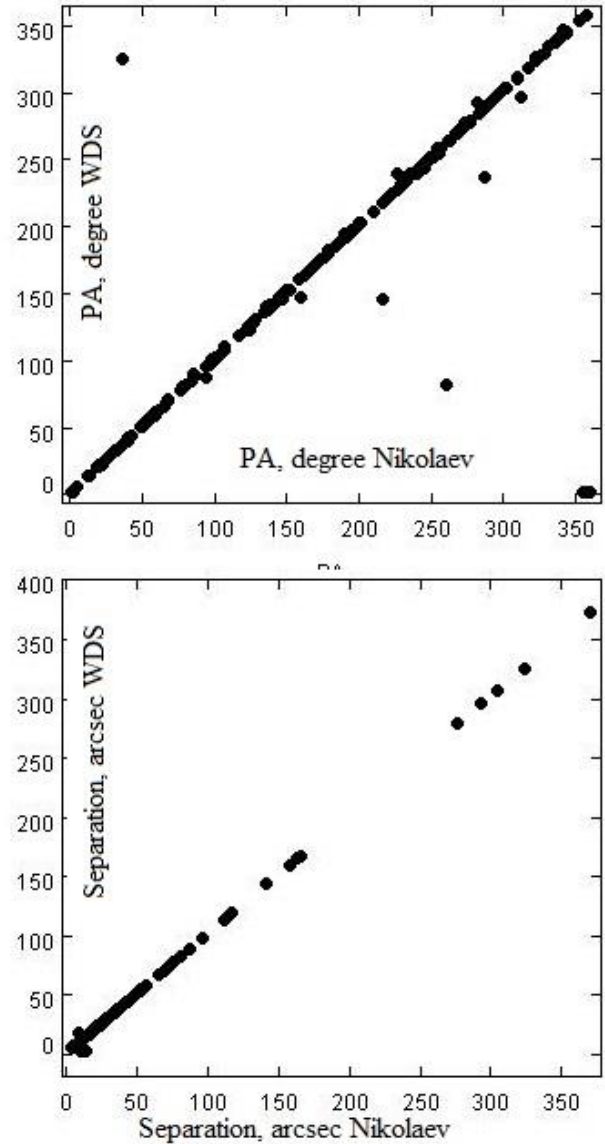


Figure 4: Measured values of separation and PA over separation and PA from WDS catalog (only double stars with separations between components more than about double FWHM were measured)

References

1. Mason B.D. et al: 2001, *Astron. J.*, 122, 3466
2. <http://www.astrometrica.at/>
3. Zacharias N. et al: 2004, *Astron. J.*, 127, 3043
4. Zacharias N. et al: 2013, *Astron. J.*, 145, 44Z
5. <http://www.star.bris.ac.uk/~mbt/topcat/>
6. <http://www.astrosurf.com/hfosaf/uk/download.htm>

INVESTIGATION OF DIFFUSE INTERSTELLAR BANDS OF ORGANIC MOLECULES IN THE SPECTRA OF CEPHEID STARS

Kashuba S.V.¹, Andrievsky S.M.¹, Chehonadskih F.A.¹,
Korotin, S.A.¹, Kovtyukh V.V.¹, Luck R.E.²

¹ Astronomical Observatory, Odessa National University,
Shevchenko Park, 65014, Odessa, Ukraine

² Department of Astronomy, Case Western Reserve University, 10900 Euclid
Avenue, Cleveland, OH 44106-7215, USA

ABSTRACT. We describe an effective method of investigation of the Diffuse Interstellar Bands (DIBs) in the spectra of Cepheid stars. DIBs are believed to originate from the absorption of such carriers as polycyclic aromatic hydrocarbons in the interstellar gaseous clouds located between an observer and the stars whose spectra were recorded. We performed a detailed consideration of the DIB at 6613 Å in our sample of spectra for more than 250 stars. The quantitative characteristics of the DIB absorption features will be studied in connection with the interstellar absorption data, and after that, they will be used in the mapping of the Galactic disc.

Keywords: ISM: bands – variables: cepheids

1. Introduction

The Diffuse Interstellar Bands (DIBs) are observed in spectra of astronomical objects in ultraviolet, visible and infrared wavelengths. The central wavelengths of DIBs don't correspond to any known spectral lines of a chemical elements. This phenomena is one of the most difficult conundrums for astrophysics. However, presence the unknown bands in the spectra of stars confirms existence the inhomogeneous distribution of the interstellar medium. Therefore, we investigated in detail the one of the DIBs of organic molecules in the spectra of Cepheid stars for determining of some characteristics ISM.

2. Data

We used the spectra of Cepheid stars with resolution of 30000, which had been obtained by R. E. Luck with the Hobby–Eberly Telescope Spectrograph (McDonald Observatory, Texas, United States). Using spectra of the variable stars for investigation DIBs is unique. In our research, we analyzed 253 spectra.

3. The method

The object of the research was DIB at 6613 Å. As a rule it blend with two stellar spectral lines: Y II at 6613.73 Å and Fe I at 6613.82 Å. But sometimes our band don't blend with any stellar spectral lines.

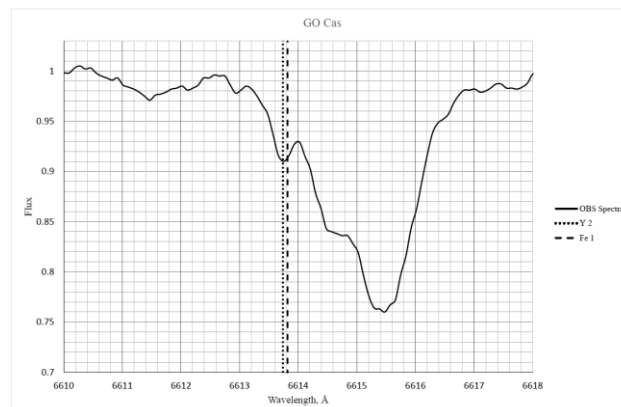


Figure 1: The DIB at 6613 Å in spectrum of GO Cas

We had to neutralize the influence of these two lines on our DIB. For this purpose, we developed an effective method, which consists of the following stages:

1. Verifying oscillator strength for Y II at 6613.73 Å and Fe I at 6613.82 Å. We used spectra of Sun with high resolution (Kurucz et al. 2004) and VALD (Vienna Atomic Line Database).
2. Creating synthetic spectra of Cepheid stars. For that, we used the basic atmospheric parameters stars, which are presented in the paper Luck & Lambert (1). The models of stellar atmospheres were generated with program ATLAS9 (Kurucz, 2004). The synthetic spectra were calculated with the SynthV program (Tsybal, 1996). We also used the chemical structure database from the paper Luck et al. (2).
3. The observed spectra processing. All procedures of spectra processing were conducted in DECH20t (Galazutdinov).
4. The observed spectrum was divided by the synthetic and we received a «clean» profile of the DIB.

Our aims were to analyze the «clean» profiles of the DIB at 6613 Å and to make map of the distribution density of interstellar matter in the Galactic disc.

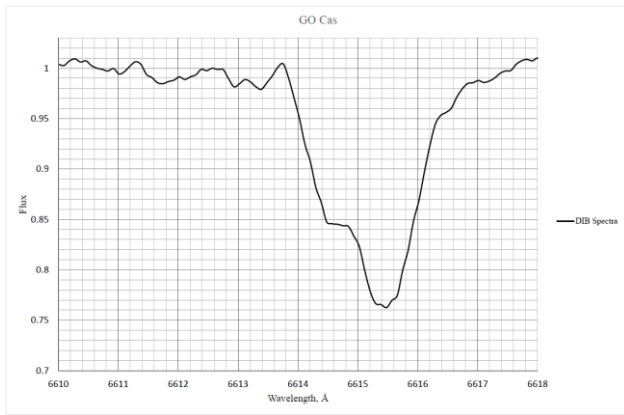


Figure 2: The «clean» profiles of the DIB at 6613 Å in spectrum of GO Cas

In our paper, we investigated the DIB of organic molecules at 6613 Å in the 253 spectra of Cepheid stars.

We «cleared» the chosen DIB's profiles of the stellar spectral lines Y II at 6613.73 Å and Fe I at 6613.82Å.

We defined the equivalent width of DIB at 6613 Å in 253 spectra.

Finally, we made map of the distribution density of interstellar matter in the Galactic disc. Our results were presented in tables and graphs.

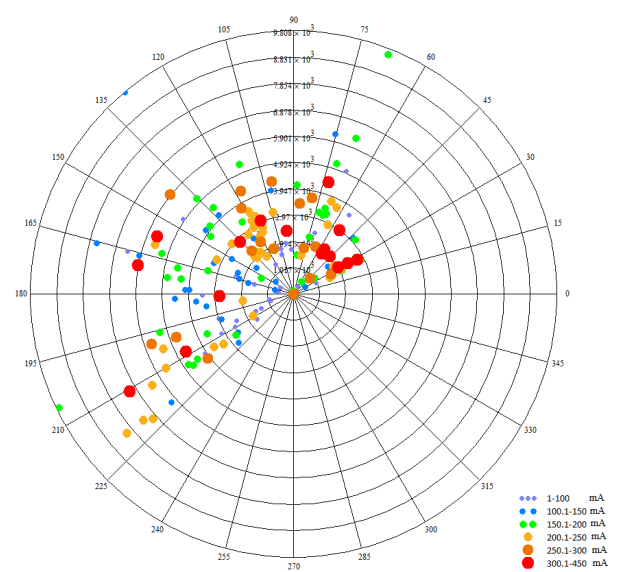


Figure 1: The Map of the Distribution Density of Interstellar Matter in the Galactic Disc

References

Luck, R.E., & Lambert, D. L. 1981, *ApJ*, 245, 1018.
 Luck R.E. et al.: 2007, *ApJ*, **133**, 2464.

NUCLEAR MAGICS AT MAGNETOROTATIONAL SUPERNOVA EXPLOSION

V.N.Kondratyev^{1,2}, Yu.V.Korovina³, T.V.Mishenina⁴

¹ Physics Department, Taras Shevchenko National University of Kyiv, 03022-UA Kyiv, Ukraine, vkondrat@univ.kiev.ua

² BLTP, JINR, 141980-RU Dubna, Russia

³ Moscow Institute of Open Education, 125167-RU Moscow, Russia

⁴ Astronomical Observatory, Odessa National University, 65014-UA Odessa, Ukraine

ABSTRACT. Nucleosynthesis at magnetorotational supernova explosion is considered by employing arguments of nuclear statistical equilibrium. Effects of ultra-strong nuclear magnetization are demonstrated to enhance the portion of titanium product. The relation to an excess of ^{44}Ti revealed from the Integral mission data and galactic chemical evolution is discussed.

Keywords: Stars: supernovae, magnetic field. – Nucleosynthesis: abundances, galactic chemical evolution.

1. Introduction

Supernovae (SNe) represent promising sites for synthesis of heavy atomic nuclei (Woosley, Heger & Weaver, 2002) and give major stellar nucleosynthetic contributions to nuclide inventories during the Galaxy chemical evolution. Magnetization of hot dense plasma due to magnetorotational instability (MRI) is considered as an inherent feature and makes plausible explosion mechanism. In present study we argue that such a feature affects nucleosynthesis (cf., e.g., (Kondratyev, 2004; 2014 and refs. therein) and, in particular, magnetic effects lead to an increase of titanium portion in the synthesis of nuclides close to the iron "peak". Consequently, the characteristic lines of respective nuclei in spectra of astrophysical objects are considerably enhanced and allow for an analysis of synthesized elements. The radioactive

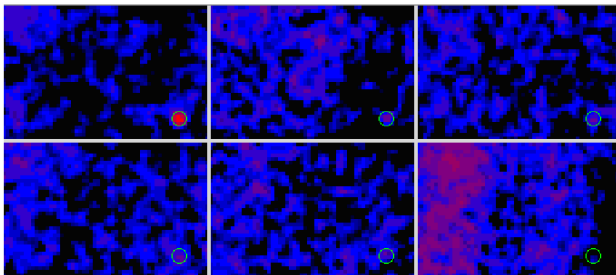


Figure 1: Direction (pixel number) dependence of the registered gamma-ray flux at different energy ranges. top: left – 20–50 keV, middle – 50–67 keV, right – 67–70 keV, bottom: left – 70–77 keV; middle – 77–82 keV, right – 82–100 keV; for the Cassiopeia region. SNR CAS A, (J2000) R.A. 350.86°, decl. 58.81°, indicated by circle.

decay chain $^{44}\text{Ti} \rightarrow ^{44}\text{Sc} \rightarrow ^{44}\text{Ca}$ gives rise to an emission of lines with energies of 67.9 keV and 78.4 keV (from $^{44}\text{Sc}^*$) and 1157 keV (from $^{44}\text{Ca}^*$) of approximately equal intensity. The respective image-mosaics from Integral data (Kondratyev, 2004; 2014) for the Cassiopeia region in various energy ranges of registered photons are presented in Fig. 1. The color (brightness) is proportional to the gamma-quanta flux: as larger the flux as lighter (brighter) the color of a pixel. As is seen the SNR CAS A gives the brightest spot for energies matching ^{44}Sc lines.

Table 1: Volume M_{Ti} of nuclides ^{44}Ti (in solar masses M_{Sun}) initially synthesized in young SNe, Tycho, CAS A and SN1987A (see Kondratyev & Korovina, 2015).

SN	$M_{\text{Ti}}[10^{-4} M_{\text{Sun}}]$
CAS A	$3.3^{+0.9}_{-0.7}$
SN1987A	3.1 ± 0.8
Tycho	< 0.84

Then ^{44}Ti half-life, about 60 years, allows to determine this isotope initial mass in SN remnants. Table. 1 shows the observational results for the total mass of ^{44}Ti nuclide synthesized in SN explosions from (Kondratyev & Korovina, 2015). These values are significantly larger as compared to model predictions, see. (Woosley, Heger & Weaver, 2002), giving the mass of initially synthesized ^{44}Ti , $M_{\text{Ti}} \sim 10^{-5} M_{\text{Sun}}$ (in solar masses M_{Sun}) in an absence of magnetic effects.

2. MRI explosive nucleosynthesis

Abundances of iron group and nearby nuclides are described very successfully within nuclear statistical equilibrium (NSE) approach for over half a century (Woosley, Heger & Weaver, 2002). At such conditions nuclide abundance is determined mainly by the binding

energy of corresponding atomic nuclei. The magnetic effects in the NSE were considered by Kondratyev (2014) and refs. therein. Recall that at temperatures ($T \leq 10^{9.5}$ K) and field strengths ($H \geq 0.1$ TT), the magnetic field dependence of relative output value $y = Y(H)/Y(0)$ is determined by a change in the binding energy of nuclei in a field and can be written in the following form

$$y = \exp\{\Delta B / kT\}. \quad (1)$$

We consider examples of ^{56}Ni and ^{44}Ti . Such a choice of symmetric nuclei, double magic and anti-magic for vanishing magnetization, gives a clear picture of magnetic effects in the formation of chemical elements and fundamental conclusions about transmutation and synthesis of nuclei in ultramagnetized plasma.

The binding energy B can be written as $B = B_{\text{LDM}} + C_n + C_p$, where shell corrections C_i for protons and neutrons, and the component B_{LDM} is calculated in semiclassical liquid drop model and varies only slightly in the magnetic field, according to the Bohr-van Leuven theorem, see (Kondratyev, 2014).

Spin magnetization of Pauli type dominates for the neutron magnetic reactivity. Interaction of a field and the spin-magnetic moment corresponding to a spin projection m_n on a field vector gives rise to a linear shift of energy levels $\Delta = m_n g_n \omega_L$, where $\omega_L = \mu_N H$ with nucleon magneton μ_N , and g_n – neutron g -factor. Accordingly, the shell energy in a field H is modified as follows

$$C_n(H) = C_n^+(E_F + \Delta) + C_n^-(E_F - \Delta), \quad (2)$$

where the indices + and – indicate a sign of the projection of spin magnetic moment on field direction. The proton magnetic response is represented by a superposition of the field interaction with spin and orbital magnetic moments and exceeds the neutron component for an open shell.

As is demonstrated by Kondratyev & Korovina (2015) at field strengths $H < 10$ TT, the binding energy shows nearly linear H dependence for considered nuclei $B = B_0 + \kappa_i H$ [MeV] with magnetic susceptibility parameters κ_i depending on a nucleus $nucleus = {}^A_Z$. For ^{44}Ti the value of this parameter is positive $\kappa_{\text{Ti}} \sim 0.3$ MeV/TT, and in case of ^{56}Ni it becomes negative $\kappa_{\text{Ni}} \sim -0.3$ MeV/TT. Evidently, for anti-magic at zero field strength nuclei the shell energy always increases with field H , and for magic one – decreases, indicating positive and negative values of magnetic susceptibility κ_i , respectively. Then for an average relative yield over MRI region V , see sect. 1, $\langle y \rangle = V^{-1} \int_V d^3r y(H(\mathbf{r}))$ one gets (Kondratyev & Korovina, 2015)

$$\begin{aligned} \langle y \rangle &= b^{-1} \left(\exp\{a\} + \int_1^b \exp\{a/x\} dx \right) \\ &= \left(\exp\{a/b\} + \frac{a}{b} [\text{Ei}(a) - \text{Ei}(a/b)] \right), \end{aligned} \quad (3)$$

where $a = \kappa_i H_0 / kT$, $b = (r_a/r_0)^2$. The radius r_0 relative to the MRI center corresponds to a maximum in field strength H_0 , and radius r_a is determined from conditions of comparable values for magnetic pressure gradients and gravitational force at R corresponding to material irruption, i.e., $dH^2(r)/dr = 4H_0^2/b^2 r_a \sim 8\pi \text{GM} n(R)/R^2$. Here the gravitational constant G , and the star mass M inside the bifurcation radius R is related to the matter density $n(R)$ as $4\pi R^2 n(R) = -dM/dR$, and the integral

$$\text{Ei}(x) = \int_{-\infty}^x \frac{\exp\{t\}}{t} dt.$$

In Fig. 2 one sees significant difference for magnetic field dependence of nuclide output, magic and anti-magic at vanishing field. For anti-magic nuclei and, therefore, increasing binding energy with increasing field strength or positive magnetic susceptibility relative volume of nucleosynthesis increases significantly with increasing a . At the same time, the relative production of magic nuclides, i.e., negative value a , is not substantially changed with increasing field. This behavior significantly differs from the case of a spatially uniform magnetization, see Fig. 2, which corresponds to the exponential dependence of $\langle y \rangle$ or $b = 1$ in Eq. (3). In this case the coefficients of suppression and enhancement are the same with the same absolute value of a . The presence of the diffusion layer, corresponding to a fade-out field strength with increasing r (or $b > 1$) in a real MRI region leads to substantial differences of relevant factors. Significant increase in a synthesis of anti-magic nuclei is accompanied by a slight change in mass volume magic nuclides. Model predictions in the absence of magnetic effects, see. (Woosley, Heger & Weaver, 2002), give the mass of initially synthesized ^{44}Ti , $M_{\text{Ti}} \sim 10^{-5} M_{\text{Sun}}$ (in solar masses M_{Sun}). For realistic characteristics of Type II SN explosion (sect. 1) enhancement factor $\langle y \rangle_{\text{Ti}} \sim 30 - 300$ corresponds to a mass $M_{\text{Ti}} \sim 10^{-3.5} - 10^{-2.5} M_{\text{Sun}}$. It is worthy to notice that not all the material ejected from the central part of a star is formed in MRI areas, see (Kondratyev, 2014). Such an enhancement of ^{44}Ti is in an agreement with direct observations in young SN II remnants, see Table I. At the same time for SN I the ^{44}Ti volume is significantly smaller. One might expect, therefore, noticeable correlations in enrichment of anti-magic nuclides with other metals, e.g., ^{56}Fe , ^{26}Al .

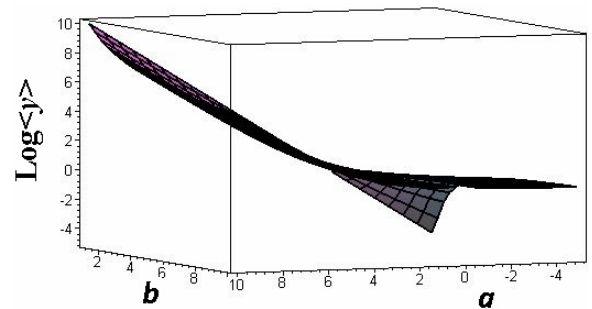


Figure 2: Relative field of nucleosynthesis products depending on parameters a and b .

3. Galactic chemical evolution

An important application of the nucleosynthesis computations is represented by a description of the enrichment of our Galaxy and the Universe as a whole with various chemical elements. Despite considerable progress in the chemical evolution modeling, as well as in the nucleosynthesis computations, a number of issues remain unresolved. In this paper, we dwell on potential sources of calcium and titanium production.

For this purpose we use the abundances of these elements, which we had obtained earlier for the Galactic disc dwarfs (Mishenina et al., 2008), and compared them with the chemical evolution computations (Timmes, Woosley & Weaver, 1995) (Figs. 3, 4). In the recent study (Timmes, Woosley & Weaver, 1995) the yields of isotopes ^{48}Ti and ^{44}Ca , produced by massive supernovae, from Woosley & Weaver (1995) were used to develop a Galactic chemical evolution model. As can be seen from Figs. 3 and 4, the employed data describe the trend of $[\text{Ca}/\text{Fe}]$ vs. $[\text{Fe}/\text{H}]$ quite well; however, the adopted yield of isotope ^{48}Ti is insufficient to describe the behavior of $[\text{Ti}/\text{Fe}]$ vs. $[\text{Fe}/\text{H}]$. A similar pattern for calcium and titanium is presented in the study by Timmes, Woosley & Weaver (1995; see their Figs. 25 and 27). It proves that the investigated sources of calcium production, such as massive stars, are dominant suppliers of calcium in the interstellar medium while further improved computations for the titanium sources are required. In respect with titanium the authors point out that "both the ^{48}Ti yield and the ration $[\text{Ti}/\text{Fe}]$ are sensitive to the parameters of the explosion and the amount of material that falls back onto the neutron star". The nucleosynthesis computations (Woosley & Weaver, 1995) were carried out not accounting for the magnetic field.

We suggest another possible mechanism of additional titanium enrichment when taking into account the increased yield of anti-magic nuclides in ultramagnetized astrophysical plasma. As is seen on an example of the radioactive isotope ^{44}Ti the direct observational data, see sect. 1, confirm such an enrichment which can be understood in terms of magnetic effects. The resulting enrichments of M44 isobars are collaborated with observational data

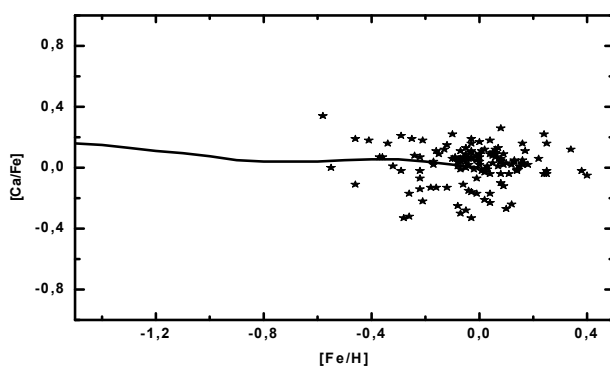


Figure 3: Comparison of observed abundance of Ca (Mishenina et al., 2008, marked as asterisks) with the trend of galactic chemical evolution (Timmes, Woosley & Weaver, 1995, marked as solid line).

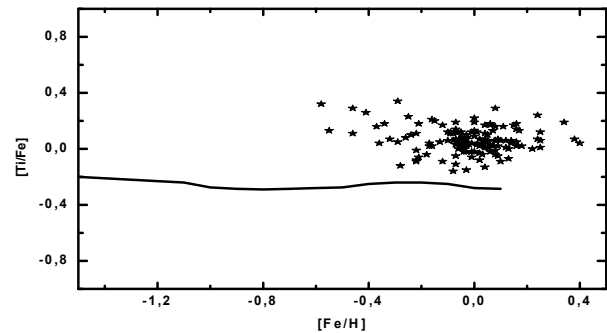


Figure 4: The same as Figure 3, but for Ti abundance.

(Kondratyev, 2014; Magkotsios, 2010). The proton magnetic reactivity dominates in a change of binding energy, see Eq. (2). Therefore, one can expect to meet a noticeable increase in production of other titanium isotopes, as well. At the same time a yield calcium isotopes can be expected unchanged because of the proton shell closure, see Eq. (3).

4. Conclusion

Effects of ultra-magnetized astrophysical plasma in supernovae on synthesis of chemical elements were investigated at conditions of nuclear statistical equilibrium. Magic-antimagic switches in the nuclear shell structure in varying magnetic field lead to an increase of titanium binding energy and, consequently, to a noticeable increase of the portion of ^{44}Ti in explosive nucleosynthesis products. Magnetic effects in nuclide creation are favorably compared to observational Integral data and galactic chemical composition.

Acknowledgements. This work is supported in part by Integral scientific data center and by the Swiss National Science Foundation (SCOPEs project No.~IZ73Z0152485).

References

- Kondratyev V.N. et al.: 2004, *Proc. 54th Intern.Symp. on Nuclear Spectroscopy and Structure of Atomic Nuclei* (Belgorod, Russia), p. 83.
- Kondratyev V.N.:2014, *EPJ A*, **50**, 7.
- Kondratyev V.N., Korovina Yu.V.: 2015, *JETP L*, **102**, 131.
- Mishenina T.V., Soubiran C., Bienayme O. et al.: 2008, *Astron. Astrophys.*, **489**, 923.
- Magkotsios G. et al.: 2010, *ApJS*, **191**, 66.
- Woosley S.E., Weaver T.A.: 1995, *Astrophys. J. Suppl. Ser.*, **101**, 181.
- Woosley S.E., Heger A., Weaver T.A.: 2002, *Rev. Mod. Phys.*, **74**, 1015.
- Timmes F.X., Woosley S.E., Weaver T.A.: 1995, *Astrophys. J. Suppl. Ser.*, **98**, 617.

THREE-DIMENSIONAL NUMERICAL HYDRODYNAMICAL SIMULATION OF LOW/HARD AND HIGH/SOFT STATES IN ACCRETION DISCS OF MICROQUASARS AND QUASARS ON BASE OF UNDEFINED PRECESSION

V.V. Nazarenko, S.V. Nazarenko

Astronomical Observatory of I.I.Mechnikov Odessa National University,
Odessa, Ukraine, *astro@paco.odessa.ua*

ABSTRACT. In this study, the models of slaved precession of accretion disc and donors radiation-driven wind were performed using three-dimensional numerical astrophysical methods by the example of microquasar Cyg X-1. As is shown, in the course of precession of the accretion disc blown by the donor's wind the states with high and low temperature (low and high mass accretion rate, respectively) start being generated in the centre of disc. Our computations of disc precession performed on base of undefined precession that means each point of rotation axis of accretion disc makes unclosed difficult curve instead of a circle as it is in case of definite precession. In this case, the transition between states of high and low temperature takes place irregularly and not depend on precession period. The duration of transition between these both states is less than intervals of states on several orders of magnitudes.

Key words: Stars: close binary system; microquasars; quasars.

1. Introduction

In present work we continue to simulate high/soft and low/hard (ON- OFF-: active and passive) states in accretion discs of microquasars and quasars. Our idea consists in that in precession accretion disc having been blown by the donor's wind begins to generate the states of low and high temperature in the disc centre. Since these states are unti correlated with mass accretion rate we interpreted them as ON- and OFF-states in accretion discs of microquasars. In the previous our work (Nazarenko, 2014) we had simulated ON- and OFF-states on the base of defined precession. The result of it was the transition between ON- and OFF-states was every precession period. But it occurs irregularly in real microquasars and not depends from precession period. By such the way to improve the results of previous work in the present

one we simulate ON- and OFF-states on the base of undefined precession. It means that each point of rotation axis of accretion disc makes unclosed curve. Thus our goal in the present research is to make the change between both ON- and OFF-states to be irregular and don't depended from precession period.

2. The numerical approach

To obtain the goal stated above we use special numerical technique. This one is as follows: to simulate 3D mass flow in the calculation area from initial time to stationary state we use non-stationary Euler's hydrodynamical equations. We resolve these equations by astrophysical variant of 'Big-particles' code by Belotserkovsky and Davydov (Nazarenko, 2014). This astrophysical variant is distinct to the standard 'Big-particles' code (Belotserkovskii et al., 1982) that in this one the internal energy on first time substep is used (in standard code the total energy on first time substep is used). To decrease the effects of numerical viscosity attributing the cold in use we use the special technique to decrease radial velocity in accretion disc and do the temperature in calculation area to the real one. We use rectangular numerical grid and also the rectangular Cartesian coordinate system that is connected hardly with the donor. To simulate the precession of accretion disc we use the slaved precession. In the chosen coordinate system the accretor makes the unclosed curve.

To decrease large computer expenses and order to run our calculation over long time we use the accretion disc precession period equal to orbital one. In the present calculation we use the following dimensionless units: the velocities are given in units of the orbital speed; the temperatures are given in units 10^4K ; the numerical time units are such that 2π is corresponding to the orbital period; mass accretion rate is given in units of solar mass per year in logarithmic scale. We cut the space around the accretor with the radius of

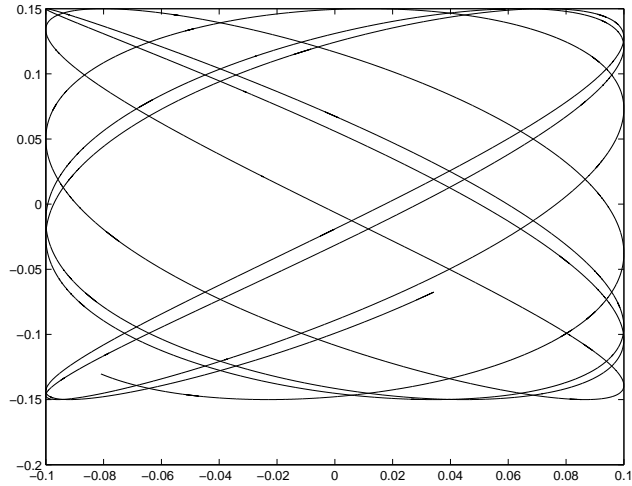


Figure 1: The time change of the accretor's coordinates in z-y plane.

0.025 (10% of the outer disc radius) to avoid singularity. This space has the size of 5000 Schwarzschild radii and it means that our simulations are running far away from accretor.

The time changes of the accretor's coordinates are given below.

$$\begin{aligned} x_{ac1} &= 1.0, & \text{if } t < 0 \\ y_{ac1} &= 0.0, & \text{if } t < -0.25 \\ z_{ac1} &= 0.0, & \text{if } t < 0 \end{aligned}$$

$$\begin{aligned} x_{ac1} &= 1.0 + A \sin\left(2\pi \frac{t}{P_x}\right), & \text{if } t > 0 \\ y_{ac1} &= 0.0 + B \cos\left(2\pi \frac{t}{P_y}\right) \cdot N_{prec}, & \text{if } t > -0.25 \\ z_{ac1} &= 0.0 + C \sin\left(2\pi \frac{t}{P_z}\right), & \text{if } t > 0 \end{aligned}$$

where $A = B = C = 0.15$, $N_{prec} = -1$ for retrograde precession, $N_{prec} = 1$ for prograde precession and P_x, P_y, P_z are precession periods for appropriate accretor's coordinates. The time is given in units of precession period.

3. The numerical results

The unclosed curve made by the accretor over on the time of calculation is shown in Fig. 1. The evolution of the accretion disc central temperature in time is shown in Fig. 2. The dependance of mass accretion rate of our accretion disc model versus time is shown in Fig. 3. The mass accretion rate is negative since it is accretion process. As it is led from Fig. 2 we run our calculation over long time as large as 17th precession period. It shows that the essential physical values are strong conserved in our present simulation in code in use. First we see in Fig. 2 it is the high temperature interval is from 4 to 13.5 precession period. The interval of low temperature in Fig. 2 is on 13.75-14.50 precession pe-

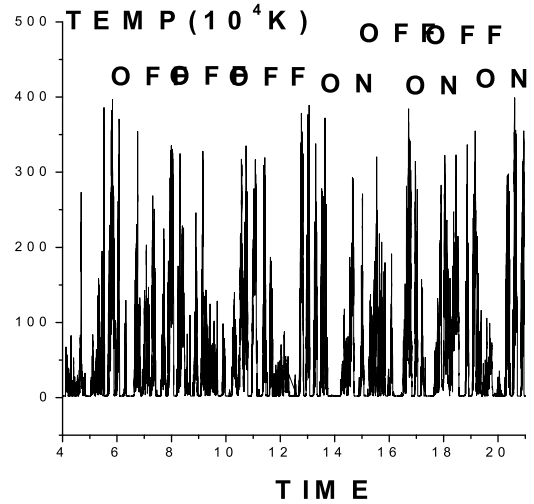


Figure 2: The dependance of the temperature in the disk's centre versus time.

riod. This interval is over 0.75 precession period. We have interpreted these intervals of low and high temperature as generation low/hard and high/soft states in our accretion disc model. We have make such the interpretation since the both time intervals of temperature stated above are anti correlated with mass accretion rate in our accretion disc model (see Fig. 2 and Fig. 3). Accordingly mentioned above we may say that the change between both low/hard and high/soft states is not making every precession period in our present calculation and is strong irregular. As we think such the fine result occurs due to the using undefined precession in the present work. To show the time structure of low/hard and high/soft states in more details we have plotted partially low/hard state (Fig. 4) and high/soft one (Fig. 5). As it is good seen from these figures, the time characteristics of low/hard state in first turn are strong discrete i.e. it is in the view of partial peaks. The amplitudes of these peaks are in the interval from 2 to 400 (maximal values). By the other words, the central disc temperature is changing in time in 200 times. As it is led from Fig. 4 and Fig. 5, the relation between both low/hard and high/soft states time intervals is order of 10. This magnitude is in good accordance with the corresponding value in real Cyg X-1 in which the low/hard states are over several years and the high/soft states are over several months (Lachowicz et al., 2006). In order to see in more details the transition between both low/hard and high/soft states on time of 13.75 (see Fig. 2) we are plotted the vicinity of this time on high resolution scale (see Fig. 6). As it is led from these figures, the time interval of the transition stated above is order of 0.005 of precession period or 40 minutes of orbital time.

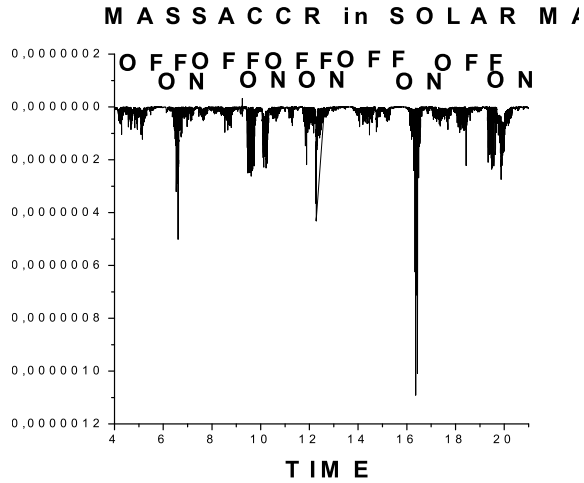


Figure 3: The dependance of the mass accretion rate in the disk's centre versus time.

The work of the mechanism to produce low/hard and high/soft states is very simple in the present paper. In the precession accretion disk having been blown by the donor's wind to states of low and high densities in the centre of disk is formed. When the densities in the disk centre are low, the radiation cooling is not efficient and instantly due to the action of the disk viscosity the kinetic energy of the disk rotation are transformed in thermal one. In this case the temperature in the disk centre is high. When the densities in the disk centre are high, the radiation cooling is strong effective and temperature in the disk centre is low.

4. Summary and discuss

Analyzing the numerical results described above we may say that the goal stated introduction is obtained and we have simulated low/hard and high/soft states and the change between both states is irregularly and is not depending from precession period. We may to mark also that the essential microquasar properties were have simulated in our present work. First of all, we show that the relation between both states is the factor of 10; the changes of central disc temperature and mass accretion rate in both states are order of 200 and 100 respectively; the transition between both states is order of 40 minutes of orbital time; the time structure of low/hard state has discrete character in the present simulation. All four properties of low/hard and high/soft states are qualitatively and quantitatively in a good accordance with observations (Lachowicz et al., 2006; Fender et al., 2003; 2004). The evolution of our calculation in the future works we see to run jet produc-

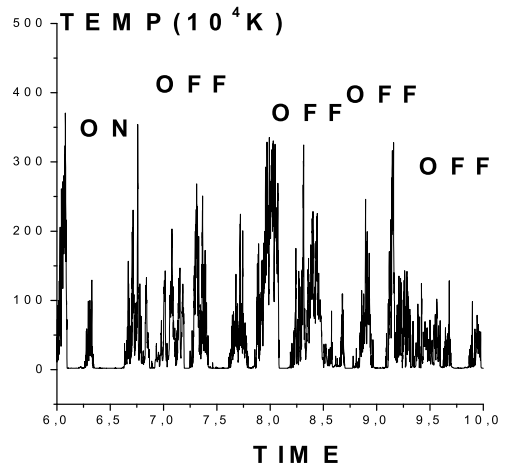


Figure 4: The dependance of the temperature in the disk's centre versus time over the interval of 6-10 precession periods.

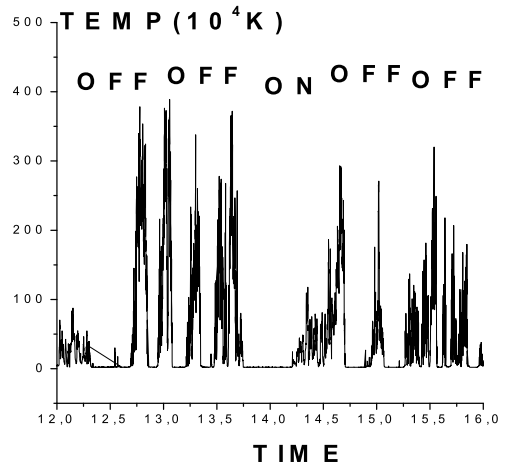


Figure 5: The dependance of the temperature in the disk's centre versus time over the interval of 12-16 precession periods.

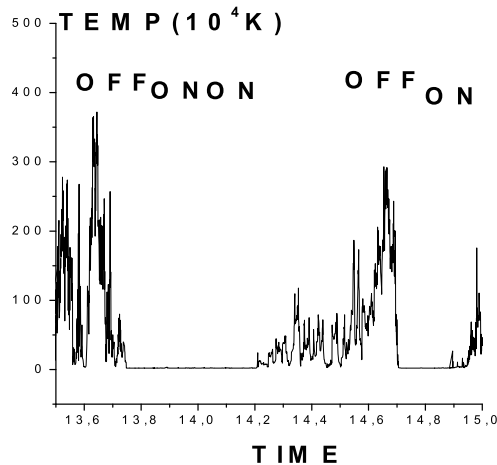


Figure 6: The dependance of the temperature in the disk's centre versus time on the high time scale over the interval of 13.6-15.0 precession periods.

tion and also its appearance and disappearance in simulated low/hard and high/soft states by us. We have planned to simulate radiation-driven jets since with our point of view such the jets may easy explained the microquasar phenomenon. Such the conclusion is based on three points on our opinion:

1) In low/hard state the temperature near the accretor in disc hot corona is increased by factor of 10 (from 10-20 KeV to 100 KeV, Fender et al., 2003; 2004). The last means that in these terms the radiation pressure will be rather able to produce jets.

2) The luminosities of microquasars are close to super critical one by factor of 0.3 - 0.7 (Fender et al., 2003; 2004).

3) The formation of radiation-driven jets in the view of narrow stream may be easy explained by radiation flux configuration on the bottom of the funnel of disc hot corona: this flux is distance from zero only in the direction in parallel to the disc rotation axis, since namely in this direction the disc central source radiation may freely leave a funnel.

In the last conclusion we implicitly imply that funnels are exist in all the microquasars.

References

- Belotserkovskii O.M., Davydov Yu.M.: 1982, "The big particles code in gas dynamics", Moskaw, Scientist, 391.
- Fender R.P., Gallo E., Jonker P.: 2003, *MNRAS*, **343**, 99.
- Fender R.P., Belloni T., Gallo E.: 2004, *MNRAS*, **355**, 1105.
- Lachowicz P., Zdziarski A.A., Schwarzenberg-Czerny A., et al.: 2006, *MNRAS*, **368**, 1025.
- Nazarenko V.V., Nazarenko S.V.: 2014, *OAP*, **27**, 137.

THE RELATIVE WAVELENGTH INDEPENDENCE OF IR LAGS IN ACTIVE GALACTIC NUCLEI: IMPLICATIONS FOR THE DISTRIBUTION OF THE HOT DUST

V.L. Oknyansky¹, C.M. Gaskell², E.V. Shimanovskaya¹

¹ Moscow M.V. Lomonosov State University, Sternberg Astronomical Institute,
Moscow, 119991, Russian Federation, *oknyan@mail.ru*

² Department of Astronomy and Astrophysics, University of California,
Santa Cruz, USA, *mgaskell@ucsc.edu*

ABSTRACT. We show that, contrary to simple predictions, most AGNs show at best only a small increase of lags in the J , H , K , and L bands with increasing wavelength. We suggest that a possible cause of this near simultaneity of the variability from the near-IR to the mid-IR is that the hot dust is in a hollow bi-conical outflow of which we only see the near side. Although most AGNs show near simultaneity of IR variability, there was at least one epoch when NGC 4151 showed the sharply increasing IR lag with the increase of the wavelength. This behaviour might also be present in GQ Comae. We discuss these results briefly. The relative wavelength independence of IR lags simplifies the use of IR lags for estimating cosmological parameters.

Keywords: galaxies: active – galaxies: nuclei – galaxies: Seyfert – infrared: galaxies – galaxies: individual: NGC 4151, NGC 6418, NGC 7469, NGC 5548, NGC 3783, Fairall 9, GQ Comae, WPVS48, PGC 50427, Ark 120, Mrk 509, MCG-6-30-15; optical and IR variability, time delay, data analysis, dust torus, cosmology.

1. Introduction

The variable near-IR radiation of active galactic nuclei (AGNs) is usually associated with the part of the optically-thick dusty torus closest to the central source (Hönig & Kishimoto 2011). The presence of such a torus is the key to explaining the observed differences in the spectra of type-1 and type-2 Seyfert nuclei by the torus blocking our direct view of the broad emission lines and the thermal continuum emitted by the accretion disc (AD). It is also believed that the dusty torus radiates in the infrared, as a result of heating by shorter wavelength radiation from the accretion disc and X-ray emitting corona. Closer to the centre the dust is completely (or largely) sublimated and delayed infrared

variability gives us the estimate of radius of the “dust holes” around the central source (Oknyanskij & Horne 2001), i.e., the radius of the region where the dust is absent. The work we present here is a continuation of our series of papers in which we measure the radius of the “dust holes” in the NGC 4151 and other AGNs from the delay of the variability in the near infrared relative to the optical variability (see details and references at Oknyanskij et al. 1999, Oknyanskij & Horne 2001, Oknyansky et al. 2014a,b). Despite the significant growth in theoretical and observational studies of AGNs in the IR, our knowledge of the dust, its origin, kinematics, and detailed morphology remains very incomplete.

The number of IR lags determined at different wavelengths for AGNs is not large. At the time of publications by Oknyansky et al. (1999), Oknyanskij & Horne (2001), there were just a few estimates of IR lags at different wavelengths. The first results were somewhat controversial. Some objects (NGC 4151, GQ Comae) showed a sharp increase of lag with wavelength in the IR. These differences in the lags (the lags in the L band were 3 times longer than in the K band) were in a good agreement with simple model predictions that cooler dust is farther from the centre than hotter dust (Barvainis 1987). Therefore Oknyansky & Horne (2001) considered those results to be normal and used the observed increase to correct observed IR lags for red shift. However, at that time at least one object, Fairall 9, was known to have about the same lags for the H , K and L bands. Oknyanskij et al. (1999) interpreted this in the following way: if the minimum distance from the central source to the dust clouds corresponds to a brighter state of the nucleus well before the interval under study, then the differences in the lags for K and L will be insignificant, as was observed in the Fairall 9. If, alternatively, this minimum radius roughly corresponds to the maximum nuclear luminosity in the interval under consideration,

then a marked difference in the lags for K and L must be observed, as it was the case for NGC 4151. This interpretation gives us observational prediction for NGC 4151 - at another time when it goes into a low state we will see similar IR lags for different IR wavelengths. This was indeed found for NGC 4151 in subsequent papers by Oknyansky et al (2006, 2014a,b). In order to investigate the reliability of these results, we have been collecting all available time lag data in different IR bands for AGNs to see how often this phenomenon is observed.

2. Observed IR time lags

Table 1 gives published and new measurements of time lags between variations in different near- and mid-IR bands relative to variability of the optical or UV continuum for as many AGNs as possible. Some new results in Table 1 were obtained applying our MCCF (Modified Cross-Correlation Function) method (Oknyanskij 1993) to published photometric data. Examples of MCCFs are given just for NGC 7469 in Fig. 1. In most cases our results are in a good agreement with results obtained before using other methods. In a few cases, our new results (for Ark 120, Mrk 509) disagree with the values obtained before by Glass (2004). These differences arise in part because of possible misprints in Glass (2004), some differences in the optical data sets used, reduction to a common photometric system, and the cross-correlation methods used. Glass took into consideration some unpublished optical data whereas we have used some additional published optical data, which were not used by Glass. Support for our values for the IR lags for Ark 120 and Mrk 509 comes from them being in good agreement with the luminosity-IR delay relation (Oknyanskij 1999; Oknyanskij & Horne 2001). As can be seen from Table 1, for most of the objects, time lags at different IR bands are similar. Only for one object, GQ Comae, do we see difference at about a factor of three between lags in the L and K bands. A similar difference was seen for NGC 4151 but only during the long, very high state which was the only one during last 110 years (Oknyanskij et al. 2013). The probability of observing an object exactly in its highest state is not large. Perhaps this is the reason why we see similar IR lags at different wavelengths for most of objects. The similar IR lags at the near and mid-IR were recently predicted in the model of a compact IR region as a part of dust torus by Hönlig & Kishimoto (2011). They considered the case in which the dust is located much farther then the sublimation distance. For the more realistic case of an IR region that is not too compact, the predicted values of the peak of the cross-correlation functions are too low in comparison to observed ones. Some new observations show that

hot dust clouds radiating in the mid-IR are located more in the polar regions (Hönlig et al. 2013) than in the torus. Those results were explained by optically-thin, dusty wind which is launched from the hottest and inner region of an optically-thick dusty disk. The beginning of this outflow with the hottest dust can be connected also with near-IR radiation. So we considered an alternative model where the variable near- and mid-IR radiation arises from the near side of a hollow, bi-conical outflow of dust clouds.

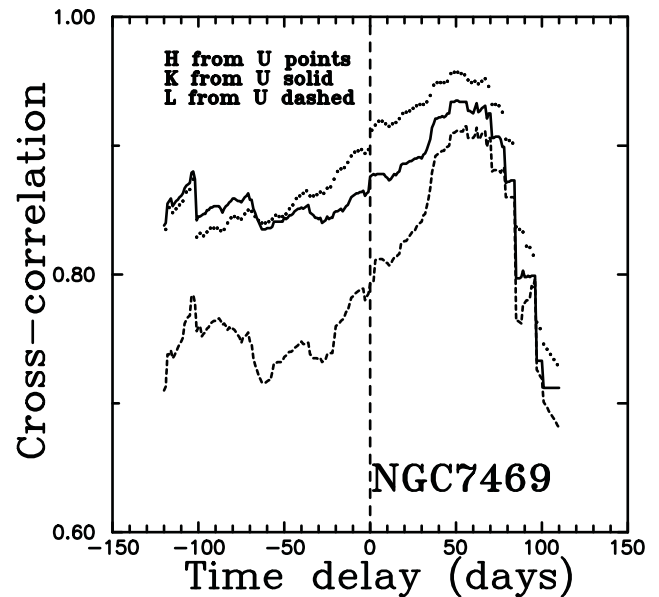


Figure 1: Cross-correlation functions calculated with the MCCF method for NGC 7469 using IR (Glass 1998) and optical (Lyuty 1995) observations during 2008-2013. See also Oknyansky (1999) and Oknyanskij & Horne (2001) where the IR lags for the object were found first time.

3. A hollow, bi-conical, outflow model

If, as it is often depicted, the dust is in a flattened distribution in a plane approximately perpendicular to the line of sight, the lag, τ , gives the distance, $c\tau$, of the emitting region from the central source. Therefore, if the IR lags are similar, as seems here usually to be the case, dust of different temperatures would be at approximately the same radii. An alternative possibility, that does not require dust of different temperatures to be at similar radii, is that the hot dust is the inner surface of a hollow conical outflow. As it is shown in Fig. 2, the part of the cone on the nearside of the AGN has its surface approximately tangential to the iso-delay surfaces for response to variations of the continuum when viewed from near face-on (as is usually the case for type-1 AGNs). The cone on the far side gives a much more spread out response and, since the

Table 1: Infrared lags in different bands, previously published and measured in this work.

Object	Time delay, days (1 from 2)	Bands 1(2)	Time Interval	References to results	References to data (for new results)
NGC4151	18 ± 6	K(U)	1969-1980	Oknyanskij (1993)	
	24 ± 6	L(U)		Oknyanskij & Horne(2001)	
	35 ± 8	K(U)	1985-1998	Oknyanskij et al. (1999)	
	8 ± 4	H(U)			
	97 ± 10	L(U)			
	104 ± 10	K(U)	1998-2003	Oknyanskij et al (2006)	
	94 ± 10	H(U)			
	105 ± 10	L(U)			
	41 ± 5	KH(U)	2003-2006	Oknyanskij et al. (2008)	
	105 ± 5	L(U)			
	94 ± 10	L(J)			
	37 ± 5	K(U)	2003-2007		
	40 ± 6	JHKL(B)	2008-2013	Oknyansky et al. (2014a,b)	
NGC 6418	37 ± 2	3.6 μ m(B)	2011-2013	Vazquez et al.(2015)	
	47 ± 3	4.5 μ m(B)			
	40 ± 5	3.6 μ m(B)		This work	Vazquez et al.(2015)
NGC 7469	50 ± 5	4.5 μ m(B)			
	52 ± 15	K(U)	1984-1996	Oknyanskij & Horne(2001)	Glass(1998), Luty(1995)
	60 ± 10	L(U)			
	50 ± 10	H(U)		This work	
	88	K(V)	2001	Suganuma et al.(2006)	
	54	K(V)	2002		
	87	K(V)	2001-2002		
	70 ± 5	H(V)	2001	This work	Suganuma et al.(2006)
	88 ± 5	H(V)	2002		
	53 ± 5	K(V)			
NGC 5548	48 ± 5	H(V)			
	47	K(V)	2001-2003	Suganuma et al.(2006)	
	48	K(V)	2001		Suganuma et al.(2006)
	48 ± 4	K(V)	2001-2003	This work	
	37 ± 6	H(V)			
	55 ± 4	K(V)	2001		
NGC 3783	52 ± 4	H(V)			
	41 ± 8	J(B)	2006-2009	Lira et al. (2011)	
	66 ± 6	H(B)			
	76 ± 14	K(B)			
	74 ± 5	J(B)		This work	Lira et al. (2011)
	75 ± 8	H(B)			
F9	86 ± 8	K(B)			
	-20 ± 100	J(UV)	1982-1998	Clavel et al.(1989)	
	385 ± 100	K(UV)			
	250 ± 100	H(UV)			
GQ Comae	410 ± 110	L(UV)			
	250	K(UV)	1980-1989	Sitko et al. (1993)	
	700	L(UV)			
	260 ± 20	K(UV),K(V)		Oknyanskij (1999)	Sitko et al. (1993)
WPVS48	70 ± 20	L(V)			
	66 ± 4	J(B)	2013	Pozo Nuñez et al. (2014)	
	74 ± 5	K(B)			
PGC 50427	68 ± 4	K(B)		This work	Pozo Nuñez et al. (2014)
	48 ± 2	J(B)	2013	Pozo Nuñez et al. (2015)	
M 509	47 ± 2	K(B)			
	100	K(U)	1985-2001	Glass (2004)	
	60	L(U)			
	104 ± 20	J(B)		This work	Glass (2004)
MCG-6-30-15	139 ± 20	HK(B)			Chuvaev et al.(1997)
	153 ± 20	L(B)			
	11 ± 4	J(B)	2006-2011	Lira et al.(2015)	
	17 ± 4	H(B)			
Ark 120	19 ± 4	K(B)			
	315	U(L)	1986-2001	Glass (2004)	
	95 ± 30	JHKL(B)		This work	Glass (2004) Doroshenko & Lyuty(1999)

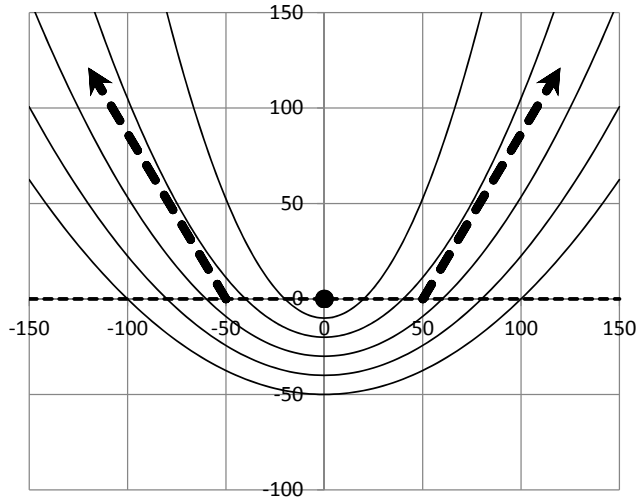


Figure 2: Cross section (in light days) of the inner wall of the near side of a hollow, bi-conical outflow (thick dashed arrows). Iso-delay paraboloids are shown at 20 day intervals. The horizontal dashed line shows the location of the optically-thick mid plane which obscures our view of the other side of the bi-cone (not shown).

material in the equatorial plane (what will be come the accretion disc) is optically thick, the response of the far side of the cone is probably not seen. We show the inner wall of the near side of the hollow bi-cone in Fig.3.

IR and optical light curves of an object are connected through a response function $\Psi(\tau)$ that depends on geometry and physical properties of the emitting medium:

$$F_{IR}(t) \sim const + \int_{-\infty}^{\infty} \Psi(\tau) F_{opt}(\tau - t) d\tau \quad (1)$$

$\Psi(\tau)$ can be explained as a response of the medium to a central source's UV impulse in the form of the δ -function. We assume that the optical and UV variability occurs almost simultaneously. We can obtain $\Psi(\tau)$ from a model or we can try to estimate it from the real data using some methods for solving ill-posed inverse problems (see the next paragraph). Then we can investigate the structure and physical properties of the emitting medium through comparison of response functions, obtained from observational data, with ones, predicted by different models.

We have calculated $\Psi(\tau)$ directly for our model *via* Monte-Carlo simulations with 10000 dust cloudlets distributed randomly within the hollow bi-conical space given by parameters H , R_{min} , R_{max} , β , α , $\Delta\alpha$ (see Fig. 3). We also take into account the dependence of the UV flux on distance to the central source S and the anisotropy of the UV radiation. To get the $\Psi(\tau)$, we consider a short δ -function UV pulse at $t = 0$ and treat each cloud as a point-like object which

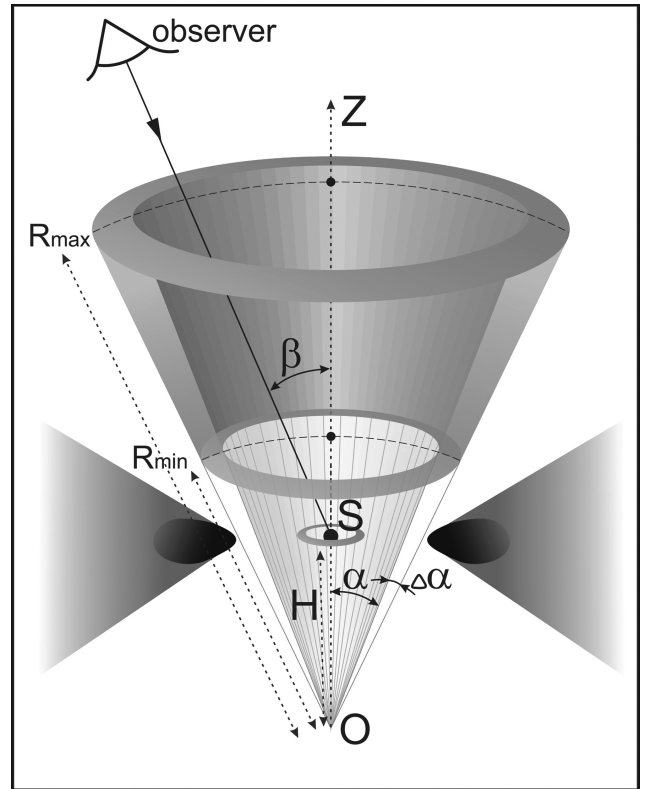


Figure 3: Geometry of the near side of the proposed hollow bi-conical dust distribution.

re-radiates in the IR only when it receives the UV pulse at a time lag τ . The lag is simply due to light travel effects. We obtain two response functions for two different regions: one close and one further away from S (see Fig. 4).

4. Reconstruction of response functions from real data

Unfortunately, we cannot obtain $\Psi(\tau)$ directly from (1), because the observational data are unevenly spaced and have long gaps. So we propose a new approach for recovery of the response function that combines the cross-correlation analysis of observational unevenly spaced time series and Tikhonov regularization.

As can be easily shown, the cross-correlation function $CCF_{F_{IR}F_{opt}}$ is a convolution of the auto-correlation function $ACF_{F_{opt}}$ with $\Psi(\tau)$:

$$CCF_{F_{IR}F_{opt}} \sim \int_{-\infty}^{\infty} \Psi(\tau) ACF_{F_{opt}}(\tau - t) d\tau \quad (2)$$

There are several methods of cross-correlation analysis which allow obtaining cross-correlation function for unevenly spaced time series. We use the MCCF method (see details and references at Oknyansky et al. 1999, 2014a). The advantage of the MCCF method is that it imposes a limit on the interpolation which is

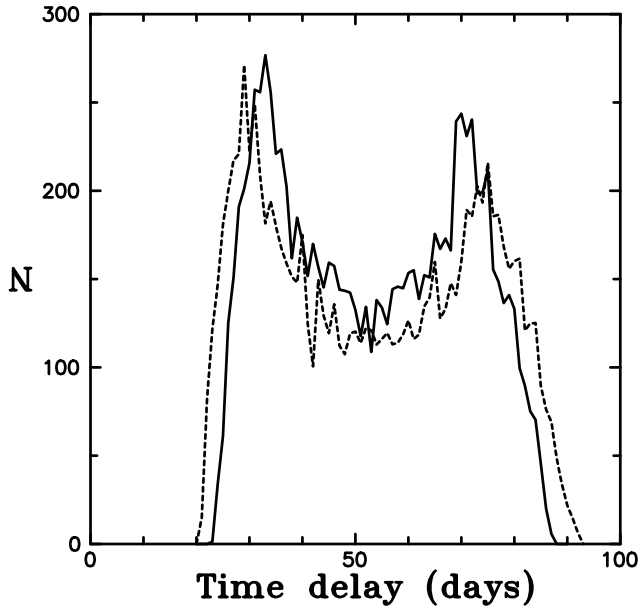


Figure 4: Monte Carlo simulations (using 10,000 clouds) of response functions for thin conical shells. $H = 90$ ld, $\beta = 20^\circ$, $\alpha = 30^\circ$, $\Delta\alpha = 5^\circ$, $F_{UV} \sim 1/R^2$, axial anisotropy of the UV radiation is given by $F_{UV} \sim [\cos(\gamma)(1 + 2\cos(\gamma)/3)]^{1/2}$ (Netzer 2015). Solid line: $R_{min} = 120$ ld, $R_{max} = 140$ ld; dashed line: $R_{min} = 140$ ld, $R_{max} = 160$ ld. N is the number of clouds responding per day.

necessary for unevenly spaced data. For our purposes we used only the central part of the MCCF peak with the length 80 days (± 40 days from the peak delay).

The eq. (2) is a Fredholm integral equation of the first kind with the convolution kernel. This is an ill-posed problem. Such problems can be solved using the Tikhonov regularization approach (Tikhonov et al. 1995) that allows one to find approximate solution, taking into account *a priori* information about the function sought, e.g., the smoothness of the solution or its closeness to some model (Koptelova et al. 2005).

Assuming that $\Psi(\tau)$ is a square integrable function, we compose the Tikhonov smoothing function:

$$M^\alpha[\Psi] = \|CCF_{F_{IR}F_{opt}} - ACF_{F_{opt}} * \Psi\|_{L_2}^2 + \alpha\|\Psi\|_{L_2}^2 \quad (3)$$

Provided that the regularization parameter α is chosen according to the discrepancy principle, the solution Ψ^α of the minimization problem for $M^\alpha[\Psi]$ can be considered as an approximate solution of (2).

Results of the reconstruction of the response function for the Seyfert galaxy NGC 7469 with the suggested approach based on observational K and V light curves in 2002 (Suganuma et al. 2006) are presented in Fig. 5. The reconstructed response function has two peaks. Two peaks are also observed in the theoretical response function in Fig. 4. Perhaps this is a characteristic feature of our proposed model.

It will be of interest to investigate this in other objects.

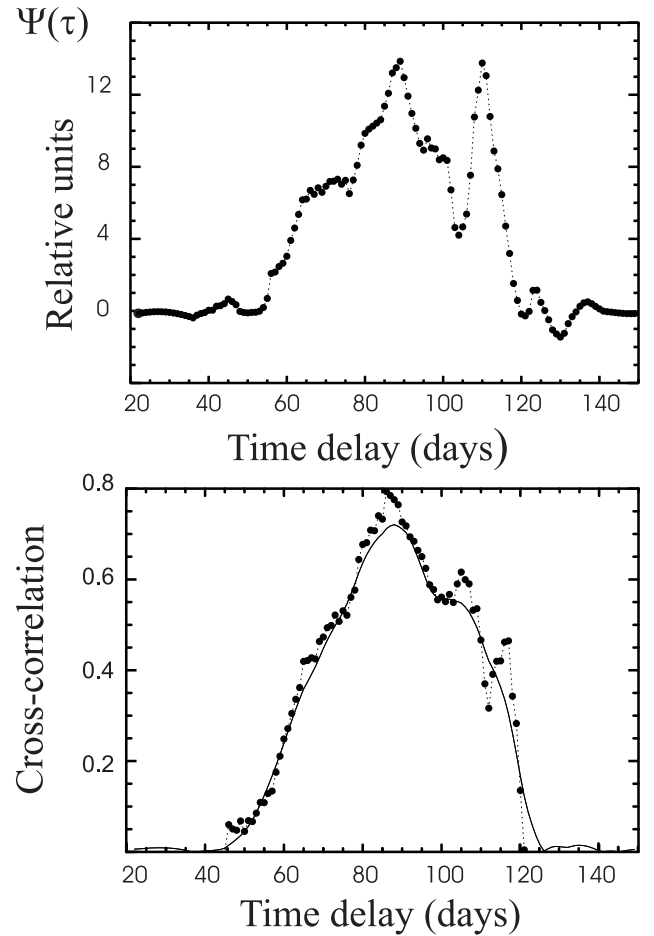


Figure 5: Upper: the reconstructed response function $\Psi(\tau)$ for the Seyfert galaxy NGC 7469. Lower: $CCF_{F_K F_V}(t)$, calculated from K and V band lightcurves (dotted line), and $ACF_{F_V} * \Psi$ for the reconstructed response function (solid line).

5. Cosmological applications

The ability to measure cosmological constants using the time delays of the near-infrared variability relative to the optical one was first mentioned by Kobayashi et al. (1998) and independently by Oknyanskij (1999, 2002). At the same time it was first shown (Oknyanskij 1999, 2002; Oknyanskij & Horne 2001) that for a number of AGNs the time delay of variability (in the K band) depends on the UV luminosity as $\tau \propto L_{UV}^{1/2}$ in accordance with the theoretical result of Barvainis (1987, 1992). In the recent publications Yoshii et al. (2014) and Hönic (2014) considered in detail the possibility of estimating cosmological parameters on the basis of measuring the dust sublimation radii in AGNs. Of particular interest is the ability to measure distances to objects with large redshifts, z .

For large z it is necessary to take into account the possible dependence of the delays on wavelength in the IR range and to make any appropriate correction. The equation for such a correction was derived by Oknyansky & Horne (2001) on the basis of the theory (Barvainis 1987) and observational data available at that time. However, as we have found now, the IR delays do *not* depend significantly on wavelength for most AGNs. The significant difference in IR lags with wavelengths can be just a temporary, rare situation in particular objects, as happened in the case of NGC 4151 just when it was in its very high state. Therefore for most of cases for a wide range of z the IR lags can be easily corrected to the rest frame just by allowing for the time dilation (i.e., dividing by $(1+z)$).

6. Conclusions

We find that most AGNs show at best only a small increase of lags in the J , H , K , and L bands. Just one object, GQ Comae (which is a high-luminosity AGN), probably has big differences in the IR lags (lag for L is about 3 times bigger than for K). A similar difference in IR lags was observed temporarily in NGC 4151 when it was in a very high state. Probably this big difference in IR lags is at epochs when the dust is intensively sublimated. During more normal times when the dust region is located much farther out than the sublimation distance, the time lags are about the same.

Our model with hollow bi-conical outflow of the dust clouds does not contradict to the existence of the dust torus. Moreover, the torus and accretion disc in the model are needed to block the IR light from farther part of the conical outflow. Also the torus can be a reservoir for the dust in the outflow.

In the Table 1, a significant number of the objects (5 out of 11) with similar IR lags have been observed to change their Seyfert type. This could just be the result of these objects having been studied particularly well. At the same time our model can explain cases of changing Seyfert type. In the very low luminosity states of some objects, when they look like Seyfert 2s, dust creation can commence in the gas clouds in the hollow of the conical outflow. So the thickness of the conical shell with dust clouds will be bigger and some of the dust clouds can be on the line of sight and block the broad line region from view and the object will be classified as a type 2 (see the same idea for the torus model in Mason 2015).

Our model can explain not only the similar IR lags at different wavelengths but also the high correlation values for IR and optical variations. Furthermore, the model can better explain the observed luminosity in IR since the IR-emitting region (i.e., the dust cone) has a higher covering factor and hence is getting more UV radiation than in the case of the flat compact IR-

emitting region.

Finally, we note that the relative wavelength independence of time lags in the IR simplifies the use of these time delays to estimate luminosities and hence estimate cosmological parameters.

Acknowledgements. We are thankful to Sebastian Hönig for useful comments, to Boris Artamonov for fruitful discussions, and to graphic designer Natalia Sinugina for producing Figure 3. This work has been supported by the Russian Foundation for Basic Research through grant no. 14-02-01274.

References

- Barvainis R.: 1987, *Ap.J.*, **320**, 537.
 Barvainis R.: 1992, *Ap.J.*, **400**, 502.
 Clavel J. et al.: 1989, *Ap.J.*, **337**, 236.
 Chuvaev K.K. et al.: 1997, *Astron. Lett.*, **23**, 355.
 Doroshenko V.G., Lyuty V.M.: 1999, *Astron. Lett.*, **25**, 771.
 Glass I.: 1998, *MNRAS*, **297**, 18.
 Glass I.: 2004, *MNRAS*, **350**, 1049.
 Hönig S.F., Kishimoto M.: 2011, *A&A*, **524**, A121.
 Hönig S.F. et al.: 2013, *Ap.J.*, **771**, 87.
 Hönig S.F.: 2014, *Ap.J. Lett.*, **774**, L4.
 Kobayashi Y. et al.: 1998, *Proc. SPIE*, **3352**, 120.
 Koptelova E. et al.: 2005, *MNRAS*, **356**, 323.
 Lira P. et al.: 2011, *MNRAS*, **415**, 1290.
 Lira P. et al.: 2015, *MNRAS*, **454**, 368.
 Lyuty V.M. et al.: 1995, *Astron. Lett.*, **21**, 581.
 Mason R.E.: 2015, *P&SS*, **116**, 97.
 Netzer H.: 2015, *ARA&A*, **53**, 365.
 Oknyanskij V.L.: 1993 *Astron. Lett.*, **19**, 416.
 Oknyanskij V.L.: 1999, *Odessa Astron. Publ.*, **12**, 99.
 Oknyanskij V.L. et al.: 1999, *Astron. Lett.*, **25**, 483.
 Oknyanskij V.L., Horne K.: 2001, *ASP Conf. Proc.*, **224**, 149.
 Oknyanskij V.L. et al.: 2006, *ASP Conf. Ser.*, **360**, 75.
 Oknyanskij V.L. et al.: 2008, *Odessa Astron. Publ.*, **21**, 79.
 Oknyanskij V.L.: 2002, *ASP Conf. Proc.*, **282**, 330.
 Oknyanskij V.L. et al.: 2013, *Odessa Astron. Publ.*, **26**, 212.
 Oknyansky V.L. et al.: 2014a, *Astron. Lett.*, **40**, 527.
 Oknyansky V.L. et al.: 2014b, *Odessa Astron. Publ.*, **27**, 47.
 Pozo Nuñez et al.: 2014, *A&Ap*, **561**, L8.
 Pozo Nuñez et al.: 2015, *A&Ap*, **576**, 73.
 Sitko M.L. et al.: 1993, *Ap.J.*, **409**, 139.
 Suganuma M. et al.: 2006, *Ap.J.*, **639**, 46.
 Tikhonov A.N., Goncharsky A.V., Stepanov V.V., Yagola A.G.: 1995, *Numerical Methods for the Solution of Ill-Posed Problems*. Kluwer Academic Press, Dordrecht.
 Vazquez B. et al.: 2015, *Ap.J.*, **801**, 127.
 Yoshii Y. et al.: 2014, *Ap.J. Lett.*, **784**, L11.

REVISION OF THE PHENOMENOLOGICAL CHARACTERISTICS OF THE ALGOL-TYPE STARS USING THE NAV ALGORITHM

M.G.Tkachenko¹, I.L.Andronov¹, L.L.Chinarova²

¹Department “High and Applied Mathematics”, Odessa National Maritime University, Mechnikova st., 34, 65029, Odessa, Ukraine, *masha.vodn@yandex.ua*, *tt_ari@ukr.net*

²Astronomical Observatory, Odessa National University, Shevchenko Park, 65014, Odessa, Ukraine, *lidia_chinarova@mail.ru*

ABSTRACT. Phenomenological characteristics of the sample of the Algol – type stars are revised using a recently developed NAV (“New Algol Variable”) algorithm (2012Ap.....55..536A, 2012arXiv 1212.6707A) and compared to that obtained using common methods of Trigonometric Polynomial Fit (TP) or local Algebraic Polynomial (A) fit of a fixed or (alternately) statistically optimal degree (1994OAP.....7...49A, 2003ASPC..292..391A).

The computer program NAV is introduced, which allows to determine the best fit with 7 “linear” and 5 “non-linear” parameters and their error estimates. The number of parameters is much smaller than for the TP fit (typically 20 – 40, depending on the width of the eclipse, and is much smaller (5 – 20) for the W UMa and β Lyrae – type stars. This causes more smooth approximation taking into account the reflection and ellipsoidal effects (TP2) and generally different shapes of the primary and secondary eclipses. An application of the method to two – color CCD photometry to the recently discovered eclipsing variable 2MASS J18024395 + 4003309 = VSX J180243.9 +400331 (2015JASS...32..101A) allowed to make estimates of the physical parameters of the binary system based on the phenomenological parameters of the light curve. The phenomenological parameters of the light curves were determined for the sample of newly discovered EA and EW – type stars (VSX J223429.3+552903, VSX J223421.4+553013, VSX J223416.2+553424, USNO-B1.0 1347-0483658, UCAC3-191-085589, VSX J180755.6+074711= UCAC3 196-166827). Despite we have used original observations published by the discoverers, the accuracy estimates of the period using the NAV method are typically better than the original ones.

Keywords: Stars: variable – stars: eclipsing

1. Introduction

Phenomenological modeling is an effective tools to study newly discovered or poorly studied eclipsing binary stars, for which there is no sufficient information on spec-

tra/temperatures and mass ratio. This additional information is needed for physical modeling using the algorithm of Wilson and Devinney (1971) also discussed by Wilson (1994). This method is implemented in some different programs, like BinaryMaker (Bradstreet, 2005), PHOEBE (Prsa A. et al., 2011), series of programs written in the Fortran language (Zola et al. 1997, 2010).

The physical modeling of close binary stars is discussed in detail by Kopal (1957), Tsessevich (1971), Kallrath and Milone (2009).

The phenomenological modeling of variable stars has a long history starting from hand-drawing of the light curve and further algebraic polynomial fits of the parts of the light curve or trigonometric polynomial (TP) fits.

The statistically optimal degree of the polynomial (or other more complicated model) may be determined using at least three criteria and their modifications (see Andronov 1994, 2003 for reviews).

2. Approximations of Minima

The “local” approximations of the extrema including polynomials, splines, asymptotic parabolae, asymmetric hyperbolae, running parabolae and sines were discussed by Andronov (2005). The Gaussian shape was an usual approximation for spectral lines in the era preceding synthetic spectra, and, besides measuring Doppler shifts, was used also for minima determination of eclipsing variables and, in a modified form, by Mikulášek et al. (2012). However, the Gaussian function has no abrupt switch from zero to the zero profile, thus it is not possible to determine from the fit the value of the eclipse duration – one of the main parameters needed for the General Catalogue of Variable Stars (Samus’ et al., 2015).

Andronov (2012ab) compared few limited – width approximations and proposed the following approximation:

$$x_C = C_1 + C_2 \cos(2\pi\phi) + C_3 \sin(2\pi\phi) + C_4 \cos(4\pi\phi) + C_5 \sin(4\pi\phi) + C_6 H(\phi / C_8, C_9) + C_7 H((\phi - 0.5) / C_8, C_{10}) \quad (1)$$

Here the shape of the eclipse is described as

$$H(z, \alpha) = \begin{cases} (1 - |z|^\alpha)^{3/2}, & \text{if } |z| \leq 1 \\ 0, & \text{if } |z| > 1 \end{cases} \quad (2)$$

The usual determination of phase is $\phi = \zeta - \text{int}(\zeta - \zeta_0)$, where $\zeta = (t - T_{00})/P_0$, T_{00} is the initial epoch, P_0 is period, and ζ_0 is the minimal limit of the interval ($\zeta_0 \leq \phi < \zeta_0 + 1$) of possible values of ϕ . Classical approach is the interval of phases $[0, 1)$, i.e. $\zeta_0 = 0$, with an additional notification that one may extend the main interval by adding any integer number E to the phase, as the light curve is suggested to be periodic: $m(\phi + E) = m(\phi)$. This obvious extension may be realized at computer programs either by doubling the data with a shift of $E = 1$, or by using suitable values of ζ_0 for different parts of the light curve. As typically the initial epoch and period are defined so that the primary minimum corresponds to $\phi = 0$ (or close to 0) and the secondary minimum – to $\phi = 0.5$. Thus for Eq. (1) it is suitable to choose $\zeta_0 = -0.25$.

In previous papers, we have used the values T_{00} and P_0 , which were determined by other methods (e.g. trigonometric polynomial). Andronov et al. (2015b) improved the method NAV to make possible differential corrections

$$\phi = \zeta - \text{int}(\zeta - \zeta_0) + C_{11} + C_{12} \cdot (t - T_1), \quad (3)$$

where T_1 is some moment of time, which is recommended to be close to the mean time \bar{t} for partial orthogonalization of basic functions (Andronov, 1994, 2003). The corrected values of the light elements are (Andronov et al. 2015b):

$$T_{01} = \frac{T_{00} + C_{11}P_0 - C_{12}P_0T_1}{1 - C_{12}P_0} \quad (4)$$

$$P_1 = \frac{P_0}{1 - C_{12}P_0} \quad (5)$$

We also use additional parameters (the relative depths of the primary and secondary minima, respectively) $d_1 = 1 - 10^{-0.4C_6}$, $d_2 = 1 - 10^{-0.4C_7}$ and their combinations $Y = d_1 + d_2$ and $\xi = d_1 / d_2 = F_1 / F_2$. Here F_1 and F_2 are relative values of the mean brightness of the eclipsed part of star. The value of Y varies from 0 (no eclipses) to 1 (both full eclipses).

Assuming a simplified model of uniform brightness distribution and spherical symmetry of components (Tsessevich 1971, Shulberg 1971, Andronov 1991, Malkov et al. 2007, Andronov and Tkachenko 2013), one may estimate physical parameters.

As generally the primary minimum is defined to be more deep than the secondary one (however, it may be not

the case, if the minima are of the same depth within error estimates), it corresponds to the case, when the star with larger surface brightness (and so temperature) is eclipsed by a cooler component.

Papageorgiou et al. (2014) proposed the simplest parabolic approximation of the light curve in four fixed phase intervals, which has the simplest program realization. The number of parameters (12) is the same as in our NAV approximation, but the NAV approximations are continuous, allow to determine the width and corrections to the initial epoch and period. However, the NAV approximation needs more computational time.

Mikulášek (2015) proposed another special shape for the eclipse as

$$F_e = A \left(1 + C \frac{\phi^2}{D^2} + K \frac{\phi^4}{D^4} \right) \left\{ 1 - \left[1 - \exp \left[1 - \cosh \left(\frac{\phi}{D} \right) \right] \right]^r \right\} \quad (6)$$

from which some are similar to that we used in the NAV approximation, i.e. the characteristic width D is proportional to the eclipse half-width C_8 , $A = C_6$ (for a primary minimum) or $A = C_7$ (for a secondary minimum), and, for small phases $\phi \rightarrow 0$, $\alpha \rightarrow 2r$ for “sharp” eclipses $r \leq 1$ and else $\alpha \rightarrow 2$. Two additional parameters C , K should generally produce closer coincidence of the approximation to the observations, but also larger statistical errors of the parameters. Obviously, the number of parameters may also be increased in the NAV algorithm, as was discussed by Andronov (2012ab), but currently we try to make studies using small modifications of the initial algorithm.

3. Application to Concrete Stars

For the analysis, we have used photometric observations of 6 newly discovered eclipsing binary stars of different types, which were published in the “Open European Journal on Variable Stars” (OEJV).

The phase light curves and their best fit approximations (including non-linear optimization for the parameters $C_8 \dots C_{12}$) are shown in Fig. 1 – Fig. 6. For the preparation of figures, the program MCV (Andronov and Baklanov 2004) was used. The parameters are listed in Table 1.

The analysis shows that the corrections of the period related to the parameter C_{12} range typically from 1σ to 7σ , so sometimes are statistically significant. The error estimates for the period using our method are typically better than the original ones, for two stars from 6 by a factor of 10–12. Similar situation is present for the initial epochs. We conclude that the current improvement of the method by adding parameters C_{11} and C_{12} is efficient for the determination of the initial epoch and the photometric period.

Among the coefficients $C_2 \dots C_5$ for this sample of stars, the largest value for a given star is typically of C_4 , which corresponds to a “double frequency wave” due to the ellipticity effect.

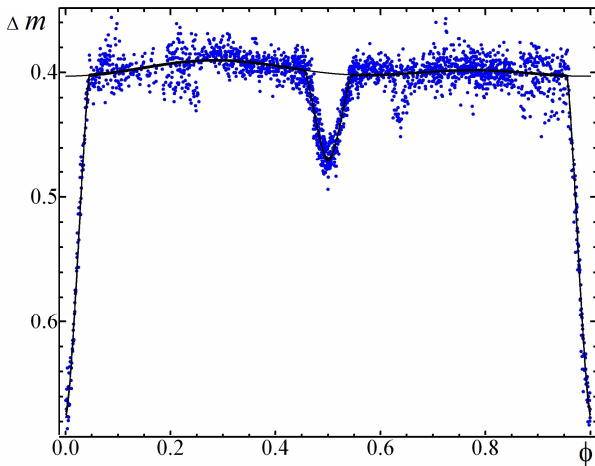


Figure 1: The phase light curve for the star VSXJ223421.4+553013. The observations are shown as blue dots, the black lines show the NAV approximation and $\pm 1\sigma$ error corridors.

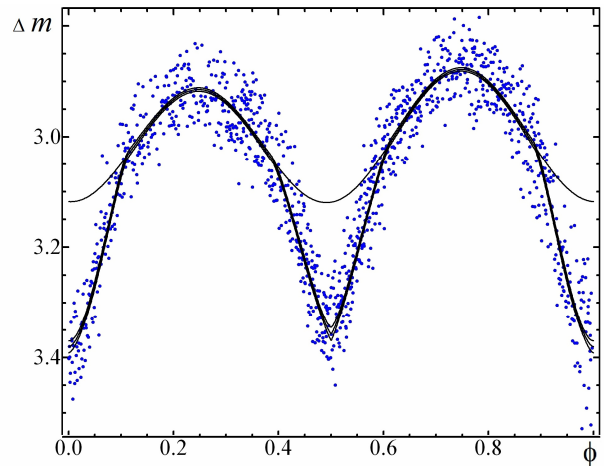


Figure 4: The phase light curve for the star USNO-B1.0 1347-0483658. The observations are shown as blue dots, the black lines show the NAV approximation and $\pm 1\sigma$ error corridors.

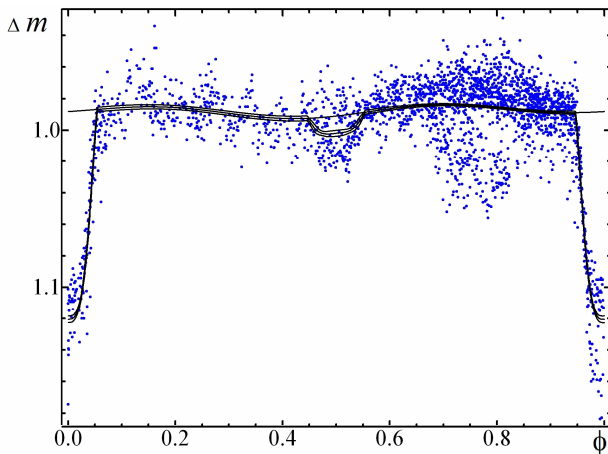


Figure 2: The phase light curve for the star VSXJ223416.2+553424. The observations are shown as blue dots, the black lines show the NAV approximation and $\pm 1\sigma$ error corridors.

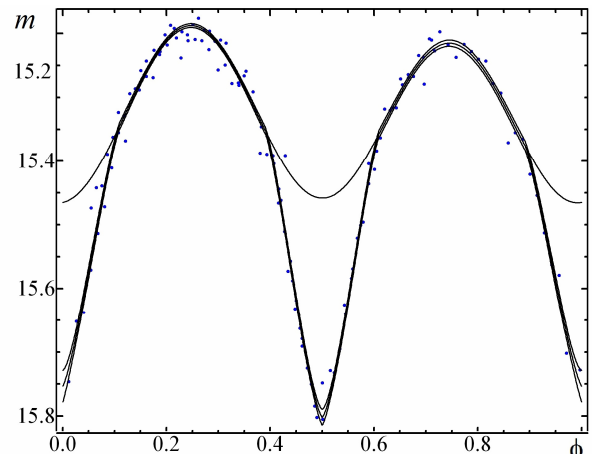


Figure 5: The phase light curve for the star UCAC3 191-085589. The observations are shown as blue dots, the black lines show the NAV approximation and $\pm 1\sigma$ error corridors.

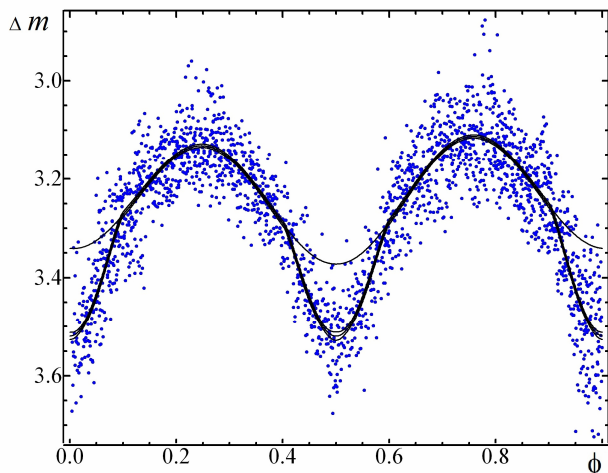


Figure 3: The phase light curve for the star VSXJ223429.3+552903. The observations are shown as blue dots, the black lines show the NAV approximation and $\pm 1\sigma$ error corridors.

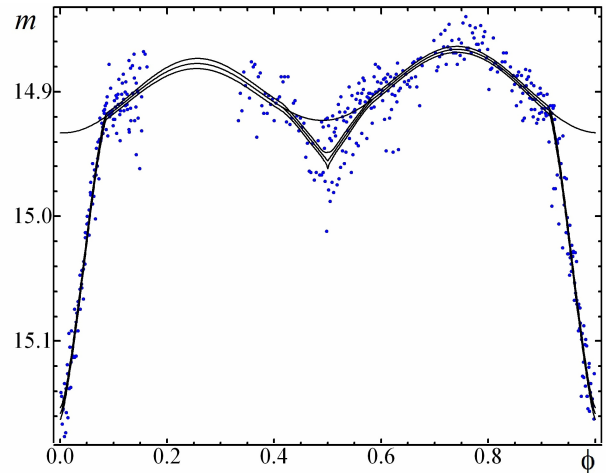


Figure 6: The phase light curve for the star UCAC3 196-166827=VSX J180755.6+074711. The observations are shown as blue dots, the black lines show the NAV approximation and $\pm 1\sigma$ error corridors.

Table 1. Characteristics of the NAV approximations

	VSX J223421.4+553013 (Lehký 2009a, OEJV 99, #3)	VSX J223416.2+553424 (Lehký 2009a, , OEJV 99, #2)	VSX J223429.3+552903 (Lehký 2009a, OEJV 99, #1)
C_1	0.3980±0.0003	0.9876±0.0006	3.2393± 0.0027
C_2	0.0013±0.0004	-0.0014±0.0009	-0.0159±0.0032
C_3	-0.0038±0.0004	0.0014±0.0007	0.0092±0.0020
C_4	0.0036±0.0004	0.0019±0.0007	0.1170±0.042
C_5	0.0015±0.0004	-0.0024±0.0007	0.0040±0.0038
C_6	0.2714±0.0026	0.1325±0.0025	0.1786±0.0103
C_7	0.0695±0.0015	0.0109±0.0023	0.1475±0.0109
C_8	0.0456±0.0004	0.0546±0.0008	0.0985±0.0042
C_9	1.56±0.04	3.19±0.19	1.93±0.24
C_{10}	1.69±0.08	3.97±2.33	1.96±0.30
C_{11}	-0.0002±0.0001	0.0010±0.0003	-0.0067±0.0014
C_{12}	$(-1.89±0.93) \cdot 10^{-6}$	$(4.08±1.93) \cdot 10^{-6}$	$(-3.35±0.50) \cdot 10^{-5}$
T_{00}	54373.28108±0.00035	54387.58563±0.00040	54387.35274±0.00040
P_0	1.324325±0.000150	1.105815±0.000009	0.387245±0.000009
T_{01}	54442.14572±0.00017	54466.09957±0.00035	54462.47568±0.00056
P_1	1.3243217±0.0000012	1.1058209±0.0000021	0.3872400±0.0000020
d_1	0.2212±0.0018	0.1148±0.0020	0.1517±0.0080
d_2	0.0620±0.0013	0.0100±0.0021	0.1270±0.0087
Y	0.2832±0.0024	0.1248±0.0030	0.2787±0.0140
γ	3.5662±0.0759	11.4929±2.4366	1.1941±0.08260
Min I	0.674 ±0.002	1.121±0.002	3.519 ±0.007
Max I	0.390 ±0.001	0.984±0.001	3.112 ±0.003
	USNO-B1.0 1347-0483658 (Lehký 2009b, OEJV 115, #1)	UCAC3 191-085589 (Moos et al. 2013, OEJV 156, #6)	VSX J180755.6+074711 (Franco et al. 2010, OEJV 135, #1)
C_1	3.0073±0.0033	15.3314±0.0035	14.8996±0.0012
C_2	-0.0005±0.0033	0.0034±0.0040	0.0050±0.0017
C_3	0.0180±0.0018	-0.0139±0.0025	0.0056±0.0018
C_4	0.1109±0.0047	0.1301±0.0051	0.0278±0.0026
C_5	-0.0035±0.0034	-0.0066±0.0038	-0.0006±0.0014
C_6	0.2627±0.0142	0.2882±0.0256	0.2250±0.0061
C_7	0.2383±0.0140	0.3432±0.0153	0.0324±0.0071
C_8	0.1124±0.0042	0.1095±0.0037	0.0866±0.0023
C_9	1.65±0.18	1.24±0.18	1.41±0.08
C_{10}	1.23±0.13	1.38±0.11	0.41±0.63
C_{11}	0.0012±0.0012	0.0022±0.0011	-0.0011±0.0007
C_{12}	$(3.64±3.94) \cdot 10^{-6}$	0.0048±0.0014	0.0004±0.0002
T_{00}	55068.50679± 0.00075	55948.67692±0.00405	55381.44874±0.00344
P_0	0.2576355± 0.0000009	0.27448±0.00107	0.861209±0.00013
T_{01}	54881.46373± 0.00030	55949.22649±0.00029	55387.47629±0.00058
P_1	0.2576357±0.0000010	0.27484 ±0.00038	0.86154±0.00014
d_1	0.2149±0.0103	0.2331±0.0181	0.1879±0.0055
d_2	0.1971±0.0104	0.2710±0.0103	0.0294±0.0064
Y	0.4120±0.0171	0.5041±0.0227	0.2165±0.0083
γ	1.0906±0.0613	0.8602±0.0674	6.3740±1.3713
Min I	3.380± 0.011	15.753±0.025	15.157±0,004
Max I	2.878± 0.003	15.187±0.003	14.866±0.002

The stars USNO-B1.0 1347-0483658 and UCAC3 191-085589 show unequal maxima (O'Connell (1951) effect). This effect is more pronounced in the coefficient C_3 than C_5 . This is in a good agreement with theoretical expectations (cf. Davidge and Milone, 1984).

In future, possibly it will have sense to exclude the term with C_5 from the mathematical model (1), if still being within the error estimates. This will be decided after analyzing a larger sample of stars.

The parameter α (Eq. (2)) (i.e. C_9 , C_{10} for the primary and secondary minimum, respectively) is typically seen in the range from 1 to 2. The outstandingly small value of $C_{10}=0.41\pm 0.63$ for VSX J180755.6+074711 also does not differ from this range within error estimates.

In our sample, the exception for both minima is present in VSX J223416.2+553424. The secondary eclipse is very shallow, but is still seen in the noisy observations,

Large values $\alpha \gg 2$ typically correspond to a total eclipse or a transit and a large difference in radii. For this case, Andronov (2012a) proposed a possible extension for the expression (2) assuming that the eclipse starts at some non-zero value z_0 , so

$$0 \leq z_0 \leq z \leq 1. \quad (7)$$

For the present noisy observations, such a complication due to using an additional parameter z_0 seems not to be effective. This object is also extreme in our sample due to a very large brightness ratio $\gamma=11.5\pm 2.5$ and thus large relative temperature difference. Multi-color are needed for a more detailed study similar to that described by Andronov et al. (2015a) for the object 2MASS J18024395 + 4003309 = VSX J180243.9 + 400331.

4. Conclusions

Parameters of the phenomenological modeling are determined for 6 newly discovered eclipsing binary stars of different types.

The initial algorithm (Andronov, 2012ab) was improved by adding two parameters allowing to make corrections to the initial epoch and period. The corresponding error estimates are typically significantly better than that obtained using other methods. This improvement of accuracy is more efficient for the EA – type stars, i.e. relatively short eclipses.

In our sample, there are 3 stars of the W UMa – type. They all show distinct eclipses, contrary to the GCVS statement that EB and EW – type objects are systems “having light curves for which it is impossible to specify the exact times of onset and end of eclipses” (Samus’ et al. 2015). We propose to correct this definition.

The presence of eclipses is to be justified by statistical significance of the parameters C_6 and C_7 (eclipse depth), otherwise should be classified as “elliptic” (ELL).

For a fixed declination i , one may expect an increase with relative radii of the components (and thus from EA to EW types) of the parameters C_8 (eclipse half-width), C_2 , C_4 (proximity effects), C_6 and C_7 (eclipse depth).

Acknowledgements. The authors are thankful to Professors S. Zoła and Z. Mikulášek for fruitful discussions over the years. This research is a part of the projects “Inter – Longitude Astronomy” (Andronov et al., 2010) and “Ukrainian Virtual Observatory” (Vavilova et al., 2012).

References

- Andronov I.L.: 1991, Structure and Evolution of Stars. *Odessa Inst. Adv. Teachers*, 84p.
- Andronov I.L.: 1994, *OAP*, **7**, 49.
- Andronov I.L.: 2003, *ASP Conf. Ser.*, **292**, 391.
- Andronov I.L.: 2005, *ASP Conf. Ser.*, **335**, 37.
- Andronov I.L.: 2012a, *Astrophys.*, **55**, 536,
- Andronov I.L.: 2012b, *Częstochowski Kalendarz Astronomiczny – 2013*, 133; 2012arXiv 1212.6707A.
- Andronov I.L. et al.: 2010, *OAP*, **23**, 8.
- Andronov I.L., Baklanov A.V.: 2004, *Astronomy School Reports*, **5**, 264.
- Andronov I.L., Tkachenko M.G.: 2013, *OAP*, **26**, 204.
- Andronov I.L. et al.: 2015a, *Journal of Astronomy and Space Science*, **32**, 127.
- Andronov I.L, Tkachenko M.G., Chinarova L.L.: 2015b, *Physics Journal* (accepted); 2015arXiv151000333A
- Bradstreet D.H.: 2005, *SASS*, **24**, 23.
- Davidge T.J., Milone E.F.: 1984, *ApJS*, **55**, 571
- Franco L., Marchini A., Papini R.: 2010, *OEJV*, **135**, 1.
- Kallrath J., Milone E.F.: 2009, *Eclipsing Binary Stars: Modeling and Analysis*, Springer-Verlag New York, 444p.; 2009ebs..book.....K
- Kopal Z. (1959). Close Binary Systems. *Chapman & Hall, London*, 558p.
- Lehký M.: 2009a, *OEJV*, **99**, 1.
- Lehký M.: 2009b, *OEJV*, **115**, 1.
- Malkov Y. et al.: 2007, *A&A*, **465**, 549.
- Mikulášek, Zdeněk; Zejda, Miloslav; Janík, Jan: 2012, *Proc. IAU Symp.*, **282**, 391; 2012IAUS..282..391M
- Mikulášek Z.: 2015, *A&A* **584A**, 8; 2015A&A...584A...8M.
- Moos C., Hamsch F.-J., Krajci T.: 2013, *OEJV*, **156**, 1.
- O'Connell D.J.K., 1951: *PRCO*, **2**, 85-100
- Papageorgiou A., Klefogiannis G., Christopoulou P.-E.: 2014, *Contrib. Astron. Obs. Skalnaté Pleso*, **43**, 470.
- Prsa A. et al.: 2011. PHOEBE: Physics Of Eclipsing Binaries. *Astrophysics Source Code Library*, (record ascl: 1106.002; 2011ascl.soft06002P).
- Samus N.N. et al.: 2015, *General Catalogue of Variable Stars, CDS/ADC Collection of Electronic Catalogues*, 1, 2025, code 2009yCat....1.2025S, electronically available at <http://www.sai.msu.su/gcvs/gcvs/>
- Shul'berg A.M.: 1971. *Close Binary Systems with Spherical Components*, Moscow, Nauka, 246
- Tsessevich V.P. (ed.): 1971, *Eclipsing Variable Stars*. Moscow: Nauka, 350p.; 1971isme.conf.....T
- Vavilova I.B. et al.: 2012, *KPCB*, **28**, 85.
- Wilson R.E. 1994, *PASP*, **106**, 921-941.
- Wilson R.E., Devlinney E.J.: 1971, *ApJ*, **166**, 605-619.
- Zoła S. et al.: 1997, *A&A*, **324**, 1010.
- Zoła S. et al.: 2010, *MNRAS*, **408**, 464.

PHOTOMETRY AND MODULATION OF LIGHT CURVES IN THE BLAZHKO STAR V365 HER

S.N. Udovichenko

Astronomical Observatory of I.I.Mechnikov Odessa National University
T.G.Shevchenko Park, Odessa 65014, Ukraine, *udovich222@ukr.net*

ABSTRACT. The photometric CCD observations for the Blazhko RR Lyr type star V365 Her in Astronomical stations near Odessa (Ukraine) have been carried out. The light curves in V system were obtained and the frequency Fourier analyse was performed. The strong Blazhko effect and modulation of the light curves were detected. From Fourier spectra 15 frequencies were identified.

Key words: Stars: oscillations – stars; variables: RR Lyr – stars: individual: V365 Her.

1. Introduction

The variability of the star was found by C.Hoffmeister in 1936. The star thoroughly was investigated by V.P.Tsessevich, which determined the primary elements of period: Max. hel. J.D. = $2436047.522 + 0.6130535 \cdot E$, and discovered the sophisticated shape of light variation curves, known as Blazhko effect (40.64 day) (Tsessevich, 1961, 1966). He mentioned, that the curve of maximum height shows considerable dispersion, and it seems, that the most part of time we observe the weakened maxima and only in some time intervals (short-term) we observe the maxima in the considerable heights. It indicates in modulation of a light curves by additional frequencies, and the star represents the scientific interest for observations. Visual observations in 20 century were carried out by Hoffmeister and Tsessevich. Now V365 Her is known as RR Lyr-star type (RRab) with amplitude $12.^m7 - 14.^m0$ (P), has period $0.^d613138$, Kholopov et al. (1985).

2. Observations

The photometric CCD observations of V365 Her in Astronomical stations near Odessa in observation season 2009-15 have been carried out. Two stars were chosen as comparison and check stars (comp=UCAC4-558-060233, check=UCAC4-558-060246). The 48 cm reflector AZT-3 with the f/4.5 Newtonian focus and CCD photometer with chip Sony ICX429ALL (600x800

pixels), equipped with V filter, Peltier cooler were used (Udovichenko, 2012). The hermetic housing and thermoelectric (Peltier) cooler provide a temperature difference between the crystal and the environment of about -40°C , and the temperature was supported by a constant. The exposure time for variable and comparison stars for the most part were chosen to except a saturation of frame and consist 90 sec. More then 5600 CCD frames were gathered during 55 nights. The reductions of the CCD frames were carried out using the MUNIPACK (Motl) software. The procedures for the aperture photometry are composed of the dark-level and flat-field corrections and determination of the instrumental magnitude and precision. The all set of observations are shown in fig.1. The errors on individual data points vary between 0.005 mag to 0.01 mag.

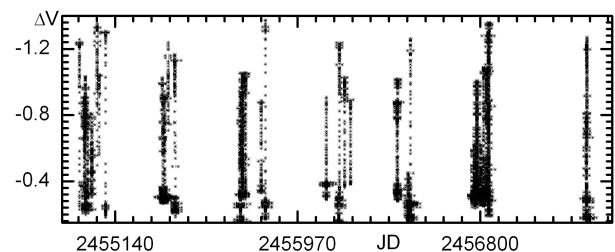


Figure 1: The all data set of observations V365 Her.

3. Frequency analysis

For all observations of V365 Her were determined the magnitudes comparatively of comparison star.

The frequency analyses were performed using a package of computer programs with single-frequency and multiple-frequency techniques by using utilize Fourier as well as multiple-least-squares algorithms (program Period04, Lenz and Breger, 2004). The pulsation period was determined with this package as the highest peak on the Fourier amplitude spectra. The all light curves V365 Her with pulsating period are shown on fig. 2. These phase curves were computed from elements:

$$MaxHJD = 2454978.403 + 0.613182 \cdot E.$$

Table 1: Identified Fourier amplitude and phases of the pulsation and modulation frequencies in light curves of V365 Her.

Identif.	Frequency	Amplitude	Phase	S/N
f0	1.630835	0.346	0.15	6.6
2f0	3.26168	0.127	0.86	26.7
3f0	4.89255	0.086	0.89	20.2
4f0	6.52330	0.061	0.22	13.1
5f0	8.15355	0.052	0.15	11.7
6f0	9.78498	0.021	0.43	6.1
7f0	11.41402	0.021	0.68	4.6
f0+fm	1.65552	0.085	0.33	17.2
f0-fm	1.60613	0.054	0.54	11.7
2f0-fm	3.22425	0.034	0.74	6.6
3f0+fm	4.91979	0.034	0.83	7.1
3f0-fm	4.85806	0.026	0.85	7.0
4f0+fm	6.5530	0.034	0.26	7.6
5f0+fm	8.1788	0.038	0.80	6.7
6f0-fm	9.74763	0.024	0.47	6.1

Table 2: Time of maxima V365 Her.

Time J.D.	Time J.D.	Time J.D.
2454978.406	2455718.538	2456425.517
2455000.510	2455720.377	2456785.478
2455002.334	2455734.480	2456815.517
2455005.391	2455804.382	2456828.398
2455059.338	2455823.383	2456836.361
2455067.319	2456159.387	2456839.427
2455097.367	2456183.311	2457283.362
2455355.527	2456210.284	
2455411.336	2456422.466	

The maximum of the light curves amplitude variation is 1.3 mag, minimum 0.8 mag, and strong Blazhko modulation of amplitude reach about 0.5 mag and phase modulations up to 0.05. The power spectra of basic frequency and after prewhitening is shown in Fig. 3.

After prewhitening of basic frequency the harmonics of basic frequency kf_0 and triplet of frequencies $kf_0 \pm f_m$, responsible for modulation of light curves was found. The Fourier amplitude and phases of the pulsation component identified in the spectra of the light curves of V365 Her are presented in Table 1. The basic frequency denoted as f_0 , the modulation frequency of Blazhko effect denote as f_m . We find triplet of frequencies $f_0 \pm f_B$, but, perhaps, there are more frequencies in the pulsation spectra of V365 Her. From obtained data the mean period of Blazhko effect amount $14^d.6$.

The time of maxima V365 Her presents in Table 2.

References

- Hoffmeister C.: 1936, *Astron. Nachrichten.*, **259**, 37.
 Lenz P., Breger M.: 2004, *Comm.in Asteroseismology*, **144**, 41.

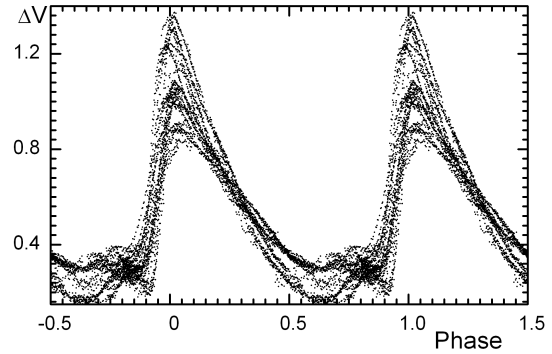


Figure 2: The light curves V365 Her with phase of basic period. The strong Blazhko modulation of amplitude reach about 0.5 mag and phase modulations up to 0.05.

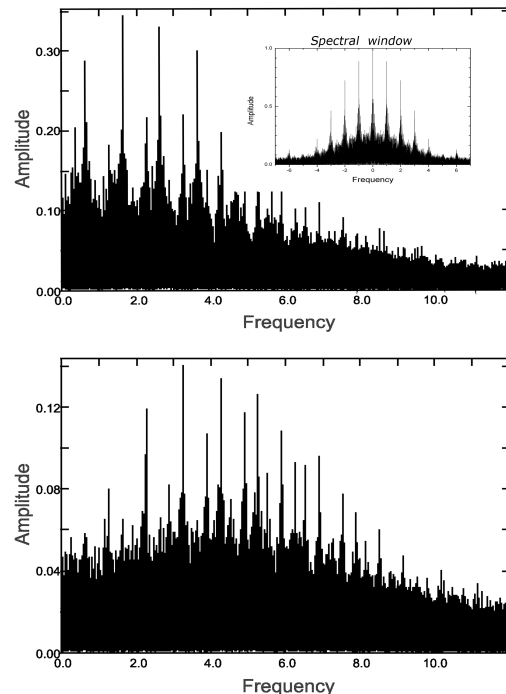


Figure 3: The Fourier amplitude spectrum of basic frequency and after prewhitening. The spectral window shows inside first picture.

Motl D.: <http://sourceforge.net/projects/c-munipack/files>.

Samus N.N., Durlevich O.V., Kazarovets E.V., Kireeva N.N., Pastukhova E.N., Zharova A.V. et al.: 2011, *General Catalogue of Variable Stars* (GCVS database, Version 2011Jan).

Tsessevich V.P.: 1980, *Sov. Astron.Jurn.*, **38**, 293.

Tsessevich V.P.: 1966, RR Lyrae-type variable stars, Naukova Dumka, Kiev.

Udovichenko S.N.: 2012, *Odessa Astron. Publ.*, **25**, 32.

Subsection Virtual observatories and intensive data

COMPARISON OF ZERO ZONE CATALOGUES OF THE FON PROGRAM BASED ON THE KYIV AND KITAB OBSERVATIONS

V.M.Andruk¹, H.Relke², Yu.I.Protsyuk³, M.M.Muminov⁴, Sh.A.Ehgamberdiev⁴,
Q.X.Yuldoshev⁴, V.V.Golovnia¹

¹ Main Astronomical Observatory of National Academy of Sciences,

27 Akad. Zabolotnogo St., 03680, Kyiv, Ukraine, *andruk@mao.kiev.ua*

² Walter Hohmann Observatory, Wallneyer St.159, 45133 Essen, Germany,

helena_relke@yahoo.com

³ Research Institute “Nikolaev Astronomical Observatory”,

1 Observatornaya St., 54030, Mykolaiv, Ukraine, *yuri@nao.nikolaev.ua*

⁴ Ulugh Beg Astronomical Institute of the Uzbek Academy of Sciences,

33 Astronomicheskaya St., 100052, Tashkent, Uzbekistan, *muminov_mm@mail.ru*

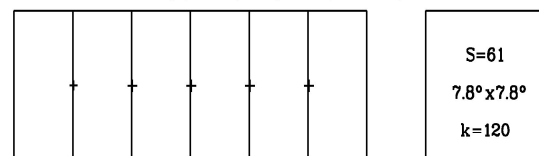
ABSTRACT. The two new catalogues for the zero zone of the FON project were created after the processing of two different collections of digitized photographic plates. The photographic plates were received at the DAZ and DWA telescopes of the Kitab observatory of the Republic of Uzbekistan (KO UAS) and of the Main astronomical observatory in Kyiv (MAO NASU) in the number of 90 and 120 plates, respectively. The digitization of these photographic plates in the frame of the Ukrainian Virtual Observatory project was performed by means of the Epson Expression 10000XL scanner with the scanning resolution of 1200 dpi. The coordinates of stars and galaxies for the both catalogues are determined in the system of the Tycho2 catalogue. The stellar magnitudes of all objects are done in B-magnitudes of the photoelectric standard system. The difference between the calculated and the reference positions is equal $\sigma_{\alpha\delta} = \pm 0.06-0.07''$. The internal accuracy of the both catalogues for all objects is $\sigma_{\alpha\delta} = \pm 0.20''$, $\sigma_B = \pm 0.18^m$ and $\sigma_{\alpha\delta} = \pm 0.27''$, $\sigma_B = \pm 0.17^m$, respectively. We present the comparison of these both catalogues with each other and with the Tycho2, UCAC4 as well as PPMX catalogues and discuss the results.

Keywords: photometric – methods: data analysis – catalogs, virtual observatory tools – astrometry - techniques

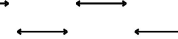
1. Introduction

On the basis of the processing of different sets of observational data of the FON project (Kislyuk et al., 2000, Yatsenko et al., 2011) for the zero zone were created two star catalogues of the positions and stellar magnitudes. This work was done by the using of the resources of the Ukrainian Virtual Observatory UkrVO (Vavilova et al., 2012, Vavilova et al., 2012). The sets of observational data consist of the photographic plates exposed with the Double Wide Angle Astrograph (DWA, 40/200, 103"/cm, Golosevo, h=186m) and the Zeiss Double Astrograph (DAZ, 40/300, 76"/cm, Kitab, h=657m). The catalogues were created on the basis of photographic plates digitized

KIEV, MAO NASU, DWA(D/F=40/200), 103"/mm, 1px=2.17", 13000x13000



$\Delta\alpha = 16\text{min}$



KITAB, UBAl UAS, DAZ(D/F=40/300), 67"/mm, 1px=1.45", 13000x13000

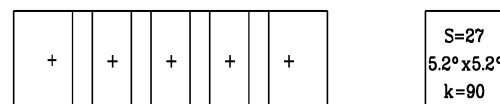


Figure 1: Scheme and the relative size of the overlapping zones for the MAO NASU and KO UAS.

by the using of the Epson Expression 10000XL scanner (Andruk et al., 2010, Golovnya et al., 2010, Protsyuk et al., 2014, Protsyuk et al., 2014, Protsyuk et al., 2014). The reduction procedure was done with the software that was previously used in the series of works (Andruk et al., 2014, Muminov et al., 2014, Yizhakevych et al., 2014, Protsyuk et al., 2014, Kazantseva et al., 2015) and is described in detail in the following publications (Muminov et al., 2015, Andruk et al., 2015, Andruk et al., 2016). The photographic plates were scanned with a spatial resolution of 1200 dpi, the size of each plate is 30 x 30 cm (13000 x 13000 pixels). The working areas (see Figure 1) are 7.8° x 7.8° (1 px = 2.17 ") and 5.2° x 5.2° (1 px = 1.45") for the DWA and DAZ telescopes respectively. The versions of both catalogues were obtained by the processing of single scans without the rotation of the plates on the 90°. This approach allows to save resources for the storing and processing information more than twice times without the loss of accuracy of the results. The software concept and the steps of the processing of digitized photographic plates

for the zero zone will be then applied for all photographic plates of the FON project exposed as in Kyiv (sky area from 0 to 90 degrees) and as well as in Kitab (sky area from 0 to -20 degrees) respectively.

2. The processing of the digitized photographic plates and creating of the catalogues

The processing of these two digitized sets of photographic plates exposed with the DWA (120 plates) and DAZ (90 plates) telescopes was performed on the base of the common method which was developed and has been applied in practice in the MAO NASU. The steps of the processing of the scanned photographic plates are:

1. Conversion of the tiff-format files to the fit-format files using the GIMP package.
2. The processing of the scans using the MIDAS/ROMAFOT package to obtain the rectangular coordinates X, Y and instrumental magnitudes of registered objects.
3. The dividing of the registered objects into two exposures for each digitized plate.
4. The creating of the files with the reference stars for each digitized plate using the Tycho2 catalogue.
5. The creating of the files for the relationship between the rectangular and equatorial coordinate systems of reference stars.
6. Correction of the rectangular coordinates of registered objects for systematic errors.
7. Reduction of the rectangular coordinates X, Y of registered objects in the system of equatorial coordinates α, δ of the Tycho2 catalogue.
8. Conversion of the instrumental photometric values of objects to the system of photoelectric B_{pe} stellar magnitudes of the Johnson's system.

For the calibration of the characteristic curves of the photographic plates, the recording photometric field errors and the conversion of the instrumental photometric values to the system of photoelectric B_{pe} stellar magnitudes of the Johnson system were used data from the catalogues (Kornilov et al., 1991, Mermilliod, 1991, Andruk et al., 1995, 1996, Relke, et al., 2015). For the plotting of the characteristic curves of photographic plates was used the photometric information of both exposures.

The process of the creating of the CAT1 and CAT2 catalogues for the two sets of observations at the DWA and DAZ telescopes was as follows. In the overlapping zones of the photographic plates the identification and selection of candidates in stars and galaxies was carried out according to the following criteria:

- 1) the difference between equatorial coordinates should not be greater than the size of the one pixel
- 2) the difference between stellar magnitudes should not exceed ± 2 mag (because of the accounting of variable stars).

If the found candidate meets the selection criteria at least on two plates, it was included in the list of the objects for the catalogues. For the non-overlapping areas of the plates of DAZ telescope the candidates in stars and galaxies were implemented by the direct identification with the objects from the UCAC4 catalogue (Zacharias et al., 2013). The CAT1 and CAT2 catalogues contain

1320108 and 1795840 stars and galaxies up to $B_{ph} \leq 16.5^m$ (the photographic magnitudes of the Johnson system) for the epoch of 1990.35 and 1983.29 respectively. The CAT1 and CAT2 catalogues cover the zones of width up to 8° (from -4° to $+4^\circ$) and of width up to 5.2° (from -2.6° to $+2.6^\circ$), respectively. As the result of the comparing CAT1 and CAT2 catalogues was received a third MCAT catalogue, which contains the averaged data for the 669480 stars and galaxies.

3. Internal errors of the catalogues

The distribution of internal errors of defined equatorial coordinates $\sigma_\alpha, \sigma_\delta$ and photometric magnitudes $\sigma_{B_{ph}}$ of stars and galaxies on the intervals of stellar magnitudes of the three catalogues are given in the table 1. The average errors are provided at the top of the table 1 and their corresponding values for three catalogues are equal:

$$\sigma_\alpha = \pm 0.279", \pm 0.208", \pm 0.105"; \sigma_\delta = \pm 0.273", \pm 0.201", \pm 0.157"; \sigma_{B_{ph}} = \pm 0.168^m, \pm 0.176^m, \pm 0.140^m.$$

Table 1. The errors of the defined equatorial coordinates and stellar magnitudes for the three catalogues

B_{ph} mag	$\sigma_\alpha, \sigma_\delta$ arcsec		$\sigma_{B_{ph}}$ mag
CAT1			
6.6	± 0.286	± 0.249	± 0.204
7.6	0.218	0.178	0.155
8.6	0.138	0.119	0.116
9.6	0.086	0.082	0.081
10.6	0.066	0.066	0.061
11.6	0.062	0.064	0.068
12.6	0.106	0.108	0.094
13.6	0.190	0.192	0.119
14.6	0.285	0.278	0.162
15.3	0.355	0.346	0.212
16.3	0.395	0.396	0.262
17.1	0.455	0.416	0.156
CAT2			
6.6	± 0.203	± 0.356	± 0.296
7.6	0.264	0.224	0.264
8.6	0.148	0.143	0.231
9.6	0.097	0.094	0.175
10.6	0.064	0.064	0.134
11.6	0.057	0.059	0.086
12.6	0.106	0.107	0.093
13.6	0.162	0.159	0.116
14.6	0.179	0.177	0.144
15.5	0.218	0.215	0.201
16.2	0.263	0.253	0.193
17.1	0.258	0.289	0.278
MCAT			
6.7	± 0.173	± 0.203	± 0.333
7.6	0.139	0.142	0.209
8.6	0.093	0.095	0.160
9.6	0.070	0.061	0.110
10.6	0.056	0.046	0.077
11.6	0.050	0.045	0.067
12.6	0.062	0.078	0.087
13.6	0.090	0.133	0.103
14.6	0.111	0.167	0.148
15.3	0.123	0.191	0.170
16.2	0.132	0.207	0.182
17.1	0.132	0.187	0.491

4. Actual accuracy (external errors) of the catalogues

The results of the comparison of the three catalogues with the reference Tycho2 catalogue are presented in the second part of the table 2 as well as on the figure 2.

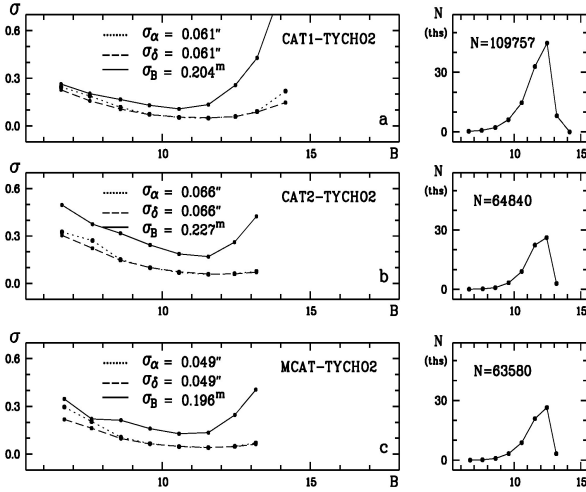


Figure 2: The trend of the errors of astrometric reduction with the B-magnitude for the three catalogues relative to the reference Tycho-2 catalogue.

We point out that the errors of astrometric reduction for the reference stars of the Tycho2 catalogue do not exceed the value of $\sigma_{\alpha\delta} = \pm 0.07''$. The comparison of the calculated equatorial coordinates of the created catalogues was also made with the equatorial coordinates of the UCAC4 (Zacharias et al., 2013) and PPMX (Roeser et al., 2008) catalogues. The results of the comparison are given in the third and fourth parts of the table 2 as well as on the figures 3 and 4.

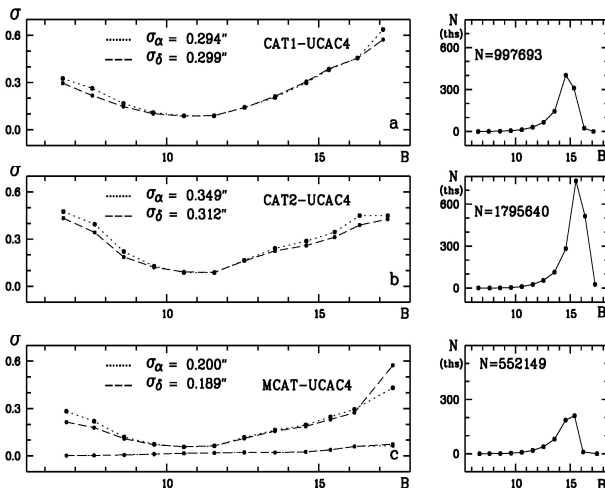


Figure 3: The trend of the errors of differences in equatorial coordinates with the B-magnitude for the three catalogues relative to the UCAC4 catalogue.

The astrometric errors of the created catalogues relative to the UCAC4 catalogue are: $\sigma_\alpha = \pm 0.294''$, $\pm 0.349''$, $\pm 0.200''$; $\sigma_\delta = \pm 0.299''$, $\pm 0.312''$, $\pm 0.189''$. The error values relative to the PPMX catalogue are: $\sigma_\alpha = \pm 0.260''$, $\pm 0.274''$, $\pm 0.186''$; $\sigma_\delta = \pm 0.273''$, $\pm 0.261''$, $\pm 0.188''$.

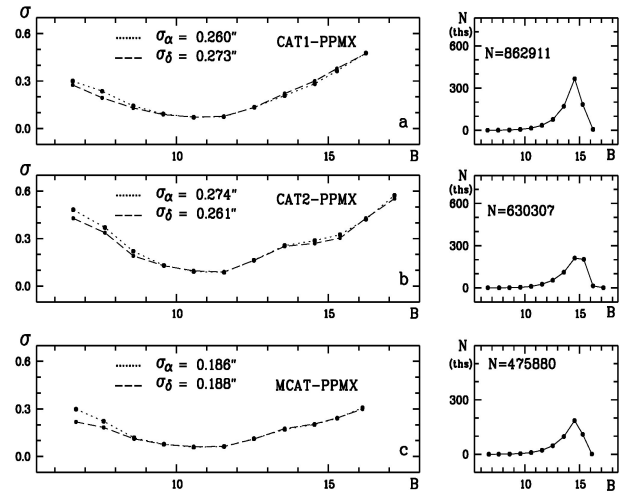


Figure 4: The trend of the errors of differences in equatorial coordinates with the B-magnitude for the three catalogues relative to the PPMX catalogue.

The photometric errors for the new three catalogues are presented on the figure 5.

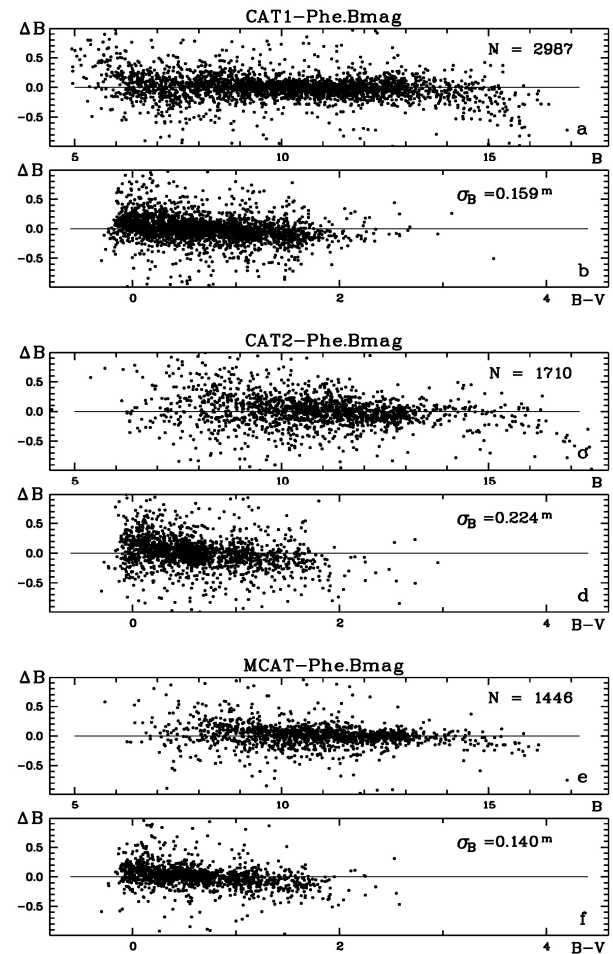


Figure 5: The trend of the errors of differences in magnitudes with the B-magnitude for the three catalogues relative to the photo electrical B-magnitudes.

The photometric errors were determined by the comparing of the stellar magnitudes of our three catalogues

with the photoelectric values of reference photometric catalogues. The calculated results are presented at the bottom of the table 2. For the three catalogues the error values are as follows: $\sigma_{\text{Bph}} = \pm 0.159^{\text{m}}, \pm 0.224^{\text{m}}, \pm 0.140^{\text{m}}$.

Table 2. The external errors of the three catalogues

	CAT1	CAT2	MCAT
N	320108	1795840	669480
σ_{α}	0.279"	0.208"	0.105"
σ_{δ}	0.273"	0.201"	0.157"
σ_{Bph}	0.168 ^m	0.176 ^m	0.140 ^m
TYCHO2			
	109757	64810	63580
	0.061"	0.066"	0.049"
	0.061"	0.066"	0.049"
	0.204 ^m	0.227 ^m	0.196 ^m
UCAC4			
	997693	1795840	552149
	0.294"	0.349"	0.200"
	0.299"	0.312"	0.189"
PPMX			
	862911	630307	475880
	0.260"	0.274"	0.186"
	0.273"	0.261"	0.188"
Pe.Bmag			
	2987	1710	1448
	0.159 ^m	0.224 ^m	0.140 ^m

5. Some remarks

The "Photographic Survey of the Northern Sky" (FON project) was proposed by the Main astronomical observatory Academy of Sciences of Ukraine, Kyiv (MAO NASU) (Kolchinsky et al., 1977; Kolchinsky et al., 1979). The idea of this project was due by the situation in the field of photographic astrometry in the early seventies of the twenties century. Some observatories of the former Soviet Union (Goloseevo, Zvenigorod, Dushanbe, Abastumani and Kitab) equipped with identical astrographs produced by the "Carl Zeiss Jena" (DDR) took part in this project. The observatories finished the observations at the end of the 90s of the XX century and have in their archives thousands of the photographic plates waiting for the reduction. The archive of the Kitab observatory (zone from -20° to $+30^{\circ}$) contains about 2600 photographic plates. Now the staff members of the Kitab observatory have organized the digitalization of the photographic plates of the "FON" project.

6. Conclusion

The created star catalogues of the positions and stellar magnitudes (Bph) of the zero zone of the Kyiv and Kitab parts of the FON project will be posted on the web pages of the MAO NASU and the Astronomical Institute of the Uzbek Academy of Sciences. The catalogues contain the equatorial coordinates of stars (α , δ) on the equinox 2000.0 as well as the stellar magnitudes (Bph). We provide the errors definitions of these values and number of determinations as well as an additional information in the form of the average values for the diameters of star images f (FWHM) and the values of the maximal intensity in the center of object images ($cInt$).

Acknowledgements. The authors are thankful to anybody who has read this contribution to the end. This work was partially supported by the Ukrainian Astronomical Association.

References

- Andruk V.M. et al.: 1995, *Astron. Nachr.*, **316**, **N4**, 225.
 Andruk V.N. 1996, *Kinem. Phys. Cel. Bodies*, **12**, **N4**, 60.
 Andruk V.M. et al.: 2010, *Kinem. Phys. Cel. Bodies*, **26**, **N3**, 146.
 Andruk V.M. et al.: 2014, *Odessa Astron. Publ.*, **27/1**, 53.
 Andruk V.M. et al.: 2015 ArXiv (in press).
 Andruk V.M. et al.: 2016, *Kinem. Phys. Cel. Bodies*, **32**, **N1**, 56.
 Golovnya V. et al.: 2010, *J. of Phys. Studies*, **14**, **N2**, 2902.
 Kazantseva L.V. et al.: 2015, *Kinem. Phys. Cel. Bodies*, **31**, **N1**, 58.
 Kislyuk. V.S. et al.: 2000, *Kinem. Phys. Cel. Bodies*, **16**, **N6**, 483.
 Kolchinsky I.G., Onegina A.B.: 1977, *Astrometry and Astrophysics*, **N33**, 11.
 Kolchinsky I.G., Onegina A.B.: 1979, *Astrometry and Astrophysics*, **N39**, 57.
 Kornilov V.G. et al.: 1991, *Trudy GAIS*, **63**, 1.
 Mermilliod J.C.: 1991, *Homogeneous means in the UBV system*.
 Muminov M.M. et al.: 2014, *Odessa Astron. Publ.*, **27/1**, 57.
 Muminov M.M. et al.: *Izvestija GAO*, Pulkovo, 2016 (in press).
 Protsyuk Yu.I. et al.: 2014, *Odessa Astron. Publ.*, **27/1**, 59.
 Protsyuk Yu.I. et al.: 2014, *Odessa Astron. Publ.*, **27/1**, 61.
 Protsyuk Yu.I. et al.: 2014, *Odessa Astron. Publ.*, **27/1**, 63.
 Protsyuk Yu.I. et al.: 2014, *Kinem. Phys. Cel. Bodies*, **30**, **N6**, 54.
 Relke H. et al.: 2015, *Odessa Astron. Publ.*, **28**, **N1**.
 Roeser S. et al.: 2008, *A&A*, **488**, 401.
 Vavilova I.B. et al.: 2012, *Kinem. Phys. Cel. Bodies*, **28**, **N2**, 85.
 Vavilova I.B. et al.: 2012, *Baltic Ast.*, **21**, **N3**, 356.
 Yatsenko A.I. et al.: 2011, *Kinem. Phys. Cel. Bodies*, **27**, **N5**, 249.
 Yizhakevych O. et al.: 2014, *Odessa Astron. Publ.*, **27/1**, 67.
 Zacharias N. et al.: 2013, *Astron. J.*, **145**, 44.

CATALOG OF POSITIONS AND B MAGNITUDES OF STARS IN THE CIRCUMPOLAR REGION OF NORTHERN SKY SURVEY (FON) PROJECT

V.M.Andruk¹, L.K.Pakuliak¹, V.V.Golovnia¹, G.A.Ivanov¹, O.M.Yizhakevych¹,
Yu.I.Protsyuk², S.V.Shatokhina¹

¹ Main Astronomical Observatory of National Academy of Sciences,
27 Akad. Zabolotnogo St., 03680, Kyiv, Ukraine, andruck@mao.kiev.ua

² Research Institute "Nikolaev Astronomical Observatory",
1 Observatornaya St., 54030, Mykolaiv, Ukraine, yuri@nao.nikolaev.ua

ABSTRACT. The catalog of star positions and B-magnitudes for the circumpolar region (from 58° to 90° in declination) of Northern Sky Survey project has been created under the motto of the rational use of resources accumulated in UkrVO JDA (Joint Digital Archive) in MAO NASU. The total amount of processed plates is 477. Digitizing of astronegatives has been carried out using Microtek ScanMaker 9800XL TMA and Epson Expression 10000XL scanners, with the scanning mode – 1200 dpi, the linear size of the plates – 30x30 cm or 13000x13000 px. The catalog contains 1 975 967 stars and galaxies with $B \leq 16.5^m$ for the epoch of 1985.28. The coordinates of stars and galaxies were obtained in the Tycho-2 reference system, and B-value in the system of photoelectric standards. The internal accuracy of the catalog for all the objects is $\sigma_{\alpha\delta} = \pm 0.23''$ and $\sigma_B = \pm 0.12^m$ (for stars in the range of $B = 8^m - 14^m$ errors are $\sigma_{\alpha\delta} = \pm 0.11''$ and $\sigma_B = \pm 0.06^m$). Convergence between the calculated and reference positions is $\sigma_{\alpha\delta} = \pm 0.06''$ (for 171 124 stars from Tycho-2), and the convergence with photoelectric stellar B-magnitudes is $\sigma_B = \pm 0.15^m$ (for 5130 stars). External accuracy from the comparison with UCAC-4 is $\sigma_{\alpha\delta} = \pm 0.33''$ (1 928 367 stars and galaxies were cross identified).

Keywords: virtual observatory tools – astrometry – techniques; photometric – methods: data analysis – catalogs

1. Introduction

For the creation of the circumpolar region star catalogue 477 plates of the FON project (Kislyuk, 2000; Yatsenko, 2011) were digitized and processed. The catalogue covers the region from 58° to 90° in declination and includes positions and B-magnitudes of stars. The work is done with the involvement of collected resources of UkrVO JDA (Joint Digital Archive) (Vavilova, 2012; Vavilova, 2012).

The process of digitizing the UkrVO archives was not limited to photographic surveys relatively homogeneous in quality. Plates, obtained in a variety of observational programs and received on different instruments with different methods, different structures of object images, digitized with different models of scanners were taken into processing. The variety of digitized material required constant upgrading of software and finding new approaches to its solution. The algorithms and methods developed in this

investigation permit to resolve many problems of plates processing from different observational archives.

The FON plates were obtained with four-fold overlapping on both coordinates. For this catalogue in some areas with distances $\pm 2^\circ$ from the centers of plates on the declination the two-fold overlapping was used. The overlapping along the strips on the right ascension is made with $4^\circ/\cos\delta$ shift of plate centers. The centers of adjacent strips are spaced apart from each other by 4° on declination. The number of plates in the RA stripes shown in the Table 1.

All the plates were obtained with MAO NASU DWA (Double Wide-angle Astrograph, D/F=40/200, 103"/mm, h=186m). The linear dimensions of the most plates are 30x30 cm (8x8°).

Table 1. Number of plates in each RA stripe.

DEC	N	DEC	N	DEC	N
88°	8	76°	53	64°	50
84°	25	72°	51	60°	102
80°	24	68°	58	56°	106

The plates were digitized using Microtek ScanMaker 9800XL TMA and Epson Expression 10000XL commercial scanners with the resolution 1200 dpi. The dimensions of the digital image fields are up to 13000x13000 px (1px = 2.17"). This version of the catalogue is obtained from the processing of single scans without turning the plate by 90°. This permits to save resources for storage and processing the data in half without losses in accuracy (Andruk, 2016). The results of scanners' testing, principles and stages of astronegative digital image processing are stated in the series of publications (Andruk, 2005, Andruk, 2007, Andruk, 2010, Golovnya, 2010, Protsyuk, 2014, Protsyuk, 2014, Protsyuk, 2014). The results of the software testing are described in (Kazantseva, 2015; Protsyuk, 2014; Andruk, 2014; Muminov, 2014; Vavilova, 2014; Yizhakevych, 2014).

2. Separation of stars into two exposition sets

The FON plates were obtained with two expositions: the long and short of 16-20 minutes and 30-60 second respectively. For astrometric catalogue star images of short expo-

sition are not used and should be excluded at the initial step before the astrometric solution. Stages and functional dependences of different parameters in the separation of detected objects into two sets are shown on Fig.1. Upper panels demonstrate the correlation between instrumental photometric values of long and short expositions m_2 и m_1 at initial and final stages of separation on the left and right sides of the figure correspondingly. Differences of magnitudes Δm reduced to the mean value are given on the panels **b, d** in relation to m_1 and the distance from the center of the plate R . The differences of distances between centers of images Δr are given on the panel **c** in relation to m_1 . The differences of rectangular coordinates ΔX , ΔY are presented on the panels **e, f** relative to the rectangular coordinates Y , X . The lower panels (**g, h, j**) show the real and pre-calculated histograms of distribution Δm , ΔX , ΔY , shown with solid and dashed lines, respectively. It will be recalled that the value of the ΔX , ΔY differences' rotation in relation to the center of rectangular coordinates Y , X depends on the declination of the plate. The mutual rotation of two frames is absent at the equator.

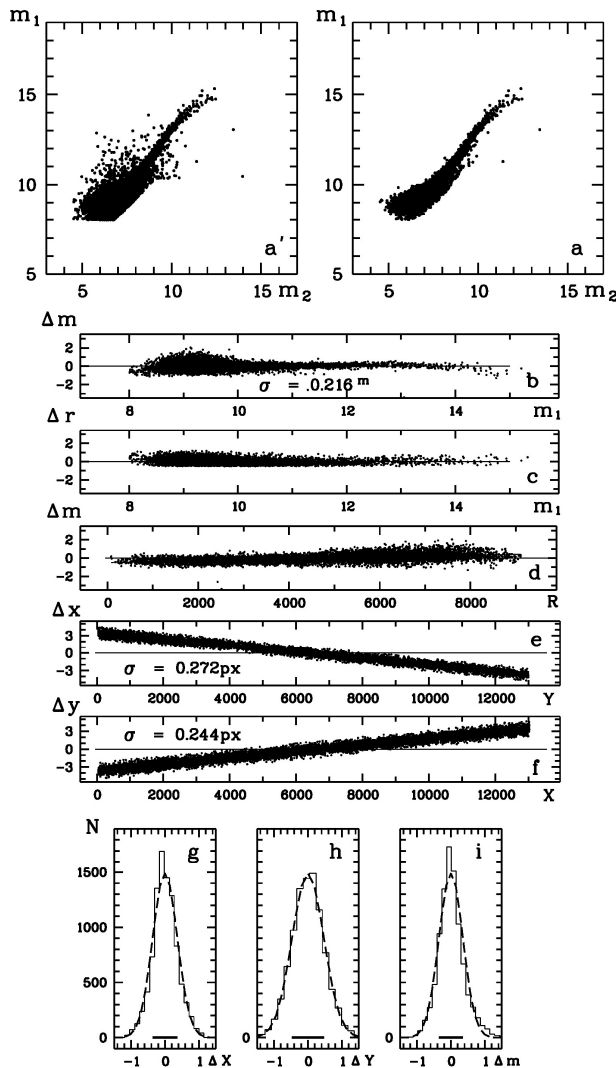


Figure 1: Stages of processing and functional dependences of different parameters in separation of star images into two exposition sets on the example of the test plate.

3. The magnitude equation

When calculating the tangential coordinates the special attention is given to the accounting of the magnitude equation $mdtX$ and $mdtY$. It was found that for the plates exposed on astrographs the magnitude equation becomes significant for stars from $B \approx 11^m$ and its influence increases with the brightness of stars.

Fig. 2 shows the magnitude equation for the long exposition of the test plate with two expositions and Fig.3 presents the residual differences after its elimination. Fig.2 demonstrates the differences $\Delta\alpha$, $\Delta\delta$ between observed and catalogue positions in relation to star image diameters $f_{1/2}$, instrumental photometric values m_1 , magnitudes B and color indices $B-V$ of Tycho-2 before the corrections for systematic errors of the scanner. From plots it is obvious that the magnitude equation is linear on all sections of $f_{1/2}$ and B and there the quadratic dependence on instrumental photometric values m_1 exists. Fig.3 shows the trend of residual differences in coordinates after the correction for the magnitude equation and the errors of the scanner.

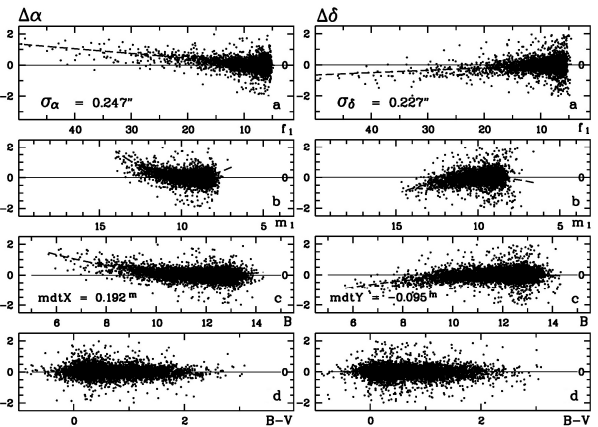


Figure 2: The magnitude equation for the long exposition detected on the plates with two expositions of the FON project.

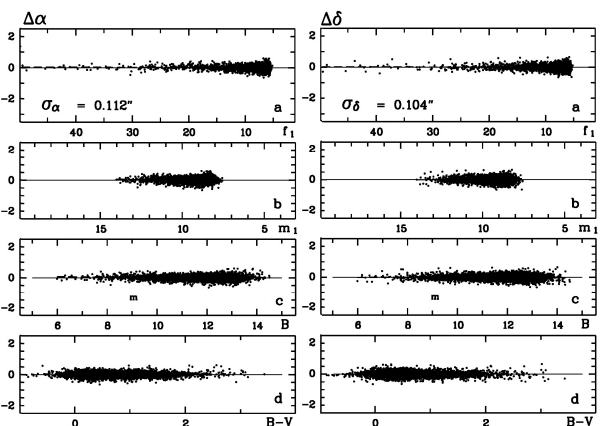


Figure 3: The residual differences in coordinates after the corrections for the magnitude equation and the scanner errors.

4. Astrometric solution in the Tycho-2 reference system

In each step of catalogue creation the star catalogue TYCHO-2 was taken as reference. The accuracy of it is $\sigma_{\text{RA,DEC}} = \pm 0.060''$, $\sigma_{\mu} = \pm 0.0025''/\text{yr}$, $\sigma_m = \pm 0.10^m$ for its all 2 539 913 stars.

For all scans of plates with the field dimensions up to $8 \times 8^\circ$ the tangential coordinates ξ , η were calculated by equations (1). The same formulae were used on the stage of scanner systematic errors $\Delta\alpha$, $\Delta\delta$ studying.

$$\begin{aligned} \xi_i &= a_1 + a_2 X_i f_{1/2i} + a_3 Y_i f_{1/2i} + a_4 R_i m_i + a_5 f_{1/2i} + \sum b_{lm} X_i^l Y_i^m, \\ (l=0 \div 6, m=0 \div 6, l+m=n, n=1 \div 6) \\ \eta_i &= c_1 + c_2 X_i f_{1/2i} + c_3 Y_i f_{1/2i} + c_4 R_i m_i + c_5 f_{1/2i} + \sum d_{lm} X_i^l Y_i^m, \\ (l=0 \div 6, m=0 \div 6, l+m=n, n=1 \div 6) \end{aligned} \quad (1)$$

Here, $i = 1, 2, \dots, n$ – number of reference stars; X_i , Y_i and R_i – rectangular coordinates and distances of stars from the centers of plates; m_i – photometric measured data of stars; $f_{1/2i}$ – diameters of star images (FWHM); coefficients a_2 , a_3 , a_4 and c_2 , c_3 , c_4 define coma affects, coefficients a_5 , c_5 – taking into account the magnitude equation, which is calculated separately; coefficients of the full sixth-order polynomial b_{lm} и d_{lm} (27 terms) in the generalized case describe the aberrations of telescope optics with the systematic errors of the scanner included. A step-by-step description of scanner systematic errors exclusion is set out in (Andruk, 2015).

Fig. 4 shows the results of the test plate processing. On the left side the trend of telescope systematic errors σ_α , σ_δ over the plate field is shown. Right panels demonstrate the trend of the residual differences $\Delta\alpha$, $\Delta\delta$. Negative and positive values of differences are shown by horizontal and vertical strokes which have linear dimensions according to the scale of values presented on the figure. Errors are obtained by averaging within 250×250 px cells.

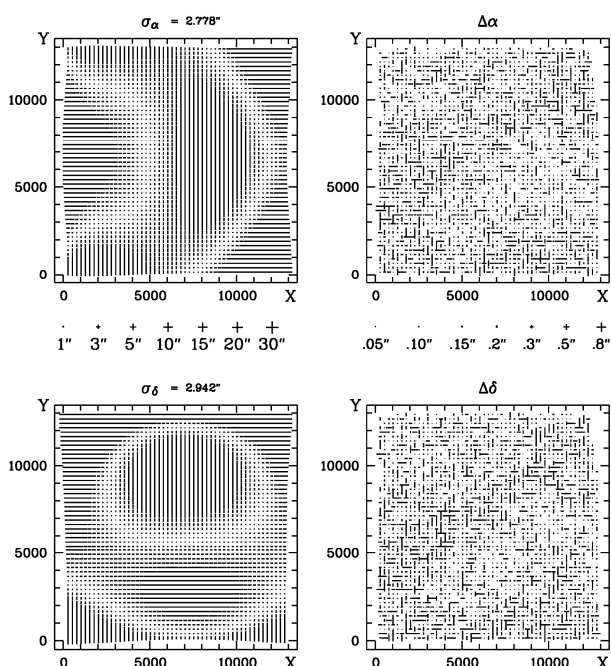


Figure 4: The distribution of errors and residual differences over the plate field as a result of the astrometric solution.

5. Photometric reduction into the system of photoelectric B-magnitudes

The reference system for the photometric solution is based on the photoelectric B_{pe} -values from catalogues (Kornilov, 1991, Mermilliod, 1991). The stages and principles of astronegative characteristic curve restoration accounting the field photometric equation and the data of two expositions are described in (Andruk, 2012). The approximation of the characteristic curve and determination of photographic B-magnitudes B_{ph} for all 477 plates were carried out by the least square method solution of the set of equation (2):

$$B_i = e_1 + e_2 X_i + e_3 Y_i + e_4 R_i + e_5 R_i^2 + e_6 R_i^4 + \sum f_n m_i^n \quad (n=1, 2, \dots, 5) \quad (2)$$

Here, $i = 1, 2, \dots, n$ is the number of photoelectric data for standard star on the plate; X_i , Y_i и R_i are the rectangular coordinates and the distances from the center of the plate; m_i – instrumental photometric evaluations; coefficients e_2 , e_3 , e_4 , e_5 , e_6 define the field photometric equation; f_1 , f_2 , f_3 , f_4 , f_5 describe the functional form of the characteristic curve. The equation (2) was chosen as minimizing the errors of the reduction into the reference B_{pe} system in the best way.

6. Catalogue creation

When creating the catalogue the next steps were undertaken:

1. Digitizing of astronegatives using Microtek Scan-Maker 9800XL TMA and Epson Expression 10000XL scanners with 1200 dpi resolution.
2. Conversion of the tiff-format files to the fit-format files using the GIMP package.
3. Calculation of the rectangular coordinates X , Y , photometric instrumental evaluations m , $f_{1/2}$ and other parameters using the MIDAS/ROMAFOT package for all registered objects.
4. Astrometric reduction of all objects into Tycho-2 reference system to obtain their position α , δ at the epoch of plates' exposure.
5. Conversion of instrumental photometric evaluations m into the reference system of photoelectric B_{pe} -magnitudes.
6. Calculation of mean values of equatorial coordinates α , δ and stellar magnitudes B for stars and galaxies in the limits of RA-overlapping of scans for each RA stripe. Elimination of artefacts.
7. Averaging of α , δ , B values in the overlapping areas between RA stripes.
8. Preparation of the catalogue of positions α , δ and stellar magnitudes B and its supplementation with proper motions data μ_α , μ_δ from UCAC4 (Zacharias, 2013).

The processing of scans was carried out using MIDAS/ROMAFOT software package. The photometric equalization of scans was made by taking into account the individual flat-field calculated for each plate separately (Andruk, 2005). The number of registered objects on the astronegatives, exposed in the areas of Milky Way reaches 300 000. The total number of objects found on the

whole set of 477 plates is around 25.933 million ones of different origin. Equatorial coordinates α , δ for all objects are obtained in the reference system of Tycho-2 at the epoch of exposition of each plate. As a rule, the reduction was made for full fields of plates with dimensions $8^\circ \times 8^\circ$, the exception was made for the high-latitude zones (84° and 88°) with a much smaller dimensions of processed fields. Photographic B_{ph} -magnitudes of objects were derived from equations (2) for characteristic curves of astro-negatives calibrated with photoelectric B_{pe} -magnitudes.

The final positions and B-magnitudes of stars and galaxies as well as their errors were calculated by equations (3) and (4):

$$\begin{aligned} \alpha &= (\alpha_1/\sigma_{\alpha 1}^2 + \alpha_2/\sigma_{\alpha 2}^2) / (1/\sigma_{\alpha 1}^2 + 1/\sigma_{\alpha 2}^2) \\ \delta &= (\delta_1/\sigma_{\delta 1}^2 + \delta_2/\sigma_{\delta 2}^2) / (1/\sigma_{\delta 1}^2 + 1/\sigma_{\delta 2}^2) \\ B_{ph} &= (B_1/\sigma_{B 1}^2 + B_2/\sigma_{B 2}^2) / (1/\sigma_{B 1}^2 + 1/\sigma_{B 2}^2) \end{aligned} \quad (3)$$

$$\begin{aligned} \sigma_\alpha &= (1 / (1/\sigma_{\alpha 1}^2 + 1/\sigma_{\alpha 2}^2))^{1/2} \\ \sigma_\delta &= (1 / (1/\sigma_{\delta 1}^2 + 1/\sigma_{\delta 2}^2))^{1/2} \\ \sigma_B &= (1 / (1/\sigma_{B 1}^2 + 1/\sigma_{B 2}^2))^{1/2} \end{aligned} \quad (4)$$

7. The accuracy of the catalogue

The comparison of 171 124 reference stars of the catalogue with Tycho-2 gives the errors of the astrometric reduction $\sigma_{\alpha\delta} = \pm 0.06''$.

The errors of photometry were derived from comparison of calculated stellar magnitudes with the photoelectric values of 5130 stars from the photometric reference catalogues. The errors are $\sigma_B = \pm 0.12^m$.

The comparison of the catalogue with UCAC-4 gives the positional errors in relation to UCAC4 at the level of $\sigma_{\alpha\delta} = \pm 0.33''$ (1 928 367 stars and galaxies were cross-identified in both catalogues).

8. Conclusion

The comprehensive software was developed and implemented in the Department of the Astrometry MAO NASU to process the digitized astronomic negative plates as well as to obtain the final product in the form of a catalogue of positions and stellar magnitudes of stars and galaxies. The above version of the catalogue created in the circumpolar zone of FON project contains 1 975 967 stars and galaxies down to $B \leq 16.5^m$ at the epoch 1985.28. The positions of objects are obtained in the reference system of Tycho-2. The stellar magnitudes B are in the system defined by photoelectric standards. The internal accuracy of the catalogue for all objects is $\sigma_{\alpha\delta} = \pm 0.23''$ and $\sigma_B = \pm 0.12^m$. For the stars in the interval of magnitudes $B = 8^m - 13^m$ the errors are $\sigma_{\alpha\delta} = \pm 0.11''$ and $\sigma_B = \pm 0.06^m$.

The convergence of the coordinates with the Tycho-2 reference system obtained on 171 124 stars is $\sigma_{\alpha\delta} = \pm 0.06''$. The convergence of magnitudes with the photoelectric values B_{pe} for 5 130 stars is $\sigma_B = \pm 0.15^m$. The positional errors of the catalogue derived on 1 928 367 cross-identified stars in comparison to UCAC4 are $\sigma_{\alpha\delta} = \pm 0.33''$.

The algorithms and methods of plate digitizing and processing and the software developed in the Department of Astrometry MAO NASU is now applied for the total

set of exposed plates of the FON project with the aim of creating the catalogue of positions and B-magnitudes of the whole northern sky from 0° to 90° on declination.

The created star catalogue of the positions and stellar magnitudes of the circumpolar zone of the FON project will be posted on the web pages of the MAO NASU and UkrVO. The catalogue contains the equatorial coordinates of 1 975 967 stars and galaxies (α , δ) on the equinox 2000.0 and the epoch 1985.28 as well as the stellar magnitudes (Bph). We provide the errors definitions of these values and number of determinations as well as an additional information in the form of the average values for the diameters of star images $f_{1/2}$ (FWHM) and the values of the maximal intensity in the center of object images (cInt).

Acknowledgements. The authors are grateful to the MAO NASU ACISS for the technical assistance. The authors thank Ph.D. P.F.Lasorenko for consultations. This work was partially supported by the Ukrainian Astronomical Association.

References

- Andruk V.M. et al.: 2005, *Kinem. Phys. Cel. Bodies*, **21**, N5, 396.
- Andruk V.M. et al.: 2005, *Kinem. Phys. Cel. Bodies. Supl.*, **N5**, 413.
- Andruk V.M. et al.: 2007, *J. Phys. Studies*, **11**, N3, 329.
- Andruk V.M. et al.: 2010, *Kinem. Phys. Cel. Bodies*, **26**, N3, 75.
- Andruk V.M. et al.: 2012, *Visnyk KNU, Astronomy*, **N48**, 11 (in ukrainie).
- Andruk V.M. et al.: 2014, *Odessa Astron. Publ.*, **27/1**, 53.
- Andruk V.M. et al.: 2015, 2015arXiv, in press.
- Andruk V.M. et al.: 2016, *Kinem. Phys. Cel. Bodies*, **32**, N1, 56 (in press).
- Golovnya V.V. et al.: 2010, *J. Phys. Studies*, **14**, N2, 2902.
- Kazantseva L.V. et al.: 2015, *Kinematics and Physics of Celestial Bodies*, **31**, N1, 58.
- Kislyuk V.S. et al.: 2000, *Kinem. Phys. Cel. Bodies*, **16**, N6, 483.
- Kornilov V.G. et al.: 1991, *Trudy GAIS*, **63**, 1.
- Mermilliod J.C.: 1991, *Homogeneous means in the UBV system*.
- Muminov M.M. et al.: 2014, *Odessa Astron. Publ.*, **27/1**, 57.
- Protsyuk Yu.I. et al.: 2014, *Odessa Astron. Publ.*, **27/1**, 59.
- Protsyuk Yu.I. et al.: 2014, *Odessa Astron. Publ.*, **27/1**, 61.
- Protsyuk Yu.I. et al.: 2014, *Odessa Astron. Publ.*, **27/1**, 63.
- Protsyuk Yu.I. et al.: 2014, *Kinematics and Physics of Celestial Bodies*, **30**, N6, 54.
- Vavilova I.B. et al.: 2012, *Kinem. Phys. Cel. Bodies*, **28**, N2, 85.
- Vavilova I.B. et al.: 2012, *Baltic Ast.*, **21**, N3, 356.
- Vavilova I.B. et al.: 2014, *Odessa Astron. Publ.*, **27/1**, 65.
- Yatsenko A.I. et al.: 2011, *Kinem. Phys. Cel. Bodies*, **27**, N5, 249.
- Yizhakevych O. et al.: 2014, *Odessa Astron. Publ.*, **27/1**, 67.
- Zacharias N. et al.: 2013, *AJ*, **145**, 44.

CATALOGUES OF THE FAINT OBJECTS IN THE AREAS WITH GAMMA-RAY BURSTS

V.V. Golovnia¹, Yu.I. Protsyuk², V.M. Andruk¹, I.B. Vavilova¹, L.K. Pakuliak¹,
I.V. Kulyk¹, Ya.O. Romanyuk¹, O.R. Baransky³

¹ Main Astronomical Observatory NAS of Ukraine, Kyiv, Ukraine,
golov@mao.kiev.ua, andruk@mao.kiev.ua,

² Nikolaev Astronomical Observatory, Mykolaiv, Ukraine, *yuri@nao.nikolaev.ua*

³ Taras Shevchenko National University of Kyiv, Kyiv, Ukraine

ABSTRACT. The results of GRB observations are being published in the GCN Circulars in real-time. To study all the objects in the sky areas around the GRBs we identified them on the digitized MAO Double Wide angle Astrograph (DWA) plates (D/F=40/200) within a circle with the radius of dozens of arcminutes. We selected only GRBs with the positional accuracy between $\pm 0.3''$ and $\pm 7.5''$ and the range of magnitudes between 14^m and 20^m .

We used MIDAS/ROMAFOT package to obtain the catalogues of the faint objects in small areas in the GRBs vicinity. For the plates of DWA telescope the positional rms errors are $\pm 0.20''$ for RA and DEC, the photometric errors are $\pm 0.20^m$. All positions were obtained in Tycho-2 system.

Keywords: gamma-ray burst, astronomical data base, methods: data analysis

1. Introduction

Gamma-ray bursts are the most powerful explosions known in the Universe. Now they are identified with the regions of formation of massive stars in galaxies and the parent short-lived explosions of massive stars, which have a random spatial distribution in the sky (Sokolov et al., 2009; Raikov et al., 2010; Kienlin et al., 2014; Gerasim et al., 2015).

The astroplates give us an unique opportunity to identify the optical counterparts of the GRBs and study all the objects in the vicinity of the registered GRB (Golovnya et al., 2012, 2014; Pakuliak et al., 2013; Vavilova et al., 2014). With this aim we used MIDAS/ROMAFOT software package to obtain catalogues of the faint objects in small areas in the vicinity of the registered GRB. This software was developed at the MAO NAS of Ukraine for processing the scanned records to get a high precision astrometric and photometric data of objects (Andruk et al., 2005, 2007, 2010, 2014; Yatsenko et al., 2011; Golovnya et al., 2010).

2. Search of optical analogs of GRB

The results of GRB observations are being published in the GCN Circulars in real-time (Barthelmy, 2015). The Database of Joint Digital Archive (JDA) of Ukrainian Virtual Observatory (UkrVO), which contains observational data obtained at Ukrainian observatories, was used to search for optical analogs of GRBs on the astroplates (Sergeeva et al., 2004; Vavilova et al., 2010, 2012a, 2012; Pakuliak et al., 2012; Protsyuk et al., 2014).

Table 1 shows the optical coordinates of some GRBs and their precision (sigma) from GCN Circulars, for which the optical identifications were successful (Beardmore et al., 2015; Goad et al., 2015; Osborne et al., 2015; Evans et al., 2015). The table also lists numbers of the plates (N) from JDA UkrVO for the corresponding objects.

Table 1: The number of plates (N) in JDA UkrVO

GRB	RA, Dec, J2000 h m s deg ' "	Sigm ", \pm	N
150728A	19:28:55.28+33:54:57.8	4.1	3
150626B	12:30:32.04+66:46:18.6	1.7	5
150607A	09:19:57.25+68:26:09.6	1.4	3
150530A	21:50:02.94+57:30:59.8	1.6	9
150527A	19:15:50.32+04:12:06.9	1.5	9
150423A	14:46:18.96+12:17:00.6	1.8	10
150323A	08:32:42.74+45:27:52.8	1.9	6

However, the identification process was not always successful. Let us give an example of the search for GRB 140419A (Osborne et al., 2014). At the first detection this object had a magnitude of ~ 13.5 , then it was increased to 12.5 in ~ 70 sec and then the brightness decayed fast to $\sim 14.3^m$ for about 350 sec (Guver et al., 2014). We found two plates obtained in 1978 and 1990 with the desired areas, but we could not find the optical analogue of this GRB. Also, no optical counterpart was found in the close vicinity of GRB 140818B (Beardmore et al., 2014). But inspecting larger area around this object, we found some images near GRB position on both selected plates. Brightness of the objects was estimated as $V=15.0$ and $V=16.5$ (Golovnya, 2014).

The five plates were found in JDA UkrVO for GRB 150212A and GRB 150213B, but they had no optical analogue (Evans et al., 2015, Golovnya, 2015, Osborne et al., 2015, Golovnya, 2015).

Three plates with the GRB150220A (Evans et al., 2015) were found with a limited magnitude of 16.4, 15.6 and 15.7 respectively. Two objects were found on plate GUA040C002183, EPOCH=1993.2192. Fig. 1 shows $13' \times 13'$ area around GRB150220A with these two objects. The coordinates and B magnitudes were obtained in the system of TYCHO-2 catalogue with rms errors of $0.093''$, $0.099''$, 0.21^m for right ascension, declination, and magnitudes respectively (Golovnya & Andruk, 2015).

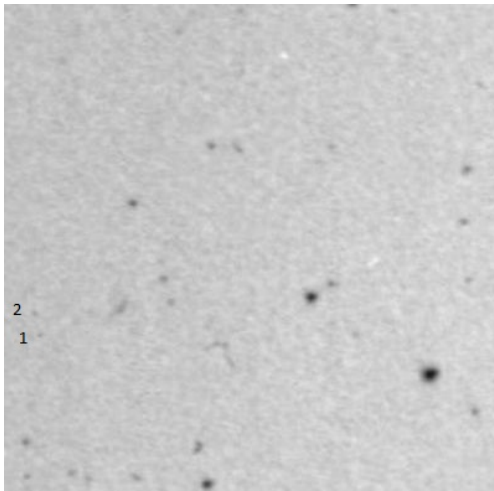


Figure 1: The area of GRB150220A with identified Obj1 and Obj2

We observed the same field around GRB 150220A with 0.7-m f/4 reflector of Kyiv comet station on Mar 10, 2015 during 18 days after the burst has been occurred. The telescope is equipped with CCD (1027x1056 pixels with a scale of 0.95"/px). We obtained 21 CCD frames with 60 sec expositions in R-filter (Romanyuk et al., 2015). The individual frames were summed in order to increase the signal. We did not find aforementioned images of Obj1 and Obj2 on the final CCD frame. However, we confirmed some of the positions of X-ray sources reported early by P.A. Evans. Table 2 contains the coordinates of X-ray sources given by Evans et al. (2015) and their optical identifications made with the CCD.

Table 2: Source's position as follows by P.A.Evans (GCN 17501) and Ya.O.Romanyuk (GCN 17645).

	GCN 17501			GCN 17645		
	h	m	s	°	'	"
1	9 01	31.65		-01 39	07.6	outside our field
2	9 01	30.74		-01 38	27.0	outside our field
3	9 02	08.55		-01 36	59.1	9 02 08.1 -01 36 35
4	9 02	08.90		-01 40	20.1	extremely faint
5	9 01	28.27		-01 39	06.3	outside our field
6	9 02	25.29		-01 41	14.9	9 02 25.3 -01 41 15
7	9 01	46.37		-01 38	13.9	9 01 46.4 -01 38 14

We detected the optical counterpart (18.3^m) of the GRB 151027A with 0.5-m telescope Mobitel KT-50 of the Nikolaev observatory with Alta-U9000 CCD with R-filter (Protsyuk & Kovalchuk, 2015).

3. Creation of catalogs of objects in the areas around GRBs

As it was shown above, the optical counterparts of some GRBs and X-ray sources can be identified with the plates from the JDA UkrVO. With this aim we decided to create the catalogues of faint stars in the vicinity of GRBs (the catalogues are under development). At the first step we scanned the plates with resolution of 1200 dpi, but in order to increase a positional accuracy, we shall rescan the plates with resolution of 1600 dpi.

Special tools were also developed, which allowed obtaining the positions and magnitudes of faint stars with accuracy of about $\pm 0.20''$ and $\pm 0.20^m$ respectively. Each catalogue covers the sky area of about 10-20 arcmin and contains the coordinates and magnitudes of about hundreds of stars. The TYCHO2 or UCAC4 catalogues are used as reference ones. The developed tools allow us the fast cross-identification between the lists of the obtained optical positions of the faint stars and GRB coordinates (Protsyuk et al., 2014a, 2014). The catalogues will be put on the UkrVO web-site after completing.

Acknowledgements. This work was partially supported by the Ukrainian Astronomical Association.

References

Andruk V.N. et al.: 2005, *Kinematika i Fizika Nebesnykh Tel*, **21**, N5, 396.
 Andruk V. et al.: 2007, *J. Phys. Studies*, **11**, No3, 329.
 Andruk V.M. et al.: 2010, *Kinem. Physics Celest. Bodies*, **26**, No3, 146.
 Andruk V.N. et al.: 2014, *Odessa Astron. Publ.*, **27/1**, 53.
 Barthelmy S.: 2015, *gcn.gsfc.nasa.gov*.
 Beardmore A.P. et al.: 2014, *GCN 16712*.
 Beardmore A.P. et al.: 2015, *GCN 18088*.
 Evans P.A. et al.: 2015, *GCN 17879*, *GCN 17735*.
 Evans P.A. et al.: 2015, *GCN 17452*.
 Evans P.A.: 2015, *GCN 17501*.
 Gerasim R.V. et al.: 2015, *Astrophys.*, **58/2**, 204.
 Goad M.R. et al.: 2015, *GCN 17615*.
 Goad M.R. et al.: 2015, *GCN 17968*, *GCN 17889*.
 Golovnya V. et al.: 2010, *J. Phys. Studies*, **14**, No 2, 2902.
 Golovnya V. et al.: 2012, *Kyiv Univ. Messenger. Astronomy*, **49**, 36 (in ukrainian).
 Golovnya V.V.: 2014, *GCN 16757*.
 Golovnya V. et al.: 2014, www.astroplate.cz/wp-content/uploads/2014/01/Golovnya_UkrVO_new_life.pdf
 Golovnya V.V.: 2015, *GCN 17473*.
 Golovnya V.V.: 2015, *GCN 17484*.
 Golovnya V.V., Andruk V.M.: 2015, *GCN 17589*.
 Guver T. et al.: 2014, *GCN 16120*.
 Kienlin A. et al.: 2014, *Astroph. J. Suppl. S.*, **211**, 13.
 Osborne J.P. et al.: 2014, *GCN 16124*.
 Osborne J.P. et al.: 2015, *GCN 17475*.
 Osborne J.P. et al.: 2015, *GCN 17905*.
 Pakuliak L et al.: 2012, *IAUS*, **285**, 389.
 Pakuliak L. et al.: 2013, *Odessa Astron. Publ.*, **26/2**, 236.
 Protsyuk Yu., Kovalchuk O.: 2015, *GCN 18533*.
 Protsyuk Yu.I. et al.: 2014, *Odessa Astron. Publ.*, **27/1**, 59.
 Protsyuk Yu.I. et al.: 2014, *Kinemat. Physics Celest. Bodies*, **30**, N6, 54.
 Raikov A.A. et al.: 2010, *Astrophys.*, **53**, 3, p.396.
 Romanyuk Ya. et al.: 2015, *GCN 17645*.
 Sergeeva et al.: 2004, *Baltic Astronomy*, **13**, No 4, 677.
 Sokolov V.V. et al.: 2009, Workshop "Many faces of GRB phenomena – optics vs high energy".
 Vavilova I.B., Pakuliak L.K., Protsyuk Yu.I.: 2010, *Kosmichna Nauka i Tekhnologiya*, **16**, 62.
 Vavilova I.B. et al.: 2012, *Kinem. Physics Celest. Bodies*, **28**, No2, 85.
 Vavilova I.B. et al.: 2012, *Baltic Astronomy*, **21**, 356.
 Vavilova I. et al.: 2014, *Odessa Astron. Publ.*, **27/1**, 65.
 Yatsenko A.I. et al.: 2011, *Kinem. Physics Celest. Bodies*, **27**, No5, 249.

RESEARCH OF THE LONG-TERM BEHAVIOUR OF THE PLEIADES BY USING OF PHOTOGRAPHIC PLATES FROM UKRVO DIGITAL ARCHIVE AND BALDONE OBSERVATORY

L.V.Kazantseva¹, V.M.Andruk², S.V.Shatokhina², Yu.I.Protsyuk³, I.Eglitis⁴, M.Eglite⁴

¹Astronomical Observatory of Kyiv Shevchenko National University, Observatorna St. 3, Kyiv, 04053, Ukraine, *likaz@observ.univ.kiev.ua*

²Main Astronomical Observatory of National Academy of Sciences, Akad. Zabolotnogo St. 27, Kyiv, 03680, Ukraine, *andruk@mao.kiev.ua*, *svetash@mao.kiev.ua*

³Research Institute Nikolaev Astronomical Observatory, Observatornaya St. 1, Mykolaiv, 54030, Ukraine, *yuri@nao.nikolaev.ua*

⁴Baldone Observatory, Institute of Astronomy, University of Latvia Baldones Riekstukalns, Rigas raj., LV 2125, Latvia, *ilgmars@latnet.lv*

ABSTRACT. The Pleiades Star Cluster (M45) is one of the most studied star clusters in the galaxy. At the same time as part of the Pleiades are many long-period variable stars, including flashing that need further study. Recent work on the processing of photographic images of the Pleiades obtained at different observatory revealed a number of star clusters with large variations in coordinates, the reason you want to understand. Collection of UkrVO unified digital archive contains a number of plates with images of the stars of the Pleiades obtained on different instruments. Processing of this material allows to test out standard programs for digital astronomical images processing. Also we will add information about variable stars and will improve the coordinates and proper motions of cluster stars. Selected material covers the period 1909 – 1999 years. The plates have different margins, scale, number of stars on images and obtained limiting magnitude. Exactly this diverse set of options lets you to be sure of results.

Keywords: virtual observatory tools – astrometry – techniques: data analysis: star cluster – M45.

1. Introduction

Pleiades Star Cluster (M45) is one of the most studied star clusters in the Galaxy, but still continues its active research: rotation, inflation, and lithium in the Pleiades (Somers, 2015); search for free-floating planetary-mass objects in the Pleiades (Zapatero Osorio, 2014); empirical isochrones, luminosity, and mass functions of the Pleiades cluster (Bouy, 2015).

The Pleiades became the object of interest for digitization: possible Cyclic Activity of the Pleiades' Star (Hambaryan, 2003); for studying the long-term behaviors of the Pleiades flare stars (Tsvetkov, 2002); search for extrasolar Planets in the Pleiades (Yamamoto, 2013).

We are considering two problems: testing of a comprehensive program digitized images processing (Andruk, 2010) and search for changes in the laws of time astrometric and photometric data for the stars of the Pleiades.

2. Plates with Pleiades Star Cluster in UkrVO archives and taken for processing

Now Joint Electronic Archive of UkrVO (Vavilova, 2012) has 339 M45 images in 16 particular archives, which were obtained in the 8 observation points.

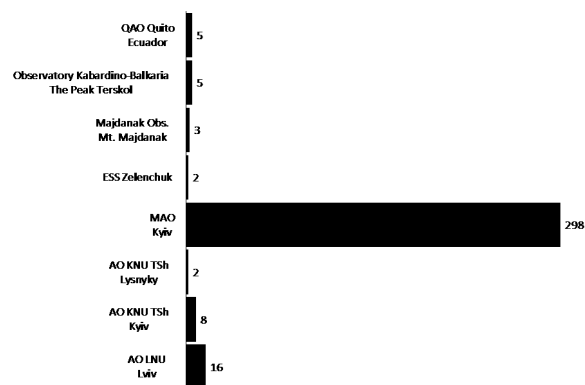


Figure 1: Distribution of observation points data

In addition, we have included in the processing 38 plates of Research Institute “Nikolayev Astronomical Observatory” and 60 plates of Baldone observatory of Institute of Astronomy, University of Latvia.

Photographic plates were scanned using different scanners. Digital images processing was carried out by one and the same comprehensive program. Already wear processed 36 plates for different instruments.

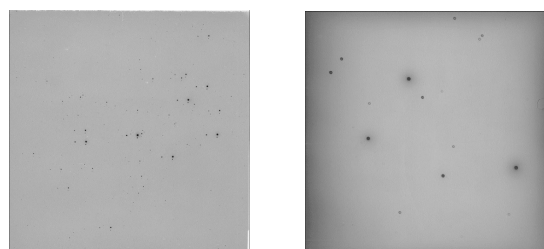


Figure 2: Scan images of plates with different scales.

Work began recently, made only its initial stage, was processed only 1/10 of the planned material, continues to develop a standard approach to the accurate identification of the stars in a large number of objects in an image, were obtained astrometric and photometric data.

Table 1. Number of plates for each telescope.

Instrument	AO	D	F	N
		m	m	
Zeiss Zonal Astrograph	NAO	0,1	2,0	10
Zeiss-600	Terskol	0,6	7,5	4
Double Astrograph Repsold	AOKNU	0,2	4,3	2
Double Long Focus Astrgraph	MAO	0,4	5,5	9
Double Wide Angle Astrograph	MAO	0,4	2,0	3
Baldone Schmidt Telescope	BAO	1,2	2,4	4
Three-Camera Astrograph	MAO	0,1	1,7	2
Unknown	AOKNU			2

3. Preliminary results

The scans processing was carried out using MIDAS/ROMAFOT software package, with the individual flat-field calculated for each plate separately (Andruk, 2005; Andruk, 2014).

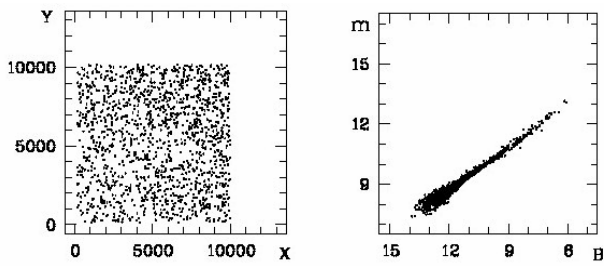


Figure 3: Digital image and the dependence of the magnitude for plate N0078.

The processing of digital images of various sources has been described repeatedly (Kazantseva, 2015; Protsyuk, 2014). We used the standard method of complex processing and compared the results virtually the same region of the sky for the various epochs and observation conditions.

Table 2. The internal accuracy for all objects on the coordinates.

Instrument	mean rmsRA	mean rmsDE
Zeiss Zonal Astrograph	0,135"	0,150"
Zeiss-600	0,283	0,090
Double Astrograph Repsold	0,089	0,093
Double Long Focus Astrograph	0,056	0,050
Double Wide Angle Astrograph	0,096	0,087
Baldone Schmidt Telescope	0,129	0,108
Three-Camera Astrograph	0,092	0,087
Unknown	0,541	0,493

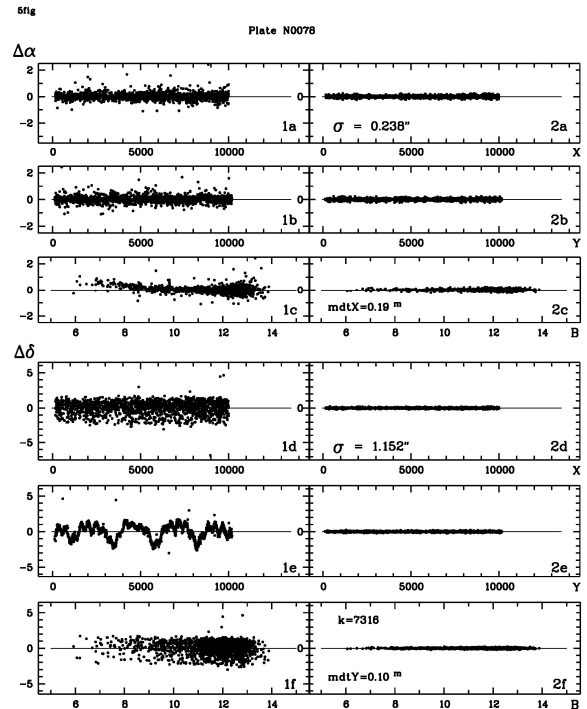


Figure 4: The residual differences in coordinates after the program corrections for plate N0078.

Preliminary analysis of the material obtained allows us to make some conclusions:

- Standard image processing of brightest stars requires improvement.
- Photometric data require additional account information (filters, emulsion, exposure time, etc.).
- Preparation of O-C coordinates on different epochs of observations demonstrate the manifestation of his own movements, which are known for certain stars reach 21 mas/year for RA and 47 mas/year Dec.

References

Andruk V.M. et al.: 2010, *Kinem. Phys. Cel. Bodies*, **26**, N3, 75.
 Andruk V.M. et al.: 2005, *Kinem. Phys. Cel. Bodies*, **21**, N5, 396.
 Andruk V.M. et al.: 2014, *Odessa Astron. Publ.*, 27/1, 53.
 Bouy H. at al.: 2015, *A&A*, **577**, id. A148, 17.
 Hambaryan V. et al.: 2012, *PASRB*, **11**, 259.
 Kazantseva L.V. et al.: 2015, *Kinem. Phys. Cel. Bodies*, **31**, N1, 58.
 Protsyuk Yu.I. et al.: 2014, *Odessa Astron. Publ.*, 27/1, 59.
 Protsyuk Yu.I. et al.: 2014, *Odessa Astron. Publ.*, 27/1, 61.
 Somers G. et al.: 2015, *MNRAS*, **449**, N 4, 4131.
 Tsvetkov M. et al.: 2005, *Kinem. Phys. Cel. Bodies, Supl.*, **5**, 567.
 Vavilova I.B. et al.: 2012, *Kinem. Phys. Cel. Bodies*, **28**, N2, 85.
 Yamamoto K. et al.: 2013, *PASJ*, **65**, N 4, 19
 Zapatero Osorio M. R. et al.: 2014, *A&A*, **568**, id A77, 16.

CROSS-MATCHING OF VERY LARGE CATALOGS

M. V. Martynov, D. V. Bodryagin

Research Institution “Mykolaiv Astronomical Observatory”
Observatorna St., 54030, Mykolaiv, Ukraine

ABSTRACT. Modern astronomical catalogs and sky surveys, that contain billions of objects, belong to the “big data” data class. Existing available services have limited functionality and do not include all required and available catalogs. The software package ACrId (Astronomical Cross Identification) for cross-matching large astronomical catalogs, which uses an sphere pixelation algorithm HEALPix, ReiserFS file system and JSON-type text files for storage, has been developed at the Research Institution “Mykolaiv Astronomical Observatory”.

Keywords: database, catalogs, virtual observatory.

1. Introduction

Cross-identification is a powerful tool which is used for solving many astrometric and astrophysical problems. Numerous programs and Web services (like CDS X-Match Service <http://cdsxmatch.u-strasbg.fr/xmatch>) has been developed for this in frames of Virtual Observatory (VO). Unfortunately, their functionality and options are restricted by next reasons:

- the limited list of catalogs which are available for cross-identification;
- rigorously specified object identification algorithms;
- some restrictions and difficulties in cross matching and uploading/downloading of large (hundreds of thousands or more objects) user data sets.

2. Cross-matching of the astronomical data with the software package ACrId (Astronomical Cross Identification)

This software product is a package of console scripts written in the Python programming language. There were implemented the following steps:

- 1) Data preparation (preprocessing and pixelation of selected catalogs);
- 2) Cross-identification of the objects;
- 3) Output and saving of the cross-matching results in the user formats.

Most of astronomical catalogs and surveys are available in two types: text (XML-format VOTable) or binary and have different patterns of records. The first stage is carried out to convert the selected digital catalogs into a common format of the JSON-type text file. This

conversion allows you to describe all the different catalogs with help of uniform rules and makes easier adding other catalogs and lists of absolutely various structure, origin and type. Standard form of catalog description includes three files

- 1) General description;
- 2) List of files of the catalog (original, before pixelation);
- 3) Description format.

The next stage of the preparation data of “big data” type to cross-matching consists in partitioning the selected file into separate fragments. The pixelation of the sphere is frequent and efficient solution of many problems because in astronomy we have deal with data distributed on the celestial sphere. Pixelation means subdivision spherical surface on numbered fragments of equal area. Usage of pixelation allows not only to solve the problem of celestial map representation and analysis, but is also essential by constructing databases that require quick search of celestial objects. Pixelation also does possible to use several PC simultaneously for cross-matching of large surveys. There are some systems of pixelation. We used hierarchical grid with equal squares HEALPix (Hierarchical Equal Area isoLatitude Pixelization) (Górski et al., 2005). Pixelation sphere has a number of advantages over the previously used method of the sphere division using the equatorial coordinates. However, there is a technical problem when we divide sphere into pixels to place them on the HDD (if the pixel size is about half an arc minute, then their number will exceed 805 million). Not every system can create so many files. For example, the NTFS file system (OS MS Windows) allows you to create more than 4 billion files, but the creation of empty 805 million files of zero size takes about 320 GB of disk space. You can't also change the maximum number of files available without formatting the partition in the ext3 and ext4 file systems (OS Linux) and there is need more than 200GB (depending on the size of the cluster partition) for the creation of 805 million empty files. It turned out that the best choice for solving the problem is ReiserFS file system, which was designed specifically to work with a lot of small files. There are no restrictions on the maximum available number of system files and 805 million zero size files occupy only 82 GB. After the “zero” pixelation sphere, that is, after the creation of zero

size files, it is necessary to fill in their by respective objects from the catalogs. As noted earlier list of catalogs can be arbitrary because the unified files JSON-type text format were created for all catalogs before pixelation process. The actual process filling the pixels can last from several hours to several weeks depending on the computing capacity and size of the input catalog. It should be noted that this version of the data preparation for cross-identification requires high-capacity HDD for long-term storage of the results of catalogs pixelation. The advantage of this option is lack of necessity to build additional indexes to locate the data quickly, since the role of the search tree plays the file system itself in which files and folders are named and arranged so that they are playing the role of "frozen" fast path to data.

In general, the task of cross-identification astronomical objects in different catalogs is search the same source in some lists of coordinates. The main problems in this case are different epochs of observations and different limiting magnitudes of the catalogs. The first one requires taking account proper motions and their error. This leads to the fact that the use of only coordinate criterion for identification does not always yield successful results. The object may be absent in this neighborhood, or there may be several candidate objects from another catalog. Preliminary pixelation allows us to carry out a so-called "cascade" cross-identification with using more than two catalogs. This enables the construction of additional filters, which ultimately reduces the error of false identifications.

The ACrId software package has a wide range of applications in our observatory. HealPix pixelation of some basic astrometric catalogs, including the catalog of XPM (Fedorov et al., 2009), which is not in the database CDS, have performed. The results are used to calculate and the study of the proper motions of stars.

Usage the software allowed us to obtain the first version of the compiled catalog of stars with high proper motion (HPM) on the whole celestial sphere (about 968,251 objects). The distribution of the stars in the equatorial coordinates is shown in Figure 1.

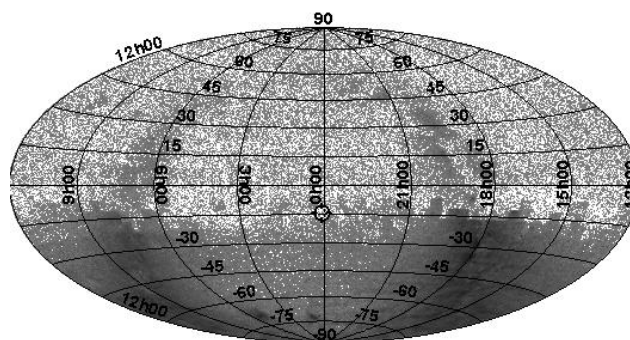


Figure 1: Distribution HPM stars on celestial sphere in equatorial coordinates.

As can be seen from the fig. 1, there are a huge number of HPM stars with proper motion more than 150mas/year on the Southern hemisphere. To validate this result, it is planned to get a second version of the catalog using the represented software with an expanded list of modern celestial catalogs and surveys.

3. Conclusion

The software package of extra-large astronomical catalogs pixelation and cross-identification "ACrId" is used to division the celestial sphere on small plots of equal area (pixels) for the following usage pixel numbering as search index. Program "ACrId" allows you to cross-matching an arbitrary number of catalogs with any format and carry out multi-stage objects cross-identification for the search common objects and determinations their parameters.

References

- Górski K. M.: 2005, *AphJ*, **622**, 2, 759.
 Fedorov P.: 2009, *MNRAS*, **393**, 133.
<http://cdsxmatch.u-strasbg.fr/xmatch>

DETERMINATION OF PROPER MOTIONS OF CIRCUMPOLAR STARS BY USING IMAGES FROM UKRVO PLATE ARCHIVES

Yu. Protsyuk¹, V. Andruk², A. Mazhaev¹, O. Kovylianska¹, S. Protsyuk¹, V. Golovnya²

¹ Research Institute: Nikolaev Astronomical Observatory (RI NAO), Ukraine,
yuri@nao.nikolaev.ua, mazhaev@nao.nikolaev.ua

² Main Astronomical Observatory (MAO) of National Academy of Sciences (NAS),
Ukraine, andruk@mao.kiev.ua, golov@mao.kiev.ua

ABSTRACT. UkrVO plate archives contain information obtained at different time periods and in different observatories for the same regions of the sky [3, 5, 6, 7, 8]. It allows us to carry out joint processing of plates and to receive new results for interesting objects. To obtain proper motions of stars in circumpolar areas, we selected 34 photographic plates from the RI NAO archive and 161 plates from the archive of the MAO NAS. A mean epoch difference between the plates from these archives is 55 years. Scanning of the plates and data processing were independently carried out by both observatories. A catalog of equatorial positions for 195 thousand stars up to 15^m was compiled in the RI NAO (black dots in Fig. 1). A catalog of equatorial positions for 1050 thousand stars up to 16.5^m was compiled in MAO (gray dots in Fig. 1). A comparison of positions for common stars contained in these catalogs was conducted. A catalog of proper motions for 30 thousand common stars up to 15^m was compiled using these two input catalogs. The obtained result suggests the advisability of processing of all observations to receive proper motions of stars up to 14-15^m in the declination zone of 65° to 90°.

Keywords: Astrometry – Proper motions – Astronomical data bases – Catalogs – Virtual observatory tools.

1. Introduction

We selected photographic plates containing circumpolar stars in declination zone of 65° to 90°. All plates in the RI NAO archive were obtained with the Zonal Astrograph (ZA, D/F = 12/204, 101"/mm, FoV 5°x5°). Selected plates from the MAO archive were obtained with the Double Wide-angle Astrograph (DWA, D/F = 40/200, 103"/mm, FoV 8°x8°). The plates were obtained with up to four fold overlap in MAO and usually without overlapping in the RI NAO. Therefore, the same star was observed two to four times in the MAO and one or two times in the RI NAO.

2. Virtual observatory tools

We compiled both catalogs in accordance with the VOTable standard, which was produced and endorsed by the Executive Committee of the International Virtual Observatory Alliance. Usage of the VOTable standard allows us to apply wide range of VO tools to visualize and examine tabu-

lar data. For example, Aladin sky atlas allowed us to visualize obtained equatorial positions, which are shown in Figure 1. Tool for OPERations on Catalogues And Tables (TopCat) allowed us to carry out cross correlation of stars contained in different astrometric catalogs and to examine linear correlation of proper motions for found common stars.

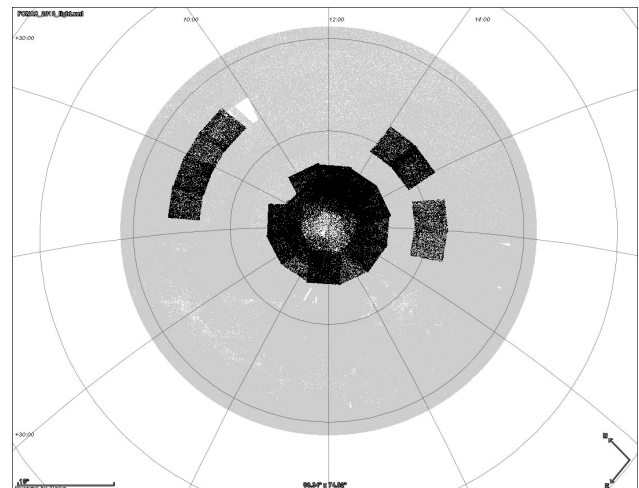


Figure 1: Equatorial positions of stars from two catalogs.

3. Data processing

The mean first epoch of 34 selected plates is 1930.3. Total number of plates for the first epoch of observations of circumpolar stars in the RI NAO archive is 196. The mean second epoch of 161 selected plates is 1985.7. The MAO archive contains about 2000 plates in the declination zone of 65° to 90°. These plates were obtained during the observation campaign of FON project. The Russian or Ukrainian acronym FON stands for Photographic Survey of the Northern Sky.

Each selected plate from the MAO archive was scanned only once with a resolution of 1200 dpi. Each selected plate from the RI NAO archive was scanned five or six times with a resolution of 1200, 1500 or 1600 dpi. As the result of plate scanning at the MAO, we obtained two to four equatorial positions for every star. The number of positions depends on number of available plates, which cover a given region of interest (ROI) in the sky. As the result of plate scanning at the NAO, we obtained six to twelve equatorial positions for each

star. The number of positions depends on number of scans for one or two available plates in a given ROI. Both observatories conducted the raw image processing by using the same procedures and MIDAS/ROMAFOT package to obtain (X, Y) coordinates [4]. Both observatories carried out astrometric reduction in the Tycho-2 system by using different software, namely 00plate in MAO and plate_gr in NAO [1] to compare obtained results of data processing.

4. Comparison of catalogs

The catalog of positions for 195 thousand stars up to 15^m was compiled in the RI NAO. The catalog of positions for 1050 thousand stars up to 16.5^m was compiled at the MAO. Numbers of stars versus magnitude are shown in the left part of Figure 2 as empty and filled circles for the RI NAO and the MAO catalogs respectively. Common ROI in the sky for both catalogs are shown in Figure 1. Numbers of stars in the common ROI are shown in the right part of Figure 2 as filled and empty circles for the RI NAO and the MAO catalogs respectively.

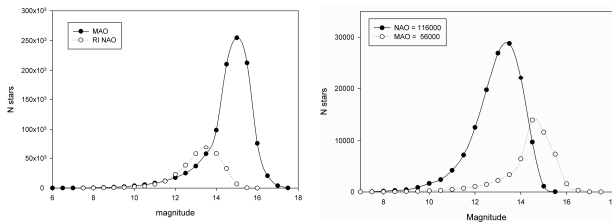


Figure 2: Number of stars for two input catalogs (left) and number of stars in common ROI (right) vs magnitude.

Standard deviations (SD) of positions of input catalogs are $\sigma_\alpha = \pm 0.24''$ and $\sigma_\delta = \pm 0.23''$ for the MAO catalogue, and $\sigma_\alpha = \pm 0.10''$ and $\sigma_\delta = \pm 0.17''$ for the RI NAO. Inner accuracies of equatorial positions versus declination are shown in Figure 3 for both input catalogs. The plate_gr software used in NAO provides us better results than 00plate software used in MAO, especially near 90° (Figure 3).

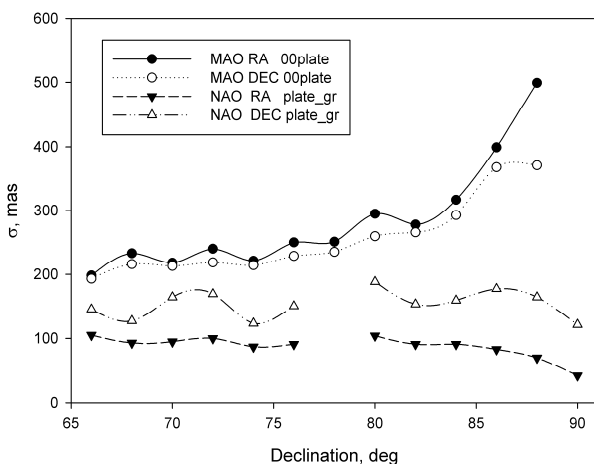


Figure 3: The SD of equatorial positions vs declination.

Using these two input catalogs as the first and the second epoch of observation, we obtained a resulting ZA_DWA catalog of positions and proper motions for about 30 thousand common stars. Number of stars versus magnitude for the ZA_DWA catalog is shown in the left part of Figure 4. We calculated inner accuracies of equatorial positions for

the ZA_DWA catalog. The SD of positions in right ascension (RA) and declination (DE) are ± 73 mas for both equatorial coordinates. The SD of equatorial positions versus magnitude are shown in the right part of Figure 4.

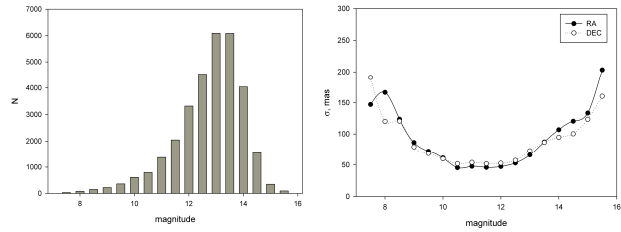


Figure 4: Number of stars (left) and SD of positions (right) in the ZA_DWA catalog vs magnitude.

We compared proper motions for the common stars in the ZA_DWA and Tycho2 catalogs. TopCat allowed us to find common stars for these catalogs and to calculate parameters of linear correlation (LC) for proper motions of stars in RA – $\mu_\alpha \cdot \cos\delta$ and DE – μ_δ . The coefficients of LC in $\mu_\alpha \cdot \cos\delta$ (Figure 5) and μ_δ are equal to 0.92 and 0.94 respectively for about 16 thousand common stars.

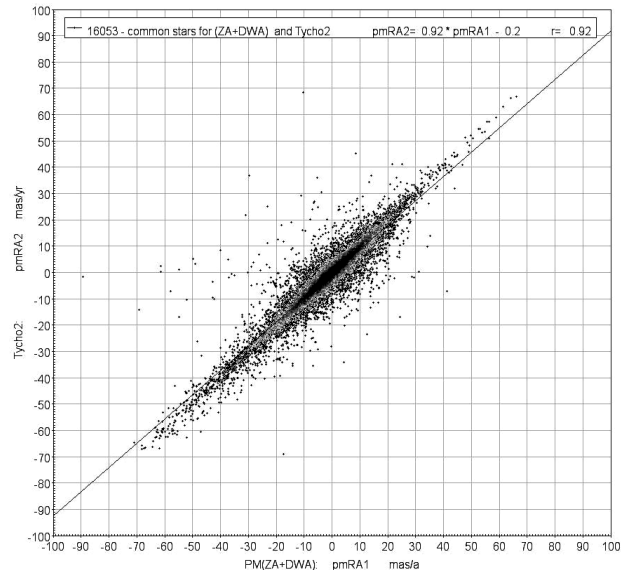


Figure 5: LC of $\mu_\alpha \cdot \cos\delta$ for our and Tycho2 catalogs.

The obtained result suggests the advisability of processing of all observations to receive proper motions of stars up to 14-15^m in the declination zone of 65° to 90°.

Acknowledgements. This research has made use of "Aladin sky atlas" developed at CDS, Strasbourg Observatory, France 2000A&AS..143...33B and 2014ASPC..485..277B TopCat as an interactive graphical viewer and editor for tabular data were helpful in this research work (2005ASPC..347...29T).

References

2. Andruk V. et al.: 2016, *KPCB*, **32**, 1 (in press).
3. Andruk V. et al.: 2014, *Odessa Astron. Publ.*, **27/1**, 53.
1. Protsyuk Yu. et al.: 2014, *Odessa Astron. Publ.*, **27/1**, 59.
4. Protsyuk Yu. et al.: 2014, *KPCB*, **30**, N6, 296.
6. Protsyuk Yu. et al.: 2014, ISBN: 978-80-7080-918-1, 131.
5. Vavilova I. et al.: 2014, ISBN: 978-80-7080-918-1, 8.
7. Vavilova, I.B. et al.: 2012, *KPCB*, **28**, N2, 85.
8. Vavilova, I.B. et al.: 2012, *BA*, **21**, N3, 356.

DATA PROCESSING OF PLATES CONTAINING IMAGES OF URANUS AND NEPTUNE FROM UKRVO DIGITAL ARCHIVE: STRUCTURE, QUALITY ANALYSIS

Protsyuk Yu.¹, Yizhakevych O.², Kovylianska O.¹, Protsyuk S.¹, Andruk V.², Kashuba S.³, Kazantseva L.⁴

¹ Research Institute: Nikolaev Astronomical Observatory, Ukraine, yuri@nao.nikolaev.ua

² Main Astronomical Observatory, National Academy of Sciences, Ukraine, andruk@mao.kiev.ua

³ Astronomical Observatory, Odessa National University, Ukraine, sv.kashuba@gmail.com

⁴ Astronomical Observatory, Kyiv National University named after T. Shevchenko, Ukraine, kazl@ukr.net

ABSTRACT. To use accumulated resources of UkrVO digital archive, analysis of the available photographic plates containing images of Uranus and Neptune was conducted. Data processing of selected plates was also carried out to provide an estimate of positional precision and accuracy. Archives of the Research Institute: Nikolaev Astronomical Observatory (NAO), Main Astronomical Observatory of National Academy of Science (MAO), Astronomical Observatory of Odessa National University (AO ONU), Astronomical Observatory of Kyiv National University (AO KNU) were used. Numbers of plates containing images of Uranus and Neptune are, respectively, the following: 220 and 218 plates in NAO, 64 and 35 plates in MAO, 54 and 44 plates in AO ONU, 3 and 1 in AO KNU. Plates of NAO and MAO have 2 or 3 exposures per plate, and other plates have only one exposure per plate. The epoch of observation for most plates is 1960 to 1998, and for only one plate is 1908.

All plates were scanned with the resolution not less than 1200 dpi. Each plate of NAO was scanned 5 to 6 times. Plates containing images of Uranus and Neptune were, respectively, scanned 618 and 952 times in NAO. All plates of other observatories were scanned only once. Raw image processing for scans containing images of Uranus and Neptune was conducted for all scans obtained in observatories. (X, Y) coordinates, (I) intensities and FWHM values were obtained for images of all objects.

Star identification for scans containing images of Uranus and Neptune was, respectively, conducted for 600 and 936 scans in NAO and for 71 scans in MAO. Coordinates of all objects were obtained. Positional accuracy of reference stars was estimated for 244 plates of NAO and 66 plates of MAO, and has value of 0.08"-0.26".

Keywords: astronomical data bases – astrometry – methods: data analysis – catalogs

1. Introduction

In 2014 we used Joint Digital Archive (JDA) database of UkrVO (Vavilova et al., 2012a, 2012b) to find and recalculate all Ukrainian observations of Pluto (Kazantseva et al., 2015). In 2015 we continue this work and analysis of the available photographic plates in JDA, containing images of Uranus and Neptune, was conducted.

Archives of the NAO (Zonal Astrograph (ZA, D/F=12/204, 101"/mm), MAO (Double Wide-angle Astrograph (DWA, D/F = 40/200, 103"/mm), Double Long Focus Astrograph (DLFA, D/F=40/550, 37"/mm)), AO ONU (Seven Wide Angle Astrograph (SWA, D/F=12/60, 313"/mm)) and AO KNU were used. Then, we start scanning of this plates and make processing of a received images. Using different kind of software we obtained coordinate of the planets and comparing results with well known ephemerides.

2. Structure of archive and plate scanning

We found more than 600 plates with Uranus and Neptune in UkrVO. Structure of plate archives is shown in Table 1.

Table 1. Structure of plate archives

	Telescope, epoch	Uranus, plates	Neptune, plates
NAO	ZA 1961-1998	220	218
MAO	DLFA, DWA, Z600 1963-1991	64	35
AO ONU	SWA 1960-1989	42+12	32+12
AO KNU	AZT8, DAMR 1988, 1908	3	1

All plates in NAO and MAO have 2 or 3 exposures per plate. Another one have only one exposure. 12 plates of AO ONU have Uranus and Neptune in same plate.

After searching in JDA all plates were scanned with the resolution not less than 1200 dpi (part of plates in NAO were scanned with the resolution 1600 dpi). Current status of the scanning shows in Table 2.

Table 2. The current status of the plate scanning

	Uranus, plates	scanned, plates/scans	Neptune, plates	scanned, plates/scans
NAO	220	104/618	218	160/952
MAO	64	39/39	35	35/45
AO ONU	42+12	48/54	32+12	38/38
AO KNU	3	3/3	1	1/1

Each plate of NAO was scanned 5 to 6 times without turning. Plates containing images of Uranus and Neptune were, respectively, scanned 618 and 952 times in NAO. All plates of other observatories were scanned only once (except one plate of MAO and AO ONU with 6 scans for testing purpose).

3. Data reduction and quality analysis

For raw image processing we used MIDAS/ROMAFOT software (Andruk et al., 2010; Protsyuk et al., 2014a, 2014b). Raw image processing for scans containing images of Uranus and Neptune was, respectively, conducted for 618 and 952 scans in NAO and for all scans obtained in other observatories. (X, Y) coordinates, (I) intensities and FWHM values were obtained for images of all objects. The current status of raw image processing shows in third column of Table 3 (considering that 1 plate in NAO usually have 6 scans).

Table 3. The current status of the raw image processing and identification

	scanned, plates	processed in MIDAS, plates	identified, plates	no identified, plates
RI NAO	264	264	244	8
MAO	74	74	66	8
AO ONU	86	85	2	-
AO KNU	4	4	1	-

For star identification we used two different software package for LINUX and WINDOWS system (Protsyuk et al., 2014; Andruk et al., 2016). Star identification for scans containing images of Uranus and Neptune was, respectively, conducted for 600 and 936 scans in NAO and for 71

scans in MAO. Some of plates no identified due to quality of images and errors in observation. After identification coordinates of all objects on plates were obtained in Tycho-2 system (Protsyuk et al., 2014; Andruk et al., 2016). Positional accuracy of reference stars shows in Table 4. In first column scale of one pixel in seconds of arc specified. In columns from 4 to 6 standart deviation (SD) of planet's position (in arcsec and pixel) and magnitude shows. Table 4 shows, that SD of planet's position is in ranges 0.10-0.12 pixel in main part of archive, that corresponds depending on the scale from 0."08 to 0."26. Plates of AO ONU have large scale and big distortion near the border, so, errors in seconds of arc also big.

Table 4. The current status of the reduction

	Proc., plates	Ident., plates	SD of planet RA position, arcsec pix	SD of planet DEC pos., arcsec pix	SD of mag
NAO 2.1 1.6	264	244	0.19 0.11	0.19 0.11	0.01-0.07
MAO DLFA 0.8			0.09 0.11	0.08 0.10	0.01-0.03
MAO DWA 2.2	74	66	0.22 0.10	0.26 0.12	0.04-0.05
AO ONU 16.9	85	2	2.2 0.13	2.7 0.16	0.01-0.03
AO KNU	4	1	-	-	

Since the NAO has a 6 scans for each plate we obtained inner accuracy of planets coordinate. Distribution of quantity of SD of positions in seconds of arc shows on Fig. 1 for Uranus and on Fig. 2 for Neptune.

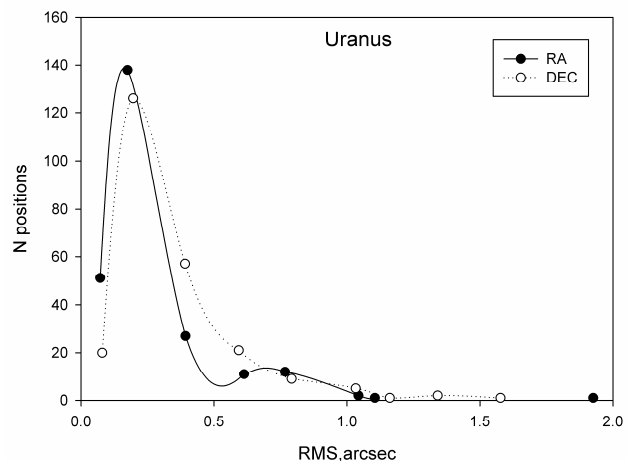


Figure 1: Distribution of quantity of SD of Uranus position in seconds of arc

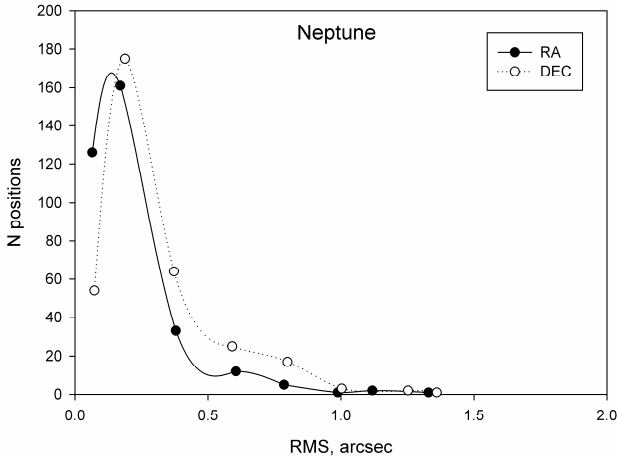


Figure 2: Distribution of quantity of SD of Neptune position in seconds of arc

Some plates of NAO have 5 exposures, so, we obtained track of planet position during time of observation (Fig. 3, Fig. 4).

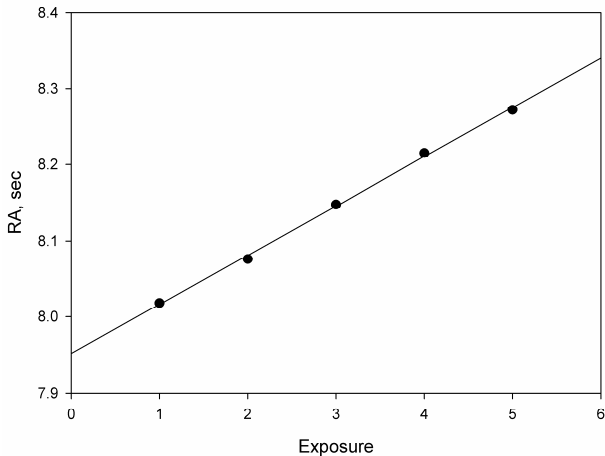


Figure 3: Track of the Uranus in RA direction on one of a plates

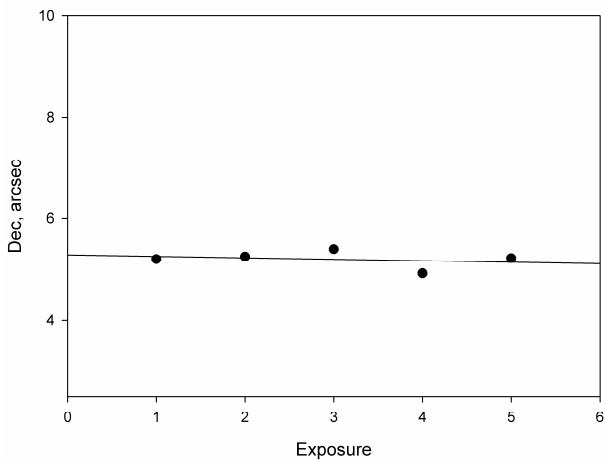


Figure 4: Track of the Uranus in DEC direction on one of a plates

For all moments of planet's observation we downloaded planet's position from The Institut de Mecanique Celeste et de Calcul des Ephemerides (IMCCE) ephemeris website and were compared our results with well known ephemerides.

4. Conclusion

We were found in UkrVO archive 627 plates with 1701 exposures of the Uranus and Neptune. Were scanned and processed in MIDAS software 428 plates on date. And were identified 313 plates with 932 positions of Uranus and Neptune. Obtained positions were compared with known orbital theories and were received (O-C) for them.

For next period we will modify program for processing AO ONU observations, finishing scan, reduction and identification of all UkrVO plates with Uranus and Neptune. Also we shall include satellites of the planets in workset and using of those coordinates for improvement of the orbital theory of the planets and their satellites.

Acknowledgements. The authors are thankful to anybody who has read this contribution to the end.

References

- Andruk V.M. et al.: 2010, *Kinem. Phys. Cel. Bodies*, **26**, N3, 146.
- Andruk V. et al.: 2016, *Kinem. Phys. Cel. Bodies*, **32**, N1 (in press).
- Kazantseva L.V. et al.: 2015, *Kinem. Phys. Cel. Bodies*, **31**, N1, 58.
- Protsyuk Yu.I. et al.: 2014a, *Kinem. Phys. Cel. Bodies*, **30**, N6, 54.
- Protsyuk Yu. et al.: 2014b, *Odessa Astron. Publ.*, **27/1**, 59.
- Vavilova I.B. et al.: 2012a, *Kinem. Phys. Cel. Bodies*, **28**, N2, 85.
- Vavilova I.B. et al.: 2012b, *Baltic Ast.*, **21**, N3, 356.

CREATION OF LARGE CATALOGUES BY USING OF VIRTUAL OBSERVATORIES

Yu.I.Protsyuk, O.M.Kovalchuk

Research Institute “Nikolaev Astronomical Observatory”,
Mykolaiv, Ukraine, yuri@nao.nikolaev.ua

ABSTRACT. We developed an application program to search images in the registers and databases of Virtual Observatories and to download them to local computer. The program has the ability to process XML file in VO Table format to generate links to images, as well as to work directly with the astronomical servers. To improve the efficiency for downloading of large number of images, we used multi-threaded mode. The program runs under the Windows operating system. Using the program in 2014 year, we found and downloaded more than 145 thousand of images of open clusters, having total volume of about 300 GB. Total download time was about 7 days. To process the downloaded images, we created and configured a complex of 10 virtual machines on two PCs for parallel image processing by using Astrometrica program. Total processing time was about 14 days. An application program was also created to analyse the obtained results, which were used to create four catalogues of stellar coordinates at the average epoch of 1953 to 1998. The total number of stars in the catalogues is more than 35 million. The standard error is $0.04''$ to $0.07''$, and the average number of observations is 4 to 6. The catalogs are used to improve proper motions of stars in and around of open clusters.

Keywords: Astrometry – Astronomical data bases – Catalogs – Virtual observatory tools.

1. Introduction

In recent years through the development of panoramic receivers and information technology astronomers must respond to an avalanche increasing amount of data that contain information on many celestial objects at different wavelengths. Existing and future huge databases can not afford to use in one isolated institution, but provides such opportunities for international cooperation and organization wide access to collected data. International Virtual Observatories Alliance (IVOA) created to pool resources astronomical data at the national and international levels and provide convenient unified search engine to access the data. Since 2011 Ukrainian Virtual Observatory (UkrVO) included to IVOA (Vavilova et al., 2010, 2011, 2012).

New scientific results can be obtained using data accumulated on different instruments for a long time. One example of this is the study of open clusters (OC) of our Galaxy, formations of stars that have a common origin. It helps

solve a wide class of problems concerning formation of stars, structure and evolution of the Galaxy and others. Currently, the number of OC estimated near one hundred thousand and only a small percentage of them have been studied in detail. In particular, we don't know the exact distances and middle proper motions of about half of all known OC.

To solve this problem at the Research Institute: Nikolaev Astronomical Observatory (RI NAO) we studied of stars in regions around the OC several last years using the achievements of a decade of work on the creation and implementation of modern information technologies in astronomy, including the UkrVO creation (Protsyuk et al., 2007; Mazhaev et al., 2014; Vavilova I. et al.: 2010, 2011, 2012, 2014). With the assistance of our own observations and data from IVOA registries received at different times and at different telescopes, an accurate catalogs of positions and proper motions of stars around OC in creating (Protsyuk et al., 2014).

2. Develop an application program to search images in VO databases

Search and downloading of astronomical images obtained at different times and on different instruments through specialized astronomical websites or through existing specialized software requires a big amount of manual work and time if there is a need for a large number of observations. For this purpose we developed methodics and software to search for images in the IVOA registers and astronomical databases (DB) and automatically download them to computer. Software provides features for finding information about astronomical images and automatically download them to your computer when matching predetermined criteria. Search criteria, given in a prepared list, include the angular coordinates and search radius. The program has the ability to process XML files in VO Table format to create links to the images and work directly with astro-servers. Software running in the Windows operating system and consists of several functional modules – namely: content downloads module, module of content analysis of Web page and formation of links to files and image downloads module. The program works in multithreaded mode and provides full control of downloading and processing of possible network errors. Download speed is limited only by the speed of the Internet connection. The modular construction principle of the program provides high stability that is essential for automatic downloading large file sets.

3. Processing and analysis of the obtained images

We used developed program for 500 selected fields around OC and were found and downloaded more than 145 thousand images in 2014. Images were obtained at various of telescopes from 1952 to 1999 with total capacity near 300GB. Total duration of the work of program was about 7 days of continuous operation. By automating the process productivity increased about 200 times.

For processing the images arrays we created complex of 10 virtual machines on 2 PCs, which is configured for parallel automatic processing of large volumes of observations using Astrometrica (<http://www.astrometrica.at>) with additional program for automation. Images were downloaded from Aladin Images Server (<http://aladin.u-strasbg.fr>) for infrared photometric reviews 2MASS (Skrutskie M.F. et al., 2006.) and DENIS (DENIS Consortium, 2005) and from the server <http://archive.stsci.edu> for The Digitized Sky Surveys (DSS) array. Also we include near the 20 thousand own observations at the telescope Mobitel KT-50. The UCAC4 catalog (Zacharias et al., 2013) were used for all reduction as reference one. The total number of processed images – more than 160 thousand. Were received coordinates for more than 235 million objects with good precision. For processing of the entire array of images with 10 virtual machines took about 14 full days job.

Also software for the analysis of the results were created. The accuracy analysis of (O-C) (UCAC4 reference catalog) depending on the Mag, Dec, Ra and Color band. Calculation of the standard deviation and the mean (O-C) made in 3-iteration. This number of iterations is selected because the number of exceptions by the criterion 3σ in third iteration decreases sharply. Part of the results of calculations for one source (2MASS) set out in the form of a graphs of Figures 1-4.

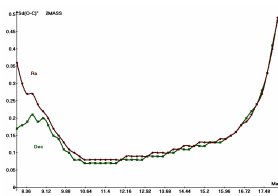


Figure 1: Dependence of the standard deviation (SD) of O-C to magnitude

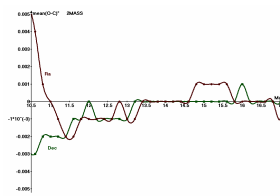


Figure 2: Dependence of the mean O-C to magnitude of O-C to magnitude

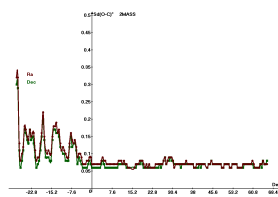


Figure 3: Dependence of the SD of O-C to declination

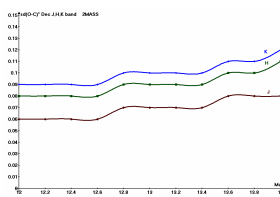


Figure 4: Dependence of the SD of O-C in declination to magnitude in bands J, H, K

We made analysis of accuracy of the results from all 4 sources by magnitude, coordinates and color band.

4. Creation and analysis of the catalogs

Image processing conducted using the program Astrometrica and additional program, created in the RI NAO, for batch mode processing. Were processed over 160 thousand images with UCAC4 reference catalog. All data is divided into five parts and we obtained five catalogs at different epochs.

First consider the catalog, obtained from 2MASS set. We received more than 135 million objects on it in sites containing OC. With this data we obtained astrometric catalog of over 19.7 million stars (9-18.5)^m (Fig.5) which observed three and more times with the average number of observations (ANO) of a star about 6.3 times and the average accuracy of catalog position (ACCP) in right ascension (RA) 40 mas and declination (DEC) 39 mas (Fig. 6). The average epoch of catalog is 1998.7.

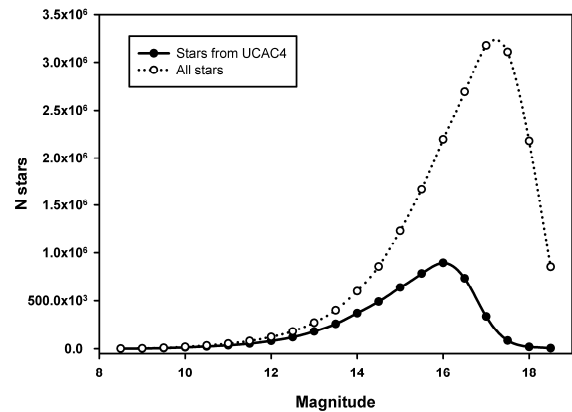


Figure 5: Distribution of stars of 2MASS set catalog to magnitude

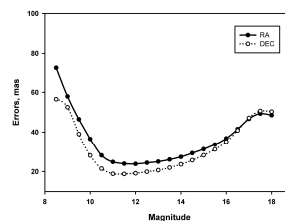


Figure 6: Dependence of precision of 2MASS set catalog to magnitude.

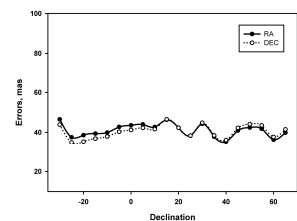


Figure 7: Dependence accuracy of 2MASS set catalog to DEC

As shown in Figure 7 the accuracy distribution to declination without major deviations. In comparison, the reference catalog on the same data, which includes over 5.1 million stars from UCAC4 that were observed 3 or more times with ANO of a one star about 4.9 times have ACCP 32 mas by RA and 28 mas by DEC.

Next consider the catalog, obtained from the DENIS set. We received more than 24.5 million objects in regions, containing OC. With this data we obtained astro-

metric catalog of more than 3 million stars (9-18.5)^m (Fig. 8) which observed three and more times with the ANO of a star about 5.2 times and AACP in RA 52 mas and DEC 68 mas (Fig. 9). The average epoch of catalog is 1998.8.

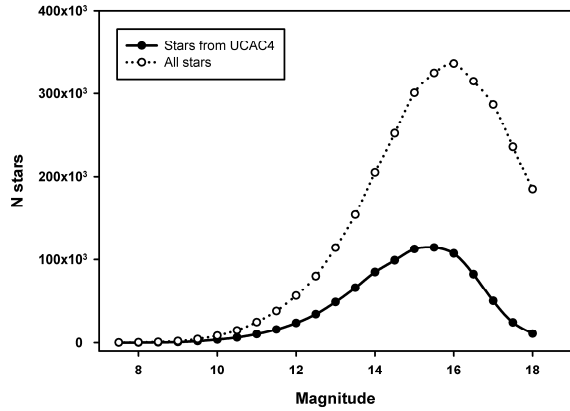


Figure 8: Distribution of stars of DENIS set catalog to magnitude

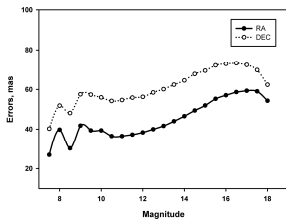


Figure 9: Dependence of precision of DENIS set catalog to magnitude.

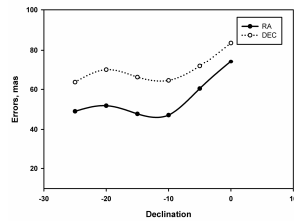


Figure 10: Dependence accuracy of DENIS set catalog to DEC

As shown in Figure 10 the accuracy distribution to declination have the noticeable dependence. In comparison, the reference catalog on the same data, which includes over 0.9 million stars from UCAC4 that were observed 3 or more times with ANO of a one star about 5.3 times have AACP 41 mas by RA and 52 mas by DEC.

Next consider the catalog, obtained from the DSS-A set. We received more than 19.5 million objects in regions, containing OC. With this data we obtained astrometric catalog of about 3 million stars (13-18.5)^m (Fig. 11) which observed three and more times with the ANO of a star about 4.1 times and AACP in RA 65 mas and DEC 70 mas (Fig. 12). The average epoch of catalog is 1953.2.

As shown in Figure 13 the accuracy distribution to declination have the noticeable dependence with accuracy deviation. In comparison, the reference catalog on the same data, which includes about 0.7 million stars from UCAC4 that were observed 3 or more times with ANO of a one star about 3.6 times have AACP 65 mas by RA and 70 mas by DEC.

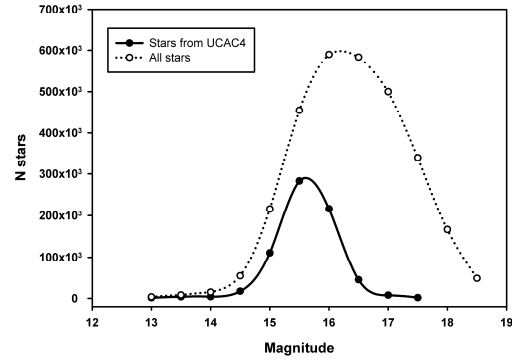


Figure 11: Distribution of stars of DSS-A set catalog to magnitude

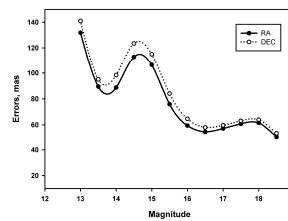


Figure 12: Dependence of precision of DSS-A set catalog to magnitude.

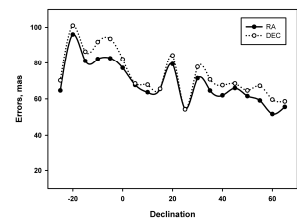


Figure 13: Dependence accuracy of DSS-A set catalog to DEC

Next consider the catalog, obtained from the DSS-B set. We received more than 52.5 million objects in regions, containing OC. With this data we obtained astrometric catalog of more than 8 million stars (13-18.5)^m (Fig. 14) which observed three and more times with the ANO of a star about 5.7 times and AACP in RA 47 mas and DEC 54 mas (Fig.15). The average epoch of catalog is 1988.3.

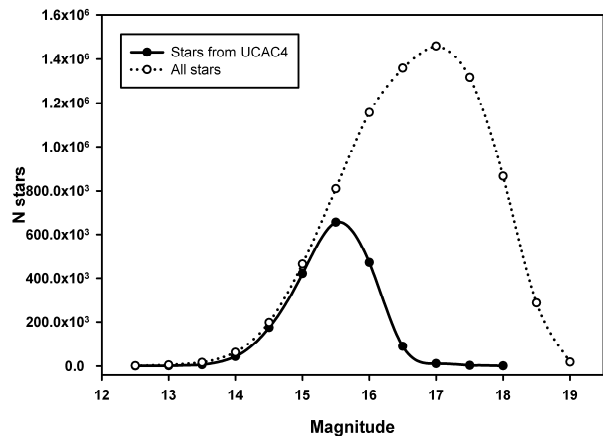


Figure 14: Distribution of stars of DSS-B set catalog to magnitude

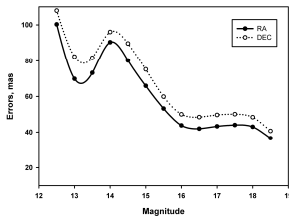


Figure 15: Dependence of precision of DSS-B set catalog to magnitude.

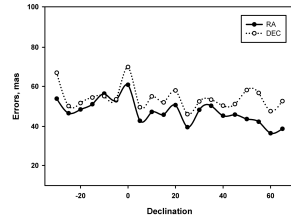


Figure 16: Dependence accuracy of DSS-B set catalog to DEC

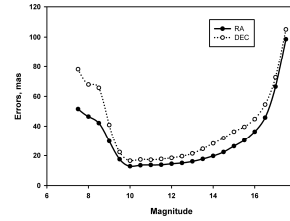


Figure 18: Dependence of precision of MOBITEL set catalog to magnitude.

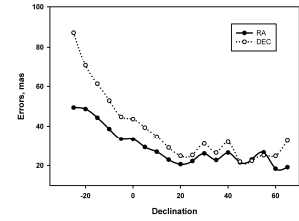


Figure 19: Dependence accuracy of MOBITEL set catalog to DEC

As shown in Figure 16 the accuracy distribution to declination have the some dependence and the picture is somewhat reminiscent of the behavior of the system in the Mobitel telescope (Fig. 19) but zero-point is not at zenith but around the equator. When you move to north accuracy difference between the two coordinates increases. In comparison, the reference catalog on the same data, which includes over 1.8 million stars from UCAC4 that were observed 3 or more times with ANO of a one star about 5.6 times have AACP 50 mas by RA and 56 mas by DEC. This is worse, than accuracy of general catalog and is associated with significantly worse accuracy of bright stars.

Finally consider the MOBITEL-2014 catalog, which include data from more than 20 thousands of CCD images, observed in RI NAO in 2011-2014. We received more than 90 million objects in regions, containing OC in the area of $\pm 20^\circ$ from the Galactic plane. With this data we obtained astrometric catalog of over 3.7 million stars (8-17)^m (Fig. 17) which observed three and more times with the ANO of a star about 21 times and AACP in RA 29 mas and DEC 38 mas (Fig. 18). The average epoch of catalog is 2013.6.

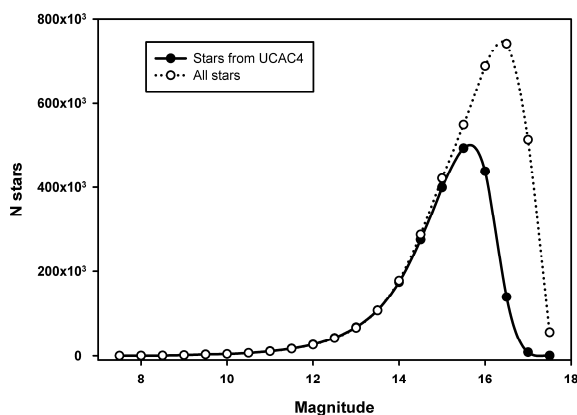


Figure 17: Distribution of stars of MOBITEL-2014 set catalog to magnitude

As clearly shown in Figure 19 the accuracy distribution to declination have the dependence from the zenith distance. Perhaps the reason is related to the lack of telescope alignment in south, which is usually performed only in the direction of the zenith ($\delta = 47^\circ$) and pole ($\delta = 90^\circ$) without alignment control to south of the zenith.

5. Conclusion

By using software, created in NAO in 2014, at 500 selected areas of sky within a 7 days of continuous operation more than 145 thousand astronomical images obtained at various telescopes from 1952 to 1999 was found and downloaded. For processing the arrays of images, including 20 thousand of own observations, the complex of 10 virtual machines was created on 2 PCs. Complex was set up to automatic processing of large volumes of observations in parallel and worked about 14 full days. As a result, we received more than 235 million coordinates of sky objects with good precision. All the processing is performed in a single system with the same software. And we obtained astrometric catalogs with more than 38 million stars.

Thus, the implementation of this investigation resulted in the increase performance of processes from 10 to 200 times. It shows how important for modern astronomy is to use modern information technology when working with large volumes of information.

Acknowledgements. The authors are thankful to Herbert Raab for the Astrometrica program, Yevgen Kozyryev for the Astrometrica automation program and anybody who has read this contribution to the end.

References

- Mazhaev A. et al.: 2014, *Odessa Astron. Publ.*, **27/1**, 55.
- Protsyuk Yu.I. et al.: 2007, *Proc. of IAU Symp.*, **N248**, 548.
- Protsyuk Yu.I. et al.: 2014, *Kinem. Phys. Cel. Bodies*, **30**, **N6**, 54.
- Skrutskie M.F. et al. : 2006, *AJ*, **131**, 1163.
- Vavilova I. B. et al.: 2010, *Kosmichna Nauka i Tekhn.*, **16**, **N5**, 62 (in russian).
- Vavilova I. B. et al.: 2011, *Kosmichna Nauka i Tekhn.*, **17**, **N4**, 74 (in russian).
- Vavilova I.B. et al.: 2012, *Kinem. Phys. Cel. Bodies*, **28**, **N2**, 85.
- Vavilova I. et al.: 2014, *Odessa Astron. Publ.*, **27/1**, 65.
- VizieR Online Data Catalog: 2005, *The DENIS database*
- Zacharias N. et al.: 2013, *AJ*, **145**, 44

THE COMPILED CATALOGUE OF PHOTOELECTRIC UBVR STELLAR MAGNITUDES IN THE TYCHO2 SYSTEM

E.Relke¹, Yu.I.Protsyuk², V.M.Andruk³

¹ Walter-Hohmann-Observatory, 159 Wallneyer St., 45133 Essen, Germany, helena_relke@yahoo.com

² Research Institute: Nikolaev Astronomical Observatory, 1 Observatornaya St., 54030, Mykolaiv, Ukraine, yuri@nao.nikolaev.ua

³ Main Astronomical Observatory of National Academy of Sciences, 27 Akad. Zabolotnogo St., 03680, Kyiv, Ukraine, andruk@mao.kiev.ua

ABSTRACT. In order to calibrate the images of astronomical photographic plates from the archive of UkrVO was created the compiled catalogue of photoelectric UBVR stellar magnitudes. It is based on: the Kornilov catalogue of 13586 WBVR stellar magnitudes (Kornilov et al., 1991), the Mermilliod catalogue of 68540 UBVR stellar magnitudes (Mermilliod, 1991) and the Andruk catalogue of 1141 UBVR stellar magnitudes (Andruk et al., 1995). All original coordinates have the different epoch and equinox. We performed the cross reference of stars from these three catalogues with the Tycho2, UCAC4 and XPM catalogues and created a new photometric catalogue on the epoch and equinox of J2000.0.

Keywords: Photometric – methods: data analysis – catalogues virtual observatory tools – astrometry - techniques

1. Introduction

For the goals and objectives of photometric calibration of the astronomical photographic plates exposed for the sky areas from -30° to 90° was created the first version of the compiled star catalogue of the positions, proper motions and photoelectric U(W)BVR stellar magnitudes in the Johnson system. The reason for the creation of this catalogue was the low precision of the equatorial coordinates and the absence of any information about the proper motions of stars, that have photoelectric U(W)BVR stellar magnitudes in all source catalogues. For our purposes were chosen three source catalogues:

1. Photometric catalogue of UBVR stellar magnitudes (Kornilov et al., 1991)
2. Photometric catalogue of WBVR stellar magnitudes (Mermilliod et al., 1991)
3. Photometric catalogue of UBVR stellar magnitudes of the MEGA project (Andruk et al., 1995; Andruk 1996; Andruk 1996; Andruk 1996).

The corresponding number of stars with the photoelectric stellar magnitudes in three source catalogues is following: 13586 (down to $\delta \leq -26^\circ$), 47022 (down to $\delta \leq -30^\circ$) and 1141 (down to $\delta \leq -13^\circ$). Altogether the whole list has 61749 stars. The precision of the equatorial coordinates of the stars in these catalogues is not high enough, (especially

for the second catalogue), that complicated the identification of the calculated coordinates of stars obtained as the result of the processing of digitized images of photographic plates. The difficulties by the identification are significant for the faint stars and growing up for the photographic plates recorded in the first half of the twentieth century.

2. The results of the identification with the Tycho2, UCAC4 and XPM catalogues

All stars of the created list were consistently identified with the stars of the Tycho2, UCAC4 (Zacharias et al., 2013) and XPM (Fedorov P. et al., 2009) catalogues. The corresponding amounts of stars of the individual source catalogues identified with the Tycho2 catalogue were following: the 38837, 13202 and 633 stars for the first, second and third catalogues respectively. Then the not identified stars from the whole list were compared with the UCAC4 catalogue. The results of this second identification were: the 7803, 289 and 460 stars for the first, second and third source catalogues respectively. The same procedure of the identification for the rest of not identified stars using the XPM catalogue gave out the following results: the 75, 3 and 7 stars. So the first version of our catalogue contain 61309 stars. Due to the errors of identification and because of the duality of a certain amount of stars, the number of the stars in the final catalogue will be decreased.

3. The using of the two exposures on the same photographic plate for the photometry

The combination of characteristic curves of the two exposures on the same photographic plate makes possible to build a new combined characteristic curve for the whole interval of stellar magnitudes on the photographic plate. The photoelectric stellar magnitudes (Bpe) from the source catalogues were used as the photoelectric standards. The steps and methods of the construction of such combined characteristic curves for photographic plates, are shown on the figures 1 and 2. The photometric field errors were also taken into account. The difference between stellar magnitudes of two exposures in the scale of the photoelectric standards (Bpe) is $\Delta B = 3.223$ mag. The errors of photome-

try are $\sigma_1 = \pm 0.229$ mag for the first exposure and $\sigma_2 = \pm 0.374$ mag for the second one. The characteristic curves for the binding of the instrumental photometric values of m_1 and m_2 with the scale of photoelectric standards B_{pe} are displayed on the d-panel. The photometric errors are $\sigma_1 = \pm 0.146$ mag and $\sigma_2 = \pm 0.179$ mag.

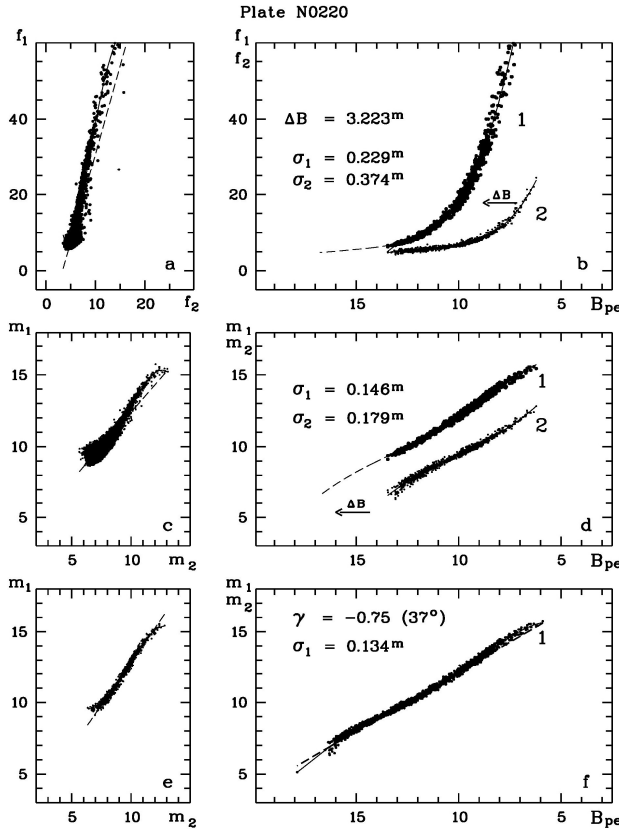


Figure 1: Photometry of stars using the information about the two exposures for the photographic plate N0220.

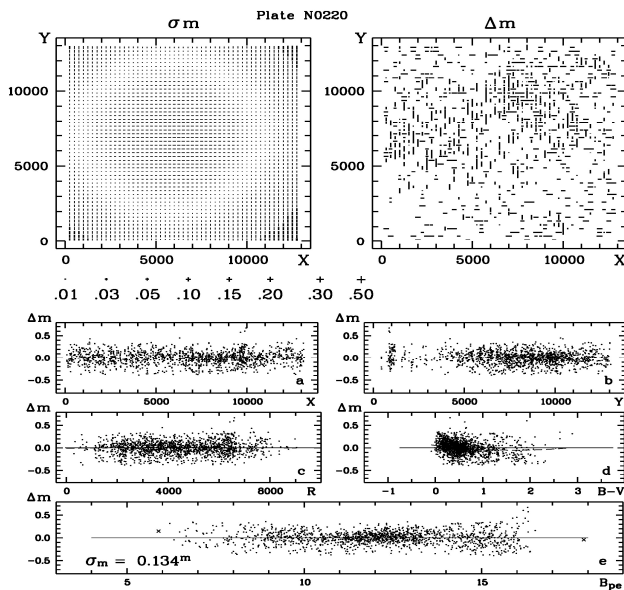


Figure 2: The photometric field errors (upper panels and panels a, b, c, d) for the photographic plate N0220.

4. About the compiled catalogue of photoelectric U(W)BVR magnitudes

As a result of this succeeding identification was created a compiled star catalogue of the equatorial coordinates and proper motions in the system of the Tycho2 catalogue and photoelectric U(W)BVR magnitudes adopted to the Johnson system. The electronic form of this catalogue is presented in the 14 columns. The first seven columns contain information from the original source catalogues: equatorial coordinates α , δ (1 and 2 columns); U(W), B, V and R magnitudes (3, 4, 5 and 6 columns); the 7 column contains the references on the original photometric catalogues (1 – Andruk et al., 1995, 2 – Kornilov et al., 1991 and 3 – Mermilliod et al., 1991). The next seven columns contain the results of the identification: the equatorial coordinates of the stars on the epoch and equinox 2000.0 (8 and 9 columns); the proper motions $\mu\alpha\cos\delta$ and $\mu\delta$ (arcsec/year, 10 and 11 columns); B and V magnitudes from the Tycho2, UCAC4 and XPM catalogues recorded in columns 12 and 13; the last column (14) contains the references on the catalogues where data taken from (1 – Tycho2, 2 – UCAC4 and 3 – XPM).

5. Conclusion

This work was performed within the framework of work on the creation of software for data reduction of Joint Digital Archive of Ukrainian Virtual Observatory (Vavilova et al., 2012; Vavilova et al., 2012). The photoelectric calibration of the photographic plates was already used by the authors in series of works (Andruk et al., 2010, Andruk et al., 2014, Andruk et al., 2016, Kazantseva et al., 2014, Prot-syuk et al., 2014). The created catalogue will be posted on the websites of the RIO NAO (Ukraine), MAO NASU (Ukraine) observatories and as well as will be transferred to the Strasbourg astronomical Data Centre.

Acknowledgements. The authors are thankful to anybody who has read this contribution to the end.

References

- Andruk V.M. et al.: 1995, *Astron. Nachr.*, **316**, N4, 225.
- Andruk V.M. et al.: 1996, *Astron. Nachr.*, **317**, N2, 49.
- Andruk V.M. et al.: 1996, *Astron. Nachr.*, **317**, N2, 127.
- Andruk V.N.: 1996, *Kinem. Phys. Cel. Bodies*, **12**, N4, 60.
- Andruk V.M. et al.: 2010, *Kinem. Phys. Cel. Bodies*, **26**, N3, 146.
- Andruk V.M. et al.: 2014, *Odessa Astron. Publ.*, **27**, N1, 53.
- Andruk V.M. et al.: 2016, *Kinem. Phys. Cel. Bodies*, **32**, N1, 56.
- Fedorov P. et al.: 2009, *Mon. Not. R. Astron. Soc.*, **393**, 133.
- Kazantseva L.V. et al.: 2015, *Kinem. Phys. Cel. Bodies*, **31**, N1, 58.
- Kornilov V.G. et al.: 1991, *Trudy GAIS*, **63**, 1.
- Mermilliod J.C.: 1991, *Homogeneous means in the UBVR system*.
- Prot-syuk Yu.I. et al.: 2014, *Kinem. Phys. Cel. Bodies*, **30**, N6, 54.
- Vavilova I.B. et al.: 2012, *Kinem. Phys. Cel. Bodies*, **28**, N2, 85.
- Vavilova I.B. et al.: 2012, *Baltic Ast.*, **21**, N3, 356.
- Zacharias N. et al.: 2013, *Astron. J.*, **145**, 44.

CATALOG OF ASTRONOMICAL POSITIONS OF SATURN'S MOONS OBTAINED BY PHOTOGRAPHIC OBSERVATIONS AT THE MAO NASU IN 1961-1991

O.M.Yizhakevych, V.M.Andruk, L.K.Pakuliak

Main Astronomical Observatory of National Academy of Sciences,
27 Akad. Zabolotnogo St., 03680, Kyiv, Ukraine, izhak@mao.kiev.ua

ABSTRACT. In the framework of UkrVO national project the new methods of plate digital image processing are developed. The photographic material of the UkrVO Joint Digital Archive (JDA, <http://194.44.35.19/vo-mao/DB/archivespecial.php>) is used for the solution of classic astrometric problem – positional and photometric determinations of objects registered on the plates including Saturn's moons. The results of tested methods show that the positional RMS errors are better than ± 150 mas for both coordinates and photometric ones are better than $\pm 0.20^m$ with the Tycho-2 catalogue as reference.

Keywords: astrometry – methods: catalogs – planets and satellites: individual: Saturn

1. Introduction

A decade ago we created the database of metadata of photographic astronomical plates DBGPA on the base of the MAO NASU glass archive. Later it formed the basis for the creation of Ukrainian VO Joint Digital Archive (JDA) (Vavilova et al., 2012, Vavilova et al., 2012). The efficient structure of the JDA database facilitates a quick search and selection of the desired information for the solution of specific problems such as the determination of the coordinates of celestial bodies and creation of catalogues of stars and galaxies (Kazantseva et al., 2015).

Here we present the results of the reduction of photographic observations of Saturn and its moons, made in 1961 – 1991 at the MAO NASU using 4 telescopes. In DBGPA, we found the data of almost 300 photographic observations of these objects. For further processing, we select 253 plates matching the quality criteria. These plates were scanned using Epson Expression 10000XL (EE) commercial scanner. The complete reduction of the set of plates was made using the software package specially developed and customized for this case at the MAO NASU Department of Astrometry. The catalogue of more than 1100 astrometric positions of the eight Saturn's moons (S2-S9) was obtained in the system of the Tycho-2 star catalogue. The internal accuracy of RMS reduction on the data of three telescopes DLFA, DAZ, and Z600 is about $\pm 0.03'' - \pm 0.11''$, for the DWA plates the accuracy appears to be a little bit worse $\pm 0.15'' - \pm 0.21''$. The temporal distribution of calculated positions of moons is presented in the histogram of Fig. 1.

The most effective observations were those done in 1980 and 1982 with DWA and the observations conducted in 1990 with Z600 (Yizhakevych et al., 2014).

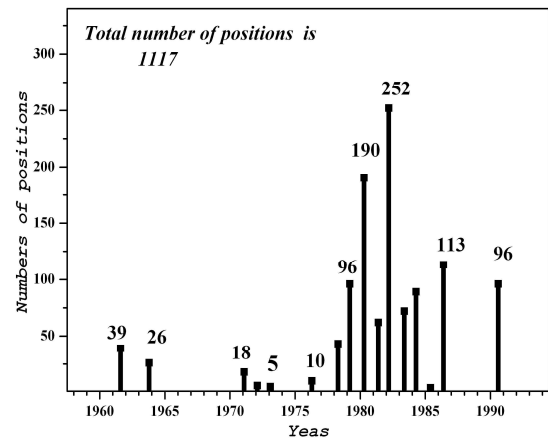


Figure 1: The distribution of the calculated positions of Saturn's moons observations using 4 telescopes of the MAO NASU.

2. Observational data

The first series of photographic observations (193 plates, 71 observational nights) were obtained during 1961–1988 using two astrographs: Double Long Focus Astrograph DLFA (D/F=400/5500 mm) and Double Wide Angle Astrograph DWA (D/F= 400/2000). A few short series of observations were made in field conditions: in 1986 with the Double Zeiss Astrograph DAZ (D/F= 400/3000) in Kitab observatory of the Tashkent University (Uzbekistan) (8 plates, 7 observational nights) and in 1989 (7 observational nights), 1990 (9 nights), 1991 (7 nights) with the Zeiss Reflector Z600 (F = 7500 mm; mt. Maidanak, Usbekistan) (54 plates). Table 1 presents the more information about the telescopes and the observational material.

The most efficient observers for 30 years who collected data for more than 10 plates each were Ledovskaya (Kulyk) I.V., Lysiakova R.F., Major S.P., Onegina A.B., Sereda E.M., Shatokhina S.V., Yizhakevych O.M.

The technique of observations of moving objects with a different brightness (from 8^m to 14^m) is the exposition of multiple images of varying duration on the same plate. Obviously, the effectiveness of such observations depends

on the mutual random placement of the Saturn's moons at the moment.

Table 2 shows the availability of Saturn's moons observations using MAO NASU telescopes. The highlighted data apply to the maximum distances between the moon and the planet (in mm) on the plate depending on the telescope scale. In the other words, they concern the cases when the moon being in the opposition can be found on the plate.

Table 1. Additional information about telescopes.

Telescope, Tube	Scale "/mm	Field degree	Emulsion	Years
DLFA, I	37.5	2.5x2.5	ORWO -ZU21, -ZU2	1961-1984
DLFA, II	37.5	1.8x2.5	ORWO -NP27	1982
DWA, I,II	103.1	8.0x8.0	ORWO -ZU21	1976-1988
DAZ, I,II	68.8	0.5x0.5	ORWO -ZU21	1986
Z-600	27.5	5.5x5.5	ORWO -ZU21, -ZU2, -NP27	1989-1991

Table 2. The availability of the observations of Saturn's satellites (S2–S9) with telescopes of the MAO NASU.

Satellite	MgV	Distance from the Planet (mm) on the plate depending on the telescope scale			
		DLFA 37"/mm	DWA 103"/mm	DAZ 68"/mm	Z600 27"/mm
<i>I</i>	<i>2</i>	<i>3</i>	<i>4</i>	<i>5</i>	<i>6</i>
S2	11.7	1.1	0.4	0.6	1.5
S3	10.3	1.4	0.5	0.7	1.8
S4	10.4	1.7	0.6	0.9	2.3
S5	9.7	2.4	0.9	1.3	3.2
S6	8.3	5.5	2.2	3.1	7.5
S7	14.2	6.7	2.7	3.7	9.1
S8	11	16.1	5.9	8.9	21.8
S9	16.4	111.	41.	62.	152.

T exposure: from some seconds of time to some minutes

In fact, various reasons make the chance for the satellite detection lower, for example, because of photographic irradiation, mismatched exposure duration, unfavorable mutual placement of moons, and others.

The special attention was paid to the estimation of the moments of observation. As a rule, the observer recorded the moments of cassette shutter opening and closing at the hearing using stellar chronometer or stellar clock with the further connection to the precise time signals by the «6 points» technique. Before the start of the processing, the corrections of chronometers and stellar clocks were

newly qualified and the UT moments of the middle of the exposition were also redefined for each image in contrast to DBGPA data, where the moments of observation have the different format of presentation. They are the start moments of the exposure and its duration.

Search files for the identification of the moons were prepared due to the IMCCE (Paris) ephemeris (http://www.imcce.fr/hosted_sites/aimirror/nssephe.php).

3. Reduction

The algorithm of calculation of the positions by photographic observations is as follows: the first step is the determination of the rectangular coordinates x, y of objects in the plate coordinate system; on the second step, the objects are identified in the reference star catalogue, and finally the positions in the equatorial coordinate system α, δ are derived.

The connection between two coordinate systems x, y and α, δ is determined by the infinite power series, whose members depend on many factors. Among them are the quality of the telescope optics, the field of view of the telescope, the tilt of the plate to the focal plane of the optical system, the reference system used, the number of reference stars on the plate and other factors. The calculations using the formulae of the linking are possible only after the application of restrictions on the number of members of the power series in the result of the evaluation of their relevance on the basis of the adopted model of aberrations. By varying this number, we can get results with the highest level of accuracy, leaving only the significant members of the series (Andruk et al., 2005; Andruk et al., 2014). The scanning of plates was made using Epson Expression 10000XL scanner at 16-bit gray levels and a resolution of 1200 dpi. (Golovnya et al., 2010). Previously, the detailed study of the device, namely the additional errors, connected with the scanner mechanics behavior, has showed its applicability to the solution of problems of ground-based astronomy (Protsyuk et al., 2014).

The software package, specially developed and customized for the case in the LINUX-MIDAS-ROMAFOT environment (Andruk et al., 2007; Andruk et al., 2010), allowed to make a reduction of **253** scans with Saturn's moons images. In fact, the amount of processed material appeared to be approximately three times larger because of multiple images on the each plate. It requires the additional efforts to improve the software algorithm for splitting the digitized image into separate files according to the number of exposures on the plate.

Initially, the software was developed for the processing of the astronegatives of the FON project (Yatsenko et al., 2011). Its plates have large fields of view and are obtained with two expositions: long (16–20 min.) and short (30–60 sec) ones. This allows selecting a few hundred reference stars from the Tycho-2 catalogue homogeneously distributed across the plate field. The more reference stars are on the plate, the more accurate solution for the relation of two coordinate systems could be obtained. In our case, the number of exposures exceeds two.

The processing of the DWA (8°x8°) and DAZ (5°x5°) plates was made using the polynomial of the sixth degree. In addition to them in the observations of Saturn's moons another two telescopes were involved having different

scales of images and star fields (Table 1). So, the reduction of DLFA plates (2°x2°) needs the polynomial of the third degree, and the linear model was applied to the reduction of Z600 (0.5°x 0.5°) plates.

The first step of the reduction includes the full analysis of the image for detecting the blemishes and damages of the emulsion on the plate as well as their removal. The elimination of scanner errors is done on the same step too.

The next step was the full reduction of the selected plates. On this step, the plates with failed observations were found and excluded from the processing. These include plates with aiming errors (plates of Z600, obtained in 1991), improper exposition duration when observing faint objects (plates with Phoebe – S9, 16.4^m; plates of Z600, obtained in 1989), errors in the recording of times and in the determination of chronometer corrections, etc.

Finally, we obtained the catalogue of 1100 astrometric positions of eight Saturn’s moons (S2–S9) using 193 photographic plates exposed on four telescopes during 87 productive observational nights.

The comparison of observed positions with the theory of moons’ motion DE431 was made using the ephemeris of IMCCE, France, and the residuals (O–C)_α and (O–C)_δ, as well as their standard deviations σ, were obtained according to (1):

$$\sigma = \sqrt{\sum((o - c)_i - \overline{(o - c)})^2 / (n - 1)} . \quad (1)$$

The results of the comparison are given in Table 3. The internal accuracy of the astrometric reduction into the Tycho-2 reference system lies within ±0.03" – ±0.11" for the three telescopes DLFA, DAZ, Z600. For the DWA, the internal accuracy is worse, and it is equal ±0.15"– ±0.21".

Figures 2, 3, 4, 5 show the scattering of (O–C) deviations from their average value for S6 satellite as the most efficient object for all four telescopes. The comparison between these four histograms demonstrates that the scattering of O–C from their average value lies in the limits of 1" and is random for DLFA, DAZ and Z600. In the case of DWA, this scattering is much larger and lies within ±2". The dispersion analysis for the Fisher test shows that it may indicate the presence of an undetected source of residual systematic errors.

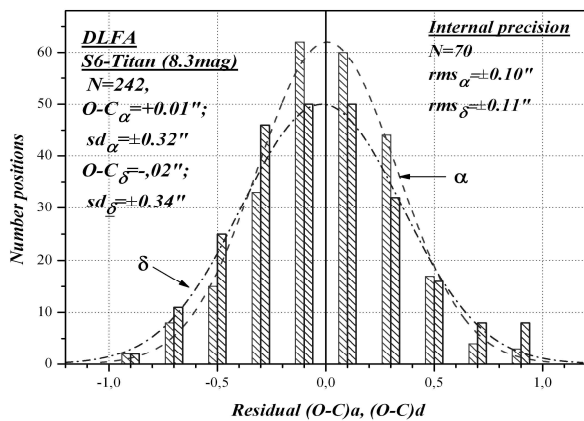


Figure 2: Residuals (O–C); DLFA

Table 3. Statistic parameters of the results of the astrometric solution for 7 satellites and 4 telescopes.

Obj	DLFA (1961–1984 yrs)				
	N	O-C _α "	σ _α "	O-C _δ "	σ _δ "
S2	9	+0.402	0.32	+0.184	0.17
S3	71	-0.094	0.38	+0.085	0.46
S4	118	-0.015	0.33	+0.067	0.39
S5	186	+0.071	0.34	+0.018	0.35
S6	248	+0.005	0.32	-0.018	0.37
S8	212	-0.019	0.36	+0.019	0.37
Σ	844	+0.007	±0.34	+0.022	±0.37
Obj	DWA (1978–1986 yrs)				
	N	O-C _α "	σ _α "	O-C _δ "	σ _δ "
S5	5	-0.744	0.85	-0.214	1.11
S6	55	+0.209	0.60	+0.109	0.64
S8	36	-0.744	0.85	-0.214	1.11
Σ	96	-0.198	±0.72	-0.004	±0.87
Obj	Z600 (1990)				
	N	O-C _α "	σ _α "	O-C _δ "	σ _δ "
S3	4	+0.166	0.25	+0.041	0.30
S4	11	-0.160	0.30	+0.089	0.24
S5	12	-0.252	0.46	+0.183	0.26
S6	35	-0.032	0.43	-0.219	0.30
S7	5	-0.252	0.51	+0.099	0.39
S8	29	+0.313	0.41	+0.016	0.34
S9	1	+0.439		-0.268	
Σ	97	+0.027	±0.41	-0.035	±0.31
Obj	DAZ (1986)				
	N	O-C _α "	σ _α "	O-C _δ "	σ _δ "
S4	4	-0.451	0.27	+0.096	0.15
S5	18	-0.093	0.47	+0.070	0.29
S6	29	-0.052	0.34	+0.040	0.27
S8	29	-0.012	0.31	-0.012	0.31
Σ	80	-0.055	±0.33	+0.025	±0.26

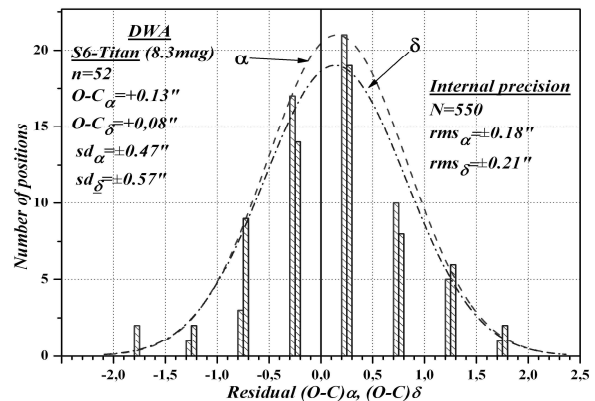


Figure 3: Residuals (O–C); DWA.

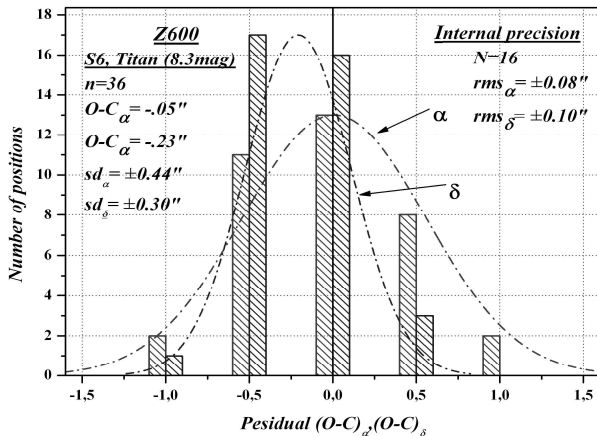


Figure 4: Residuals (O–C); Z600.

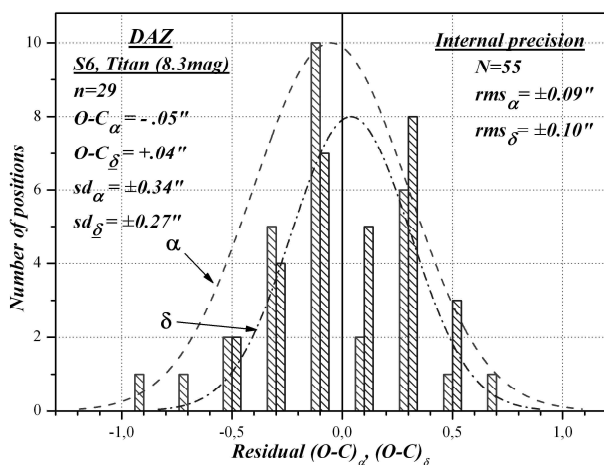


Figure 5. Residuals (O–C); DAZ.

4. Conclusion

The catalogue of 1100 astrometric positions of eight Saturn's moons S2-S9 was obtained based on the reduction of four independent series of observations from different telescopes. For the moment, we have processed 193 plates from the set of 253 plates found in the database of UkrVO JDA.

The internal accuracy of the reduction for three telescopes with the scales from 28 to 68 arcsec/mm lies within $\pm 0.03''$ – $\pm 0.11''$. The fourth instrument with the scale 103 arcsec/mm gives the accuracy in the interval $\pm 0.15''$ – $\pm 0.21''$ and the larger dispersion of O–C.

For three telescopes DLFA, DAZ, Z600 standard deviations σ are in the range from $\pm 0.25''$ to $\pm 0.37''$ for both coordinates, while those for DWA exceed the above values of 1.5–2 times.

The dispersion analysis for the Fisher test shows that the larger dispersion of O–C for DWA may indicate the presence of an undetected source of residual systematic errors. In order to identify the cause of these errors, we assume to perform the additional analysis of the reduction of DWA observations.

The problem of the reduction of Z600 plates exists. Most of them were eliminated because of insufficient results of the preliminary digital analysis of images for defects and damages of emulsions. The considerable number

of moons' images close to the planet was not found on the scans of those plates using the digital procedure in contrast to the previous reductions based on the classic technique of measurements (Izhakevich, 1991; Yizhakevych, 1991; Yizhakevych, 1994, Kaltygina, 1992; Pakuliak, 2012; Yizhakevych, 2012). These points to the possible limitations of the processing algorithm, which could misidentify the few pixel images of faint moons as the "dirt" on the emulsion. This requires the further improvement of the software for the processing of digital images of plates with the Solar System bodies.

Acknowledgements. This work was partially supported by the Ukrainian Astronomical Association.

References

- Andruk V.M. et al.: 2005, *Kinem. Phys. Cel. Bodies*, **21**, N5, 396.
- Andruk V.M. et al.: 2007, *J. Phys. Studies*, **11**, N3, 329.
- Andruk V.M. et al.: 2010, *Kinem. Phys. Cel. Bodies*, **26**, N3, 75.
- Andruk V.M. et al.: 2014, *Kinem. Phys. Cel. Bodies*, **27**, N1, 53.
- Golovnya V.V. et al.: 2010, *J. Phys. Studies*, **14**, N2, 2902.
- Izhakevich E.M.: 1991, *Scientific paper deposited in All-russian institute of scientific and technical information*, No. 4553-B91, 1991PDR14553_1.
- Kaltygina S.V. et al.: 1992, *Scientific paper deposited in All-russian institute of scientific and technical information*, No. 1044-Uk92, 5.
- Kazantseva L.V. et al.: 2015, *Kinem. Phys. Cel. Bodies*, **31**, N1, 58.
- Pakuliak L. et al.: 2012, in *Proc. of the Conf. NAROO-GAIA "A new reduction of old observations..."*, June 20–22, 2012, France, Paris, p. 161.
- Protsyuk Yu.I. et al.: 2014, *Odessa Astron. Publ.*, **27/1**, 59.
- Vavilova I.B. et al.: 2012a, *Kinem. Phys. Cel. Bodies*, **28**, N2, 85.
- Vavilova I.B. et al.: 2012b, *Baltic Astronomy*, **21**, N3, 356.
- Yatsenko, A.I. et al.: 2011, *Kinem. Phys. Cel. Bodies*, **27**, N5, 249.
- Yizhakevych O.M. et al.: 1991, *Kinem. Phys. Cel. Bodies*, **7**, N2, 98.
- Yizhakevych O.M. et al.: 1994, *Kinem. Phys. Cel. Bodies*, **10**, N1, 88.
- Yizhakevych Ye. et al.: 2012, in *Proc. of the Conf. NAROO-GAIA "A new reduction of old observations..."*, June 20–22, 2012, France, Paris, p. 153.
- Yizhakevych O. et al.: 2014, *Odessa Astron. Publ.*, **27/1**, 67.

RADIOASTRONOMY

THE STUDY OF EXTRAGALACTIC SOURCES 3C 446 AND 3C 345 WITH USING THE SINGULAR SPECTRUM AND WAVELET ANALYSIS

G.I.Donskykh¹, M.I.Ryabov², A.L.Sukharev², M.F.Aller³

¹ Department of Astronomy, I.I.Mechnikov Odessa National University, Ukraine

² Odessa observatory "URAN-4" of the Institute of Radio Astronomy NAS, Ukraine

³ Radio observatory of Michigan University, Ann Arbor, USA

ABSTRACT. We investigated the data of monitoring of flux density of extragalactic sources 3C446 and 3C345, which was held on 26-meter radio telescope of University of Michigan at frequencies 14.5, 8 and 4.8 GHz. The data of observations were investigated using singular spectrum analysis and wavelet-analysis. According to the results of wavelet analysis for each year of observations, graphics of "spectra periods" were built to determine the contribution of individual periods in the activity of the radio source. The results obtained with two different methods showed a good correlation between them. For a long time component of the flux the periods of $\sim 5 - 9$ years were found. For short term components the periods of $\sim 1 - 4$ years are presented. The results obtained using two different methods were compared with VLBI radio maps, which were obtained by the program MOJAVE. The changes of periods over time are associated with certain physical processes in the system "core – accretion disk – jet" and with appearing of new bright components (knots) in the jet.

Keywords: AGN, jet.

1. Introduction

The source 3C 446 is located at the distance 10138 Mpc. It refers to optically violently variable quasars.

Blazar 3C 345 is located at a distance of 3473 Mpc. This source refers to the radio loud quasars. Some authors (eg, Lobanov & Roland, 2005) assume the existence in the source of binary systems of supermassive black holes. In the article (Caproni & Abraham, 2004) the discovery of precession in jet of source 3C 345 is reported.

2. Data reduction

In this paper 3C 446 and 3C 345 are studied. The observations were taken by the radio telescope RT-26 Michigan Observatory, at frequencies of 14.5 GHz, 8 GHz and 4.8 GHz. Graphs of flux density 3C 446 and 3C 345 at three frequencies are presented at Figures 1 and 2. Details of the calibration methods and the methods of analysis are described in paper (Aller et al., 1985).

Based on daily observations of flux average values of 7 days with an irregular grid of counting are defined. According to the histogram of distribution of time

intervals between counting the interpolation interval in 0.02 years (7,3 days) has been chosen. With using a polynomial moving average (half-width an interval of 5 points) reduction of noise has been reached and random emissions have been removed. By means of trigonometric interpolation the data have been reduced to an even step on time. Allocation of short component in signals against the main period Fourier filtering (O – C) was used (Gaydyshev, 2001).

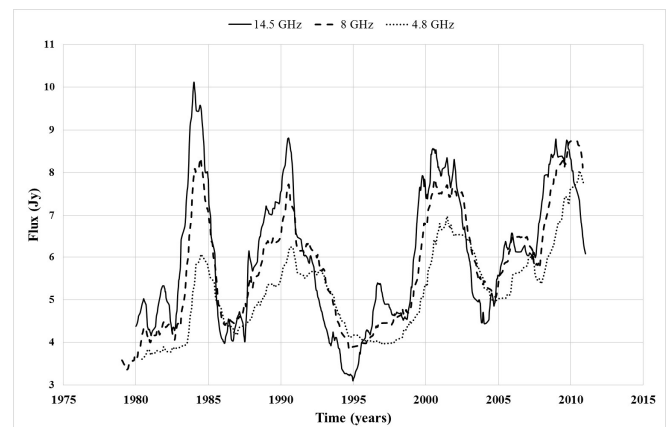


Figure 1: A graph of flux density 3C 446 at three frequencies

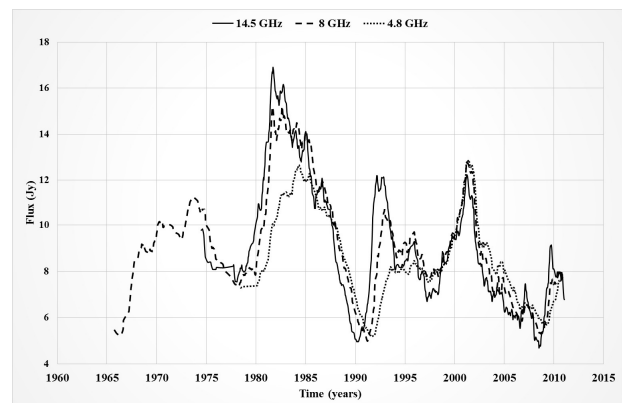


Figure 2: A graph of flux density 3C 345 at three frequencies

3. Wavelet-analysis

Two-parameter analyzing function of one-dimensional wavelet transform is well localized both in time and frequency. This distinguishes it from the ordinary Fourier analyzing function which covers the entire time axis. Thus, it is possible to see the detailed structure of the process and the evolution of the harmonic components of the signal in time (Smolentsev, 2010). We used a continuous wavelet transform based on Morlet function. On the wavelet spectra of the harmonic components of the signal are visible as bright spots, stretching along the time axis. The examples of the wavelet spectrum are shown in Fig. 3 and 4.

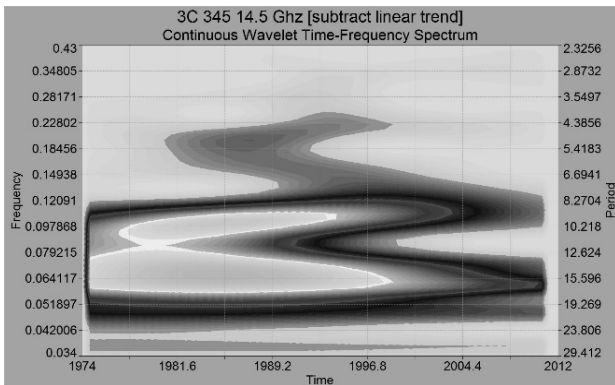


Figure 3: A continuous wavelet-spectrum of the initial smoothed data for 3C 345 at a frequency of 14.5 GHz

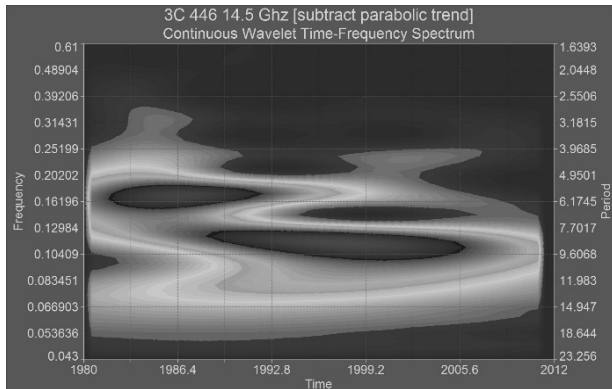


Figure 4: A continuous wavelet-spectrum of the initial smoothed data for 3C 446 at a frequency of 14.5 GHz

Periods and times of the manifestation obtained by wavelet analysis for the sources 3C 345 and 3C 446 are shown in Tables 1 and 2.

At all three studied frequencies for a longtime component of the source 3C 345 the presence of periods in the range of ~ 9 – 12.7 and 16 years is characterized. At frequencies 14.5 and 8 GHz the periods in the range ~ 4.6 – 6.1 years are present. For a short periodic component at all frequencies periods ~ 1.3 – 1.7 and 3 – 4 years are marked. The long ~ 16-year period is marked at all three frequencies and had a maximum of spectral power at 14.5 GHz in 1985, at 8 GHz – in 1988, and at 4.8 GHz – in 1994. The spectral power of 16-year period, was the highest at a frequency of 8 GHz.

Table 1. Periods obtained by wavelet-analysis for 3C 345

The trend					
Frequency (GHz)	Period (years)	Beginning of the period	End of the period	Maximum spectral power	Date of maximum spectral power
14.5	16.4-15.9	1976.8	2004.8	3545	1985.7
	10.5-9.1	1980.2	1998.0	3180	1984.6
	5.3-4.6	1984.4	1991.3	808	1987.5
8	16.1-12.7	1969.6	2007.5	4050	1988.8
	12.7-9.3	1969.6	2004.5	2800	1985.1
	6.5-6.1	1970.4	2000.7	707	1994.8
4.8	16.3-15.9	1984.5	2005.3	3200	1994.6
	9.3-8.7	1983.4	2004.3	890	1992.4
O-C					
14.5	4.0-3.4	1980.4	1999.4	384	1993.0
	1.7-1.5	2001.5	2009.1	46	2008.8
	1.4-1.2	1982.6	1992.3	44	1985.1
8	5.0-4.2	1970.0	2003.4	188	1995.0
	2.7	1971.1	1983.5	42	1976.6
	3.0	1990.1	2007.8	118	1994.2
	1.3	1979.0	1986.0	34	1981.8
	1.7-1.3	1968.2	1975.1	7	1970.5
4.8	4.0	1979.1	2006.0	32	2002.7
	1.3	1981.8	1986.2	8	1984.3

Table 2. Periods obtained by wavelet-analysis for 3C 446

The trend					
Frequency (GHz)	Period (years)	Beginning of the period	End of the period	Maximum spectral power	Date of maximum spectral power
14.5	5.8	1981.7	1995.2	1037	1986.7
	8.8	1997.6	2008.4	1092	1998.6
8	6.0	1981.4	1994.0	343	1986.2
	9.2	1997.0	2008.6	808	1998.8
4.8	5.8	1983.0	1993.7	114	1986.9
	9.2	1996.7	2009.0	407	2000.1
O-C					
14.5	3.0-2.7	1981.0	1998.5	175	1983.6
	2.0-1.3	1988.5	2001.8	32	1990.1
	2.1-1.9	2005.5	2010.3	10	2009.0
	0.8	2000.4	2005.6	7	2001.2
8	2.4-2.1	1980.8	1989.8	8	1983.5
	1.7	2002.5	2009.2	7	2008.4
	1.7-1.1	1988.7	1995.3	4	1991.9
4.8	2.7-2.4	1985.6	2008.7	7	2006.8
	1.4-1.2	1998.8	2008.3	0.7	2000.0

For a long time component of the source 3C 446 at all three frequencies by the presence of periods of 6 and 9 years is characterized. For a short time component at all frequencies the long 6-year period had a maximum of spectral power in 1986. The spectral power of this period was the highest at a frequency of 14.5 GHz. Another long ~ 9-year period had a maximum of spectral power at frequencies of 14.5 and 8 GHz in 1998, and at a frequency of 4.8 GHz – in 2000.

4. “Period – spectral power” dependence

As a result of the wavelet analysis "period – spectral power" graphs were build for each year of observation. They allow to define the periods, making the largest contribution to the formation of phase of activity of the investigated source and the time and duration of their existence.

To study the structure of radio sources in the periods of maximum activity, the VLBI maps from the database MOJAVE for the period 1995 -2012 at the frequency of 15.4 GHz (Lister et al., 2009) were investigated.

Figures 5 and 6 show examples of “period – spectral power” dependence graphs for long term and short-term components of source 3C345 during one phase of its increased activity in 2001 (see. Figures 5 and 6). From these graphs we learn that at this time the periods of ~ 9.2 and 16 years (trend), and the period of ~ 1.7 years (O-C) are seen.

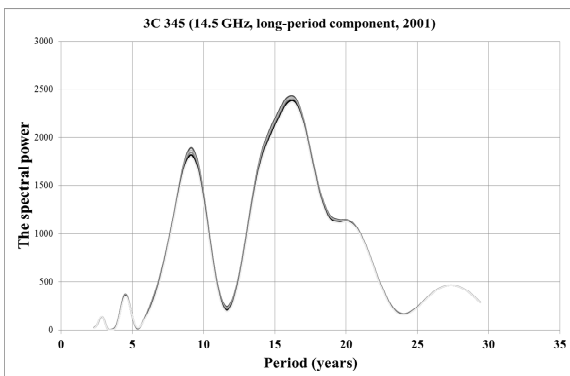


Figure 5: “Period – spectral power” dependence graph for phase of activity for the source 3C 345 in 2001 at a frequency of 14.5 GHz (trend component).

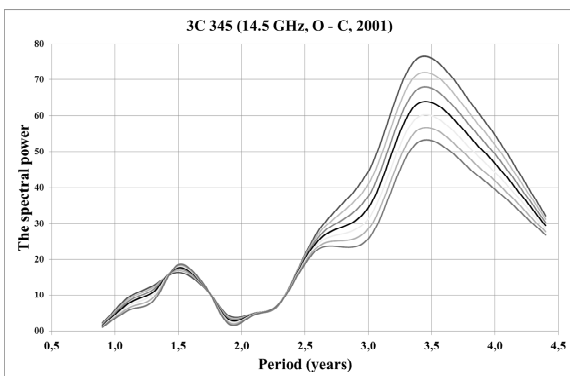


Figure 6: “Period – spectral power” dependence graph for phase of activity for the source 3C 345 in 2001 at a frequency of 14.5 GHz (O-C component).

At the VLBI maps (MOJAVE) for that epoch of observations structural changes in the jet 3C 345 are visible (see. Fig. 7).

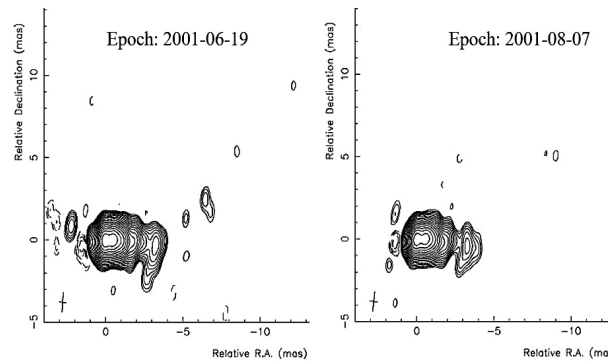


Figure 7: VLBI maps of the source 3C 345 during one of its phases of activity.

Figures 8 and 9 show "period-spectral power" graphs for the source 3C 446 in the phase of its increased activity in 2008. At this time the periods ~ 8.7 years (long-period) and ~ 1.9 years (short-period) are presented. The VLBI maps MOJAVE for this epoch of observations are shown in Figure 10.

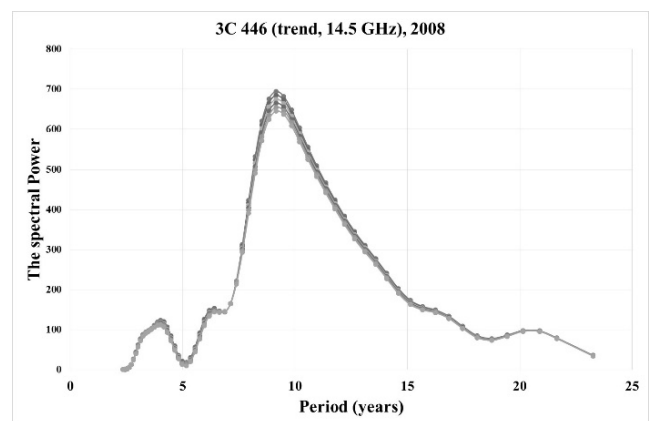


Figure 8: “Period – spectral power” dependence graph for phase of activity for the source 3C 446 in 2008 at a frequency of 14.5 GHz (trend component).

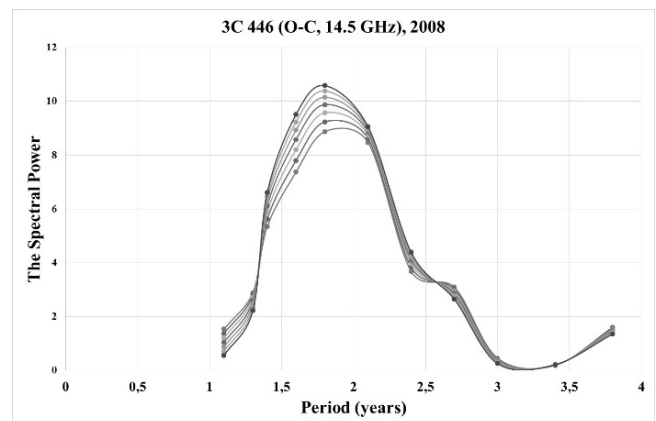


Figure 9: “Period – spectral power” dependence graph for phase of activity for the source 3C 446 in 2008 at a frequency of 14.5 GHz (O-C component).

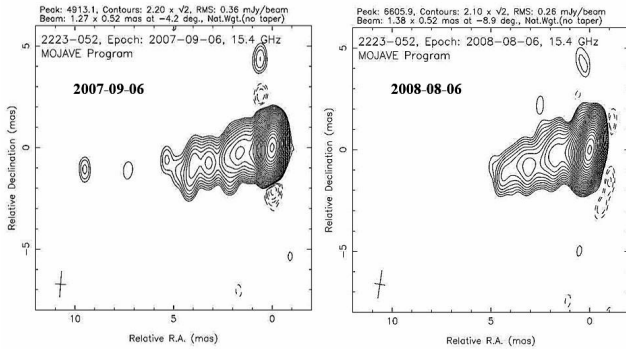


Figure 10: VLBI maps of the source 3C 446 during one of its phases of activity.

5. Singular spectrum analysis

Using the singular spectrum analysis we decompose the original signal into a set of narrow-band filters, which include trend components, periodic components and noise signal (Alexandrov, 2006). Using this set of narrow-band filters, the periods of sinusoidal oscillations in years were determined. To obtain spectral power distribution depending on time in study narrowband component obtained by analysis of a singular spectrum short Fourier transform was used, i.e. Fourier transform used a moving window where each window with overlaps calculated Fourier spectrum and as a result we get a step by step presentation of the temporal evolution of the spectral power and the frequency of the signal. Thus, it is possible to relate the formation of a certain period of time with the moment in which it was the highest. Examples of the obtained principal components are shown in Figures 11 and 12. The eigentriples (principal components) with the numbers 2 – 11 correspond to the required harmonics, and the eigentriples with numbers equal to or greater than 12 are noise.

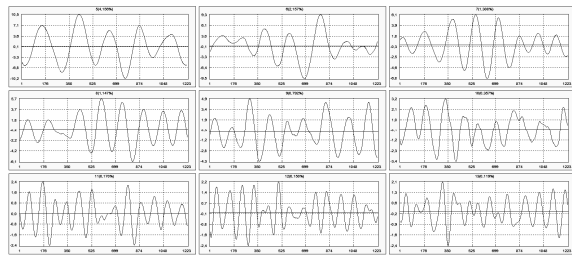


Figure 11: The principal components for 3C 345 at 14.5 GHz (one- dimensional diagram)

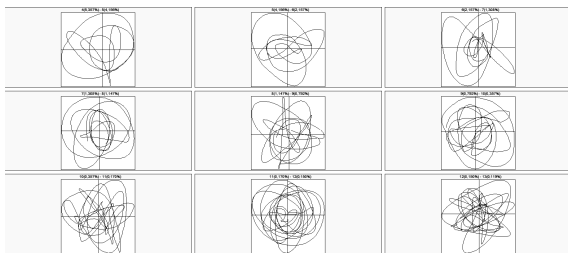


Figure 12: The principal components for 3C 345 at 14.5 GHz (two-dimensional diagram)

The main drawback of methods with the analyzing function such as Fourier or wavelet analysis is that there is some test function used for comparison with the original series. Singular spectrum analysis allows to avoid the test function, so its calculations allow us within high accuracy distinguish various components of the test series.

Periods for sources 3C 345 and 3C 446 obtained by singular spectrum analysis are shown in Tables 3 and 4. The dates of maximum activity are the same for several periods are typed in bold.

Table 3: Periods obtained by singular spectrum analysis for 3C 345.

Frequency 14.5 GHz		
8.1	2(18,34%), 3(6,80%)	1983.4 , 1984.3, 1987.8 , 1993.1
6.1	4(5,36%)	1982.4, 1985.8
4.9	5(4,16%)	1987.9 , 2001.1
4.1	6(2,16%)	1983.8 , 1996.9 , 2000.7
3.5	7(1,31%)	1983.6 , 2000.2
3.1	8(1,15%)	1987.4 , 1989.6
2.7	9(0,79%)	1987.9 , 1997
2.4	10(0,36%)	1987.2 , 1989.6 , 2007.8
1.7 – 1.9	11(0,17%), 12(0,15%)	1983.4 , 1988.1, 1989.9 , 1997.3 , 2000.7 , 2007.8 , 2008.5
Frequency 8 GHz		
15.1	1(27,94%),2(25, 73%)	1977.8, 1981.3 , 1984.9, 1987.9, 1992.7
10	3(12,36%), 4(6,33%)	1989.6, 1995.2 , 1997 , 2001.7
6	4(6,33%), 5(3,23%), 12(0,17%)	1981.5 , 1995.2 , 1995.9 , 1998.6 , 2000.8, 2001.7
4.3	6 (1,498%)	1997.95
3.3 – 3.8	7(1,28%), 8(1,16%), 11(0,44%),12(0, 17%)	1972.8 , 1981.5 , 1983, 1989.8, 1991.6, 1997.6 , 1998.6 , 2002.6
2 – 2.7	9(0,78%), 10(0,62%), 12(0,17%)	1972.9 , 1981.5 , 1998.4 , 2002.6
Frequency 4.8 GHz		
Period (years)	Principal components	Date of maximum activity
4.3	5(1,85%), (1,20%)	1985.4, 1987.9 , 1999.1, 2000.9
2.7	7(0,73%), (0,56%), 9 (0,22%)	1998.3 , 2000.9 , 2001.1 , 2004.9, 2006.6
1.8 – 2.2	9(0,22%),10(0,2 0%), 11(0,19%),12(0, 15%)	1998.5 , 2000.5 , 2006.5

Table 4. Periods obtained by singular spectrum analysis for 3C 446.

Frequency 14.5 GHz		
10.4	1(27,62%), 2(25,24%)	1984.6, 1988.8, 1992.9, 1994.7, 2004.6
5.2	3(16,12%), 4(8,88%)	1983.1, 1984.7, 1994.1, 1996.1
4.1	5(2,99%), 8(0,74%)	1983, 1989.1, 1992.6, 1995.2, 2000.8, 2006.9
2.6 – 3	6(2,14%), 7(1,88%), 8(0,74%)	1983, 1985, 1989.1, 1992.6, 1995.8, 1998.7, 1999.9, 2006.9, 2007.1
2.3	9(0,35%)	2000.3
1.7 – 2	10(0,28%), 11(0,25%), 12(0,24%)	1983.1, 1984.6, 1985, 1985.2, 1985.9, 1989.9, 1992.6, 2005.3
Frequency 8 GHz		
10.6	1(28,00%), 2(26,22%)	1996.7, 2000.9
5.3	3(13,41%), 4(7,64%), 6(1,87%)	1983.2, 1983.9, 1990.4, 2000.7, 2009.7
4.25	5(3,95%), 8(0,85%)	1983.8, 1985.5, 1990.4, 1995.9
2.7 – 3	6(1,87%), 7(1,52%), 8(0,85%), 11(0,23%)	1983.9, 1985.6, 1990.3, 1991.9, 1994.5, 1995.9
1.9	9(0,41%), 10(0,38%)	1985.3, 1990.9, 1992.1, 1995.9, 2009.7
1.5	12(0,17%)	1983.9, 1995.8
Frequency 4.8 GHz		
Period (years)	Principal components	Date of maximum activity
10.2	1(30,61%), 2(29,51%)	1995.6, 1998.9, 2000.8, 2006.2
5.1	3(9,38%), 6(0,88%), 7(0,70%), 8(0,56%), 11(0,14%)	1983.7, 1984.8, 1995, 1995.7, 1997.4, 2001.4, 2007.2
4.1	4(4,18%), 5(2,15%)	1985, 1993.9, 1994.3, 2000.6, 2001.5, 2004.6
2.6 – 2.9	6(0,88%), 7(0,70%), 8(0,56%), 11(0,14%)	1983.7, 1984.8, 1994.9, 1995.3, 1997.4, 2001.6, 2007.2
2	9(0,29%), 10(0,28%)	1993.9, 2000.4
1.6	11(0,14%), 12(0,10%)	1985.8, 1995.6, 1998.6, 2001.8

The common manifestation of several periods at the same time corresponds to maximum amplitude of flux.

Summary

We investigated the data of monitoring of flux density of extragalactic sources 3C446 and 3C345, which was held on 26-meter radio telescope of University of Michigan at frequencies 14.5, 8 and 4.8 GHz. The data of observations were investigated using singular spectrum analysis.

In investigated sources trend components were found in the range $\sim 6 - 10$ years (3C345) and $5 - 9$ years (3C446). Short-component is characterized by manifestation of periods $\sim 1.2 - 5$ years (3C 345) and $0.8 - 3$ years (3C 446). It is assumed that the long-period components correspond to the core activity, and short-components correspond to structural changes in the jet. Data analysis was carried out by two supplementing each other methods: wavelet analysis and singular spectrum analysis. Wavelet analysis is based on the Fourier transform, while the singular spectrum analysis does not use the analyzing function. The results of calculations of the singular spectrum analysis of fluxes of extragalactic sources were compared with the results of the wavelet analysis. The results obtained with two different methods showed a good correlation between them. The obtained data were compared with the VLBI maps (database MOJAVE) to study the evolution of component in the jets of the quasars studied. There was found the relationship of manifestation of certain periods of variability with changes in the jet.

References

- Alexandrov F.I.: 2006, Development of software system for automatic selection and forecast of additive components of time series in the framework of the "Caterpillar SSA", Publishing House of St. Petersburg State University.
- Aller H.D. et al.: 1985, *ApJS*, **59**, 513.
- Caproni A., Abraham Z.: 2004, *Proc. of the International Astronomical Union*, Issue IAUS **222**, 83.
- Gaydyshev I.: 2001, *Analysis and data processing (the special directory)*, St.Petersburg Publishing house.
- Lister M.L. et al.: 2009, *AJ*, **138**, Issue 6, 1874.
- Lobanov A.P., Roland J.: 2005, *A&A*, **431**, N 3, 831.
- Smolentsev N.: 2010, *Veyvlet-analiz in MATLAB*, DMKPress.

MONITORING THE COMMUNICATION CHANNEL FROM PUSCHSHINO TO MOSCOW IN THE PROJECT OF SPACE RADIO TELESCOPE "RADIOASTRON"

D.V. Dumsky^{1,2}, E.A. Isaev^{1,2}, V.A. Samodurov^{1,2}, K.A. Isaev³

¹ P.N. Lebedev Physical Institute, RAS,

53 Leninskiy Prospekt, Moscow, 119991, Russia, *dumsky@prao.ru*

² National research university Higher school of economics, *is@itaec.ru*
Moscow, 101000, Russia

³ Institute of Mathematical Problems of Biology, RAS,

4, Institutskaja str., Pushchino, Moscow Region, 142290, Russia

ABSTRACT. The need for transmission and storage of large amounts of scientific data in the project space radio telescope "Radioastron" required us to organize a reliable communication channel between the tracking station in Pushchino and treatment centers in Moscow. Network management data requires us to an integrated approach and covers the organization secure access to manage network devices, timely replacement of equipment and software upgrades, backups, as well as documentation of the network infrastructure. The reliability of the channel is highly dependent on continuous monitoring of network and server equipment and communication lines.

Keywords: Radioastron; monitoring; telecommunications.

1. Introduction

The RadioAstron is an international space VLBI project led by the Astro Space Center of Lebedev Physical Institute in Moscow, Russia. The payload - Space Radio Telescope, is based on spacecraft Spektr-R, that have been designed by the Lavochkin Associations. The purpose of the project is to use the space telescope for radio astronomical observations using VLBI (Very Long Baseline Interferometry) techniques in tandem with ground-based VLBI networks located in Australia, Chile, China, Europe, India, Japan, Korea, Mexico, Russia, South Africa, Ukraine, and the USA. The scientific objective of the project is to produce an image coordinate measurement and angular movements of different celestial radio sources with extremely high angular resolution (Kardashev et. al., 2012, Kanevskiy et al., 2014).

Ground tracking support of the spacecraft is currently provided using the 22-m antenna (RT-22)

located at the radio observatory near Pushchino, outside of Moscow (Fig.1). Flow of digital data received by tracking station can reach 128 Mbit/s. For efficient data exchange the direct communication fiber channel between PRAO and processing center ASC FIAN was created. The capacity of channel is 1Gbit/sec. In addition to tracking station the buffer data-center created as a reference node communication and file storage accomodation. The scientific data channel is used for transmission of telemetry information from the board of the spacecraft too. The channel of communication provided by ISP with guarantee of redundancy via two independent optical lines, and organized using technology MPLS (Multiprotocol Label Switching).

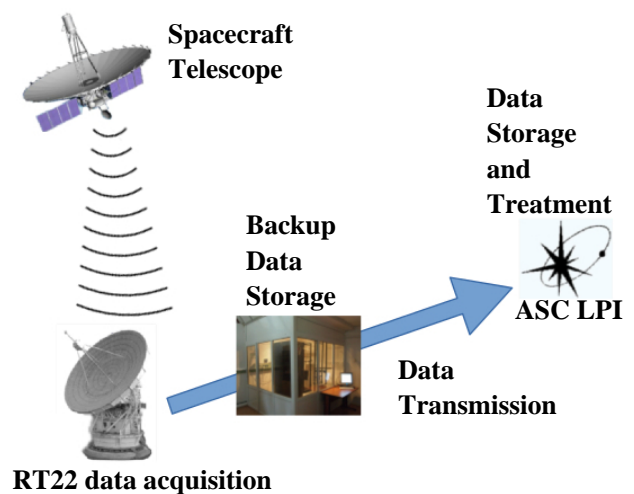


Figure 1: Radioastron data channels.

2. Chanell monitoring

Failsafe operation of the communication channel is especially relevant for the space telescope. For example, uninterrupted reception of telemetry data allows specialists to take further decisions on the correction of its orbit and receive important information about the performance of the onboard equipment. The success of the scientific experiments directly related to the reliability of the transmission of scientific data. This requires solutions that can automatically detect and respond to threats and channel performance issues in real time, as well as predict possible issues in the future. Monitoring system gives us the opportunity to have the right information about data transmission at the right time.

Real-time monitoring of hundred of metrics collected from network devices and servers is an important prerequisite for the smooth operation of the scientific data channel and the equipment in its structure. Monitor of availability, syslog messages, power consumption, temperature conditions and other various aspects of equipment performance help us maintained overall performance of the channel at an acceptable level. The main features of monitoring system is alerts when a fault occurs and storage of events history in DB.

We choose Zabbix as monitoring system because it is easy to use, it is Open Source and met most of the requirements we had for a monitoring tool in our environment for channel maintenance (Dumsky et al., 2014). The monitoring system is a powerful network tool that helps us to ensure that critical systems, applications and services are always up and running. It must provides features such as alerting, event handling, reporting and performance statistics. With items collecting data and triggers designed to “fire“ upon problem situations, we have alerting mechanism in place that is notify us about important events by email even when we are not directly looking at Zabbix frontend panel. We can see in which of the sites of the channel detects a problem with the help of interactive map monitoring in real-time. The current values of monitored parameters, as well as their changes can be viewed as separate graphs with scale changes by the hour, day, week and month (Fig.2).

2. Conclusion

Every day about 50 to 300 GB of unique information about the structure and evolution of various astrophysical objects (blazars, pulsars, cosmic masers and black holes) is transmitted through the channel. The same amount of data backed up in the PRAO ASC LPI buffer data storage. The average data rate of the channel transmission is typically 300-400 Gbit/s.

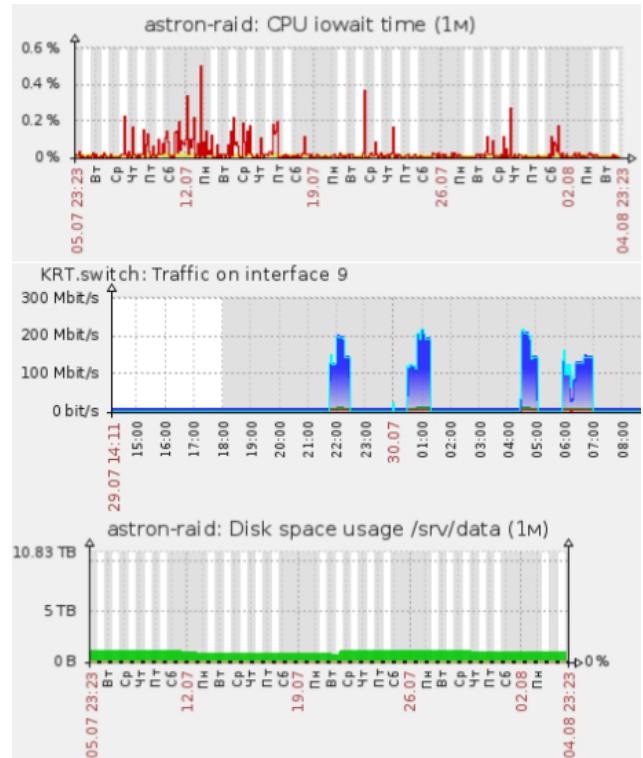


Figure 2: Graphs of important channel parameters.

The monitoring system over the past two years, allows us quickly resolved emergency situations caused by the power failure and failures of the network equipment, and cooling system of the buffer data center, as well as identify the causes of failures of channel associated with the failure of the individual switching devices and optical modules. We were promptly detected and eliminated two cases of the optical lines damage, allowing to minimize the idle time of the channel work. Monitoring of disks in buffer storage allows us for timely replacement of failed drives, that would prevent the destruction of RAID-array and prevent permanent loss of scientific data.

References

- Kardashev N.S., Kovalev Y.Y., Kellermann K.I.: 2012, *The URSI Radio Science Bulletin*, **343**, 22.
- Kanevskiy B.Z. et al.: 2014, *Bulletin of S.A.Lavoshkin Federal Research and Production Association*, **3**, 47.
- Dumsky D., Isaev E., Samodurov V.A. et al.: 2014, *Odessa Astron. Publ.*, **27**, 71.

SECULAR DECREASE THE FLUX OF SUPERNOVA REMNANT CAS A ON MONITORING RESULTS TO RADIOTELESCOPE "URAN-4" IRA NASU

A.A.Gorbynov¹, M.I.Ryabov², S.K.Panishko²

¹ Astronomy Department of I.I.Mechnikov Odessa National University

² Odessa observatory "URAN-4" of the Institute of Radio Astronomy NASU

ABSTRACT. This work is dedicated to the study of secular decrease of the flux of young supernova remnant Cas A according to observations by radio-telescope "URAN-4" of Odessa Observatory IRA NASU from 1987 to 2001 years on frequency of 25 MHz. On the investigation base there is a relationship analysis of flux CasA to the "stable" source – radio-galaxy Cyg A (CasA/Cyg A) which is located on a small angular distance. Results of the observations held on RT «URAN-4» show that there is no noticeable decrease of fluxes in the period 1987-1993, with the relationship ratio (CasA/Cyg A) = 1.5. While considering data from 1987 to 2001 manifested a slight decrease trend in flux equal to 8.4% for the all period. At the same time, according to various investigations the average value flux of Cas A in the interval of frequencies 38-2924 MHz is 0.8% per year. At the meantime in this frequency the range ratio (CasA/Cyg A) has become less than one. Thus, there is a noticeable contradiction of secular decrease of the flux Cas A on this radio frequencies in comparison with the predictions of the theory in 1.7% per year.

Keywords: supernova remnant, radioemission.

Introduction

In 1948 British radioastronomers Riley and Smith discovered an extremely bright radio source in the constellation Cassiopeia. They named it Cassiopeia A. This source became calibration for the majority of radio astronomy catalogs. It soon turned out that the flux varies systematically. The reason for these changes is the expansion of the supernova remnant. The theoretical explanation of the expansion of the supernova remnant was represented in the work of Shklovskii (1960).

Result of multifrequency observations

Observations of Cassiopeia A flux changes were at different wave lengths. At shorter wave lengths dominated secular decrease in flux. At longer wave lengths decrease flux was less noticeable. At the same time, at longer wave lengths we observed episodic change of flux associated with the state of the ionosphere.

Carrying out absolute changes of fluxes of radio sources is due to technical difficulties with their organizing and observations. In this regard the

determination of flux changes of Cas A is considered its relation to the flux of the radio galaxy Cygnus A (Cyg A) that is located on a small angular distance. This ratio is recorded as Cas A/Cyg A.

The results of such measurements at frequencies of 81.5, 151.5 and 290 MHz are shown in Fig. 1.

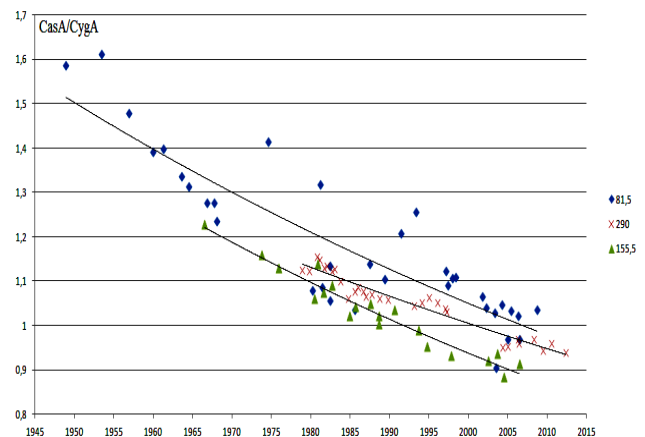


Figure 1: The ratio of fluxes Cas A / Cyg A at frequencies 81.5, 151.5 and 290 MHz.

Studies have been conducted at certain frequencies, indicated in the figures. One of the conditions is the stability of the radiation Cyg A. As a result, the rate d_v was obtained - secular decrease of the flux density of the radio emission in Cas A (Vinyakin, 2014).

$$d_{81.5}(2005.0) = 0.71 \pm 0.06 \% \text{ year}^{-1}$$

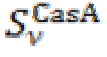
$$d_{151.5}(2005.0) = 0.78 \pm 0.04 \% \text{ year}^{-1}$$

$$d_{290}(2005.0) = 0.61 \pm 0.03 \% \text{ year}^{-1}$$

Nick Rees (1990) has studied the relationship Cas A / Cyg A. He found anomalous behavior relationships CasA/Cyg A at a frequency 38MHz (Rees, 1990). Such a deviation requires a detailed study on a longer period of time. Studies have been conducted on the meter and decimeter waves. We found four periods in the spectrum of variations relationships Cas A/Cyg A: (3.1 ± 0.02) ; (5.1 ± 0.3) ; (9.0 ± 0.2) and (24 ± 2) years. If the flux Cyg A is constant, they can be attributed to the secular variation Cas A.

According to various studies, the average decrease of flux Cas A in the frequency range 38-2924 MHz is detected in interval 0.39-0.99 % per year (see Table 1) (Bovkoon, 2010; Vinyakin, 2014).

Table 1:

ν	Epoch measurement	$-d\nu(2005)$, % year ⁻¹	 S _ν CasA (2015.5), Ян
20 MHz	1984.5	0.71 ± 0.12	37265 ± 3120
25 MHz	1984.5	0.99 ± 0.09	32095 ± 1890
38 MHz	1980.1	0.73 ± 0.13	26540 ± 2015
927 MHz	1991.2	0.68 ± 0.03	2360 ± 140
2924 MHz	1983.2	0.50 ± 0.09	1038 ± 64
22680 MHz	2005	0.51 ± 0.01	219.7 ± 3.0
32940 MHz	2005	0.55 ± 0.02	169.4 ± 1.8
33000 MHz	2002.9	0.39 ± 0.02	171.6 ± 0.6
40620 MHz	2005	0.56 ± 0.02	144.6 ± 1.7

Currently, as a result of the secular decrease of flux Cas A over frequency intervals 38 MHz ratio of the fluxes Cas A / Cyg A was less than one. Thus, there is a noticeable difference in the magnitude of the secular decrease in flux Cas A on radio frequencies than the theoretical predictions of 1.7% per year.

Observations on radiotelescope «Uran-4»

Observation Cas A on radiotelescope "URAN-4» of Odessa Observatory IRA NASU have been held for monitoring programme of fluxes of powerful radio sources at a frequency of 25 MHz since 1987 till present time. The study is based on analysis of the ratio of the flux to the Cas A "stable" source - radio galaxy Cyg A (Cas A / Cyg A).

In 1987-1993 observations were conducted in analog regime registration during 10-14 days a month. In 1999-2014 observations were carried out continuously in digital regime registration.

The procedure for processing the observation data was the following:

1. Flux of radio emission of the source was determined in relation to the power calibration signal noise generator.

2. The effective area of the antenna in different hour angles is different.

Therefore, the data obtained in different hour angles cited to the direction of the culmination radio source.

3. Matrix of observation data was processed to detect accidental releases. After their exclusion, we determined the average daily values, average for the entire period of observation and their dispersion.

Results of observations on RT «Uran-4»

According to observation results it has been found that for a correct consideration of changes of fluxes Cas A / Cyg A it is best to divide into two intervals of data. The first interval includes observations from 1987 to 1993 (Fig.2).

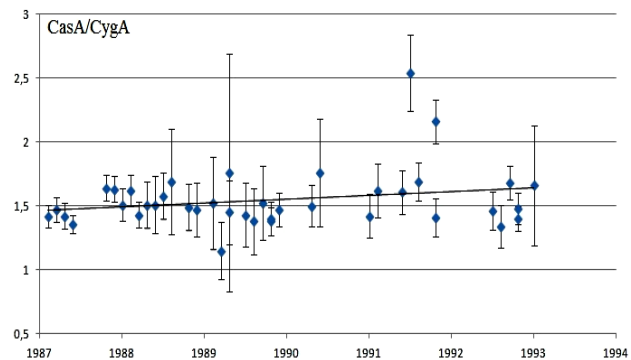


Figure 2: Observations of flux ratio Cas A / Cyg A from 1987 to 1993.

The results of observations carried out at RT "URAN - 4", show no appreciable drop in fluxes between 1987 and 1993 when the value of the flux ratio (Cas A / Cyg A) = 1,5.

The second period includes observational data from 1998 to 2002 (Fig. 3).

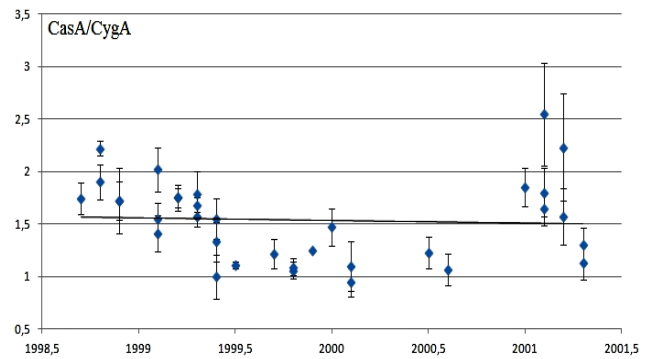


Figure 3: Observations of flux ratio Cas A / Cyg A from 1998 to 2002.

When considering the data from 1987 to 2001, there is a tendency of the flux decreasing, equal to 8.4% over a period of 14 years.

Conclusion

As a result of observations on the RT Uran-4 we received a marked contrast of the flux changes of Cas A at a frequency of 25 MHz compared to higher frequencies. The results of observations carried out at RT "URAN-4", show no appreciable drop in fluxes between 1987 and 1993 when the value of the flux ratio (Cas A / Cyg A) = 1,5.

The reason of regime change from the stability to reducing the flux of Cas A at decameter wavelengths may be the existence of a compact component in the center, especially the angular structure of the residue found in the X-ray space telescope "Chandra" and variations of the state of the ionosphere in the changing solar and geomagnetic activity. This can be quite a strong modulation of the flux of source, due to the influence of solar activity and seasonally-day effects. Hence, for solving the problem of secular decrease of Cas A radio flux at low frequencies, the season-day effect determined by observation should be taken into account. This effect

results in scatter of the ratio $3C461/3C405$ within the range 1.3-1.7 and enhanced dispersion if one or both sources are observed through non-stable ionosphere (Ryabov, 1993).

When considering the evolution of the flux of Cas A it should be taken into account: the existence of a compact source in remnant, rupture of the shell, the lifetime of individual condensations, the presence of shock waves in the remnant, modulation of the flux under the influence of changes in the state of the ionosphere. All this will help to better understand the processes that occur in the evolution flux of Cas A on the radio waves. In this regard, it is likely variability of Cyg A flux due to these effects will study in the future.

References

- Rees N.: 1990, *R. Astron. Soc.*, **243**, 637.
Bovkoon V.P. et al.: 2010, *Radiophys. and Radioastron.*
Ryabov M.I. et al.: 1993, *Astron. and Astrophys. Trans.*, **4**, 29.
Shklovsky I.: 1960, *AJ*, **37**, No2, 256.
Vinyakin E.N.: 2014...91, 9, 720.

LIGHT CURVE TYPES OF CLASSIC T TAURI STARS

N.Z.Ismailov, H.N.Adygezalade

Shamakhy Astrophysical Observatory after named N.Tusi of ANAS
AZ 5626, Y.Mamedaliyev set., ShAO, Shamakhy, Azerbaijan, *ismailovn@yahoo.com*

ABSTRACT. By using the archive photometric data's obtained for a long time intervals we have carried out a master light curves of 28 classical T Tauri type stars. For the physical character of variability mainly 5 type light curves can be separated. We have proposed a new scheme of classification among the examined light curves. The proposed scheme suggests a qualitative interpretation in terms of interaction of the central star with its circumstellar accretion disk.

Keywords: T Tauri stars, variability, master light curves, classification.

1. Introduction

T Tauri stars were first identified as an interesting pre-main sequence class of objects because of their unusual spectral and photometric properties (Joy, 1945, Herbig, 1962). Classical T Tauri stars are possess strong emission lines (hereafter CTTS) (stars with equivalent widths $W(H\alpha) \geq 10\text{\AA}$) and are now recognized as pre-main sequence stars accreting material from an extended circumstellar disk. There are also T Tauri stars (hereafter TTS) with weak emission lines and circumstellar disk indicators (so-called "weak-line" TTS: WTTS) or without emission lines and disks (hereafter naked TTS: NTTS). Despite a large amount of observational material obtained for last 60 years, there remains unclear a physical causes of the light variations of TTS.

Researches of last year's show that there are only a rather limited number of plausible mechanisms by which a star could conceivable change its apparent brightness. At this time such mechanisms were proposed: 1) the rotation of the star with an asymmetrical distribution of cool spots, 2) variable hot spots on the stellar surface, 3) stellar flares and accretions, 4) grows and decay of large active regions on the photosphere and, 5) obscuration by circumstellar dust (e.g., Herbst et al., 1994).

The classification scheme for "Orion variables"—now called T Tauri stars — firstly suggested in 1954 by Parenago (1954) based on photographic observations is still relevant today. In this scheme, the most important factor is the shape of the light curve. Following Parenago's (1954) scheme Herbig (1962) classified the forms of light curves into four classes. Then Herbst et al.(1994) were divided TTS light curves into four types based on the color and spectral variations.

The relationship between Herbig's "class" and Herbst et al.'s "type" is not clear, but may reflect the different time scales of variability, i.e., longer for the "class" (10-100 days) and shorter for the "type" (0.5-30 days). Moreover,

both proposed classification schemes make difficulties in separation of the different type of light curves. Our purposes in this report are consideration of the forms of CTTS light curves obtained on the more rich observational data.

2. Observational data and results

We used the photoelectric *UBVRI* observation results from the Wesleyan University database (<ftp://sun.astro.wesleyan.edu>) (Herbst et al.1994) and from archive Grankin et al. (2005) which is a collection of many-year observations by various authors. These data do not cover all available observations for individual objects, but the amount of material is sufficient to study the general characteristics of the T Tauri stars represented in the database. To avoid biases due to observational selection effects, we chose objects with as many data points as possible accumulated over decades. Moreover we included to this material for some stars results from ASAS database (www.astrouw.edu.pl/asas) for *V* and *I* bands.

We selected a total of 28 classical T Tauri stars with more than 300 observations as a minimum in various filters. The typical photoelectric photometry uncertainties are about $\pm 0.01^m$ in *B* and *V* and, as a rule, no more than $\pm 0.03^m$ in *U*. For the ASAS data average uncertainties is relatively large (at $\pm 0.05^m$), while we have not discovered some systematic differences with data's from other catalogues. We were not able to correct for systematic differences between the data of different authors, but most of the observations for individual stars appear uniform, indicating that such systematic differences are not significant. In the Figure 1 demonstrated plotted master light curves of some CTTS.

After plotting the light curves for all 28 stars, we attempted to identify general tendencies and differences among these curves. Figure 2 displays an example of each of the light curve types we found among the T Tauri stars in our sample. The arrows in Figure 1b schematically explain our approach to estimating the amplitudes of brightness variations for (i) active states with high amplitudes (ΔV_1) and (ii) quiet states with low amplitudes (ΔV_2), at approximately the same brightness level. A list of selected objects, amplitudes ΔV_1 and ΔV_2 , full amplitudes of color indexes $\Delta(U-B)$, $\Delta(B-V)$ and determined types on our classification scheme are presented in the Table 1.

Both existing photometric studies of T Tauri stars and our results show the following common features in the light curves. All the T Tauri stars display irregular brightness variations over several days during various observing seasons. The stars show both quiet and active

states. In the quiet state, the daily brightness variations (we will use this term to refer to all brightness variations with time scales within 1–15 days) for individual stars can have amplitudes from 0.07^m to 1.6^m (V866 Sco), but, in most cases, the V amplitude is within 1^m .

Rapid daily brightness variations are observed in both the active and quiet states. The amplitudes of the brightness variations in the active and quiet states, ΔV_1 and ΔV_2 (Fig. 1b), differ, with their ratio being almost constant, on average higher than two.

We determine the active and quiet states of a star as follows. As a rule, during a given time interval, a star displays brightness variations that can be described with two parameters: the mean brightness and the amplitude of the daily variations. Both parameters can differ considerably from season to season. To study these variations, we selected the extreme states of both parameters. Thus, we can characterize the states of the highest and lowest mean brightness. We call these extreme states of the amplitude of the daily variations the star's "active" and "quiet" states. The star's mean brightness in its active and quiet states can be different or virtually the same.

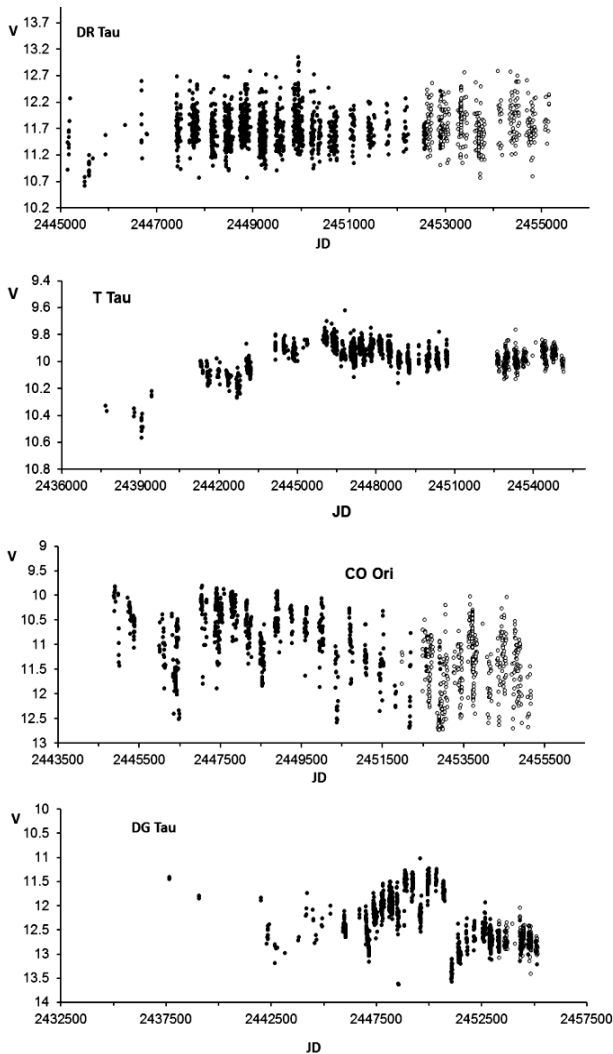


Figure 1: Examples of master light curves for some CTTs. Dark cycles—from catalogue Herbst et al.(1994), open cycles from ASAS database.

Our analysis shows that we can clearly distinguish five different types of light-curve shapes. We distinguish the following principal types based on light-curve shape:

- type I:** constant mean brightness without changes in the amplitude of the rapid brightness variability;
- type II:** constant mean brightness with changes in the amplitude of the rapid variability;
- type III:** varying mean brightness without changes in the amplitude of the rapid variability;
- type IV:** variations of both the mean brightness and the amplitude of the rapid variability;
- type V:** the variable is often bright, and rare brightness decreases (dimming) are observed.

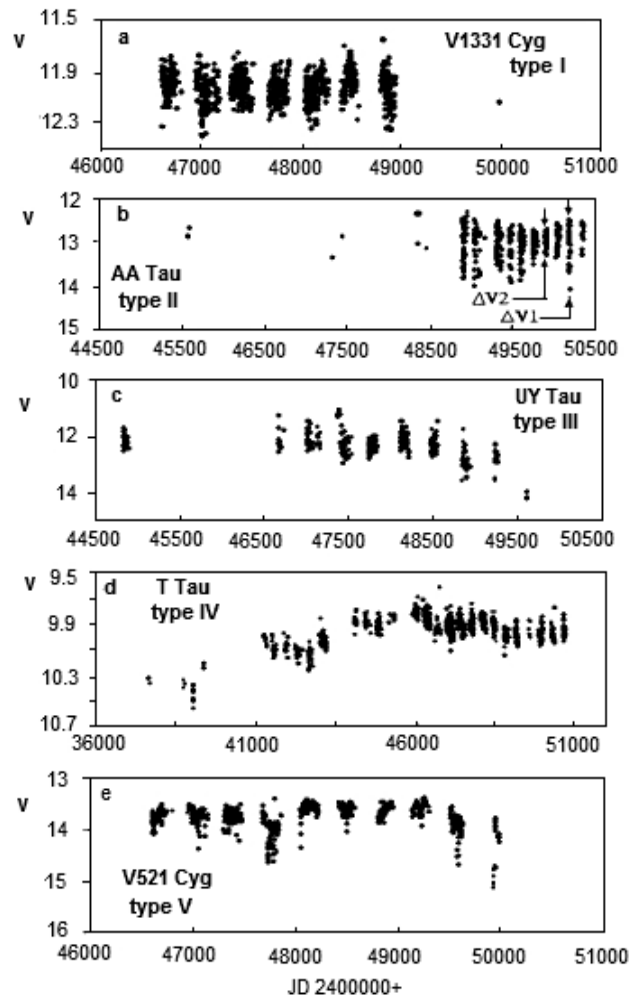


Figure 2: Selected typical examples of CTT light curves. The arrows in panel (b) explain our technique for estimating amplitudes during different brightness states of the stars.

Type I stars exhibit brightness variations whose amplitude is almost the same in different years, and whose mean brightness does not vary. Only two stars like this were found in our sample, DL Tau and V1331 Cyg (Fig. 1a). Despite the presence of some scatter about the mean level, the mean brightness itself does not vary. Such variability can be explained by brightness modulation of a cool spot on the surface due to axial rotation of the star. In

this case, we must assume that the spots are very stable and that their relative area does not vary within a season or from season to season.

The mean brightness of the type II stars does not vary, but their rapid variations on time scales of several days are accompanied by gradual changes in their amplitude over several years. Typical representatives of this group are DR Tau and AA Tau (Fig. 1b). This type has the most members in our list (13 stars of 28). Such variations could be due to modulation of the star's brightness in the presence of a hot spot or to variable activity of the star itself, similar to cyclic solar activity, as well as to the appearance of additional radiation associated with non-stationary disk accretion. The light curves of this type suggest that such activity appears and then gradually disappears over five years.

Similar to the type I stars, the type III stars do not show variations in the amplitude of their rapid daily brightness variability; smooth changes of the mean brightness (trends) on time scales of several years are observed. A typical example is DN Tau (Fig. 1c). In our opinion, this

type of variability requires the presence of a stellar companion whose brightness is comparable to that of the variable star and comparatively constant. Then, in principle, the brightness variations can be described fairly well using a cool spot model.

In addition to their rapid daily variations, the type IV stars exhibit simultaneous changes in their variability amplitude within a season, as well as long-term changes in their mean brightness over several years. Most ETT stars are of this type; typical representatives are T Tau and RY Tau. It is likely that, along with seasonal changes due to the star's chromospheric activity, eclipses by an invisible companion or a protoplanet also occur (Fig. 1d).

The type V stars are as a rule, in bright condition. There are sometimes rapid daily variations with amplitudes of up to 0.5^m , but abrupt dimmings with amplitudes exceeding $\sim 1^m$ in V are also observed in some years. A typical representative is V521 Cyg. If objects such as this exhibit dimmings often and within short time intervals, then the star's light is probably blocked by circumstellar gas and dust (Fig. 1e).

Table 1. Observational data for the studied sample of T Tauri stars

Star	ΔV_1	ΔV_2	$\Delta(U - B)$	$\Delta(B - V)$	Sp	Type
BM And	2.35	1.04	0.79	0.38	K5V	III
RW Aur a	2.66	1.09	0.93	0.69	K1V	IV
SU Aur	1.1	0.17	0.51	0.38	G2III	III
UY Aur	3.18	0.82	1.06	1.61	K7V	II
GM Aur	0.74	0.3	1.36	0.49	K3V	IV
DI Cep	0.57	0.19	0.54	0.37	K1V	V
V521 Cyg	1.77	0.31	0.32	0.47	G8	II
V1082 Cyg	1.05	0.74	0.82	0.4		I
V1331 Cyg	0.73	0.42	0.58	0.12		III
V1121 Oph	0.74	0.45	0.68	0.51	K5	IV
CO Ori	2.68	0.45	0.72	0.37	F8	V
GW Ori	0.63	0.07	0.43	0.23	G5V	II
V866 Sco	3.56	1.6	0.42	0.58	K5V	IV
T Tau	1.1	0.18	0.79	0.26	K1V	IV
RY Tau	1.25	0.23	0.39	0.15	K1IV	V
UX Tau ab	2.13	0.93	0.78	0.51	K2V	II
AA Tau	1.77	0.66	1.5	1.04	K7V	II
BP Tau	1.31	0.19	0.78	1.25	K7V	II
CI Tau	1.51	0.41	1.12	0.49	K7V	II
DF Tau	1.95	0.23	1.8	1.22	M0	III
DG Tau	2.15	0.75	0.36	0.36	M?	VI
DK Tau	1.95	0.23	0.42	0.81	K7V	III
DL Tau	2.02	0.8	0.44	0.69	K7V	III
DN Tau	0.55	0.34	0.42	0.18	M0V	II
DR Tau	3.67	1.81	0.74	0.78	K5V	II
GG Tau	0.58	0.15	0.62	0.75	K7V	
GI Tau	2.95	1.39	2.18	1.29	K6V	
GK Tau	1.13	0.68	1.23	0.54	K7V	

3. Conclusion

Let us obtain a simple estimate of the accreted mass needed to provide a V -brightness variation of $\Delta V=0.5^m$, as is typical of most CTT stars (Herbst et al. 1994)

Many photometric observations of T Tauri stars show brightness variations in the quiet phase of up to several tenths of a magnitude. Let the star have a mass and luminosity equal to the solar values (G2V spectrum). A brightness change $\Delta V = 0.5^m$ will then imply an increase of the radiated flux by a factor of 1.58, and the additional flux for such a brightness variation is $\Delta E=2.2 \times 10^{33} \text{ erg}\cdot\text{s}^{-1}$. The characteristic fastest motions indicated by the observed emission lines of T Tauri stars (including those related to accretion onto the star) have velocities of about 300 km/s (e.g. Petrov et al., 1999). With such velocities for the accreting matter, the energy balance of the additional radiation flux requires a mass of up to $\Delta M = 4.7 \times 10^{22} \text{ kg}$, which is about a factor of 100 lower than the mass of the Earth and is comparable to the mass of the Moon. This demonstrates that the variability of stars having type I light curves (constant mean brightness and constant amplitude) can probably not be due to the accretion of matter from a circumstellar disk, because the rate of accretion onto a star cannot be constant. Type I brightness variations could be due to the presence of a cool spot and/or an active chromosphere

A simple calculation shows that a large mass, comparable to that of the solar system's planets, can fall onto the stellar surface during an outburst, apparently within a short time (days). Such large brightness variations are characteristic of type IV T Tauri stars. Various stars experience such substantial variations from once every several years to once every several decades.

This shows that the interaction between the circumstellar disk and central star is active, and is accompanied by appreciable mass transfer through the circumstellar disk.

All this suggests that a typical, comparatively inactive T Tauri star should have a type I light curve. The other types of light curves can result from additional physical processes influencing the star, such as the accretion of matter from a circumstellar disk, eclipses by circumstellar matter, outbursts, effects associated with binarity, etc. This suggests that the main "stationary" object for all the light-curve types is the star itself, which probably has a magnetically active, spotted surface (e.g. Petrov et al., 1999).

Thus, the proposed classification scheme for T Tauri light curves is in reasonable consistency with current concepts concerning mechanisms for the variability of young stars. Note, however, that, bearing all these general features in mind, individual interpretation is needed for each particular observed T Tauri light curve.

Acknowledgements. This work supported by Azerbaijan National Academy of Sciences as a priority field of scientific researches.

References

- Grankin K.N. et al.: 2007, *A&A*, **461**, 183.
- Herbig G.H.: Adv. 1962, *A&A*, **1**, 47.
- Herbst W. et al.: 1994, *AJ*, **108**, 1906.
- Joy A.H.: 1945, *ApJ*, **102**, 168.
- Parenago P.: 1954, *Publ. Shtern. Astron. Institute*, 25.
- Petrov P.P. et al.: 1999, *A&A*, **341**, 553.
- Pojmanski G.: 2002, *Acta Astronomica*, **52**, 397.

HE I 5876 LINE STRUCTURE IN THE SPECTRA OF IL CEP A

N.Z.Ismailov, O.V.Khalilov, G.R.Bahaddinova

Shamakhy Astrophysical Observatory after named N.Tusi of ANAS
AZ 5626, Y.Mamedaliyev set., ShAO, Shamakhy, Azerbaijan, *ismailovn@yahoo.com*

ABSTRACT. We are presents the results of researches of the He I $\lambda 5876$ Å (D_3) line in the spectrum of Herbig Be type star IL Cep A. This line represents the absorption structure which has a width on the level of the continuum about 15-18 Å, and a FWHM about 6-8 Å. It is shown that the line He I $\lambda 5876$ Å has a complex, multi-component structure. The average value of the radial velocities showed smooth variability, and the maximum value V_r achieved in 2009-2010. Large scatter in radial velocity was obtained in 2013 and 2014.

The equivalent width of the line also shows significant changes from year to year, and during the observation season. The total average value of this parameter remains constant for all observations. For all of the data, a mean value of the equivalent width of the absorption is equal 0.56 ± 0.025 Å, and the standard deviation ± 0.16 Å from the mean. The observed features in the line indicates that the field of origin this line has a complex structure and physical conditions.

Keywords: Pre-Main Sequence stars, spectral variability, helium D_3 line, IL Cep A.

1. Introduction

Herbig Ae/Be stars (HAeBes) are pre-main sequence (PMS) objects of intermediate mass approximately from 2 to 8 M_\odot (Herbig, 1960; Finkenzeller & Mundt, 1984; Thé et al., 1994), spectral classes from B0 to F2 and types of luminosities IV-V. They are surrounded by dust/gas accretion disks. Disks of HAeBes have a complex spatial structure and contains an accretion regions and matter outflows in the form of a stellar/disk wind at higher latitudes.

HAeBe stars may be the precursors of young main sequence β -Pictoris and Vega-type stars. These latter systems are surrounded by circumstellar debris disks, which perhaps contain planetary bodies. This would imply that the environment around HAEBE stars represents an early phase in the formation of planets.

HAeBe stars are important astrophysical objects because they represent the late formative stages of intermediate mass stars. They are therefore significant for understanding general and specific phenomena involved in star formation. Moreover, HAeBe stars can help us to understand a number of perplexing properties of their main sequence (MS) descendants: in particular chemical peculiarities, very slow rotation, and magnetic fields, observed in individually or in combination in a significant fraction of MS A/B stars.

The star HD 216629 = IL Cep A ($\alpha_{2000} = 22^{\text{h}}53^{\text{m}}16^{\text{s}}$, $\delta_{2000} = +62^\circ 08' 45''$, $V \sim 9.3$) is a member of young starformation region Cep OB3. At the distance 6.9" (IL CepB=ADS 16341B) (Pirzkal et al., 1997) and even 0.44" (Wheelwright et al., 2010) of the star it were separated two companions which are weaker in brightness to $\Delta B = 3.5^{\text{m}}$ than the main component.

On the data of different authors the spectral type of IL CepA was determined as B2IV-V (Garmany, 1973), B3e (Finkenzeller, 1985), or as a components in visual binary B3 and B9 (Alecian et al., 2013). Radial velocities, equivalent widths and profiles of hydrogen lines are variable (see, e.g. Ismailov et al. 2013 and references there).

Hill (1967) firstly have determined the periodical variation in brightness of the star with the period 1.^d401, but later in the work (Hill et al., 1976) this periodicity was not confirmed.

One of consider question in the HAeBes spectrum is a structure and origin of the line D_3 . This problem firstly in detail was studied by Böhm and Catala (1995). These authors showed that the line D_3 in HAeBes has mainly 2 type profiles: 1) clean absorption profiles and 2) absorption profiles which have blue shifted emission components. Some stars shows more complex structure. A question of the nature of different components in the line D_3 of young stars is object of discussion.

In this work we have presented results of long time researches the line D_3 structure in the spectrum of IL CepA.

2. Observations and results

The spectra were taken in 2006–2014 in the Cassegrain focus of the 2 m telescope of the Shamakhy Astrophysical Observatory of the Azerbaijan National Academy of Sciences. We used the UAGS-based spectrometer (Ismailov et al., 2013). A CCD detector is fixed in the focal plane of the camera. The 530×580 px CCD has a linear size of $9.5 \times 13.9 \text{ mm}^2$ and a pixel size of $18 \times 24 \mu\text{m}^2$. The dispersion is equal to 10.5 \AA/mm and about 6 \AA/mm in the red and blue parts of the spectrum, respectively. The entire observed region of the spectrum can be covered by two frames. The spectrometer operates in 70–140 orders. The CCD window accommodates 28 and 50 orders in the red and blue parts of the spectrum, respectively. The normal spectrograph slit width determined by the CCD pixel size is 0.35 mm, which, given the effective Cassegrain focal length of 29 500 mm, corresponds to 2.

The spectrometer has a spectral resolution of $R = 14\,000$, and a signal-to-noise ratio $S/N=80-100$ in the $H\alpha$ region and $S/N=20-40$ in the HeI 5876 Å region. To control the stability of the system, the spectra of standard stars, the flat field image, and the comparison spectrum were taken every observing night at the beginning and end of the exposure of the object. Wavelength calibration was based on the spectrum of sunlight scattered in the Earth's atmosphere. We used the DECH20T program and its components developed at the Special Astrophysical Observatory (Galazatdinov, 1992) to perform all the image reduction tasks and subsequent measurements of the spectra.

We used the lines of the Th-Ar lamp comparison spectrum to estimate the instrumental contour width, which we found to be 0.36 and 0.44 Å in the blue and red parts of the spectrum, respectively. The measured half widths of some lines exceed significantly the width of the instrumental profile: they are equal to 6–8 Å, 2–4 Å, and 4–7 Å, for $H\alpha$, $H\beta$, and D_3 , respectively, and 0.8–1 Å and 1.5–2.0 Å for NaI D_1, D_2 and DIBs $\lambda\lambda 5780, 5798$ Å, respectively.

We acquired a total of 50 pairs of spectrograms of the star for 2006-2014 years. Each pair consists of two identical spectra taken one after another. Three to four identical spectra of the star were taken on some nights.

The errors of the measured equivalent widths and intensities were equal to 5% and about 1%, respectively. The mean error of position measurements in the spectra of standard stars was 2–3 km/s. The measurement errors for the equivalent widths D_3 absorption sometimes exceed this limit because of the lower S/N ratio in the corresponding parts of the spectrum.

The line D_3 in the spectrum of IL CepA is represented as a wide absorption profile with width on the continuum at 15–18 Å and with a half width FWHM 6–8 Å. For this star in the work Tuairisg et al. (2000) was determined equivalent width of D_3 as 250 mÅ for absorption and 5 mÅ for emission components.

Because the line in our spectra has a complex structure the equivalent width we have determined by integration method for all boundary of contours. The radial velocity of the line was measured on the displacement of the line center at the half intensity level.

In the Figure 1 has shown a time variation of equivalent widths W_λ (up panel) and radial velocities V_r for the line D_3 (top panel).

As seen from the Figure 1 values of the equivalent width have some scatter from night to night but mean of this parameter is not so large changes during all time of observation. For all measurements mean value of equivalent width is equal 0.56 Å with dispersion ± 0.16 Å and with mean error of measurement ± 0.025 Å.

In 2013 radial velocities has shown variation from -12 to -32 km/s, this scatter bigger than in previous years. In 2014 the scatter in V_r is maximal, from -27 to +44 km/s. Moreover one can see smooth decrease of mean values V_r still 2010, then return to previous values. This character of variation in V_r of the line D_3 in more little scale is repeated variations of radial velocity of the emission component of $H\alpha$. This event also followed with unusual decreasing of equivalent width of $H\alpha$ emission from -14 Å to -7 Å (Ismailov et al., 2013).

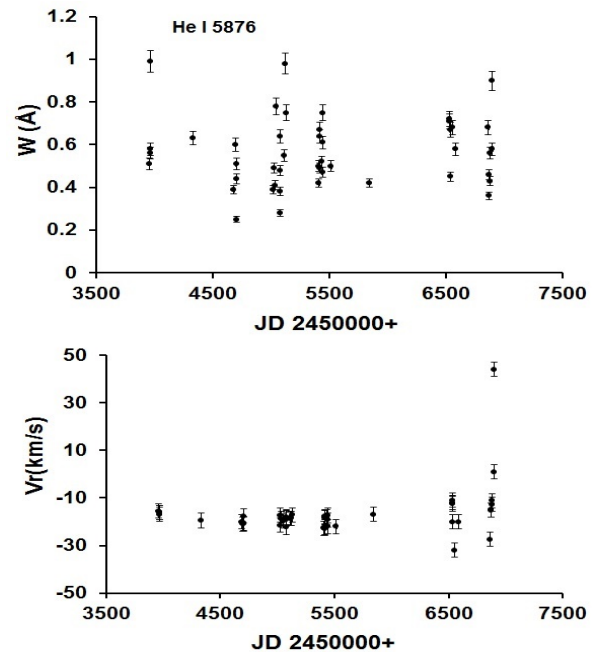


Figure 1: Time variation of equivalent widths W_λ (top panel) and radial velocities V_r (bottom) of the line D_3 .

In Figure 2 are shown profiles of the line D_3 obtained in various nights. The profile shows complex structure which are consisting of some components. The structure shows variations for different nights. Moreover one can see some stable observable per night components. These components at 10-20 times stronger than the noise level, because we think that they are real components, possible consisting of emission components imposed to the weak absorption. Actually as has shown in Figure 2, the limit of noise intensity must be less or equal of the intensities of atmospheric H_2O lines placed near of lines D_1, D_2 NaI.

In detail a theory gives the following atomic transitions of the line He I 5876 Å (see, http://physics.nist.gov/PhysRefData/ASD/lines_form.html) (Table 1).

Table 1: Atomic parameters of the line D_3 .

Wavelength, Å	Transition level	$\log gf$	relative intensity
5875.5987	$2p\ ^3P^o - 3d\ ^3D$	-1.511	
5875.6140	$2p\ ^3P^o - 3d\ ^3D$	0.480	5
5875.6148	$2p\ ^3P^o - 3d\ ^3D$		5
5875.6251	$2p\ ^3P^o - 3d\ ^3D$	-0.338	5
5875.6404	$2p\ ^3P^o - 3d\ ^3D$	0.138	5
5875.9663	$2p\ ^3P^o - 3d\ ^3D$	-0.214	1

In columns were presented: wavelength in Å, levels of transition, $\log gf$, where g -factor and f - the strength of oscillator, relative intensity. In our spectrum the lines 5875.61, 5875.62 and 5875.64 we have got as one unresolved line. The line 5875.966 is relative weak than previous lines. Indeed as have seen in Figure 2 as a minimum we obtained 2-3 relative strong separated components in this line. But we count that these components may be results of variable emission which imposed to the wide absorption of this line.

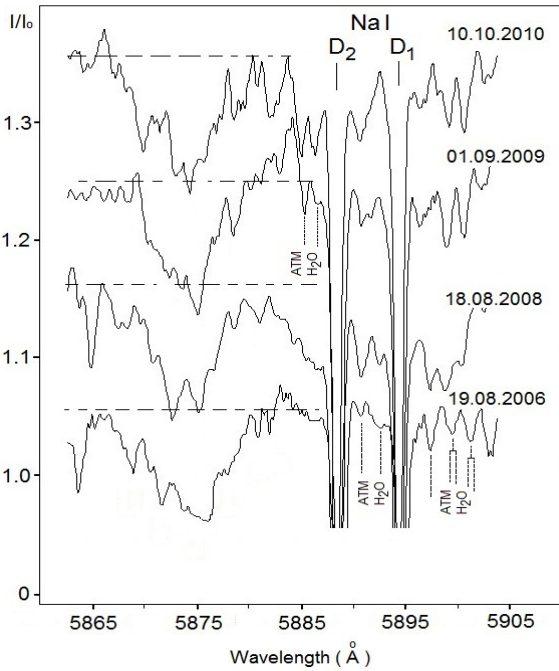


Figure 2: The structure of the line D₃ in the spectrum IL CepA.

In favor of our assumptions in Figure 3 have presented the profile of the line D₃ He I for spectrum of different HAeBes – AB Aur (Sp B9-A0V), HD 200775 (Sp B2-B3V) and supergiant 55 Cyg (Sp B3 Ia) which were observed in the same up mentioned equipment. As seen from the Figure 2 in spite of the fact that all these stars have in the spectrum the line D₃, the structure of the line as in IL Cep A is not detected. Moreover we have presented the profile of this line, for the spectrum IL Cep A obtained by Böhm and Catala (1995), where we see the same multicomponent structure in the line D₃. This comparison allows us to suppose that the complex structure in the line D₃ may be connected of additional emission components in the line.

In the work by Tuairisg et al. (2000) authors tired determination of contribution of additional emission in this line for IL CepA. For it they are subtracted a theoretical profile of the line for corresponded spectral class from the observed profile of the line. As mentioned these authors, this procedure is followed many errors: to determination of real fundamental parameters of the star, influence of the noise, model calculations etc. Main of them on our opinion are connected with determinations of the real spectral class of IL Cep A, because as mentioned in Ismailov et al.(2013) the spectral class of the star were determined by different authors is different.

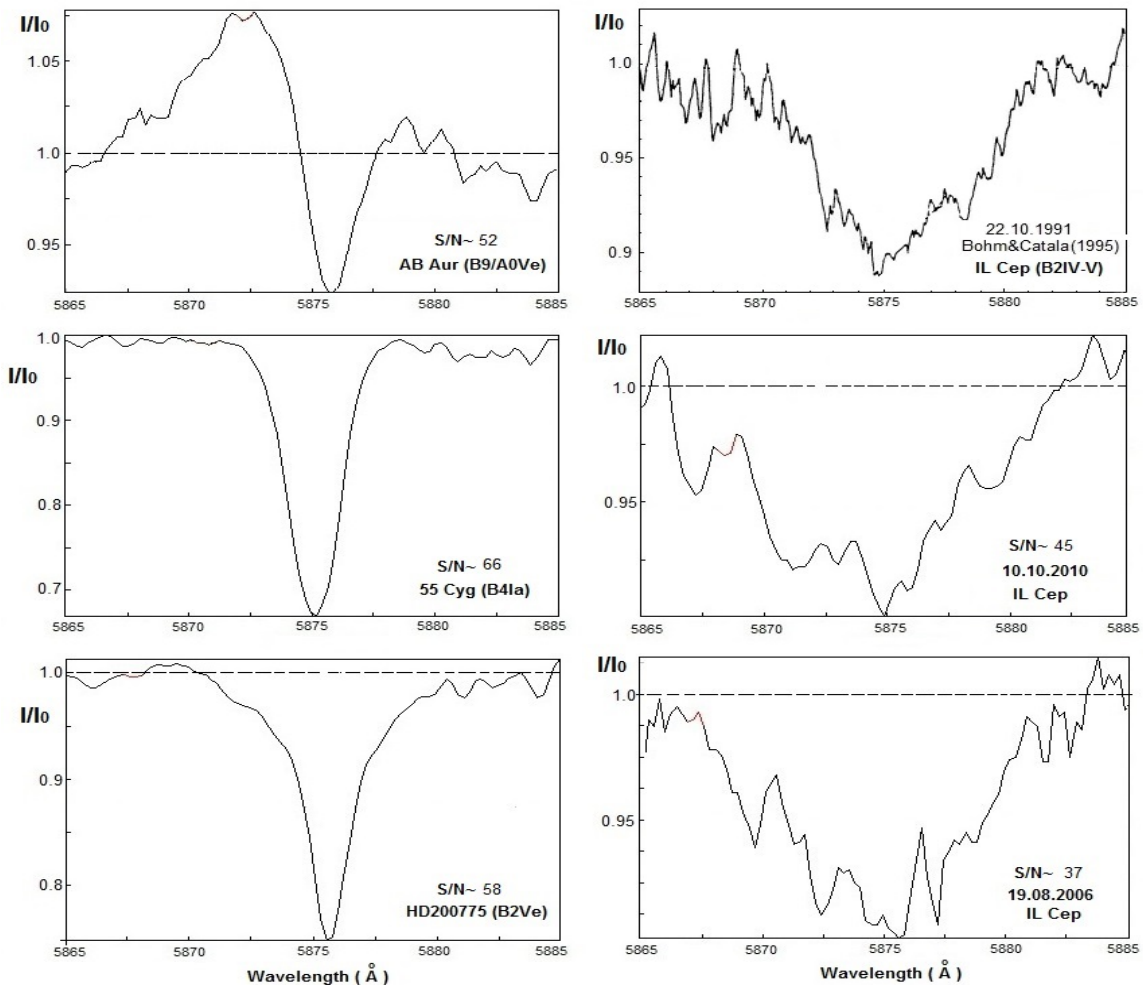


Figure 3: Profiles of the line He I 5876 Å for different stars obtained in the same equipment: on the top right panel presented a profile of the line from the work by Bohm and Catala (995). For each panel S/N level have presented.

As a first step by using Mihalas (1964) theoretical profiles of the line HeI 5876 Å (for $T_{\text{eff}}=20000$ K and $\lg g=4.0$) and taking into account a rotational velocity of IL Cep A as 180 km/s (Ismailov et al.2013, Melnikov et al. 1996) we have try to determine the contribution of emission component imposed to the helium absorption. In Figure 4a,b for example we have presented a residual profiles of the line for 2007 and 2009 obtained by dividing the observational profile to the theoretical with corresponding parameters. As seen from this figures in each case we have residual emission components. This fact as a minimum shows that the observational profile of the star perhaps is consisting of superposition of emission and absorption components.

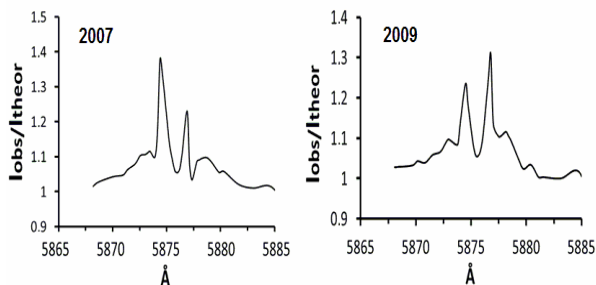


Figure 4: The residual structure obtained by dividing of the observational profile to the model.

3. Conclusions

Thus we have analyzed a structure of the D₃ line helium in the spectrum of HAeBes IL Cep A. We concluded that the line has complex multicomponent and variable structure. Some of components in the profile are real and connected with emission from the star envelope or disk. This line represents the absorption structure which has a width on the level of the continuum about 15-18 Å, and a FWHM about 6-8 Å. Although equivalent widths of the

line demonstrated some scatter for different seasons of observation, the mean value of this parameter is not varied from year to year.

The radial velocity in the line D₃ shows the smooth variation with a minimum in 2010. This character of variation in V_r of the line D₃ in more little scale is repeated variations of radial velocity of the emission component of H α . In 2013 and 2014 we have observed large scatter in radial velocities perhaps connected with activity in the circumstellar environment. A long time smooth variation in V_r perhaps occurred by dynamical motion in the binary system.

Acknowledgements. This work supported by Azerbaijan National Academy of Sciences as a priority field of scientific researches.

References

- Alesian E. et al.: 2013, *MNRAS*, **429**, 1001A.
- Böhm T., Catala C.: 1995, *A&A*, **301**, 155.
- Finkenzeller U.: 1985, *A&A*, **151**, 340.
- Finkenzeller U., Mundt R.: 1984, *A&AS*, **55**, 109.
- Galazutdinov G.A.: 1992, *Preprint of the Special Astrophysical Observatory*, No. 92.
- Garmany C.D.: 1973, *AJ*, **78**, 185.
- Harvey J.V., Tandberg-Hanssen E.: 1968, *SoPh.*, **3**, 316.
- Herbig G.H.: 1960, *ApJS*, **4**, 337.
- Hill G. et al.: 1976, *Publ. Dom. Astrophys. Observ.*, **15**, 1.
- Hill G.: 1967, *ApJSS.*, **14**, 263.
- Ismailov N.Z. et al.: 2013, *Astrophys. Bull.*, **68**, 196.
- Mel'nikov S.Yu. et al.: 1996, *Astron. Reports*, **40**, 350.
- Mihalas D.M.: 1964, Pasadena, California, 220 p.
- Pirzkal N. et al.: 1997, *ApJ*, **481**, 392.
- Thé P.S. et al.: 1994, *A&AS*, **104**, 315.
- Tuairisg S.O. et al.: 2000, *A&AS*, **142**, 225.
- Wheelwright H.E. et al.: 2010, *MNRAS*, **401**, 1199.

SEASONAL VARIATIONS OF THE IONOSPHERE SCINTILLATIONS PARAMETERS OBTAINED FROM THE LONG OBSERVATIONS OF THE POWER COSMIC RADIO SOURCES AT THE DECAMETER WAVE RANGE

O. A. Lytvynenko, S. K. Panishko

Observatory URAN-4, Institute of Radio Astronomy NASU
Pushkinskaya str., 37, Odessa, 65125, Ukraine, spanishko@ukr.net

ABSTRACT. Observations of the four power cosmic radio sources were carried out on the radio telescope (RT) URAN-4 during 1987-1990 and 1998-2007 at the frequencies 20 and 25 MHz. Effects of ionosphere and in particular existence of intensity fluctuations on the cosmic radio sources records, or scintillations, are essential at the decameter wave range. Long series of the ionosphere scintillations parameters such as indices, periods and spectrum slopes were obtained after observation data proceeding. Behavior of the seasonal variations was investigated on this data. Obtained dependencies were compared with the indices of the solar and geomagnetic activity.

Keywords: radio sources: ionosphere scintillations, seasonal dependence

1. Introduction

Ionosphere scintillations are essential effect during observations in the decameter range of the radio waves. Long series of the ionosphere scintillations parameters such as indices, characteristic times (periods) and spectrum slopes of the signal from source might be obtained after processing of long standing measurements of discrete cosmic radio sources records. Previous investigations of the scintillation parameters time variations were showed an existence of the year cycle or seasonal-daily dependence in parameter's behavior (Kravetz et al., 2004; Panishko et al., 2008). This behavior is very variability on the small time intervals because intensity fluctuations (scintillations) are arises in such variable medium as ionosphere. Monthly meaning is the most optimum interval for studying of the scintillation parameter long time variations. The aim of this work is investigation of ionosphere scintillation parameter behavior on the base of the long measurement series.

2. Observations

The index, period and spectrum slope values of the ionosphere scintillations were calculated by processing of the four power radio source (3C144, 3C274, 3C405, 3C461) records, which were obtained on the radio telescope URAN-4 during 1987-1990 and 1998-2007 at the frequencies 20 and 25 MHz. Processing method was presented in the work (Derevyagin et al., 2005). Observations that carried out during 1987-1990 were

registered on the paper tape of recorder and processed by manual manner. The spectrum calculating do not carried out in this case therefore only scintillation index and period data are available. Time interval 1998-2007 was decided to 1998-2002 and 2003-2007 because the long data interruption was in the beginning 2003 on the technique reasons. The monthly mean values of studying parameters were obtained from initial data.

3. Results and their discussion

The ionosphere scintillation index data would considered in this work. Monthly mean values of scintillation indices SI for interval 1987-2007 at frequencies 20 and 25 MHz are plotted in the Fig. 1. The long time variations are remarkable in a behavior of the values SI , which corresponds previously observed seasonal-daily dependence. Others scintillation parameters – periods and spectrum slopes – are showed similar behavior but do not considered here because paper volume is limited.

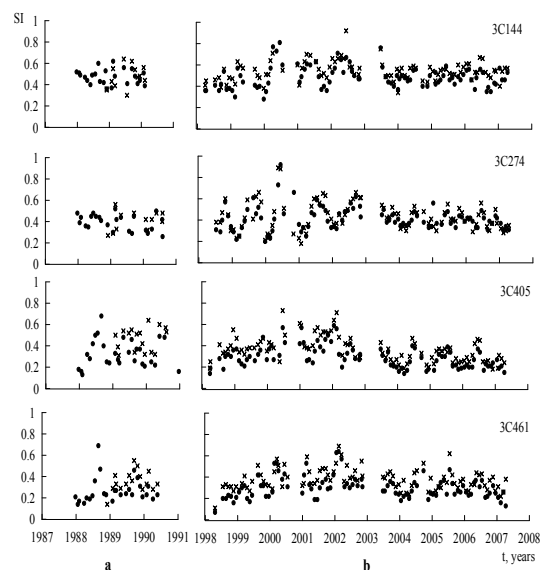


Figure 1: Monthly mean values of the ionosphere scintillation indices for 4-th radio sources: a – for time interval 1987-1990; b – for 1998-2007. Here and further crosses are marked values obtained at frequency 20 MHz, circles – at 25 MHz.

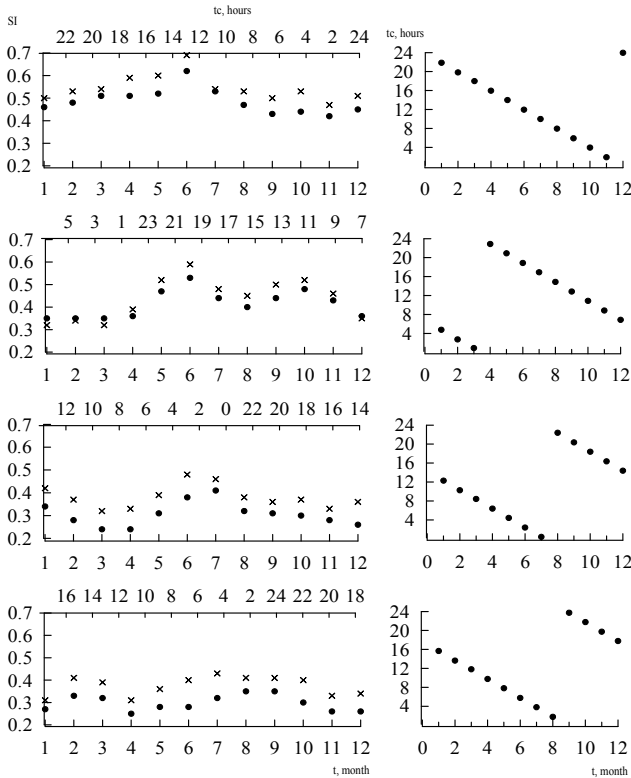


Figure 2: Scintillation indices for 4-th radio sources and 2-th frequencies meaning during month interval for all years observed. On the top axe are showed radio source culmination times for middle of the month. On the right: changing of the culmination time during year

Table 1: Correlation coefficients between data series at two frequencies

Years	1987-1990	1998-2002	2003-2007
Source			
3C144	0.84	0.77	0.99
3C274	0.51	0.69	0.53
3C405	0.40	0.79	0.73
3C461	0.34	0.87	0.71

It can be note that this is sufficient coincidence between scintillation index data on two frequencies. Corresponding values of the correlation coefficients are presented in Table 1. This result demonstrates similar conditions in which ionosphere scintillations arises at two frequencies.

The values meaning during the month intervals for all scintillation index data considered are presented in the Fig. 2. It can be seen that behavior of the index *SI* is similar at two frequencies but different for radio sources. If compared graphics in the Fig. 2 with contour maps in the Fig. 3 we can see that scintillation index behavior depends on that how culmination time of the radio sources change during the year. In general it may be noted that scintillation index maximum values reached in June-August and October and minimum values – in March-April, August-September and November.

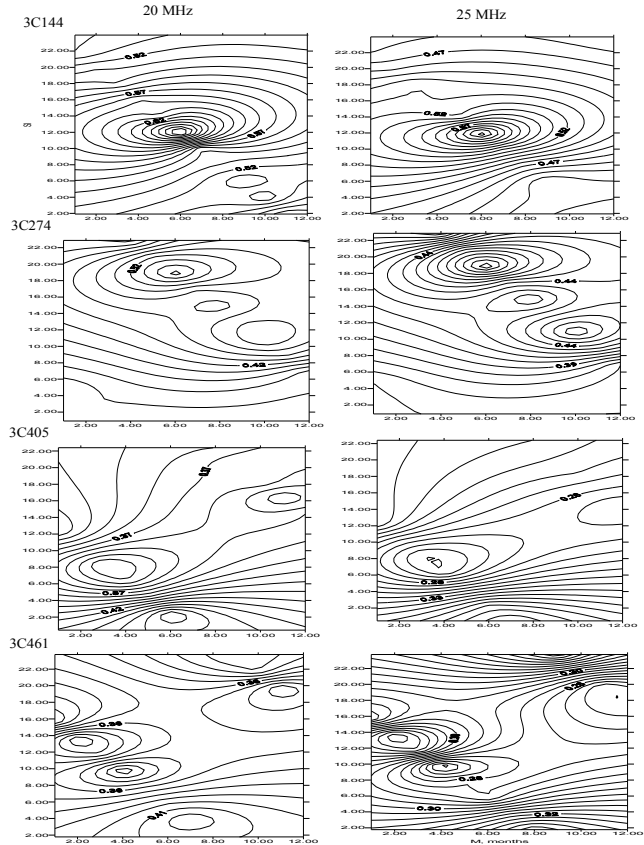


Figure 3: Contour graphics of scintillation index dependence on month of year and radio source culmination time

Besides year cycle scintillation indices are showed long time trend which caused by influence of the solar activity cycle. For second and third observation time intervals the low frequency part was distinguished by fitting of the second order polynomial function. Such procedure was fulfilled for the monthly mean of solar and geomagnetic indices – number of solar spots, radio flux at the frequency 10 cm and *Ap*-index. In result we obtained those values of the correlation indices between low frequency part of scintillation indices dependence and solar and geomagnetic index behavior change in following limits with:

- a) number of solar spots: 0.38-0.99;
- b) radio flux at the frequency 10 cm: 0.39-0.99;
- c) geomagnetic index *Ap*: 0.46-0.96.

It's sufficiently high means and confirmed the connection with solar activity.

4. Conclusions

Investigations of the ionosphere scintillation index seasonal dependence were carried out for 4-th power cosmic radio sources at two frequencies in the decameter wave range. Following results were obtained.

Previously known seasonal-daily dependence in behavior of the scintillation index monthly mean of the 4-th power discrete cosmic radio sources at the

frequencies 20 and 25 MHz was confirmed for a long time interval of data.

It was established that scintillation index series at the two frequencies of the decameter range of radio waves have sufficiently good correlation.

It was investigated that the type of changing of scintillation index behavior during season and daily depended on that how culmination time of the radio source change during year.

Low frequency part of ionosphere index dependence has sufficiently high values of the correlation coefficients with solar number spots, radio flux at the frequency 10 cm and geomagnetic Ap-index.

References

- Kravetz R.O. et al: 2004, *Odessa Astron. Publ.*, **17**, 42.
Panishko S.K. et al.: 2008, *Radiofizika i Radioastronomiya*, **13**, S130 (in russian).
Derevyagin V.G. et al.: 2005, *Astron. and Astrophys. Trans.*, **91**, 421.

LUMINOSITY-LINEAR SIZE RELATION FOR GALAXIES AND QUASARS WITH STEEP RADIO SPECTRUM

A.P.Miroshnichenko

Institute of Radio Astronomy, NAS of Ukraine
4, Chervonopraporna Str., 61002, Kharkiv, Ukraine
mir@rian.kharkov.ua

ABSTRACT. Our data for sources with steep radio spectrum, detected with radio telescope UTR-2 at the decametre band give evidence on the great luminosities, linear sizes, characteristic ages of these objects. In connection with such peculiarities, we examine the luminosity-linear size relation of galaxies and quasars with steep radio spectrum at the decametre band. It turned out, that this relation has similar trends for considered radio sources with linear steep spectrum and break steep spectrum. Also we presented the luminosity ratio-linear size relation at different frequency ranges. We discuss the obtained evolution relations for galaxies and quasars with steep low-frequency radio spectrum.

Keywords: Galaxies: steep radio spectrum – Galaxies: luminosity – Quasars: steep radio spectrum – Quasars: luminosity

1. Introduction

For the purpose of further study of the peculiar class of objects – galaxies and quasars with low-frequency steep radio spectrum (the spectral index values are larger 1), we consider the relation of their radio luminosity and linear size. This relation, as pointed out Shklovskii (1963), may contain the information on the source's evolution. A number of authors (Kapahi, 1989; Gopal-Krishna & Kulkarni, 1992; Neeser et al 1995; Singal, 1996; Luo & Sadler, 2010) have studied the dependence of linear size on luminosity for radio galaxies and quasars, but there is no the single opinion. For instance, Kapahi (1989) obtained for powerful radio galaxies an increase of source's sizes at large luminosities, while Luo & Sadler (2010) established the same trend only for sources with low radio luminosity. Note, that majority of the authors have used samples of objects irrespective of range of the spectral indices. It is known, spectral indices of non-thermal radio spectra may be connected with acceleration mechanisms of relativistic particles and evolution of sources. The detailed study of the identified radio sources with steep spectra at the decametre band (Miroshnichenko, 2010, 2012a, 2012b, 2013, 2014, 2015) shows, that these radio sources have interesting properties. In particular, these objects have great luminosity ($L_{25} \sim 10^{28}$ W/Hz ster), great characteristic age (10^8 years), giant radio structure (~ 1 Mpc). It is noteworthy that the obtained energy ratio for steep-spectrum sources (Miroshnichenko, 2014) testifies that the energy of relativistic particles prevails over the energy of magnetic field in the galaxies and quasars with steep radio spectra.

2. Luminosity – linear size relation for powerful giant sources

From the UTR-2 catalogue (Braude et al., 1978, 1979, 1981a, 1981b, 2003) we have formed sample of radio sources with steep spectrum including objects with linear steep spectrum (S-type) and spectrum with low-frequency steepness after a break (C+ type). Within the declination ranges from -13 to +20 degrees and from 30 to 40 degrees of the UTR-2 catalogue we have identified 78 galaxies and 55 quasars with linear steep spectrum (S-type) and 52 galaxies and 36 quasars with break steep spectrum (C+type) (with flux density at 25 MHz $S_{25} > 10$ Jy and spectral index larger 1). We use the NED database (<http://nedwww.ipac.caltech.edu>) for the high-frequency and optical identifications. Estimates of the angular sizes of examined sources we have derived from the corresponding radio images of the NVSS survey (at frequency 1400 MHz), presented at NED database. We suppose, that angular sizes from NVSS are close to angular sizes of corresponding sources at low frequencies. Calculations of the physical parameters of considered radio sources are carried out at cosmological parameters $\Omega_m = 0.27$, $\Omega_\lambda = 0.73$, $H_0 = 71$ km/s Mpc. Table 1 presents the characteristic values of derived parameters of sample objects: $\langle z \rangle$ – is the mean value of the redshifts of considered class of objects; z_{median} – is the median value of the redshifts; $\langle L_{25} \rangle$ – is the mean value of the monochromatic luminosities at the frequency 25 MHz; $\langle R \rangle$ – is the mean value of the linear sizes of objects.

Table 1. Parameters of the sample sources

Objects	$\langle z \rangle$	z_{median}	$\langle L_{25} \rangle$ (W/Hzsr)	$\langle R \rangle$ (cm)
G_S	0.697 (+0.105)	0.364	$3.27(+1.18)$ 10^{28}	$6.09(+0.64)$ 10^{24}
G_{C+}	0.308 (+0.076)	0.182	$8.14(+5.73)$ 10^{27}	$3.50(+0.52)$ 10^{24}
Q_S	1.029 (+0.070)	0.944	$5.17(+1.35)$ 10^{28}	$9.75(+0.53)$ 10^{24}
Q_{C+}	0.950 (+0.092)	0.857	$4.78(+1.73)$ 10^{28}	$8.73(+0.75)$ 10^{24}

As one can see from the Table 1, galaxies and quasars with steep low-frequency spectrum are characterized by

great radio luminosity at the decameter band and the giant linear size. We examine relationship $L_{25}(R)$ of radio luminosity at 25 MHz and linear size for each class of objects in our sample, that is, in 4 subsamples, which are: galaxies with linear steep spectrum (G_S), galaxies with break steep spectrum (G_{C+}), quasars with linear steep spectrum (Q_S), quasars with break steep spectrum (Q_{C+}). At this, the relation $L_{25}(R)$ is considered at different ranges of redshift z relatively to median values z_{median} in given subsamples (see Figure 1 – Figure 6).

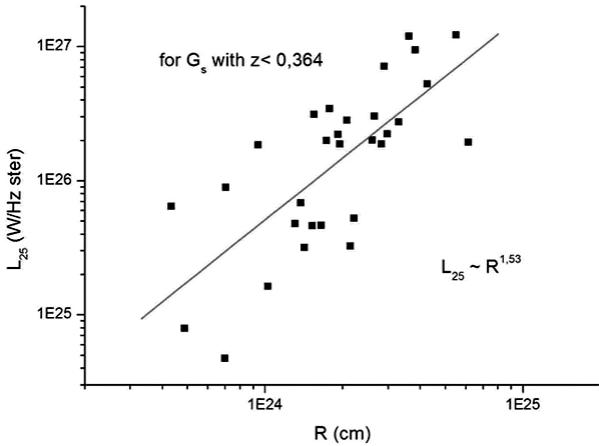


Figure 1: Luminosity at 25 MHz versus linear size for G_S at $z < z_{median}$

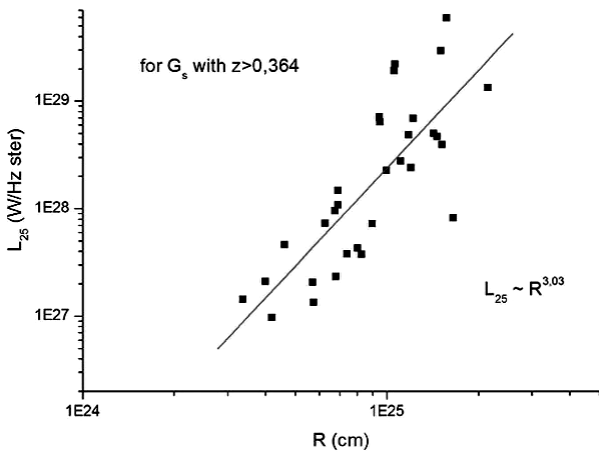


Figure 2: Luminosity at 25 MHz versus linear size for G_S at $z > z_{median}$

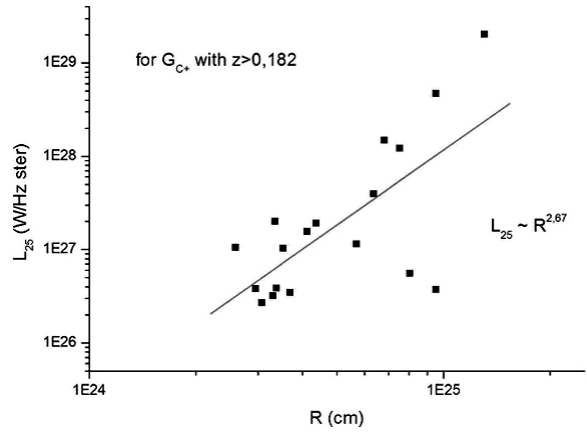


Figure 3: Luminosity at 25 MHz versus linear size for G_{C+} at $z > z_{median}$

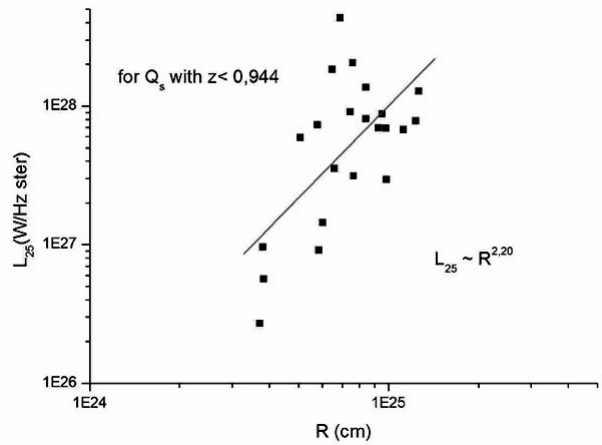


Figure 4: Luminosity at 25 MHz versus linear size for Q_S at $z < z_{median}$

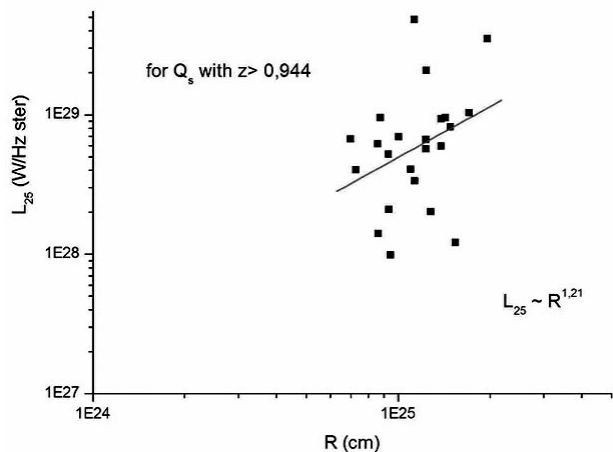


Figure 5: Luminosity at 25 MHz versus linear size for Q_S at $z > z_{median}$

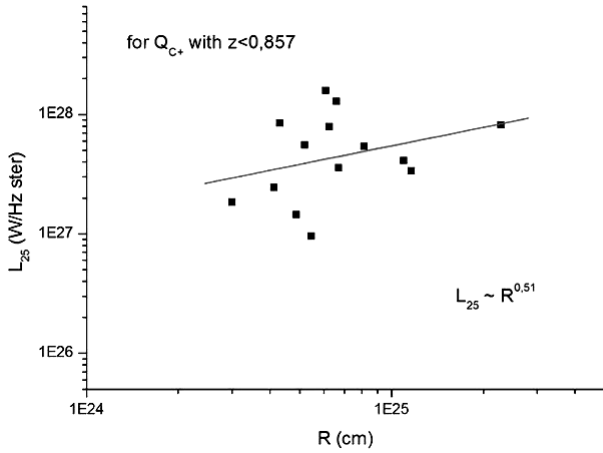


Figure 6: Luminosity at 25 MHz versus linear size for Q_{C+} at $z < z_{\text{median}}$

The derived relations $L_{25}(R)$ have the power trend (see Figures 1 – 6 and Table 2).

Table 2. Relations $L_{25}(R)$ in 4 subsamples (G_S , G_{C+} , Q_S , Q_{C+}) at redshift ranges z , less z_{median} , and larger z_{median}

Objects /and their z_{median}	$L_{25}(R)$ at $z < z_{\text{median}}$	$L_{25}(R)$ at $z > z_{\text{median}}$
$G_S / 0.364$	$L_{25} \sim R^{1.53 (+0.27)}$	$L_{25} \sim R^{3.03 (+0.43)}$
$G_{C+} / 0.182$	$L_{25} \sim R^{0.98 (+0.40)}$	$L_{25} \sim R^{2.67 (+0.70)}$
$Q_S / 0.944$	$L_{25} \sim R^{2.20 (+0.60)}$	$L_{25} \sim R^{1.21 (+0.75)}$
$Q_{C+} / 0.857$	$L_{25} \sim R^{0.51 (+0.44)}$	$L_{25} \sim R^{1.57 (+0.98)}$

It is interesting that the ratio of corresponding luminosities at decameter and optical bands (L_{25} / L_{opt}) for sample objects displays the similar correlation with linear size of sources (see Figure 7, Figure 8).

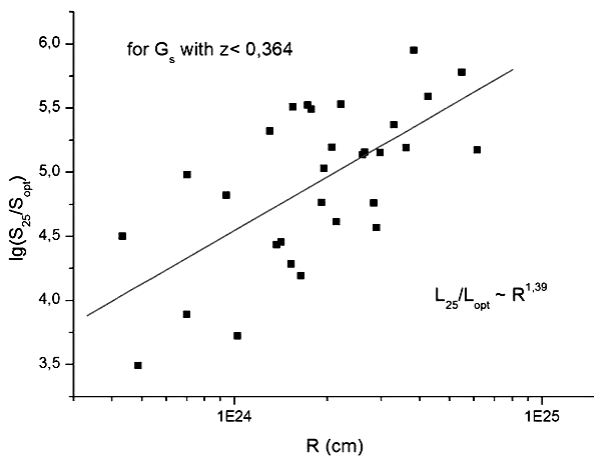


Figure 7: Ratio of luminosities at decameter and optical bands versus linear size for G_S at $z < z_{\text{median}}$

We can consider the ratio of decametre and optical luminosities of source as the ratio of emission of extended component and central component of source. As it follows from Figure 7 and Figure 8, the relative contribution of the decametre emission in steep-spectrum sources increases for more extended objects.

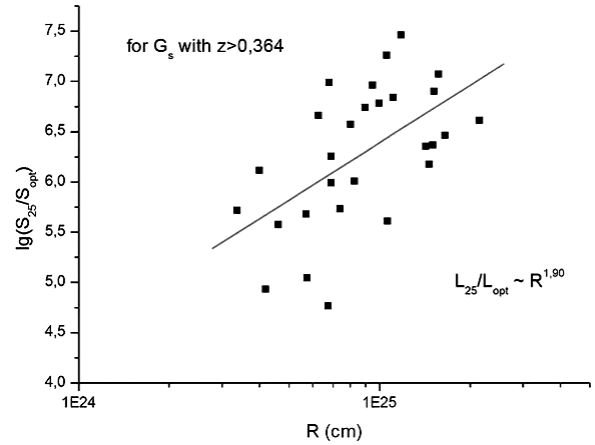


Figure 8: Ratio of luminosities at decametre and optical bands versus linear size for G_S at $z > z_{\text{median}}$

Also, we study the relation $L_{25}(R)$ at the same range of redshifts: $z = 0 - 0.5$ for each subsample of objects. It turned out that obtained relations have the power shape:

$$\begin{aligned} \text{for } G_S : L_{25} &\sim R^{1.93 (+0.22)} \\ \text{for } G_{C+} : L_{25} &\sim R^{1.81 (+0.25)} \\ \text{for } Q_S : L_{25} &\sim R^{1.80 (+1.06)} \\ \text{for } Q_{C+} : L_{25} &\sim R^{0.25 (+0.94)} \end{aligned}$$

So, galaxies and quasars with steep spectrum and giant radio structure reveal the positive correlation of their radio luminosity and linear size. Within the limits of statistical errors the derived power indices of the relation $L_{25}(R)$ are enough close in values for galaxies and quasars of our sample. The noticeable disperse at the each found relation $L_{25}(R)$ for sources with steep radio spectrum may be caused by cosmological evolution of linear size, that is, the relation of linear size and redshift, $R(z)$. To exclude the influence of itself cosmological model used at calculation of source's physical parameters, we search for the relation $R(z)$ only at given bins of luminosity L_{25} (at bin value $\Delta \lg L_{25} = 1$). For example, at the luminosity bin $L_{25} = 10^{28} - 10^{29}$ (W/Hz ster) the derived relation $R(z)$ shows power trend in 4 subsamples:

$$\begin{aligned} \text{for } G_S : R &\sim (1+z)^{0.74 (+0.38)} \\ \text{for } G_{C+} : R &\sim (1+z)^{0.97 (+0.27)} \\ \text{for } Q_S : R &\sim (1+z)^{0.83 (+0.52)} \\ \text{for } Q_{C+} : R &\sim (1+z)^{1.87 (+0.42)} \end{aligned}$$

One can note the more considerable evolution of the linear size of quasars with break steep radio spectrum (C+type). This corresponds to great characteristic age of these objects. According to our previous estimates of characteristic age of sources with steep radio spectrum (Miroshnichenko, 2013) the age of galaxies and quasars with spectrum of C+type is $\sim 10^8$ years, and near one order is larger than the characteristic age of sources with steep spectrum of S – type.

3. Conclusion

Empirical relations of luminosity and linear size have been derived for samples of powerful galaxies and quasars with low-frequency steep spectrum and giant radio structure.

Within the limits of statistical errors the power shape of the relation of luminosity and linear size is, practically, the same for galaxies and quasars with steep spectrum.

The cosmological evolution of linear size of galaxies and quasars with steep radio spectrum have been revealed, at that quasars with spectrum C+ show the more considerable evolution.

The found relation of decametre luminosity and linear size points out on the huge power of the “central engine” of sources with steep radio spectrum, which provides for rejection of jets to giant distances (~ Mpc).

References

- Shklovskii I.S.: 1963, *SvA*, **6**, 465.
Kapahi V.: 1989, *AJ*, **97**, 1.
Gopal-Krishna & Kulkarni V.: 1992, *A&A*, **257**, 11.
Neuser M. et al.: 1995, *ApJ*, **451**, 76.
Singal A.: 1996, in *Extragalactic Radio Sources*, Dordrecht, 563.
Luo Q. & Sadler E.: 2010, *e-print*, arxiv: 1003.0667.
Miroshnichenko A.: 2010, in *Astrophysics and Cosmology after Gamow*, New York, AIPC, **80**, 335.
Miroshnichenko A.: 2012a, *Radio Physics and Radio Astronomy*, **3**, 215.
Miroshnichenko A.: 2012b, *Odessa Astron. Publ.*, **25**, 197.
Miroshnichenko A.: 2013, *Odessa Astron. Publ.*, **26/2**, 248.
Miroshnichenko A.: 2014, in *Multiwavelength AGN Surveys and Studies*, Cambridge, 96.
Miroshnichenko A.: 2015, *e-print*, arxiv: 1505.01870.
Braude S. et al.: 1978, *Astrophys. Space Sci.*, **54**, 37.
Braude S. et al.: 1979, *Astrophys. Space Sci.*, **64**, 73.
Braude S. et al.: 1981a, *Astrophys. Space Sci.*, **74**, 409.
Braude S. et al.: 1981b, *Astrophys. Space Sci.*, **76**, 279.
Braude S. et al.: 2003, *Kinem. Phys. Celest. Bod.*, **19**, 291.

THE DAILY 110 MHz SKY SURVEY (BSA FIAN): ON-LINE DATABASE, SCIENCE AIMS AND FIRST RESULTS OF DATA PROCESSING

V.A.Samodurov^{1,2}, A.E.Rodin^{1,2}, M.A.Kitaeva¹, E.A.Isaev^{1,2}, D.V.Dumsky¹,
D.D.Churakov³, M.O.Manzyuk⁴

¹ Pushchino Radio Astronomy Observatory ASC LPI, Pushchino, Russia, *sam@prao.ru*

² National research university Higher school of economics, Moscow, Russia

³ TSNIIMASH, Moscow, Russia

⁴ Internet portal BOINC.Ru

ABSTRACT. From 2012 on radio telescope BSA FIAN multi beams diagram was started. It capable at July 2014 daily observing by 96 beams in declination -8 .. 42 degrees in the frequency band 109-111.5 MHz. The number of frequency bands are from 6 to 32, the time constant are from 0.1 to 0.0125 sec. In receiving mode with 32 band (plus one common band) with a time constant of 12.5 ms (80 times per second) respectively produced 33x96x80 four byte real and so daily we produced 87.5 Gbt (yearly to 32 Tbt). These data are enormous opportunities for both short and long-term monitoring of various classes of radio sources (including radio transients) and for space weather and the Earth's ionosphere monitoring, for search for different classes of radio sources, etc. The base aims of our work are:

a) to obtain new scientific data on different classes of discrete radio sources, the construction of physical models and their evolution - obtained on the basis of the clock continuous digital sky radio monitoring at frequency 109-111.5 MHz and cross-analysis of data from third-party reviews on other frequencies;

c) launch the streaming data on various types of high-performance computing systems, including to create a public system of distributed computing for thousands of users on the basis of BOINC technology. The BOINC client for astronomical data from the monitoring survey of the big part of entire sky almost have not analogies.

We have some first science results (new pulsars, and some new type of radiosources).

Keywords: Stars: abundances – Galaxy: abundances – stars: late-type

1. Observations

In 2012 the multi-beam feed array has become operational on the BSA FIAN radio telescope (Oreshko et al, 2012). As of July 2015 it is capable of 24-hour observation using 96 beams in declination of -8 to +42 degrees in the 109-111.5 MHz frequency band.

The number of frequency bands range from 6 (417 kHz per band as the “wide observational mode” or “light” mode) to 32 (78 kHz per band as the “narrow observational mode” or “heavy” mode) while the time constant ranges from 0.1 sec (“wide observational mode”) to 12.5 ms (“narrow observational mode”). Such type of continu-

ous daily survey of the major observable part of the sky is not yet done by any observatories worldwide. Observations have already been carried out for more than 2.5 years, with a typical daily data production of 2.3 GB (gigabytes) in wide observational mode, equating to a total of 0.8 TB (terabyte) of data per year. Respectively, in narrow observational mode the data produced amounts to 87.5 GB daily, or 32 TB yearly.

It is now possible to record data in both modes at the same time. The narrow observational mode will be used in the near future for the purpose of searching for radio transients of different types (for example, pulsars). At the end of October 2015 we accumulated over 16 months of observations “heavy” mode (total volume of about 41.6 TB) and more than 3 years for “light” mode (total volume of about 3 TB).

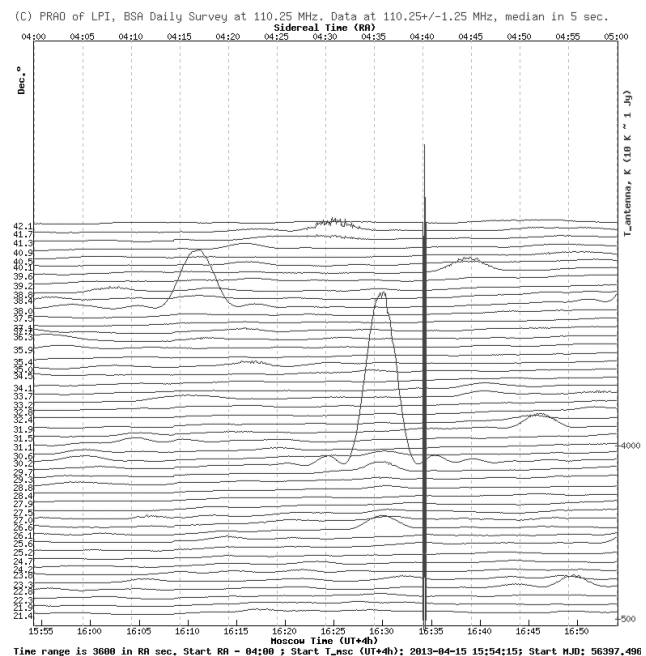


Figure 1: The sample of calibrated data from the multi beams diagram BSA at 15 April 2013. It showed the calibration signals (at RA = 4 h 40 m) of galaxy background with the some radio sources on it. The some sources (for example is upper sources) are showed phenomenon of flicker produced by interstellar medium scintillations from small sources with scales nearly fraction of arc second.

2. Database and data processing

A specialized database needs to be constructed to facilitate the large amount of observational data. In the period between 7 July 2012 and 20 October 2013 an experimental database collected more than 8 million calculated 5-second sample data from each beam for more than 27 parameters. The observational data parameters are maximal, minimal, median, average, dispersion etc. for 5-second periods of time in different frequency bands. Using this data close to one million images has been built. The figure 1 present example median data on hourly scale.

By the end of 2014 work will be completed on the on-line database, which will be publically available on <http://astro.prao.ru/>. This database will enable users, both local and remote, to use different ways to processing the observation data. The total size of the database is over than 200 GB.

We should highlight the fact that storing the compressed data in SQL database formats allows us to use the power of selection, sorting, matching, filtering and initial processing of data by using standard SQL commands. This will greatly simplify the interaction and the comparative analysis of the data for different sorts of data and their cross-temporal analysis, averaging etc. These data are enormous opportunities for both short and long-term monitoring of various classes of radio sources (including radio transients) and for space weather and the Earth's ionosphere monitoring, for search for different classes of radio sources, etc.

One of our goals is to launch data streaming processes on various types of high-performance computing systems, including creating a public system of distributed computing for thousands of users on the basis of BOINC technology. The BOINC client for astronomical data from the monitoring surveys of large parts of the entire sky almost has no analogies.

Preliminary estimates show that we may reach of data processing speeds practically bordering on "on-line" mode (with a time lag of no more than 2-3 hours following the observations). All data, including the original observations and the results of data processing for the purpose of various scientific objectives will be continuously displayed on the PRAO of LPI website. The data will be displayed in graphical form for external public users, while the project participants will also be able to access the data in its original digital form.

For mutual benefit it is possible to also facilitate for this database to include additional low-frequency (10-25 MHz) observation data from the Ukrainian UTR radio telescope.

3. The scientific goals

This monitoring system allows a potential to solve a tremendously wide range of classes of problems, not only fundamental scientific ones, but also challenges within applied sciences. The proposed project allows to continuously monitor celestial radio sources in most parts of the sky on time scales from milliseconds to years.

The following is a list of our primary goals:

1) Monitoring of the ionosphere state and its fluctuations (with a characteristic time scale of tens of seconds).

2) Analysis of meteor tracks in the higher layers of the Earth's atmosphere.

3) Monitoring of active phenomena on the Sun such as sporadic outbursts with the time scales from seconds to hours as well as the state of the near-solar plasma. This is a broad field of research on near-solar source flicker interplanetary plasma. This solar behavior will be monitored and its most common parameters will be displayed in graphical form on the PRAO of LPI website.

4) Radio monitoring of transient (flare) phenomena in the solar system such as ionospheric and storm phenomena of the giant planets, tracking of radio transient phenomena on the Moon and other radio phenomena in the solar system.

5) Monitoring of transient phenomena in our Galaxy. This covers a wide class of scientific problems, from studies of outbreaks of radio emission from cataclysmic variables to search for candidates in exoplanets around alien stars. Not all of them can be implemented on our radio telescope, however some of these events are available to us.

6) Monitoring of flux density of extragalactic radio sources. For this purpose we are able to perform daily monitoring of about 400-500 radio sources outside of 15-degree declination from the plane of our Galaxy.

7) Monitoring of extragalactic transient phenomena. The most interesting problem is searching for fast radio transient events in other galaxies (on the scale of a few milliseconds). According to several studies such radio transients have been discovered in the decimeter wavelength range in the last few years. Theorists associate these transient events with the possible merges of neutron stars. Phenomena of this magnitude emit great amounts of energy, the levels of which are high enough to be detected by our telescope even from galaxies as distant from us as hundreds of Mpc. This problem is currently a very popular topic for Astrophysics.

Ultimately, the multi-beam observations of the BSA of LPI telescope will take advantage of the wide-field survey capabilities to enable the discovery and investigation of variable and transient phenomena from the intra- to the extra-galactical, including flare stars, intermittent pulsars, X-ray binaries, magnetars, extreme scattering events, interstellar scintillation, radio supernovae and orphan afterglows of gamma-ray bursts. In addition, it will allow us to probe unexplored regions of parameter space where new classes of transient sources may be detected.

4. The first scientific results

We have today from base data processing of the some first science results. It is the first results for search of the new pulsars and search results of the other objects.

It is best test of our data is the pulsars search. The best solving of this problem on our data can be processing by a on supercomputers computing or a by BOINC distributed computing (look on <http://boinc.berkeley.edu/>).

The example of the last way is the Einstein@Home project in the decimeter band of radio wave for the data from Arecibo radio telescope (Cordes, J.M. et al: 2006) and from Parkes Observatory data (Knispel et al, 2013). The project found in the observatory data more than 50 new pulsars at a frequency of 1440 MHz.

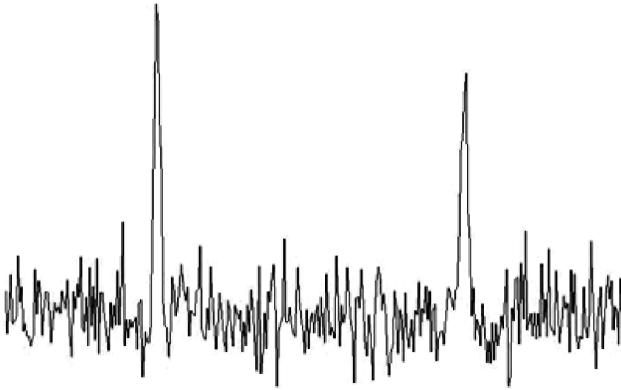


Figure 2: The result of search for new pulsar PSR $\alpha_{2000}=09^{\text{h}}28^{\text{m}}00^{\text{s}}\pm 30^{\text{s}}$; $\delta_{2000}=+30^{\circ}37'\pm 20'$ with period $P=2.0919\text{s}$ and $DM=22-24$ (from S.A.Tulbashev, V.S.Tulbashev, 2015). It is showed 2 pulsar periods.

BSA of LPI is one of the best in the world in antennas sensitivity parameter. Really, BSA effective area of approximately 30,000 square meters, which is about the same order as that in Arecibo and significantly more than Parkes radio telescopes. The pulsars is brighter by order on our frequency 110 MHz in additional. So although our frequency band is less (2.5 MHz against the tens of megahertz in Parkes and Arecibo), we may hope discover of some new pulsars in our data.

We began in April 2015 pulsars search in the standard regime by single personal computers as part of the work data testing. We have been using two searches methodic.

First method is classical folding – that is testing different periods and dispersion delay for pulsar candidate. Four new pulsar was already discovered by this work (S.A. Tulbashev, V.S. Tulbashev, 2015).

On the figure 2 is showed the result of searching for one from new pulsars that found by folding method (S.A. Tulbashev, V.S. Tulbashev: 2015).

The second method is search for new periodic objects by using spectral analysis. We dividing observation time in each beam scans on data segments that contain 2048 points (i.e., 2 in power 11, for to using of classical Fast Fourier Transform algorithms). So for the "small" mode of observation with a time constant of 0.1 seconds is provided time interval data equally 205 seconds. So we have near beam width BSA temporal scale (at the half power) that has about 5-6 minutes. Thus the range of 205 seconds is about twice less than the actual exposure time of sources. But this method allows summarizing the observations data from day to day. In result we will can find hundreds possible pre-candidates pulsar list with roughly defined periods $\pm 0.0005^{\text{s}}$ by preprocessing FFT spectral analysis over all the sky. This big list of pre-candidates will be processing at next stage by BOINC computing. In result we hope found some very weak pulsar computing after preprocessing by FFT spectral analysis plus BOINC computing.

On the figure 3 is showed the result of checking data for this pulsar by FFT spectral analysis for sum all 3 year data (2012-2015) in observational "light" mode (with 0.1 sec time constant). We may look that both methods work very satisfactorily.

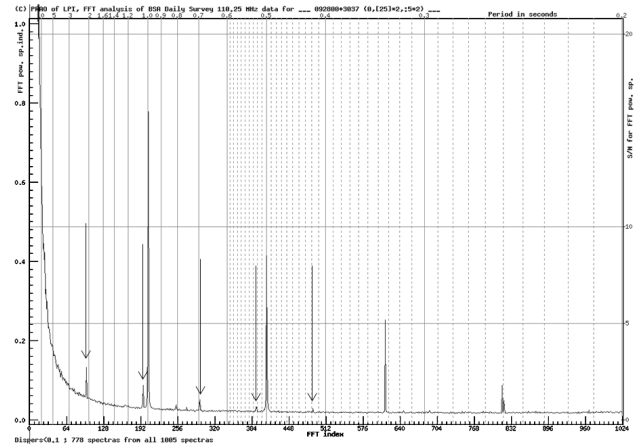


Figure 3: The result of testing for new pulsar PSR from figure 2 by FFT spectral analysis on 2012-2015 year data. The arrows marked 5 harmonics of the period $P=2.0919\text{s}$. We may look also 4 harmonics of the period $P=1.000\text{s}$ that unfortunately produced by interferences from local GPS time receiver.

There are other scientific problems (sometimes quite unexpected nature) that can be solved with the help of your data. So, as an example of practical problems that proposed by one of the authors is search radar echoes from satellites that produce by ILS in airport near Moscow. An instrument landing system (ILS) is a ground-based instrument approach system that provides precision lateral and vertical guidance to an aircraft approaching and landing on a runway, using a combination of radio signals. ILS carrier frequencies range between 108.10 MHz and 111.95 MHz (with the 100 kHz first decimal digit always odd, so 108.10, 108.15, 108.30, etc., and are not used for any other purpose).

We not look (to our luck) direct radiation from ILS but we may look its echoes from Earth satellites. We really find reflections from the International Space Station in the target multi-beam diagram of BSA.

We did analysis of the 2 month statistics of detecting reflected radar signals indicated airfield complexes from the International Space Station. It is showed that in September-October 2013 there were 85 events across the track of the ISS (at a distance of 500-800 km away from the observer) target through diagram BSA. This 35-40 are reliably identified as short bursts of radio flux equally 10-20 Jy. Figure 4 shows one from these cases, where the ISS passing through BSA multi-beam diagram (which are directed along the South-North line). This work demonstrates that found radio transients in our survey data can be, unfortunately, also be produce manmade.

The figure 4 is showed that satellites track on the data is very symmetrical. But we also finding transient phenomena second timescale in non-symmetrical form and with traces of the influence of the dispersion delays. We will preparing in future some statistical work for this phenomena.

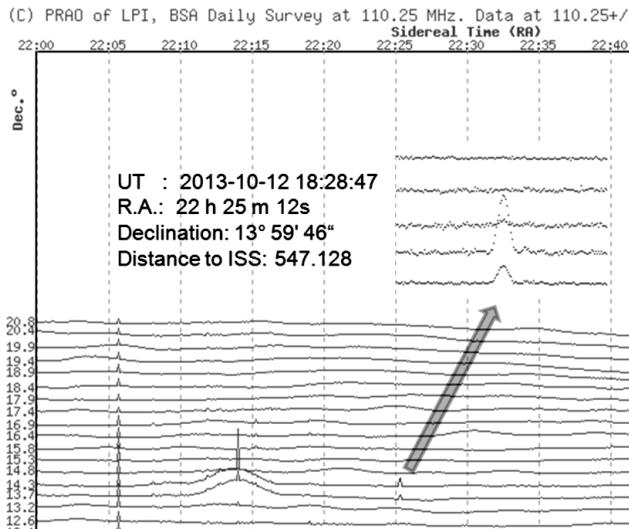


Figure 4: The result of ISS passing through BSA multi-beam diagram at 2013-10-12 in 18:28:47 UT. We may look that ISS at distance 547.1 km passing through diagram about 1.6 sec and has very symmetrical form.

5. Future prospects

This BSA monitoring system allows a potential to solve a tremendously wide range of classes of problems. The proposed project allows to continuously monitor of celestial radio sources in most parts of the sky on time scales from milliseconds to years. We hope produce thus regime of processing that all the work of patrol and processing possible transient phenomena, also as monitoring of known radio sources, searching for new sources and so on will be conducted in automatic mode.

The observational data will be automatically preprocessing and locating in total data base. At next stage we will find from this data base of some interesting goal for scheduled and will start processing on BOINC-server by method of distributed computing.

The part of the work will be produced from the known coordinates of some type of sources (for example the giant planets of the solar system, transients associated with cataclysmic variables, etc.).

Other part of sky targets will be produced by third-party information sources. It is in first different data base for example gamma-ray bursts data base and so on.

In our data reduction can be also included other long wave radio survey for cross testing. For example is the most low-frequency survey observations in word from the Ukrainian radio telescope UTR, also as Netherlands radio interferometric system LOFAR and so on.

Acknowledgements. This work is supported by RFBR grant 14-07-00870a.

References

- Cordes J. M. et al: 2006, *AJ*, **637**, Issue 1, 446.
 Knispel B. et al: 2013, *AJ*, **774**, Issue 2, article id. 93.
 Oreshko V.V. et al : 2012, *Transactions of the Institute of Applied Astronomy (Russia)*, **24**, 80.
 Tulbashev S.A., Tulbashev V.S.: 2015, *Astron. Tsirkular*, **1624**.

HIGH-FREQUENCY CUTOFF IN TYPE III BURSTS

A.A.Stanislavsky^{1,2}, A.A.Konovalenko¹, Ya.S.Volvach¹, A.A.Koval¹

¹ Institute of Radio Astronomy, Kharkiv, Ukraine, *astex@ukr.net*

² V.N. Karazin Kharkiv National University, Kharkiv, Ukraine

ABSTRACT. In this article we report about a group of solar bursts with high-frequency cutoff, observed on 19 August of 2012 near 8:23 UT, simultaneously by three different radio telescopes: the Ukrainian decameter radio telescope (8-33 MHz), the French Nançay Decametric Array (10-70 MHz) and the Italian San Vito Solar Observatory of RSTN (25-180 MHz). Morphologically the bursts are very similar to the type III bursts. The solar activity is connected with the emergency of a new group of solar spots on the far side of the Sun with respect to observers on Earth. The solar bursts accompany many moderate flares over eastern limb. The refraction of the behind-limb radio bursts towards the Earth is favorable, if CMEs generate low-density cavities in solar corona.

Keywords: Sun: radio emission – bursts: UTR-2 radio telescope

1. Introduction

Sporadic radio emission of the Sun is observed in a wide range of wavelengths, from millimeters to kilometers. The radio waves emerge from different heights (layers) of the solar atmosphere: radiation of millimeter range is emitted by the lower chromosphere, cm-waves are produced by the middle and upper chromosphere, decimeters originate from the transition region, meters come from the lower corona, and the radio emission in the decameter range is generated by the upper corona and so on (Zheleznyakov, 1970). An important component of solar activity is various types of solar bursts. Solar bursts can serve as a probing signal to study properties of solar corona plasma. Multi-frequency observations of solar radio emission allow ones to determine the electron density, temperature and magnetic field strength in the solar corona at different heights.

In the decameter range the solar activity are observed in the type III bursts associated with IIIb bursts, U and J bursts, the type II and IV bursts, striae, drifting pairs and S-bursts as well as other events (Krüger, 1979). They occur with varying frequency of occurrence. The main parameters characterizing the bursts are the frequency drift rate, instantaneous bandwidth, duration, flux, polarization, etc. All these parameters indicate the type of solar bursts. The type III bursts is the most numerous collection of solar bursts recorded in radio observations. They occur on the whole Sun. However, the most of observations are performed by ground-based instruments, and a significant part of solar radio events is unavailable for the radio astronomy tools. This situation is improved by space mis-

sions such as WIND and STEREO, but they are not as sensitive as the newest radio telescopes LOFAR, UTR-2, GURT and others. Nevertheless, some solar bursts from the far side of the Sun can arrive at ground-based telescopes due to specific conditions in solar corona. Such events are related to solar bursts with high-frequency cutoff. Recall, the low-frequency cutoff (radio emission below 10 MHz cannot reach to ground-based instruments) in cosmic radio emission appears due to the ionosphere. As for the high-frequency cut-off, its cause is totally different. This effect is explained by the burst's source position in solar corona with respect to the observer. Really, if the source is moved radially from behind the solar limb, it may be occulted by solar corona. Therefore, the most high-frequency part of the solar burst spectrum is reflected away from the direction of the Earth. The propagation of radio emission of behind-limb solar bursts in the solar corona imposes a number of features on the characteristics of these bursts for terrestrial observers.

In this work we present preliminary results related to the observations of solar bursts with high-frequency cutoff (Fig.1), demonstrating clearly the properties typical for the type III ones. The identification is useful for understanding their nature and frequency-time evolution.

2. Instruments and observations

On 19 August of 2012 starting with 8:23 UT the Ukrainian decameter radio telescope UTR-2 (8-33 MHz) has registered about a dozen of solar bursts following each other. Their main peculiarity was high-frequency cutoff near to the upper boundary frequency of observations for UTR-2. Note that we used only four sections of the north-south antenna array of this radio telescope. The total effective area of such an antenna part is 50 000 m², and the beam pattern size is 1°×15° at 25 MHz. The solar radio data were recorded by the digital DSP spectrometer operating in the frequency range of 9-33 MHz with the time resolution of 100 ms and frequency resolution of 4 kHz. Some of these solar bursts had their cutoff frequency above frequency capabilities of UTR-2. To get a full view of all the events, we have studied the observations of two different radio telescopes at the same time: the French Nançay Decametric Array (10-70 MHz) and the Italian San Vito Solar Observatory of RSTN (25-180 MHz). Both the instruments also show the registration the given bursts. This allowed us to find the frequency of cutoff of each bursts in the collection. They were different from burst to burst and lie in the range of 30-55 MHz. The simultaneous

observations in different parts of the world indicate that the given bursts and their characteristic features have solar origin rather than either ionospheric or instrumental links.

The frequency drift rate of the solar bursts was negative, 1.1-3.3 MHz/s that corresponds to the characteristic values as applied to the type III bursts in decameter wavelengths. The same is related to their duration. The flux of the set does not exceed 1000 s.f.u. ($1 \text{ s.f.u.} = 10^{-22} \text{ W m}^{-2} \text{ Hz}^{-1}$) that points to the moderate character of bursts in intensity.

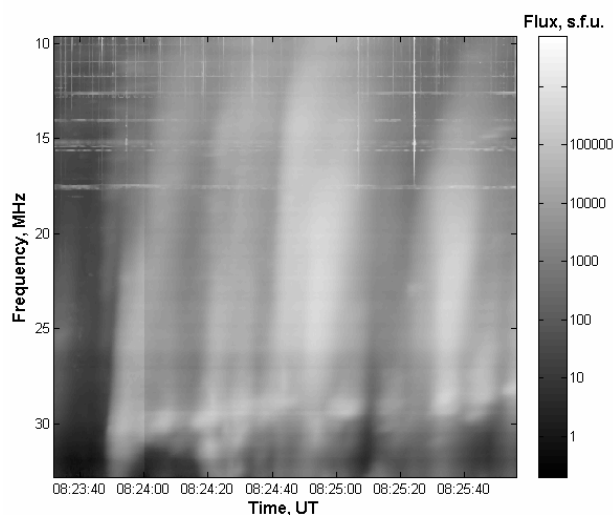


Figure 1: Dynamical spectrum of solar radio bursts with high-frequency cutoff, observed on 19 August of 2012 after 8:23 UT by the telescopes UTR-2. Horizontal bright lines are disturbances due to broadcasting radio stations. Vertical lines in the range about 8-18 MHz indicate terrestrial lightning discharges.

In this connection it should be mentioned that recently a solar burst with high-frequency cutoff in the decameter range of wavelengths has been described by Brazhenko et al. (2012). This was a single radio event on 3 June of 2011. It had the cutoff at ~ 27.5 MHz, the half-power duration 17-22 s, the frequency drift rate 100-500 kHz/s. Moreover, the dynamical spectrum of this event demonstrates an unusual fine structure with filaments called “caterpillar”. The unique properties of this burst make it difficult to classify, according to the conventional scheme of types of solar bursts. Therefore, the further patrol of new events with high-frequency cutoff is very important for a successful interpretation of the phenomena.

3. Interpretation

As it has been shown by Melnik et al. (2012), one of plausible interpretations, explaining features of the unusual burst on 3 June of 2011, is that the origin of the event came from behind the solar limb, and the cutoff of its radio emission appeared because the high-frequency part of the burst’s spectrum does not pass towards the Earth. This approach also can be applied for the group of solar bursts observed on 19 August of 2012. Really, the solar activity was connected with a new group of solar spots (AR 11548, about N19E87) born 17 August 2012 on

the far side of the Sun for terrestrial observers. This is supported by the STEREO observations (see <http://stereo-ssc.nascom.nasa.gov/data.shtml>). However, the plasma dispersion of solar corona influences on the direction of radio wave propagation that can lead to the reflection of radio rays away from the Earth rather than their refraction towards the Earth (see, for example, Thejappa and MacDowall, 2010). Consequently, the purely spherical model of solar corona density is not favorable for behind-limb solar bursts to detect them by ground-based tools. The situation may be rescued by coronal mass ejections (CMEs) associated with the post-limb flare activity. In particular, the CMEs generate lower-density cavities in solar corona (Gibson S.E. et al., 2010) through which the radio emission of behind-limb bursts can fall to Earth. This problem will be considered in more detail elsewhere.

4. Conclusions and future work

In this work we have shown that the solar bursts with high-frequency cutoff can be identified as usual type III bursts. Because of various effects of radio wave propagation in solar corona (generally speaking, the latter is an inhomogeneous medium), being originally the type III bursts, the behind-limb bursts are distorted. Maybe that is why the bursts on 3 June of 2011 looks like “caterpillar”. Anyway, the analysis of ray tracing in inhomogeneous solar corona for the solar bursts with cutoff requires a separate examination. Additionally, notice that it would be useful to check the functional evolution of frequency drift rates and durations in frequency for the events on 19 August of 2012 considered in this paper. According to Alvarez and Haddock (1973), as well as Elgarøy and Lyngstad (1972), there are characteristic dependences of the frequency drift rate and the duration in frequency, supported by ordinary type III bursts. It would be useful to check them as applied to the bursts of this paper in future.

Acknowledgements. This research was supported particularly by Research Grant “Synchronized simultaneous study of radio emission of solar system objects by low-frequency ground- and space-based astronomy” from National Academy of Sciences of Ukraine. We want to thank the STEREO and SOHO teams for developing and operating the instruments as well as for their open data policy.

References

- Alvarez H., Haddock F.T.: 1973, *Sol. Phys.*, **29**, 197.
- Brazhenko A.I. et al.: 2012, *RPRA*, **3**, 279.
- Elgarøy Ø., Lyngstad E.: 1972, *A&A*, **16**, 1.
- Gibson S.E. et al.: 2010, *ApJ*, **724**, 1133.
- Krüger A.: 1979, *Introduction to Solar Radio Astronomy and Radio Physics*, Springer, Berlin.
- Melnik V.N. et al.: 2012, *RPRA*, **17**, 199 (in Russian).
- Thejappa G., MacDowall R.J.: 2010, *ApJ*, **720**, 1395.
- Zheleznyakov V.V.: 1970, *Radio Emission of the Sun and Planets*, Pergamon Press, Oxford.

ON THE E/P-COSMIC RAYS AS MEDIATORS OF VISCOUS FORCES THAT CREATE SHOCK AND VORTEX STRUCTURES IN THE RADIO GALAXIES

N.O.Tsvyk

Institute of Radio Astronomy of NAS of Ukraine,
Chervonopraporna 4, 61002, Kharkiv, Ukraine, natalitsv69@gmail.com

ABSTRACT. There are for the galaxies of FR II type (like Cygnus A) studied a number of hydrodynamic and kinetic processes to transport of magnetized plasma with cosmic rays, and a stratification process of RG-lobe because of e/p-cosmic rays. We found that the jet and bow shock in radio galaxies are supported by the processes of e/p-cosmic rays (acceleration, radiation), and the effects of changes in viscosity inside the cocoon. Cosmic rays are working inside the "jet head" into the cocoon stratification: to the light caviton (with high kinematic viscosity) and to the heavy shock cover (with high magnetic viscosity). The post-jet-vortex is injected by diffusion of e-rays through the area of "jet head" MHD-turbulized, and it is flowing a caviton around. Alternatively, the bow shock accompanied super sound turbulent waves and flows with p-rays.

Keywords: Radio galaxy; cosmic rays, viscosity, shocks

1. Introduction. A history for the simulation of the FR II-type radio galaxy lobes

There was in Kaiser (1997) shown a self-consistent hydrodynamical model for the jet-cocoon of FR II radio galaxy (RG), with reconfinement jet-shock (that connected with e-jet plasma production). The other main work, Zanni (2003), show a simple of self-consistent cocoon shock model of FR II RG; and in a work of Kino (2004) was illustrated a hot spot of two-shocks dynamic in details (the parameters of Cygnus A galaxy found).

There are Mathews (2011, 2012) recently shown a model for self-consistent evolution of gas and cosmic rays (CRs) in Cygnus A, in assuming a wind-injection of the viscous e-gas with e-CRs into the lobe (cocoon) of Radio Galaxy. This model shows the post-jet-wind with e-CRs; how e-CRs mix with cluster gas; how viscosity supports the e-wind-flow.

In work of Tsvyk (2010) was discussed a model of RG with two-layer cocoon that separated by e- and p-CRs; and this model is developed here. New points in this report: p-CRs are the shock-inductors; effects of CRs in turbulence and current production; effect of viscosity changes as flow-regulator. We grounded in main assumptions of Mathews (2012), but show the cocoon dynamics in consist with two simple physical structures: a shock-like-outer-layer and a vortex-flow winding the inner-layer. The aim of this work is to study when the main structures of FR II-

RG (jet, cavity-lobes and bow-shocks) are grown up because of stratification effects in the magnetized plasma through the e/p cosmic rays as mediators.

2. The main impacts of the CRs to the FR II-lobe

There key assumptions are: (1) a cocoon matter composed of electron-positron e-plasma (density of $n_e = n_{e1} + n_{e2}$), and ion-proton plasma ($n_p \approx n_{th}$), atoms and neutrals (n_a), e- and p-CRs; (2) a cocoon matter is quasi-neutral ($n_{e1} - n_{e2} = n_{th}$) but current exists in it; (3) the CRs, that have being accelerated by DSA-mechanism near HS and bow shock, are the main mediator of exchanges due to they relativistic properties; (4) the e- and p-CRs separate in different area because of flow dynamics and viscosity changes; (5) a magnetic field (B) is produced by regular part from the CR-diffusion currents, and by dynamical part (the jet elongated) from pumping in the frozen of e-flows and from the p-CR kinetic effects of mixed matters (mainly within the shock areas). Out the scope are the ions-CRs decays, e-annihilation and many other processes.

The main part of cocoon energy contains in p-CRs; and some essential part is in e-CRs too. The less part cocoon energy contains in B -field, but frozen effects do B -field rule the flow cocoon dynamics. Cocoon energy contains in the p-CRs, the e-CRs, the turbulence (waves and vortexes), the thermal matter and the magnetic field. A jet consists of the e-plasma, with some part of p-plasma; but the p-flows are the most inert and energetically. The e-plasma flows are much frozen in B -fields and they fill the inner-cocoon; against to the p-plasma fills the outer cocoon and pumping shocks because of there momentum. Cocoon stratifies because of viscosity changes and injection of Hill's vortex flows (jet-supported). The radiation of e-CRs (synchrotron in radio, IC in X-ray band) helps for e-plasma vortex glues together and separated from p-plasma turbulence flows.

The jet and the lobes parameters of RG are differ in the shock-like (Zanni, 2003) or wind-like (Mathews, 2011) models. For example, RG of Cygnus A located in cluster of $3 \cdot 10^{14}$ sun-mass and with Virial radius of 1Mpc. The jet length is 60 kpc, bow-shock velocity is ~ 6000 km/s ($0.02c$), and the age of this source is ~ 10 Myr (it adjusts with the observations of e-CRs radio-age, see Machalski (2007)). So, the shock-like model (Zanni, 2003) predicts the RG jet-power of $L_j \sim 10^{47}$ erg/s and the energy of $E_c = 3 \cdot$

10^{61} erg; against to the wind-model Mathews (2012) that give us $L_j \sim 10^{46}$ erg/s and $E_c = 3 \cdot 10^{60}$ erg, that predicts only 1/20 part of cocoon volume fills with e-CRs without p-CRs energy in this wind-model. We review later shock-like model (illustrated in fig.1), and consider that p-CRs energy is essentially.

Bow shock properties in the outer lobe area. Shock-presser equals to the presser of p-CRs in outer lobe, both and nearly equal to the e-CRs presser in the inner lobe (see fig.1: 2, 3-arias, respectively). Pressure of B -field is negligible. The number of p-CRs in the outer lobe is some part of p-plasma (~ 1 -10%); and it is comparable to the number of e-CRs in this area.

Shock dynamic was shown in Zanni (2003). This a shock scale $R_s(t, \theta)$ grows with velocity u_{sh} that defines from the shock presser and the ICM-plasma density, $u_{sh} = dR_s(t, \theta)/dt \sim [P(t)/\rho_1(t)]^{1/2}(\cos^2\theta + a_1)$, and has an elongation along the jet-direction (for $\theta=0$ we have $1+a_1 \sim 1.3$). The other way, the energy of cocoon defines from the jet burst power (that comes with flow injection of e-CRs plasma), and as well as from shock presser multiplied to cocoon volume, $E_c(t) \sim \int L_j(t)dt \sim P(t) R_s(t, 0)^3$. The jet plasma is strongly blown to the inner lobe (3-area in fig.1), and it compresses the cluster matter of outer lobe (1-area, ICM) into the bow-shock front (2-area).

The flow velocities are super-sonic and not regular behind the shock front. Here is the turbulence dominated in plasma dynamics that pumps the Meshkov-vortex instabilities and ejects the inner-lobe-flow vortex surrounding bow-front. The e/p-CRs help to transport shock energy because there high transcalency. The jet-hot-spot, being the shock-center-point, forms the caviton-like feature in density map (see fig.1: 3, 4-arias) which may work to focus the wave-shock energy and support the jet.

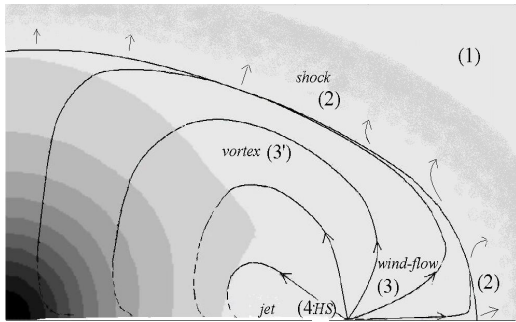


Figure 1: The density field (gray scales) and the velocity field (vector-lines) within the inner (3) and outer lobes (2).

Wind-flow properties in the inner lobe-caviton area. Wind-flow dynamic was shown in Mathews (2011, 2014); the simplest model is “simple-source” injection of e-flux-matter with e-CRs into the outer-lobe ep-plasma (with some part of neutral atoms). It illustrated in fig. 1 see aria 3; and the model of parameters done in Tables 1, 2. The pressure (P) and flow velocity (u) make the dynamical variations such as in the injection point (hot spot at jet-head) we have $P \rightarrow 0$ and u -velocity is maximum. The average flow velocity consists with regular and diffusion parts, the density varies with velocity profile, as $\rho \propto r_s^{q-2}$ when $u \propto (c/3)r_s^{-q}$, ($q \leq 2$, r_s is a scale from HS to

the chosen point). It is likely that post-jet e-plasma wind to the lobe (3) as nearly regular flow together with e-CRs and some part of thermal plasma from area (2), because this matters have mixed gradually within the HS-area and accompanied the accelerations of the e-CRs. That way, in the injection HS-point we have a purely post-jet flow with the density as in Kino (2004) model (see Table 1); and then the post-jet flows mix with $\sim 0.2n_{th}(r)$ of outer thermal plasma because of e-CR diffusion (see Table 2; r is a scale from RG-center to the chosen point, a density derives in the King’s model as $n_{th}(r) \propto (1+r^2/a_K^2)^{-1.13}$). This e-dominated-flow becomes regular because of viscosity in wind-injection area. Latter, in outside, the flux-collision-front give us the maximum of presser, that exhibit as $u=0$ and thermal-heats dominate. In this flow-stress cover, where the wind-flow transforms into the macro-scale Hill’s-2 vortex, we have: $\rho_1 u \sim \rho_{th} u_2$, $u_2 \approx 0.75 u_{sh}$; and the matters are mixed strongly by vortex-turbulence and MHD-waves, as e-CRs pressure is comparable to thermal pressure, $P_{th} \geq P_{eCR}$. So, the wind-velocities and Hill’s vortex velocity are correlated here.

Table 1: The parameters of Cygnus A at near HS-area based on Kino (2004) model: the density (ρ and n_a , n_p , n_e), magnetic field (B), scattering time (τ), viscosities (η_K , ν_K , ν_m), collision ($X = \omega_B \tau$, $\beta \sim 0.3$) and Reynolds (Re) numbers.

	1-ICM	2-HS	3-HS	4-jet
$Presser$, dyne/cm ²	10^{-10}	$2 \cdot 10^{-8}$		$< 10^{-8}$
n_a/n_p	0.20	0.05	< 0.01	0
n_p , cm ⁻³ ,	0.025	0.1	10^{-5}	10^{-7}
n_e , cm ⁻³	0.025	0.1	10^{-3}	10^{-4}
B , G	10^{-5}	$7 \cdot 10^{-5}$	$2 \cdot 10^{-4}$	$2 \cdot 10^{-5}$
ρ , m_p /cm ³	0.03	0.1	10^{-5}	$6 \cdot 10^{-7}$
$\omega_B \tau_{ii}$, [$\omega_{Be} \tau_{ee}$]	10^{11}	$[10^{14}]$	$[10^{20}]$	$[10^{19}]$
τ_{ei} [τ_{ee}], yr	10^5	10^7	$[10^{12}]$	$[10^{12}]$
η_K , gm/(s cm) ($\beta=0.3$)	$5 \cdot 10^{-5}$	0.25	35	10
ν_K , ($\beta=0..0.3$)	$10^{25..21}$	$10^{29..24}$	$10^{37..30}$	$10^{36..31}$
ν_m , cm ² /s	10^{21}	10^{20}	10^{14}	10^6
$Re = \lambda_0 c / \nu_K$ ($\beta=0.3$, $\lambda_0 \sim 1$ kpc)	10^{11}	$5 \cdot 10^7$	50	10

Vortex properties in the inner lobe-caviton area. Some of the vortex-flow dynamic with vortex-injection was shown in Antonuccio-Delogu (2010). We add this sketch of processes some more connection with shock-structures. This way, the main vortex is injected by Carioles force in around of min-pressure-focus ($P \rightarrow 0$) that forms as a ring near the hot spot points because of flux-stress dynamic in the post-jet structures of e-flux-matter blows. The injection provides within Kelvin’s low frames: $d(\bar{\omega} / \rho) / dt = (\bar{\omega} / \rho) \nabla \bar{u}$ ($\bar{\omega}$ -circulation is constant, $\bar{\omega} = rot \bar{u}$). And the gravity-buoyant and F_η -viscosity forces help us to form the vortex flux of Hill’s-2 like type

in the post-jet cavity surface around (see fig.1, 3' area), because of the matter difference and e-CR presser variation:

$$\frac{\partial \vec{u}}{\partial t} + \rho^{-1} \nabla P + \frac{1}{2} \nabla (u^2) = [\vec{u} \times \vec{\omega}] + \vec{F}_\eta + \vec{F}_g.$$

A simple model of Hill's-2 vortex of R_{s3} size (limited of e-plasma contact border, $R_{s3} \sim 0.7 R_s$) may describe as main-flow-vortex in nearly uncompressed matter by the velocity profile in spherical (r - θ) geometry with the RG centre as zero-point and jet aligns to $\theta=0$:

$$u_r \propto \rho_{th}(r)^{-1} (R_{s3}(t, \theta)^2 - r^2) \cos \theta \cos(2\theta);$$

$$u_\theta \propto \rho_{th}(r)^{-1} (R_{s3}(t, \theta)^2 - r^2) \cos \theta \sin(2\theta).$$

A fine density variation is accounted as $u \propto \rho_{th}(r)^{-1}$ in attached to the King's model. This main-vortex excites the vortex-turbulence in contact with shock-surface that runs plasma density to mix by everyone small or large flow-velocity lines. The turbulence makes to shift dynamically this Hill's vortex forward together with bow-shock surface. The plasma presser inside the any macroscopic flow tube is decrease because the e-CRs are radiated, and this supports the Carioles force in Hill's-2 vortex structure.

Vortex flux matter composed with e-plasma and e-CRs that predominates over the thermal ep-plasma in the inner cocoon part ($n_e > n_{th}$). This forms a cavity-vortex structure within the inner e-Lobe density field, $\rho = (n_{th} + n_a) m_p + n_e m_e$, and the Hill-2 vortex injection helps to separate the inner-matters with e-CRs from outer-matters with p-CRs. The particles are sorted by quasi-neutrality low ($n_{e1} - n_{e2} = n_{th}$).

The average flux velocity (u) obtains as to dominate the e-plasma flux and the relativistic e-CR diffusion flux: $u = (\sum n_\alpha m_\alpha u_\alpha) / \rho$ (α is types of particles: $e1, e2$ – electron/positrons, p – protons, a – neutral atoms, and e/p -CR – relativistic particles). Superposition of the vortex and the shock velocity gives up the flux relaxation ($u \rightarrow 0$) at $\theta = \pi/2$. Near the e-lobe edge (R_{s3} -surface) we have $u \sim u_2$; and in this area the matter composition changes: the e-plasma is depressed and the thermal plasma with p-CRs is added, whit the presser is conserved.

To construct the density model (fig. 1, Table 2) we use the continuity matter equation with referred assumptions and with u -flux model chosen.

3. Magnetic fields impact to FRII-lobe structure

The magnetic field is grown both the dynamical and regular field parts inside the cocoon. The dynamical field is pumping from cosmic turbulence B_{turb} field by adiabatic and alpha-pump turbulent effects; the regular part of B_θ -field induced from CR-diffusion currents.

Only estimation lobe model parameters are represented in Table 2, and the B -field calculations in this model show in fig.2. If the current is estimated in the inner lobe because of diffusion motion of the e-CR-particles with the different singles, $\Delta n_e \sim \Delta n_{CR} \sim 0.1 n_{th}$ (despite of $n_e \gg n_{th}$ in the 3-area) and $\Delta v \sim |v_e - u| \sim v_{dif} > \sim 10^6$ cm/s (that is smaller then sound and Alfvénic velocities, $c_{s,A} \sim 10^7..10^9$ cm/s), so the regular part of magnetic field give us tor-

oidal-field of $B_\theta \sim 3 \cdot 10^{-4}$ G that mainly induced by radial and jet-elongate current components.

Beside this, the p-CRs diffusion give us a moves B -field lines together with cosmic matter, and pumps dynamically the turbulent field component as alpha-pump turbulent effects in (2) and HS areas (fig.1). These effects are dominated within the outer lobe that is near the bow shock-wave surface; we assume that $B_{turb} \propto (P_{eCR} + P_{pCR})$. Stress of these turbulent fields must be $B_{turb} \sim 3 \cdot 10^{-4}$ G, compare to the regular B_θ -field near the jet-HS surface.

Maximum strength of regular magnetic field (B_θ) is nearly denoted to the areas of minimum plasma presser (the same as areas of with minimum of Hill's-flow velocities). This effect comes to gluing of local e-flows with e-CRs, and it may appear as bright features (look likes as an additional HS-spot) in radio emission map of the RG-lobe. However the turbulent pumping may be so strong that to exhibit only one HS-point in the lobe map as the jet head.

Table 2: The model parameters of inner and outer lobe for typical FRII-RG (like Cygnus A) based on assumption of the wind-vortex-shock cocoon transformation because of the CR-flow dynamics (see the text and Table 1 in detail).

AREA	3 (HS)	2 (HS)	3 (e-Lobe)	2 (outer)
n_e	0.001	0.0005	10^{-4}	$<10^{-4}$
n_{th}, cm^{-3}	0.001	0.04	0.002	0.003
n_a	10^{-6}	0.0003	$<10^{-4}$	$<10^{-4}$
B_θ, mG	0.15..0.2	0.03	0.3..0.2	0.06
$\Lambda_{ll} ..$	0.1 ..	0.1 ..	0.5 ..	10 ..
Λ_r, kpc	10^{-5}	10^{-6}	0.1	0.5
v_m	10^{13}	10^{15}	10^{18}	10^{19}
v_K^*	10^{35}	10^{31}	10^{13}	10^{20}
$Re = \lambda_0 c / v_K^*$	<1 (reg. flow)	~ 2	$10^7..10^{20}$ (turb.)	$\sim 10^{13}$
λ_{min}, pc ($Re \sim 1000$)	$>10\ 000$	>1	$<10^{-6}$	<0.1

* parameters at magnetic line intermittency $\beta=0.3$;
 Λ is min CR-diff. length; λ_{min} is min vortex scale at $Re \sim 1000$

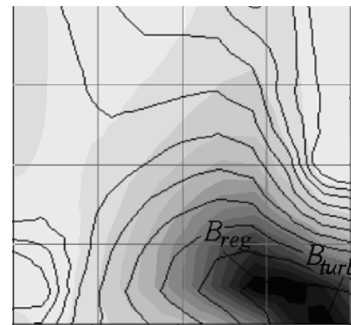


Figure 2: The model of magnetic field strength (in the gray scales: dark is $B \sim 3 \cdot 10^{-4}$ G, white is $B \sim 10^{-6}$ G) and the low-band synchrotron radiation (contour lines).

4. Model for the RG lobe viscosity as cosmic plasma

Cosmic plasma is low-collision matter (the collision term is $X_\alpha = \omega_{B\alpha} \tau_\alpha \gg 1$, and the magnetic pressure is smaller than thermal one $P_B < P_{nT}$), and this plasma is composed of the different types (α) of particles, that parameters are changed within the RG-cocoon.

The contact layer that splitting the inner lobe (3) with e-plasma and the outer lobe (2) with thermal plasma plus p-CRs, is the front of viscosity stress that comes to change the matters dynamics. Viscosity consists of kinematical and magnetic parts, and the physics of cocoon are coordinated by these types of viscous vary.

This way, the kinematical viscosity η_K coordinates the changes of the velocity along B_0 (by η_{Kl}), and the viscous dump of transverse velocity fluctuations (by $\eta_K \sim \eta_{K0}$). Here we are: $\eta_{Kl} \sim \eta_{K0} X_j^{-2+\beta}$, where $\eta_{K0} = \sum \{ \eta_j T_j \tau_j X_j^{-\beta} \}$ and $0 < \beta < 1$ is the magnetic turbulence parameter. The p-CRs make to change the characteristics X and β of the slow matter turbulence that handle the viscous forces.

The magnetic viscosity, $\eta_m = \rho v_m = \rho c^2 / \sigma_{eff}$ coordinates the currents induction and the enhanced of MHD-turbulence within the shock both and in the jet surface; both and it enhanced the magnetic dynamo in the dense matter area. Here is the effective conductivity within e-lobe depends on the neutral density $\sigma_{eff} \sim e^2 n_e \tau_e m_e^{-1} (1 + (n_a m_p \rho^{-1})^2 X_e X_i)$ as accounted in Bykov (2007) model.

Table 1 and 2 demonstrate the typical parameters in cocoon as changes of the kinematical and the magnetic viscosity, both and as turbulent exiting changes (by Reynolds number). The fig.3 demonstrates the relative viscosity changes of v_m/v_K that response the areas where magnetic turbulence may pump strongly.

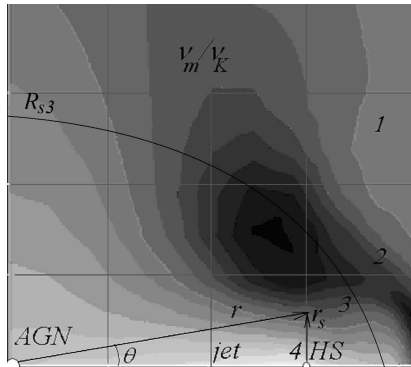


Figure 3: The model of relative viscosity changes (in the gray scales: dark is $v_m/v_K \sim 10^{10}$, white is $v_m/v_K \sim 10^{-20}$; the 2-3 contact R_{s3} -boundary outline schematically sketched).

5. Radiation and streaming of the e-CRs in FR II lobe

In the inner lobe, the wind-flow consists of the local flows with e-CRs which are gluing because of viscosity, magnetize effects and radiating cooling of e-CRs. The diffusion effect of the e-CRs, because of vortex and Alfvén-wave turbulence, are smoothing the flow dynamic and dumping turbulence by viscosity driven. The effect of e-CRs radiation leads to cool of the lobe matter and it helps a current production and gluing of local e-CR-flows.

The e-CRs are radiating mainly by synchrotron (in radio bands at f -frequency) and synchrotron-inverse Compton (in X-ray bands) processes, which are frequency-dependent. So, the lobe radio brightness is $I_{syn} \propto n_{eCR} B f^{-(s+1)/2}$, and the X-ray brightness depends on n_{eCR} and radiation field.

The e-p-CRs flow together with the thermal plasma (that frozen in B -field tubes) and drift with energy-dependent diffusing velocity, $v_{eCR} = u + v_{diff_eCR}$. A diffusion velocity defines by turbulence parameters and regular magnetic field (B_0): $v_{diff_eCR} \sim (\kappa_{e0}/\Lambda_{diff}) \gamma^{2-s} \propto (B_0/B_{turb})^2 r_g c/\Lambda_{syn}$. Thus, the low-energy particles of e-CRs, that was cooling by radiation to energy $\gamma \sim 1..10$, have to flow with thermal plasma better than diffuse. Alternatively, the p-CRs particles have to correct a local B_{turb} -lines with any diffusion act, thus in a bow shock area this effects are limited the magnetic field correlation scales (λ_0) with the p-CRs energy spectrum (γ_{p_max}) and with $R_s(t)$ lobe-size.

This way, taking account the trends of B-field and e-flows, we may predicted that a powerful radio emission of low-energy e-CRs in MHz-band comes from areas where e-rays are pulled together into streams, due to the turbulence by viscous forces dumping, and e-rays cooling. And the radiation-cooling of e-CRs give us the main mediator-effects that coordinate all cocoon dynamics.

6. Conclusions

1. The viscosity of RG matter rules in the lobe-phenomenology. It is switching the instabilities, and directing the gluing flows, and heating or accelerating of CRs in the cocoon, and the magnetic-viscosity divides the vortexes into small modes (B -pumping).

2. The bow-shock transports by wave-turbulence, and by the p-CRs, that getting up of magnetic-viscosity the biggest. The e-p-CRs ejects by diffusion-shock acceleration mechanism.

3. The magnetic field turbulence prevents the mixing of cocoon fluid. The e-CRs frozen into magnetic turbulence critically, beginning with $>10^{-6}$ pc-size modes (the smallest). The p-CRs help to mix the matters.

4. The e-CRs and p-CRs are separated by injection of Hill's-2 vortex from relativistic post-jet e-plasma-flow winding. The ties of e-CRs are gluing by viscosity and radiate-cooling effects.

5. The e-CRs diffuse (in adding to flow-transport) by energy-dependent, because of B-turbulence that has been generated by vortexes and MHD-waves.

After synchrotron-radiate-cooling, the low-energy e-CRs are filling nearly all cocoon-volume, adding to the p-CRs that holding up the B -turbulence within the cocoon-surface.

References

- Kaiser C.R. et al.: 1997, *MNRAS*, **286**, 215.
 Zanni C. et al.: 2003, *A&A*, **402**, 949.
 Kino M. et al.: 2004, *MNRAS*, **349**, 336.
 Mathews W.G. et al.: 2011, *ApJ*, **736**, 6.
 Mathews W.G. et al.: 2012, *ApJ*, **755**, 13.
 Tsyk N.: 2010, in: *Proc. of 10th Gamow's Odessa Astron. Conf.*, Odessa, Ukraine, 142.
 Machalski J. et al.: 2007, *A&A*, **462**, 43.
 Antonuccio-Delogu V. et al.: 2010, *MNRAS*, **405**, 1303.
 Bykov A.M. et al.: 2007, *Physics-Uspekhi*, **50**, 141.

DECAMETER PULSARS AND TRANSIENTS SURVEY OF THE NORTHERN SKY. STATUS, FIRST RESULTS, MULTIPARAMETRIC PIPELINE FOR CANDIDATE SELECTION

V.V.Zakharenko¹, I.P.Kravtsov¹, I.Y.Vasylieva^{1,2}, S.S.Mykhailova³, O.M.Ulyanov¹,
A.I.Shevtsova¹, A.O.Skoryk¹, P.Zarka², O.O.Konovalenko¹

¹ Institute of Radio Astronomy of the National Academy of Sciences of Ukraine (IRA NASU)
4, Chervonopraporna St., 61002, Kharkiv, Ukraine, rian@rian.kharkov.ua

² LESIA, Observatoire de Paris, CNRS, UPMC, Universite Paris Diderot, Meudon, France

³ V. N. Karazin Kharkiv National University, 4 Svobody Square, 61022, Kharkiv, Ukraine,
info@karazin.ua

ABSTRACT. We present the results of processing first 20% of Northern sky pulsars and transients survey using UTR-2 radio telescope. Data processing is done by an automatic pipeline that detects and outputs a large number of transient candidates (usually dispersed bursts). We have developed a multivariate pipeline for visual inspection of these candidates. By adjustment of input parameters of the pipeline the observer can substantially increase signal-to-noise ratio of detected signals as well as discriminate them from residual low-intensity interference with high significance. About 450 transient signals have passed the examination by the multivariate pipeline. Their distributions on the Galactic latitude and dispersion measure have been derived. The shape of the distributions suggests that these signals might be associated with cosmic sources of radio emission.

Keywords: pulsars, transients, survey, decameter range

1. Introduction

First decameter-wavelength census of known pulsars (Zakharenko et al., 2013) aimed at re-detection and study of nearby pulsar population was highly successful. More than a half of observable pulsars with dispersion measure (DM) $< 30 \text{ pc cm}^{-3}$ were re-detected, despite the extremely difficult conditions of observations in the decameter range, such as high Galactic background temperature, large scattering time constant of pulsar pulses, enormously high radio frequency interference (RFI) level etc. The major result of that study was confirmation of pulse profile broadening observed for the majority of aforementioned pulsars, compared to their widths at higher observational frequencies. This opened a new parameter space for searching new sources of pulsed radiation in the closest Galactic neighborhood. Pulse profile broadening can make ‘unfavourably’ oriented pulsars, rotating radio transients (RRATs) and other radio-emitting neutron stars visible at low frequencies. This makes a low-frequency blind pulsar and transient survey of the entire Northern sky both useful and required.

Such a survey was started in 2010 (Zakharenko et al., 2011). One of the first important results was first detection of decameter emission (Vasylieva et al., 2014) of the re-

cently discovered pulsar J0243+6257 (Hessels et al., 2008). The dispersion measure of this pulsar was substantially refined (an error became less than 0.01 pc cm^{-3} instead of previous one near 0.2). It became possible due to the important advantage of the low-frequency range and broad observational band (16.5 - 33 MHz) of the above survey – the precise determination of the dispersion measure. Observations in a broad frequency band allow to distinguish with high confidence between a real signal that had passed through the interstellar medium and local interference. The real signals have a characteristic dependence of pulse arrival time on the frequency ($\propto f^{-2}$), being delayed at lower frequency f_{\min} compared to higher frequency f_{\max} by

$$dt = 10^{16} / 2.410331 \cdot \text{DM} \cdot (f_{\min}^{-2} - f_{\max}^{-2}) \quad (1)$$

seconds. The local signals may have a different origin and time-frequency structure, e.g. signals with linear frequency modulation.

Stream processing of a part of survey data revealed many transient ‘candidates’. The goal of the present work is to check each ‘candidate’ by means of the interactive data reduction pipeline, all intermediate results of which can be inspected simultaneously. For instance, raw dynamic spectra (before de-dispersion) show whether signal’s time-frequency shape is not $\propto f^{-2}$ (Vasylieva et al., 2014) or has features similar to those described in (Petroff et al., 2015). Presence of signal only in a narrow frequency band is also an indicator of its artificial origin. However, as the signal-to-noise ratio (SNR) of the candidates after integration of the entire frequency band is quite low, generally 6-8 standard deviations (σ), inspection in the fractional sub-bands reduces it further, sometimes equalizing signal with noise. Therefore, additional criteria are required to verify the signals’ origins. Subsequent stage of our work is an analysis of distribution of the ‘candidates’ on the galactic coordinates and dispersion measures (that can be translated to distance). Similarity of these distributions to distributions of known pulsars and RRATs will imply the cosmic origin of the ‘candidates’.

2. Data analysis

The blind decameter drift-scan survey (Zakharenko et al., 2011; Vasylieva et al., 2014) should cover a range of declinations (δ) between -10° and 90° . To date, more than 90% of planned sky region is covered, and about 75% of data is automatically pre-processed (i.e. spared from interference, compensated for interstellar dispersion in the range $0 < DM < 30 \text{ pc cm}^{-3}$ with 0.01 pc cm^{-3} step, producing 3000 spectral-integrated time series that form a “DM-Time” plane, see Fig. 1a). After processing of each observation session, the database of candidates is updated with parameters (occurrence time, DM and signal-to-noise ratio) of detected signals if their SNR exceeds 5.5σ .

At the next stage signals with $DM < 1$ and signals which form regular structures (usually slanted lines) in the “DM-Time” plane are rejected as they are most likely RFI. Taking into account scattering in the interstellar medium that smears pulses of regular pulsars over tens of milliseconds and pulse width itself, we also reject the events that occupy only a single sample ($8 \text{ ms} \times 0.01 \text{ pc cm}^{-3}$) in the “DM-Time” plane.

In order to reveal spurious (RFI-induced) candidates, and to maximize the SNR of real candidates, we have developed a multivariate pipeline for candidate selection. A set of adjustable input parameters includes:

- thresholds in RFI mitigation routine (Vasylieva et al., 2013),
- step between adjacent trial DM values (up to 0.002 pc cm^{-3}),
- cutoff frequency of a high-pass filter that reduces effects of ionospheric scintillations.
- cutoff frequency of a low-pass filter that increases an integration time for the pulses
- width of partial frequency sub-bands
- time interval for search of repetitive signals

When optimal, the above settings lead to 2-5-fold increase in SNR which is vital for exploring spectral features of candidates and their shape in the ‘DM-Time’ plane with a higher contrast.

Fig. 1 shows visual inspection of a ‘candidate’ that at first glance didn’t provide any reason for rejection (a red disk in the panel a). However, after examining the raw data and its de-dispersion using the correct DM value, we found a signal behavior, very different from that described by equation (1). The signal was relatively narrowband (panel b) and had a linear frequency modulation (panel c, top). Its shape in the time-DM plane is smeared over many adjacent DM values (panel c, bottom) as it happens with RFI signals. Signals like in Fig. 1 are of course excluded from ‘candidates’ database.

3. Results and discussion

As a result, ‘candidates’ from about 20% of the survey have been checked for compliance with the dispersion law (equation 1). These signals have a relatively broad band and don’t show any RFI features. We determined approximate coordinates of each ‘candidate’ by deriving direction of UTR-2 pointing at the moment of its detection.

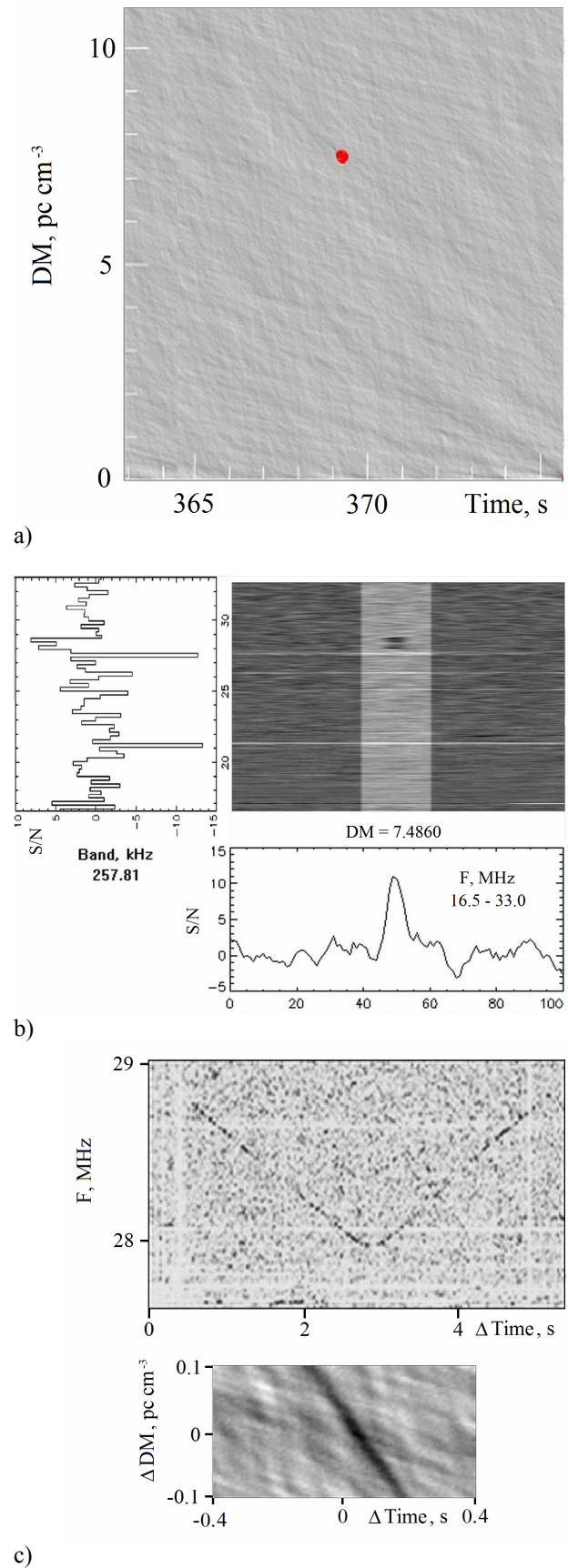


Figure 1: (a) “DM-time” plane, (b) de-dispersed spectrogram (grey-scale image) with cut-sets over time and frequency, (c) zooms of raw spectrogram (top) and “DM-time” plane (bottom)

A map of Galactic background radio emission (Sidorchuk et al., 2008) and superimposed coordinates of the corresponding transient sources are shown in Fig. 2. Only recordings of low declinations are (partly) processed so far.

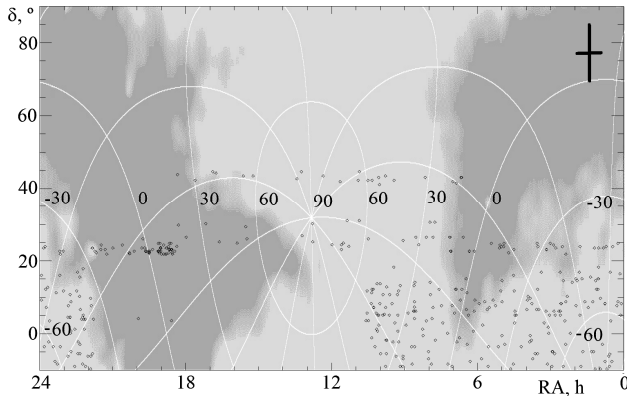


Figure 2: Sky map with coordinates of transient candidates and pattern of directivity of the UTR-2

A promising result is a lack of preferable directions in the distribution of the sources, except for a region of $RA=19^h$ and $\delta = 23^\circ$. But as this region is located close to Galactic disk, in the direction not far from its center, this concentration of detected events seems expected.

To analyze statistically whether the above sources are a part of Galactic disk population, we have derived a histogram of their galactic latitudes. As expected, the histogram has a local maximum near $b=0^\circ$ (Fig. 3 a), similar to the histogram for close pulsars (period > 0.2 s, $DM < 30$ pc cm^{-3}), shown in Fig. 3b (derived from Manchester et al., 2005).

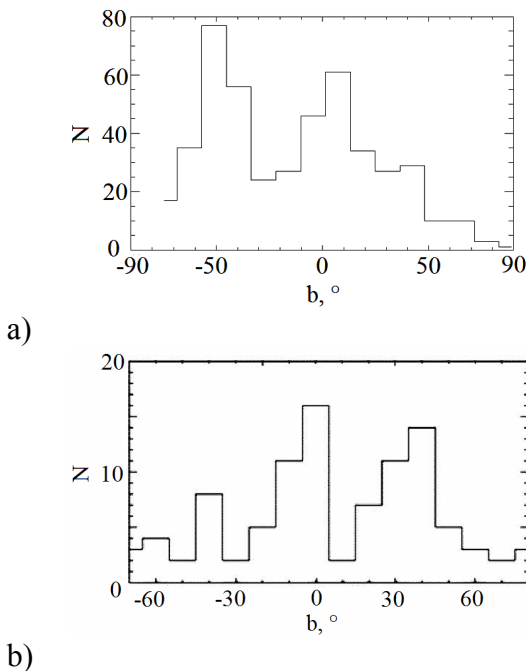


Figure 3: Histogram of transients' (a) and known close pulsars' (b) (Manchester et al., 2005) galactic latitudes

The main maximum of the histogram is at $b = -50^\circ$. But from Fig. 2 it is evident that the data with galactic latitude from -45° to -90° is processed completely, whereas the remaining areas are processed partly. Therefore, along with further data processing the number of events at galactic latitudes above -45° will increase, while below -45° will remain unchanged. Furthermore it is possible that at low radio telescope beam positions (corresponding to low declinations in Fig. 2 and regions with $-90^\circ < b < -45^\circ$) the number of residual low-intense broadband RFI in the data is higher.

The distribution on the galactic latitude thus implies that if not all, but the majority of detected signals are of cosmic origin and their coordinates tend to low Galactic latitudes. It is possible that there is a number of interference among the 'candidates', but they do not have a large impact on the shape of the distribution.

The expected distribution of cosmic sources on DM is shaped by the following factors. With increasing DM (and therefore distance between a source and an observer) the geometrical size of the considered region (layer), and therefore the number of sources that it contains, should increase. For the closest ones (while the considered layer doesn't extend beyond the width of the Galactic disk) the number of sources grows approximately as a square of distance (and hence of DM). For more distant sources the increase will be close to linear. However at some point this distribution will reach the maximum and the number of sources will start to decrease, because the more distant sources are generally weaker. Additionally, with decreasing frequency, the scattering of pulsed signals comes into play (the scattering time constant is $\propto f^{-4}$). I.e. at lower frequencies this turnover should happen at lower values of DM, compared to higher frequencies.

For comparison, a simulation of similar distributions for pulsars, expected to be detected by SKA1-LOW and SKA1-MID is shown in Fig. 4 (Keane et al., 2015). A distribution, obtained for the above 'candidates' is shown in Fig. 5a, and is generally in agreement with the simulated one (Fig. 4), as we see the increase in number of 'candidates' up to $DM=10-15$, followed by a gradual decrease.

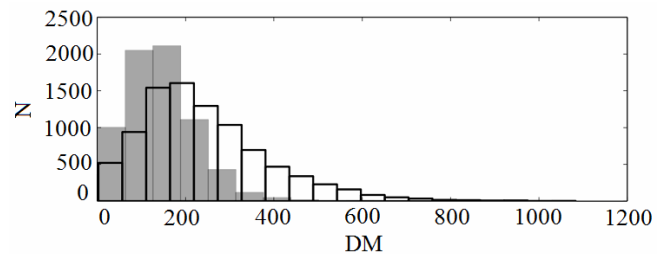


Figure 4: Simulated histograms of DM of pulsars, expected to be observed with SKA Phase 1, for SKA1-LOW (dark bars) and SKA1-MID (clear bars) (Keane et al., 2015)

Apart from an outlier at a low DM value (that can be related either to RFI or to unidentified source of repetitive pulsed emission, e.g. a pulsar) the distribution is smooth. For comparison, Fig. 5b shows a distribution of known

RRATs on dispersion measure, derived from ‘RRATalog’. It has a fragmented structure due to a small number of sources, but as a whole, it is also similar to those shown in Fig. 4 and Fig. 5a. We should note that the shape of RRAT distribution is a result of their discoveries in high-frequency surveys – at decimeter wavelengths, which means the lower influence of the interstellar medium and a larger DM range that can be explored.

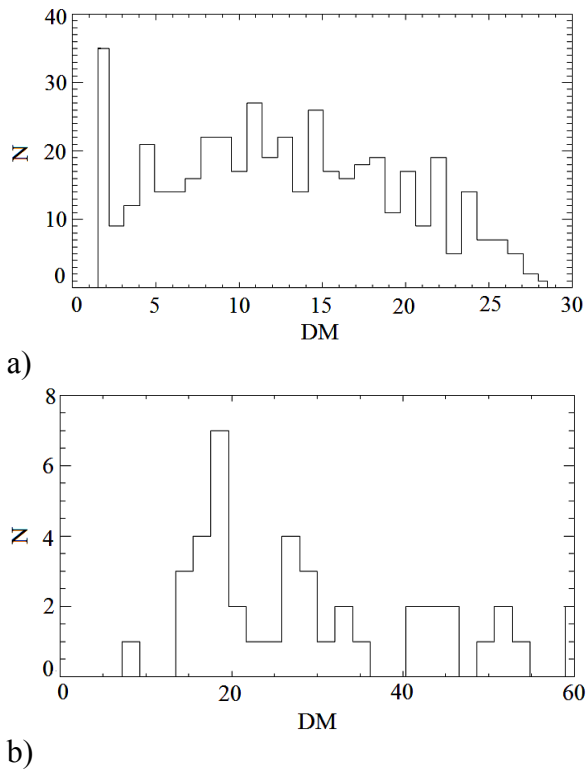


Figure 5: Distribution of DM of transient events detected in this study (a) and known RRATs (b) (RRATalog)

Thus, the both distributions that we derived (on the galactic latitude and DM) suggest that the majority of detected signals are most likely of cosmic origin. The shape of the received pulses is similar to pulsar or RRAT pulses. We assume that the detected ‘candidates’ could originate from:

- neutron stars that are unfavorably oriented in space for higher frequency observations,
- RRATs with low dispersion measures that have been misinterpreted as RFI in the high-frequency surveys,
- pulsars that present an increase of flux density towards low frequencies (such as PSR B0943+10, see Stappers et al., 2011),
- giant pulses of millisecond pulsars (usually flux density of millisecond pulsars grows with decreasing frequency) that are either sporadic or unfavorably oriented. Although giant pulses are short, they will arrive significantly scattered at our frequencies and will be noticeable in the survey data,
- anomalously intense pulses (see Ulyanov et al, 2006) of close weak pulsars.

4. Conclusions

Using the developed routines of multivariate candidate selection, we have analyzed the transient signals from about 20% of the decameter pulsars and transients survey of northern sky. Adjustment of filtering parameters and simultaneous access to all intermediate stages of processing serves for rejection of RFI-induced candidates even with low SNR.

Histograms of candidates’ galactic latitudes and dispersion measures show that corresponding sources tend to be located at low Galactic latitudes and have an expected distribution on dispersion measure. This allows us to suppose that the majority of above signals must be associated with cosmic sources.

Complete processing of all survey data give more significance to these distributions and possibly will allow to link such parameters as galactic longitude, intensity, probability of occurrence etc. This will help to attribute the sources to certain structures, such as Gould belt, Galactic spiral arms and subsequently to improve general knowledge of close neutron star population.

References

- Zakharenko V.V. et al.: 2013, *MNRAS*, **431**, 3624.
 Zakharenko V.V. et al.: 2011, *Odessa Astron. Publ.*, **24**, 117.
 Vasylieva I.Y. et al.: 2014, *RP&RA*, **19**, 197.
 Hessels J.W.T. et al.: 2008, *AIP Conf. Ser.*, **983**, 613.
 Petroff E. et al.: 2015, *MNRAS*, **451**, 3933.
 Vasylieva I.Y. et al.: 2013, *Odessa Astron. Publ.*, **26**, 159.
 Sidorchuk M.A. et al.: 2008, *Astrophysics with E-LOFAR*, http://www.hs.uni-hamburg.de/DE/Ins/LoFar/lofar_workshop/poster_abstracts.html.
 Manchester R.N. et al.: 2005, *AJ*, **129**, 1993.
 RRATalog: <http://astro.phys.wvu.edu/rratalog>
 Keane E. et al.: 2015, *AASKA14*, **1**, 40.
 Stappers B.W. et al.: 2011, *A&A*, **530**, A80.
 Ulyanov O.M. et al., 2006, *IAU Joint Discussion*, **2**, 12.

SUN, SOLAR ACTIVITY AND ASTROBIOLOGY

EVALUATION OF CORONAL SHOCK WAVE VELOCITIES FROM THE II TYPE RADIO BURSTS PARAMETERS

V.V.Galanin¹, E.A.Isaeva^{1,2}, R.O. Kravetz¹

¹Institute of Radio astronomy of NAS of Ukraine, URAN-4 observatory

²Astronomy observatory institute of I.I.Mechnikov ONU

Odessa, Ukraine

¹gvv@breezein.net, ^{1,2}isaeva-ln@mail.ru

ABSTRACT. The work presents the results of research of connection between the coronal shock waves and the parameters of type II (mII) meter-decameter bursts in 25-180 MHz band for 66 solar proton events. The velocities of coronal shock waves for this two cases were determined. In the first case the velocities of the shock waves was evaluated according to the Newkirck model and in the second case – directly from the type II radio burst parameters. The calculated values of shock waves velocity was compared with the same velocity values that is published on NGDC site. The comparative analysis showed that precision of coronal shock waves velocity estimation which gets directly from type II radio bursts parameters was higher than the same one which used the Newkirck model. Research showed that there is exist the sufficiently strong connection between the shock wave velocity and the delay of type II burst intensity maximum on the second harmonica. Correlation coefficient between the studied parameters was equal to ≈ 0.65 .

Key words: shock speed, drift velocity

1. Introduction

It is well known that solar proton events (SPE) have great influence on the space weather. An SPE which is accompanied with streams of high energy particles, coronal mass ejections (CME) and shock waves are cause some geoeffects (Pudovkin et. al., 1992; Rivin, 1985). In this connection it is expedient to evaluate beforehand an intensity of high energy particle streams, velocity of CME and shock waves before it is reach the Earth orbit. It can be easy done by the radio burst parameters (Mel'nikov et. al., 1991; Chertok et. al., 2009). In this paper we examine the estimation of coronal shock waves (CSW) velocity. It is considered that shock waves in solar corona can be generated either in the energy output burst region (Classen et. al, 2002) or upon CME movement (Gopalswamy et. al., 1998). Most reliable indicator of shock waves in solar corona is type II radio bursts. It is considered that plasma mechanism of radio bursts (Cairns et. al., 2003) is responsible for it generation.

2. Results

For the analysis we have used the original dynamic spectra records obtained on Solar Radio Spectrograph (SRS) in 25-180 MHz range

(<http://www.ngdc.noaa.gov/stp/space-weather/solar-data/solar-features/solar-radio/rstn-spectral/>). Fig.1 show an example of dynamic spectrum of proton event type II burst 31.05.2003. As it seen we can distinguish two bars corresponding to main and second harmonic. They are approximated good enough by the functions (1) (light lines on fig.1)

$$\lg f_{i,j} = k_j \cdot \lg t_i + d_j \quad (1),$$

where t_i - time of maximum intensity of type II burst on the $f_{i,j}$ frequency, k_j and d_j - coefficients of linear regression, $i=1,2..n$ – counting number, $j=1,2$ – number of harmonic. Zero point of time counting for all events has corresponded to the beginning of the first harmonic on 180 MHz frequency.

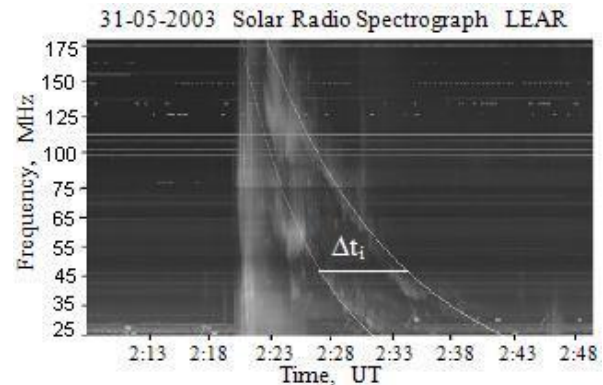


Figure 1: An example of dynamic spectrum of proton event type II burst 31.05.2003.

Main frequency of plasma radiation f is proportional to electron density $Ne^{0.5}$ (2)

$$f_{i,1} = \sqrt{\frac{e^2 N_e}{\pi m_e}} = 8.98 \times 10^{-3} \sqrt{N_e} \quad \text{MHz} \quad (2)$$

So, using empirical dependence of frequency from time $f_{i,j}$ (1) and suitable model of coronal electron density we can calculate heights and velocities of type II radio burst sources. To find the height distribution of electron density we had use the Newkirck model (3) (Newkirk, 1961):

$$N_e = N_0 \times 10^{4.32R_{\odot}/R} \quad (3),$$

where $N_0=4.2 \times 10^4 \text{ cm}^{-3}$ - concentration, R_{\odot} - solar radius, R - distance from solar center to source of type II burst.

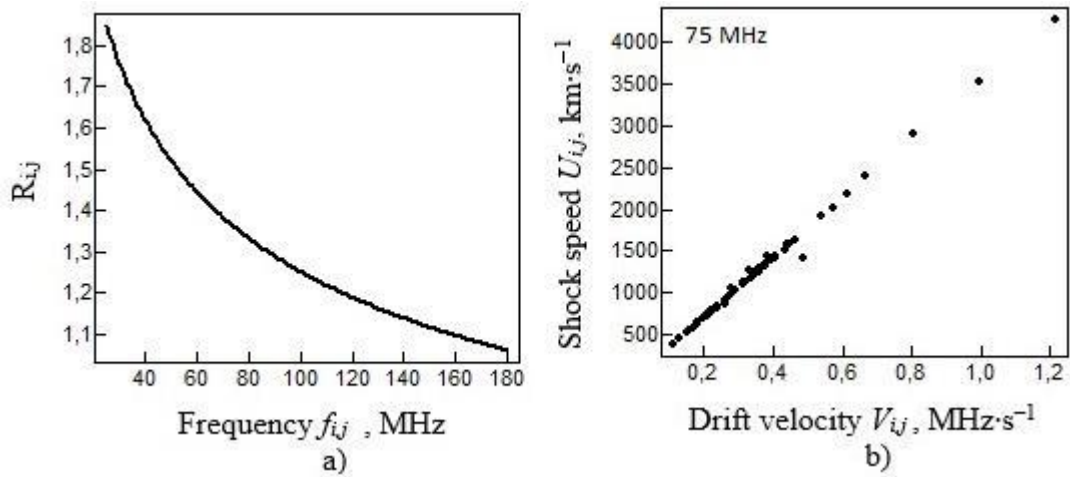


Figure 2: a). Relationship between the frequency f_{ij} and the height R_{ij} of source of type II radio burst
 b). Relationship between the drift velocity V_{ij} and the shock speed U_{ij}

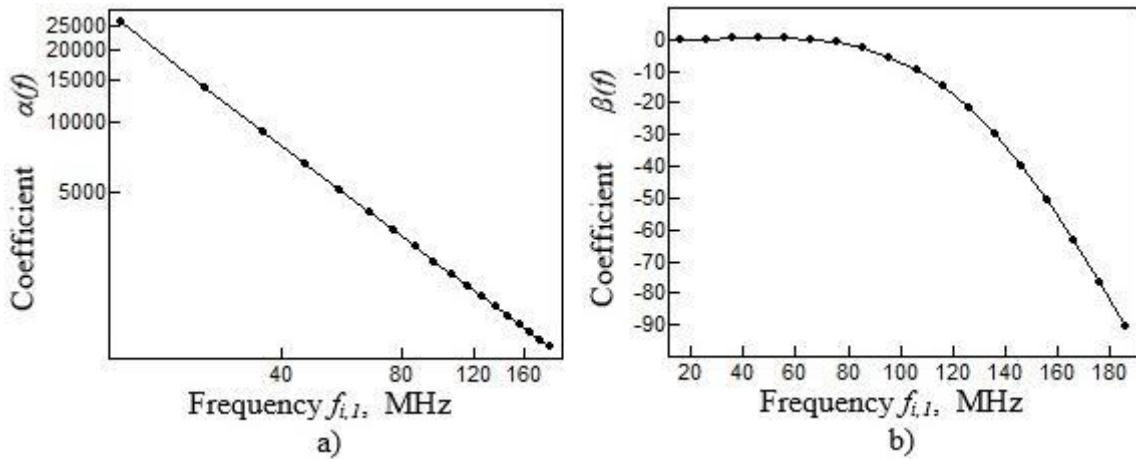


Figure 3: The dependence of linear regression coefficients $\alpha(f_{i,j})$ and $\beta(f_{i,j})$ (5) from frequency $f_{i,j}$.

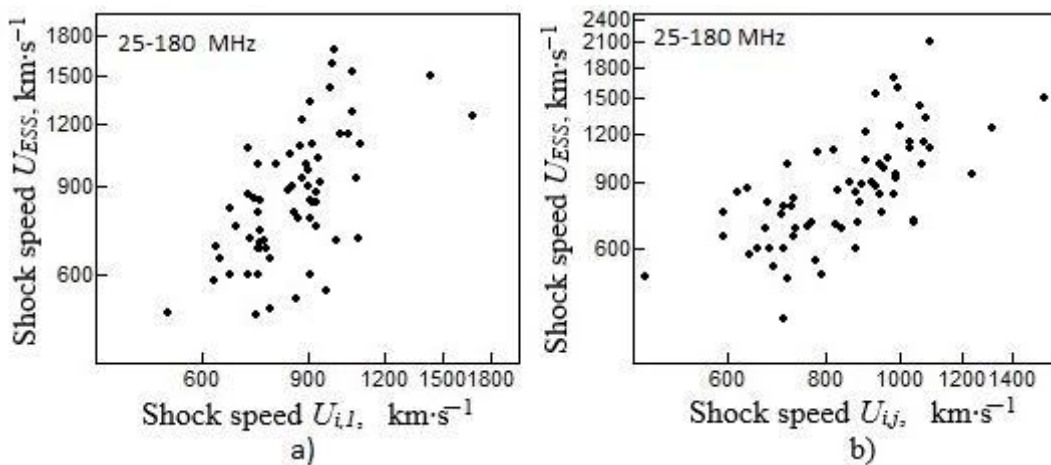


Figure 4: Disperse diagram of calculated velocity values $U_{i,j}$ and U_{ESS} :
 a). $\lg U_{i,1} = 0.3335 \cdot \lg ((R_{i+1,j} - R_{i,j}) / (t_{i+1,j} - t_{i,j})) + 3.2758$, $r(U_{i,1}, U_{ess}) \approx 0.56$
 b). $\lg U_{i,j} = -0.2408 \cdot \lg \Delta t_i + 3.2758$, $r(U_{i,j}, U_{ESS}) \approx 0.65$

Thus, when determine the electron density from formula (2) and using model (3) we can determine the height $R_{i,j}$ of source in the given time moment t_i and hence the velocity of shock wave $U_{i,j}$. As the result of the research it was ascertain that there is exist the clear connection between the frequency $f_{i,j}$ and the height $R_{i,j}$ of source of type II radio burst, and also between the shock wave velocity $U_{i,j}$ and drift velocity $V_{i,j}$ in the given time moment. Fig. 2 a) show dependence between $f_{i,j}$ and $R_{i,j}$, fig,2 b) – between $U_{i,j}$ and $V_{i,j}$ on 75 MHz frequency for all of 66 proton events.

More detailed research has shown, that dependence between $f_{i,j}$ and $R_{i,j}$ was found approximately identical for all of 66 events (4), but dependence between $V_{i,j}$ and $U_{i,j}$ was found more complex because there is exist the strong dependence of linear regression coefficients $\alpha(f_{i,j})$ and $\beta(f_{i,j})$ (5) from frequency $f_{i,j}$ fig. 3 a) and b).

$$\lg R_{i,j} = -\alpha \cdot \lg f_{i,j} + \beta \quad (4)$$

$$\lg U_{i,j} = \alpha(f_{i,j}) \cdot \lg V_{i,j} + \beta(f_{i,j}) \quad (5)$$

Thus, it is enough to know the dependence of frequency from time (1) and also the dependence of height of type II burst source from frequency (4) to evaluate the velocity of shock wave in any given time moment (6).

$$U_{i,j} = (R_{i+1,j} - R_{i,j}) / (t_{i+1,j} - t_{i,j}) \quad (6)$$

Calculated values of velocity $U_{i,j}$ we have compare with the values of coronal shock wave velocities U_{ESS} which is publish on NGDC site in 25-180 MHz range (<http://www.ngdc.noaa.gov/stp/space-weather/solar-data/solar-features/solar-radio/radio-bursts/tables/spectral-sgd/>).

Fig. 4a) show disperse diagram of this values. Correlation coefficient r between this values was found low: $r(U_{i,j}, V_{i,j}) \approx 0.56$. It is testified that Newkirk model (Newkirk, 1961) is not allow to evaluate quite exactly the velocity of coronal shock waves. That is why we had performed the research of relationship directly between U_{ESS} and type II radio burst parameters. As the parameters which is characterizes the velocity of shock wave we used such parameters as the velocity of frequency drift $V_{i,1}$ and $V_{i,2}$ on first and second harmonics, relative distance b_i between harmonics on the dynamic spectra in the given time moment (Tsap and Isaeva, 2013) and time delay Δt_i (7) of intensity maximum of type II burst on second harmonic relatively first one on the given frequency $f_{i,j}$ (fig.1).

$$\Delta t_i = t_{i+\Delta t,2} - t_{i,1} \quad (7)$$

Comparative analysis showed that the strong enough relationship between time delay Δt_i and U_{ESS} exist. Correlation coefficient between Δt_i and U_{ESS} was equal ≈ 0.65 , that is somewhat high then between $U_{i,j}$ and U_{ESS} (fig. 4b). In the same time, relationship of U_{ESS} with drift velocities $V_{i,1}$ and $V_{i,2}$ was found approximately the same as the relationship between $U_{i,1}$ and U_{ESS} that is correlation coefficient is equal ≈ 0.56 .

3. Conclusions

Evaluation of coronal shock waves velocity that use Newkirk model and directly from type II radio burst parameters has reveal some interesting peculiarities. So, using Newkirk model it was show that clear dependence between frequency and height of type II burst radio source exist. Also dependence between drift velocity and shock wave velocity exist. Presence of such dependencies indicates that it is possible to evaluate coronal shock waves velocity directly from type II radio burst parameters. Confirmation of this is the strong enough dependence between shock waves velocity which is published on NGDC site and time delay of type II burst maximum on the second harmonics relatively first one on the given frequency $f_{i,j}$.

References

- Cairns I.H., Knock S.A., Robinson P.A., Kuncic Z.: 2003, *Space Sci. Rev.*, **107**, 27.
 Classen H.T., Aurass H.: 2002, *Astro. And Astrophys.*, **384**, 1098.
 Chertok I.M., Grechnev V.V. and Meshalkina N.S.: 2009, *Astron. Zh.*, **86**, 1133.
 Gopalswamy N., Kaiser M.L., Lepping R.P., Kahler S.W., Ogilvie K. et. al.: 1998, *J. Geophys. Res.*, **103**, 307.
 Mel'nikov V.F., Podstrigach T.S., Daibog E.I. and Stolpovskii V.G.: 1991, *Kosm. Issled.*, **29**, 95.
 Newkirk G.: 1961, *Astrophys. J.*, **133**, 983.
 Pudovkin M.M., Raspopov O.M.: 1992, *Geomagnetism and Aeronomy*, **32/5**, 1.
 Rivin Yu.R.: 1985, *Geomagnetism and Aeronomy*, **25/6**, 990.
 Tsap Yu.T. and Isaeva E.A.: 2013, *Cosmic Reseach*, **51/2**, 108.

CONNECTION BETWEEN THE CME VELOCITIES AND DECAMETER RADIO BURSTS PARAMETERS FROM URAN-4 OBSERVATIONS

Galanin V.V.¹, Isaeva E.A.^{1,2}, Kravetz R.O.¹

¹ Observatory URAN-4 of the Institute of Radio Astronomy of the National Academy of Sciences of Ukraine, gvv@breezein.net, krro@ukr.net

² Research Institute “Astronomy Observatory of Odessa I.I. Mechnikov National University” isaeva-ln@mail.ru

ABSTRACT. The paper reports the results of the research of connection between the coronal mass ejections (CME) with the IV type continual decameter bursts parameters. As the parameters characterizing the CME velocity, we used the integrated flux of the radio bursts and background intensity on 20 and 25 MHz frequencies. The analysis demonstrated that the connection between the CME velocity and IV type bursts increases, if we take into account the intensity of the radio bursts and background on two polarizations at a given frequency. In this case, the correlation coefficient is ≈ 0.75 .

Keywords: coronal mass ejection, radio burst.

1. Introduction

The most simple and accessible way for diagnostics of the coronal mass ejection (CME) parameters is using the parameters of the radio bursts. It is well known that the vast majority of metric and hectometric bursts of IV and II type are connected with the CME (Tsap et al., 2013). This paper demonstrates that there is a sufficiently strong connection between the CME velocity and integral flux of the microwave bursts, however the connection between CME velocity and parameters of metric and decametric bursts of II type proved to be low.

2. Basic data and processing results

The measurements were carried out by decametric radio telescope Uran-4 (PT) (Galanin et al., 1989). Radio telescope URAN-4 is a part of the very long base radio interferometer system (VLBI), which is located on the territory of Ukraine from west to east. The operating range of the instrument is 10-30 MHz.

Radio telescope antenna is represents the electrically controlled phased array with linear size 232.5 x 22.5 m. and consist of 128 crossed dipoles. It enables to select two polarization components of the signal. Width of the instrument antenna direction diagram at the level of half-power on 25 MHz frequency is 2.7 X 22 degrees. In VLBI mode of the interferometer, the resolution of 2 seconds is provided.

After the modernization of equipment in 2011, the observations were initiated on 20 and 25 MHz

frequencies. For our measurements, we used the method of “translucence” of the outer regions of the corona by radiation of discrete radio sources. This method allowed us to obtain information about the environment of radio waves propagation and to measure the intensity of the solar radio radiation.

Figure 1 demonstrates an example of recording on two polarizations on 20 and 25 MHz frequencies of the continual burst fixed by RT Uran-4 on June 27.2012. Fig. 2 provides a record of the same burst fixed by SVTO observatory.

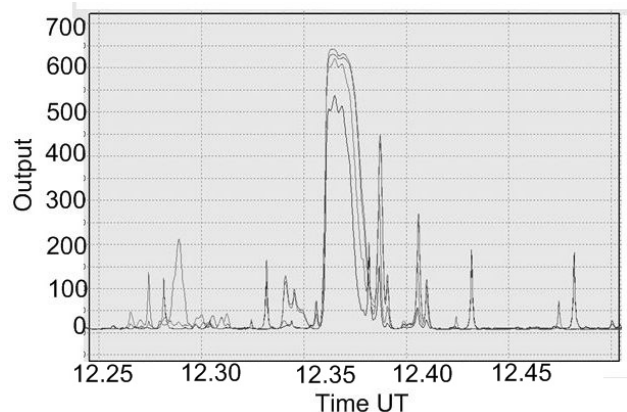


Figure 1: Record of the continual solar burst recorded on 27.06.2012 by radio telescope URAN-4 on two polarizations on 20 and 25 MHz frequencies.

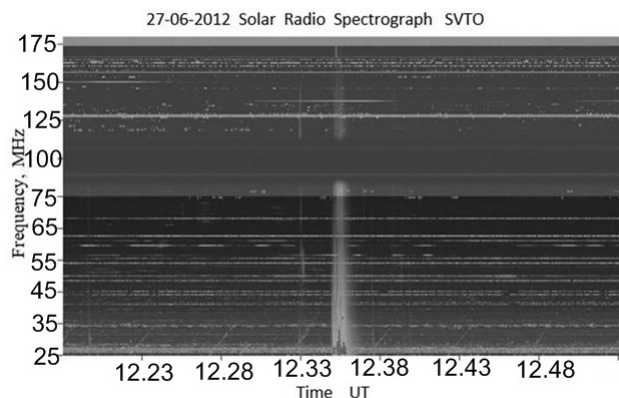
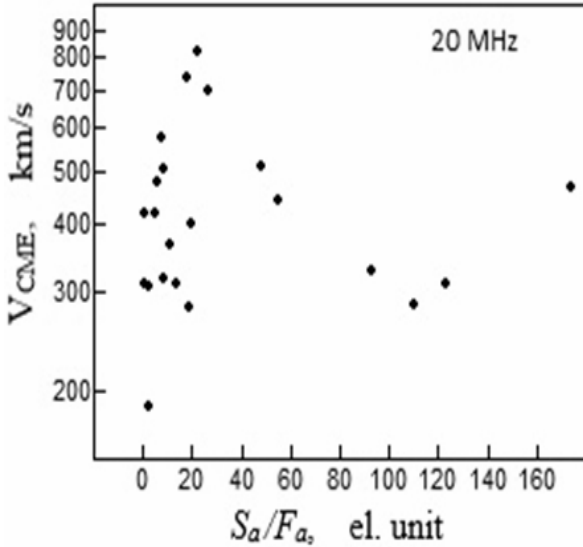
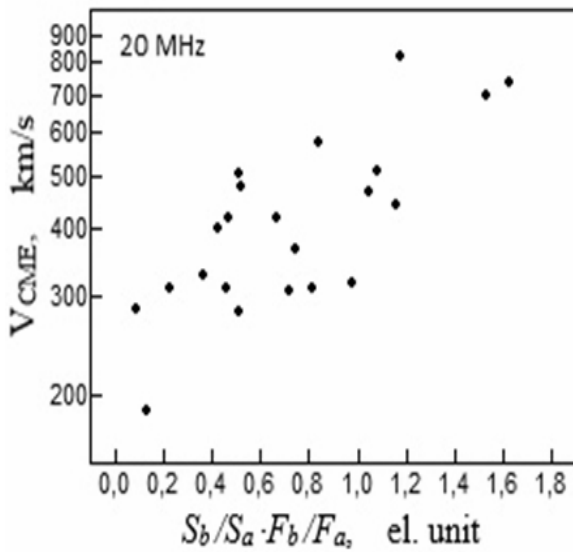


Figure 2: Observation on spectrograph of SVTO observatory of the continual burst connected with CME, 27.06.2012.

In this paper we restrict ourselves to the research of the connection between CME velocity V_{CME} and parameters of the IV type continual decametric bursts obtained from measurements by the radio telescope URAN-4. We selected the CME velocity from catalog SOHO / LASCO. We analyzed the connection between the CME velocity with such parameters as the duration, maximum and integral value of the burst flux for two polarizations, as well as the value of background.



a)



b)

Figure 3: a) Correlation coefficient r between V_{CME} and S_a/F_a , $r \sim 0.06$; b) Correlation coefficient r between V_{CME} and $S_b/S_a * F_b/F_a$, $r \sim 0.75$.

Comparative analysis demonstrated that the connection between the CME ejection and each listed parameter proved to be low, which is quite consistent with previous results (Tsap et al., 2013). Fig. 3 a) shows an example of the research of CME velocity and integral flux of burst S_a normalized to the value of background F_a . In this case, the connection between V_{CME} and S_a/F_a is absent. However, the connection between the CME velocity and the parameters of the radio bursts significantly increases if values of the burst flux and background on two polarizations are used simultaneously (1), see. Fig. 3b).

$$\text{Lg } V_{CME} = -0.0002 \cdot S_a - 0.02220 \cdot F_a + 0.0002 \cdot S_b + 0.0539 \cdot F_b \sim S_b/S_a * F_b/F_a, \quad (1)$$

where S_a , F_a and S_b , F_b – integral flux of the burst and value of the background on two polarizations a and b , respectively.

From correlation (1) it is seen how the CME velocity is connected with the parameters S_a , F_a and S_b , F_b . Specifically, the ratio between the flux of burst and ratio of the background on two polarizations proved to be of fundamental importance. Unfortunately, such selection includes only 22 events, which didn't enable to get a true dependence of the CME velocity on radio burst parameters due to the small amount of data.

3. Conclusions

1. The results of implemented researches indicate that the CME velocity is connected to some extent with the polarization characteristics of IV type decametric radio bursts.

2. Further research in this direction is necessary.

References

- Tsap Yu.T. et al.: 2013, *J.CrAO*, **109**, 4, 121.
Galanin V.V. et al.: 1989, *Cinematics and Physics of Celestial Bodies*, **5**, 5, 87-90.

THE REACTION OF PHOSPHORUS-CONTAINING INTRACELLULAR INCLUSIONS TO SPACE WEATHER CHANGES

Gromozova E.N., Kachur T.L., Voychuk S.I., Kharchuk M.S.

Danylo Zabolotny Institute of Microbiology and Virology of NAS of Ukraine, Kiev
gren.elen@gmail.com

ABSTRACT. It is known that the bio-astronomical effect of Chizhevsky-Velhover is based on the cytochemical metachromatic reaction of polyphosphate-containing volutin granules of microorganisms. As a result of long-term monitoring (2001-2015 years) of this of cytochemical index in yeasts *Saccharomyces cerevisiae*, it was shown that metachromatic staining of the granules possessed rhythmicity and connection with space weather. Under laboratory conditions the change of metachromasy was achieved by applying different stress factors: anaerobiosis, low temperature, acidity. Simulation of metachromatic staining in vitro by using solutions of inorganic polyphosphate with other compounds showed that this reaction was possible for the low concentrations of these polymers. The effect of the low concentrations was more expressed with increasing chain length of polyphosphate. The inhibition of the metachromasy in solution with added protein and calcium chloride indicated that this of reaction involved the presence of the protonated sites in the polymers. It is assumed that metachromatic staining of volutin granules *in vivo* may depend on other conditions including conformational restructuring of a polymer or sol-gel phase transitions. Thus, the question whether the metachromatic reaction of intracellular polyphosphate granules to the space weather changes is driven by a response to associated stress or despite the apparent similarity of the effects they are of a different nature remains unclear.

Key words: space weather, polyphosphate, volutin granules, bio-astronomical effect, metachromatic reaction

1. Introduction

To date, there is a significant amount of data about the influence of space weather on the biological processes. The connection between the behavior of microorganism and cosmophysical factors was reflect in bio-astronomical effect of Chizhevsky-Velhover [1]. reflected in bio-astronomical effect of Chizhevsky-Velhover [1]. This effect is based on the metachromatic reaction of volutin granules stained with basic dyes such as (methylene and toluidine blue) [2]. Volutin granules are intracellular structures which widely spread among microorganisms both prokaryote and eukaryote. Inorganic polyphosphates are the main component of granules. These polymers are known to perform different functions depending on localization in the cell [3, 4]. It is assumed that one of these functions can be a reception of the cosmophysical signals [5]. Inorganic polyphosphates, so-

called "fossil molecules", are the most ancient molecules arisen in inanimate nature and accompanied biological objects at all stages of evolution [3]. The formation of evolutionary and adaptive scenario of ancient biosystems functioning was, first of all, under the action of helio- and geophysical factors. So, we can assume that variation of these conditions took part in the formation of rhythmic biological processes with the participation of polyphosphates. Thus, investigation of the inorganic polyphosphate features of volutin granules manifested using metachromatic staining may bring us closer to understanding of the mechanisms of the biotopic cosmic weather action.

The objective of the present work was to research the effects of the stress factors on the metachromatic reaction of volutin granules and its simulation in vitro.

2. Methods

In the experiments, the yeasts *Saccharomyces cerevisiae* Y-517 from Ukrainian Collection of Microorganisms of Danylo Zabolotny Institute of Microbiology and Virology of NAS of Ukraine were used. Cultures were grown on the wort agar for 24 hours at temperature 28°C. Everyday in set time (12:00 Kiev time), cells were stained with methylene blue according to Loeffler for determining the presence of the metachromatic reaction [5]. Simultaneously, they were subcultured on the fresh nutrient medium. Assessment of the metachromatic reaction was performed by stained smears in light field using light microscopy (microscope "PrimaStar", Zeiss). Three-point system assessment was used, where "1" – absence of metachromasy (blue color of the granules), "2" and "3" – different degree of expressing metachromasy (violet and violet-red colour of the granules, respectively). Stress conditions were low temperature (-4°C), anaerobiosis and acidity (150 mM acetic acid). We prepared solutions of inorganic polyphosphates with chain length 18 and 200 residues of phosphoric acid at a final concentration of 0.025 to 5 mg/ml. pH was adjusted to neutral values by titration of 1 N solution of NaOH. Concentration of methylene blue in test samples was 0.005 mg/ml. Glucose (0.01, 0.1 and 1%), calcium chloride (1, 15 and 30 mM) and bovine serum albumin (BSA; 0.1, 0.5 and 1 mg/ml) were added to polyphosphate solutions. The uptake spectra of methylene blue in the samples were evaluated using the spectrophotometer DU-8B (Beckman, USA) with water as a blank sample. Data was treated statistically by program of Statistica 6.0 (StatSoft, Inc. 2002).

3. Results and discussion

As a result of long-term monitoring which was conducted from 2001 to 2015 years it was found that the metachromatic reaction of volutin granules of *S. cerevisiae* yeast had rhythmicity and connection with space weather [6]. Rhythm of metachromasy almost completely coincided with the known space periods. This coincidence could mean conjugation of rhythms or synchronization of biological rhythms with cosmophysical variations but it has not a causal relationship [7]. Except the presence of rhythmicity statistically reliable correlation of this reaction with whole range of cosmophysical factors at the same period [6] could be the evidence of connection of metachromasy with space weather.

In our experimental studies under laboratory conditions the metachromatic reaction of volutin granules of the yeast cells was observed when using different stress factors: low temperature, anaerobiosis and acidity. Full colour change of volutin granules to violet-red ("3") was observed at low temperature and acidity (see Fig. A and B), whereas at anaerobiosis it was marked 90% of cases with such colouring (see Fig. C). Thus, the changes of the phosphoric metabolism of the cell might probably take place as a result of the stress impact, and were reflected in the appearance of metachromatic staining of volutin granules.

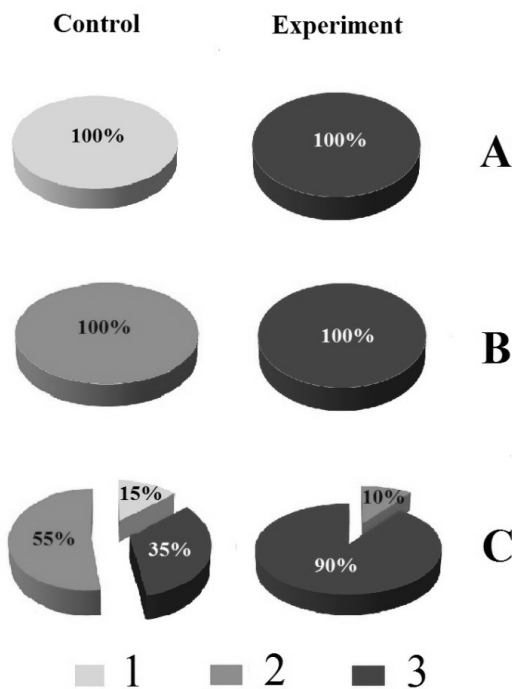


Figure 1: Impact of stress factors on the metachromatic reaction: A – low temperature (-4°C); B – acidity (0,15 M); C – anaerobiosis; 1 – absence of metachromasy (blue colour of granules); 2 – weakly expressed metachromasy (violet colour of granules); 3 – well expressed metachromasy (violet-red colour of granules).

The simulation of the metachromatic reaction *in vitro* with polyphosphate solutions in combination with other compounds, showed that protein and calcium chloride inhibited aggregation of methylene blue on a polymer. Glucose, in turn, did not interfere with the appearance of the metachromatic staining. Thus, inhibition of the

metachromatic staining by, adding protein and calcium chloride to the solution indicated that this reaction took place in the presence of the protonated sites in the polymers. It was shown that (Fig. 2) the metachromatic shift in the spectrum of uptake of the dye was caused by a decrease of polyphosphate concentration (of 0.1 mg/ml to 0.025 mg/ml). The effect of the low concentrations was more expressed with increasing chain length of polyphosphate (Fig. 2 B).

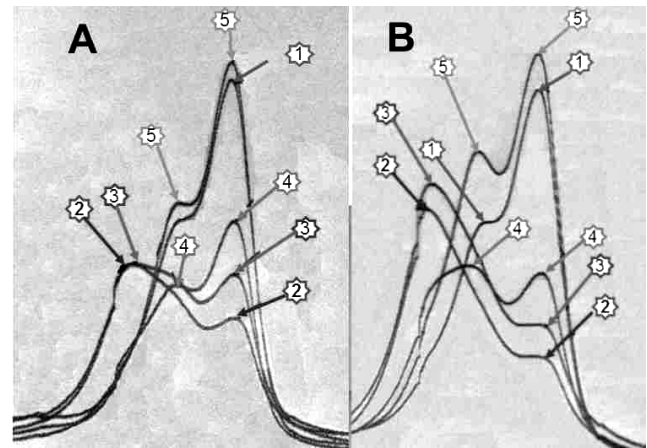


Figure 2: The uptake spectra of the methylene blue solution (0.005 mg/ml) and its complexes with polyphosphates. Polyphosphates chain lengths: 18 (A) and 200 (B) of phosphoric residues at concentrations: (1) 0 (control); (2) 0.025; (3) 0.1; (4) 0.4; (5) 2.5 (mg/ml).

The cause of the metachromatic staining is known to be aggregation of the dye on the polyanions serving as a matrix [8]. Polyphosphates are one of such polyanionic compounds. A metachromasy does not occur if polyphosphates have chain length less than 10 residues of phosphoric acid [9]. As these polymers are known to be actively involved in the antistress reactions of microorganisms [10] the metachromasy of volutin granules can be assumedly caused by stress impact of the cosmophysical events. However, the reaction to the stress factors usually is accompanied by the polyphosphate accumulation [10], which should not cause metachromatic staining of the polyphosphate-containing structures. Thus, the processes causing metachromasy *in vivo* differed from those which took place *in vitro*. It is assumed that this reaction might be also caused by the physico-chemical factors conformational changes of a chain, where the distance between the reaction groups is 5 and less Å [11], or sol-gel phase transitions.

Thus, the question whether the metachromatic reaction of intracellular polyphosphate granules to the space weather changes is driven by a response to associated stress or despite the apparent similarity of the effects they are of a different nature remains unclear.

References

1. A quick reference guide to space biology and medicine. Moscow: Medicine, 1967 (in russian).
2. Serafim L.S., Lemos P.C., Levantesi C., Tandoi V., Santos H., Reis M.A.M.: 2002, *Journal of Microbiological Methods*, 51, 1-18.

3. Brown M.R.W., Kornberg A.: 2004, *PNAS*, **101**, №46, 16085.
4. Lichko L., Kulakovskaya T., Pestov N., Kulaev I.: 2006, *Biosci. Rep.*, **26**, 45.
5. Practicum for microbiology: tutorial guide /ed. Egorov N.S., Moscow: Moscow University Press, 1976, 307 p. (in russian).
6. Gromozova E.N., Grigoriev P.E., Kachur T.L., Voychuk S.I.: 2010, *Biophysical processes and Biosphere*, **9**, No 2, 67 (in russian).
7. Vladimirsky B.M. Impact of solar activity on biosphere-noosphere (Heliobiology from Chizhevsky A.L. to the present days) /B.M.Vladimirsky, N.A.Temurjyants, M: Publishing house, 2000, 374 p. (in russian).
8. Shirai M., Nagatsuka T., Tanaka M.: 1977, *Micromol. Chem.*, **178**, 37.
9. Lorenz B., Schröder H.C.: 1999, *Inorganic Polyphosphates. Biochemistry, Biology, Biotechnology*, Springer, 217 (in russian).
10. Ault-Riche D., Fraley C.D., Tzeng C.-M., Kornberg A.: 1998, *Journal of Bacteriology*, **180**, No7, 1841.
11. Pierce E. Histochemistry theoretical and applied /ed. E. Pearce, Moscow: Univ. foreign. literature, 1962, 962 p. (in russian).

LONGTERM CHANGES OF SOLAR ACTIVITY ASYMMETRY

U.M.Leiko

Astronomical Observatory of Taras Shevchenko National University of Kyiv,
Observatorna 3, Kyiv, 04053, Ukraine, leikoum@ukr.net

ABSTRACT. We report results of analysis of the north-south asymmetry of solar activity, solar magnetic fields. The analysis is based on the sunspot data, 1875–2015 (<http://solarscience.msfc.nasa.gov/greenwch.shtml>), large-scale solar magnetic field (solar mean magnetic field, SMMF) and solar polar magnetic field time series, 1975–2015 (<http://wso.stanford.edu>). To study long-term changes of solar activity asymmetry we applied analysis of cumulative sum. Cumulative sum averages short-periodic changes and identifies long-term periodicity.

Minimum of cumulative sum of sunspot area mean monthly values time series occurs in ~1910, maximum – in ~1980. Perhaps this is branch growth of long-term (~140-years) cycle of solar activity asymmetry. Cumulative sums of polar magnetic field of different pole have ~22-years periodicity. Change of cumulative sum of SMMF time series has different character. But long-run trend with intervals of positive and (or) negative polarity of ~22 years is observed.

Keywords: Sun: Solar activity – Sunspots area: Solar activity – Magnetic fields: Data analysis – Methods: Cumulative sum.

1. Introduction

Solar activity (SA) is a variety of phenomena and processes associated with the formation and the decay of the magnetic field in the solar atmosphere. The most studied type of SA is variations of sunspots number. Magnetic fields on the Sun were first measured in sunspots by Hale (1908). It was established that the spots of the present cycle are opposite in polarity to those of the last cycle (“the law of polarity Hale”). It was found that the Sun’s polar fields changed polarity as well. Thus, the physical cycle is 22-year cycle (Babcock, 1961).

A distinctive feature of SA is asymmetry regarding the hemispheres. It is known that the asymmetry is not random in nature, and occurs at long time intervals. To investigate the feature of SA asymmetry different methods were used: a variety of statistical tools (Carbonell et al., 1993) a wavelet analysis (Donner & Thiel, 2007), cumulative sum (Mordvinov, 2006; Leiko, 2013) et al.

The present work is continuation of investigation of long-term changes of asymmetry using different SA time series.

2. Data and Method

We applied analysis of cumulative sum (CS) of such indicators of solar activity: sunspots area data, 1875–2015

(<http://solarscience.msfc.nasa.gov/greenwch.shtml>), solar mean magnetic field (SMMF) and solar polar magnetic field time series, 1975–2015 (<http://wso.stanford.edu>).

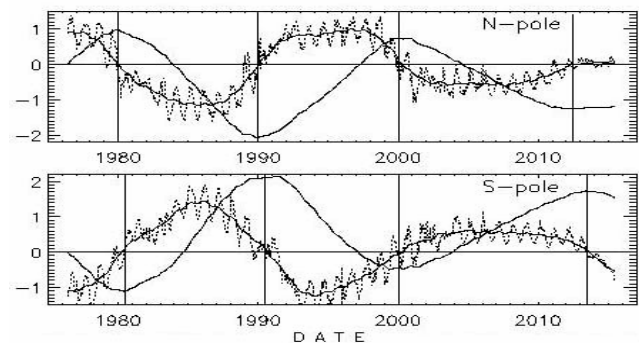


Figure 1: The solar polar field strength, in gauss (G) (line by dot, smoothed data – thin solid line) and its cumulative sums (thick solid line). Times of polar field reversals are shown by solid vertical lines.

CS adds the current value of the analyzed series with all previous, averages short-periodic changes and identifies long-term periodicity (Mordvinov, 2006; Leiko, 2013). If the CS increases, then positive values dominate, if the CS decreases, then negative values dominate. Fig. 2 presents the changes of solar polar field at N- and S-pole. Both lines of CS have wavy shape. One can see that times of reversal of magnetic field agree with extrema of CS. The distance between the two maximums or two minimums is ~22 years. So, the period of CS of polar field is solar magnetic cycle.

3. Results

The nature of the asymmetry is often characterized in different ways that can lead to different conclusions. Simply quantifying the asymmetry itself is problematic. Absolute asymmetry $NSA = A_N - A_S$ produces strong signals around the times of maxima. Relative asymmetry $NSAr = (A_N - A_S) / (A_N + A_S)$ produces strong signals in minima. And variations of these indexes are different (Leiko, 2011).

The CSs of absolute and relative asymmetry are shown on fig. 2. Both CS have wavy shape, change more or less synchronously and have one minimum and one maximum. This curve is a part of quasi-periodic process. Interval from minimum to maximum (the branch growth) is half of full period. During the interval 1875–1915 CS wanes (southern hemisphere dominates), during 1915–1980 CS increases (northern hemisphere dominates), after 1980 CS again wanes (southern hemisphere dominates). Both extremums

have two different in intensity humps, the second hump more intense in both cases. Solid thick vertical lines showing moments for these humps. The distance between first and second pairs of humps in the minimum and maximum is $\sim 65\text{--}70$ years. It can be assumed that the length of a full cycle should be $\sim 130\text{--}140$ years.

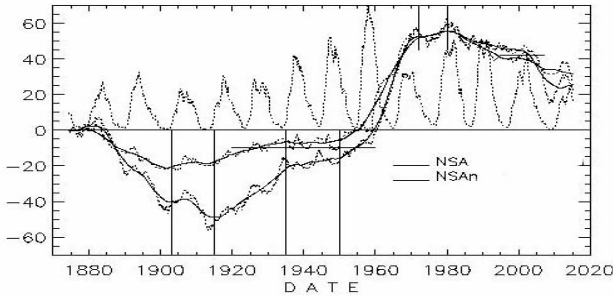


Figure 2: The monthly sunspot's area scaled by 1/50 and smoothed cumulative sums of absolute (NSA) and relative (NSAn) asymmetry.

A feature of curves CS is the availability of plateau, time intervals, when the CS almost unchanged. Plateau marked by solid thin horizontal lines, thin solid vertical lines – moments of their beginning and end. This time intervals are 1935–1950 (at branch growth) and 1995–2003 (on branch droop). In these short intervals was not dominance regarding hemispheres by index of total spots area.

Fig. 3 shows the change of SMMF values, its sector structure (upper and middle panels). On the bottom panel lines by dots are their CS, thick solid line – smoothed values of the CS of SMMF, dashed thick line – smoothed values of CS of sector structure. Oblique straight lines are their linear trends.

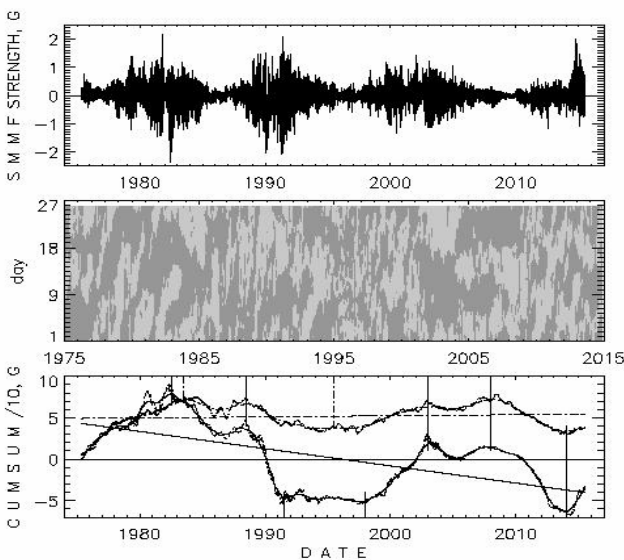


Figure 3: Daily Solar Mean Magnetic Field, its sector structure and their cumulative sums.

Although the CS curves have a different course, however, is visible in the course of synchronicity. Both curves have two maximums and two minimums, both maximum have two humps, the first minimum is the plateau, the second minimum until visible one hump. However, trends of these curves are completely different. The CS of the sector structure has almost no trend, while the cumulative sum of the SMMF has a significant trend. This means that

the sector structure having ~ 22 years cycle in the predominance of the square of fields of positive and negative polarities has no long cycle. A significant negative trend of CS curve of SMMF indicates that the index field value has a long cycle of changes and available monitoring interval is on decrease branch of this cycle.

We compared the curves course of the CS of daily values of SMMF and the CS of daily asymmetry of value total area of sunspots on interval 1975–2015 timeframe. Despite the different nature of these curves, their changing is synchronously to 2005.5. After this time the change occurs in antiphase. In the fig. 4 this point shows a solid vertical line across the panel. Both curves have a plateau at about the same time. One can see that the trend of these curves are almost identical. This means that the above suggestion (the asymmetry index of field value has long cycle of change and monitoring interval is on a branch of the recession this cycle) is true.

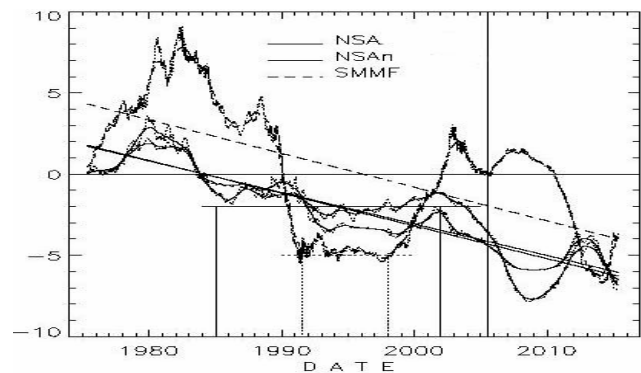


Figure 4: Cumulative sums of daily values of SMMF, sunspot's area and their trends.

Parallelism of trendlines suggests that this cycle may be the same length as the cycle asymmetry of spots area. The area of spots is proportional to the magnitude of their magnetic fields. Therefore asymmetry of magnetic fields values of both large- and small-scale have $\sim 130\text{--}140\text{-year}$ cyclicity.

3. Conclusions

The long-term cycle (~ 140 years) of north-south asymmetry of solar activity was selected on the time series of the sunspot area.

Probably the photospheric large-scale magnetic fields have this long-term cycle also. But sector structure of large scale magnetic fields has not this long-term cycle.

Variations of the asymmetry of large-scale and small-scale magnetic fields (area of sunspots) are in sync until 2005.5, after this time the dynamics asymmetry passes in antiphase.

Acknowledgements. The author is thankful to all for possibility of using the data of solar activity by Internet.

References

- Babcock, H.W.: 1961, *Astrophys. J.*, **133**, 572.
- Carbonell M. et al.: 2007, *Astron. Astrophys.*, **476**, 951.
- Donner R. Thiel M.: 2007, *Astron. Astrophys.*, **475**, L33.
- Hale, G.E.: 1908, *Astrophys. J.*, **28**, 315.
- Leiko U.M.: 2011, *Visn. Kiev. Univ. Astronomy*, **47**, 23.
- Leiko U.M.: 2013, *Izv. Crim. Astrofiz. Obs.*, **109**, 67.
- Mordvinov A.V.: 2006, *Astron. Zh.*, **83**, 1042.

PROBLEM OF MISTAKES IN DATABASES, PROCESSING AND INTERPRETATION OF OBSERVATIONS OF THE SUN. I.

N. I. Lozitska

Astronomical Observatory of Taras Shevchenko National University of Kyiv
Observatorna 3, Kyiv, 04053, Ukraine, nloz@observ.univ.kiev.ua

ABSTRACT. In databases of observations unnoticed mistakes and misprints could occur at any stage of observation, preparation and processing of databases. The current detection of errors is complicated by the fact that the works of observer, databases compiler and researcher were divided. Data acquisition from a spacecraft requires the greater amount of researchers than for ground-based observations. As a result, the probability of errors is increasing. Keeping track of the errors on each stage is very difficult, so we use of cross-comparison of data from different sources. We revealed some misprints in the typographic and digital results of sunspot group area measurements.

Keywords: Sun: – Areas of sunspot groups, Observations, Identification of errors, correction of datasets

1. Introduction

Systematic and isolated errors can be found in various datasets. The difference of sunspot group areas from different observatories had been considered as systematic errors in publication by Gnevysheva (1968), Baranyi (1999, 2013). In present paper we identify and correct some isolated errors in databases of sunspot group areas.

2. Data of Observations

Data of sunspot groups area is available at the sites of Solar-Terrestrial Physics Division (STP) NOAA <http://www.ngdc.noaa.gov/stp/space-weather/solar-data/> (Solar Observing Optical Network USAF), Solar Physics Group (SPG) of NASA's Marshall Space Flight Center <http://solarscience.msfc.nasa.gov/>, Debrecen Observatory (Györi, 2011) <http://fenyi.solarobs.unideb.hu/>, Pulkovo Interactive database of solar activity (Miletsky, 2005) <http://www.gao.spb.ru/database/csa/>.

3. The Cross-comparison Method and Results

We made the comparison of sunspot group areas from databases of Pulkovo, Greenwich, and Debrecen Observatories. Our interest was focused on revealing especially large random errors. The greatest isolated errors were detected in Pulkovo's datasets.

Table 1 presents such comparison for whole group area and for leading spot of group SD 1939264 with same group RGO 13394 (transition of 1939, August 26 – September 7).

Table 2 contains the comparison for whole group area and for leading spot of group SD 1939-274 with same

group RGO 13405 (transition of 1939, September 4–16). From these tables we can see the significant excess of area of sunspot groups, up to 1500 millionth parts of hemisphere (m.p.h.) Even greater differences were found for the leading spots in some days. In first case, we can suppose the transfer printing slips from Catalogues of solar activity to electronic dataset. In second one, the probable explanation is contribution of heterogeneous data from different observatories in average value presented in SD catalogue without necessary alignment to same measuring system. Observations in the 1930th – 1940th were just being started. Likely, two parameters – provisional areas in millionth parts of a disk and corrected areas in millionth parts of a hemisphere – were mixed.

Table 3 demonstrates analogous data for the largest groups SD 194618 and SD 1947057 which were observed in 1946, January 29 – February 12, and in 1947, March 4 – 17, respectively.

Table 4 shows how significant errors in measurement result records of areas in SOON USAF observatories lead to overestimation of average daily group areas, calculated by SPG, using the primary data of SOON observatories. Our calculations of daily values USAF_{corr} which were made after removal of errors coincide well with DPD observatory values. These essential errors of measurements of USAF observatories we have identified as the values that go beyond 3 standard deviations. Some of them were misspellings during numbers input when the number of adjacent columns are shifted to the right so that added to the fourth rank in the value of the area. The rest seems to have been the case of records in the database in millionth parts of the disc, which are sometimes found among the correct values of the area, measured in millionth parts of the hemisphere. In this case, situation is analogous to Pulkovo catalogue. Measurements carried out on different observatories had contained the provisional data among corrected ones. The Solar Physics Group had used this data for calculation of daily averaged data without eliminating errors of each measurement. As a result, many areas of daily values of sunspot groups are significantly overestimated.

Acknowledgements. We express our gratitude to all the observers, whose measurements are used in the work.

References

- Gnevysheva R.N.: 1968, *Sov. Phys. Astron.*, **11**, 976.
- Baranyi T. et al.: 2013, *MNRAS*, **434**(2), 1713.
- Baranyi T. et al.: 1999, in Proc. ESA **SP-448**, 569.
- Györi, L. et al.: 2011, in Proc. IAU, **S273**, 2011, 403.
- Miletsky, E. et al.: 2005, in Proc. of Pulkovo conf., **9**, 47.

Table 1:

Data	S_{gr} SD, mph	S_{gr} , RGO, mph	S_{gr} SD - S_{gr} RGO, mph	S_{lider} SD, mph	S_{liter} RGO, mph	S_{lider}/S_{gr} SD,	S_{lider}/S_{gr} SD,
1939 09 03	2376	2295	81	1476	1125	0,62	0,49
1939 09 04	3666	2513	1153	1730	1472	0,47	0,59
1939 09 05	3272	2785	487	1362	1053	0,42	0,38
1939 09 06	6174	3054	3120	6174	1438	1	0,47

Table 2:

Data	S_{gr} SD, mph	S_{gr} , RGO, mph	S_{gr} SD - S_{gr} RGO, mph	S_{lider} SD, mph	S_{liter} RGO, mph	S_{lider}/S_{gr} SD,	S_{lider}/S_{gr} SD,
1939 09 08	2561	2282	279	425	404	0,17	0,18
1939 09 09	3045	2561	484	3045	431	1,00	0,17
1939 09 10	3810	2623	1187	3674	497	0,96	0,19
1939 09 11	3876	2927	949	3653	499	0,94	0,17
1939 09 12	4226	2723	1503	4114	513	0,97	0,19
1939 09 13	4442	2993	1449	2543	557	0,57	0,19

Table 3:

Data	S_{gr} SD, mph	S_{gr} RGO, mph	S_{gr} SD - S_{gr} RGO, mph	Data	S_{gr} SD, mph	S_{gr} RGO, mph	S_{gr} SD - S_{gr} RGO, mph
1946 02 02	6402	4940	1462	1947 03 08	5630	3615	2015
1946 02 03	7406	5080	2326	1947 03 09	6826	3886	2940
1946 02 04	5633	4952	681	1947 03 10	7500	4179	3321
1946 02 05	5692	4533	1159	1947 03 11	5091	4547	544
1946 02 06	6655	4799	1856	1947 03 12	6744	4554	2190
1946 02 07	5732	5202	530	1947 03 13	5208	4205	1003
1946 02 08	5763	4898	865	1947 03 14	5199	4052	1147
1946 02 09	5716	4596	1120	1947 03 15	6292	3989	2303

Table 4:

Data	NOAA №	S_{gr} , mph			Data	NOAA №	S_{gr} , mph		
		SPG	USAF _{corr}	DPD			SPG	USAF _{corr}	DPD
1982 09 13	3804	2240	228	299	1989 09 01	5670	250	206	241
1983 05 14	4173	2110	1782	1754	1989 09 07	5670	220	56	40
1983 12 05	4373	1010	28	8	1990 02 14	5927	800	504	427
1984 02 19	4421	1560	1464	1310	1990 02 15	5927	1160	564	446
1984 04 27	4474	2500	3174	3215	1990 02 16	5927	850	546	523
1988 07 18	5076	230	42	38	1990 02 22	5954	670	14	13
1988 10 10	5175	2540	1022	1043	1990 06 28	6129	170	70	59
1988 12 05	5261	290	249	193	1990 08 10	6204	680	42	36
1989 02 05	5350	1650	24	14	1990 08 18	6197	180	84	104
1989 02 09	5355	1380	252	383	1990 08 18	6224	80	50	3
1989 02 27	5378	1460	88	104	1990 08 19	6206	810	32	37
1989 03 07	5383	350	178	293	1990 08 25	6212	670	308	322
1989 06 30	5555	450	395	445	1990 09 27	6283	990	703	605
1989 07 02	5563	570	378	390	1990 10 18	6314	590	478	470
1989 06 29	5569	960	493	506	1990 11 06	6353	1060	428	20
1989 07 02	5569	520	322	427	1990 11 10	6361	870	322	349
1989 07 02	5572	740	145	186	1990 12 27	6427	290	238	228
1989 07 27	5612	660	248	234	1991 03 28	6560	120	67	89
1989 08 09	5638	110	48	58	2011 06 17	11234	100	70	200
1989 08 14	5644	210	59	57	2011 06 17	11236	260	424	522
1989 08 31	5668	270	91	146	2011 06 24	11236	180	109	267
1989 08 29	5669	2630	1403	663					

SIMULTANEOUS MAGNETIC FIELD MEASUREMENTS IN SUNSPOTS USING SPECTRAL LINES WITH DIFFERENT LANDE FACTORS

S.N.Osipov ¹, V.G.Loizitsky ²

¹Main Astronomical Observatory of National Academy of Sciences,
Zabolotnoho 27, Kiev 03680, Ukraine, osipov@mao.kiev.ua

²Astronomical Observatory of Taras Shevchenko National University of Kyiv,
Observatorna 3, Kyiv 01053, Ukraine, loizitsky@observ.univ.kiev.ua

ABSTRACT. We present magnetic field measurements in several sunspots observed in June-July 2015 on Horizontal Solar Telescope ATsU-5 of Main Astronomical Observatory of National Academy of Sciences of Ukraine. The Zeeman splittings were measured using $I \pm V$ profiles of about ten spectral lines of Mn I, Fe I and Ni I including three lines with negative Lande factors, namely Fe I 5434.527 Å, Fe I 6094.419 Å and Fe I 4995.411 Å ($g_{\text{eff}} = -0.014, -0.218, \text{ and } -0.25$, respectively). Our main conclusions are the following:

a) as rule, spectral lines with largest Lande factors give the strongest measured magnetic fields B_{obs} in sunspot umbra that can be interpreted as a result of blending the Zeeman π - and σ -components in case of non-longitudinal magnetic field.

b) in some places of sunspots, B_{obs} differs also for lines with close Lande factors, e.g. by Fe I 5432.950 and Ni I 5435.871 ($g_{\text{eff}} = 0.67$ and 0.5 , respectively).

c) lines Fe I 6094.419 Å and Fe I 4995.411 Å with $g_{\text{eff}} < 0$ have in sunspots signs of splitting which corresponds to $g_{\text{eff}} > 0$.

The possible causes of named effects are discussed in short form.

Keywords: Sun: Solar magnetic fields – Sunspots: direct measurements – Lande factors.

1. Introduction

Magnetic field measurements in different spectral lines allow obtain very important information about vertical and horizontal magnetic fields inhomogeneity in solar atmosphere. In case of homogeneous magnetic field, we can expect the same measured magnetic field strengths by different spectral lines. If magnetic field is inhomogeneous, measured field values can depend from depth of line formation, its temperature sensitivity, etc. Let us remember some important results to last case.

Gopasyuk et al. (1973) found very interesting effect for non-sunspots regions: measured magnetic field strength depends from magnetic sensitivity factor $g\lambda^2$. This effect, obtained by magnetographic method from analyze of Stokes V parameter, was confirmed lately in Stokes I using photographic method (Loizitsky, 1980). As it was argued in last paper, probable cause of this dependence is

the presence of spatially unresolved magnetic fields with strength of 8-10 kG.

In the same year, Stenflo (1973) discovered the most important observational effect to existence of the spatially unresolved magnetic fields with kG fields in the quiet atmosphere. He used two spectral lines of the same multiplet (No. 1) of Fe I, 5247.1 Å and 5250.2 Å, which have practically equal heights of formation and temperature sensitivity, but different Lande factors g_{eff} , 2.0 and 3.0, respectively. It was found that, in general, $B_{\text{obs}}(5247.1) \neq B_{\text{obs}}(5250.2)$. According to simulations, Stenflo's (1973) observations correspond to $B_{\text{true}} = 1.1\text{--}2.3$ kG in spatially unresolved magnetic fluxtubes.

Semel (1981) had compared the measured magnetic fields B_{obs} in 12 spectral lines using lambda-meter for observations of plages and sunspots. He found a good agreement of such fields for sunspots, but very essential differences (till 5 times) for plages.

Solanki and Stenflo (1984) studied the statistical properties of the Stokes I and V line profiles of 400 unblended Fe I lines in areas of photospheric network and plages. Observations were carried out at Kitt Peak McMath telescope using FTS technique. They concluded that true magnetic field B_{true} in fluxtubes is typically 1.4–1.7 kG, and the filling factor is 3–4% for network and 5–15% for plages. In addition, it was found that 12 lines of high multiplets (No. 823-1177) have very different observed and theoretical (for LS coupling) Lande factors. As to Fe I 5434.527 Å line ($g_{\text{eff}} = -0.014$), authors had concluded: "Our data show no sign of this line in the V spectra, consistent with a g_{eff} of zero".

However, another effect was found later in this line. In spectra of powerful solar flares this line has sometimes appreciable splitting of narrow emissive peaks at its core that correspond to magnetic field strength of about several tens kG (see, e.g., Loizitsky, 2011, 2015).

The purpose of this paper is to analyze the new observational data on the Zeeman splitting in sunspots of different spectral lines, which have both well-known and "doubtful" Lande factors.

2. Observations

Observations were carried out on Horizontal Solar Telescope ATsU-5 of Main Astronomical Observatory of

National Academy of Sciences of Ukraine. Spectra recordings were performed using the SBIG ST-8300 CCD camera. For observations of $I+V$ and $I-V$ spectra, the polarization mosaic made by V.I. Skomorovsky and quarter-wave plate were used. Measured spectra were corrected for flatfield, parasitic interference and curvature of spectral lines.

During June-July 2015, we observed several sunspots placed no far from disk center, in particular, the greatest spots on following dates: June 10, 20, 23 and 26, 2015 and July 08 and 18, 2015.

Stokes $I \pm V$ spectra were recorded in about $\pm 4 \text{ \AA}$ ranges around following wavelengths: 4995.4, 5434.5 and 6094.4 \AA (Fig. 1). About 6–8 well-visible spectral lines with different Lande factors were observed in named wavelength ranges. In this short paper, we present the most obvious effects only, without many details of our study, which is planned to presentation in a separate article.

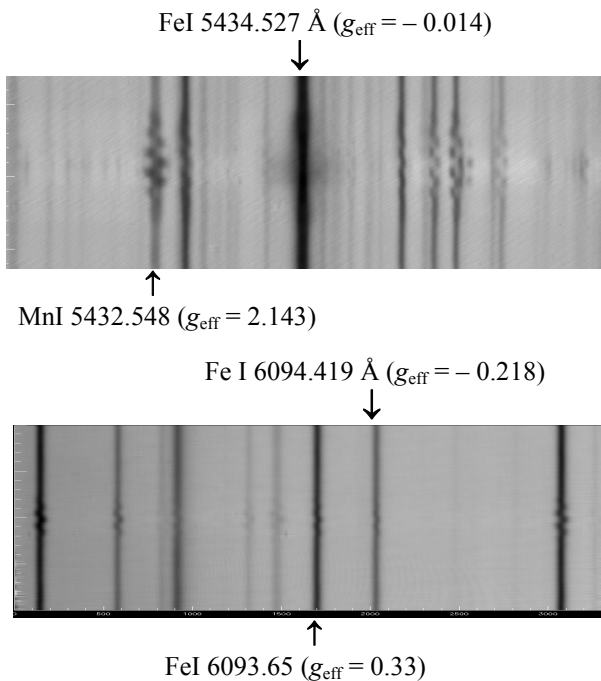


Figure 1: The examples of observed spectra around 5434.5 \AA (July 08, 2015, UT = 7^h30^m) and 6094.4 \AA (July 18, 2015, UT = 7^h20^m).

3. Results

Our main conclusions are the following:

a) as rule, spectral lines with largest Lande factors give the strongest magnetic fields in sunspot umbra (Fig. 2) that can be interpreted as a result of blending the Zeeman π - and σ -components in case of non-longitudinal magnetic field.

b) in some places of sunspots, B_{obs} differs also for lines with close Lande factors, e.g. by Fe I 5432.950 \AA and Ni I 5435.871 \AA ($g_{\text{eff}} = 0.67$ and 0.5 , respectively).

c) Fe I 6094.419 \AA and Fe I 4995.411 \AA lines with $g_{\text{eff}} < 0$ have in sunspots signs of the Zeeman splitting which corresponds to $g_{\text{eff}} > 0$ (see, for example, Fig. 1).

Effect b) in our case can occur as a result (at least, partly) of different temperature sensitivity of lines. For

example, lines Fe I 5432.950 \AA and Ni I 5435.871 \AA have different excitation potentials of lower atomic levels, namely 4.43 and 1.98 eV, respectively.

Effect c) was discussed earlier by Lozitsky (2009). For Fe I 6094.419 \AA line, a wrong Lande factors is excluded because the empirically determined Lande factor ($g_{\text{eff}} = -0.218$) is known here. So, we should search any solar effects. Two solar effects were discussed: (i) real changes of magnetic polarity at close levels ($\approx 10 \text{ km}$) of solar atmosphere and (ii) Paschen-Back effect. Last effect can change of the Lande factors for Fe I lines, but in case of very strong magnetic fields ($\sim 10^5 \text{ G}$). At present, both interpretations seem as 'exotic' because they suppose extreme magnetic field changes in subtelescopic scales. In addition, such picture should be both in sunspots and outside sunspots where extremely strong magnetic fields are unlikely. True, there is one argument in favour of (ii) case. According to Solanki and Stenflo (1984), all 12 spectral lines with 'wrong' Lande factors are lines of high multiplets. Namely for such Fe I lines the Paschen-Back effect is more probable than for lines of low multiplets.

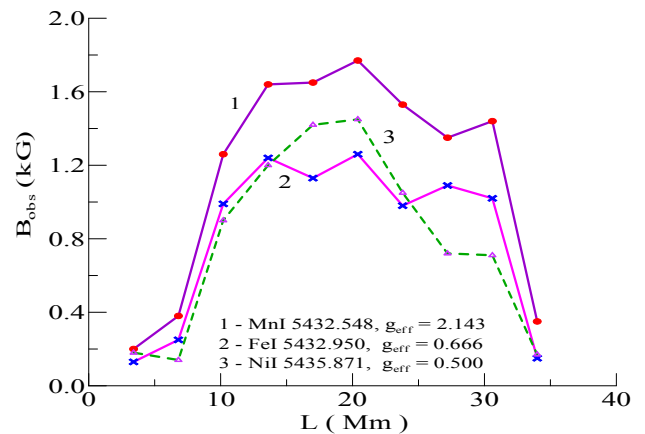


Figure 2: Comparison of observed magnetic fields B_{obs} in a sunspot (AR2381, July 08, 2015) by three spectral lines with different Lande factors; L – distance on the Sun surface.

As to Fe I 5434.527 \AA line, we found very weak Zeeman-like effects in this line which were observed against a background of strong Evershed effect. Our preliminary conclusion is that this line shows spectral manifestation of the Zeeman effect in sunspot umbra which corresponds to $g_{\text{eff}} < 0$.

Acknowledgements. The authors are thankful to N.I. Lozitska for helpful discussions and notes.

References

- Gopasyuk S.I. et al.: 1973, *Solar Phys.* **31**, 307.
 Lozitsky V.G.: 1980, *Phys. Solariterr., Potsdam*, **14**, 88.
 Lozitsky V.G.: 2009, *Bull. Crim. Astrophys. Obs.* **104**, No.6, 132.
 Lozitsky V.G.: 2011, *Int. J. Astron. Astrophys.* **1** (3), 147.
 Lozitsky V.G.: 2015, *Adv. Space Res.* **55**, 958.
 Semel M.: 1981, *Astron. Astrophys.* **97**, 75.
 Solanki S.K., Stenflo J.O.: 1984, *Astron. Astrophys.* **140**, 185.
 Stenflo J.O.: 1973, *Solar Phys.*, **32**, 41.

PECULIARITIES OF A GROUP RESPONSE OF CARDIOVASCULAR SYSTEM OF VOLUNTEERS AT DIFFERENT LATITUDES TO CHANGES OF SPACE WEATHER PARAMETERS

Parshina S.S.¹, Samsonov S.N.², Manykina V.I.², Afanasyeva T.N.¹, Vishnevsky V.V.³, Petrova P.G.⁴, Petrova V.D.¹, Strekalovskaya A.A.⁴, Tokayeva L.K.¹, Kaplanova T.I.¹, Potapova M.V.¹

¹ V. I. Razumovsky Saratov State Medical University of the Russian Ministry of Health, Russia, Saratov, parshinasvetlana@rambler.ru

² Yu.G.Shafer Institute of Cosmophysical Research and Aeronomy of Siberian Branch of the Russian Academy of Sciences, Russia, Yakutsk, s_samsonov@ikfia.ysn.ru

³ Institute of Mathematical Machines and Systems Problems, NSA of Ukraine, Ukraine, Kiev

⁴ M.K.Ammosov Medical Institute of North-Eastern Federal University, Russia, Yakutsk

ABSTRACT. A simultaneous monitoring in evaluating of the response of a cardiovascular system of healthy volunteers was performed. The research was oriented to changes of a space weather parameters in auroral (Tiksi), subauroral (Yakutsk) and medium (Saratov) areas. In each of the experimental groups there was revealed an effect of synchronization between repolarization processes of ventricular myocard responding (according to a T-wave symmetry coefficient of a cardiogram) and geomagnetic activity (according Kp-index). At rest the group effect of synchronization (GES) of myocard in geomagnetic activity change was noticed in 33,3%-61,3% of the respondents. The origin of GES has features depending on the area of habitation and an age of the volunteers.

The study is performed with the partial financial support in partnership with Russian-Ukrainian grant RFFI №14-02-90424 ukr_a.

Keywords: geomagnetic activity, cardiovascular system, T-wave symmetry coefficient.

1. Introduction

Changes in the pulse of a geomagnetic field of the Earth caused by active processes on the Sun and in the magnetosphere of the Earth [1] are one of the most significant factors of an adaptation failure and acute exacerbation of chronic diseases. It's known that a healthy person can stand it without pain. Revealing of the peculiarities of an adaptation of a healthy cardiovascular system to geomagnetic activity changes will allow to elaborate a number of preventing cardiologic measures.

Aim: to reveal a group response of a cardiovascular system in geomagnetic activity change at a long monitoring of healthy volunteers from different areas of habitation. The study was performed as an international multilatitudinal synchronous biophysical experiment "Heliomed".

2. Results and discussing

Monitoring of a cardiovascular system state was organized simultaneously in auroral (Tiksi – 11 people), subauroral (Yakutsk – 2 groups with 18 and 15 people) and medium (Saratov – 31 people) areas. An average age of the volunteers was in different groups: 51,3±3,8 years (Tixie), 43,0±2,5 years (Yakutsk-1), 21,6±1,7 years (Yakutsk-2) and 40,6±2,2 years (Saratov).

The duration of screening was 60 days in spring period March – April in 2014. the daily control of the repolarization processes of ventricular myocard according of ECG with a T-wave symmetry coefficient evaluation (TSC), with the help of Phazagraph device (Ukraine). The given method is good at screening of an ischemic heart disease and evaluation of changes of a space weather parameters, especially, of a solar activity, in morphological parameters of a cardiac muscle [2-4]. The daily research protocol included 4 measures of TSC: initial (at rest), after emotional load, after a physical load, at restoration after a 10-minute rest, blood pressure measuring.

Geomagnetic activity was estimated by the global geomagnetic perturbations – Kp-index, which had been detected every day during all the period of studying.

To evaluate the dynamics of the myocard state of the volunteers in geomagnetic perturbations change we had introduced the parameter "group effect of synchronization – "GES" [5], which reflected the coincidence between TSC and Kp-index maximums. If there is a presence of TSC-Kp synchronization of 66,7% from a total number of Kp maximums, it is registered into a GES group. It's proved that GES is different at rest and at various types of load [5]. In the present study the results of GES of volunteers from different areas were analyzed: examinees were at rest initially and at rest after a 10-min rest after a physical load.

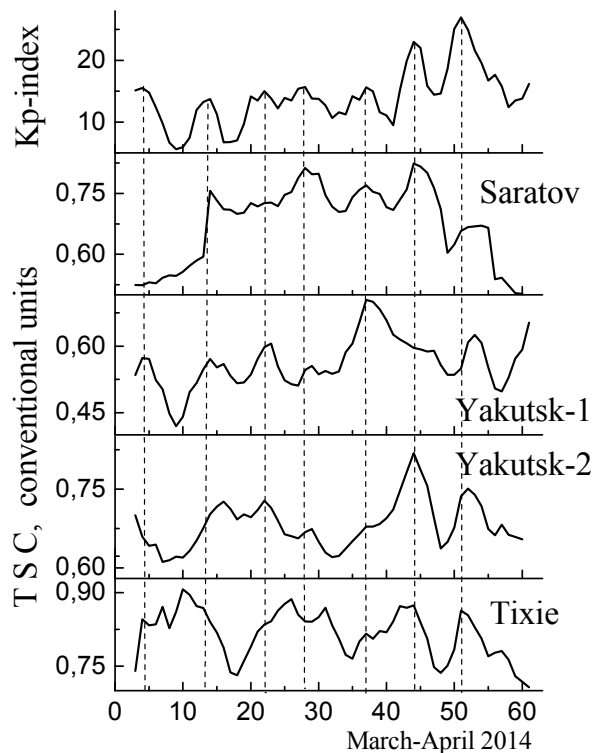


Figure: Kp-index and TSC on the different latitudes

It was noticed that GES was in all groups of volunteers. In the medium areas it was 61,3% of volunteers (Saratov), in subauroral – 33,3% (Yakutsk-1) and 39,0% (Yakutsk-2), in auroral – 45,5% (Tixie). There was no statistically significant difference between these parameters ($p > 0,05$), which may be connected with a low number of samplings. So, the presented analysis isn't able to confirm that various regions are different in the proportion of "sensible" and "insensible" volunteers.

Together with this, it was discovered that GES has peculiarities connected with the regions of screening and the age of the examinees (Figure). During the period of studying there had been noticed 7 Kp maximums, the highest levels of the geomagnetic perturbations had been fixed at the 6th and the 7th maximums (Figure). In the medium areas (Saratov) the TSC-Kp synchronization was at 2,4,5,6th Kp maximums and was absent in the strongest – the 7th – maximum. Probably, the response on the strong enough 6th maximum led to the reducing of the adaptation ability of a cardiovascular system, which became evident in the absence of a TSC and Kp synchronization in the 7th Kp maximum.

In subauroral areas (Yakutsk-1, Yakutsk-2) GES is different from the medium areas, as well as between the groups of various age. The volunteers of an average age (Yakutsk-1) demonstrated GES at the 1,2,3,4,5th Kp

maximums. There was no response at the 6th Kp maximum, but there was – at the stronger 7th Kp maximum, although, it was not at the day of the geomagnetic perturbations. It was 2 days later. In the group of the young volunteers (Yakutsk-2) the TSC-Kp synchronization had been registered at the 6th and the 7th Kp maximums, and it was also 1 day later in the 7th maximum. In the given group there was also noticed the TSC and Kp synchronization in the 3rd Kp maximum.

Interesting regularity was revealed in GES in auroral areas (Tixie). TSC and Kp synchronization was noticed only at the strongest Kp maximums – the 6th and the 7th (Figure). There was no myocard response on the other, not as strong geomagnetic perturbations.

The analyzing of the TSC-Kp synchronization effect in different groups of studying shows that the leading factor for synchronization of a myocard state and geomagnetic perturbations is a value of a Kp-index, as well as a state of adaptation abilities of a cardiovascular system of the volunteers.

3. Conclusions

The group effect of the TSC-Kp synchronization is revealed at all studying areas (medium, subauroral and auroral). The degree of incidence of volunteers with myocard "sensitive" to geomagnetic perturbations doesn't depend on the region of habitation. At the same time, the origin of GES has peculiarities in various – medium, subauroral and auroral – areas. The groups of volunteers of different age, living in the same area, are also characterized by different variants of myocard response on geomagnetic activity change. Besides, an initial state of adaptation ability of a cardiovascular system of the volunteers also determines peculiarities of myocard state response on geomagnetic activity change.

The study performed with the financial support of collaborative Russian-Ukrainian grant 14-02-90424 «The role of normal and extreme heliogeophysical processes in evolution of biosphere».

References

1. Obridko V.N. et al.: 2014, *Psychosomatic and integrative research*, **1**, <http://pssr.pro/articles/237>.
2. Samsonov S.N.: 2013, *Odessa Astron. Publ.*, **26**, 297.
3. Fainzilberg L.S.: 1998, *Control systems and machines*, **4**, 40.
4. Vishnevsky V.V. et al.: 2003, *Biomedical technologies and radioelectronics*, **3**, 3.
5. Parshina S.S. et al.: 2015, IT + M&Ec'2015, Spring session, 316, http://gloriz.com/doki/me/2015/2015_5.pdf.

SUN'S POLAR MAGNETIC FIELD REVERSALS IN SOLAR CYCLE 24

M.I.Pishkalo¹, U.M.Leiko²

Astronomical Observatory of Taras Shevchenko National University of Kyiv,
Observatorna 3, Kyiv, 04053, Ukraine

¹pish@observ.univ.kiev.ua, ²leiko@observ.univ.kiev.ua

ABSTRACT. It is known that polar magnetic field of the Sun changes its sign at the maximum of solar cycle. These changes were called as polar field reversals. We investigated dynamics of high-latitude solar magnetic fields separately in northern and southern hemispheres. Solar polar field strength measurements from the Wilcox Solar Observatory and low-resolution synoptic magnetic maps from the SOLIS project and from Helioseismic and Magnetic Imager (HMI) onboard Solar Dynamics Observatory were used. We analyzed total magnetic flux at near-polar zones, starting from 55, 60, 65, 70, 75, 80 and 85 degrees of latitude, and found time points when the total magnetic flux changed its sign. It was concluded that total magnetic flux changed its sign at first at lower latitudes and finally near the poles. Single polar magnetic field reversal was found in the southern hemisphere. The northern hemisphere was characterized by three-fold magnetic field reversal. Polar magnetic field reversals finished in northern and southern hemispheres by CR 2150 and CR 2162, respectively.

Keywords: Sun: Solar activity – Solar magnetic fields: Polar field reversals

1. Introduction

Polar magnetic fields of the Sun are maximal in solar activity minima and minimal in maxima. Besides, at the epoch of solar maximum polar magnetic fields reverse their sign (Babcock, 1959; Petrie et al., 2014).

Polar magnetic fields are predominantly connected with large-scale dipolar magnetic field of the Sun. Its evolution, in a general way, may be described by the Babcock-Leighton solar cycle mechanism (Babcock, 1961; Leighton, 1969). At the photosphere level the polarity reversal may be described by a surface flux transport process (Wang et al., 1989; Sun et al., 2015).

Polar magnetic field reversals are usually asymmetric (Svalgaard & Kamide, 2013). They occur usually at different time in northern and southern solar hemispheres. Sometimes the polarity reversal in northern or southern hemisphere is three-fold. So, Makarov and Sivaraman (1986, 1989) found that three-fold reversals occurred in solar cycles 16, 19 and 20 in N-hemisphere, and in cycles 12 and 14 in S-hemisphere. In solar cycles 21-23 polarity reversals were single in both hemispheres (see Pishkalo et al., 2005, and references therein).

In the present work we study evolution of near-polar magnetic fields of the Sun at the maximum of the current solar cycle 24 to find the time of polarity reversals.

2. Data and analysis

We analyzed data on sunspot number from the SIDC (<http://sidc.oma.be/html/sunspot.html>) and solar polar magnetic field measured in the Wilcox Solar Observatory (WSO, <http://wso.stanford.edu/Polar.html>) near the maximum of sunspot cycle 24.

Low-resolution synoptic magnetic maps from the SOLIS project (Fe I 630.2 nm, 360×180 pixels; http://solis.nso.edu/0/solis_data.html) and from Helioseismic and Magnetic Imager (HMI, 720×360 pixels, <http://jsoc.stanford.edu/data/hmi/synoptic/>) onboard Solar Dynamics Observatory (SDO) were also analyzed in details. We summed up total magnetic flux at near-polar zones starting from 55, 60, 65, 70, 75, 80 and 85 degrees of northern and southern latitude, and found then time points when the total magnetic flux changed its sign. We considered the time points as the time of polarity reversal in the corresponding zones.

3. Results

Fig. 1 illustrates evolution of international monthly sunspot number from the SIDC and polar magnetic field measured by the WSO near the maximum of solar cycle 24, in 2012-2015. Smoothed data are plotted by solid lines. It should be noticed that polar fields measured at the WSO are mean fields over the $|\pm 55|^\circ$ of solar latitude. In the top panel, times of polar field reversal in northern and southern hemispheres (according to the WSO data, bottom panel) are shown by solid and dashed vertical lines respectively.

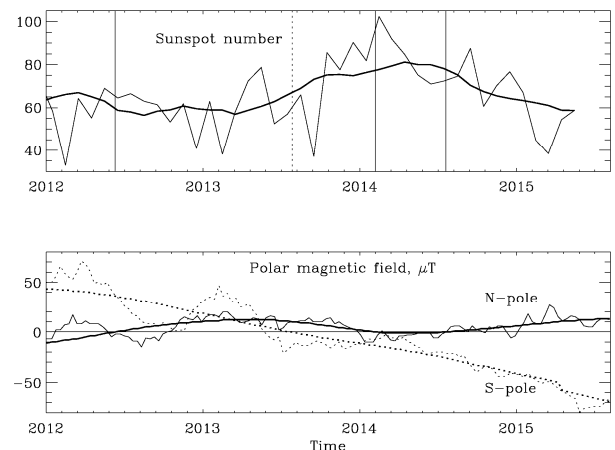


Figure 1: Monthly sunspot number from the SIDC (top) and polar magnetic field measured by the WSO (bottom) since 2012. Smoothed data are plotted by solid lines

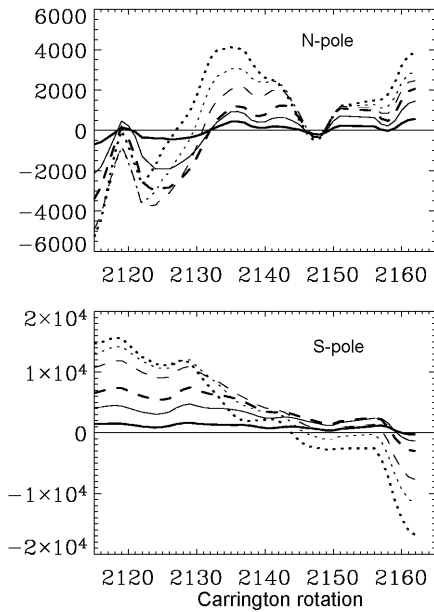


Figure 2a: Evolution of total near-polar magnetic flux in different near-polar zones (SOLIS data, see, the text).

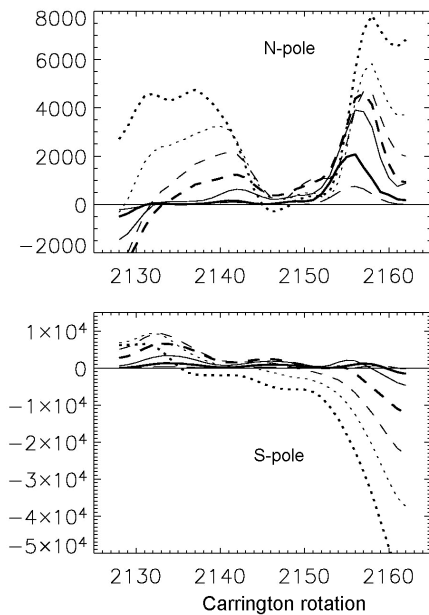


Figure 2b: the same as in fig. 2a for HMI data.

One can see that the polarity reversal in the northern hemisphere was three-fold and it came to the end in the middle of 2014, a year after completion of the polarity reversal in the southern hemisphere in the middle of 2013.

Evolution of total magnetic flux in different near-polar zones is shown in Fig. 2a (SOLIS) and 2b (HMI) by thin and thick solid (75° and $\geq 80^\circ$), dashed ($\geq 65^\circ$ and $\geq 70^\circ$) and dotted ($\geq 60^\circ$ and $\geq 55^\circ$) lines. Line with long dashes in fig. 2b represents near polar zone of $\geq 85^\circ$. Note: Fig. 2 was plotted after triple 3-points smoothing.

The current solar cycle began in December, 2008 after a prolonged and weak solar minimum. Polar magnetic fields in minimum of solar cycle 24, measured by the WSO, were almost twice weakened as compared with three previous cycles. Before the cycle maximum, total magnetic flux in near-polar zones was positive in the S-hemisphere and nega-

tive in the N-hemisphere. Near the cycle maximum total magnetic flux changed its sign from negative to positive in the N-hemisphere and from positive to negative in the S-hemisphere. These changes occurred first at low latitudes. It seems that polarity reversal was single in the S-hemisphere and three-fold in the N-hemisphere. The process of polarity reversal in the S-hemisphere and first reversal in the N-hemisphere are gradual when it “moves” from zones of $\geq 55^\circ$ to poles during 7 rotations to 2 years. Second and third polarity reversals in the N-hemisphere are fleeting and cover all the zones nearly simultaneously. Polarity reversal in the S-hemisphere finished in the first half of 2015, about one year later than in the N-hemisphere. Time of polarity reversals against lower limits of near-polar zones are plotted in fig. 3.

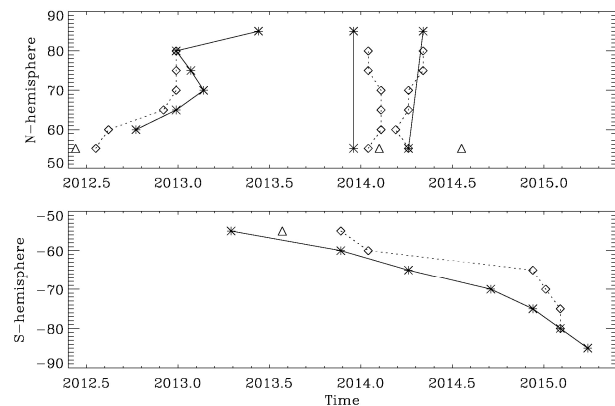


Figure 3: Time of polarity reversal in different near-polar zones in the northern (top) and southern (bottom) hemispheres obtained using data from SOLIS (rhombuses) HMI SDO (asterisks) and WSO (triangles). Note: points of ± 55 along y-axis correspond to zones from $\pm 55^\circ$ to poles, and so on.

Conclusions

In solar cycle 24, polar field reversals occur near the cycle maximum, at different time in N- and S-hemisphere according to the hemisphere activity.

There were three-fold polar magnetic field reversal in the N-hemisphere and single reversal in the S-hemisphere.

The magnetic field reversal in N-hemisphere was completed one year earlier than in the S-hemisphere.

The whole reversal process, from $\pm 55^\circ$ to poles, lasted about two years in both hemispheres.

References

Babcock H.D.: 1959, *Astrophys. J.*, **130**, 364.
 Babcock H.D.: 1961, *Astrophys. J.*, **133**, 572.
 Leighton R.B.: 1969, *Astrophys. J.*, **156**, 1.
 Makarov V.I., Sivaraman K.R.: 1986, *Bull. Astr. Soc. India*, **14**, 163.
 Makarov V.I., Sivaraman K.R.: 1989, *Solar Phys.*, **119**, 35.
 Petrie G.J.D. et al.: 2014, *Space Sci. Rev.*, 2014, **186**, 325.
 Pishkalo M.I. et al.: 2005, *Vestnik Kiev Univ. Astronomy*, **41–42**, 98.
 Sun X. et al.: 2015, *Astrophys. J.*, **798**, article id. 114.
 Svalgaard L., Kamide Y.: 2013, *Astrophys. J.*, 2013, **763**, article id. 23.
 Wang Y.-M. et al.: 1989, *Science*, **245**, 712.

SOLAR SYSTEM

THE PHYSICAL PARAMETERS OF THE GAS AND DUST IN COMETARY ATMOSPHERES

Churyumov K.I., Ponomarenko V.O., Kleschonok V.V.

Taras Shevchenko National University of Kyiv Astronomical observatory

Observatorna str. 3, 04053 Kyiv, Ukraine

klivch@mail.ru, vasilyponomarenko@gmail.com

ABSTRACT. The results of observations and studies of comets on the basis of the optical spectra with an average resolution were presented. Spectral material was mainly produced in 2009–2012 with the help 2-m telescope Zeiss ($F_1 = 6.3$ m; $F_2 = 16$ m) at high mountain astronomical station "Terskol" of Main Astronomical Observatory of National Academy of Sciences of Ukraine and the Institute of Astronomy RAS. The resolution of the spectra $R \approx 1500$, $R \approx 4500$, $R \approx 14000$; wavelength ranges $\lambda\lambda = 3850\text{--}8000$ Å.

Using the spectra of comets, based on the model Hazer, was performed the following work: carried out the identification of spectral emission lines, obtained physical parameters of the neutral gas atmosphere of comets. And also, physical parameters the dusty atmosphere.

Keywords: comet, spectrophotometric gradient, emission lines.

1. Introduction

The observations of comets, which are the objects of the research paper were obtained in 2009-2012 at the astronomical observatory "Terskol" of International Center of Astronomical, Medical and Ecological Research of National Academy of Sciences of Ukraine and the Institute of Astronomy RAS (Russia, the North Caucasus, $43^\circ 16' 29''$ n. l., $42^\circ 30' 03''$ e. l., Altitude 3136 m). The code observatory in the Minor Planet Center (MPC) – B18. Instrument for observations was 2-m reflecting telescope Zeiss ($F_1 = 6.3$ m; $F_2 = 16$ m) with outboard spectrometer-photometer of Cassegrain focus (the spectrograph slit had the height $\approx 11''$ and the width $\approx 3''$). In the spectrograph was installed the CCD camera FLI PL4301E (with chip 50×50 mm, field $11' \times 11'$, 1247×1151 pixel). In the spectrograph set alternately the different modes: prism ($R \approx 1500$), echelle ($R \approx 14000$). All spectra were obtained in the optical range ($380 \text{ nm} \leq \lambda \leq 850 \text{ nm}$).

All studied comets can be divided into two dynamic groups: Jupiter-family comets (JFCs) and long-period comets (LPC) with retrograde motion. The orbital elements, some physical parameters and characteristics for observations JFCs are presented in Table 1, for LPC in Table 2. In the tables can see differences between the types of comets, which are displayed in the value of the angle of inclination of the orbit to the ecliptic plane, the eccentricity and the period of rotation, geocentric distance.

Table 1. Parameters of observations and orbital elements of JFCs

Parameter		22P	81P	103P
Heliocentric distance	r , AU	1.77	1.63	1.06
Geocentric distance	Δ , AU	0.78	0.68	0.13
Integral magnitude	T	$\approx 12^m$	9.8^m	9.1^m
Phase angle	s-t-o	10°	13°	56°
Elongation angle	s-o-t	160°	157°	116°
Position angle	PA	259°	274°	271°
Diameter of comet's nucleus	D , km	≈ 3	≈ 5	≈ 0.6
Geometrical albedo of surface	A	0.05	0.059	0.028
Eccentricity of orbit	e	0.54	0.538	0.694
Inclination to ecliptic	i	4.7°	3.24°	13.6°
Period of rotation	P , y.	6.43	6.42	6.46

Table 2. Parameters of observations and orbital elements of LPC

Параметр		C/2006 W3	C/2009 K5	C/2009 P1
Heliocentric distance	r , AU	3.13	1.50	2.09
Geocentric distance	Δ , AU	2.33	1.43	1.61
Integral magnitude	T	$\approx 12^m$	$\approx 11^m$	10.7^m
Phase angle	s-t-o	13°	40°	27°
Elongation angle	s-o-t	137°	75°	104°
Position angle	PA	160°	272°	122°
Eccentricity of orbit	e	1.00005	1.001	1.001
Inclination to ecliptic	i	127.1°	103.9°	106.2°

The calculations of the physical parameters of gas-dust cometary atmospheres were based on the Hazer's model. This model is used in the processing of the surface brightness profiles of the neutral atmosphere of comet obtained on the basis the photometric and spectroscopic observations (Hazer, 1957). It is easy and convenient, as it

includes a small number of parameters that can be determined theoretically or obtained from observations, which greatly simplifies the process of obtaining the physical quantities.

Hazer's model based on the following approximations:

1) the comet nucleus is spherical with a radius r_0 ; its substance is vaporized by absorption of solar radiation. The molecules leave the surface of the nucleus, moving in all directions with the radial velocity v_0 ;

2) the reason of radiate energy is the mechanism of resonance fluorescence (under the action of the solar flux);

3) the decomposition of molecules occurs as a result of photodissociation under the law $n = n_0 e^{-t/\tau_0}$, where n_0 – the number of molecules, which are presented at the moment $t=0$; τ_0 – half-life for this type of molecules;

4) at a distance r from the comet's nucleus the density of molecules characterized by the expression

$$D(r) = D(r_0) \left(\frac{r_0}{r} \right)^2 e^{-\frac{t-t_0}{\tau_0}}$$

This model does not take into account the effects of solar radiation pressure on the molecules, anisotropic (non-radial) the escaping of parent molecules from the nucleus and non-radial movement of daughter molecules, as well as the distribution of velocities of their movement. The model can be used only to the photodegradation products and it is impossible in cases where the daughter molecules formed by the chemical reactions.

2. The identification of emissions in cometary comae

Was carried out a detailed identification of emission spectral lines in comae of comets 81P/Wild 2, 103P/Hartley 2, C/2007 N3 (Lulin), C/2009 K5 (McNaught). For identification were used the catalogues of Cochran (Cochran, 2001) and Brown (Brown et al., 1996). Most revealing is the identification that was conducted for the comet Hartley 2 and McNaught, since the lines in the spectra of comets were identified with the equal resolution ($R \approx 14000$) and in the equal wavelength ranges ($\lambda = 4690-7000 \text{ \AA}$). At the time of observations the comet 103R had a higher integral magnitude and was on a much smaller heliocentric distance. In spite of this, the number of emission lines, that could be identified in this JFCs significantly less than their number in the C/2009 K5 (McNaught). We can assume that this fact is characteristic of the vast majority of JFCs in compared with LPC with retrograde motion and can be explained by the disintegration time or differences in origin between the two types of comets. The results of identification are presented in Table 3.

Also, the identification of spectral emission lines was carried out for the comet C / 2007 N3 (Lulin) based on the spectra with echelette ($R \approx 4500$; $\lambda = 3800-9000 \text{ \AA}$), and for the comet 81P/Wild 2 ($R \approx 14000$; $\lambda = 4700-8500 \text{ \AA}$). The search of emission lines in the spectra of other comets are not implemented because their gas activity was weak.

We should also note the identification of the doublet Na ($D_1 = 588.9 \text{ nm}$, $D_2 = 589.6 \text{ nm}$) in the spectra of comets 22P/Kopff ($r = 1.8 \text{ AU}$), 103P/Hartley 2 ($r = 1.06 \text{ AU}$), C/2009 K5 (McNaught) ($r = 1.5 \text{ AU}$). As is known, the identification of Na on heliocentric distance of $> 1 \text{ AU}$ is a rare phenomenon.

Table 3. Emission lines in the spectra of comets 103P/Hartley 2 и C/2009 K5 (McNaught)

Emission	Comet 103P	Comet C/2009 K5
C ₂	928	1248
NH ₂	162	189
H ₂ O ⁺	25	31
[OI]	3	3
Na	2	2
CN	24	36
no ident	651	675
All	1795	2184

3. Accuracy of spectrophotometry

For the processing the spectra of comets obtained with a CCD have been used specialized programs DECH95, DECH20T and other software designed or adapted for the processing of cometary spectra. The part of the work was done based on the MATLAB programs. At the stages plot charting and separate works in large data arrays used Microsoft Office Excel.

In accordance with the method of processing and features of observational material was analyzed possible errors. The error of measurement results was mostly accidental, since the systematic component was removed by corrections and reductions. The random component of measurement error for a single image is equal 10/1 and determined by the ratio the signal/noise ratio. However, due to the fact that during the night snapshot the object was obtained several times (were carried out reusable measurement), the random component of measurement error for each of the research subjects was reduced to a level that does not exceed 5%. In addition, to the final results was introduced error of measurement processing. Theoretically it determined that the error processing of measurement results does not exceed 6%. Therefore, the total maximum possible error (worst case) does not exceed 11%. Also, the error was evaluated by the method of comparison with exemplary measure, which was a star-standard. Methods of assessment lay in the fact that every night observation was obtained not one snapshot, but two snapshots of star-standards (solar-type star and a star with higher temperature – "divayzer"). With the help of single star-standard were calculated the fluxes from another star in absolute units. By means of comparison with spectrophotometric catalog of Burnashev (Burnashev, 1985) was determined an error of measurements and calculations. For the different stars and nights maximum error was equal 6–10%. Fig. 1 shows an example of a comparison performed measurements and calculations for the star HD 214923 (spectral class B8V) with the data of spectrophotometric catalog of Burnashev. The resolution of the observations that submitted in the work in many times greater than the resolution of the catalog, so the resulting intensity was approximated by the polynomial.

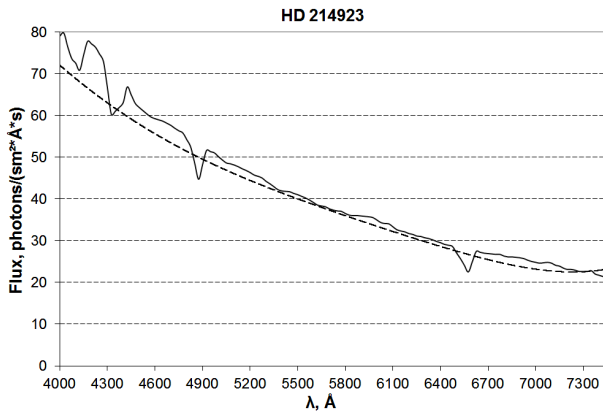


Figure 1: The intensity of the star-standard HD 214923: the continuous line shows the data of spectrophotometric catalog; the dotted line shows the results of measurements and calculations ($1 \text{ \AA} = 0.1 \text{ nm}$)

4. The spectrophotometric gradient

It was also built the ratio of the reflected by comet the solar continuum in absolute units (excluding the standard emissions and the luminescent continuum) to the original spectrum of the Sun for all the studied comets. Thus obtained spectrophotometric gradients indicate on differences in the reflective characteristics of dust between the considered JFCs and LPC with retrograde motion (Fig. 2). The figure shows that the considered comets of the Oort cloud better reflect the short-wave radiation in the visible spectral range. This may be due to an excess in their atmospheres of highly dispersed dust particles < 0.5 microns. These particles have a lower temperature and better dissipate the short wavelengths (in accordance with the mechanisms of Mie and Rayleigh). The scattered light can make a significant contribution to reducing the reflection properties of the cometary dust in the LPC, which are discussed in the work. The spectrophotometric

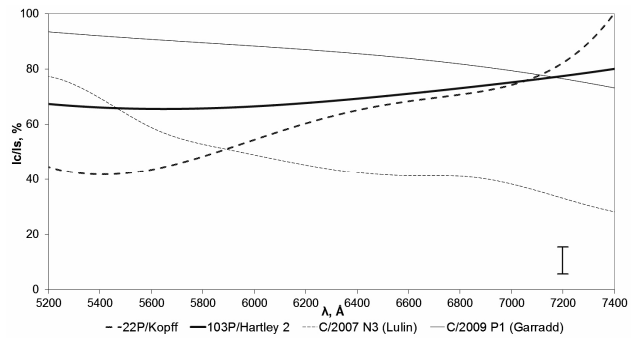


Figure 2: The spectrophotometric gradients for JFCs (22P, 103P) and LPC with retrograde motion (C/2007 N3, C/2009 P1)

gradients of the investigated JFCs increasing with wavelength in the visible range. To explain the phenomenon can lose the JFCs of a significant amount of light dust particles < 0.5 microns due to active gassing and reusable approaches to the Sun. Heavy, inert, the coarse dispersed dust (> 0.5 microns), which dominates in the atmospheres of these comets, will reflect light of Sun almost uniformly (with a small directly proportional to the wavelength). In Fig. 2 we can see, that the spectrophotometric gradients for short-period comets 22P and 103P are increasing, and for long-period comets C/2007 N3 and C/2009 P1 are falling (in the visible spectral range).

References

- A'Hearn M.F. et al.: 1995, *Icarus*, **118**, 223.
 Brown M.E.: 1996, *Astron. J.*, **112** (3), 1197.
 Burnashev V.I.: 1985, <http://sirius.bu.edu/planetary/obstoals/starflux/>
 Cochran A.: 2001, anita@barolo.as.utexas.edu.
 Haser L.: 1957, *Bull. Acad. Roy. Belg*, **43**, 740.
 Langland-Shula L.E. et al.: 2011, *Icarus*, **213**, 280.

STUDY OF QUASI-PERIODIC VARIATIONS IN DRAG OF ARTIFICIAL SATELLITE DURING 23–24 SOLAR CYCLES

Komendant V.H.¹, Ryabov M.I.², Sukharev A.L.²

¹Astronomy Department of Odessa I.I.Mechnikov National University

²Odessa observatory «URAN-4» Institute of Radio Astronomy NASU

ABSTRACT. Apply of the method of time-frequency analysis allows to reveal the detailed structure of the manifestations of the influence of the state space weather on the upper atmosphere of the Earth. Sensitive indicators of such changes are low-orbit satellites. The dynamics of drag of nineteen low-orbit satellites was viewed. The study period includes phases of declining and a long minimum of 23rd solar cycle, phases of rise and maximum of 24th solar cycle. In dynamic of inhibition of all the analyzed satellite pronounced regular inhibition effects with extended periods of 2 – 6 years and short-period effects with periods less than one year. In the satellites: 00063, 00165, 25064, 00932 and 00746 – detected periods with trend from 25 – 28 days to 1 – 1.7 months.

1. Introduction

In this work, satellites are used as indicators of the impact of space weather and manifestations of solar activity on the upper atmosphere of the Earth. Density variations cause a change in the height of the satellite in the atmosphere. The density of the atmosphere is constantly changing and doesn't only depend on the latitude and height above the Earth's surface, but also on the solar activities and space weather conditions. Evolution of the orbit and drag of satellites depends on: gravitational and tidal perturbations (the attraction of the Sun, Moon and other planets); compression of the Earth; the Earth's magnetic field; light pressure; charged and neutral particles (the effect is small and therefore neglected); aerodynamic disturbances of Earth atmosphere [1, 2].

2. Observational data

Nineteen satellites with different inclinations were taken for the analysis. Among them: polar, middle-latitude and equatorial satellites. There are nine circle orbit and ten elliptic orbit satellites. Some elements of the orbits of this satellites are listed in Table 1. In brackets (after number of satellite) period of observation of the satellite is shown.

Most of all satellites were observed during 10 years. Satellite 27700 was observed during 8 years (2005 – 2012). Observations of these satellites cover the declining phase of solar cycle 23 and the first half of solar cycle 24. It includes the rise phase and beginning of the maximum phase of solar cycle 24.

In Table 1 are listed: numbers of satellites, periods of observations, inclination of orbits – i , eccentricity – e and the minimum distance from the surface of the Earth at perigee – r_{min} .

Table 1.

Number of satellite	i	e	r_{min}
satellites with circular orbit			
25860 (2005-2013)	98.57°	0.0002	655 km
27700 (2005-2012)	97.7°	0.005	486 km
12054 (2005-2013)	65°	0.007	522 km
00397 (2005-2014)	58.3°	0.0016	613 km
00063 (2005-2014)	48.5°	0.0027	465 km
00165 (2005-2014)	47.9°	0.0013	540 km
06153 (2005-2014)	35°	0.00077	697 km
25064 (2005-2013)	34.9°	0.0007	507 km
23757 (2005-2013)	22.9°	0.0009	499 km
satellites with elliptical orbit			
00932 (2005-2014)	81.3°	0.114	522 km
00721 (2005-2014)	78.6°	0.11	592 km
00829 (2005-2014)	60.8°	0.3	393 km
00746 (2005-2014)	60.8°	0.31	399 km
00082 (2005-2014)	38.9°	0.12	631 km
00016 (2005-2014)	34.3°	0.2	649 km
00005 (2005-2014)	34.2°	0.19	647 km
00020 (2005-2014)	33.4°	0.17	505 km
00011 (2005-2014)	32.9°	0.15	551 km
00963 (2005-2014)	19.75°	0.21	265 km

3. Initial values

Variations of the B-star Drag Term were studied in this article. This Drag Term strongly correlates with the density of the atmosphere. In this case, it can be seen as drag coefficient. The B-star Drag Term is used for the model SGP 4. This mathematical model is used for prediction of the position and velocity of an artificial satellite (there are 5 mathematical model of SGP) [7]. This model uses TLE data format produced by NORAD – North American Aerospace Defense Command [5]. The B-star Drag Term measured in units of $1/R_3$ (R_3 – radius of the Earth).

4. Methods of data processing

Packages of the statistical analysis were used for our estimations, which are: Origin Pro 8.1, STATISTICA 8 и PSELab.

For primary processing of data software package – Origin Pro 8.1 was used. With it performed data interpolation by B-spline method and subtracted the trend (polynomial 3rd order and using of frequency filtering). After this package statistical analysis software package STATISTICA 8 was used. With this package periodograms for all satellites were constructed. At the last stage the PSELab package was used for construction of the spectrograms. PSELab allows to carry out the spectral and spectral–time analysis of data.

5. Application of spectral analysis of time series

Spectral analysis is one of the signal processing methods, which allows to describe the frequency content of the measured signal. The basis for this analysis is the Fourier transform. It binds the values of the time series with their representation in the frequency domain.

The disadvantage of this method is that it can't show the period of time when the amplitude of any harmonic changes. One option to eliminate this disadvantage was proposed. It is based on using the method not to the entire process, but to the process within a certain time window, which gradually shifts [3]. To recalculate the coefficients of the resulting series we used the algorithm of fast Fourier transform (FFT). In this work, for construction of the spectrograms we used algorithm "Winograd". This algorithm has a significant advantage over the others, when the multiplication operation is more difficult than addition [4].

6. Results

Due to the fact that the data series are presented on an uneven timeline, to create a time series with uniform samples we used the B-spline interpolation. Figure 1 shows an example graph of the change of the drag coefficient of the satellites: 27700, 00932 – in the investigated time interval.

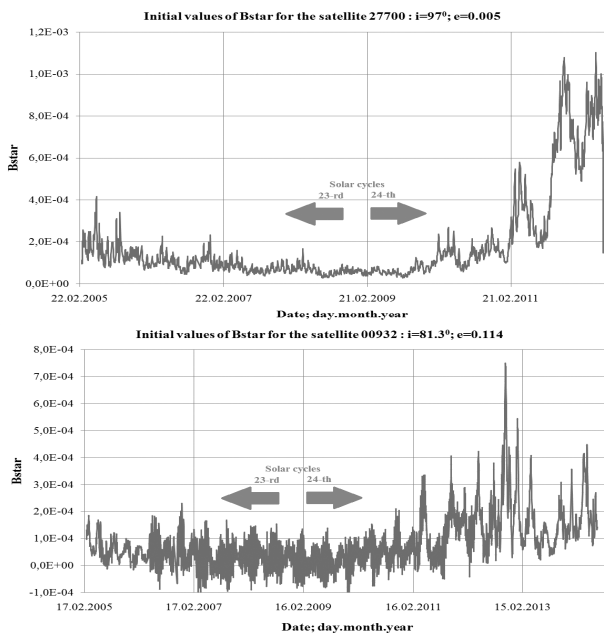


Figure 1: Initial values for polar satellites 27700 (circular orbit) and 00932 (elliptical orbit).

Fig. 1 shows a marked difference in the drag dynamics of the satellites at period of the minimum of the 23rd solar cycle and at the beginning of the 24th solar cycle.

As a result of the carried out calculations we obtained that there are quasi-periodic oscillations with an interval of 27 to 30 days in the declining phase of the 23rd solar cycle and in the phase of minimum solar activity. On this oscillations overlaid the oscillations with period of 10 to 13 days. In addition to these observations drags with a period of slowdown of about three months are marked.

6.1. Dividing the data into two intervals of observations

According to the drag dynamic of the artificial satellites, marked above, observations data was divided into two periods: 2005-2009 and 2010-2014. In STATISTICA 8, using Fourier analysis, we constructed periodograms for these intervals. An example of periodogram is shown in Figure 2.

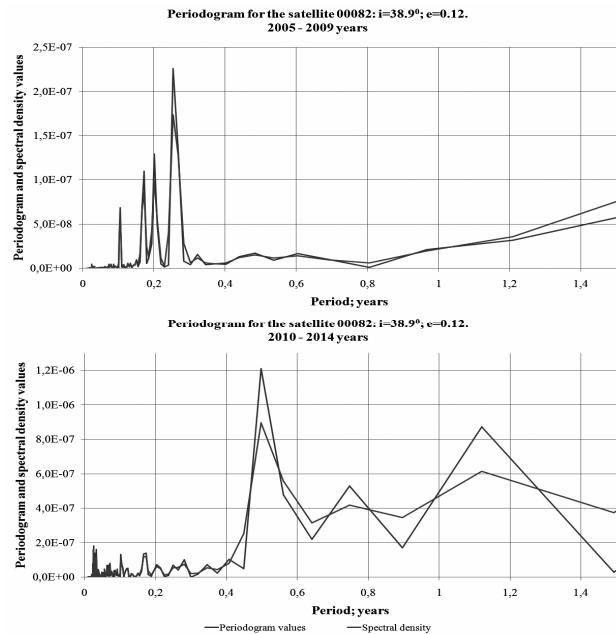


Figure 2: Periodogram of initial values for two time periods (satellite 00082).

In the resulting periodograms: for 2005 – 2009 dominated periods of up to 0,5 years. And for 2010–2014 we see increasing of period 0,5 year and manifestation of longer periods of 1 – 1,2 years («elliptic» satellites) and 2,4 year («circular» satellites). For all objects in the declining phase of the 23rd solar cycle, the maximum amplitude has a short–period variations (up to 0,5 year), in the raise phase of the 24th solar cycle the maximum amplitude has the long–period variations (from 0,5 year to 2,5 years).

6.2. Subtract of the trend component

Table 2 lists the periods of trend component. It shows existence of six years period and about two–year period. All of them have maximum spectral power. Further, to identify short–components, trend components were removed.

Table 2.

Number of satellite	Periods: Year - *, Months - **, Days - ***.		
satellites with circular orbit			
25860 $i=97.7^\circ$	6*	2*	11,1**
27700 $i=97^\circ$	1,7*	1,1*	6,6**
12054 $i=65^\circ$	6*	3*	1*
00397 $i=58.3^\circ$	6,4*	2,1*	1,1*
00063 $i=48.5^\circ$	2,1*	1,3*	8,9**
00165 $i=47.9^\circ$	2*	11,3**	8,6**
06153 $i=35^\circ$	6,4*	2,1*	1,1*
25064 $i=34.9^\circ$	2*	11,1**	8**
23757 $i=22.9^\circ$	6*	2*	11,1**
satellites with elliptical orbit			
00932 $i=81.3^\circ$	6,4*	1,8**	1,3**
00721 $i=78.6^\circ$	6,4*	2,1*	1,1*
00829 $i=60.8^\circ$	6,4*	2,1*	11,7**
00746 $i=60.8^\circ$	2,1*	1,3*	11,8**
00082 $i=38.9^\circ$	6,4*	1,6*	11,7**
00016 $i=34.3^\circ$	2,5*	11,7**	8*
00005 $i=34.2^\circ$	6,4*	2,1*	11,7**
00020 $i=33.4^\circ$	1,3*	8**	5,9**
00011 $i=32.9^\circ$	6,4*	2,1*	1,1*
00963 $i=19.75^\circ$	6,4*	2,1*	11,7**

Table 3.

Number of satellite	Periods: Year - *, Months - **, Days - ***.							
satellites with circular orbit								
25860 $i=97.7^\circ$	2,4*	1*	8**	6**	3,5**	26,2***		
27700 $i=97^\circ$	2,47*	1,7*	9,9**	6,6**	5,9**	4**	1,8**	27,6***
12054 $i=65^\circ$	2*	1*	8,5**	6**	5**	3,6**	2,5**	27,3***
00397 $i=58.3^\circ$	2,5*	1,1*	8,5**	5,9**	4,1**	1,2**	25,9***	10,9***
00063 $i=48.5^\circ$	2,5*	1,2*	9,4**	6**	4**	1,8**		27***
00165 $i=47.9^\circ$	2,4*	1*	8,2**	6,1**	3,3**	27,4***		
06153 $i=35^\circ$	2,1*	11,7**	8,5**	5,9**	4**	1,4**	25,6***	9,6***F
25064 $i=34.9^\circ$	2*	1*	8**	6**	3,5**	1,7**	27,3***	
23757 $i=22.9^\circ$	2*	1*	8**	6**	4**	27,3***		
satellites with elliptical orbit								
00932 $i=81.3^\circ$	1,3*	11,8**	9,5**	5,9**	2,9**	1,5**	27,2***	12,9***
00721 $i=78.6^\circ$	1,8*	1,1*	8,4**	5,9**	4**	2,9**	12,7***	
00829 $i=60.8^\circ$	1,8*	11,7**	9**	5,7**	4,6**	2,3**	1,6**	
00746 $i=60.8^\circ$	1,8*	11,8**	8,5**	5,7**	21,5***			
00082 $i=38.9^\circ$	2,5*	1,1*	6,1**	3,1**	2,5**	2**	1,2**	26***F 9***
00016 $i=34.3^\circ$	1,8*	11,7**	6,1**	3,6**	2,8**	2,3**	1,5**	11,2***
00005 $i=34.2^\circ$	1,8*	6,1**	4,9**	3,4**	2,2**	25,5***	11***	
00020 $i=33.4^\circ$	1,3*	8**	6**	4,4**	1,2**	25,8***		
00011 $i=32.9^\circ$	1,1*	6,1**	4,1**	2,5**	25,5***			
00963 $i=19.75^\circ$	1,8*	11,7**	6,1**	3,4**	1,8**	26,8***	9***	

F – faint period

In order to eliminate the influence of the trend components we subtracted the 3rd order polynomial. Then frequency filtering of periodicities more than three years was conducted.

As a result of calculations in Fig. 3 we found periods of 9 – 12,7 days and 1,3 – 2,5 years. For the elliptic orbit satellites periods of: 1 year; 1,8 years and 2,5 years. For the circle orbit satellites periods of: 1 year; 1,2 years; 2,4 – 2,5 years.

6.3. Calculations of the spectrograms for data with subtracted trend

To identify the time of existence of periodic components the program PSELab was used [6]. The result of its application to the Equatorial satellite 25064 is shown in Figure 4.

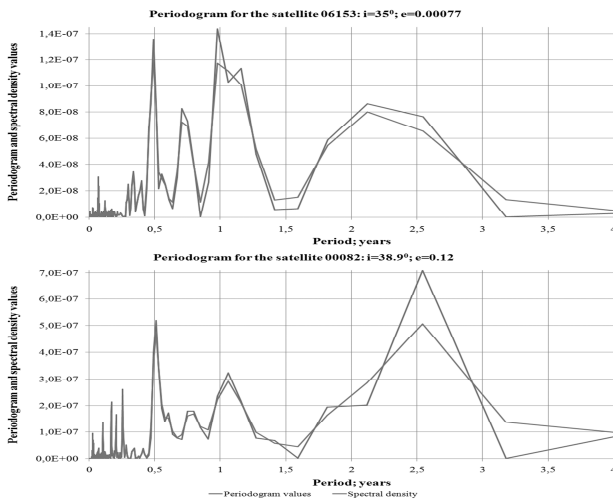


Figure 3: Periodograms with subtracted trend for satellites: 06153 and 00082.

Table 3 shows periods of «circular» and «elliptic» satellites after subtract of the trend components. It lists periods from 2,5 years to 3 months that have maximum spectral power, and periods of less than one month with less spectral power. There are: around annual, semiannual and 27 day periodicities for the «circular» and «elliptic» satellites. For the «circular» satellites we found periods of 2 – 2,5 years and for the «elliptic» satellites – near to biennial periods.

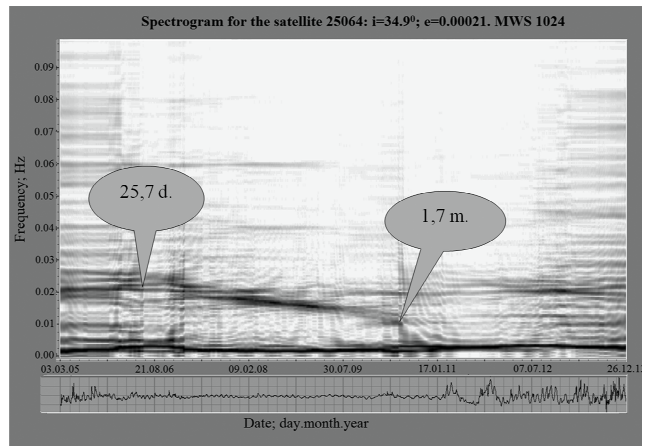


Figure 4: Spectrogram for the Equatorial satellite 25064.

In Figure 4 marked period with trend from 25,7 days to 1,7 month. For satellites: 00063, 00165, 25064, 00932 and 00746 – detected periods with trend from 25 – 28 days to 1 – 1,7 month, and for the satellite 00165 – from 6,4 to 7,2 days.

Table 4.

Number of satellite	Periods: Year - *, Months - **, Days - ***.							
satellites with circular orbit								
25860 $\varphi=97.7^\circ$	1,3*A	5,6**G(F on D,M)	26,3***F on A	14,7***F on D,M	13,6***F on D,M			
27700 $\varphi=97^\circ$	1,2*A	6,4**G(FT on D,M)	26,1***F on A	13,5***F on A	9***F on D,M			
12054 $\varphi=65^\circ$	1,4*A	5,8**G(FT on D,M)	13,5***F on A	26***F on A	13,3***F on A	8,9***F on D,M		
00397 $\varphi=53.3^\circ$	1,6*A	6**G(F on D,M)	26,1***F on A	10,6***M(F on D,G)	9***M			
00063 $\varphi=48.5^\circ$	1,5*A	5,9**G(FT on D,M)	26,2***F on A	23,2=>13,7***D,M	8,9***D			
00165 $\varphi=47.9^\circ$	1,4*A	1*G	5,9**G(F on D,M)	26,7***F on A	6,4=>7,2***M			
06153 $\varphi=35^\circ$	1,5*A	9,1**G(FT on D,M)	5,9**G(F on D,M)	2,1*D,M	26,3***F on A	11,2***D,M(F on G)	9,5***D,M(F on G)	
25064 $\varphi=34.9^\circ$	1,3*A	5,8**D,G(F on M)	25,7***F on A	29,***=>1,2**M	9***F on D,M			
23757 $\varphi=22.9^\circ$	1,4*A	5,7**G(F on D,M)	26,1***F on A	13,5***F on D,M	9***F on D,M			
satellites with elliptical orbit								
00932 $\varphi=61.3^\circ$	1,3*FT on A	6,1**G(F on D,M)	2,9**A	25,7***F on A	12,9***A	10,2=>9,7***D,M	2,2***A	
00721 $\varphi=78.6^\circ$	1,7*F on A	9,9**A	5,4**G(FT on D,M)	3,7**G(FT on D,M)	2,9**A	12,6***A	11,2***A	10,5***A
00829 $\varphi=60.8^\circ$	2,1*F on A	5,6**A(F on D,M)	2,6=>1,3**D,M	26,2***F on M	12,3***F on A			
00746 $\varphi=60.8^\circ$	1,3*FT on A	8,6**FT on A	5,4**A	12=>12,7***D,M				
00082 $\varphi=58.9^\circ$	2,5*A(F on M)	5,8**G(F on M)	3**M(FT on G)	2,4**D(FT on M,G)	2**F on A	1,2**A	11,9***G(F on D,M)	10,4**G(F on D,M)
00016 $\varphi=34.3^\circ$	1,4*D(F on M,G)	5**G	3,5**D,M(F on G)	2,2**F on A	1,4**F on A	11,2***F on A		
00005 $\varphi=34.2^\circ$	1,8*A	1,1*G	5**D,G	3,2**F on A	2,1**F on A	1,4**F on A	26,7**F on A	11***F on A
00020 $\varphi=33.4^\circ$	1,3*A	5,9**G(F on D,M)	12,6***F on D,M	10,7***F on D,M				
00011 $\varphi=32.9^\circ$	1,1*A	6,1**FT on A	25***F on A					
00963 $\varphi=19.75^\circ$	1,4*FT on A	7,3**A	1**F on A	25,6***F on A	9***D,M			

F – faint period; FT – fitful period; D – on the declining phase of the 23rd solar cycle; G – on the rise phase of the 23rd solar cycle; M – on the minimum phase; A – on all observation period.

Table 4 shows the most significant periods of spectrograms for all of the objects. The period of about 0,5 years is present on all observation period for all circle orbit satellites. Such period was detected for elliptic orbit satellites. Periods more than one year are present at the entire range of observations not for all satellites.

7. Conclusions

As a result of the calculation using the programs: OriginPro 8.1, STATISTICA 8 and PSELab have been found:

- 1) difference in the drag dynamics of the satellites at the minimum of the 23rd solar cycle and at the beginning and maximum of the 24th solar cycle;
- 2) the offset of maximum amplitude from short-period variations (up to 0,5 year) in the declining phase of the 23rd solar cycle, to the long-period variations (from 0,5 year to 2,5 years) in the raise phase of the 24th solar cycle;
- 3) periods were detected with trend from 25 – 28 days to 1 – 1,7 month, and for the satellite 00165 – from 6,4 to 7,2 days.

Using Fourier analysis identifies short-periodic components from 11 to 14 days for the circle orbit satellites and 12,7 days for the elliptic orbit satellites. Detected periods with trend probably are related to the dynamics of influence of solar and geomagnetic activity and tidal phenomena on the upper atmosphere of the Earth.

The following steps assume the equating of the received data with the manifestations of solar activity and magnetic storms. The purpose of such research is the consideration of various factors in the prediction models of the upper atmosphere of the Earth.

References

1. Beletsky V.V.: 1965, *The motion of an artificial satellite about the center of mass*, M., 416 p.
2. Roy A.: 1981, *Orbital motion*, M.: Mir, 544 p.
3. Marple S.L.: 1990, *Jr. Digital spectral analysis with applications* (Trans. from english), M.: Mir, y., 584 p.
4. Oppenheim A., Schafer R.: 2006, *Digital signal processing*, M.: Technosphere, 856 p.
5. NORAD [web resource] /North American Aerospace Defense Command. Access mode: <http://www.norad.mil/>.
6. PSELab [web resource] /Power Spectrum estimation laboratory, Access mode: <http://pselab.ru/>.
7. Felix R. Hoots, Ronald L. Roehrich. SPACETRACK Report No.3 [web resource] / Models for Propagation of NORAD Element Sets, 1980. Access mode: <https://celestrak.com/NORAD/documentation/spacetrk.pdf>.

THE STUDY OF INDICATRICES OF SPACE OBJECT COATINGS IN A CONTROLLED LABORATORY ENVIRONMENT

Koshkin N., Burlak N., Petrov M., Strakhova S.

Astronomical observatory of Odessa university, Odessa, Ukraine
nikkoshkin@onu.edu.ua

ABSTRACT. The indicatrices of light scattering by radiation balance coatings used on space objects (SO) were determined in the laboratory experiment in a controlled condition. The laboratory device for the physical simulation of photometric observations of space objects in orbit, which was used in this case to study optical properties of coating samples, is described. The features of light reflection off plane coating samples, including multi-layer insulation (MLI) blankets, metal surfaces coated with several layers of enamel EP-140, special polyacrylate enamel AK-512 and matte finish Tp-CO-2, were determined. The indicated coatings are compound reflectors which exhibit both diffuse and specular reflections. The data obtained are to be used in the development of computer optical-geometric models of space objects or their fragments (space debris) to interpret the photometry results for real space objects.

1. Introduction

The optical-geometric modelling of a target object and its observing conditions is applied to test of methods for obtaining information on the properties and behaviour of space objects in orbit using photometric observations. To that end, both computer (Melikyants, 2007; Willison & Bédard, 2015), and physical (Koshkin, 1989) simulations have been used in the Department of Space Research of the Astronomical Observatory of Odessa University.

Proper simulation supposes knowledge of optical properties of space object surfaces, namely light-scattering indicatrices and spectral reflectance. Ideal (either theoretical or empirical) functions for light scattering from uniform surfaces (Fairbairn, 2005) are often used to simplify the problem. However, when sensing man-made objects and surfaces, such ideal functions are hardly feasible and provide results which are inconsistent with observations (Früh & Schildknecht, 2012).

The spectral scattering function or its approximation in either numerical or analytical form should be factored in the computer simulation model (Kanzler, 2015). The geometric conditions of lighting and photometry similar to those for the real objects should be adhered to in case of physical simulation in a controlled laboratory environment with space object models (Koshkin, 1985). It means that when conducting measurements in the laboratory, the conditions of integrated photometric measurements of the space object model as a point-like object should be abided; the model illumination should be provided by a source of light generating the spectral intensity

distribution in the visible spectrum close to the solar one (for colorimetric measurements) with the light beam divergence of about 30'.

The kinematic design of the simulation device should provide the required motion of the model relative to the observer and light source (including the model's spatial orientation and compound rotation around given axes), as well as simulation of simultaneous change of the phase angle, etc.

Scale similarity between the model and target space object, correspondence of coatings' optical properties and simulation of the space object spatial motion ensure conformity between the model photometry and actual observations of the space object.

The aim of this study is to exploit kinematic and photometric capabilities of the laboratory device to measure indicatrices of several real coatings used to radiation balance of space objects. Then, the data obtained can be used in the development of relevant optical-geometric models of space objects or their fragments (space debris).

2. The device for simulation in a controlled laboratory environment

The manufactured device for simulation of the space object photometric observations and measurements of sample indicatrices in a controlled laboratory environment contains three component units: the unit for model (sample') placing and rotation, illumination assembly and photometer.

The model illumination assembly. In terms of design, the model illumination assembly is a collimating system. An aperture of diameter D , which is overlapped by frosted glass and backside illuminated by a high-intensity halogen lamp KGM-12-40 with heat-reflection filter, is placed in the focal plane of the collimating lens. The required light beam divergence of about 30', which simulates the divergence of solar flux, is achieved with the relevant ratio between the diameter of "illuminated" aperture and collimator focus length F .

The photometer unit. The photometer unit is designed for the measurement of the luminous flux from the model as a point-like object. In terms of design, it is achieved by using a long-focus integrating lens with a diameter which exceeds the model size, and thus, is capable to trap all parallel light rays passing from the model towards the photometer. There is a pinhole aperture with the diameter $d = 1$ mm in the focal plane of the lens, which cuts off all

rays from the model at angles exceeding .050. The Fabry lens is attached behind the aperture; it creates an image of the aperture illuminated with the light from the model on the photocathode of light detector – in our case photomultiplier tube FEU-136. The photometer is provided to mount a filter wheel containing three band-pass filters which enable to determine the model's colours in three spectral regions, namely blue, green and red, close to TV-color system.

The mounting of model (sample) placing and rotation.

This assembly comprises an annular guide to mount the small-type stepper motor on whose axis is fixed the model – that ensures proper spatial orientation of the rotation axis. The rotation axis of the observed sample or model keeps its position with respect to the light source and can rotate along with that source relative to the photometer. In the course of all motions and rotations the sample is always kept in the centre of the light beam from the light source and within the photometer field of view.

The whole device was assembled and exploited in the blacked out room. Auxiliary mechanical parts which get into the photometer field of view or the flux from the light source at some conditions, were blackened with black matte finish to eliminate glares and stray extraneous light spots.

3. The study of light-scattering indicatrix of different SO coatings

Different types of coatings are used to maintain proper thermal balance inside of a space craft when it moves outside the Earth's atmosphere, namely multi-layer insulation (MLI) blankets, enamels with various light-scattering properties, metal surfaces, etc. Moreover, spacecrafts usually equipped with solar arrays with photoelectric transducers covered with protective coatings of fused silica, other optical assemblies and components.

Coatings used in the space have different reflectance properties in the visible wavelength range depending on the coating material and its surface microstructure. In general, to describe the reflectance profile for a given surface, it is suggested to use the spectral bidirectional reflectance distribution function (sBRDF) f_r (Willison & Bédard, 2015), which is determined from formula:

$$f_r(\theta_i, \phi_i; \theta_r, \phi_r; \lambda) = \frac{dL_r(E_i; \theta_i, \phi_i; \theta_r, \phi_r; \lambda)}{L_i(\theta_i, \phi_i; \lambda) \cdot \cos \theta_i \cdot d\omega_i} \quad [\text{sr}^{-1}]$$

where L_i and L_r are incident and reflected luminous flux, respectively, and other notations can be understood from Figure 1. It should be noted that sBRDF does not depend on the surface area.

Specific character of the LEO observations is related to their motion with respect to an observer and their rotation around the centre of mass. These factors cause changes in the solar illumination angle, as well as in the angle at which the object is visible to the observer. Therefore, it is suitable to use as a representation of spatial indicatrices a set of expressions of the correlation between the coating sample brightness (in the broadband system) and the angle of its rotation α relative to the phase-angle bisector, at the fixed values of the latter. In this case, all measurements are performed in one and the same plane, that is: $\varphi_i = 0^\circ$; $\varphi_o = 0^\circ$ or 180° .

The angle α varies within the range of $\pm(\pi/2 - \beta/2)$ (see Fig. 1,b).

Using the laboratory simulation device we carried out the study of multi-layer coatings consisting of the atmosphere-resistant epoxy enamels EP-140, special polyacrylate enamels AK-512 and matte finish coatings Tp-CO-2 (Simulation, 1971; Ivanov, 1969), as well as MLI blankets covered externally of white glass fabric.

The brightness of the illuminated coating sample in the linear (or logarithmic) scale in relative units is shown along the Y-axis in the below-presented images of the spatial indicatrix sections. The brightness was determined by measuring the intensity of the reflected luminous flux and its normalisation to account for the geometric factors. The X-axis shows the angle of the sample's rotation in the phase-angle plane determined as the angle between the normal to the mean plane of the sample's surface and the phase-angle bisector.

The measurements were conducted at three different phase angles within the range of 45° - 135° . The speciality of such measurement and representation of indicatrices is that the start point of the plotted curve corresponds to grazing incidence of the light beam onto the sample therefore several first points of the curve correspond to the

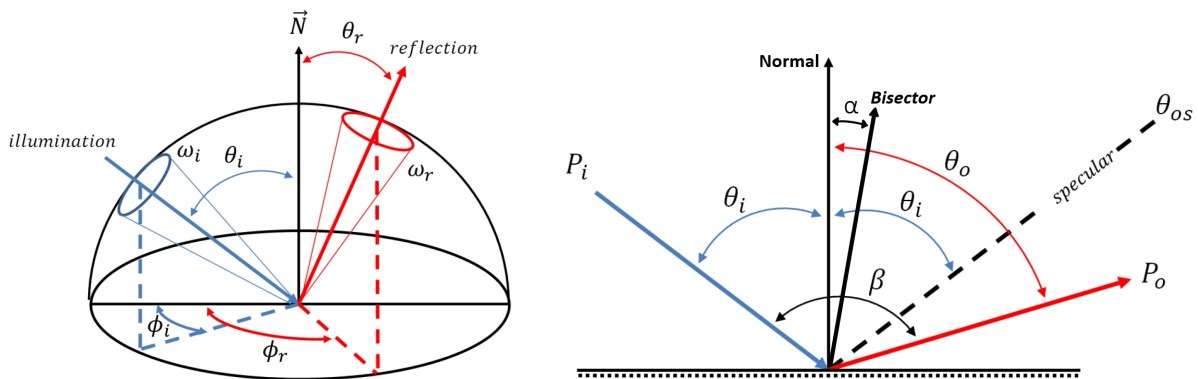


Figure 1: a) The spatial geometry of the light scattering from surface piece (adopted from Willison, 2015); b) The geometry of indicatrix measurements in the phase-angle plane; the β is phase angle.

interval when operation lighting conditions for that sample are achieved, and the indicatrix in this segment can be inconsistent with the actual brightness of the coating. The ending points of the curve must correspond to the observation of the sample surface at the angles close to 90° , and division by the relevant reflection angle cosine results in wider spread of points in this segment of the graph.

D1 – Material: Alloy AMg6M. Coating: primer AK-070 (1) Industry Standard (OST) 6-10-401-76. Enamel EP-140, white (2) Specifications (TU) 6-10-599-74. Enamel AK-512, white (2) State Industry Standard (GOST) 23171-78 and VD 23171-78.

Let us proceed to the discussion of the obtained indicatrices of light-scattering by coating samples. Fig. 2 shows the brightness indicatrices of the plane sample D1 coated with the primer AK-070 (one layer), enamel EP-140 of white colour (two layers) and enamel AK-512 of white colour (two layers). This coating is a compound reflector of light which exhibits both diffuse and specular reflections. At small phase angles ($\leq 45^\circ$), the inner diffuse reflection prevails over the brightness of specular reflection off the external layer. The diffuse reflection indicatrix is just slightly deformed comparing to the ideal Lambert's indicatrix for which the brightness does not depend on the angle at which the coating sample surface is observed (Ivanov, 1969). With the increased phase angle the specular reflection brightness increases rapidly, and at $\Phi=120^\circ$ it is 10-100 times higher than the diffuse reflection brightness.

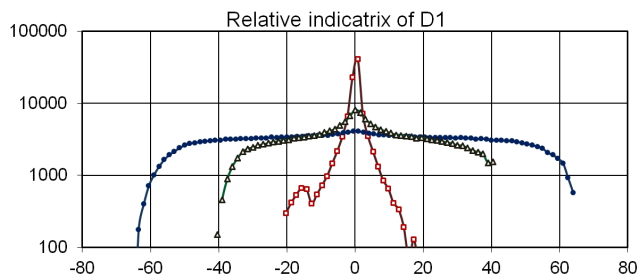


Figure 2: Brightness indicatrix of flat sample D1 for different phase angles: full circles – $\beta=45^\circ$, open triangles – $\beta=90^\circ$, open squares – $\beta=135^\circ$.

Apart from the discussed ones, the indicatrices of the same coating were obtained with different orientation of the phase-angle plane relative to the sample (the phase-angle plane is rotated by 90° with respect to the normal to the sample). The characteristics of these curves have not changed comparing to the data presented in Fig. 2, which were obtained at the same phase angles.

It is necessary to pay attention to the behaviour of spectral content of the light reflected off the coating sample D1. We conducted preliminary measurements of the three-colour reflectance for this and other samples at different phase angles. At that, a noticeable redshift of the light reflected by the coating sample D1 at the instants of specular component appearance can be marked out. The degree of this redshift increases with the increasing phase angle.

D2 – Material: Alloy AMg6M. Coating: Enamel AK-512, white (2) State Industry Standard (GOST) 23171-78. Matte finish Tp-CO-2 (2) Industry Standard (OST) 92-1000-76.

The plane surface of the second coating sample labelled in our study as D2 is coated with two layers of enamel AK-512 and two layers of white matte finish Tp-CO-2. The indicatrices of light-scattering by this coating sample are shown in Fig. 3. In contrast to the above, this coating sample only exhibits the diffuse reflection component in the studied range of phase angles with the reflection indicatrix close to the Lambert one. A perceptible specular component appears at the phase angles $\geq 160^\circ$ while the indicatrix which is just slightly elongated in the direction of the specular reflection can be observed at smaller phase angles (120° - 140°).

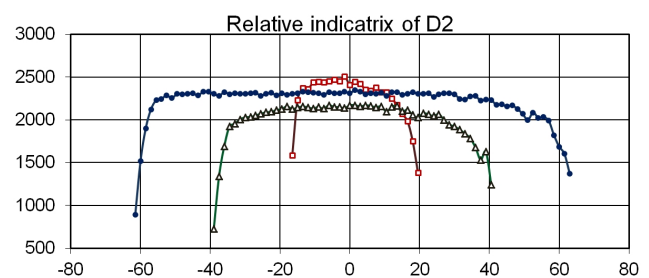


Figure 3: Brightness indicatrix of flat sample D2 for different phase angles: full circles – $\beta=45^\circ$, open triangles – $\beta=90^\circ$, open squares – $\beta=135^\circ$.

The light-scattering indicatrices of the plane sample of the MLI exterior coating which is made of white glass fabric, is presented in Fig. 4.

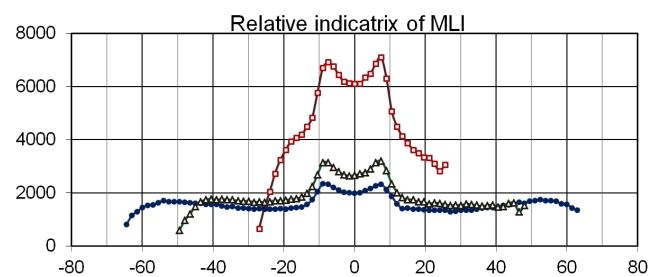


Figure 4: Brightness indicatrix of flat sample MLI for different phase angles: full circles – $\beta=45^\circ$, open triangles – $\beta=75^\circ$, open squares – $\beta=120^\circ$.

The cell structure of this coating sample, as well as its high transparency (transmission up to 40% of the solar radiation), results in complex behaviour of its brightness with changing lighting and observation conditions. Its indicatrix exhibits several brightness peaks, the highest two of them, i.e. the pre- and post-specular reflections, which are symmetric with respect to the specular reflection from the coating sample surface. Moreover, the local brightness maximums are observed when either the angle of light incidence or the angle of observation is approaching to the grazing one; at that, the maximum brightness values and their extent increase with decreasing phase angle; meanwhile, such maximums are not observed

at $\Phi > 90^\circ$. The study of indicatrices of glass fabric samples with the substrate of light-absorbing material or corrugated aluminium foil showed their identity, though the total brightness was slightly higher for the second sample. However, the presence of two accentuated directions on the glass fabric surface due to the material filament flow also results in the dependence of the spatial scattering indicatrix on the position of the phase-angle plane relative to those marked out directions.

Fig. 5 shows the indicatrices of the MLI coating sample when the phase-angle plane makes an angle of 45° with the glass fabric filament flow. In this case, the double brightness peak (corresponding to the pre- and post-specular reflections) is significantly broadened, and the brightness increase at large angles of light incidence and reflection is no longer observed. It should be noted that the angular distance between the pre- and post-specular peaks does not depend on the phase angle; however, it depends on the orientation of the MLI blanket sample.

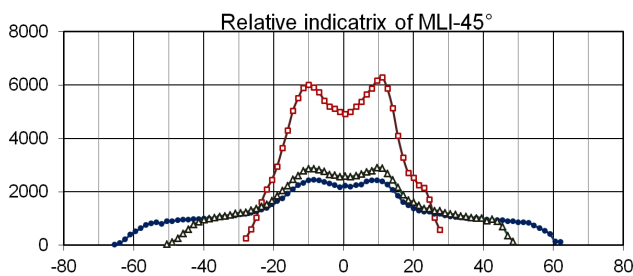


Figure 5: Brightness indicatrix of flat sample MLI for different phase angles: full circles – $\beta=45^\circ$, open triangles – $\beta=75^\circ$, open squares – $\beta=120^\circ$.

Space object surface-integrated indicatrix of this coating sample with the surface imperfections was also investigated (such ‘quilted’ MLI blanket is apparently tufted across, and there is some curvature, as well as structural elements on the space object surface). The indicatrices of the MLI blanket sample with soft plane base tufted in the square lattice points with stitch spacing of ~ 5 mm and the depth of local imperfections of ~ 5 mm, which cause a significant surface curvature of sample (MLI-G-15), are also investigated. It should be noted that at the phase angles of 40° – 60° the surface-integrated indicatrix appears smoothed with just a subtle elongation in the direction of the specular reflection from the mean surface. At the phase angles $\geq 90^\circ$ this brightness peak tends to double due to the glass fabric structure. With the lower ratio between the stitch depth and spacing, i.e. with the relatively smaller scale of imperfections on the MLI coating, the indicatrix takes the form which is typical for the plane coating sample. It is evident that any imperfections on the space object surface can not significantly change the integrated indicatrix of the MLI coating.

In addition to the above-described coating samples, the solar array cell indicatrix was also measured. Due to the smooth polished dielectric surface of the solar cell coating, the indicatrix has the form of the δ function; and the linear dynamic range of the photometric equipment is not sufficient to measure the drop in brightness when

either diffuse or specular reflection off this coating sample occurs. However, as is known, the solar arrays consist of many thousands of solar cells, and because of parallel misalignment of their surfaces the integrated indicatrix will not be close to the δ function due to large deviations in averaging of individual indicatrices; moreover, there are such design features as parallel misalignment of the solar panel sections and their flexure; therefore, when modelling photometric characteristics of the solar array working plane, it is only the similarity of the indicatrix integrated parameters that should be sought.

4. Conclusions

To ensure the photometric, as well as geometric, equivalence of models (physical and mathematical ones) and real space objects, it is essential to use coatings identical in their optical properties. Moreover, it is necessary to aim at correct simulation just of those surface-integrated photometric characteristics of large components and object integrally. To that end, we carried out the measurement of optical properties of a set of original coatings, in particular, their light-scattering indicatrices in the visible spectrum. The indicatrix of light scattering from the surface is essential in the integrated photometry (in the visible wavelength range) as an instrument of optical remote sensing, because it specifies the spatial structure of light-scattering field, and thus, the appearance of the light curve expressing the brightness change with time, which provides information on the physical properties of the object itself.

References

- Bédard D., Lévesque M., Wallace B.: 2011, in *Proc. of AMOS Conf.*
- Bédard D., Wade Gregg A.: 2014, in *Proc. of AMOS Conf.*
- Früh C., Schildknecht Th.: 2012, 63-rd International Astronautical Congress, Naples, Italy, IAC-12-A6.2.6.
- Fairbairn M.B.: 2005, *J. of the Roy. Astron. Soc. of Canada*, **99**, No. 3, p.92 (2005JRASC..99...92F).
- Ivanov A.P.: 1969, *Optics of scattering media. Nauka i Technika*, 592.
- Kanzler R. et al.: 2015, in *Proc. of AMOS Conf.*
- Koshkin N.: 1985, The laboratory device for simulating the observations of space objects. Certificate of authorship UdSSR No. 229507 – 1985.
- Koshkin N.I.: 1989, *Astronomicheskij Vestnik* (Moscow, USSR), **22**, No. 2, 159 (1989RpScT...2...13K). (English: JPRS Report: Science and Technology. USSR: Space p.13 (SEE N89-29354 24-12))
- Melikyants S., Shakun L. et al.: 2007, *Odessa Astron. Publ.*, **20**, 72 (2007OAP...20...72M).
- Simulation of thermal conditions of the spacecraft and its environment /Eds. G.Petrov and M.Kroshkin, Mashinostroenie, 1971, P. 382.
- Willison A., Bédard D.: 2015, in *Proc. of AMOS Conf.*

RESEARCHES OF LONG-TERM VARIATIONS IN URANUS AND NEPTUNE SPECTRA

Yu.Kuznyetsova¹, A.Vidmachenko¹, O.Matsiaka², Y. Shliakhetskaya¹, M.Yushkin³, V.Krushevskaya¹

¹Main astronomical observatory of National Academy of Science of Ukraine, 27 Akademika Zabolotnoho ave. 03680 Kyiv, Ukraine

²Taras Shevchenko University of Kyiv, 64/13, Volodymyrska Street, Kyiv, Ukraine, 01601

³Special astrophysical observatory of Russian Academy of Sciences, Nizhnij Arkhyz, Karachai-Cherkessian Republic, Russia 369167

ABSTRACT. The results of long-term spectral observations of Solar System giant planets Uranus and Neptune are presented here. Data were obtained in period 2002-2012 at the peak Terskol Observatory (Northern Caucasus, Russia) using 2-meter Ritchey-Chretien telescope Zeiss-2000 with help coude echelle spectrograph and at the Special astrophysical observatory (SAO RAS, Northern Caucasus, Russia) with help 6-meter telescope using echelle spectrograph NES.

Raman light scattering of solar photons by hydrogen molecules in the atmosphere spectra of Uranus and Neptune was registered in most powerful Fraunhofer lines H&K CaII as the "emission" details in center cores of these lines. Relative values of Raman scattering contribution for noted lines are estimated. Also, we have carried out long-term monitoring of Raman light scattering variations in cloudy surface spectra.

Key words: Uranus; Neptune; giant planets; Raman light scattering; Fraunhofer lines H&K CaII.

1. Introduction

Raman scattering makes contribution to spectra because of prevailing content H₂ molecules (85%) in giant planet atmospheres (Cochran & Trafton, 1978; Cochran, 1981). Raman effects in such powerful atmospheres arise in visual and UV spectral ranges. Our data were obtained in visual wavelength region. It is possible to register Raman effects only with high resolution and sufficient ratio signal/noise.

We have carried out long-term spectral observations of Solar System giant planets Uranus and Neptune. The main aims of this work are registration of Raman light scattering of solar photons by hydrogen molecules in the atmosphere spectra of Uranus and Neptune; relative value calculation of Raman scattering contribution to giant planet spectra in field of most powerful Fraunhofer lines H&K Ca II; researching of possible long-time variations of Raman light scattering in spectra of Uranus and Neptune.

2. Raman Light Scattering

Raman light scattering can be described as incoherent nonresonant scattering of photons by molecules. The

incident light which suffers the Raman scattering is just the solar spectrum. Raman light scattering is used as a diagnostic probe of planetary atmospheres because Raman spectra characterize the properties of molecules of the scattering medium (Cochran, 1981).

Raman scattering has an observable effects in planet spectra in UV and visual range. When the sunlight passes through the gas atmosphere of the planet Raman light scattering makes not deep "ghosts" in the spectrum of the scattered light (Wallace, 1972; Karkoschka, 1994). These ghosts have Rayleigh line profile and placed symmetrically on the left and on the right relatively absorption line. These shifted lines are called the Raman lines (ν_R). Each type of molecules makes own set of Raman lines:

ν_0 – Vibration frequency of incident light,

ν_R – Frequencies of shifted (Raman) lines

$(\nu_0 - \nu_R) = \omega$ – Own frequency of molecule vibration

$\nu_R^S = \nu_0 - \omega$ – Red (Stoks) «ghosts»,

$\nu_R^A = \nu_0 + \omega$ – Blue (antistoks) «ghosts».

Also Raman light scattering makes the pseudo-emission features in center cores of solar lines. About 10% of the incident photons are being Raman scattering. Intensity of Fraunhofer lines in solar light reflected by planet atmosphere is less then in Solar spectrum. Therefore after exclusion of the solar spectrum in planet spectrum at the sites of the Fraunhofer lines H&K CaII appear the "emission" details (pseudo-emission peaks). According to these works (Belton et al., 1973; Cochran & Trafton, 1978; Karkoschka, 1994) the intensities of "emission" details in cores of H&K CaII defined using low spectral resolutions can achieve 10-20%.

3. Observations and data processing

Most of spectroscopic observations were carried out at 2-meter telescope of the peak Terskol Observatory (Northern Caucasus, Russia) with using high resolution coude echelle spectrograph [<http://www.terkol.com/telescopes/maestro.htm>] (Musaev, 1999; Kuznyetsova & Bondar, 2002). Spectra were obtained during 2002-2012 in visible range about 3800-9000 Angstroms. Data for 2007 and 2008 year were obtained at

Special astrophysical observatory (SAO RAS, Northern Caucasus, Russia) with help of 6-meter telescope using echelle spectrograph NES located at the Nasmyth-2 focus (1:30). Spectra were obtained in visible range about 3500-6000 Angstroms.

Spectral resolution $R=45000$ for observations by both telescopes was used. Using such equipment it is possible to detect Raman light scattering by H_2 in the atmosphere spectra of major planets. Catalog of obtained data are presented in Tab. 1.

Solar type standard 16Cyg A was used as a comparison star for all data except Neptune (June 2002). For it was used solar type standard 35 Leo. Standard data processing were done using program pockets DECH95, DECH20T for Terskol data and MIDAS for SAO data.

4. Results

As mentioned above, Raman light scattering is the cause of appearance of pseudo-emission features in the Fraunhofer line center cores. This fact can be used as an excellent diagnostic probe of planetary atmospheres.

After exclusion of solar spectrum performed by division on the spectrum of solar-type standard, in spectra of Solar system giant planets at the sites of the Fraunhofer lines H&K CaII appear the "emission" details (Morozhenko, 1997; Kuznyetsova & Vid'machenko, 2005). So, we can obtain clear contribution of Raman light scattering in the region of cores H&K CaII after exclusion solar spectrum.

We have estimated intensity values of pseudo-emission peaks placed in centers of solar H&K CaII lines for Neptune and Uranus using our observational spectra. Results are presented in Tab. 2, Tab. 3.

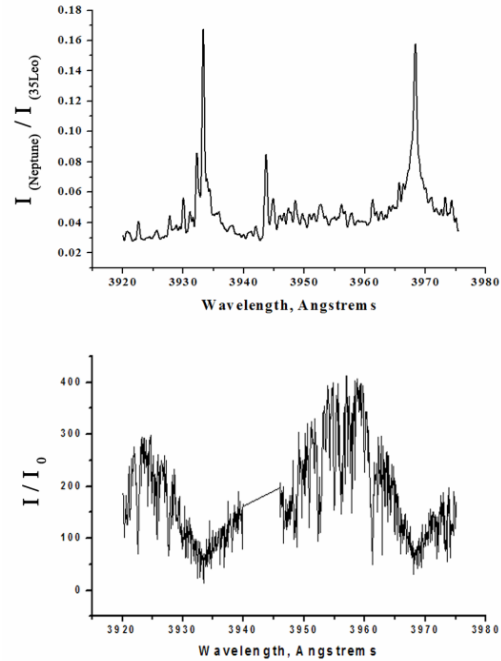


Figure 1: Spectrum of Neptune and the ratio spectrum Neptune/35 Leo in the vicinity of the Solar CaII H&K lines (June 2002).

Uranus. Comparative variations of central intensities of Raman light scattering "emission" peaks in the field of lines H&K CaII for 2007 and 2008 are shown at Fig. 2. Evaluations of central intensities of Raman light scattering "emission" peaks for Fraunhofer lines H&K CaII are presented in Tab. 2. Relative intensity values of central pseudo-emission peaks have significant variations in the range 30-57%. Probably, it can be explained due to the fact that Uranus was changing their position from 2007 to 2012 and different regions of cloudy surface fell into the field of view. Fig. 3 shows the positions for Uranus disks towards Earth for each observation date.

Table 1. Log of presented spectral data

Object	Data	Observatory	Number of expositions	Exposition time, sec
Uranus	30.09.2007	SAO, 6-m	4	900
	13.08.2008	SAO, 6-m	4	900
	01.12.2008	Terskol, 2-m	2	2700
	11.10.2011	Terskol, 2-m	2	1800
	29.11.2012	Terskol, 2-m	2	1800
Neptune	10.06.2002	Terskol, 2-m	2	3276
	30.09.2007	SAO, 6-m	3	2400
	13.08.2008	SAO, 6-m	5	2700
	02.12.2008	Terskol, 2-m	2	3600
	11.10.2011	Terskol, 2-m	2	3000
	21.11.2012	Terskol, 2-m	2	2700

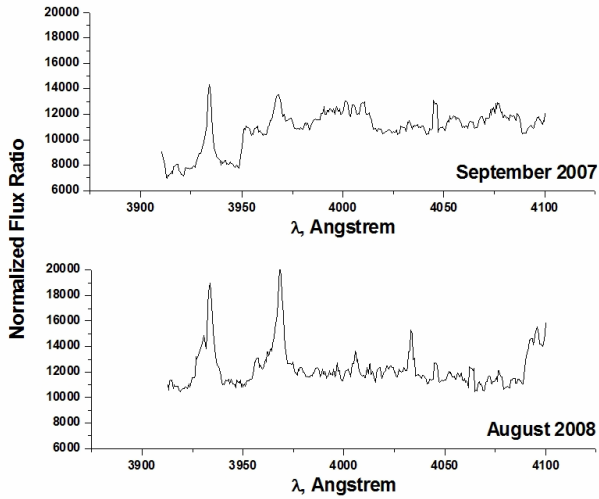


Figure 2: Raman scattering spectra of Uranus in the field of H&K CaII lines.

Table 2. Evaluations of central intensities of Raman light scattering “emission” peaks for Fraunhofer lines H&K Ca II

Data	S/N	H Ca II 3968.5 Å	K Ca II 3933.7 Å
September 2007	40	56%	43.5%
August 2008	40	57%	43.2%
December 2008	40	57%	43.1%
October 2011	40	47.6%	30%
November 2012	40	44.4%	44%

Neptune. Comparative variations of central intensities of Raman light scattering "emission" peaks in the field of lines H&K CaII for 2007 and 2008 are shown at Fig. 3. Relative intensity values of central pseudo-emission peaks in center cores of lines H&K CaII for Neptune have less noticeable variations then for Uranus. They are in the range 40-50% from 2007 to 2012. Estimations for 2002 show considerably smaller values because of low signal/noise relation. Fig. 5 shows Uranus was changing their position from 2007 to 2012. Evaluations of central intensities of Raman light scattering "emission" peaks for Fraunhofer lines H&K Ca II are presented in Tab. 3.

Table 3. Evaluations of central intensities of Raman scattering “emission” peaks for Fraunhofer lines H&K Ca II

Data	S/N	H Ca II 3968.5 Å	K Ca II 3933.7 Å
June 2002	15	25.4%	10.7%
September 2007	40	46.5%	40.1%
August 2008	40	42%	40%
December 2008	30	40%	40%
October 2011	40	45%	42%
November 2012	30	50%	40.2%

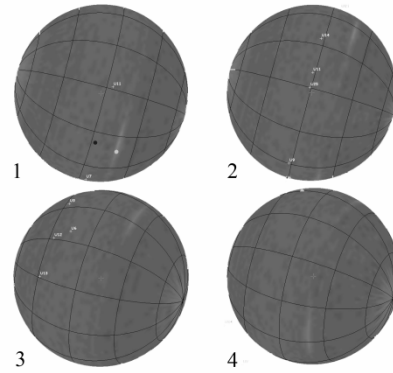


Figure 3: Positions of Uranus towards Earth for observation dates: 1-2007, 2-2008, 3-2011, 4-2012.

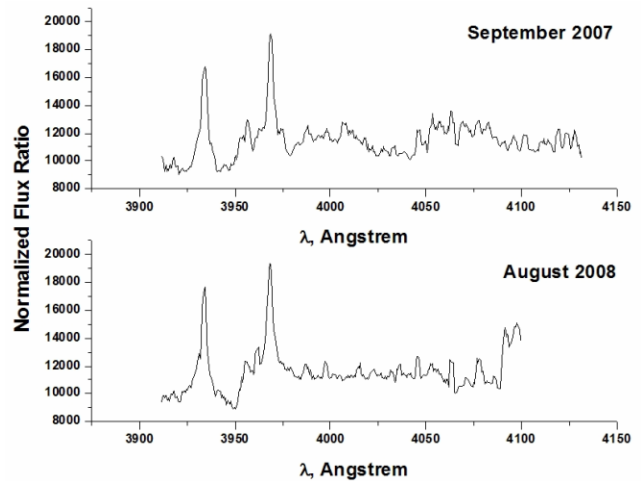


Figure 4: Raman scattering spectra of Uranus in the field of H&K CaII lines.

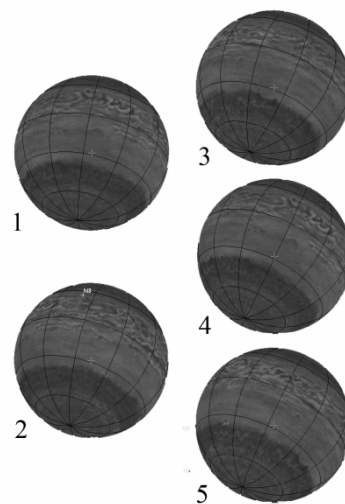


Fig.5. Positions of Neptune towards Earth for observation years: 1-2002; 2-2007, 3-2008, 4-2011; 5-2012.

5. Conclusions

So, based on the long-term spectral observations of Solar system giant planets Uranus and Neptune, we have got such results:

1. Raman scattering is registered for all Uranus and Neptune spectra obtained from 2002 to 2012 years.
2. Estimates of clear Raman light scattering contribution in central cores of H&K Ca II are changed in the range 10-56%. Such high values compared with results of other researches can be explained by the high spectral resolution ($R=45000$) of observations.
3. Reasons of variations of Raman scattering values can be aerosol clouds in planet atmosphere placed on differ heights. These clouds change the depth of gas column and respectively the values of Raman light scattering are vary.
4. "Ghosts" of H&K CaII lines were not registered due to insufficient level of ratio Signal/Noise.

References

- Belton M.J.S., Wallace L., Price M.J.: 1973, *Astrophys. J.*, **184**, №3, 143.
- Cochran W.D., Trafton L.M. et al.: 1978, *Astrophys. J.*, **219**, 756.
- Cochran W.D.: 1981, *Adv. Space Res.*, **1**, 143.
- Karkoschka E.: 1994, *Icarus*, **111**, N 1, 174.
- Kuznyetsova Y., Bondar A.: 2002, *J. Phys. Studies*, **6**, N4, 411.
- Kuznyetsova Y., Vid'machenko A.: 2005, *Kinematics and Physics of Celestial Bodies*, **Suppl. Ser.**, **N 5**, 480.
- Morozhenko A.: 1997, *Kinematics and Physics of Celestial Bodies*, **13**, **N 4**, 22.
- Musaev F., Galazutdinov G., Sergeev A. et al.: *Kinematics and Physics of Celestial Bodies*, 1999, **15**, **N 3**, 282.
- Wallace L.: 1972, *Astrophys. J.*, **176**, 249.

IDENTIFICATION OF EMISSION LINES IN A METEOR SPECTRUM OBTAINED ON AUGUST 2, 2011

A.M.Mozgova¹, J.Borovicka², P.Spurny², K.I.Churyumov¹

¹Taras Shevchenko National University, Astronomical Observatory, Kyiv, Ukraine

²Astronomical Institute, Ondrejov Observatory, 251 65 Ondrejov, Czech Republic
alenamozgova@ukr.net, jiri.borovicka@asu.cas.cz, klimchur@ukr.net

ABSTRACT. 125 emission lines were found in a meteor spectrum obtained on August 2, 2011. The identification of most of the lines is given. The following species were found in the spectrum: CrI, FeI, MgI, SiI, AlI, MnI, CaI, TiI, NaI, FeII, CaII, MgII, SiII, SrII.

Key words: meteors, spectra, line identification

1. Introduction

Meteors are phenomena in the Earth's atmosphere caused by particles of cosmic origin. Meteor is an unpredictable and short-term phenomenon. To capture it is not so easy, but it is harder to get a good meteor spectrum.

It was found that the average time interval between two penetrations of cosmic particles with masses 10^{-2} g in the atmosphere of our planet is 7.2×10^{-3} s (Churyumov et al., 2012). It is about 140 particles per second. That is a constant interaction of meteoric matter with Earth's atmosphere. Due to this we are able to explore the structure, to determine physical parameters and study the chemical composition of interplanetary matter.

The main method of study of meteoroid composition is meteor spectroscopy.

Each meteor spectrum has a great scientific value. By processing it we can get information about the chemical composition of the cosmic body that invaded into the Earth's atmosphere and the nature of the glow of its substance.

The research of meteor spectra will allow to establish the genetic relationships of meteoroids with comets and asteroids.

The results of studies of meteoric phenomena can be also used as data about the physical and chemical processes in the upper Earth's atmosphere.

Meteor spectra provide information on the ablation process, hydrodynamics of meteors and on meteoroid masses (Borovicka, 1999).

In this paper we present the results of lines identification in a meteor spectrum.

2. Observational data

The meteor spectrum studied here was obtained on August 2, 2011 at 21:56:11 UT. The observations were made at the Ondrejov Observatory (Astronomical Institute of the Academy of Sciences of the Czech Republic).

The beginning of the phenomenon was detected above the point with coordinates: $\lambda_E=15^\circ,7699$, $\varphi_N=49^\circ,3814$, and the end coordinates: $\lambda_E=15^\circ,61661$, $\varphi_N=49^\circ,13797$.

The beginning and end heights of the meteor event were $h=115,71$ km and $h=80,628$ km respectively. The average velocity of the meteoric body in the Earth's atmosphere was 48 km/s. The meteor was sporadic with very eccentric orbit with perihelion at 0,969 AU and inclination of $79,7^\circ$.

The spectral record was obtained with a fixed camera Tessar (1:4,5; $f=360$ mm) equipped with 600 grooves/mm diffraction grating.

The spectrum was recorded on FOMAPAN 200 24×18 cm sheet film. The fireball image was divided into 5 segments due to the rotating shutter, which covered the camera 15,2 times per second (Fig.1).

There are places with high intensities of spectral lines in the image. Clearly visible are the lines of the first and the second spectral order. The spectral line of CaII barely visible also in the third order. The dispersion in the first order is 45 \AA/mm . The spectral region 3500 – 6400 Å was covered. Meteor wake can be seen between the segments.

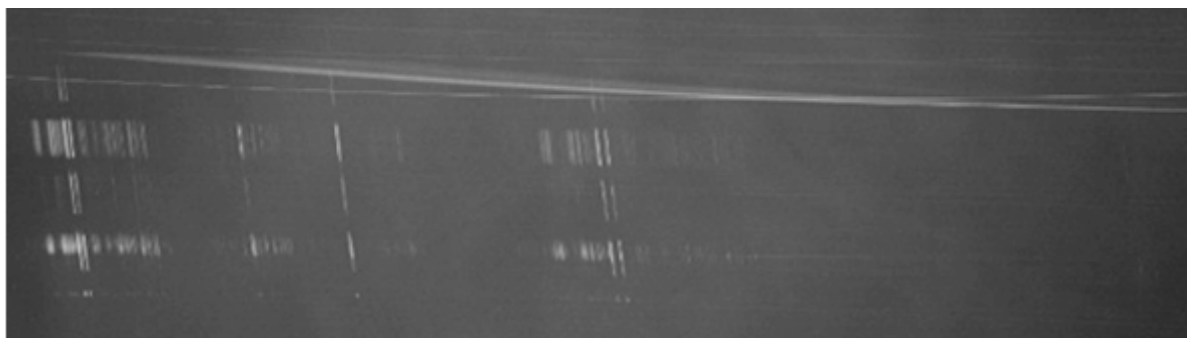


Figure 1: Meteor spectrum obtained on August 2, 2011. The flight direction was from the top to the bottom. The spectrum was divided into segments using rotating shutter. The first spectral order is on the left and a part of the second spectral order is in the middle. The horizontal trails are star zero order images. The bright star with spectrum is α Oph.

Table 1. Identification of spectral lines

no.	$\lambda_{\text{obs}} [\text{\AA}]$	$\lambda [\text{\AA}]$	Atom	Measured signal in relative units	Intensities in $\text{erg s}^{-1} \times \times \text{\AA}^{-1} \text{ster}^{-1}$	$ \Delta\lambda $	no.	$\lambda_{\text{obs}} [\text{\AA}]$	$\lambda [\text{\AA}]$	Atom	Measured signal in relative units	Intensities in $\text{erg s}^{-1} \times \times \text{\AA}^{-1} \text{ster}^{-1}$	$ \Delta\lambda $
1	3685,50	3679,92	Fel(5)	97	355	5,58	54	4427,00	4427,31	Fel(2)	4166	1033	0,31
		3683,05	Fel(5)				55	4435,00	4434,96	Cal(4)	112	34	0,04
		3687,46	Fel(21)				56	4455,00	4454,78	Cal(4)	102	33	0,22
2	3708,00	3705,57	Fel(5)	164	528	2,43	57	4461,50	4461,65	Fel(2)	2356	593	0,15
		3707,83	Fel(5)				58	4481,00	4481,24	MgII(4)	5531	1369	0,24
		3709,25	Fel(21)					4482,17	Fel(2)				
3	3720,50	3719,94	Fel(5)	784	2389	0,56	59	4489,50	4489,74	Fel(2)	235	59	
		3722,56	Fel(5)					4482,26	Fel(68)				
4		3733,32	Fel(5)				60	4493,50	4494,57	Fel(68)	109	27	1,07
		3734,87	Fel(21)				61	4528,00	4528,62	Fel(68)	234	61	0,62
	3736,50	3737,13	Fel(5)	1191	3391	0,63	62	4531,00	4531,15	Fel(39)	110	35	0,15
5	3745,00	3745,56	Fel(5)	1804	4893	0,56	63	4549,00	4549,47	Fel(38)	99	29	0,47
		3745,90	Fel(5)				64	4571,00	4571,10	MgI(1)	264	73	0,10
6		3763,79	Fel(21)					4571,98	TiII(82)				
	3766,50	3767,19	Fel(21)	298	728	0,69	65	4583,00	4583,83	Fel(38)	117	37	0,83
7		3798,51	Fel(21)				66	4647,00	4646,17	CrI(21)	53	17	0,20
	3798,00	3799,55	Fel(21)	263	556	1,55		4647,43	Fel(409)				
		3799,55	Fel(21)										
8	3815,00	3815,84	Fel(45)	314	577	0,84	67	4703,00	4702,99	MnI(11)	67	36	0,01
9	3820,00	3820,43	Fel(20)	701	1315	0,43	68	4859,50	4859,75	Fel(318)	51	37	0,25
	3824,50	3824,44	Fel(4)	1394	2562	0,06		4871,50	4871,32	Fel(318)	95	73	0,18
10		3825,88	Fel(20)				69		4872,14	Fel(318)			
		3827,83	Fel(45)					4890,76	Fel(318)				
11	3828,50	3829,35	MgI(3)	1707	3061	0,85	70	4891,00	4891,50	Fel(318)	183	156	0,50
	3832,00	3832,30	MgI(3)	2149	3767	0,30		4919,00	Fel(318)				
13	3837,50	3838,29	MgI(3)	2358	4018	0,79	71	4920,00	4920,51	Fel(318)	234	230	0,51
14	3856,00	3856,37	Fel(4)	1008	1549	0,37	72	4923,50	4923,92	Fel(42)	244	243	0,42
15	3859,50	3859,91	Fel(4)	3733	5566	0,41	73		4957,30	Fel(318)			
		3878,02	Fel(20)					4957,50	4957,60	Fel(318)	354	414	0,10
16		3878,00	Fel(4)	963	1309	0,58	74	4983,00	4982,81	NaI(9)	57	75	0,19
	3886,00	3886,28	Fel(4)	2403	3074	0,28		4981,73	TiI(38)				
17	3884,50	3895,66	Fel(4)	1161	1418	1,16	75	4994,00	4994,13	Fel(16)	44	68	0,13
19	3899,00	3899,71	Fel(4)	935	1125	0,71	76	5006,00	5006,13	Fel(318)	49	90	0,13
20		3902,95	Fel(45)				77	5012,00	5012,07	Fel(16)	61	127	0,07
	3905,50	3905,53	Sil(3)	1179	1346	0,03	78	5018,50	5018,43	Fel(42)	294	428	0,07
		3906,48	Fel(4)				79	5041,50	5041,07	Fel(16)			
	3920,26	Fel(4)				5041,76		Fel(36)	173	267	0,26		
21		3922,91	Fel(4)	1231	1250	0,41	80	5051,50	5051,64	Fel(16)	58	92	0,14
	3933,50	3933,67	CaII(1)	43294	41074	0,17		81	5056,00	5056,02	SilI(5)	86	133
23	3961,50	3961,53	AlI(1)	340	272	0,03	82	5110,50	5110,41	Fel(1)	670	1188	0,09
24	3968,50	3968,47	CaII(1)	36620	28239	0,03	83	5168,00	5167,32	MgI(2)	8369	17538	0,68
		3969,26	Fel(43)					5167,49	Fel(37)				
25	4005,50	4005,25	Fel(43)	191	122	0,25	84		5171,60	Fel(36)			
		4030,76	MnI(2)					5172,50	5172,68	MgI(2)	7948	16834	0,18
		4033,07	MnI(2)					5183,50	5183,60	MgI(2)	8033	17488	0,10
26	4034,00	4034,49	MnI(2)	941	546	0,49	86	5195,00	5194,94	Fel(36)	204	443	0,06
	4045,50	4045,82	Fel(43)	1646	921	0,32			5204,52	CrI(7)			
28	4063,50	4063,60	Fel(43)	921	488	0,10	87	5205,50	5206,04	CrI(7)	334	710	0,54
29	4071,50	4071,74	Fel(43)	827	428	0,24		88	5208,00	5208,44	CrI(7)	359	758
30	4077,00	4077,71	SrII(1)	370	212	0,71	89		5215,19	Fel(553)			
31	4131,50	4132,06	Fel(43)	606	268	0,56		5216,50	5216,28	Fel(36)	149	303	0,22
32	4143,50	4143,87	Fel(43)	753	326	0,37		5217,40	Fel(553)				
33	4201,50	4202,03	Fel(42)	721	271	0,53	90	5227,00	5227,19	Fel(37)	1287	2533	0,19
34	4216,00	4216,19	Fel(3)	1157	418	0,19	91	5233,00	5232,95	Fel(383)	122	233	0,05
35	4226,50	4226,73	CaI(2)	3824	1354	0,23	92	5270,00	5269,54	Fel(15)	6577	10405	0,46
	4251,00	4250,79	Fel(42)	492	166	0,21		5270,36	Fel(37)				
36		4250,13	Fel(152)				93	5328,00	5328,04	Fel(15)	3345	4456	0,04
	4254,00	4254,35	CrI(1)	1137	375	0,35		5328,53	Fel(37)				
38	4260,00	4260,48	Fel(152)	554	180	0,48	94		5339,94	Fel(553)			
		4271,16	Fel(152)					5341,00	5341,03	Fel(37)	161	206	0,03
39	4271,50	4271,76	Fel(42)	2174	690	0,26	95	5371,50	5371,49	Fel(15)	1440	1758	0,01
	4275,00	4274,80	CrI(1)	2006	555	0,2		96	5383,00	5383,37	Fel(1146)	25	65
40		4274,60	CrI(1)				97	5397,50	5397,13	Fel(15)	715	814	0,37
	4282,00	4282,41	Fel(71)	133	47	0,41		98	5406,00	5405,78	Fel(15)	681	766
42	4289,50	4289,72	CrI(1)	498	152	0,22	99	5415,00	5415,20	Fel(1165)	51	57	0,20
43	4293,50	4294,13	Fel(41)	692	208	0,63	100	5424,00	5424,07	Fel(1146)	48	78	0,07
44	4298,00	4299,24	Fel(152)	225	66	1,24	101	5430,00	5429,70	Fel(15)	741	786	0,30
45	4302,00	4302,52	CaI(5)	91	38	0,52	102	5434,50	5434,53	Fel(15)	285	298	0,03
46	4307,50	4307,91	Fel(42)	1750	506	0,41	103	5447,00	5446,92	Fel(15)	592	607	0,08
47	4325,50	4325,77	Fel(42)	1801	513	0,27	104	5456,00	5455,61	Fel(15)	356	350	0,39
48	4340,00	4339,45	CrI(22)	92	31	0,55	105	5506,00	5506,78	Fel(15)	26	33	0,78
		4339,72	CrI(22)					5528,50	5528,41	MgI(9)	139	105	0,09
49		4351,05	CrI(22)				107	5587,00	5586,76	Fel(686)	106	61	0,24
	4351,50	4351,77	CrI(22)	325	87	0,27			5588,76	Cal(21)			
		4351,91	MgI(14)					5593,50	5594,47	Cal(21)	27	16	0,97
50	4375,50	4375,93	Fel(2)	4774	1235	0,43	109	5616,00	5615,65	Fel(686)	183	90	0,35
51	4383,50	4383,55	Fel(41)	4671	1218	0,05	110	5688,00	5688,21	NaI(6)	101	37	0,21
52	4404,50	4404,75	Fel(41)	2015	511	0,25	111	5890,00	5889,95	NaI(1)	24016	11255	0,05
53	4414,50	4415,13	Fel(41)	769	190	0,63	112	5895,50	5895,92	NaI(1)	16425	8796	0,42

no.	λ_{obs} [Å]	λ [Å]	Atom	Measured signal in relative units	Intensities in $\text{erg s}^{-1} \times \text{Å}^{-1} \text{ster}^{-1}$	$ \Delta\lambda $	no.	λ_{obs} [Å]	λ [Å]	Atom	Measured signal in relative units	Intensities in $\text{erg s}^{-1} \times \text{Å}^{-1} \text{ster}^{-1}$	$ \Delta\lambda $
113	6101,50	6102,72	CaI(3)	53	23	1,22	119	6229,50	6230,73	FeI(207)	78	34	1,23
114	6121,00	6122,22	CaI(3)	81	34	1,22	120	6245,50	6246,33	FeI(816)	42	20	0,83
115	6136,00	6136,62	FeI(169)	87	37	0,62	121	6251,50	6252,56	FeI(169)	64	29	1,06
		6137,70	FeI(207)				122	6334,00	6335,34	FeI(62)	5206	34	1,34
116	6161,00	6162,17	CaI(3)	204	86	1,17	123	6346,50	6347,10	SiII(2)	472	354	0,60
117		6169,06	CaI(20)				124	6358,00	6358,69	FeI(13)	49	37	0,69
		6169,56	CaI(20)	54	22	0,06	125	6370,50	6371,36	SiII(2)	142	131	0,86
118	6190,50	6191,56	FeI(169)	55	24	1,06							

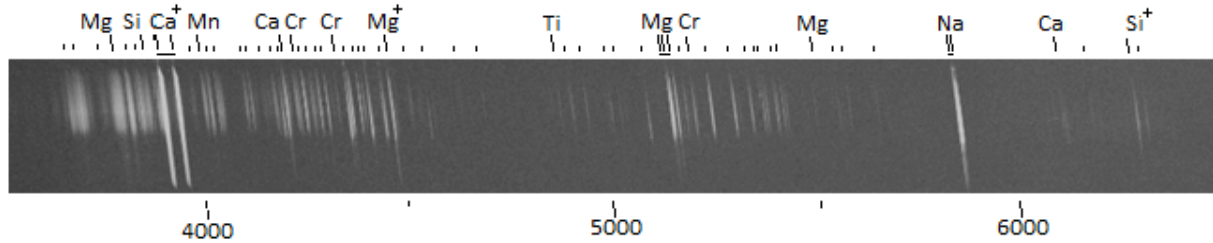


Figure 2: A part of the meteor spectrum during the flare. The important lines are identified. The short dashes show iron lines.

3. Identification of spectral lines

For spectral lines identification the brightest part of the first spectral order during the main flare which took place at the heights $h = 83,5 - 84,5$ km was used (Fig. 2). The spectrum was scanned and the spectrogram was obtained. The plate background was measured between segments. The measurements were calibrated. The wavelengths scale was determined by means of known lines in the spectrum (Borovicka, 1993). Polynomial fit of degree 3 was used to relate the instrumental lengths to wavelengths.

For photometric calibration the characteristic curve was constructed from the zero orders of stars recorded on the plate. Limiting magnitude was 4. Figure 3 shows the linear part of the characteristic curve.

The relative spectral sensitivity of the system was determined by using the first order spectrum of Jupiter and Polar Star recorded on the same plate. The real energy distribution in the Jupiter's spectrum was taken from Karkoschka (1994). The resulting relative spectral sensitivity function is shown in figure 4. The maximum of sensitivity is around 4500 Å and minimum occurs at 5200 Å.

The spectrum includes many individual emission lines belonging to atoms of different chemical elements.

There are 125 emission lines identified in the meteor spectrum. For identification the tables of Moore (1945) and Borovicka (1994) were used.

The identification of observed spectral lines is given in Table 1. The following quantities are given in Table 1: Number and wavelength of the observed line, catalogue wavelength, identification (atom and multiplet), measured signal in relative units, intensities in $\text{erg s}^{-1} \text{Å}^{-1} \text{ster}^{-1}$, difference between wavelength of the observed line and catalogue wavelength.

4. Conclusion

The basic processing of meteor spectrum was made. The meteor spectrogram was obtained and the identification of 125 emission lines found in the spectrum is presented. They were formed by CrI, FeI, MgI, SiI, AlI, MnI, CaI, TiI, NaI, FeII, CaII, MgII, SiII, SrII. Further analysis and theoretical interpretation of the spectrum is forthcoming.

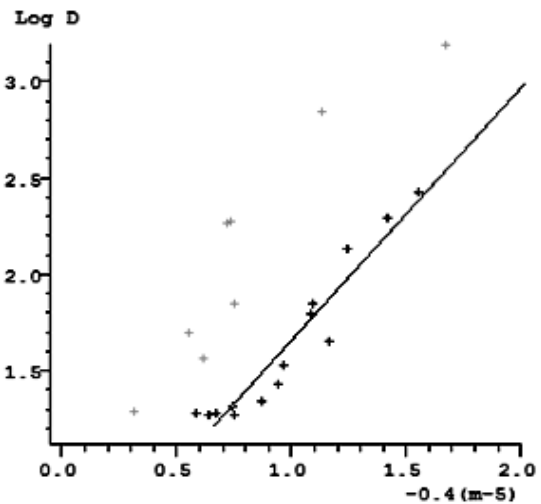


Figure 3: Characteristic curve of the plate. The opacity as a function of incident flux given by the stellar magnitude m . The crosses represent individual stars. Grey crosses were omitted from the fit.

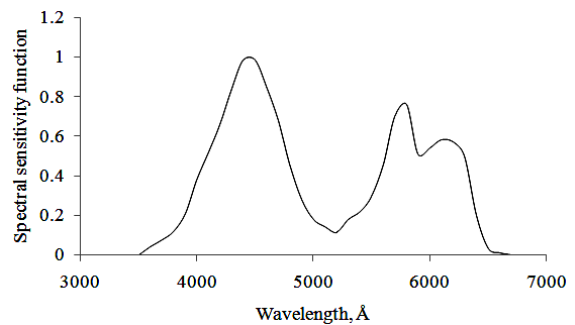


Figure 4: Relative spectral sensitivity of the spectrograph.

References

Borovicka J.: 1993, *Astron. Astrophys.*, **279**, 627.
 Borovicka J.: 1994, *Astron. Astrophys. Suppl. Ser.*, **103**, 83.
 Borovicka J.: 1999, in: *METEORIDS 1998*, Astron. Inst., Slovak Acad. Sci., Bratislava, 335.
 Churyumov K. et al.: 2012, *Physics and Astronomy in modern school*, **1**, N 16, 51.
 Karkoscka E.: 1994, *Icarus*, **111**, 174.
 Moore Ch.E.: 1945, *A Multiplet Table of Astrophys. Interest, Contrib. Princeton Univ. Obs.*, 20.

THE RESULTS OF OBSERVATIONS OF MUTUAL PHENOMENA OF THE GALILEAN SATELLITES OF JUPITER IN 2009 AND 2015 IN NIKOLAEV ASTRONOMICAL OBSERVATORY

A. Pomazan, N. Maigurova, V. Kryuchkovskiy

Research Institute “Nikolaev Astronomical Observatory”
Observatorna 1, 54030, Mykolaiv, Ukraine, antpomaz@gmail.com

ABSTRACT. The Earth and Jupiter once in 6 years have simultaneous passage of the ecliptic plane due to their orbital movement around the Sun. This makes it possible to observe the mutual occultations and eclipses in the Galilean satellites of Jupiter.

We took part in the observational campaigns of the mutual phenomena in 2009 and 2014-15. The observations were made with a B/W CCD camera WAT-902H at the telescope MCT ($D = 0.115$ m, $F = 2.0$ m) of the Nikolaev Astronomical Observatory. The light curves of mutual phenomena in the satellites of Jupiter were obtained as a result of processing photometric observations. The exact moments of maximum phases and the amplitudes of the light variation have been determined from the analysis of the light curves.

The data sets for the light curves have been sent in the IMCCE (Institute de Mecanique et de calcul des ephemerides, France) that coordinates the PHEMU campaigns.

Keywords: Jupiter: Galilean satellites: mutual phenomena

1. Introduction

Twice in orbital period which is 11.86 years, the transit of Jupiter through the nodes of its equator provides the opportunity for an edge-on view of its equatorial plane from the inner solar system. Since inclination of the orbital planes of the Galilean satellites to the planet's equator is very small the series of mutual phenomena (PHEMU) in Jovian satellites system occurs during about 9 month every 6 years.

The most observed PHEMU are eclipses and occultations. During a mutual eclipse one satellite passes through the shadow of the other satellite or Jupiter. At an occultation one satellite passes in front of another as seen from the Earth. The absence of atmosphere on the Galilean satellites permits very accurate observations allowing the determination of the time, duration and the amplitude of the observed phenomenon. The high precision photometric observations of PHEMU are an effective way of obtaining new astrometric data which has great potential in studies of secular variations and problems related to the resonances in mean motion, improve the theoretical models of the orbital motions and to determine the tidal effects in the dynamics of the Galilean satellites which not yet put into evidence.

We took part in two observational PHEMU campaigns coordinated by the IMCCE (Institute de Mecanique et de calcul des ephemerides, France). The results of the pho-

tometric observations of the Galilean satellites of Jupiter in the 2009 and 2015 are presented here.

2. Instruments for observations and reduction methods

The mutual phenomena in the Galilean satellites system of Jupiter can be easy observable. These phenomena have short duration (the mean duration of events don't exceed 10 minutes), high brightness (the Galilean satellites are 4-6 magnitude) and the magnitude drop can reach even more than one magnitude.

The observations of the PHEMU were carried out at Multichannel telescope (MCT) of the Nikolaev Astronomical Observatory (observatory code 089). Telescope MCT ($D = 0.115$ m, $F = 2.0$ m) was equipped the B/W CCD camera WAT-902H (752×582 , 8.6×8.3 mkm²), which allows to get 25 images per second. The size of field of view is $11.12' \times 8.3'$ and scale $-0.89 \times 0.86''/\text{pix}$, that allows to get images of Jupiter with four Galilean satellites simultaneously. The standard red glass filter marked RG-19 was used to reducing the light flux coming from the too bright Galilean satellites and Jupiter. Each image dated in UTC (Universal Time) with accuracy 0.001 sec by GPS.

Ephemerides for observation of mutual phenomena, calculated for Nikolaev Astronomical Observatory (089) were taken from the site of IMCCE (http://www.imcce.fr/hosted_sites/saimirror/nsszph515he.htm). According to the calculated ephemeris it was predicted 100 mutual phenomena in the Galilean satellites of Jupiter in 2009, and 186 in 2014-2015. The photometric observations of 13 mutual phenomena were carried out in 2009 and satisfactory light curves for 6 of them were obtained. During 2015 the observations of 5 mutual phenomena were performed and satisfactory light curves for 2 phenomena were obtained.

The obtained images have been processed with a Tangra software, version 3 (<http://www.hristopavlov.net/Tangra3>). The software allows to measure of the numerous successive images automatically. The aperture photometry method was used for processing. Due to the high brightness of Jupiter the most relevant processing step was choosing of the best model to determine of the sky background. The irregularities of background on the image can significantly impact on the measurement of the luminous flux of the investigated object.

The Average, Median, Background Mode, 3D Polynomial Fit and PSF-Fitting methods are implemented in Tangra software to account for the effect of sky background. The flux of the sky background nearby the investigated object was calculated by various methods and a light curves were plotted. The light curves of background flux for the occultation J2 (Europe) by J1 (Io) on August 5, 2015 derived by different reduction methods are shown in Fig.1. As can be seen, the 3D Polynomial Fit model shows the actual change of the sky background on the image caused by the displacement of the object towards to Jupiter during phenomenon. Other models due to nonoptimal algorithm of calculating do not show such changes in the background.

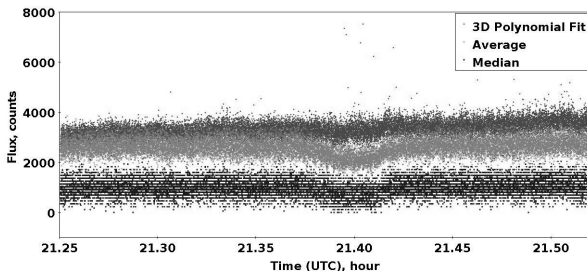


Figure 1: The light curve of background flux derived from different reduction methods.

Such analysis have been performed for each of the obtained observational series and the 3D Polynomial Fit model showed the lowest values of the relative errors of the sky background (12%). The statistical information of measurements of the sky background by various methods is given in the Table 1.

Table 1. Statistical information for background reduction method.

Reduction method	Average value, counts	Standard deviation, counts	Relative error, %
Average	2605.2	323.5	12.4
Median	965.6	289.5	29.9
Background Mode	2495.8	876.2	35.1
3D Polynomial Fit	3287.5	394.6	12.0
PSF-Fitting Background	3641.7	1790.1	49.2

More than 20 thousand images have been obtained during observation for each phenomenon. The measurements have been averaged by four points to increase the accuracy of results. It is also allows to reduce the amount of data to be sent to the IMCCE coordinating observation campaign (according to requirements only 10 thousand points are accepted).

In some cases, satellites are located close enough to each other and their light fluxes are partially overlapped. For such cases the total fluxes from related objects have been measured according to the method (F. Colas, JE Arlot, 2008).

3. The results of observations

The light curves of all Galilean satellites seen in the image were obtained because other Galilean satellites have been used as the photometric reference sources during the phenomenon. The light curve of the eclipse of J1 J2 (Io-Europe) derived from observation carried out on October 3^d, 2009 are presented in Fig.2. The background flux has been removed and clear flux averaged in 4 points (Fig.2, top). It should be noted that last part of light curves derived during phenomenon on all of observed satellites has some fluctuations. It caused by atmosphere nebulosity and the flux of satellite J2 (Europe) have been divided by flux of J1 (Io) in order to remove it. Normalized flux of J2 (Europe) by J1 (Io) presented on Fig.2, bottom.

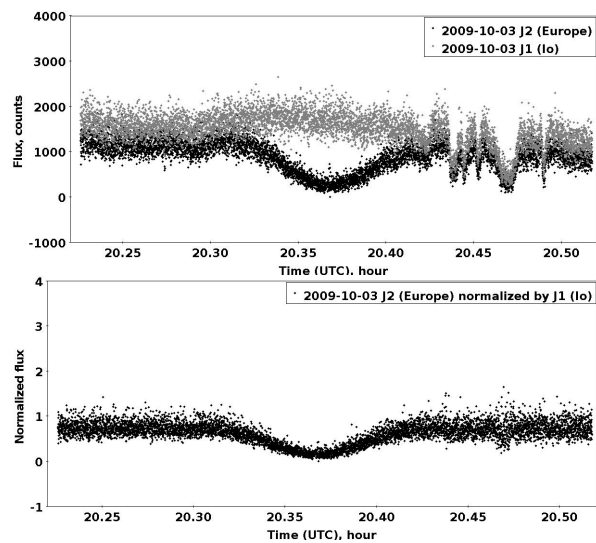


Figure 2: The light curve of eclipse J2 by J1 occurred October 3^d, 2009. Top part presents clear fluxes of J1 and J2. Normalized flux satellite J2 by J1 at bottom part.

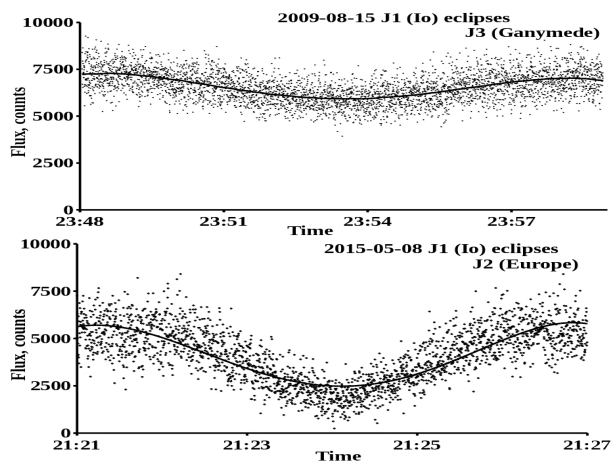


Figure 3. The light curves for observed phenomena. Solid line corresponding for approximating 4 degree polynomial function.

Unfortunately the weather conditions were not always stable during the observation of the phenomenon. The light curves, which were obtained from observation without any atmospheric fluctuations during phenomenon, have been considered as satisfactory. The approximation of such light curves has been performed by a 4 degree polynomial, which showed the smallest residuals with the actual curve. The obtained light curves and their approximating functions (solid line) of the mutual phenomena are presented in Fig. 3.

For events with satisfactory light curve the moments of maximum phase have been determined as extremes of selected approximating function. The magnitude drops for the moments of maximum phase of phenomena have been measured. Table 2 presents the predicted and determined data for the observed mutual phenomena in Nikolaev on MCT in 2009 and 2015.

Table 2. The moments of maximum phases and magnitude drop of the mutual phenomena predicted by IMCCE and observed in Nikolaev at MCT in 2009 and 2015.

Date (UTC)*	Type*	Predicted start time (UTC)*	Predicted end time (UTC)*	Expected magnitude drop *	Maximum phase (UTC)	Mag. drop
2009-08-15	1E3	23:48:00	23:59:02	0.450	23:53:32	0.26
2009-08-17	1O3	20:57:55	21:10:37	0.624	21:04:15	0.55
2009-08-17	1E3	21:08:39	21:22:26	0.436	21:15:27	0.27
2009-08-24	1O2	23:23:12	23:38:57	0.626	23:31:09	0.47
2009-10-03	1O2	18:26:41	18:33:03	0.189	18:30:09	0.23
2009-10-03	1E2	20:18:12	20:26:01	0.613	20:22:03	
2015-05-08	1E2	21:21:26	21:26:53	0.572	21:24:04	
2015-06-09	1E2	19:39:10	19:44:54	0.307	19:41:54	0.37

* Data taken from ephemerides calculated by IMCCE (<http://www.imcce.fr>) for Nikolaev Astronomical observatory (IAU code 089).

4. Conclusions

The instrumental preparation and photometric observations of the mutual events in the Jovian satellites system were carried out at Nikolaev Astronomical Observatory in 2009 and 2015 PHEMU campaigns. The relative photometry was performed and six satisfactory light curves were obtained. The moments of the maximum phases of events and the values of magnitude drop at maximum phase were estimated.

The comparison of the obtained time moments from our observations with the ephemeris calculated by IMCCE shows differences about from 0.5 to 1 minute.

The results of observations have been sent to the IMCCE for adding to international database and further analysis.

References

- Arlot J.-E.: 2005, *A&A*, **439**, Issue 2, 785.
 Arlot J.-E.: 2014, *A&A*, **572**, A 120.
 Emel'yanov N.V.: 2002, *Sol.Syst.Res.*, **36**, Issue 4, 353.
 Colas F.: 2008, *Techn.Note №5*.
 Koshkin N. et al.: 2009, *Odessa Astron. Publ.*, **22**, 28.
 Noyelles B.: 2004, in *Proc. of IAU Coll.*, **196**, 271.
 Ramírez M.E.: 2006, *A&A*, **448**, Issue 3, 1197.

SYNCHRONIZATION OF TERRESTRIAL PROCESSES WITH FREQUENCIES OF THE EARTH-MOON-SUN SYSTEM

N.S.Sidorenkov

Hydrometcenter of the Russia, Moscow, *sidorenkov@mecom.ru*

ABSTRACT. It is established that the frequencies of the quasi-biennial oscillation (QBO) of atmospheric winds and the Chandler wobble (CW) of the Earth's poles are synchronized with each other and with the fundamental frequencies of the Earth–Moon–Sun system. The QBO and CW frequencies are resonance combinations of the frequencies of the Earth–Moon system's yearly rotation around the Sun, precessions of the lunar orbit, and the motion of its perigee. The QBO and CW frequencies are in a ratio of 1:2. The synchronizations between Mul'tanovskii's natural synoptic periods and tidal oscillations of the Earth's daily rotation rate, as well as between variations in climatic characteristics and long-time fluctuations of the Earth's rotation rate are described.

Keywords: Chandler wobble, quasi-biennial oscillations of winds, cosmic effects, weather forecast, climate change.

350 years ago Christian Huygens discovered the self-synchronization of a pendulum clock. To date it has been established that synchronization is, according to I.I.Blekhman (1988), the property of material objects of various natures to generate a unified rhythm of joint motion despite the difference in their individual rhythms and their sometimes rather weak coupling.

Synchronization phenomena have been found in acoustic and electromechanical systems, electrical circuits, radio engineering, radio physical, mechanical, and engineering devices, and living systems.

Widely known is the synchronization (comparability) of the orbital and spin frequencies of planets and moons in the solar system.

By the synchronization, comparability, or resonance of a system in which the bodies rotate with orbital angular velocities ω_i , we mean linear expressions of the form

$$n_1 \omega_1 + n_2 \omega_2 + \dots + n_k \omega_k = 0, \quad (1)$$

where the coefficients n_i are small integers.

Orbital motion of planets

To date numerous comparability relations have been found for the orbital and spin angular velocities of bodies in the solar system. Following A.M. Molchanov's (1973) work, for illustrative purposes, we present comparability relations between the mean orbital angular velocities of all planets in the solar system (Table 1). Here, the up-to-date orbital periods of the planets are presented in line 4; the coefficients n_i from expression (1) for each of the planets are given in lines 5–12; and the actual and theoretical ratios of the planets' angular velocities ω_i to Jupiter's ω_5 , in lines 13 and 14, respectively. The last line gives the relative deviations of the theoretical values ω_T (calculated using formula (1)) from the actual values ω_O . It can be seen that they are small. So, given the orbital angular velocity ω_k of one planet, we can calculate the values of ω_i for the other seven planets of the solar system. For example, Venus' angular velocity ω_2 is equal to the sum of Saturn's velocity ω_6 and three times Mars' velocity ω_4 . The relative error of the result is 0.2%.

Table 1. Orbital Period of Planets

	Planet							
	1	2	3	4	5	6	7	8
	Mercury	Venus	Earth	Mars	Jupiter	Saturn	Uranus	Neptune
Orbital period	87,9693	224,7008	365,25636	686,9796	4332,8201	10755,699	30687,15	60190,03
Coefficient in expression (1)	n_1	1	0	0	0	0	0	0
	n_2	-1	1	0	0	0	0	0
	n_3	-2	0	1	0	0	0	0
	n_4	-1	-3	-2	1	0	0	0
	n_5	0	0	1	-6	2	-2	-1
	n_6	0	-1	-1	0	-5	5	0
	n_7	0	0	1	-2	0	0	7
	n_8	0	0	0	0	0	0	0
ω_O / ω_5 observed	49,2538	19,2826	11,8624	6,30706	1	0,40284	0,14119	0,07199
ω_T / ω_5 theory	49,2425	19,3240	11,758	6,2824	1	0,4000	0,14286	0,0706
$\frac{\omega_T - \omega_O}{\omega_O}$	-0,0002	0,0021	0,0011	-0,0039	0	-0,0071	0,0117	-0,019

Polar wobble

It was indicated Sidorenkov (2009) that the Chandler period is synchronized with the frequencies of the Earth–Moon–Sun system. Recall that the Earth is in two orbital motions: monthly and annual. More specifically, it rotates around the barycenter of the Earth–Moon system with a monthly period and, together with this barycenter, moves around the Sun with an annual period. The plane of the Earth and Moon's monthly orbit precesses with a period of 18.61 years, while the pericenter moves from west to east with a period of 8.85 years.

The atmospheric forcing of the polar wobble with a solar-year period of 365.24 days is modulated by the precession of the Earth's monthly orbit with a period of 18.61 years and by the motion of its perigee with a period of 8.85 years. Finally, the resulting solar annual forcing generates polar wobble with a Chandler period of 1.20 year:

$$\frac{1}{1.0} - \left(\frac{1}{18.61} + \frac{1}{8.85} \right) = \frac{1}{1.20} . \quad (2)$$

The amplitude modulation of CWP is clearly exhibited with a period about 40 years. It is known that the AAM and OAM functions are capable to account for about 90% of the required CWP excitation.

This excitation is believed to occur at the fundamental frequency of the climate system forcing with a period of 365.24 days. However, it was shown in the author's most recent works that, in addition to this basic forcing, the climate system experiences additional forcing caused by cloud amount variations with lunar-year periods. Climatic characteristics and the equatorial component of the atmospheric angular momentum h_2 were found to oscillate with a period of 355 days (Sidorenkov, 2009; Sidorenkov & Sumerova, 2012).

The wobble forcing with a lunar sidereal year period of 355 days (13 sidereal months) is modulated by the precession of the earth's monthly orbit with a period of 18.61 years and by the motion of its perigee with a period of 8.85 years. Finally, the resulting "lunar sidereal" forcing generates polar wobble with a period of 1.16 year:

$$\frac{1}{355.18 \text{days} / 365.24 \text{days} / \text{yr}} - \left(\frac{1}{18.61} + \frac{1}{8.85} \right) = \frac{1}{1.1606 \text{yr}} . \quad (3)$$

Interference of the 1.20-year Chandler oscillation and the 1.16-year oscillation leads to beats, i.e., to periodic variations in the polar wobble amplitude with a period of 35.3 years:

$$\frac{1}{1.16} - \frac{1}{1.2} = \frac{1}{35.3}$$

The "lunar" annual (13 anomalistic months) excitation can generate polar wobble with a period of 1.172 year:

$$\frac{1}{358.21 \text{days} / 365.24 \text{days} / \text{yr}} - \left(\frac{1}{18.61} + \frac{1}{8.85} \right) = \frac{1}{1.172 \text{yr}} \quad (4)$$

Interference of this wobble with CWP can generate beats with a period of 50.9 years:

$$\frac{1}{1.172} - \frac{1}{1.2} = \frac{1}{50.9}$$

Thus, interference of CWP (1.20-year period) with these moon-caused oscillations gives rise to beats, i.e., to slow periodic variations in the CWP amplitude with periods of 32 to 51 years. They are observed in reality.

Expressions (2-4) correspond to (1) with coefficients $|n_i|=1$. They describe four-frequency synchronization or resonance. In this sense, we can say that the frequency of Chandler polar wobble is synchronized with the fundamental frequencies of the Earth–Moon–Sun system.

Quasi-biennial oscillation of zonal wind

The quasi-biennial oscillation (QBO) of the atmosphere was discovered in the early 1960s in the study of the equatorial stratospheric circulation. It was found that the direction of the equatorial zonal wind reverses with a period of about 26 months in the layer 18 to 35 km. A change from westerlies to easterlies in QBO does not happen simultaneously at all altitudes, but propagates downward at about 1 km per month. An instantaneous vertical profile of zonal wind in the layer 18–31 km has the form of a wave with easterlies following westerlies. This wave always propagates downward and disappears near the tropopause (at a height of ≈ 17 km).

The QBO of the equatorial zonal wind is explained by the interaction of Kelvin waves and mixed Rossby-gravity waves with the zonal wind in the equatorial stratosphere (Lindzen, Holton, 1968). The nature of Kelvin and mixed Rossby-gravity waves is not clear. In the author's view, mixed Rossby-gravity waves are manifestations of the lunar tidal waves 2Q1 (6.86 days) and σ_1 (7.095 days) in the atmosphere (Sidorenkov, 2010). They account for an intense wide peak at a frequency of about 0.85 (day)^{-1} in the spectrum of the atmospheric angular momentum (Sidorenkov, 2009, see Section 6.5). It is believed that Kelvin waves propagate into the stratosphere, where they meet a westerly shear zone and are absorbed at the height where their phase velocity coincides with the wind velocity. As a result, the westerlies at this height strengthen, while the absorption of new waves is reduced. Since wave absorption proceeds continuously, the westerly zone gradually descends toward the tropopause at a velocity of about 1 km/month. When the westerly zone stretches down to the tropopause, the Kelvin waves have low frequencies due to the Doppler shift, while the mixed Rossby-gravity waves have high frequencies. That is why the latter propagate upward. At the height of semiannual oscillations (≈ 35 km), they can meet an easterly shear zone, where they are absorbed. As a result, the easterly velocity increases and the easterly zone descends permanently from 35 km to the tropopause, where the cycle is completed. At the same time, Kelvin wave absorption begins at the height of semiannual oscillations and a new cycle starts.

In this model, the QBO period for wind depends only on the intensity of atmospheric waves and on the distance between the equatorial tropopause and the height of semiannual oscillations in the stratosphere.

A generalization of experimental and theoretical studies has revealed that the QBO period is a linear combination of the frequencies corresponding to the doubled periods:

of the tidal year (0.97 year), precession (18.6 years), and perigee (8.85 years) of the Earth monthly orbit:

$$\frac{1}{2} \left(\frac{1}{0.97} - \frac{1}{8.85} - \frac{1}{18.61} \right) = \frac{1}{2.3} \quad (5)$$

The tidal year frequency is taken in (5) because the mechanism of QBO excitation is associated with the absorption of Kelvin and mixed Rossby-gravity waves in the equatorial stratosphere. However our observations of variations in pressure, geopotential height, temperature, and cloudiness anomaly fields suggest that planetary atmospheric waves known as Rossby and Kelvin waves behave as lunar tidal waves and have the same characteristics (Sidorenkov, 2010). The study of the equatorial angular momentum of atmospheric winds has also shown that their spectrum is dominated by semimonthly and quasi-weekly lunar waves, which are treated in meteorology as Yanai waves. In 1960 C. Eckart (p. 319) showed that Rossby waves are, in fact, oscillations described by Laplace's tidal equation. Taking into account all these findings, we believe that Rossby, Kelvin, and Yanai waves are visual manifestations of tidal waves in the atmosphere. From year to year, they repeat not with a tropical-year period of 365.24 days, but with a period of 13 tropical months, which is equal to 355.16 days ≈ 0.97 . It is called the tidal or lunar year.

In contrast to resonance expression (2), all the frequencies in (5) have doubled periods. This means that expression (5) corresponds not to the fundamental resonance, but rather to a resonance of the n -th kind, i.e., to a subharmonic oscillation, whose existence follows from Mandelstam and Papaleksi's theory (Mandelstam, 1947).

Thus, the quasi-biennial oscillation of zonal wind in the equatorial stratosphere is a combination oscillation driven

by three periodic processes affecting the atmosphere: (a) lunar-solar tides, (b) the precession of the Earth's monthly orbit around the barycenter of the Earth–Moon system, and (c) the motion of the pericenter of this orbit. In the QBO case, synchronization occurs at the combination frequencies of the n th kind.

Mul'tanovskii's natural synoptic periods

The lunar-solar tides deform the Earth's shape and change the Earth's moment of inertia. As a result, they have a noticeable effect on the velocity of the Earth's daily rotation. The tidal oscillations of the Earth's rotation rate over any time interval can be calculated theoretically (Sidorenkov, 2009). By way of illustration, Figure 1 shows the tidal deviations of the Earth's daily angular velocity v in 2016. The Earth's rotation velocity is characterized by the relative value (Sidorenkov, 2009)

$$v \equiv \frac{\delta\omega}{\Omega} = \frac{\omega - \Omega}{\Omega} \approx -\frac{\Pi_E - T}{T} \equiv -\frac{\delta\Pi}{T},$$

where Π_E is the length of Earth's day; T is the length of the standard (atomic) day, which is equal to 86400 s; and $\omega = \frac{2\pi}{\Pi_E}$ and $\Omega = \frac{2\pi}{86400}$ rad/s are the angular velocities cor-

responding to the Earth's and standard days

It can be seen that, during a tropical month, v undergoes two semimonthly oscillations with maxima occurring at the maximum distance of the Moon from the celestial equator in both Northern and Southern hemispheres (i.e., at lunar solstices) and with minima occurring when the Moon intersects the equator (i.e., at lunar equinoxes).

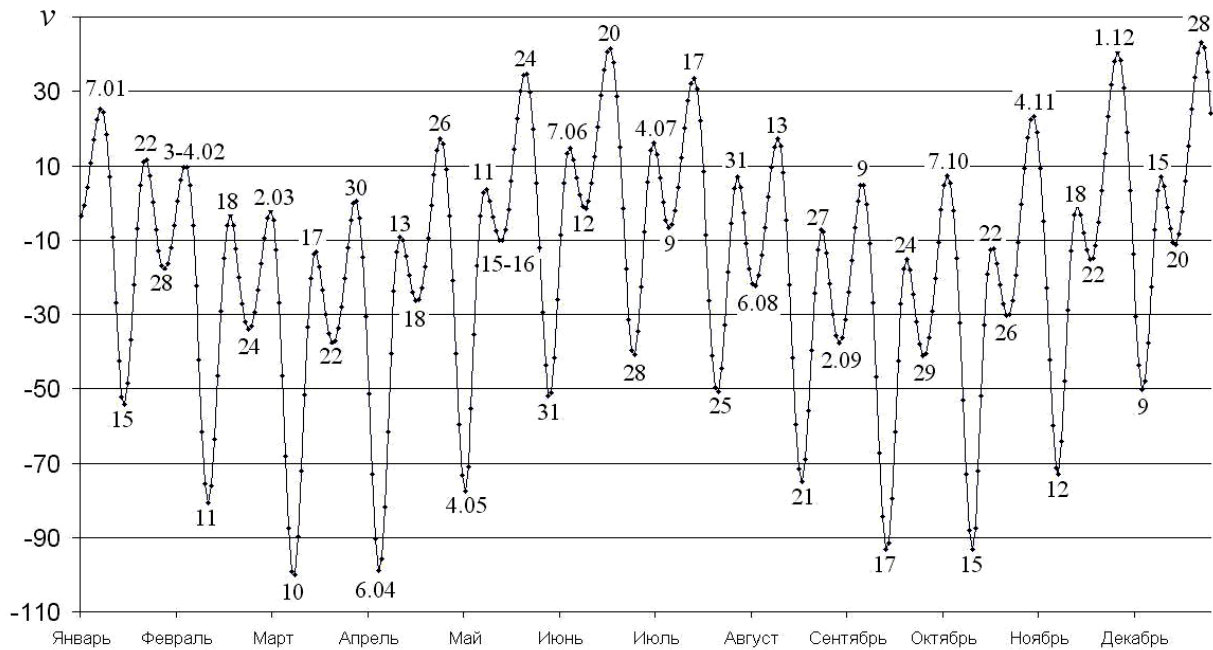


Figure 1: Tidal oscillations of the Earth's rotation velocity v in 2016. The vertical axis represents the relative deviations of v multiplied by 10^{10} . Numerals indicate the dates when maxima and minima of v occurred

The monitoring of tidal oscillations of v , the evolution of atmospheric synoptic processes, atmospheric circulation patterns, and time variations in hydrometeorological characteristics has shown that most types of atmospheric synoptic processes vary **synchronously** with the tidal oscillations of the Earth's angular velocity (Sidorenkov, 2009). Using retrospective data, we verified how frequently the extrema (minima or maxima) of v coincide in time with changes in elementary synoptic processes (ESP) in terms of the Vangengeim classification. A statistical analysis showed that 76% of the extrema of v coincide in time (up to ± 1 day) with ESP changes. In the other 24% of the cases, the extrema of v are two and more days away from the nearest ESP change (Sidorenkov, 2009).

The long-time comparative monitoring of tidal oscillations of v and variations in meteorological characteristics in Moscow, Vladivostok, and other sites clearly suggests that variations in meteorological characteristics agree in time with quasi-weekly extrema of v (<http://geoastro.ru>). Variations in weather elements at other sites of world have been monitored by S.P.Perov and L.V.Zotov. Their results also confirm that variations in meteorological characteristics are synchronized with oscillations of the Earth's angular velocity.

The tidal oscillations in the Earth's rotation velocity represent a perfect index for the features of the Earth's monthly rotation around the barycenter and time variations in the lunisolar tidal forces. They correlate with quasi-weekly and semimonthly variations in atmospheric processes and with local anomalies in the air temperature, pressure, cloudiness, and precipitation amounts depending on those variations.

Changes in weather patterns coincide with extrema of tidal oscillations of v , which correspond to lunar solstices and lunar equinoxes. By analogy with three-month seasons of the year, which are associated with the Earth's rotation around the Sun, kind of quasi-weekly weather "seasons" can be identified in weather patterns.

Quantized weather patterns were first described by B.P.Mul'tanovskii (1933) 100 years ago. He called them natural synoptic periods (NSPs). The above observations suggest that Mul'tanovskii's NSPs are possibly caused by the monthly rotation of Earth and Moon around their barycenter. Weather is synchronized with the times of lunar equinoxes and solstices. In contrast to solar seasons, the lunar NSPs are not constant: they vary from 4 to 9 days with a mean of 6.8 days. These variations are caused by the frequency modulation of the tidal force oscillations due to the motion of the lunar perigee. Plots of tidal oscillations of v provide a kind of NSP timetable, demonstrating that variations in NSP lengths are not random. Unfortunately, there still appear works in which the dynamics of NSPs is erroneously treated in terms of Brownian motion.

Note that synchronization does not determine the formation mechanisms of thermobaric structures due to the baroclinic instability of the atmosphere, but rather imposes evolution rhythms close to tidal force oscillations (more precisely, to rhythms in the Earth–Moon–Sun system) on atmospheric processes.

Decade climate changes

The synchronization of variations in meteorological characteristics with variations in the Earth's angular velocity v and the motion of bodies in the Earth–Moon–Sun system can be observed not only on intramonthly time scales, but also on interannual and decadal scales.

Hot summers and cold winters over European Russia were observed in years close to 2002/2010, 1972, 1936/1938, and 1901 (Sidorenkov & Sumerova, 2012). It is near these years that we could observe changes in the Northern Hemisphere decadal temperature tendencies, atmospheric circulation epochs, the Indian monsoon intensity, the mass of the Antarctic and Greenland ice sheets, and Earth's rotation rate regimes (Fig. 11.5) (Sidorenkov, 2009).

The results presented in Fig. 11.5 suggest that the temperature T grows when the Earth's rotation speeds up and decreases when the Earth's rotation slows down. The curve of v correlates with variations in T (with correlation coefficient $r = 0.67$) and with the accumulated sums of atmospheric circulation C (with $r = -0.70$). Singular spectral analysis (expansion in terms of empirical orthogonal functions of time) applied to series of the Earth's angular velocity and global air temperature and sea level anomalies suggests the presence of periods close to lunar periods of 18.6 and 8.85 years (Zotov, Bizouard et al., 2014).

According to observations, the values of v and T reached their maxima in 2003. In 2004 a new epoch started in the atmospheric circulation, with Earth's rotation rate v slowing down and T reducing.

A more detailed presentation can be found in Sidorenkov's publications (see <http://geoastro.ru>), where variations in meteorological elements are compared with extrema of v over the years 2012–2015.

References

- Blekhman I.I.: 1988, *Synchronization in Science and Technology*, New York, ASME Press.
- Eckart C.: 1960, *Hydrodynamics of Oceans and Atmospheres*, Pergamon Press, New York, 290 p.
- Lindzen R.S., Holton J.R.: 1968, *J. Atmos. Sci.*, **25**, 1095.
- Mandelstam L.I. Complete Collection of Works (USSR Acad. Sci., Moscow, 1947), Vol. 2 (in russian).
- Molchanov A.M. On the resonance structure of the Solar system. In *Modern Problems in Celestial Mechanics and Astrodynamics* (Moscow: Nauka, 1973) (in russian).
- Mul'tanovskii B.P. Basic Principles of Synoptic Method for Long-Term Weather Forecast TsUEGMS, Moscow, 1933 (in russian).
- Sidorenkov N.S.: 2009, The interaction between Earth's rotation and geophysical processes. Weinheim. WILEY-VCH Verlag GmbH & Co. KGaA, 2009, 317 p.
- Sidorenkov N.S., Sumerova K.A.: 2012, *Russian Meteorology and Hydrology*, **37**, № 6, 411.
- Sidorenkov N.S.: 2010, *Geofizicheskie Issledovaniya*, **11**, special issue, 119 (in russian).

EFFECT OF NON-SPHERICITY OF GRAVITATIONAL FIELD OF THE ASTEROID ON THE ITS SATELLITES ORBITS EVOLUTION

V.V. Troianskyi

Astronomical Observatory, I.I. Mechnikov Odessa National University
Shevchenko Park, 65014, Odessa, Ukraine, *v.troianskyi@onu.edu.ua*

ABSTRACT. Lately it has become possible to sufficiently precise definition of the physical and geometric characteristics of asteroid systems using radar observations (<http://echo.jpl.nasa.gov/~lance/binary.neas.html>), which allowed calculating the asymmetry of the massive component of double and multiple asteroids for studying the dynamics of motion of their satellites.

Key words: asteroid, gravitational field asteroid, satellites asteroids, evolution orbits.

1. Gravity field asteroids

If we interpret the gravitational field of the asteroid in the zero approximation as the gravitational field of a sphere with a symmetrical distribution of the density of its gravitational potential will have a very simple form:

$$U = \frac{\mu}{r}, \tag{1}$$

where r – distance from the center of the sphere, μ – gravitational constant.

In the case of the spheroid model, the gravitational potential in a spherical coordinates can be represented as an expansion using Legendre polynomial the 2nd order (Aleksandrov et al., 2004):

$$U = \frac{\mu}{r} \left[1 - \left(\frac{a}{r} \right)^2 J_2 P_2(\cos \theta) \right], \tag{2}$$

where a – equatorial radius,

$$J_2 = \frac{C - A}{Ma^2}, \tag{3}$$

where M – the mass of the asteroid. The value of J_2 , characterizes a deviation of the gravitational field of the asteroid from the gravitational field of the sphere.

$$P_2(\cos \theta) = \frac{3}{2} \cos^2 \theta - \frac{1}{2} \tag{4}$$

– the 2nd order Legendre polynomial, θ – polar angle of the asteroid’s satellite,

$$C = \int (x^2 + y^2) dM = \rho \left(\frac{1}{3} x^3 y z + \frac{1}{3} y^3 x z \right) \tag{5}$$

– the moment of inertia relative to the polar axis of the asteroid,

$$A = \int (y^2 + z^2) dM = \rho \left(\frac{1}{3} y^3 x z + \frac{1}{3} z^3 x y \right) \tag{6}$$

– moment of inertia relative to the equatorial axis of the asteroid, x, y, z – sizes of the asteroid on the axes of inertia.

$$\rho(r, \theta, \varphi) = \text{const} \tag{7}$$

– the density of the asteroid.

Similar model was used to study the dynamics of motion of the triple asteroid system (45) Eugenia (Marchis et al., 2010).

2. Calculating the magnitude of J_2

For calculation of coefficients of the second zonal harmonic, we used the formulas (3) – (6). The following Near-Earth asteroid systems were selected: (1862) Apollo, (66391) 1999KW4, (136617) 1994CC, (175706) 1996FG3, (276049) 2002CE26. For these systems, their physical parameters are known the most precisely (www.johnstonsarchive.net).

Table 1. The coefficients of the second zonal harmonic J_2 for selected asteroid systems.

Asteroids systems	Alpha J_2	Error	Beta J_2	Error	Gamma J_2	Error
(1862)Apollo	-0.03489	+0.00277 -0.00308	-0.00362	+0.00340 -3.70548	-	-
(66391)1999KW4	-0.02795	+0.00096 -0.00126	-0.05840	+0,01473 -0,02112	-	-
(136617)1994CC	-0.01339	+0.00019 -0.00001	-0.00881	+0.00609 -0.03239	-0.00729	+0.00580 -0.00692
(175706)1996FG3	0.05412	+0.00455 -0.01010	-0.00993	+0.00527 -0.01429	-	-
(276049)2002CE26	-0.01880	+0.00258 -0.00397	-0.00552	+0.00421 -0.03640	-	-

Table 1 shows the results of calculation of the coefficients J_2 and their errors for the five selected asteroid systems. In accordance with the generally accepted rules, the components of the asteroid system are identified as follows: Alpha – the main asteroid, and then, in order of the discovering of its satellites Beta, Gamma, etc.

Obtained results are used for modeling of gravitational potential of the main asteroids of asteroid systems. Due to significant error in the determination of J_2 we consider asteroid satellites as material points. Differential equations of the asteroid's satellite motion in the inertial coordinate system can be expressed as:

$$\frac{d^2 \vec{r}}{dt^2} - \text{grad} \bar{U} = 0, \quad (8)$$

where $\vec{r} = (x, y, z)$ – position vector, t – time, U – the gravitational potential due to attraction of the main asteroid.

For the integration of differential equation of motion we used the method of Everhart 15th order (Bazyey et al., 2009).

3. Accuracy of integration

When using the numerical integration of equation of motion, the control of precision of the results of the

integration is a must. Precision of integration of asteroid satellites positions of "Beta" (66391)1999KW4, "Beta" (136617)1994CC, "Gamma" (136617)1994CC do not exceed 1.5×10^{-7} meters. Magnitude of error is obtained by method of the forward and reverse integration of the motion in the 100 years interval.

4. Evolution of the orbit of asteroid satellite

For asteroid systems (66391) 1999KW4 and (136617) 1994CC orbital parameters are known

most precisely (www.johnstonsarchive.net). In Table 2 are given Kepler elements of orbits for satellites in these systems.

As a result of integration of double and multiple asteroid systems, we have obtained changes in orbital elements (solid line) of satellites considering the error (dashed line). In Fig. 1 – Fig. 9 we shows the changes in the elements of the satellites orbits considering disturbances from the compression of the main component of the system. On these figures, we conclude that the age-old changes of semi-major axis, eccentricity and inclination of orbits are hot detected.

Table 2. Kepler elements of orbits of asteroids satellites.

Satellite	a, meter	e	i, degrees	ω , degrees	Ω , degrees	Epoch, JD
"Beta" (66391)1999KW4	2540	0.0004	156.1	319.7	105.4	2456800.5
"Beta" (136617)1994CC	1720	0.002	83.3	130.9	59.2	2454994.5
"Gamma" (136617)1994CC	6100	0.19	71.7	96.2	96.2	2454994.5

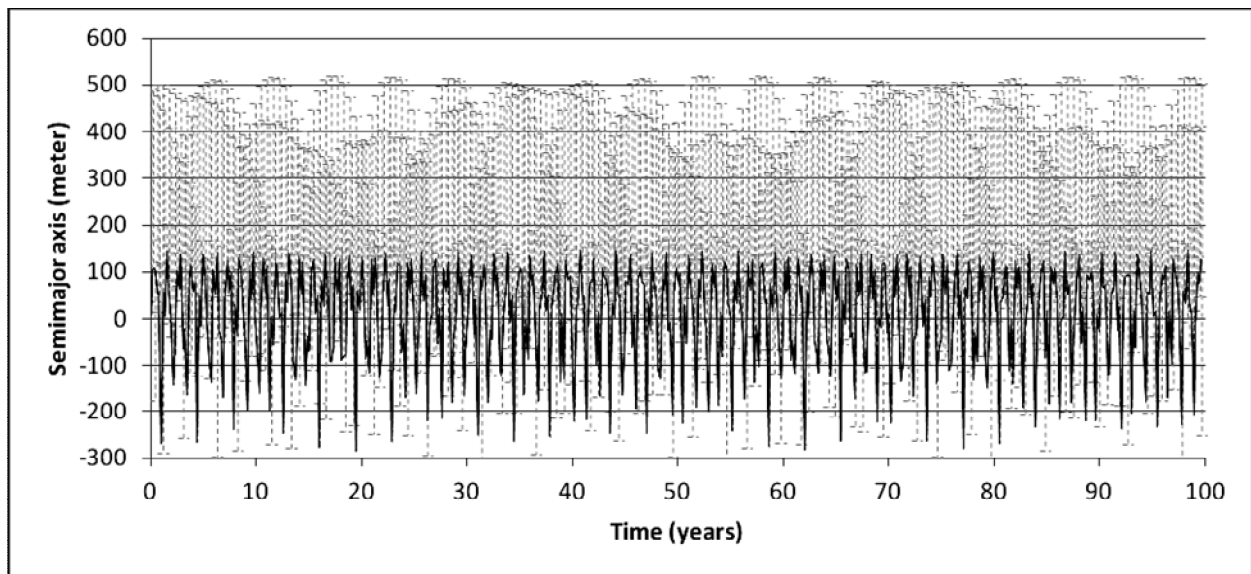


Figure 1: Change of semimajor axis of the orbit of satellite "Beta" of the asteroid system (66391)1999KW4.

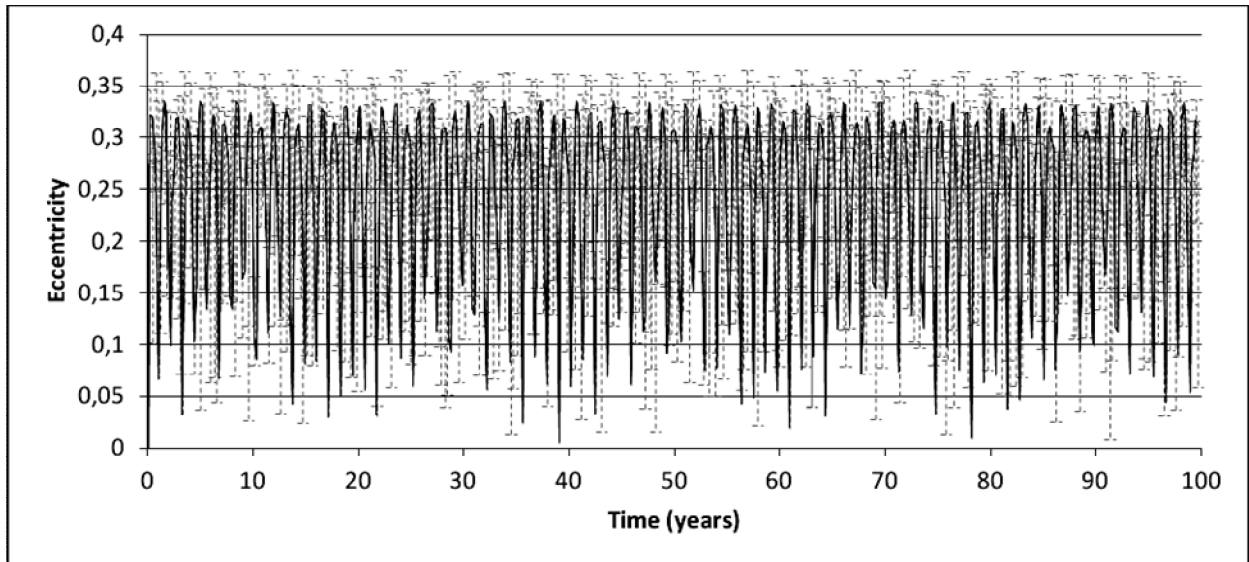


Figure 2: Change of eccentricity of the orbit of satellite "Beta" of the asteroid system (66391)1999KW4.

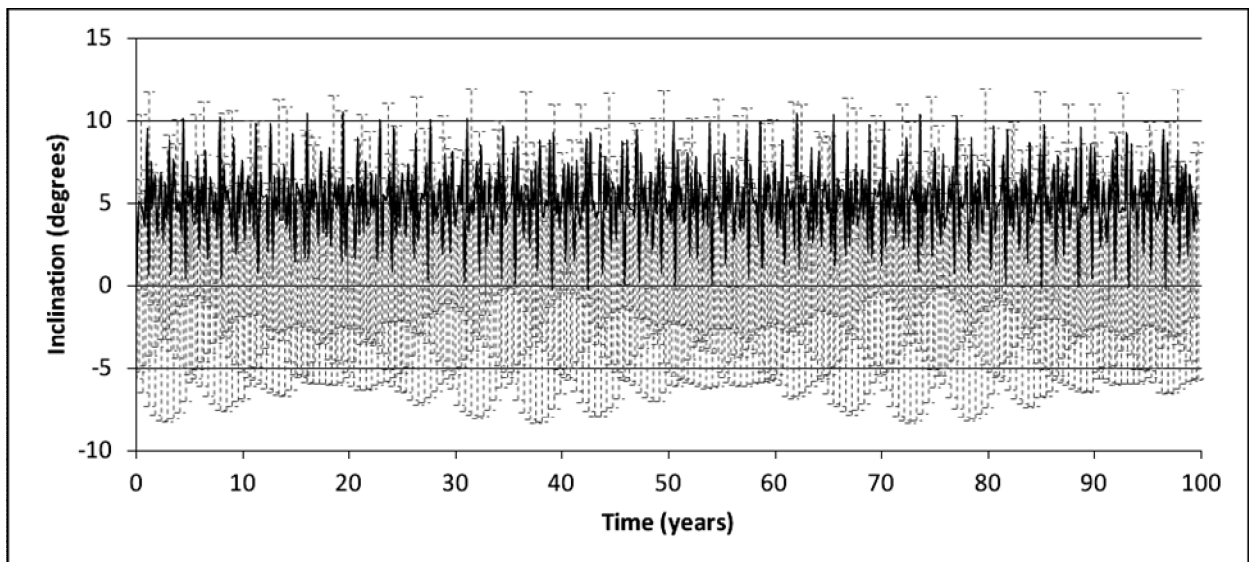


Figure 3: Change of inclination of the orbit of satellite "Beta" of the asteroid system (66391)1999KW4.

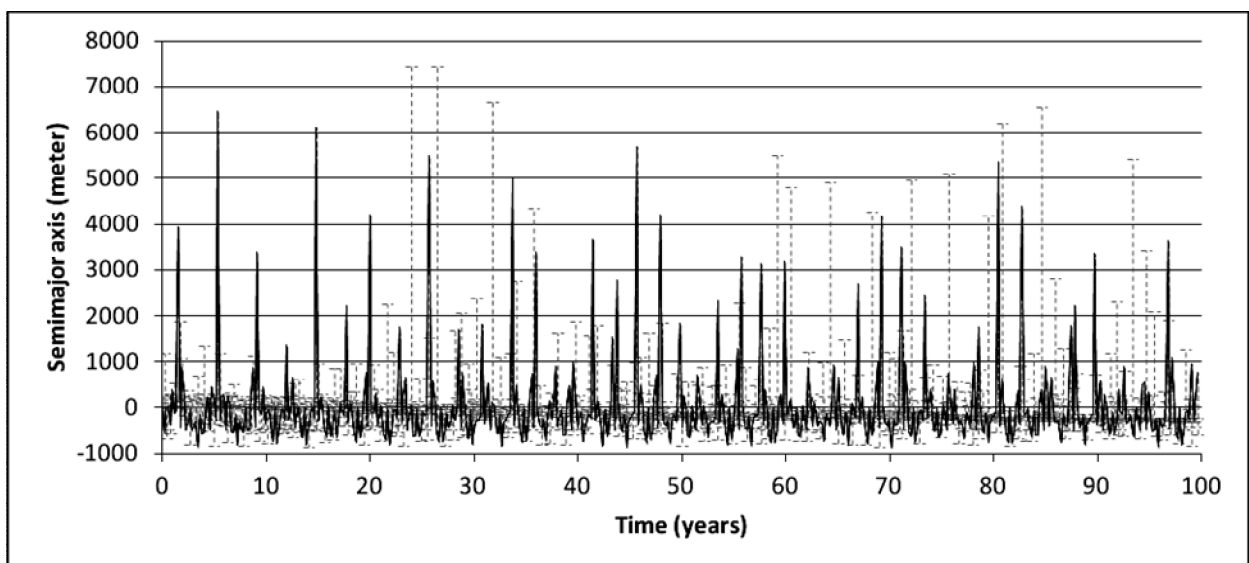


Figure 4: Change of semimajor axis of the orbit of satellite "Beta" of the asteroid system (136617)1994CC.

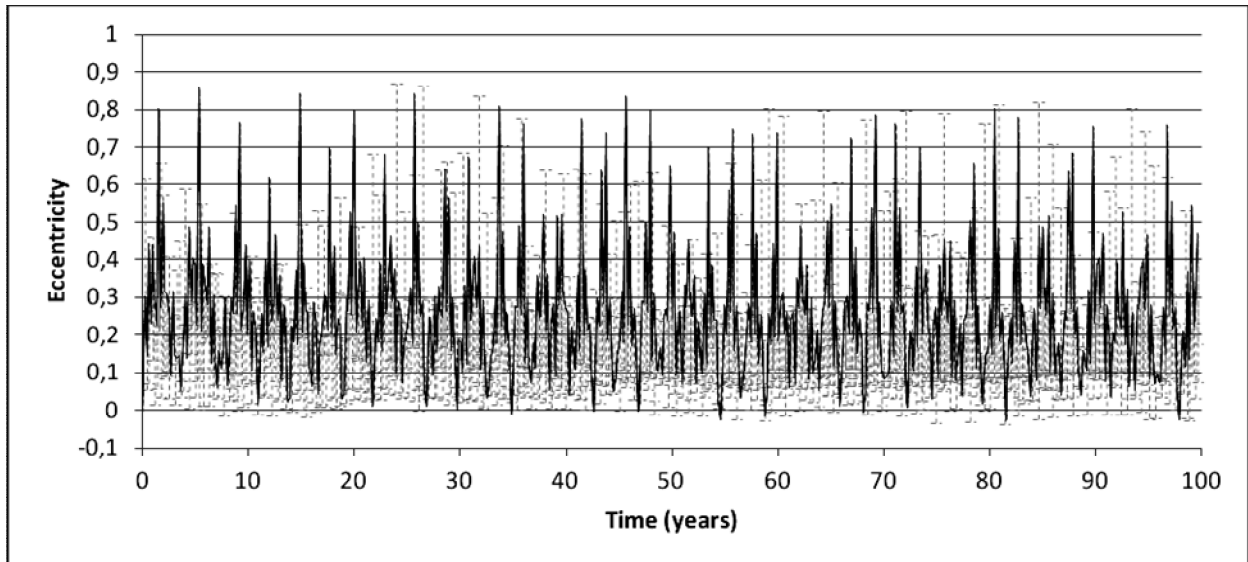


Figure 5: Change of eccentricity of the orbit of satellite "Beta" of the asteroid system (136617)1994CC.

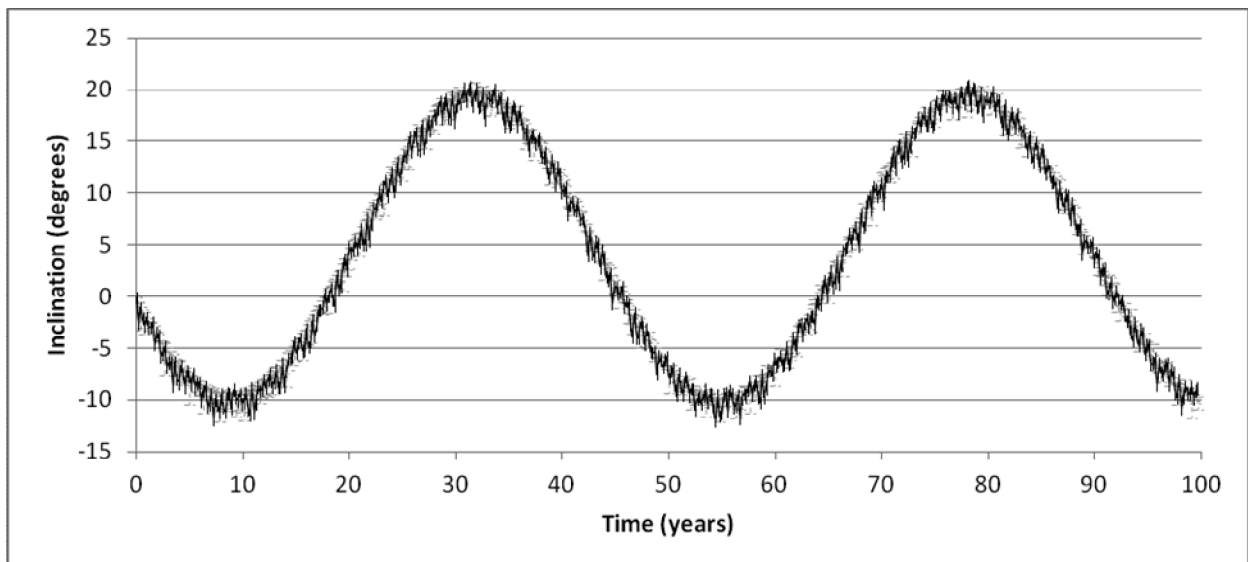


Figure 6: Change of inclination of the orbit of satellite "Beta" of the asteroid system (136617)1994CC.

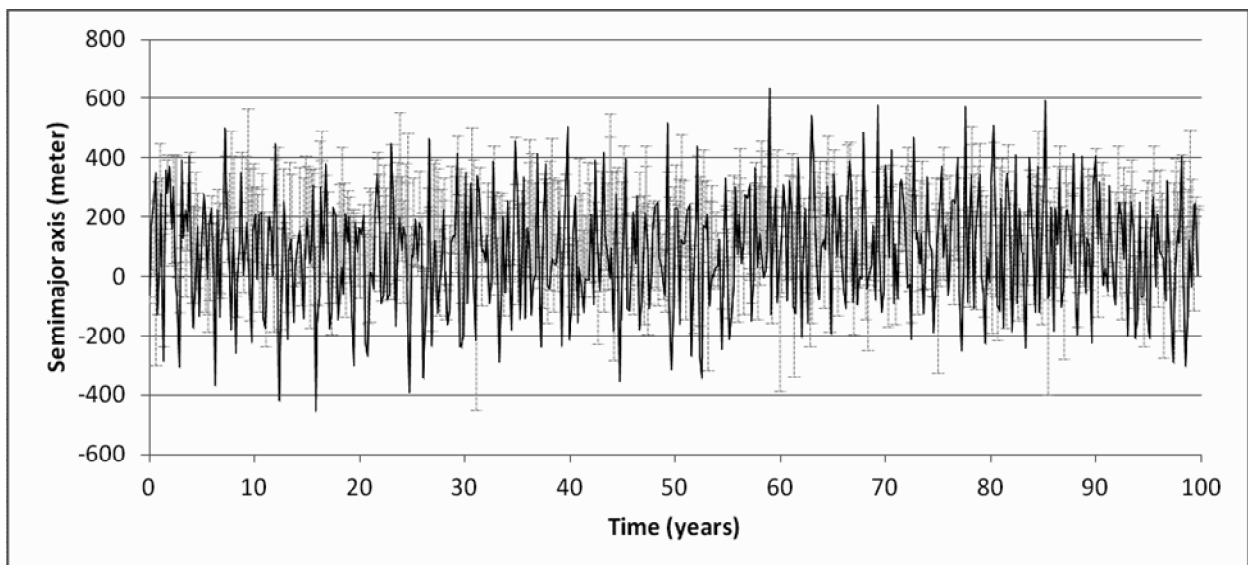


Figure 7: Change of semimajor axis of the orbit of satellite "Gamma" of the asteroid system (136617)1994CC.

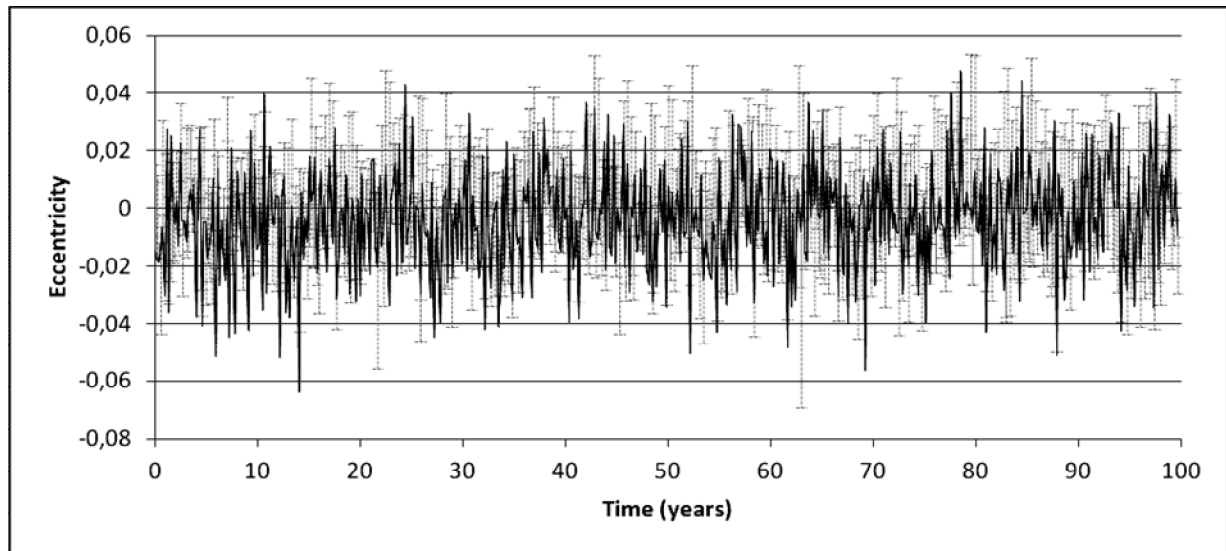


Figure 8: Change of eccentricity of the orbit of satellite "Gamma" of the asteroid system (136617)1994CC.

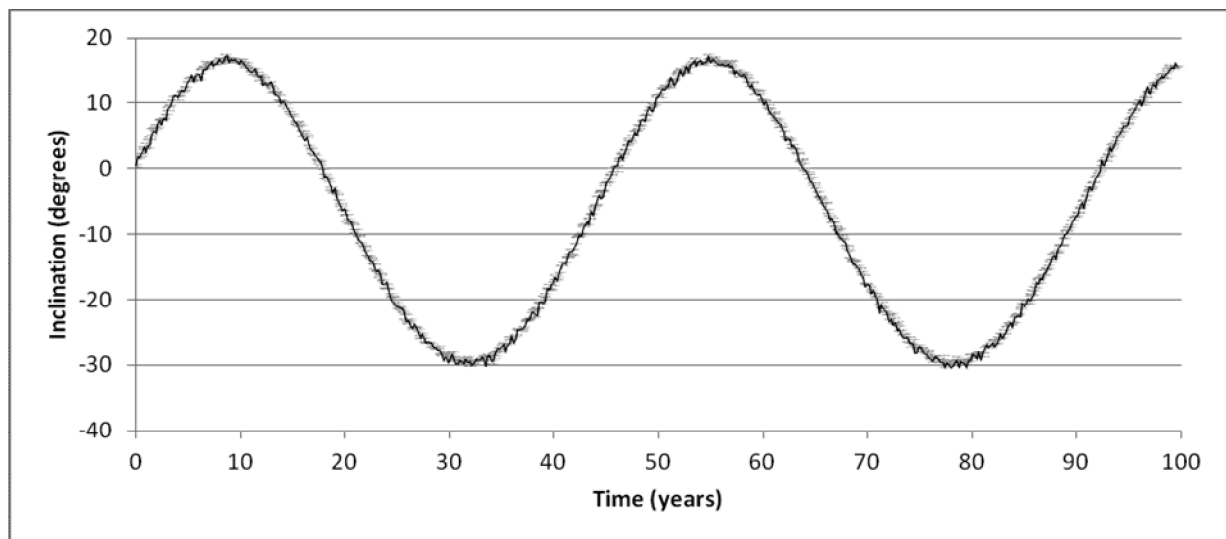


Figure 9: Change of inclination of the orbit of satellite "Gamma" of the asteroid system (136617)1994CC.

5. Conclusion

Using the known physical and geometrical parameters of the components of selected double and multiple asteroid systems we have determined the value of the second zonal. As it is seen from Table 1 error in determining of the second zonal harmonic of asteroids satellites is high due of inaccurate initial data.

We also perform the integration of equations of motion of the satellite "Beta" of the asteroid (66391) 1999KW4 in Cartesian coordinates considering the compression of the main asteroid. The modeling showed that the semimajor axis, eccentricity and inclination of the orbit of the satellite change periodically with amplitudes ≈ 216 meters, ≈ 0.168 and $\approx 5.38^\circ$, respectively.

In the asteroid system (136617) 1994CC satellite "Beta" is located very close to the surface of the central asteroid (about 650 meters), so the impact on him of the asymmetry of the gravitational field is very high. This is illustrated by Fig. 5 – Fig. 6: semimajor axis, eccentricity and inclination of the orbit of the satellite change periodically with amplitudes of ≈ 3235 m, ≈ 0.429 , $\approx 10.2^\circ$, respectively.

In the same asteroid system satellite "Gamma", is much further and therefore the influence on him of the asymmetry of the gravitational field affects not so much, semimajor axis, eccentricity and inclination of the orbit of the satellite change periodically with amplitudes ≈ 318 meters, ≈ 0.024 , $\approx 8.7^\circ$, respectively. For both satellites the period of changes in orbital inclination of 45.7 years is clearly observed.

Numerical modeling of the motion of the components of double and multiple asteroid systems shows the need to consider the asymmetry of the gravitational field of the main asteroid to describe the dynamics of movement and evolution of satellite orbits of asteroids. This task requires further and more detailed investigation.

References

- Aleksandrov V.Yu.: 2004, *Nebesna mehanika* (in Ukrainian).
 Bazyey A.A., Kara I.V.: 2009, *Visnyk Astronomichnoyi shkoly*, **6/2**, 155 (in Ukrainian).
 Marchis F., Lainey V., Descamps P. et al.: 2010, *Icarus*, **210**, 635.